frontiers | Research Topics

Community series in novel biomarkers in tumor immunity and immunotherapy, volume II

Edited by
Eyad Elkord and Takaji Matsutani

Published in
Frontiers in Immunology
Frontiers in Oncology

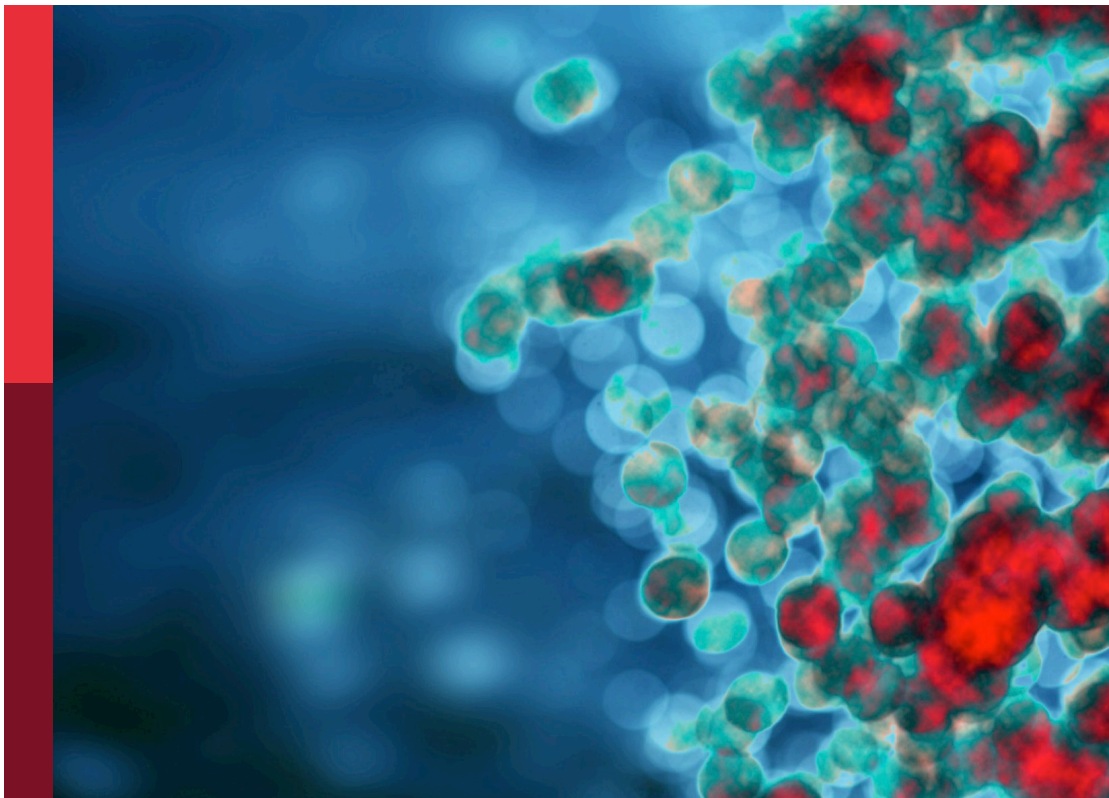

ISSN 1664-8714
ISBN 978-2-8325-6327-4
DOI 10.3389/978-2-8325-6327-4

About Frontiers

Frontiers is more than just an open access publisher of scholarly articles: it is a pioneering approach to the world of academia, radically improving the way scholarly research is managed. The grand vision of Frontiers is a world where all people have an equal opportunity to seek, share and generate knowledge. Frontiers provides immediate and permanent online open access to all its publications, but this alone is not enough to realize our grand goals.

Frontiers journal series

The Frontiers journal series is a multi-tier and interdisciplinary set of open-access, online journals, promising a paradigm shift from the current review, selection and dissemination processes in academic publishing. All Frontiers journals are driven by researchers for researchers; therefore, they constitute a service to the scholarly community. At the same time, the *Frontiers journal series* operates on a revolutionary invention, the tiered publishing system, initially addressing specific communities of scholars, and gradually climbing up to broader public understanding, thus serving the interests of the lay society, too.

Dedication to quality

Each Frontiers article is a landmark of the highest quality, thanks to genuinely collaborative interactions between authors and review editors, who include some of the world's best academicians. Research must be certified by peers before entering a stream of knowledge that may eventually reach the public - and shape society; therefore, Frontiers only applies the most rigorous and unbiased reviews. Frontiers revolutionizes research publishing by freely delivering the most outstanding research, evaluated with no bias from both the academic and social point of view. By applying the most advanced information technologies, Frontiers is catapulting scholarly publishing into a new generation.

What are Frontiers Research Topics?

Frontiers Research Topics are very popular trademarks of the *Frontiers journals series*: they are collections of at least ten articles, all centered on a particular subject. With their unique mix of varied contributions from Original Research to Review Articles, Frontiers Research Topics unify the most influential researchers, the latest key findings and historical advances in a hot research area.

Find out more on how to host your own Frontiers Research Topic or contribute to one as an author by contacting the Frontiers editorial office: frontiersin.org/about/contact

Community series in novel biomarkers in tumor immunity and immunotherapy, volume II

Topic editors
Eyad Elkord — Xi'an Jiaotong-Liverpool University, China
Takaji Matsutani — Maruho, Japan

Citation
Elkord, E., Matsutani, T., eds. (2025). *Community series in novel biomarkers in tumor immunity and immunotherapy, volume II*. Lausanne: Frontiers Media SA.
doi: 10.3389/978-2-8325-6327-4

Topic Editor Dr. Takaji Matsutani is employed by Maruho Co., Ltd. The other Topic Editors declare no competing interests with regard to the Research Topic subject.

Table of contents

frontiers | Frontiers in Immunology

TYPE Editorial
PUBLISHED 25 April 2025
DOI 10.3389/fimmu.2025.1608903

OPEN ACCESS

EDITED AND REVIEWED BY
Peter Brossart,
University of Bonn, Germany

*CORRESPONDENCE
Eyad Elkord
Eyad.Elkord@xjtlu.edu.cn
Takaji Matsutani
matsutani_fhu@mii.maruho.co.jp

RECEIVED 09 April 2025
ACCEPTED 10 April 2025
PUBLISHED 25 April 2025

CITATION
Elkord E and Matsutani T (2025) Editorial: Community series in novel biomarkers in tumor immunity and immunotherapy, volume II.
Front. Immunol. 16:1608903.
doi: 10.3389/fimmu.2025.1608903

Editorial: Community series in novel biomarkers in tumor immunity and immunotherapy, volume II

Eyad Elkord [1,2,3]* and Takaji Matsutani [4,5]*

[1]Department of Biosciences and Bioinformatics & Suzhou Municipal Key Lab of Biomedical Sciences and Translational Immunology, School of Science, Xi'an Jiaotong-Liverpool University, Suzhou, China, [2]College of Health Sciences, Abu Dhabi University, Abu Dhabi, United Arab Emirates, [3]Biomedical Research Center, School of Science, Engineering and Environment, University of Salford, Manchester, United Kingdom, [4]Translational Research Department, Drug Development Laboratories, Kyoto R&D Center, Maruho Co., Ltd., Kyoto, Japan, [5]Division of Medical Oncology/Hematology, Department of Medicine, Kobe University Graduate School of Medicine, Kobe, Japan

KEYWORDS

biomarker, ICI, bioinformatics, tumor immunology, cancer

Editorial on the Research Topic
Community series in novel biomarkers in tumor immunity and immunotherapy, volume II

Cancer immunotherapy has recently revolutionized cancer treatment. However, response rates are still modest and further improvements are urgently needed. The identification of predictive biomarkers is critical for guiding treatment and predicting outcomes. This editorial highlights contributions from recent research, showcasing a range of innovative studies that explore biomarkers in tumor immunity and their implications for cancer immunotherapy.

This Research Topic comprises twelve original articles and one systematic review. The first article by Liu et al. identified a novel immune-based subtype of poor prognosis in breast cancer, which offers implications for immunotherapy targeting tertiary lymphoid structures. The study showed the critical roles of IL-6 and IL-6R, in addition to CD46 and JAG1, in the survival and invasive capacity of cancer cells, highlighting their potential as targets in antitumor therapies.

With the emergence of COVID-19 pandemic, the relationship between viral infections and cancer outcomes has attracted investigational interests. The second study by Wang et al. developed a SARS-CoV-2-related gene signature, which can be implemented to predict prognosis and mirror the immune landscape in the tumor microenvironment in patients with lung adenocarcinoma.

Single-cell RNA sequencing has transformed our understanding of the tumor microenvironment and tumor immunity. Using single-cell RNA-seq data from the GEO database, Fan et al. uncovered the role of T cell exhaustion in osteosarcoma. Three T-cell exhaustion-related genes (RAD23A, SAC3D1, PSIP1) were identified and used to formulate a T-cell exhaustion model. This data should be useful in designing interventional studies to reinvigorate the exhausted immune responses in osteosarcoma.

Predictive models for cancer therapies are an important area of research focus. The study by Shi et al. reported that PD-L1, tumor mutational burden (TMB) and neutrophils were prognostic biomarkers for a short-term efficacy of anti-PD-1 therapy combined with chemotherapy in patients with non-small cell lung cancer.

Immune-related adverse events (irAEs) associated with cancer immunotherapies are a concern. Xing et al. identified potential biomarkers for prediction of thyroid irAEs in patients with advanced gastrointestinal cancer. The study reported that elevated levels of adenosine deaminase (ADA) were associated with the occurrence of thyroid irAEs in these patients receiving anti-PD-1 therapy.

The immune system plays critical roles in the development and treatment of different cancers. Fang et al. have further dissected the role of the immune system in thyroid cancer. The study explored the genetic means for the involvement of immune cells in tumorigenesis, which may offer insights for future clinical research in thyroid cancer.

Inflammation plays key roles in the development and prognosis of cancers. A meta-analysis study by Wang et al. identified the prognostic value of systemic immune-inflammation index (SII) in osteosarcoma. The study reported that higher SII was significantly associated with poor overall survival and advanced stage.

The identification of telomere-related long non-coding RNAs (lncRNAs) is an area of interest in cancer. The study by Xu et al. established a prognostic model for the telomere-related lncRNAs (TRLs). A six-TRLs prognostic model has been identified in ovarian cancer, which offers an avenue for targeted therapies.

Artificial intelligence in the diagnosis and prognosis of cancer is gaining great interest. Using whole slide image-based weakly supervised deep learning, Han et al. developed models to predict major pathological response to neoadjuvant chemoimmunotherapy in non-small cell lung cancer patients.

Pain is a serious issue associated with cancer. The study by Zhang et al. investigating the correlation and potential mechanisms between pain and the efficacy of cancer immunotherapy. Interestingly, baseline pain was found to be an independent prognostic factor affecting the efficacy of immune checkpoint inhibitors in non-small cell lung cancer patients, potentially through promotion of CXCL12-mediated inflammation and immunosuppression.

In search for biomarkers for therapeutic response to immune checkpoint inhibitors, a nationwide multi-centric prospective study aimed to identify pretreatment plasma exosome mRNAs as predictive biomarkers for nivolumab, a PD-1 inhibitor in head and neck cancer patients. Sato et al. reported that the plasma exosome mRNAs signature may better predict which patients respond to nivolumab, ensuring a more personalized approach to immune checkpoint inhibitors.

In another study aiming to predict which anaplastic thyroid carcinoma patients may benefit from immunotherapy, the study by Pengping et al. revealed that HLF gene hinders cancer progression by down-regulating the epithelial-to-mesenchymal transition pathway, reducing T cell exhaustion, and increasing sensitivity to sorafenib kinase inhibitor.

Finally, Wellhausen et al. showed how pembrolizumab, a PD-1 inhibitor, can enhance the efficacy of neoadjuvant chemotherapy in *in vitro* studies. This study reported that suppression of MCP-1, IFN-γ and IL-6 production by pembrolizumab in head and neck squamous cell carcinoma was linked to improved survival. This work highlights the synergistic effects of immune checkpoint inhibitors and chemotherapy, which are mediated by the inhibition of inflammatory cytokines.

Author contributions

EE: Writing – review & editing, Writing – original draft. TM: Writing – review & editing.

Acknowledgments

We would like to thank all the authors who participated in the Research Topic of "Community Series in Novel Biomarkers in Tumor Immunity and Immunotherapy: Volume II". We are also very grateful for each of the reviewers for their careful peer review and valuable assistance, and the editorial office of the Frontier Journal.

Conflict of interest

Author TM is employed by the company Maruho Co., Ltd.

The remaining author declares that the research was conducted in the absence of any commercial or financial relationships that could be construed as a potential conflict of interest.

The author(s) declared that they were an editorial board member of Frontiers, at the time of submission. This had no impact on the peer review process and the final decision.

Generative AI statement

The author(s) declare that no Generative AI was used in the creation of this manuscript.

Publisher's note

frontiers | Frontiers in Immunology

TYPE Original Research
PUBLISHED 20 March 2024
DOI 10.3389/fimmu.2024.1364506

OPEN ACCESS

EDITED BY
Takaji Matsutani,
Maruho, Japan

REVIEWED BY
Weiqi Dai,
Shanghai Shidong Hospital of Yangpu District, China
Nicole Salazar,
North Carolina Central University, United States

*CORRESPONDENCE
Xiaozhou Chen
ch_xiaozhou@163.com
Huamei Li
li_hua_mei@163.com

†These authors have contributed equally to this work and share first authorship

RECEIVED 02 January 2024
ACCEPTED 07 March 2024
PUBLISHED 20 March 2024

CITATION
Liu R, Huang X, Yang S, Du W, Chen X and Li H (2024) Discovery of an independent poor-prognosis subtype associated with tertiary lymphoid structures in breast cancer. *Front. Immunol.* 15:1364506. doi: 10.3389/fimmu.2024.1364506

Discovery of an independent poor-prognosis subtype associated with tertiary lymphoid structures in breast cancer

Ruiqi Liu[1†], Xiaoqian Huang[1†], Shiwei Yang[1], Wenbo Du[2], Xiaozhou Chen[1*] and Huamei Li[2*]

[1]School of Mathematics and Computer Science, Yunnan Minzu University, Kunming, China, [2]Department of Rheumatology and Immunology, Nanjing Drum Tower Hospital, the Affiliated Hospital of Nanjing University Medical School, Nanjing, China

Introduction: Tertiary lymphoid structures (TLSs) are ectopic lymphoid formations that arise in non-lymphoid tissues due to chronic inflammation. The pivotal function of TLSs in regulating tumor invasion and metastasis has been established across several cancers, such as lung cancer, liver cancer, and melanoma, with a positive correlation between increased TLS presence and improved prognosis. Nevertheless, the current research about the clinical significance of TLSs in breast cancer remains limited.

Methods: In our investigation, we discovered TLS-critical genes that may impact the prognosis of breast cancer patients, and categorized breast cancer into three distinct subtypes based on critical gene expression profiles, each exhibiting substantial differences in prognosis ($p = 0.0046$, log-rank test), with Cluster 1 having the best prognosis, followed by Cluster 2, and Cluster 3 having the worst prognosis. We explored the impact of the heterogeneity of these subtypes on patient prognosis, the differences in the molecular mechanism, and their responses to drug therapy and immunotherapy. In addition, we designed a machine learning-based classification model, unveiling highly consistent prognostic distinctions in several externally independent cohorts.

Results: A notable marker gene CXCL13 was identified in Cluster 3, potentially pivotal in enhancing patient prognosis. At the single-cell resolution, we delved into the adverse prognosis of Cluster 3, observing an enhanced interaction between fibroblasts, myeloid cells, and basal cells, influencing patient prognosis. Furthermore, we identified several significantly upregulated genes (CD46, JAG1, IL6, and IL6R) that may positively correlate with cancer cells' survival and invasive capabilities in this subtype.

Discussion: Our study is a robust foundation for precision medicine and personalized therapy, presenting a novel perspective for the contemporary classification of breast cancer.

KEYWORDS

tertiary lymphoid structures, tumor microenvironment, breast cancer, subtypes, prognosis

1 Introduction

As a widely utilized high-throughput sequencing method, RNA sequencing technology empowers scientists to analyze gene expression at the whole transcriptome level comprehensively. In recent years, the rapid advancements in next-generation sequencing technologies have yielded extensive biomedical data on cancer, including information on cancer genomes, transcriptomes, proteomes, and the tumor immune microenvironment. Leveraging cutting-edge analytical techniques in machine learning and deep learning, it has become possible to delve deeply into data and unearth insights into the pathogenesis, intrinsic heterogeneity, effective therapeutic targets, and other potential aspects of specific cancers within large-scale research cohorts (1–3). This process aids in achieving early and precise cancer diagnoses, selecting personalized medical treatment strategies, and accurately predicting therapeutic responses and prognostic risks.

According to the latest cancer statistics in the United States published in CA Cancer J Clin, breast cancer (BC) is the first malignant tumor with the highest incidence rate in women currently, and by 2023, it will have the highest number of new cases of all cancer types. Among all female cancer patients, the incidence rate of breast cancer is as high as 31%, and the mortality rate has been ranked second, which seriously jeopardizes women's lives and health (4, 5). Based on gene expression profile characteristics, breast cancer can be classified into five intrinsic molecular subtypes, which are known as PAM50 typing. However, gene sequencing is difficult to promote in the clinic due to its high cost, time-consuming, and other drawbacks. The widely used typing method is based on immunohistochemistry (IHC), which detects the expression of Estrogen Receptor (ER), Progesterone Receptor (PR), HER2, and Ki-67. IHC typing has a large margin of error and low robustness and requires a biopsy of the patient, for which some patients are not suitable (6, 7).

In recent years, some prognostic gene signatures associated with breast cancer have been identified in several studies and applied to clinical practice (8, 9). There is a long-standing hypothesis that secondary lymphoid organs (SLOs) are the main sites of anti-tumor immune responses (10). However, due to the distance between SLOs and tumor tissues, immune cells can only migrate inside the tumors to function. Nevertheless, recent findings have identified certain anti-tumor immune response sites within tumor tissues, known as tertiary lymphoid structures (11). TLSs are ectopic lymphoid structures formed at sites of chronic inflammation in non-lymphoid tissues (12), composed of a variety of cells such as T cells, B cells, follicular dendritic cells (FDCs), and other cells with high endothelial venules (HEV). It has been shown that TLSs play a crucial role in controlling tumor invasion. For example, the correlation between high density of TLSs and more prolonged overall survival (OS) and disease-free survival (DFS) has been demonstrated in a large number of solid tumors such as lung, colorectal, liver, breast, pancreatic, and melanoma (13–20). Not only that, TLSs in tumor tissues also play a crucial role in anti-tumor immune response and are related to the prognosis of immunotherapy closely (21–23).

Given the close relationship between TLSs and cancer prognosis, we looked at the expression levels of TLS-related genes in breast cancer. We assessed their integrated correlation with tumor microenvironment (TME) heterogeneity and clinical prognosis. Specifically, we used TLS-related gene expression profiles to typify breast cancer. Further, we explored the intrinsic heterogeneity characteristics of TLS-derived breast cancer subtypes, such as analyzing the prognosis of different subtypes, enriched genes and pathways, differences in molecular mechanisms, searching for subtype-specific biomarkers, etc., which, from the perspective of TLSs, provides an insightful understanding of the pathogenesis and progression of breast cancer, and also provides the support and foundation for precision medicine and personalized treatment.

2 Materials and methods

2.1 Molecular data and clinical information on breast cancer

In this study, transcriptome expression data and clinical information were acquired for a total of 1215 breast cancer samples from The Cancer Genome Atlas Project (TCGA). Copy number variant data, calculated using the Illumina platform based on the GISTIC2 method, were downloaded from the UCSC Xena database (https://xenabrowser.net/datapages/). The METABRIC

dataset, encompassing transcriptome expression data and clinical information for 1904 breast cancer patients, was downloaded from cbio-portal (https://www.cbioportal.org) (24). Additionally, external independent breast cancer datasets GSE19615 (n = 115) and GSE20685 (n = 327) (25, 26), the 10X single-cell RNA sequencing dataset GSE195665 (n = 167) (27), along with the cohort of triple-negative breast cancer patients receiving anti-angiogenic immunotherapy GSE103668 (n = 21) (28), were downloaded from Gene Expression Omnibus (GEO).

2.2 Consensus clustering for investigating potential breast cancer subtypes

We implemented unsupervised consensus clustering with the parameter "clusterAlg = pam, distance = euclidean, pItem = 0.8" using the "ConsensusClusterPlus" R software package (version 1.64.0) (29). This approach enabled the adjustment of the cluster number from 2 to 6, facilitating the identification of the most stable consensus matrix and the most distinct cluster assignment during the iterative clustering process.

2.3 Computational index for breast cancer-related events and immune microenvironment

We used the "method = ssgsea" function from the "GSVA" software package (version 1.48.0) to ascertain the activity scores of TLS-related genes in patients (30). To evaluate any significant variations in overall survival (OS) among subtypes, we conducted Kaplan-Meier (KM) survival analysis and applied the log-rank test using the "survival" software package (version 3.5.5) (31). To identify differentially expressed genes (DEGs) within the TLS-derived subtypes, we employed the FindAllMarkers function integrated within the "Seurat" software package (version 4.3.0) (32). Genes exhibiting adjusted $p < 0.05$ and a log2FC > 1 were classified as significantly differentially expressed. For an in-depth exploration of the distinct biological processes and pathways manifesting significant differential expression among the subtypes, we harnessed the bitr function of the "clusterProfiler" software package (version 4.0.5) to convert gene symbols to Entrez IDs (33). Subsequently, we conducted an enrichment analysis using the enrichGO function with the "ont = BP" parameter, as well as the enrichKEGG function, to elucidate and analyze the enriched Gene Ontology (GO) and Kyoto Encyclopedia of Genes and Genomes (KEGG) pathways. GO and KEGG terms demonstrating adjusted $p < 0.05$ were deemed significantly enriched. We leveraged the "ESTIMATE" software package (version 1.0.13) to estimate stromal scores, immune scores, and tumor purity in patients (34), the immune infiltration tool "CIBERSORT" was used for assessing the relative abundance of 22 immune cell types in patients (35). Furthermore, we used the "genefu" software package (version 2.32.0) to predict the PAM50 type of patients in the single-cell dataset (GSE195665) (36).

2.4 Building machine learning models to predict Cluster 1&2 and Cluster 3 subtypes of breast cancer patients

Considering that Cluster 3 identified in the TCGA breast cancer cohort has the worst prognosis, we introduced the XGBoost model to differentiate between Cluster 1&2 and Cluster 3 categories of individual breast cancer patients. The TCGA breast cancer cohort was randomly divided into training and testing sets according to 7:3, and the TLS-critical genes obtained from Lasso regression were used as features in the training set. The XGBoost model was applied to the training set using the "xgboost" function in the "XGBoost" R package (version 1.7.5.1), with parameters set to "nfold = 10, objective = binary: logistic, max. depth = 8, eval_metric = logloss", the model with the highest AUC value was kept. The model performance was tested using the testing set and other external independent datasets (METABRIC dataset, GSE195665, GSE20685, GSE195665, and GSE103668).

2.5 Performing cell communication analysis using CellChat

In the single-cell dataset, we used the CellChat package (version 1.6.1) to analyze intercellular communication in Cluster 1&2 and Cluster 3 (37). CellChat is a specialized tool for analyzing intercellular communication by integrating known intercellular communication databases and single-cell RNA sequencing data, assisting in revealing potential interactions between cell populations and contributing to the understanding of the dynamic characteristics of intercellular communication in biological processes.

2.6 Statistical analysis

All statistical analyses were performed in R4.3.0. Standard statistical tests such as Student's t-test, Wilcoxon rank sum test, log-rank test, and Cox proportional risk regression were used to analyze the expression and clinical data, and $p < 0.05$ was considered statistically significant.

3 Results

3.1 Heterogeneity of TLSs in breast cancer and potential prognostic value

TLSs are an integral part of anti-tumor immunity, and its density is closely related to patient survival, prognosis, and recurrence. Based on the existing studies on TLSs, we included 79 TLS-related genes by reviewing the literature (11, 18, 19, 21, 38–42) to analyze 1,215 breast cancer samples from TCGA (Supplementary Table S1). These genes are mainly chemokine- and immune cell-associated genes which are closely related to the formation of tertiary lymphoid structures. In the TCGA breast cancer cohort,

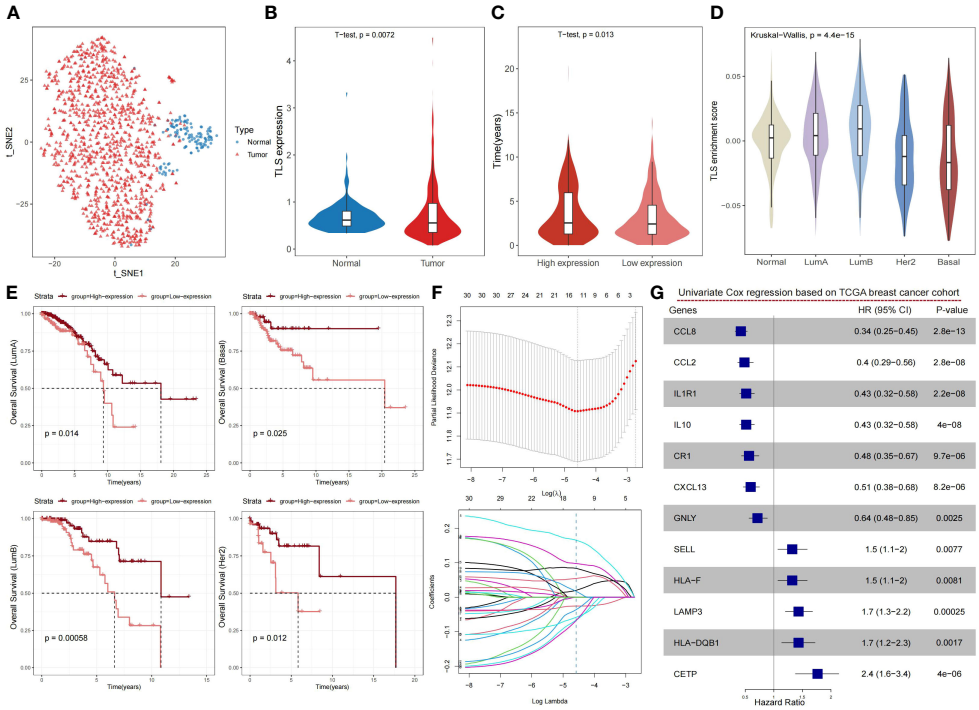

FIGURE 1
Expression levels of TLS-related genes reveal the heterogeneity of the tumor microenvironment and its impact on prognosis in breast cancer. **(A)** The t-SNE plot showing a projection of breast cancer samples based on TLS-related genes, with each point representing a sample; tumor samples are shown in red and normal samples in blue. **(B)** Violin plot showing the differences in the expression levels of TLS-related genes in normal and cancer samples of the breast cancer cohort. P-value was obtained by t-test. **(C)** Violin plot showing the distribution of overall survival time between high- and low-expression groups of TLS-related genes in the breast cancer cohort. The high- and low-expression groups were divided by the median, and the P value was obtained by t-test. **(D)** Violin plot showing the distribution of enrichment scores of TLS-related genes in PAM50 typing, with P-values obtained by Wilcoxon rank sum test. **(E)** Kaplan-Meier survival curves between the high- and low-expression groups of TLS-related genes in PAM50 typing. P-values were calculated by log-rank test. **(F)** The LASSO algorithm was used to process the TLS-related genes, and 12 critical genes were screened for subsequent analysis. **(G)** Forest plot showing the prognostic impact of the 12 TLS-critical genes on the TCGA breast cancer cohort as determined by univariate Cox regression analysis.

we observed a noteworthy disparity in the distribution of TLSs between tumor and normal samples (Figure 1A), and there were notable distinctions in the expression levels of TLS-related genes between tumor and normal samples (Figure 1B). The high-expression group had a longer overall survival time than the low-expression group (Figure 1C). To validate the strong relationship between TLSs and the prognosis of breast cancer patients, we compared the relationship between the TLS-related gene activity score and PAM50, the classical staging of breast cancer. The results showed that the Her2 and Basal subtypes, which had a poorer prognosis, had lower TLSs (Figure 1D). Although PAM50 typing can be used to predict the prognosis of patients, such as LumA has a better prognosis, whereas Her2 and Basal have a worse prognosis, we were still able to differentiate between better and worse prognostic groups from each of the PAM50 subtypes, based on the level of TLS-related gene expression. Similarly, the prognosis of the high-expression group was significantly better than the low-expression group, demonstrating the good prognostic predictive ability of TLS-related genes (Figure 1E).

To obtain more effective and reliable gene signatures for predicting the prognosis, we screened the above 79 TLS-related genes using LASSO regression and obtained 12 TLS-critical genes (Figure 1F). The univariate Cox regression analysis showed that all critical genes significantly correlated with prognosis. CCL8, CCL2, IL1R1, IL10, CR1, CETP, and GNLY were potential protective factors, whereas SELL, HLA-F, LAMP3, HLA-DQB1, CXCL13 were potential risk factors (Figure 1G). In summary, TLSs show significant heterogeneity in breast cancer and can impact the prognosis of patients.

3.2 Determination of breast cancer subtypes based on TLS-critical genes

To investigate the prognostic value of TLSs in breast cancer more precisely, we performed a consensus clustering analysis on TLS-critical gene expression profiles in the TCGA breast cancer cohort. We categorized breast cancer patients into three subtypes: Cluster 1, Cluster 2, and Cluster 3 (Figure 2A; Supplementary Table S2; see Materials and Methods). The results showed that TLS-derived breast cancer subtypes reflected significant variability in prognosis, with Cluster 1 having the best prognosis, followed by Cluster 2, and Cluster 3 having the worst prognosis (Figure 2B). By comparing the expression levels of TLS-critical genes in the three subtypes, it can be found that TLS-critical genes were expressed at the highest level in Cluster 1, followed by Cluster 2,

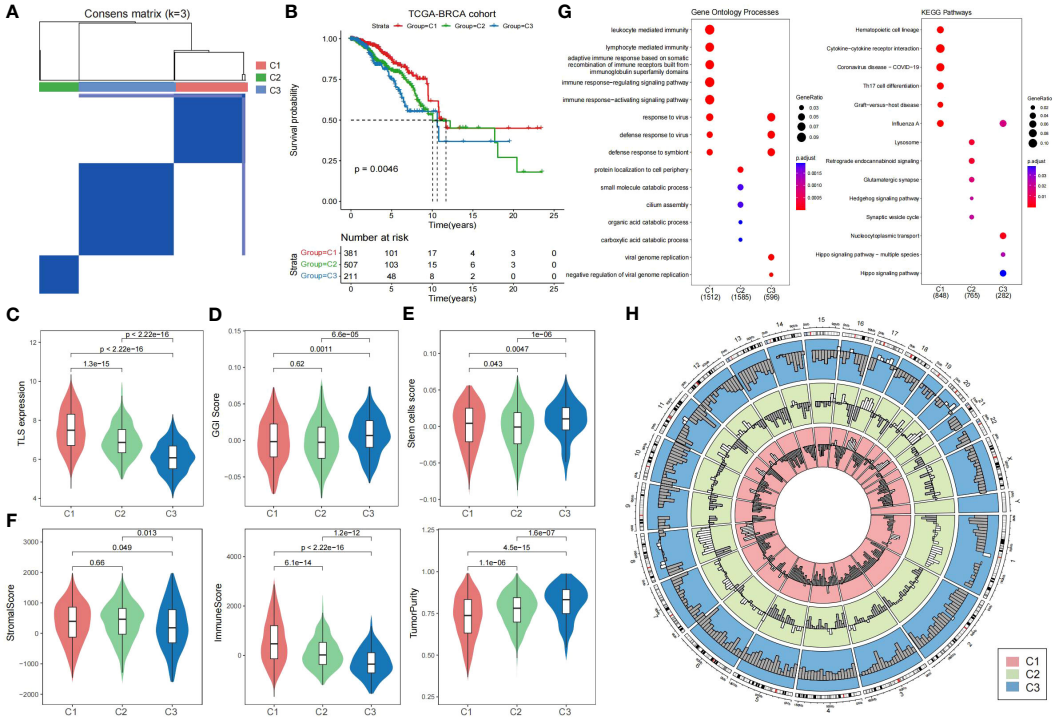

FIGURE 2
Heterogeneity of TLS-derived breast cancer subtypes. **(A)** Heatmap showing the consensus clustering matrix of the TCGA breast cancer cohort based on the TLS-critical gene expression matrix. **(B)** KM curves showing significant differences in prognosis among the three TLS-derived subtypes. P-value was obtained by log-rank test. **(C)** Violin plot showing differences in the expression of TLS-critical genes among TLS-derived subtypes. P-values were obtained by t-test. **(D)** Violin plot showing the GGI of the TLS-derived subtypes, with P-value derived by t-test. **(E)** Violin plot showing the stem cell signature gene activity scores of the TLS-derived subtypes. The P-value was derived by t-test. **(F)** Violin plot showing the distribution of different biological characteristics in the TLS-derived subtypes, including immune score, stromal score, and tumor purity, with P-values derived by t-test. **(G)** Bubble plot showing enriched gene ontology terms and KEGG pathways. **(H)** Circle plot showing the copy number variation of the TLS-derived subtypes, with white indicating copy number increase and gray indicating copy number deletion.

and at the lowest level in Cluster 3 (Figure 2C), which is in line with the results of the previous analyses: higher TLSs reflects better prognosis. To further validate the characteristics of the three subtypes, we introduced the genomic grade index (GGI), which is a gene expression signature designed to enhance the histologic grade assessment (43). It was found that Cluster 3 had the highest GGI (Figure 2D), implying that Cluster 3 had a worse prognosis and reduced responsiveness to immunotherapy treatment. We also calculated the stem cell characteristic gene activity scores of the three subtypes. Stem cell characteristic gene activity score is strongly associated with tumor aggressiveness, risk of recurrence and patient prognosis. Cluster 3 had the highest score (Figure 2E), and the resulting subtype heterogeneity may provide the basis for selecting treatment-resistant clones, leading to poor clinical outcomes. Not only that, we further analyzed the stromal score, tumor purity and immune score of these three subtypes to explore the tumor microenvironment characteristics of the three subtypes. We found that Cluster 3 had the lowest immune scores, the stromal scores, and the highest tumor purity (Figure 2F), implying that among the TLS-derived subtypes, Cluster 3 had the lowest immune cell infiltration and activity, the highest tumor cell density, and tumor invasiveness.

To elucidate the biological functions and pathways involved in TLS-derived subtypes, we performed differential gene expression analysis, as well as GO and KEGG functional enrichment analysis (Figure 2G). Cluster 1 was significantly associated with the immune system and organisms' response to external pathogens or other organisms. Cluster 2 was significantly associated with protein localization to the cell periphery, small molecule degradation, cilia assembly, and organic acid catabolism, which play essential roles in maintaining normal cellular function. Cluster 3 was significantly associated with viruses replicating their genomes and the negative regulatory processes that regulate viral genome replication, involving key processes in viral biology (Supplementary Table S3). Further functional enrichment analysis showed that Cluster 1 was significantly associated with hematopoietic cell lineage, cytokine-cytokine receptor interactions, and Th17 cell differentiation pathways, Cluster 2 was significantly associated with lysosomal, Hedgehog signaling and synaptic vesicle cycling pathways, and Cluster 3 was associated with nucleoplasmic transfer pathway and Hippo signaling pathway (Supplementary Table S4). Notably, Hippo is a very conserved signaling pathway responsible for regulating cell proliferation and apoptosis, and its major components are mutated and dysregulated in a variety of cancers, promoting the development

of malignant tumors. It has been demonstrated that transcriptional coactivators downstream of the Hippo signaling pathway, including YAP/TAZ, promote the proliferation of breast cancer cells by stabilizing the KLF5 transcription factor, survival, and tumor growth, leading to poor prognosis of breast cancer (44).

In addition, we obtained copy number variation data for the TCGA breast cancer cohort at the GDC Xena Hub (https://xenabrowser.net/datapages/). By looking at the copy number variation of TLS-derived subtypes, we found that the genetic variant profiles also exhibited significant heterogeneity. More copy number amplifications occurred in Cluster 1&2, while more copy number deletions occurred in Cluster 3 (Figure 2H). Specifically, on chromosomes 1, 8, 11, 16, 17, and 20, Cluster 1&2 showed more copy number amplification, while Cluster 3 showed only a few copy number amplifications. Besides, on chromosomes 3, 4, 5, 6, 7, 10, 12, 19, and X, copy number amplification was observed in Cluster 1&2, whereas in Cluster 3, there was no copy number amplification but only copy number deletion. This difference also reflects the molecular heterogeneity within breast cancer, and these molecular changes may lead to different characteristics and functions of tumor cells, which affects the tumor's treatment response and prognosis, leading to differences in the response of different subtypes to treatment. Therefore, this difference could be considered when developing treatment regimens. Gene amplification is usually associated with the overproliferative capacity of tumor cells, and for Cluster 1&2, which has more gene amplification, inhibiting the overproliferative capacity of tumor cells may be an effective therapeutic strategy. On the contrary, gene deletions may lead to reduced tumor suppressor function, and for Cluster 3 with more gene deletions, focusing on restoring tumor suppressor function may be another effective therapeutic strategy.

3.3 Prognostic value of TLS-derived breast cancer subtypes

To investigate the differences in immune infiltration of TLS-derived breast cancer subtypes, we used the CIBERSORT cell deconvolution tool to assess the relative abundance of 22 immune cell types in three subtypes. The results showed that Cluster 3 had the lowest degree of immune infiltration (Figure 3A). Next, we investigated the impact of potential interactions between cancer signature pathways and TLS-derived subtypes on patients and found that some pathways such as HALLMARK_UV_RESPONSE_UP, HALLMARK_ESTROGEN_RESPONSE_EARLY, and other signature signaling pathways had lower activity levels in Cluster 3 (Supplementary Table S5), may be positively correlated with survival, while HALLMARK_KRAS_SIGNALING_UP, HALLMARK_APOPTOSIS, HALLMARK_TNFA_SIGNALING_VIA_NFKB, and other signature signaling pathways were more active in Cluster 3, may be negatively correlated with survival (Figure 3B). To verify this speculation, we selected three signature signaling pathways, HALLMARK_ESTROGEN_RESPONSE_EARLY, HALLMARK_ESTROGEN_RESPONSE_LATE, and HALLMARK_E2F_TARGETS, and observed the KM curves of their OS. The results were consistent with our speculation that the high activity of HALLMARK_ESTROGEN_RESPONSE_EARLY versus HALLMARK_ESTROGEN_RESPONSE_LATE in Cluster 3 represented a better prognosis, and HALLMARK_E2F_TARGETS in Cluster 3 High activity, on the other hand, was associated with a worse prognosis (Figure 3C). We further evaluated the activity of 28 immune cells (45) in TLS-derived subtypes, and it could be seen that Cluster 1 and Cluster 2 were immunized to a better extent than Cluster 3 (Figure 3D; Supplementary Table S6). We chose Activated B cells with low activity in Cluster 3, observed the KM curve of their OS, and found that the lower activity of Activated B cells led to a poor prognosis of Cluster 3 (Figure 3E). All of these results suggest that TLS-derived breast cancer typing heterogeneity can influence breast cancer prognosis and can be utilized as a feasible factor to predict the prognosis. In addition, we investigated the association between TLS-critical genes and the survival of TLS-derived subtypes and found IL1R1 and CCL8 are protective factors (HR < 1, $p < 0.05$) (Figure 3F). IL1R1 and CCL8 are implicated in the regulation of inflammation and immune response. We next compared their expression differences in the three subtypes and found the lowest expression level of IL1R1 and CCL8 in Cluster 3, which may have contributed to the poor prognosis (Figure 3G).

3.4 Prediction of TLS-derived subtypes in external datasets using XGBoost

To develop an accurate and unsupervised clustering-independent method for predicting TLS-derived subtypes in breast cancer patients, we trained the XGBoost model for predicting Cluster 1&2 and Cluster 3 subtypes based on the breast cancer cohort of TCGA and the 12 TLS-critical genes obtained by using Lasso regression previously (see Materials and Methods). Our model achieved an accuracy of 0.92 in predicting the training set of TCGA (Figure 4A). Applying our model to external datasets of breast cancer (Metabric dataset, GSE19615, GSE20685) and combining it with clinical information, we were able to demonstrate that the predicted Cluster 1&2 and Cluster 3 subtypes differed significantly in prognosis (Figure 4B). The expression pattern of TLS-critical genes is consistent with the TCGA-BRCA cohort (Figure 4C). Furthermore, due to the extensive attention that TLSs have received in immunotherapy in recent years (21–23), we additionally collected a dataset of 21 triple-negative breast cancer patients who were treated with cisplatin and bevacizumab in a neoadjuvant setting (GSE103668), to test the predictive value of TLS-derived subtypes. Our model divided the cohort into two groups, Cluster 1&2 and Cluster 3, the differences in the expression of TLS-critical genes were also consistent with the other datasets tested (Figure 4D). Notably, while 18.8% of patients in Cluster 1&2 achieved pathologic complete remission (pCR), no patients in Cluster 3 achieved pCR, indicating a worse response to the neoadjuvant setting in Cluster 3 (Figure 4E).

We next analyzed the importance of TLS-critical genes in the XGBoost prediction model and found that CXCL13 had the highest importance (Figure 4F; Supplementary Table S7). Combining clinical information, we found that CXCL13 effectively predicted

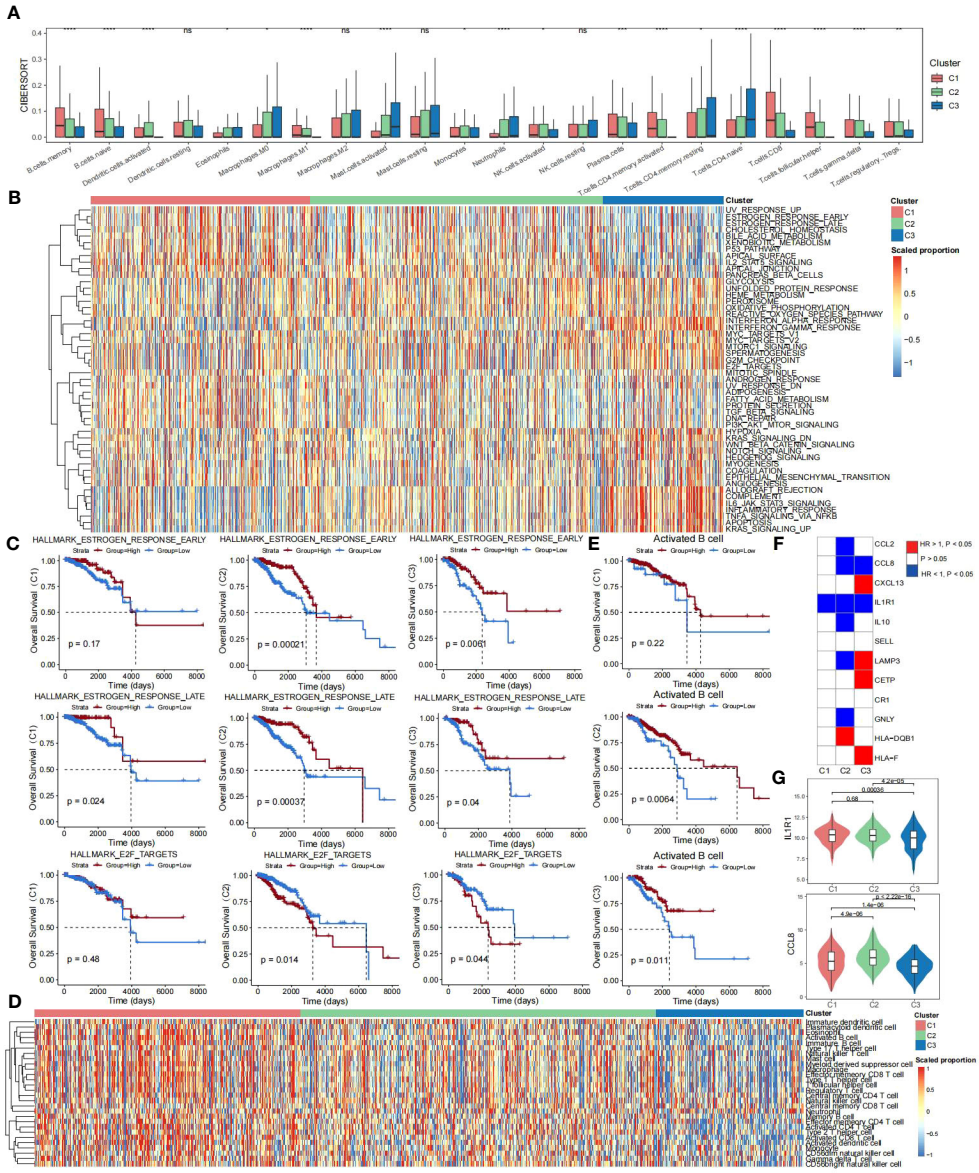

FIGURE 3
Prognostic differences in TLS-derived breast cancer subtypes. **(A)** Box line plot showing the differences in immune infiltration among the TLS-derived subtypes, P-values were derived by Wilcoxon rank sum test. ns, not significant; *$p < 0.05$; **$p < 0.01$; ***$p < 0.001$; ****$p < 0.0001$. **(B)** Heatmap showing activity scores of cancer signature pathways for the TLS-derived subtypes. These pathways were obtained from the MSigDB database. **(C)** KM curves showing the effect of the activity of cancer signature pathways on the prognosis of TLS-derived subtypes. P-values were obtained by log-rank test. **(D)** Heatmap showing the effect of the activity of 28 immune cell genomes on the prognosis of TLS-derived subtypes. **(E)** KM curves showing the effect of immune cell activity on the prognosis of patients with TLS-derived subtypes. P-values were obtained by log-rank test. **(F)** Heatmap showing the effect of the expression of TLS-critical genes on the prognosis of TLS-derived subtypes. P-values were obtained by log-rank test. **(G)** Violin plot showing the differences in the distribution of IL1R1 and CCL8 expression levels in TLS-derived subtypes. P-values were obtained by t-test.

patient prognosis in the TCGA-BRCA cohort and external datasets (Metabric dataset, GSE19615, GSE20685) (Figure 4G). Previous studies have identified that TLS production requires continuous chronic stimulation, its maintenance depends on some molecules, including CXCL13 (43, 46), and increasing CXCL13 levels promotes the formation of TLSs (47–49). These results suggest that CXCL13 is an essential biomarker for clinical studies of Cluster 3, which may be necessary for improving breast cancer patients' prognosis.

3.5 Single-cell perspective of TLS-derived subtypes

To further validate the significance of TLS-derived subtypes, we applied the model to the single-cell dataset (GSE195665) from the GEO database. We performed a detailed analysis of the single-cell transcriptome data of 834,356 cells from 167 samples, including steps of downsampling, quality control, batch-effects correction, and normalization, and finally, we used XGBOOST to predict TLS

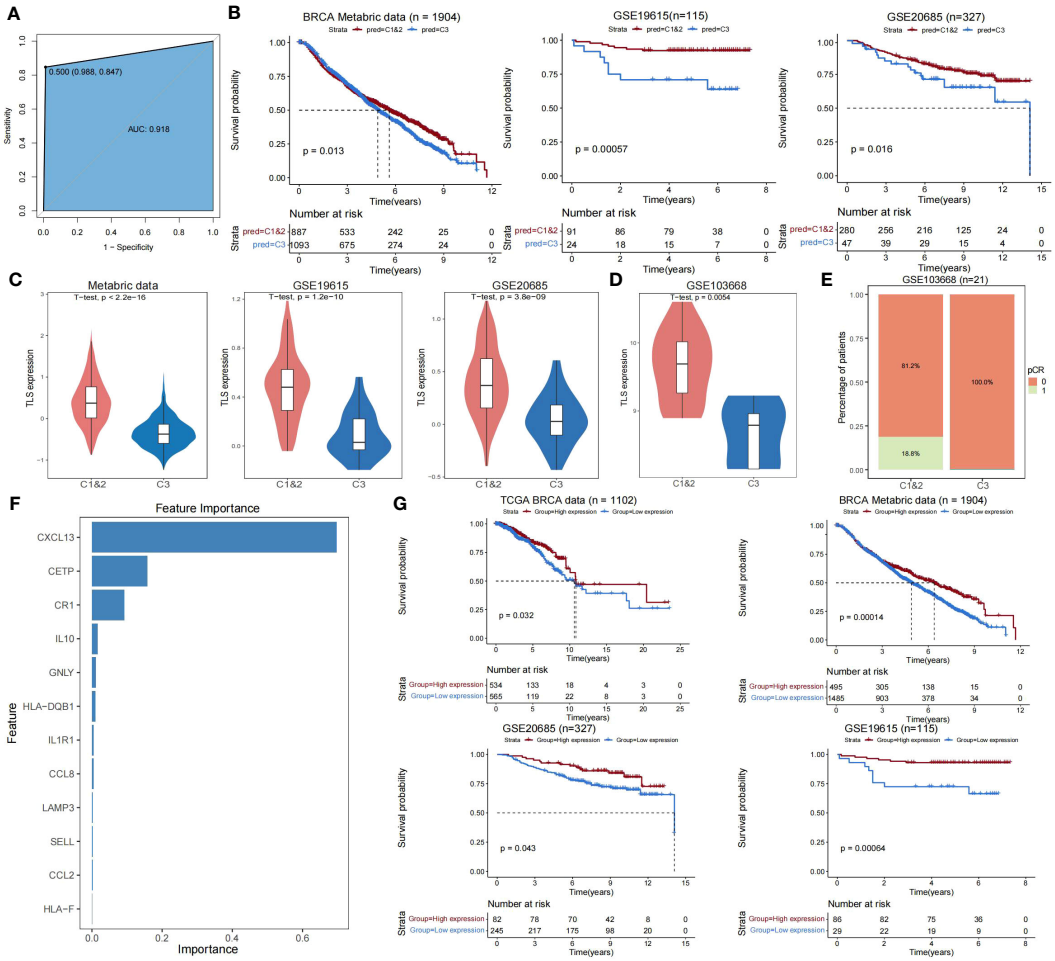

FIGURE 4
Validating the reliability of TLS-derived subtypes in external datasets. **(A)** ROC curve showing the accuracy of the XGBoost classifier in predicting specific samples in the training set. **(B)** Kaplan-Meier survival curves for Cluster 1&2 versus Cluster 3 overall survival predicted using XGBoost. P-values were obtained by log-rank test. **(C)** Violin plot showing the difference in expression levels of TLS-critical genes in Cluster 1&2 versus Cluster 3 predicted using XGBoost. P-values were obtained from the t-test. **(D)** Violin plot showing the difference in expression levels of TLS-critical genes in Cluster 1&2 versus Cluster 3 using XGBoost predictive immunotherapy cohorts. P-values were obtained by t-test. **(E)** Stacked bar graph showing the comparison of disease treatment effects between Cluster 1&2 versus Cluster 3 in the predicted immunotherapy cohort using XGBoost. pCR = 0 indicates this sample did not achieve pCR and pCR = 1 indicates this sample achieved pCR. **(F)** Bar graph showing the importance ranking of 12 TLS-critical genes (sorted by gain index) in the training set. **(G)** KM curves showing the effect of CXCL13 on the prognosis of breast cancer patients. The P-value was obtained by log-rank test.

typing for 44 tumor samples (Figure 5A). By comparing Cluster1&2 and Cluster3, we observed that the differences in expression patterns of TLS-critical genes, immune scores, and tumor purity were all consistent with our results obtained in other datasets (Figures 5B, C). Utilizing the genefu package to predict PAM50 typing for tumor samples from the single-cell dataset, we noted that samples predicted as Basal and Her2 were also predicted as Cluster 3 (Figure 5D). These findings re-emphasize the poor prognosis of Cluster 3 and confirm the feasibility of our typing strategy from a single-cell perspective.

We compared cellular fraction differences between Cluster 1&2 and Cluster 3, as well as between normal samples and Cluster 3. Notably, Cluster 3 exhibited elevated fibroblasts abundance and diminished lumhr cells abundance (Figures 5E, F). Cellchat analysis demonstrated that, compared to Cluster 1&2, fibroblasts in Cluster 3 had significantly stronger interactions with other cells, especially with myeloid cells, but weaker interactions with lumhr cells (Figure 5G; see Materials and Methods). Further analysis of receptor and ligand genes showed that the interaction of CD46-JAG1 and IL6-(IL6R+IL6ST) was significantly enhanced in Cluster 3 (Figure 5H). We observed the expression patterns of CD46 and JAG1 in fibroblasts, pericytes, and basal cells, as well as IL6, IL6R, and IL6ST in fibroblasts and myeloid cells. Within Cluster 3, the expression of CD46 was significantly increased in fibroblasts, JAG1 in basal cells, IL6 in fibroblasts, and IL6R in myeloid cells (Figures 5I, J). The KM survival curves showed that CD46, JAG1, IL6, and IL6R were all risk factors that lead to poor prognosis in breast cancer patients (Figure 5K), which implies that the enhanced interaction between CD46-JAG1 leads to poor prognosis in breast cancer patients, along with the IL6-(IL6R+IL6ST) axis. Therefore, we hypothesized that CD46 and IL6 were upregulated in fibroblasts, with enhanced interactions with basal cells and myeloid cells,

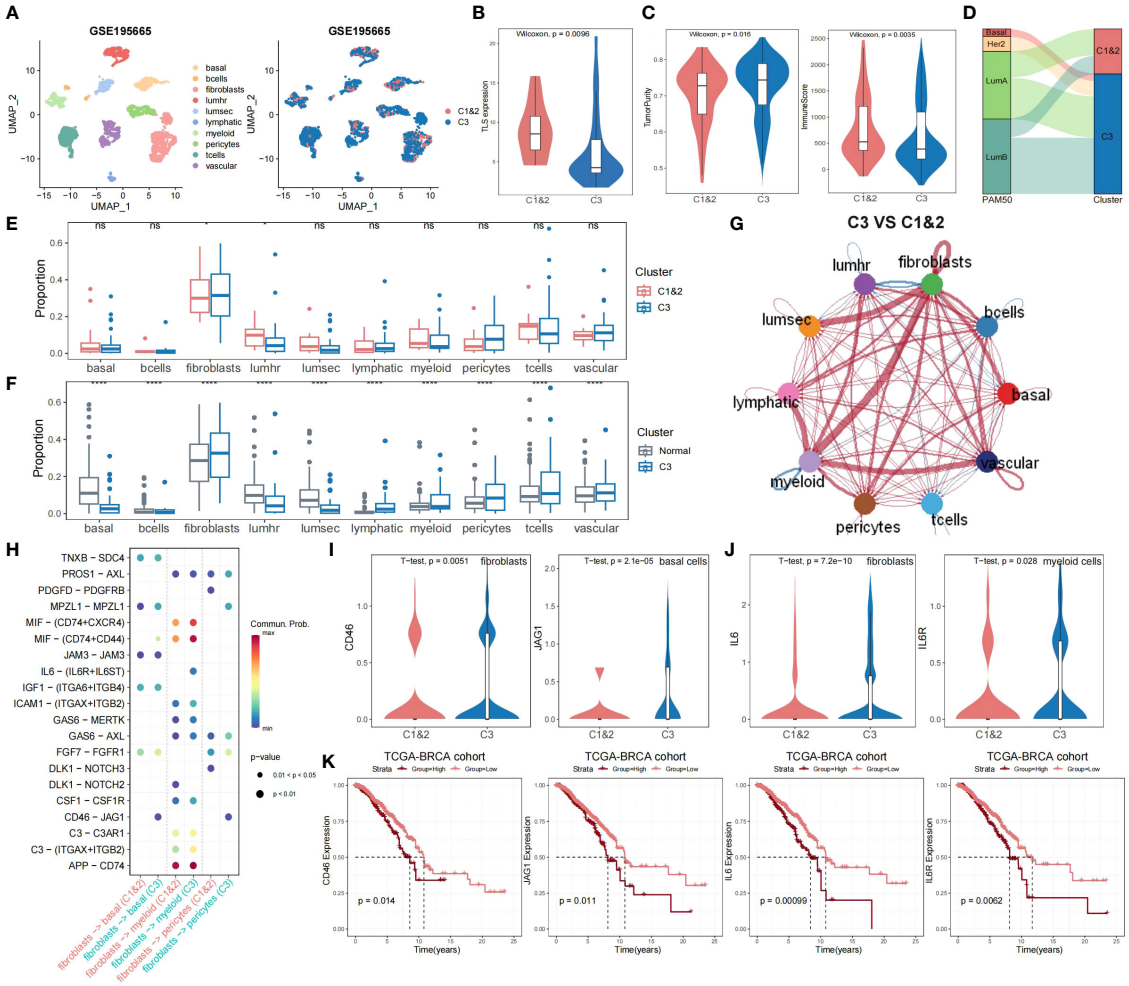

FIGURE 5
Single-cell profiling of the immune microenvironment and TLS-derived subtypes interactions. **(A)** The predictive result of the breast cancer single-cell dataset (n = 44). **(B)** Violin plot showing the difference in expression levels of TLS-critical genes in Cluster 1&2 versus Cluster 3 predicted using XGBoost. The P-value was obtained by Wilcoxon rank sum test. **(C)** Violin plot showing the difference in tumor purity and immune scores of Cluster 1&2 versus Cluster 3 predicted using XGBoost. P-values were obtained by Wilcoxon rank sum test. **(D)** Sankey plot showing the association of Cluster 1&2 versus Cluster 3 with PAM50 typing. **(E)** Grouped boxplot showing the cellular proportion of Cluster 1&2 and Cluster 3 samples. P-values were obtained from t-tests. ns, not significant, $*p < 0.05$. **(F)** Grouped boxplot showing the cellular proportion of normal and Cluster 3 samples. P-values were obtained from t-tests. $****p < 0.0001$. **(G)** Interaction map depicting the ligand-receptor interactions within the immune microenvironment. The width of edges represents the relative interaction strength. Red colored edges represent increased signaling in Cluster 3 compared to Cluster 1&2, while blue colored edges represent decreased signaling in Cluster 3 compared to Cluster 1&2. **(H)** Bubble plot showing the significant interactions between receptor and ligand genes among fibroblasts, basal cells, myeloid cells, and pericytes in Cluster 1&2 and Cluster 3. **(I)** Violin plot showing the differences in the distribution of CD46 expression levels in fibroblasts and JAG1 expression levels in basal cells of both Cluster 1&2 and Cluster 3. P-values were obtained by t-test. **(J)** Violin plot showing the differences in the distribution of IL6 expression levels in fibroblasts and IL6R expression levels in myeloid cells of both Cluster 1&2 and Cluster 3. P-values were obtained by t-test. **(K)** KM curves showing the effect of CD46, JAG1, IL6, and IL6R on the prognosis of TCGA-BRCA cohort. P-values were obtained by log-rank test.

leading to upregulation of JAG1 and IL6R expression, ultimately contributing to the poor prognosis of Cluster 3.

4 Discussion

TLSs are increasingly recognized as a focus of anti-tumor immunity, and it has been demonstrated that a higher number of mature TLSs in tumors is associated with favorable outcomes in various cancers. We explored the breast cancer microenvironment using TLS-related genes and found the heterogeneity of TLSs in breast cancer, which supports our TLS-derived typing of breast cancer. Therefore, we used consensus clustering analysis on the TLS-critical gene expression profiles of the TCGA breast cancer cohort and obtained three subtypes (Cluster 1, Cluster 2, and Cluster 3), and found that the three subtypes differed significantly in prognoses. Gene ontology annotation and pathway analysis revealed these three subtypes were associated with different biological processes. Calculation of the activity scores of signature cancer signaling pathways and immune cell genomes in TLS-derived subtypes revealed that the heterogeneity of TLS-derived subtypes may affect prognosis and may be utilized as a viable

predictor of prognosis. By further evaluating the degree of immune infiltration, stromal scores, tumor purity, GGI, and copy number variant differences of the TLS-derived subtypes, the results showed that Cluster 3 had the lowest immune scores, stromal scores, the highest tumor purity, and the highest GGI, which were all consistent with its poor prognosis. In addition, we identified many gene deletions in Cluster 3, suggesting significant heterogeneity in the characterization of genetic variation in TLS-derived subtypes at the genomic level. The above results suggest that TLS-derived subtypes could provide a new strategy for current breast cancer typing.

To validate the reliability of TLS-derived subtypes, we developed a prediction model using XGBoost to predict Cluster 1&2 versus Cluster 3 in other externally independent datasets. The model was evaluated to perform well in the TCGA training set (accuracy = 0.92). In other externally independent breast cancer cohorts, the subtypes predicted by our model showed prognostic differences and significant gene expression differences consistent with the expected pattern. This supports TLSs for typing studies in a broader range of breast cancer cohorts. In addition, we found that CXCL13 is the most critical marker gene in the Cluster 3 subtype. As mentioned in a previous study, the process of TLS formation is as follows: activation of local fibroblasts, recruitment of immune cells to maturation, and activated fibroblasts in the first step promote the recruitment and aggregation of lymphocytes through the secretion of the pro-angiogenic factors CXCL13 and CCL19 (50), so a better prognosis can be achieved by increasing CXCL13 levels to promote TLSs formation.

Finally, we applied the model to a breast cancer single-cell dataset. Again, the Cluster 3 subtype showed a worse prognosis, higher tumor purity, and lower immune scores. After observing the cellular components and intercellular communication, we hypothesized that in Cluster3, CD46, and IL6 were upregulated in fibroblasts, with enhanced interactions with basal cells and myeloid cells, leading to upregulation of the expression of JAG1 and IL6R, ultimately contributing to the poor prognosis of Cluster 3. Relevant research has demonstrated that the inflammatory cytokines IL6/IL6R amplify the signaling of the Notch-Jagged pathway, which stimulates the generation of hybrid epithelial-mesenchymal cancer stem cells, and that inhibition of CD46 gene expression reduces the effects of proliferation, invasion, and migration capacity of breast cancer cells. Knockdown of the JAG1 gene significantly reduced the potential for tumor organogenesis in triple-negative breast cancer (TNBC) cells, and JAG1-mediated adaptive resistance in Her2 breast cancer cells led to tumor recurrence (51). Overall, these studies highlight the critical roles of IL6 and IL6R, as well as CD46 and JAG1, in the survival and invasive capacity of cancer cells, and their broad promise as targets for antitumor therapies, as well as exploring the possibility of combining them with other therapeutic agents.

Data availability statement

The datasets presented in this study can be found in online repositories. The names of the repository/repositories and accession number(s) can be found in the article/Supplementary Material.

Author contributions

RL: Data curation, Formal analysis, Visualization, Writing – original draft, Writing – review & editing. XH: Investigation, Formal analysis, Writing – review & editing. SY: Writing – review & editing. WD: Writing – review & editing. XC: Conceptualization, Software, Supervision, Writing – review & editing. HL: Conceptualization, Funding acquisition, Methodology, Writing – review & editing.

Funding

The author(s) declare financial support was received for the research, authorship, and/or publication of this article. This work was supported by the Jiangsu Funding Program for Excellent Postdoctoral Talent (2022ZB699 to HL).

Acknowledgments

We would like to express our heartfelt gratitude to those who have contributed to the creation and maintenance of the databases utilized in this study.

Conflict of interest

The authors declare that the research was conducted in the absence of any commercial or financial relationships that could be construed as a potential conflict of interest.

Publisher's note

Supplementary material

The Supplementary Material for this article can be found online at: https://www.frontiersin.org/articles/10.3389/fimmu.2024.1364506/full#supplementary-material

SUPPLEMENTARY TABLE S1
List of TLS-related genes.

SUPPLEMENTARY TABLE S2
Results of consensus Clustering.

SUPPLEMENTARY TABLE S3
GO terms enriched in TLS-derived subtypes.

SUPPLEMENTARY TABLE S4
KEGG pathways enriched in TLS-derived subtypes.

SUPPLEMENTARY TABLE S5
Activity scores of cancer signature pathways of TLS-derived subtypes.

SUPPLEMENTARY TABLE S6
Activity scores of immune cell gene set of TLS-derived subtypes.

SUPPLEMENTARY TABLE S7
Importance of TLS-critical genes in the XGBoost prediction model.

References

1. Marioni JC, Mason CE, Mane SM, Stephens M, Gilad Y. RNA-seq: an assessment of technical reproducibility and comparison with gene expression arrays. *Genome Res*. (2008) 18:1509–17. doi: 10.1101/gr.079558.108

2. Stark R, Grzelak M, Hadfield J. RNA sequencing: the teenage years. *Nat Rev Genet*. (2019) 20:631–56. doi: 10.1038/s41576-019-0150-2

3. Wang ET, Sandberg R, Luo S, Khrebtukova I, Zhang L, Mayr C, et al. Alternative isoform regulation in human tissue transcriptomes. *Nature*. (2008) 456:470–6. doi: 10.1038/nature07509

4. Siegel RL, Giaquinto AN, Jemal A. Cancer statistics, 2024. *CA: Cancer J Clin*. (2024) 74:12–49. doi: 10.3322/caac.21820

5. Sung H, Ferlay J, Siegel RL, Laversanne M, Soerjomataram I, Jemal A, et al. Global cancer statistics 2020: GLOBOCAN estimates of incidence and mortality worldwide for 36 cancers in 185 countries. *CA: Cancer J Clin*. (2021) 71:209–49. doi: 10.3322/caac.21660

6. Hammond ME, Hayes DF, Dowsett M, Allred DC, Hagerty KL, Badve S, et al. American Society of Clinical Oncology/College Of American Pathologists guideline recommendations for immunohistochemical testing of estrogen and progesterone receptors in breast cancer. *J Clin Oncol*. (2010) 28:2784–95. doi: 10.1200/JCO.2009.25.6529

7. Nielsen TO, Leung SCY, Rimm DL, Dodson A, Acs B, Badve S, et al. Assessment of ki67 in breast cancer: updated recommendations from the international ki67 in breast cancer working group. *J Natl Cancer Institute*. (2021) 113:808–19. doi: 10.1093/jnci/djaa201

8. Cardoso F, van't Veer LJ, Bogaerts J, Slaets L, Viale G, Delaloge S, et al. 70-gene signature as an aid to treatment decisions in early-stage breast cancer. *New Engl J Med*. (2016) 375:717–29. doi: 10.1056/NEJMoa1602253

9. Qian Y, Daza J, Itzel T, Betge J, Zhan T, Marmé F, et al. Prognostic cancer gene expression signatures: current status and challenges. *Cells*. (2021) 10:648. doi: 10.3390/cells10030648

10. Rotman J, Koster BD, Jordanova ES, Heeren AM, de Gruijl TD. Unlocking the therapeutic potential of primary tumor-draining lymph nodes. *Cancer Immunol Immunother CII*. (2019) 68:1681–8. doi: 10.1007/s00262-019-02330-y

11. Coppola D, Nebozhyn M, Khalil F, Dai H, Yeatman T, Loboda A, et al. Unique ectopic lymph node-like structures present in human primary colorectal carcinoma are identified by immune gene array profiling. *Am J Pathol*. (2011) 179:37–45. doi: 10.1016/j.ajpath.2011.03.007

12. Dieu-Nosjean MC, Goc J, Giraldo NA, Sautès-Fridman C, Fridman WH. Tertiary lymphoid structures in cancer and beyond. *Trends Immunol*. (2014) 35:571–80. doi: 10.1016/j.it.2014.09.006

13. Cipponi A, Mercier M, Seremet T, Baurain JF, Théate I, van den Oord J, et al. Neogenesis of lymphoid structures and antibody responses occur in human melanoma metastases. *Cancer Res*. (2012) 72:3997–4007. doi: 10.1158/0008-5472.CAN-12-1377

14. de Chaisemartin L, Goc J, Damotte D, Validire P, Magdeleinat P, Alifano M, et al. Characterization of chemokines and adhesion molecules associated with T cell presence in tertiary lymphoid structures in human lung cancer. *Cancer Res*. (2011) 71:6391–9. doi: 10.1158/0008-5472.CAN-11-0952

15. Di Caro G, Bergomas F, Grizzi F, Doni A, Bianchi P, Malesci A, et al. Occurrence of tertiary lymphoid tissue is associated with T-cell infiltration and predicts better prognosis in early-stage colorectal cancers. *Clin Cancer Res*. (2014) 20:2147–58. doi: 10.1158/1078-0432.CCR-13-2590

16. Germain C, Gnjatic S, Tamzalit F, Knockaert S, Remark R, Goc J, et al. Presence of B cells in tertiary lymphoid structures is associated with a protective immunity in patients with lung cancer. *Am J Respir Crit Care Med*. (2014) 189:832–44. doi: 10.1164/rccm.201309-1611OC

17. Goc J, Germain C, Vo-Bourgais TK, Lupo A, Klein C, Knockaert S, et al. Dendritic cells in tumor-associated tertiary lymphoid structures signal a Th1 cytotoxic immune contexture and license the positive prognostic value of infiltrating CD8+ T cells. *Cancer Res*. (2014) 74:705–15. doi: 10.1158/0008-5472.CAN-13-1342

18. Messina JL, Fenstermacher DA, Eschrich S, Qu X, Berglund AE, Lloyd MC, et al. 12-Chemokine gene signature identifies lymph node-like structures in melanoma: potential for patient selection for immunotherapy? *Sci Rep*. (2012) 2:765. doi: 10.1038/srep00765

19. Schumacher TN, Thommen DS. Tertiary lymphoid structures in cancer. *Sci (New York NY)*. (2022) 375:eabf9419. doi: 10.1126/science.abf9419

20. Xu W, Ma C, Liu W, Anwaier A, Tian X, Shi G, et al. Prognostic value, DNA variation and immunologic features of a tertiary lymphoid structure-related chemokine signature in clear cell renal cell carcinoma. *Cancer Immunol Immunother CII*. (2022) 71:1923–35. doi: 10.1007/s00262-021-03123-y

21. Cabrita R, Lauss M, Sanna A, Donia M, Skaarup Larsen M, Mitra S, et al. Tertiary lymphoid structures improve immunotherapy and survival in melanoma. *Nature*. (2020) 577:561–5. doi: 10.1038/s41586-019-1914-8

22. Helmink BA, Reddy SM, Gao J, Zhang S, Basar R, Thakur R, et al. B cells and tertiary lymphoid structures promote immunotherapy response. *Nature*. (2020) 577:549–55. doi: 10.1038/s41586-019-1922-8

23. Petitprez F, de Reyniès A, Keung EZ, Chen TW, Sun CM, Calderaro J, et al. B cells are associated with survival and immunotherapy response in sarcoma. *Nature*. (2020) 577:556–60. doi: 10.1038/s41586-019-1906-8

24. Curtis C, Shah SP, Chin SF, Turashvili G, Rueda OM, Dunning MJ, et al. The genomic and transcriptomic architecture of 2,000 breast tumours reveals novel subgroups. *Nature*. (2012) 486:346–52. doi: 10.1038/nature10983

25. Kao KJ, Chang KM, Hsu HC, Huang AT. Correlation of microarray-based breast cancer molecular subtypes and clinical outcomes: implications for treatment optimization. *BMC Cancer*. (2011) 11:143. doi: 10.1186/1471-2407-11-143

26. Li Y, Zou L, Li Q, Haibe-Kains B, Tian R, Li Y, et al. Amplification of LAPTM4B and YWHAZ contributes to chemotherapy resistance and recurrence of breast cancer. *Nat Med*. (2010) 16:214–8. doi: 10.1038/nm.2090

27. Kumar T, Nee K, Wei R, He S, Nguyen QH, Bai S, et al. A spatially resolved single-cell genomic atlas of the adult human breast. *Nature*. (2023) 620:181–91. doi: 10.1038/s41586-023-06252-9

28. Birkbak NJ, Li Y, Pathania S, Greene-Colozzi A, Dreze M, Bowman-Colin C, et al. Overexpression of BLM promotes DNA damage and increased sensitivity to platinum salts in triple-negative breast and serous ovarian cancers. *Ann Oncol*. (2018) 29:903–9. doi: 10.1093/annonc/mdy049

29. Wilkerson MD, Hayes DN. ConsensusClusterPlus: a class discovery tool with confidence assessments and item tracking. *Bioinf (Oxford England)*. (2010) 26:1572–3. doi: 10.1093/bioinformatics/btq170

30. Hänzelmann S, Castelo R, Guinney J. GSVA: gene set variation analysis for microarray and RNA-seq data. *BMC Bioinf*. (2013) 14:7. doi: 10.1186/1471-2105-14-7

31. Sengupta RBD. Modeling survival data: extending the Cox model by Terry M. *Therneau; Patricia M Grambsch Sankhya Ser A*. (2003) 65:843–4. doi: 10.2307/25053321

32. Stuart T, Butler A, Hoffman P, Hafemeister C, Papalexi E, Mauck WM 3rd, et al. Comprehensive integration of single-cell data. *Cell*. (2019) 177:1888–902.e21. doi: 10.1016/j.cell.2019.05.031

33. Yu G, Wang LG, Han Y, He QY. clusterProfiler: an R package for comparing biological themes among gene clusters. *Omics: J Integr Biol*. (2012) 16:284–7. doi: 10.1089/omi.2011.0118

34. Yoshihara K, Shahmoradgoli M, Martínez E, Vegesna R, Kim H, Torres-Garcia W, et al. Inferring tumour purity and stromal and immune cell admixture from expression data. *Nat Commun*. (2013) 4:2612. doi: 10.1038/ncomms3612

35. Newman AM, Liu CL, Green MR, Gentles AJ, Feng W, Xu Y, et al. Robust enumeration of cell subsets from tissue expression profiles. *Nat Methods*. (2015) 12:453–7. doi: 10.1038/nmeth.3337

36. Gendoo DMA, Ratanasirigulchai N, Schröder M, Paré HK, Parker HK, Prat HK, et al. genefu: a package for breast cancer gene expression analysis. *Bioinformatics* (Oxford, England). (2016) 32(7):1097–9. doi: 10.1093/bioinformatics/btv693

37. Jin S, Guerrero-Juarez CF, Zhang L, Chang I, Ramos R, Kuan CH, et al. Inference and analysis of cell-cell communication using CellChat. *Nat Commun*. (2021) 12:1088. doi: 10.1038/s41467-021-21246-9

38. Finkin S, Yuan D, Stein I, Taniguchi K, Weber A, Unger K, et al. Ectopic lymphoid structures function as microniches for tumor progenitor cells in hepatocellular carcinoma. *Nat Immunol*. (2015) 16:1235–44. doi: 10.1038/ni.3290

39. Hennequin A, Derangère V, Boidot R, Apetoh L, Vincent J, Orry D, et al. Tumor infiltration by Tbet+ effector T cells and CD20+ B cells is associated with survival in gastric cancer patients. *Oncoimmunol*. (2016) 5:e1054598. doi: 10.1080/2162402X.2015.1054598

40. Kroeger DR, Milne K, Nelson BH. Tumor-infiltrating plasma cells are associated with tertiary lymphoid structures, cytolytic T-cell responses, and superior prognosis in ovarian cancer. *Clin Cancer Res*. (2016) 22:3005–15. doi: 10.1158/1078-0432.CCR-15-2762

41. Jacquelot N, Tellier J, Nutt Sl, Belz Gt. Tertiary lymphoid structures and B lymphocytes in cancer prognosis and response to immunotherapies. *Oncoimmunol*. (2021) 10:1900508. doi: 10.1080/2162402X.2021.1900508

42. Zhu X, Tian X, Ji L, Zhang X, Cao Y, Shen C, et al. A tumor microenvironment-specific gene expression signature predicts chemotherapy resistance in colorectal cancer patients. *NPJ Precis Oncol*. (2021) 5:7. doi: 10.1038/s41698-021-00142-x

43. Drayton DL, Ying X, Lee J, Lesslauer W, Ruddle NH. Ectopic LT alpha beta directs lymphoid organ neogenesis with concomitant expression of peripheral node addressin and a HEV-restricted sulfotransferase. *J Exp Med*. (2003) 197:1153–63. doi: 10.1084/jem.20021761

44. Wang C, Nie Z, Zhou Z, Zhang H, Liu R, Wu J, et al. The interplay between TEAD4 and KLF5 promotes breast cancer partially through inhibiting the transcription of p27Kip1. *Oncotarget*. (2015) 6:17685–97. doi: 10.18632/oncotarget.3779

45. Charoentong P, Finotello F, Angelova M, Mayer C, Efremova M, Rieder D, et al. Pan-cancer immunogenomic analyses reveal genotype-immunophenotype relationships and predictors of response to checkpoint blockade. *Cell Rep*. (2017) 18:248–62. doi: 10.1016/j.celrep.2016.12.019

46. Cupedo T, Mebius RE. Role of chemokines in the development of secondary and tertiary lymphoid tissues. *Semin Immunol*. (2003) 15:243–8. doi: 10.1016/j.smim.2003.08.002

47. Gu-Trantien C, Migliori E, Buisseret L, de Wind A, Brohée S, Garaud S, et al. CXCL13-producing TFH cells link immune suppression and adaptive memory in human breast cancer. *JCI Insight*. (2017) 2:e91487. doi: 10.1172/jci.insight.91487

48. Li JP, Wu CY, Chen MY, Liu SX, Yan SM, Kang YF, et al. PD-1(+)CXCR5(-)CD4(+) Th-CXCL13 cell subset drives B cells into tertiary lymphoid structures of nasopharyngeal carcinoma. *J Immunother Cancer*. (2021) 9:e002101. doi: 10.1136/jitc-2020-002101

49. Rouanne M, Arpaia N, Marabelle A. CXCL13 shapes tertiary lymphoid structures and promotes response to immunotherapy in bladder cancer. *Eur J Cancer (Oxford England: 1990)*. (2021) 151:245–8. doi: 10.1016/j.ejca.2021.03.054

50. Vella G, Guelfi S, Bergers G. High endothelial venules: A vascular perspective on tertiary lymphoid structures in cancer. *Front Immunol*. (2021) 12:736670. doi: 10.3389/fimmu.2021.736670

51. Jie LI, Jing LI. Effects of CD46-siRNA silencing on proliferation and metastasis of MCF-7 human breast cancer cell. *J Clin Surg*. (2014) 22:564–4. doi: 10.3969/j.issn.1005-6483.2014.08.009

frontiers | Frontiers in Immunology

TYPE Original Research
PUBLISHED 26 March 2024
DOI 10.3389/fimmu.2024.1366928

OPEN ACCESS

EDITED BY
Eyad Elkord,
University of Salford, United Kingdom

REVIEWED BY
Jaya Lakshmi Thangaraj,
University of California, San Diego, United States
Pengping Li,
The First People's Hospital of Xiaoshan District, China

*CORRESPONDENCE
Yi Zhang
472189926@qq.com

†These authors have contributed equally to this work and share first authorship

RECEIVED 07 January 2024
ACCEPTED 11 March 2024
PUBLISHED 26 March 2024

CITATION
Wang Y, Xu Y, Deng Y, Yang L, Wang D, Yang Z and Zhang Y (2024) Computational identification and experimental verification of a novel signature based on SARS-CoV-2–related genes for predicting prognosis, immune microenvironment and therapeutic strategies in lung adenocarcinoma patients. *Front. Immunol.* 15:1366928. doi: 10.3389/fimmu.2024.1366928

Computational identification and experimental verification of a novel signature based on SARS-CoV-2–related genes for predicting prognosis, immune microenvironment and therapeutic strategies in lung adenocarcinoma patients

Yuzhi Wang[1,4†], Yunfei Xu[2†], Yuqin Deng[3], Liqiong Yang[1,4], Dengchao Wang[1,4], Zhizhen Yang[5] and Yi Zhang[6*]

[1]Department of Laboratory Medicine, Deyang People's Hospital, Deyang, Sichuan, China, [2]Department of Laboratory Medicine, Chengdu Women's and Children's Central Hospital, Chengdu, Sichuan, China, [3]Department of Cardiology, Jianyang People's Hospital, Jianyang, China, [4]Pathogenic Microbiology and Clinical Immunology Key Laboratory of Deyang City, Deyang People's Hospital, Deyang, Sichuan, China, [5]College of Medical Technology, Chengdu University of Traditional Chinese Medicine, Chengdu, Sichuan, China, [6]Department of Blood Transfusion, Deyang People's Hospital, Deyang, Sichuan, China

Background: Early research indicates that cancer patients are more vulnerable to adverse outcomes and mortality when infected with severe acute respiratory syndrome coronavirus 2 (SARS-CoV-2). Nonetheless, the specific attributes of SARS-CoV-2 in lung Adenocarcinoma (LUAD) have not been extensively and methodically examined.

Methods: We acquired 322 SARS-CoV-2 infection-related genes (CRGs) from the Human Protein Atlas database. Using an integrative machine learning approach with 10 algorithms, we developed a SARS-CoV-2 score (Cov-2S) signature across The Cancer Genome Atlas and datasets GSE72094, GSE68465, and GSE31210. Comprehensive multi-omics analysis, including assessments of genetic mutations and copy number variations, was conducted to deepen our understanding of the prognosis signature. We also analyzed the response of different Cov-2S subgroups to immunotherapy and identified targeted drugs for these subgroups, advancing personalized medicine strategies. The expression of Cov-2S genes was confirmed through qRT-PCR, with GGH emerging as a critical gene for further functional studies to elucidate its role in LUAD.

Results: Out of 34 differentially expressed CRGs identified, 16 correlated with overall survival. We utilized 10 machine learning algorithms, creating 101 combinations, and selected the RFS as the optimal algorithm for constructing a Cov-2S based on the average C-index across four cohorts. This was achieved after integrating several essential clinicopathological features and 58 established

signatures. We observed significant differences in biological functions and immune cell statuses within the tumor microenvironments of high and low Cov-2S groups. Notably, patients with a lower Cov-2S showed enhanced sensitivity to immunotherapy. We also identified five potential drugs targeting Cov-2S. *In vitro* experiments revealed a significant upregulation of GGH in LUAD, and its knockdown markedly inhibited tumor cell proliferation, migration, and invasion.

Conclusion: Our research has pioneered the development of a consensus Cov-2S signature by employing an innovative approach with 10 machine learning algorithms for LUAD. Cov-2S reliably forecasts the prognosis, mirrors the tumor's local immune condition, and supports clinical decision-making in tumor therapies.

KEYWORDS

lung adenocarcinoma, SARS-CoV-2, prognostic signature, machine learning, immunotherapy

Introduction

Lung cancer (LC) ranks as the foremost cause of cancer-related mortality globally, accounting for about 2.3 million new cases and 1.8 million deaths annually (1, 2). The outlook for patients with metastatic cancer is very grim, as only 5% of them are expected to survive for 5 years. The survival rate for patients with tumors confined to the lungs varies between 33% and 60% (3). Based on the histological categorization of LC, around 85% of LCs are non-small-cell lung cancer (NSCLC), with the majority being lung adenocarcinoma (LUAD) (4). The clinical outcome is closely linked to the early identification and diagnosis, and the failure to do so often results in missing the best chance for clinical intervention. Surgical removal is advised for individuals diagnosed with stage I or II illness. In the treatment of NSCLC for patients in advanced stages, targeted therapy and immunotherapy are alternative systemic therapeutic approaches, in addition to traditional radiotherapy and chemotherapy. The selection of these strategies is based on the gene mutation scenarios and the expression of programmed cell death protein-ligand 1 (PD-L1) (5). The molecular and phenotypic diversity of LUAD is significant, with around 60% of cases having a driver mutation that is oncogenic. This mutation is often linked to specific clinicopathological characteristics and can help predict the response to treatment (6, 7). Despite advancements in genotype-based diagnosis and therapy modalities, the survival rate continues to be poor (8). Therefore, it is crucial to investigate new dependable biomarkers for the early detection and prediction of prognosis, as well as to offer prognostic markers and therapeutic objectives for LUAD.

Severe Acute Respiratory Syndrome Coronavirus 2 (SARS-CoV-2), a highly contagious positive-sense, single-stranded RNA virus, is believed to have originated from a zoonotic source and quickly transmitted among humans via respiratory droplets and physical contact (9). Since its emergence in late 2019, the swift worldwide proliferation of SARS-CoV-2 infection has been termed the Coronavirus Disease 2019 (COVID-19) pandemic. According to epidemiological data, individuals diagnosed with cancer, especially those undergoing anticancer therapy, have a significantly increased susceptibility to SARS-CoV-2 infection. This heightened vulnerability leads to a higher occurrence of severe complications and unfavorable prognosis due to their compromised immune system (10, 11). Furthermore, numerous symptoms may persist in numerous COVID-19 patients even after the acute infection has been eliminated. The impact of the COVID-19 pandemic on cancer is closely linked to the functioning of the immune system. There is a strong connection between viruses and cancers, as evidenced by multiple studies. Viruses are responsible for causing over 15% of malignancies (12). Cell transformation and carcinogenesis triggered by viral infections, such as those caused by human papillomavirus (HPV), hepatitis B and C viruses (HBV, HCV), Epstein-Barr virus (EBV), and human T-lymphoma virus, are well-documented (13–16). In a manner akin to SARS-CoV-2, SARS-CoV-1 disrupts numerous signaling pathways linked to malignant cell transformation (17). However, the carcinogenic potential of SARS-CoV-2 is yet to be fully understood and warrants further investigation. Policard et al. highlighted a range of genes influenced by SARS-CoV-2 infection, including the E2F transcription factor and RB1, indicating a possible role of SARS-CoV-2 in tumorigenesis. The link between malignancies and SARS-CoV-2 infection remains incompletely explored. Given that viruses can influence tumor progression via specific target genes, the role of SARS-CoV-2 target genes in cancer deserves thorough examination (18).

In this research, we provided a comprehensive overview of the SARS-CoV-2 infection–related genes (CRGs) identified in LUAD. Multiple machine learning algorithms were used to develop the

SARS-CoV-2 score (Cov-2S), which is a prognostic model designed to predict the OS of patients with LUAD. Furthermore, the Cov-2S has the capability to assess the landscape of the tumor's immune micro-environment and its responsiveness to both immunotherapy and chemotherapy. The results of our study reveal the important regulatory functions of CRGs in the progression of LUAD and offer potential targets for precise treatment of LUAD.

Materials and methods

Data resources

Transcriptome profiling data and patient survival details for LUAD were sourced from The Cancer Genome Atlas (TCGA) database to create training sets. This dataset, TCGA-LUAD, comprised 503 cases and included clinical information, genetic mutations, and copy number variation (CNV) data. For testing purposes, expression profiles from the Gene Expression Omnibus (GEO) for the following datasets were also acquired: GSE72094 (n=398), GSE68465 (n=442), and GSE31210 (n=226). All expression data were standardized to Transcripts Per Million (TPM) format to facilitate consistent dataset comparison. Following that, the "sva" package was utilized to eliminate batch effects. A total of 322 CRGs were obtained from the previous research and human protein atlas (HPA) (https://www.proteinatlas.org/) database (19), as shown in Supplementary Table 1.

Enrichment pathway exploration

Differential CRGs between adjacent normal and cancerous tissues were identified using the "limma" R package, applying criteria of an absolute fold change (FC) greater than 2 and a false discovery rate (FDR) below 0.05. For the analysis of differentially expressed genes (DEGs), Kyoto Encyclopedia of Genes and Genomes (KEGG) and Gene Ontology (GO) enrichment analyses were conducted using the R packages "clusterProfiler" and "org.Hs.eg.db". Gene set variation analysis (GSVA) was performed by integrating the "h.all.v7.5.1.symbols.gmt" gene sets from MSigDB, available at https://www.gseamsigdb.org/gsea/msigdb/index.jsp (20). This was followed by gene set enrichment analysis (GSEA) to identify significantly enriched signaling pathways and biological processes among the different groups (21).

Development and evaluation of a prognostic Cov-2S by machine learning

To develop a robust and precise prognostic signature for lung adenocarcinoma (LUAD), potential biomarkers underwent evaluation using ten integrative machine learning algorithms, namely, random survival forest (RSF), elastic network (Enet), Lasso (least absolute shrinkage and selection operator), Ridge, stepwise Cox, CoxBoost, partial least squares regression for Cox (plsRcox), supervised principal components (SuperPC), generalized boosted regression modeling (GBM), and survival support vector machine (survival-SVM). The process for signature generation involved several steps:

1. Prognostic biomarkers were initially identified using univariate Cox regression in the TCGA dataset.
2. Subsequently, 101 algorithm combinations were applied to these biomarkers to create predictive models. These models were developed using leave-one-out cross-validation (LOOCV) within the TCGA dataset.
3. All models were then tested using three GEO datasets.
4. The Harrell's concordance index (C-index) was computed for each model across all TCGA and GEO datasets. The model with the highest average C-index was deemed the most effective.

Previous studies provide more in-depth information on comparable machine learning algorithms (22). Following this, LUAD patients were stratified into high and low Cov-2S groups based on the median Cov-2S score. The predictive capability of Cov-2S was assessed with a time-dependent ROC curve, generated via the R-package "time-ROC" (23). Additionally, both univariate and multivariate Cox analyses were conducted to identify risk factors among clinical characteristics and Cov-2S for LUAD prognosis.

Univariate and multivariate Cox regression analyses were conducted to investigate the potential of Cov-2S and clinical parameters as independent prognostic indicators for LUAD patients. The independent prognostic indicators were integrated into a nomogram using the R package "rms" to predict 1-, 3-, and 5-year survival rates. Calibration plots were generated to assess the alignment between the survival rates predicted by the nomogram and the observed survival rates.

Unsupervised clustering analysis

The creation of the "ConsensusClusterPlus" R package enabled the execution of an unsupervised cluster analysis on Cov-2S mRNA expression profiles (24). The ideal number of clusters was identified by choosing the k value that minimized the sum of squares within each cluster, and the classification's stability was verified through 1000 repetitions. Moreover, the high-latitude data dimension was decreased by employing principal component analysis (PCA) from the R package "ggplot2" to examine if the gene Cov-2S could categorize patients into clusters.

Somatic variants analysis and copy number variation analysis

The R package "maftools" was used to present the waterfall plots of the top 20 genes with the highest mutation frequencies in

the mutation landscape. The calculation of the tumor mutation burden (TMB) involves determining the overall count of non-synonymous mutations present in every individual. The interaction between gene mutations was determined by using "maftools" to identify genes with significant mutations ($P< 0.05$) between the different groups. Only genes that underwent mutations exceeding 30 occurrences in at least one group were taken into account in both analyses. The GISTIC (Genomic Identification of Significant Targets in Cancer) 2.0 pipeline, accessible via GenePattern at https://genepattern.broadinstitute.org/, was employed to analyze copy number variation data. This analysis identified significant regions of amplification and deletion, as well as discrete copy number statuses of all genes across different Cov-2S groups. Additionally, to assess the extent of genomic alterations, metrics such as the fraction of genome altered (FGA), fraction of genome gained (FGG), and fraction of genome lost (FGL) were calculated for each sample (25). FGA was determined by calculating the proportion of fragment base count representing genetic variation within the genome, while FGG/FGL solely concentrated on the acquisition or depletion of genetic variation within the genome.

Tumor microenvironment

Various algorithms, such as TIP (tumor immunophenotype) tracking (26), ESTIMATE (27), TIMER (28), MCP-counter (29) and the single sample gene set enrichment analysis (ssGSEA) algorithm (30), were utilized for TME analysis. TIP concentrated on characterizing the immune microenvironment by referencing the seven-step cancer-immunity cycle and deducing the proportions of diverse tumor-infiltrating immune cells. The ESTIMATE algorithm was employed to compute the ESTIMATE score, immune score, and stromal score, thereby assessing the tumor's immune and stromal components. Additionally, the abundance of various immune cell types infiltrating the tumor was estimated using algorithms such as TIMER, MCP-counter, and single-sample Gene Set Enrichment Analysis (ssGSEA).

Evaluation of immunotherapy response

The Tumor Immune Dysfunction and Exclusion (TIDE) web tool, available at http://tide.dfci.harvard.edu, was employed to predict immunotherapy responses across various hypoxia subtypes of tumors (31). Additionally, the unsupervised subclass mapping (submap) method was utilized to assess the expression similarity between lung adenocarcinoma (LUAD) patients with different hypoxia subtypes and those exhibiting varied outcomes following immunotherapy. This approach posits that greater similarity in expression profiles between patient pairs suggests more closely aligned clinical outcomes (32). Furthermore, three independent external datasets (GSE78220, NIHMS1611472, and IMvigor210) were selected to investigate the correlation between the Cov-2S score and the efficacy of immunotherapy treatments.

Prediction of chemotherapy drug sensitivity

Cancer cell lines (CCLs) drug sensitivity data were sourced from the Cancer Therapeutics Response Portal (CTRP v2.0, available at https://portals.broadinstitute.org/ctrp) and the PRISM Repurposing dataset (PRISM, accessible at https://depmap.org/portal/prism) (2, 33). The CTRP scrutinized 481 compounds against 835 CCLs, whereas the PRISM Repurpose initiative examined 1448 compounds across 482 CCLs. Prior to further analysis, compounds with missing values (NAs) in over 20% of the samples were excluded. The ISOpure algorithm was implemented to minimize the influence of non-tumor components in the analysis (34). Additionally, the "pRRophetic" package's built-in ridge regression model was employed to predict the area under the curve (AUC) value for each compound in individual patients. This estimation utilized a combination of the meta-set purified expression profile and the drug sensitivity data (35).

Cell culture

Human lung adenocarcinoma cell lines A549 and H838, along with the normal bronchial epithelial cell line BEAS-2B, were acquired from Procell (Wuhan, China) and the American Type Culture Collection (Manassas, VA, USA), respectively. In a controlled environment at 37°C and 5% CO2, H838 cells were maintained in RPMI-1640 medium supplemented with 10% fetal bovine serum (FBS), while A549 and BEAS-2B cells were cultured in Dulbecco's Modified Eagle Medium (DMEM) also containing 10% FBS. Small interfering RNA (siRNA) constructs targeting GGH were obtained from Shanghai Hanheng and introduced into A549 and H838 cells using Lipofectamine 3000 for effective GGH knockdown. The siRNA sequences were as follows: siRNA-NC, 5'- CGGGCCATGAAACGCCCATGG-3'; siRNA1-GGH, 5'-GCT GTTTAACATGGTGATTTG-3'; siRNA2-GGH, 5'-GGGACC CACTGAGGTAGTTAA-3'. After 48 hours, the effectiveness of knockdown was assessed through immunoblotting, and the cells were then utilized for additional experiments.

Cell proliferation assay

The viability of cells was assessed using Cell Counting Kit-8 (CCK-8) and colony formation experiments. In the CCK-8 trial, 1000 cells were planted in 96-well dishes and incubated for 24, 48, and 72 hours. Subsequently, 10 µl of CCK-8 reagent (Saiku, Shanghai, China) was added to each well containing 100 µl of culture medium, and the plates were incubated at 37°C. After 2 hours, the optical density (OD) at 450 nm was measured using a micro-plate reader. In the colony formation assay, 500 cells subjected to treatment were plated in each well of 12-well plates. After an incubation period of 10 days, the plates were washed twice with phosphate-buffered saline (PBS). The cells were then fixed with 4% paraformaldehyde for 30 minutes and stained using a crystal

violet staining solution for 10 minutes. Finally, they were stained with a solution of crystal violet for 10 minutes.

Cell migration and invasion assay

For the wound healing experiment, 5x10^5 cells were seeded into each well of a 6-well plate. The following day, a sterile 20 µl pipette tip was used to create a scratch (wound) on the cell surface. Post-wounding, non-adherent cells were washed off with phosphate-buffered saline (PBS) and replaced with fresh serum-free medium for a 24-hour period. The progression of wound closure was monitored and assessed using a light microscope. For cell migration assessment, Transwell chambers (24-well, BIOFIL, China) were employed. The lower chamber was filled with 0.6 ml of Dulbecco's Modified Eagle Medium (DMEM) supplemented with 20% fetal bovine serum (FBS). Meanwhile, approximately 7x10^4 cells, resuspended in basic medium, were added to the upper chamber and incubated overnight at 37°C in a 5% CO2 atmosphere. After 24 hours, the cells were fixed with 4% paraformaldehyde and stained with 2.5% crystal violet for subsequent analysis. ImageJ was used to randomly select and count three microscopic views. Cell invasion assay also employed Transwell chambers. 70 µl of diluted Matrigel was applied to the upper chamber prior to coating. The migration was performed without coating matrigel surface. The following procedures are comparable to the migration process.

Cell viability assay

Cell viability was determined by CCK8 cytotoxicity assay. Briefly, cells were seeded in 96-well plates at 5000 cells/well and treated with at 37°C with Ispinesib (0, 30, 60, 120 or 240 nM, MedChem Express, Monmouth Junction, NJ, USA, Cat No.HY-50759), Paclitaxel (0, 10, 20, 40 or 80 nM, MedChem Express, Monmouth Junction, NJ, USA, Cat No. HY-B0015) and Epothilone-b (0, 40, 80, 160 or 320 nM, MedChem Express, Monmouth Junction, NJ, USA, Cat No. HY-17029) for 24 h, respectively. Cells were incubated with CCK8 (10 µl/well) for 2 h at 37°C and then spectrophotometrically quantified at 450 nm.

Quantitative real-time PCR and immunohistochemistry

The total RNA was extracted with RNA isolation Kit (AG, Changsha, China) according to the product protocol. The extracted RNA underwent reverse transcription using the Reverse Transcription Kit (Promega, Madison, Wisconsin) to synthesize complementary DNA (cDNA), setting the stage for quantitative real-time PCR (qRT-PCR). The qRT-PCR analysis was performed on the Roche 480II quantitative real-time gene amplification instrument (Roche, Oregon, USA), utilizing SYBR Premix Ex Taq II (Promega, Wisconsin, USA). For normalization and control purposes, GAPDH was employed as an endogenous reference. Relative gene expression levels were calculated and analyzed using the $2^{-\Delta\Delta Ct}$ method. The specific primers used in this study are detailed in Supplementary Table 2. The LUAD tissue microarray (HLugA020PG02) was acquired from Outdo Biotech, and its ethics approval was obtained. The IHC procedure was performed according to the previously mentioned protocol (36). The main antibodies used were anti-GGH (Huaan, Hangzhou, HA721359, 1:100). In this study, the immunostaining intensity was scored using the following scale: 0 for negative staining, 1 for light yellow staining, 2 for brownish yellow, and 3 for tan. Additionally, the extent of the immunostaining area was evaluated as: 1 for less than one-third coverage, 2 for coverage between one-third and two-thirds, and 3 for more than two-thirds coverage. The final score for biomarker expression was determined by multiplying the immunostaining intensity score by the immunostaining area score.

Statistical analysis

All statistical analyses in this study were conducted using R software 4.1 and GrapdPad Prism 5. For categorical data, Chi-square tests and Fisher's exact tests were employed. The Wilcoxon signed-rank test was utilized for comparing paired continuous variables. Pearson correlation analysis was applied to assess correlations between continuous variables. Statistical significance levels were defined as follows: extremely significant (****) for $p < 0.0001$, highly significant (***) for $p < 0.001$, significant (**) for $p < 0.01$, marginally significant (*) for $p < 0.05$, and not significant (ns) for $p \geq 0.05$.

Results

Transcriptional and genetic alterations of CRGs in LUAD patients

The CRGs expression patterns between adjacent and cancerous tissues were compared in the TCGA LUAD and identified 34 differently expressed SARS-CoV-2 infection-related genes (DECRGs) containing 28 upregulated and 6 downregulated genes (Figure 1A). We conducted GO and KEGG enrichment analysis for DECRGs to determine the functions and pathways that had the greatest level of involvement. In terms of GO analysis, the DECRGs were mainly enriched in "protein homodimerization activity", "endoplasmic reticulum" and "response to hypoxia" (Figure 1B). In the KEGG pathway, the DECRGs showed significant enrichment in the category of "protein processing in the endoplasmic reticulum" (Figure 1B). In order to delve deeper into the correlation between genomic changes and expressions of DECRGs in LUAD, the TCGA-LUAD project compiled the genomic modifications of these genes. Analysis of somatic mutations revealed that DECRGs mutations were present in 187 out of 616 samples (30.36%). Among these, CENPF (6%), PKP2 (5%) and ADAMTS1 (4%) exhibited the highest gene mutation

10.3389/fimmu.2024.1366928

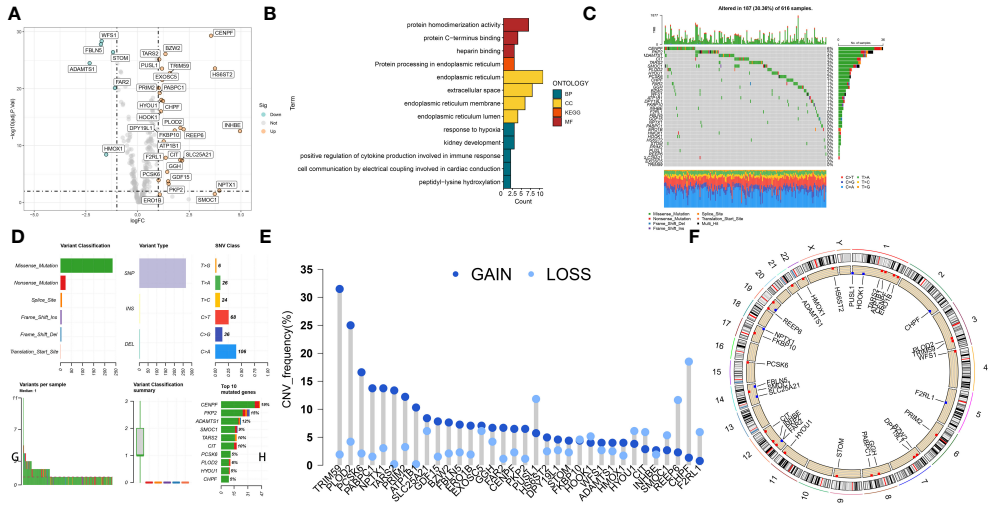

FIGURE 1
The landscape of SARS-CoV-2 infection–related proteins (CRGs) in TCGA-LUAD set. **(A)** Volcano plot of the DECRGs. **(B)** GO categories [molecular function (MF), biological process (BP) and cellular component (CC)] and KEGG pathway analysis for DECRGs. **(C, D)** The mutation summary and details of DECRGs in the LUAD patients. **(E)** CNV mutation situation of the DEPCDRGs. **(F)** The location of CNV alterations of DECRGs on chromosomes.

rates (Figure 1C). The predominant mutation types in these genes are nonsense mutations (Figure 1D). The findings presented in Figure 1E demonstrate a relatively low frequency of CNVs among the DECRGs. Notably, genes such as TRIM59, PLOD2, PCSK6, PABPC1, and NPTX1 exhibited amplifications in their copy numbers. In contrast, genes like SMOC1, REEP6, CHPF, and F2RL1 showed deletions in their copy numbers. Figure 1F depicts the chromosomal locations of these DECRGs in LUAD patients. Additionally, among these DECRGs, 16 genes were identified as having significant correlations with the prognosis of LUAD patients.

Construction of prognostic Cov-2S by integrative machine learning algorithms

After identifying 16 potential prognostic genes, a machine learning-based integrative approach was employed to create a reliable and consistent prognostic model. In total, 101 different types of prognostic models based on machine learning were acquired, and their C-index for both the training and testing sets were displayed in Figure 2A and Supplementary Table 3. The RFS framework exhibits a highest average C-index of 0.716 was suggested as the optimal model (Figure 2A, Supplementary Table 4). The Cov-2S was determined for every individual in all groups by analyzing the expression levels of 10 genes included in the model (Figures 2B, C). LUAD cases were divided into high and low Cov-2S groups based on the median value of Cov-2S. As anticipated, patients with low Cov-2S in LUAD exhibited a higher OS rate in the training, testing, and meta sets (Figures 2D-H). In addition, the discriminative ability of Cov-2S group for the prognosis of LUAD patients is not influenced by clinical feature subtypes (Supplementary Figure 1).

Evaluation of the Cov-2S signature

The discrimination of Cov-2S was assessed using Time-ROC analysis, yielding AUC values ranging from 0.94 to 0.98 in TCGA, 0.68 to 0.78 in GSE31210, 0.61 to 0.72 in GSE98465, 0.65 to 0.68 in GSE72094, and 0.72 to 0.9 in the meta-set (Figures 3A-E). Similar to the Time-ROC curve results, the C-index range for all sets is 0.62-0.93, with the TCGA set having the highest C-index (Figure 3F). The Chi-square test results indicated that individuals with advanced T, N, M stages and deceased status exhibited elevated Cov-2S levels (Supplementary Figure 2). Additionally, the prognostic prediction of Cov-2S was compared with other clinical and molecular variables. As displayed in Figures 3G-J, Cov-2S had distinctly superior accuracy than almost all clinicopathological measures including M, T, T, gender, M and TP53, KRAS, or EGFR mutations. In order to investigate if Cov-2S functioned as a standalone prognostic indicator, univariate and multivariate cox analyses were conducted by including various clinicopathological traits and Cov-2S. The results suggested the Cov-2S as a reliable prognostic indicator for LUAD patients independently (Tables 1-4). Incorporating independent predictors into the nomogram construction, we observed that Cov-2S exerted the most significant influence on survival prediction (Supplementary Figures 3A-D). Evaluation of the prediction accuracy of the model using calibration curves revealed close alignment between the predicted calibration curves at the 1-, 3-, and 5-year calibration points and the standard curve (Supplementary Figures 3E-H). Numerous predictive patterns have been developed for LUAD. In order to assess the predictive efficacy of Cov-2S in relation to other prognostic indicators, a random selection of 58 constructed prognostic indicators for LUAD were gathered and their C-index was computed. As shown in Figure 4, the C-index of our Cov-2S exceeded that of the majority of these prognostic signatures across all analyzed datasets.

10.3389/fimmu.2024.1366928

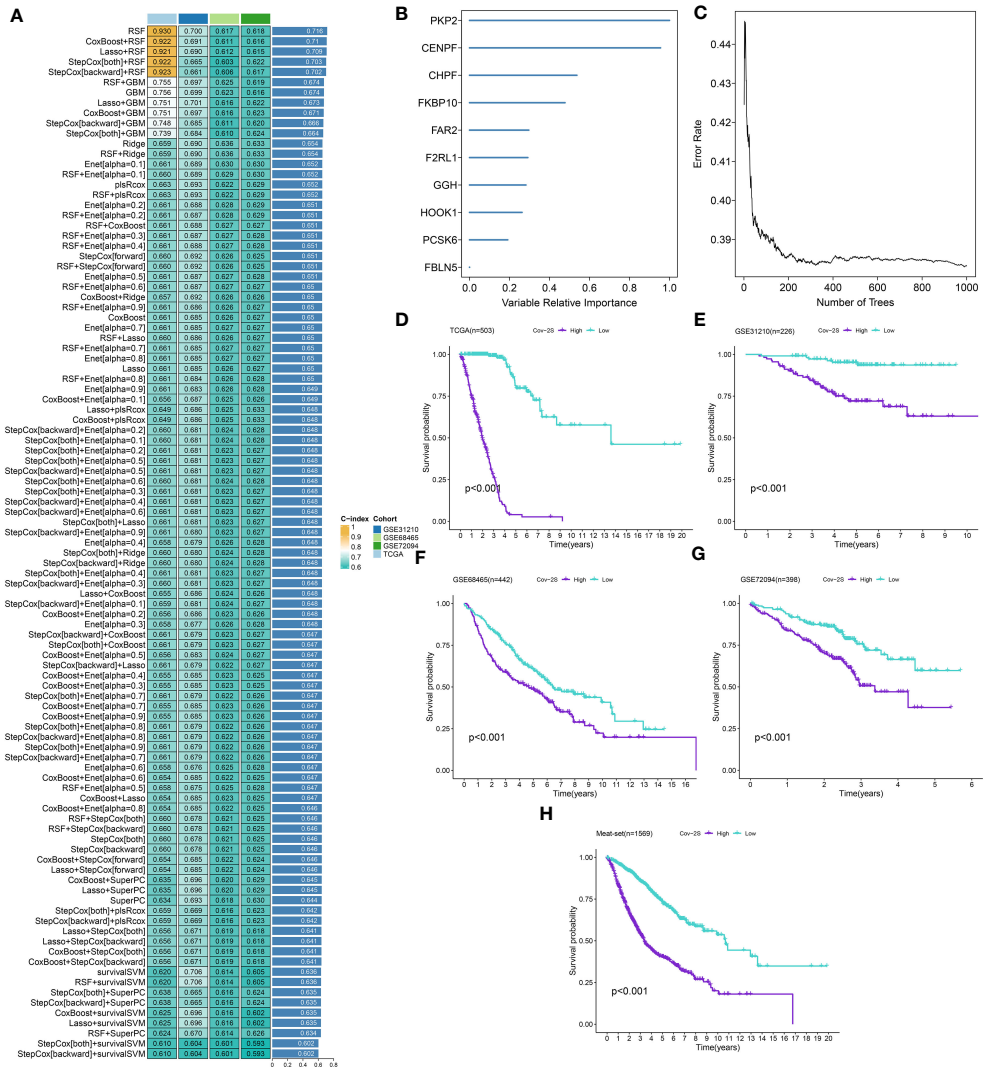

FIGURE 2
A SARS-CoV-2 score (Cov-2S) was established and validated via the machine learning-based integrative procedure. **(A)** A total of 101 kinds of machine learning algorithms were used to obtain the optimal model and calculated the C-index of each model for all sets. **(B, C)** The number of trees for determining the Cov-2S with minimal error and the importance of the 10 CRGs based on the RSF algorithm. **(D-H)** Kaplan–Meier curves of OS according to the Cov-2S in TCGA, GSE31210, GSE68465, GSE72094 and meta-set.

Generation of Cov-2S modification patterns

In order to gain a deeper understanding of the impacts of Cov-2S on LUAD, a consensus clustering analysis was conducted to categorize LUAD patients based on various alteration patterns. The heatmap of the consensus matrices and cumulative distribution function (CDF) curve (Supplementary Figure 4) identified that there were two clusters (cluster A, cluster B and cluster C) which were considered optimal. The PCA analysis confirmed a strong distribution between different groups based on the expression profiles of the Cov-2S (Figure 5A). Significantly, the analysis of survival demonstrated a significant difference in survival rates between the three clusters, where cluster A showed a more positive outcome and cluster B had a poorer prognosis (Figure 5B). Figure 5C illustrates the proportion of surviving and dying patients in three cluster and two Cov-2S groups. In cluster A, GSVA revealed prominent activation of various metabolic biological processes, while cluster B and cluster C were markedly enriched in various cell proliferation pathways (Figures 5D-F). Moreover, the ssGSEA method detected obvious disparities in the immune scores of the three distinct clusters (Figure 5G).

Somatic mutation and CNV status between the different groups

Our analyses suggested a specific somatic mutation distribution among two Cov-2S groups. As shown in Figures 6A, B, TP53, TTN, MUC16, CSMD3, RYR2, and LRP1B were commonly mutated in both the high and low Cov-2S groups. Somatic mutation profiles indicated that synonymous and non-synonymous mutations, as

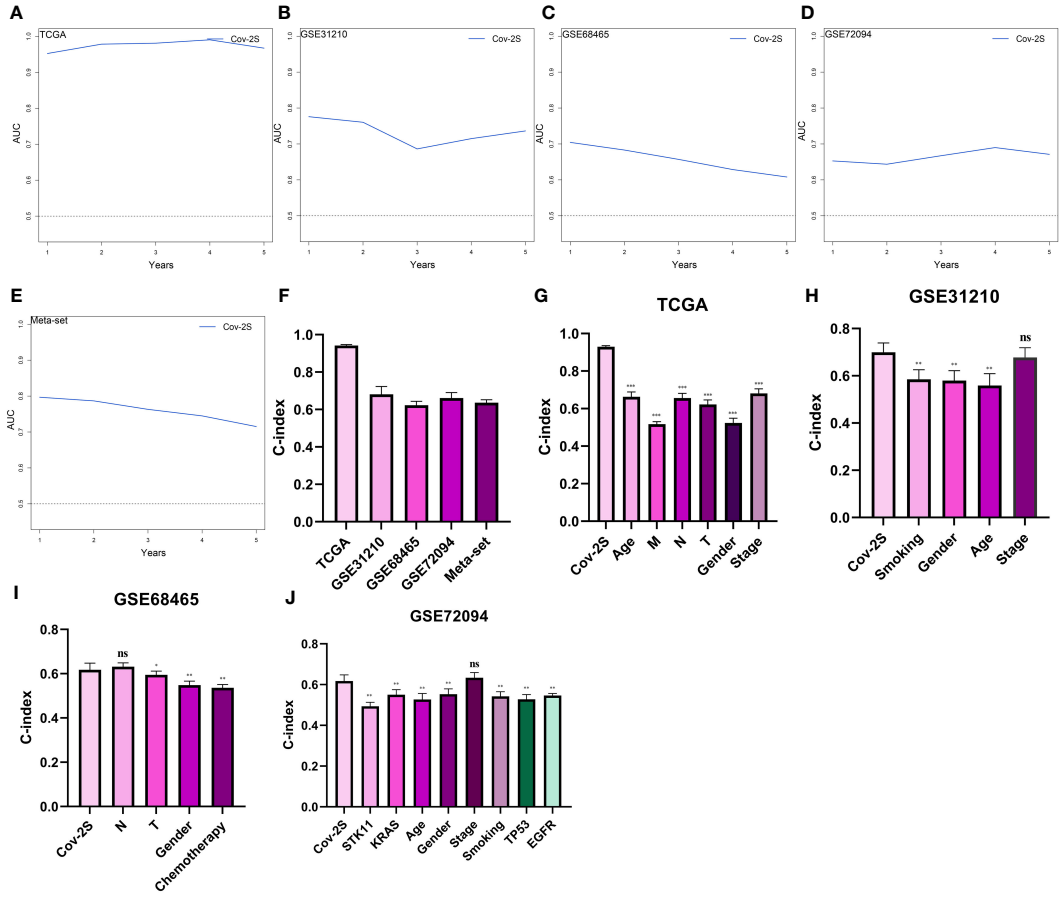

FIGURE 3
Evaluation of the Cov-2S. **(A-E)** Time-dependent receiver operating characteristic curve of Cov-2S for predicting the prognosis of LUAD patients from TCGA, GSE31210, GSE68465, GSE72094 and meta-set. **(F)** The C-index of the Cov-2S for the TCGA, GSE31210, GSE68465, GSE72094 sets. **(G-J)** The C-index of the Cov-2S and other clinical factors in the TCGA, GSE31210, GSE68465, GSE72094 sets. ns, not significant. *P < 0.05, **P < 0.01, ***P < 0.001.

well as overall mutation counts, did not display any noteworthy variances between the high and low Cov-2S groups. However, 8 genes demonstrated significantly distinct mutation frequencies between the two groups, along with a notable presence of co-mutations (Figures 6C-G). Moreover, there was no statistically different variation in TMB between the high and low Cov-2S groups (Figure 6H). Additionally, the study revealed the correlation between TMB, Cov-2S, and prognosis, indicating that patients with low TMB and high Cov-2S experience the most unfavorable prognosis (Figure 6I). Following that, CNV analysis revealed distinct chromosomal alteration patterns between the high and low Cov-2S groups (Figure 6J). Regrettably, there were no

TABLE 1 Univariate and multivariate Cox analysis of the clinicopathological features and Cov-2S with OS for TCGA cohort.

	Univariate Cox		Multivariate Cox	
Characteristics	HR(95%CI)	*P* value	HR(95%CI)	*P* value
Stage	1.977(1.586-2.463)	< **0.001**	1.487(1.049-2.109)	**0.026**
N	1.942(1.575-2.394)	< **0.001**	1.251(0.93-1.681)	0.139
T	1.816(1.386-2.38)	< **0.001**	1.423(1.034-1.958)	**0.03**
Age	1.038(0.822-1.31)	0.754	NA	NA
Sex	1.041(0.847-1.28)	0.7	NA	NA
M	1.727(1.18-2.527)	**0.005**	0.756(0.479-1.191)	0.227
Cov-2S	0.106(0.075-0.149)	< **0.001**	0.127(0.086-0.187)	< **0.001**

Significant value is given in bold.

TABLE 2 Univariate and multivariate Cox analysis of the clinicopathological features and Cov-2S with OS for GSE68465 cohort.

	Univariate Cox		Multivariate Cox	
Characteristics	HR(95%CI)	*P* value	HR(95%CI)	*P* value
N	2.029(1.689-2.438)	< **0.001**	1.947(1.603-2.366)	< **0.001**
T	2.062(1.587-2.68)	< **0.001**	1.797(1.36-2.374)	< **0.001**
Gender	1.262(1.051-1.516)	**0.013**	1.267(1.044-1.539)	**0.017**
chemotherapy	1.412(1.15-1.734)	< **0.001**	1.246(1.004-1.545)	**0.046**
Cov-2S	0.728(0.607-0.875)	< **0.001**	0.784(0.648-0.948)	**0.012**

Significant value is given in bold.

statistical difference in genomic loss, gain, and alteration between the two Cov-2S groups (Figure 6K).

TME and molecular characteristics of the Cov-2S

The immune condition of the TME impacts the outcome of cancer cells and anticipates responsiveness to immune checkpoint inhibitors (ICIs). Initially, we examined the correlation between Cov-2S and the infiltration of immune cells. As depicted in the illustration, the majority of individuals in the low Cov-2S group exhibited an elevated quantity of immune infiltrating cells (Figure 7A). Analyzing the correlation between the Cov-2S signature and the functions of the anticancer immunity cycles helps in understanding the status of anticancer immunity. Patients in the low Cov-2S group exhibited marked upregulation of various processes, including priming, activation, recruitment of CD4 T cells, and infiltration of immune cells into the tumor (Figure 7B). The findings indicated that patients with a low Cov-2S displayed a comparatively elevated expression of the majority of immune checkpoint genes (Figure 7C). Moreover, the Cov-2S exhibited a positive correlation with pathways associated with immunotherapy response and various metabolic pathways, such as the IFN-γ signature, DNA repair, nicotinamide adenine metabolism, and biotin metabolism (Figure 7D). GSVA was conducted to explore the underlying cancer mechanism of the Cov-2S.The findings indicated that individuals with elevated Cov-2S levels exhibited an abundance of pathways associated with cancer, including the EMT, proliferation, metabolites, and DNA repair (Figure 7E). Interestingly, these pathway results were confirmed in the GSEA analysis (Figures 7F-I).

Sensitivity prediction of different groups to immunotherapy and chemotherapy

The treatment of LUAD has demonstrated a promising potential for the application of immunotherapy. Through TIDE and submap analysis, we assessed the immunotherapy response of two Cov-2S groups. The results showed that individuals with low Cov-2S have a decreased TIDE score, suggesting that these patients are more prone to receiving advantages from immunotherapy (Figure 8A). Furthermore, the Submap analysis module revealed that patients with low Cov-2S exhibit similarities to melanoma patients who responded favorably to anti-PD-1 treatment (Figure 8B). Given the potential of Cov-2S to accurately forecast the efficacy of immunotherapy for LUAD, we aim to investigate its ability to predict the response to ICIs in groups of patients undergoing immunotherapy. In the IMvigor210 dataset, survival analysis revealed that a high Cov-2S score was associated with a poorer prognosis compared to a low Cov-2S score (Figure 8C). Additionally, the complete response/partial response (CR/PR) group exhibited a lower levels of Cov-2S than the stable disease/progressive disease (SD/PD) group, as demonstrated in Figure 8D. In the GSE78220 and NIHMS1611472 cohorts, we also discovered that decreased Cov-2S is associated to positive response to ICIs treatment (Figures 8E, F). Overall, these findings suggest that Cov-2S may be linked to immunotherapy response. To identify potential drugs with the desired properties, we conducted drug

TABLE 3 Univariate and multivariate Cox analysis of the clinicopathological features and Cov-2S with OS for GSE31210 cohort.

	Univariate Cox		Multivariate Cox	
Characteristics	HR(95%CI)	*P* value	HR(95%CI)	*P* value
smoking	1.417(0.882-2.277)	0.15	NA	NA
gender	1.344(0.839-2.152)	0.219	NA	NA
age	1.263(0.777-2.052)	0.346	NA	NA
stage	2.774(1.732-4.441)	< **0.001**	2.015(1.233-3.293)	**0.005**
Cov-2S	0.286(0.153-0.532)	< **0.001**	0.356(0.186-0.682)	**0.002**

Significant value is given in bold.

TABLE 4 Univariate and multivariate Cox analysis of the clinicopathological features and Cov-2S with OS for GSE72094 cohort.

	Univariate Cox		Multivariate Cox	
Characteristics	HR(95%CI)	*P* value	HR(95%CI)	*P* value
STK11	1.028(0.72-1.469)	0.879	NA	NA
KRAS	0.767(0.588-0.999)	**0.049**	0.907(0.69-1.192)	0.484
Age	1.258(0.836-1.894)	0.27	NA	NA
Gender	0.733(0.564-0.952)	**0.02**	0.725(0.553-0.95)	**0.02**
Stage	1.969(1.477-2.625)	< **0.001**	1.921(1.43-2.58)	< **0.001**
Smoking	1.248(0.694-2.245)	0.459	NA	NA
TP53	0.861(0.645-1.151)	0.313	NA	NA
EGFR	2.58(1.274-5.226)	**0.008**	2.147(1.047-4.4)	**0.037**
Cov-2S	0.575(0.438-0.755)	< **0.001**	0.64(0.483-0.847)	**0.002**

Significant value is given in bold.

response prediction separately using drug response data derived from CTRP and PRISM. CTRP and PRISM datasets encompass gene expression profiles and drug sensitivity profiles of numerous CCLs, offering a foundation for constructing drug response prediction models. A subset of 160 compounds was common to both datasets, resulting in a cumulative count of 1770 unique compounds across the combined datasets after eliminating redundancies (Figures 9A, B). During the cross-validation of the two pharmacogenomics databases, we identified four drugs or compounds (paclitaxel, SB-743921, cabazitaxel, epothilone-b, and ispinesib) that show promising therapeutic potential for patients with high Cov-2S. These drugs have lower estimated AUC values and exhibit a negative correlation with Cov-2S, as depicted in Figures 9C, D.

Predictive efficacy of Cov-2S from a pan-cancer perspective

To assess the generalizability of Cov-2S application in different solid tumors, we constructed Cov-2S in the TCGA pan-cancer set and evaluated the distribution and predictive efficacy of Cov-2S. Our results showed a significant distribution of Cov-2S in most solid tumors, with the highest evaluated Cov-2S being in rectum adenocarcinoma and testicular germ cell tumors (Figure 10A). In addition, Cov-2S can be a significant risk factor for glioma, ovarian cancer, cervical squamous epithelial cell cancer, pancreatic cancer, colon cancer, bladder cancer, uterine carcinosarcoma, sarcoma, thyroid carcinoma and uveal melanoma (Figure 10A). Finally, we evaluated the differential expression of Cov-2S in tumor tissues in

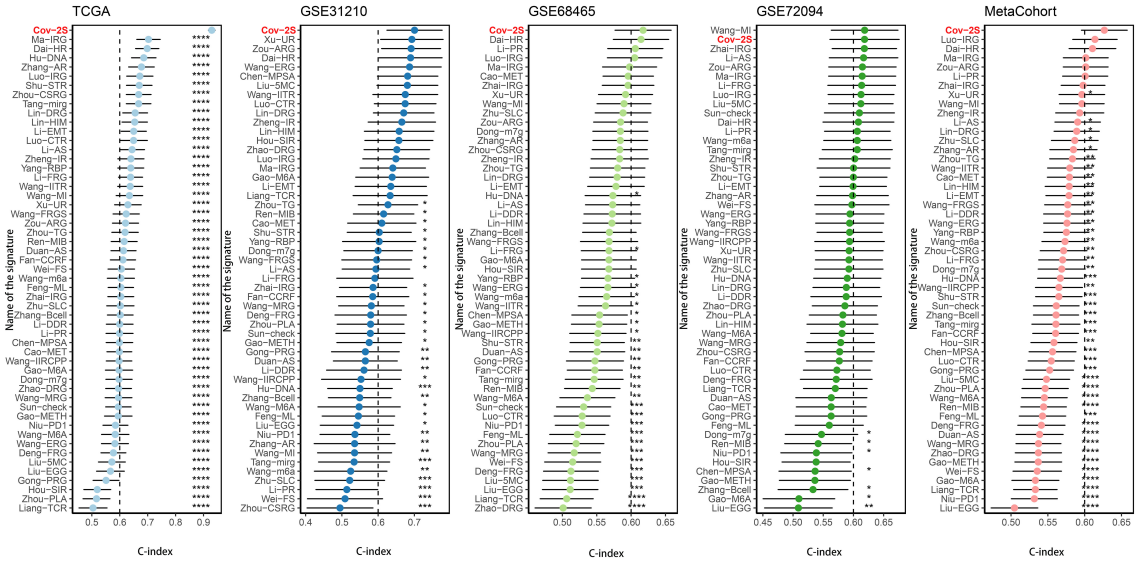

FIGURE 4
Comparison of Cov-2S and other gene expression-based prognostic signatures in LUAD based on the TCGA, GSE31210, GSE68465, GSE72094 and meta-set. ns, not significant. *P < 0.05, **P < 0.01, ***P < 0.001, **** P < 0.0001.

10.3389/fimmu.2024.1366928

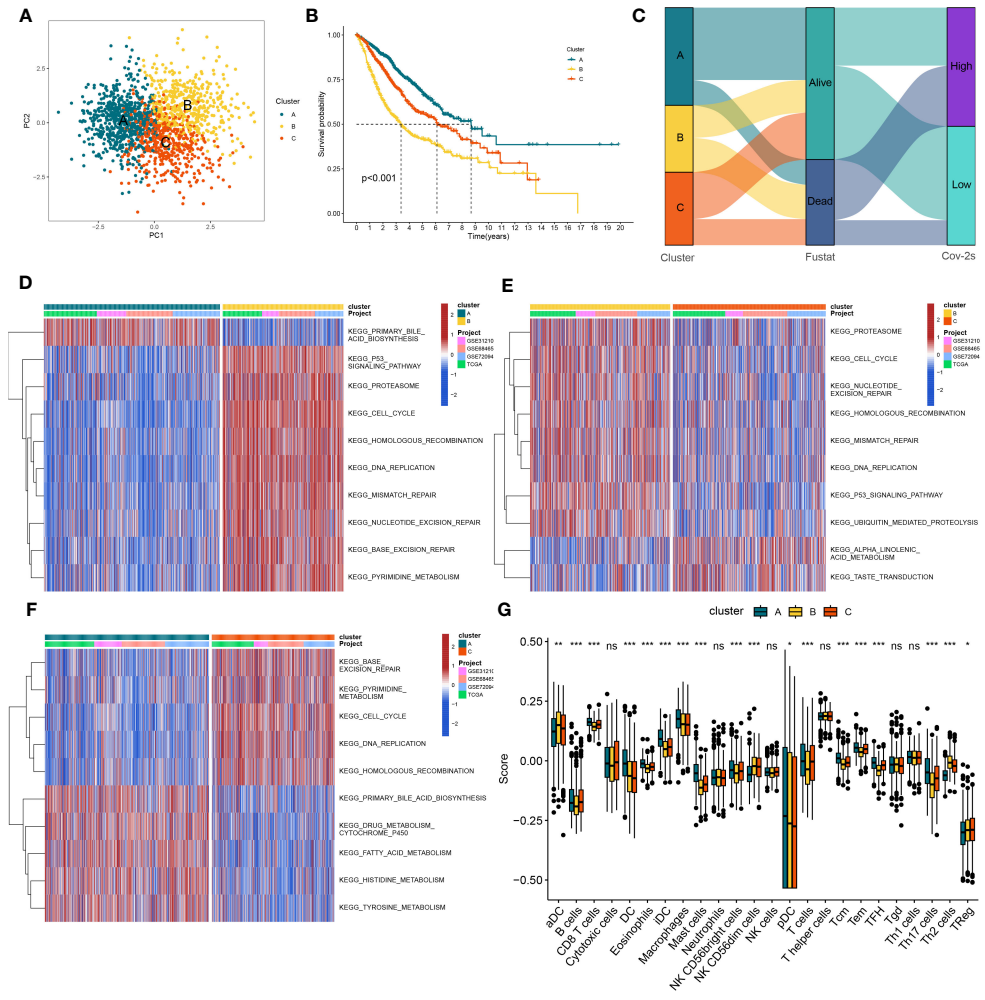

FIGURE 5
The construction of clusters based on Cov-2S. **(A)** PCA plot of three clusters. **(B)** Kaplan-Meier survival analysis between three clusters. **(C)** Alluvial diagram of clusters distributions in groups with different Cov-2S and survival outcomes. **(D-F)** GSVA analysis indicating significant enrichment of pathways in the three clusters. **(G)** The proportion of 24 kinds of immune cells in three clusters. ns, not significant. *P < 0.05, **P < 0.01, ***P < 0.001.

different organs. Cov-2S exhibits significant elevation in organs such as the esophagus, stomach, colon, gallbladder, and uterus in female cancer patients; while Cov-2S exhibits significant elevation in organs such as the lungs, esophagus, stomach, colon, gallbladder, and testes in male cancer patients (Figure 10B).

GGH in LUAD progression

In order to examine the function of Cov-2S in cellular processes, we performed a comparative analysis of relative expression. The expression levels of CENPF, F2RL1, GGH, HOOK1 and PK92 were significantly elevated in LUAD cell lines by qRT-PCR experiment, while FBLN5, PCSK6 were significantly depressed in in LUAD cell lines (Figure 11A). IHC experiments further validated the high expression of GGH protein in LUAD tissues (Figures 11B, C). Given that GGH exhibits the most prominent upregulation in LUAD cells, and there is a lack of prior research on its involvement in LUAD, we have opted to investigate GGH in subsequent experiments. Successful GGH knockdown were detected by qRT-PCR (Figure 12A). The CCK-8 test showed a markedly diminished in cellular growth capacity after transfection with GGH siRNA (Figure 12B). Transfection with GGH siRNA resulted in a significant reduction in the number of colonies formed, as demonstrated by the clonogenic assay (Figure 12C). The results suggest that GGH can inhibit the growth of cells in LUAD. The wound healing assay results, as shown in Figure 12D, demonstrated a reduced wound healing capability in LUAD cells following the silencing of GGH. The outcomes of transwell migration and invasion assays, depicted in Figure 12E, further indicated a decline in the migration and invasion abilities of the cells upon GGH silencing. Moreover, downregulation of GGH enhances the susceptibility of LUAD cells to ispinesib and epothilone-b (Supplementary Figure 5).

Discussion

Cancer remains a leading cause of mortality worldwide (37). The prevalence and death rate of LC have been steadily rising

10.3389/fimmu.2024.1366928

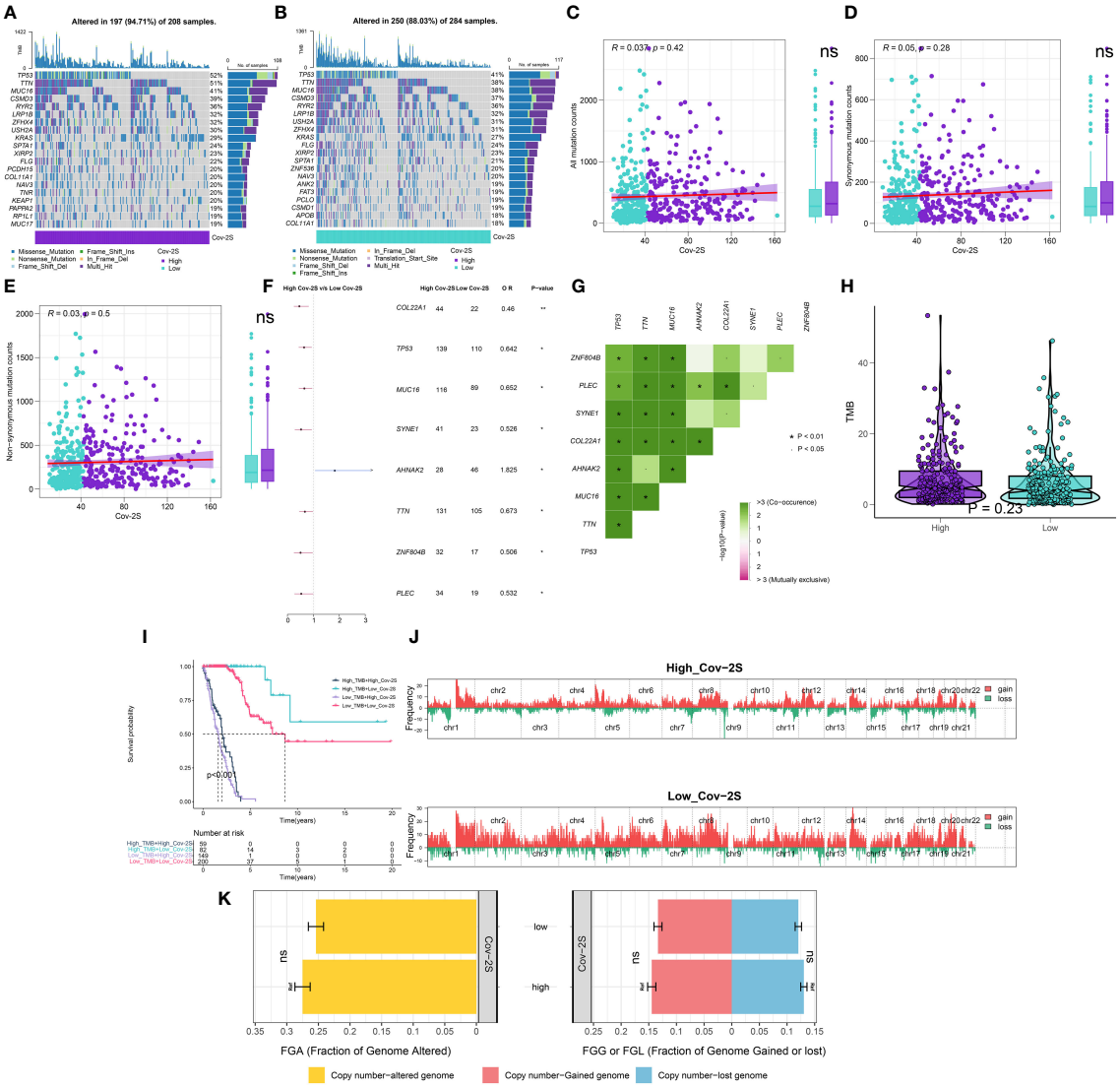

FIGURE 6
Integrated comparisons of somatic mutation and CNVs between high and low Cov-2S groups in the TCGA set. **(A, B)** Waterfall plots showing the mutation information of the top 20 genes with the highest mutation frequency in the Cov-2S groups. **(C-E)** Association between all mutation counts, synonymous mutation counts, nonsynonymous mutation counts, and Cov-2S and their distribution in the Cov-2S groups. **(F)** Differentially mutated genes between high and low Cov-2S groups are displayed as a forest plot. **(G)** Interaction effect of genes mutating differentially in patients in the Cov-2S groups. **(H)** Distribution of TMB in the Cov-2S groups. **(I)** Kaplan–Meier curves for patients stratified by both TMB and Cov-2S. **(J)** Gene fragments profiles with amplification (red) and deletion (green) among the Cov-2S groups. **(K)** Comparison of the fraction of the genome altered, lost, and gained between the Cov-2S groups. ns, not significant. * P < 0.05.

annually (38). LUAD is the primary form of lung cancer, and its occurrence continues to be significant (3). The traditional TNM staging system, although fundamental in cancer diagnosis and management, exhibits considerable limitations in precisely assessing patient prognosis and informing treatment choices. This underscores the necessity for the discovery and implementation of new predictive tools to improve accuracy in prognosis and tailor treatment strategies more effectively (4). The COVID-19 outbreak is evolving into a significant worldwide issue concerning public health. New research indicates that CRGs may have crucial functions in viral infection, and they are also involved in the progression of numerous types of cancer. In LC cells, the study conducted by Kim et al. revealed that the suppression of MUC1-C signaling leads to a decrease in the levels of proteins associated with cell growth and an increase in the levels of proteins associated with cell death following SARS-CoV-2 infection (39). Additionally, a different study indicates that individuals with increased levels of ACE2, TMPRSS2, TLR1, TLR2, and TLR6 in LC are at a higher risk of contracting SARS CoV-2. This can result in a more severe SARS-CoV-2 infection and further contribute to the progression of cancer by activating NF-κB through TLR2 (40). The researches offer valuable starting points for further investigating the connection between COVID-19 and LUAD. This also motivated us to conduct additional bioinformatics analyses and study LUAD samples in

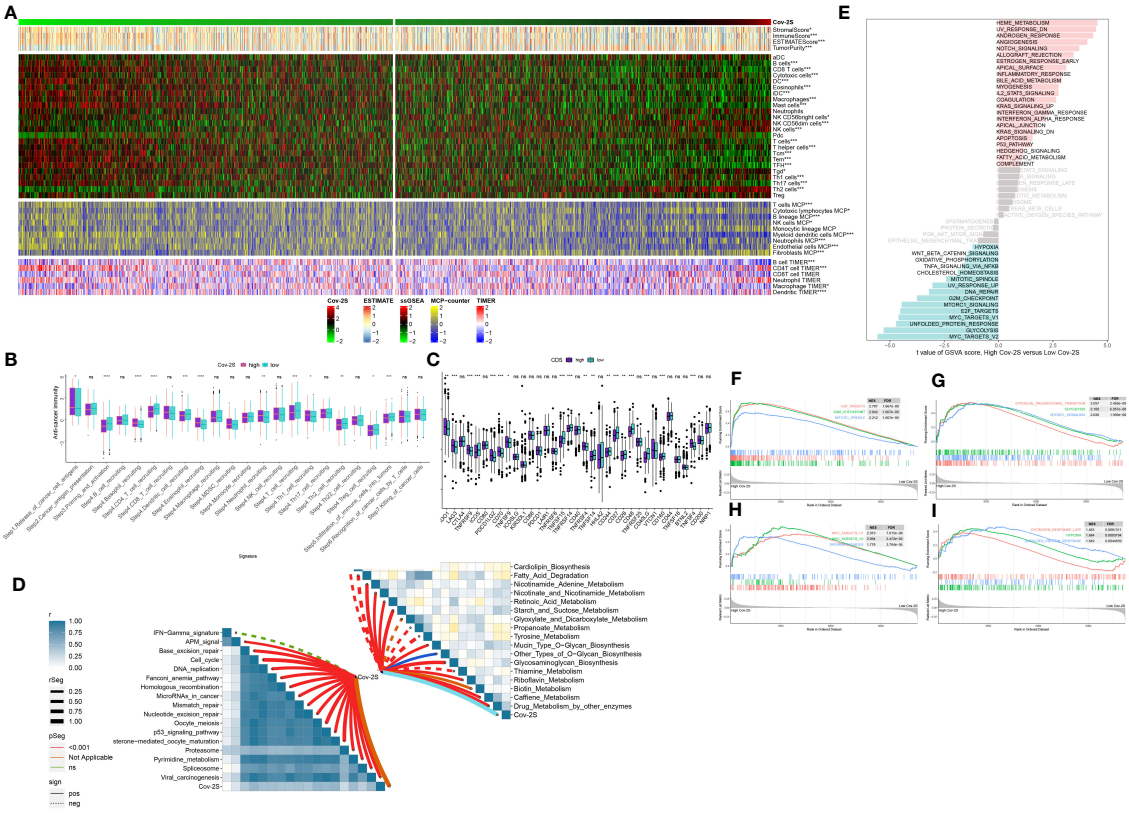

FIGURE 7
Immune-related characteristics of the Cov-2S. **(A)** Heatmap displaying the correlation between the Cov-2S and immune infiltrating cells in the meta-set. **(B)** Boxplot showing the differences of anti-cancer immunity score between Cov-2S groups. **(C)** Comparison of immune checkpoint-related genes levels between Cov-2S groups in the meta-set. **(D)** The correlations between the Cov-2S and immune-related pathways, metabolic pathways based on GSVA of GO and KEGG terms were displayed in butterfly plot. **(E)** The difference in the hallmark gene sets between different Cov-2S groups. **(F-I)** The GSEA results for the 12 overlapping upregulated hallmark pathways in terms of the high Cov-2S groups. ns, not significant. *P < 0.05, **P < 0.01, ***P < 0.001, **** P < 0.0001.

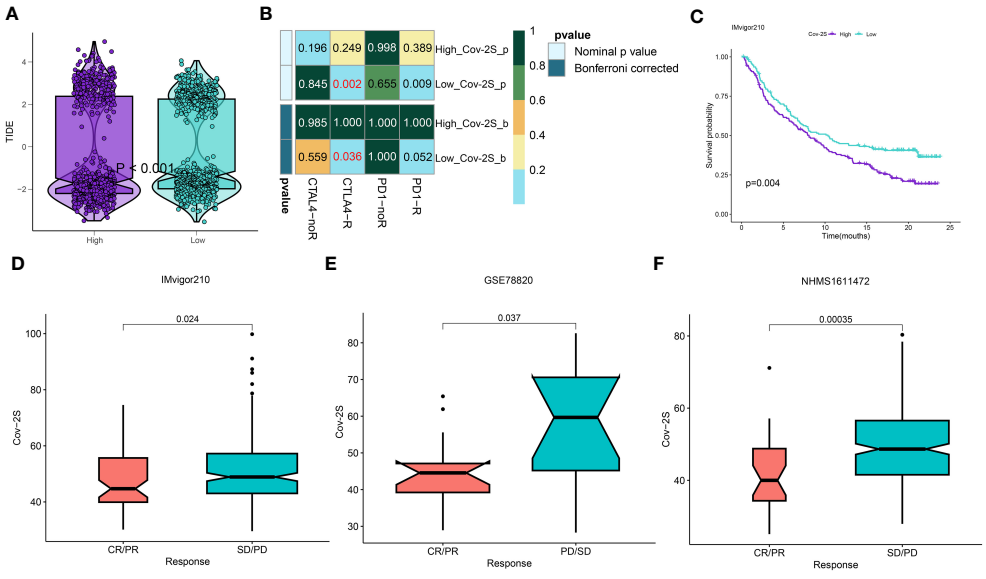

FIGURE 8
Differential putative immunotherapy response for patients from high and low Cov-2S groups. **(A)** Violin plot showing different TIDE scores from patients with different Cov-2S. **(B)** Submap analysis of the meta-set and melanoma patients with detailed immunotherapeutic information. **(C)** Kaplan-Meier curve for patients in high and low Cov-2S groups in the IMvigor210 set. **(D-F)** Box plot showing different Cov-2S from patients with immunotherapy responses in the IMvigor210, GSE78820, NHMS1611472 sets.

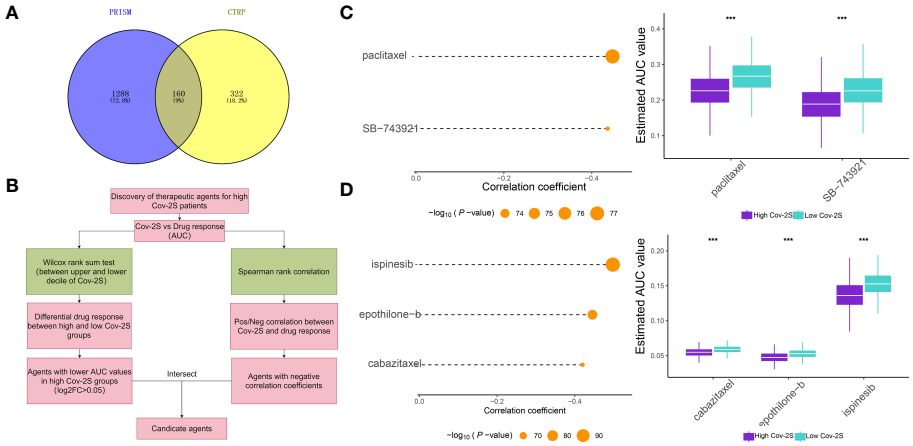

FIGURE 9
Identification of candidate drugs for high Cov-2S patients. **(A)** Data for drug prediction were sourced from the CTRP and PRISM databases. The Venn diagram illustrates the compounds contained within each database. **(B)** The process involved in exploring the drug databases of CTRP and PRISM is depicted in the flowchart. This exploration primarily encompassed the utilization of the Wilcoxon rank sum and Spearman correlation statistical algorithms. **(C)** Spearman's correlation analysis and the analysis of differential drug response were conducted for two compounds derived from CTRP data. **(D)** Spearman's correlation analysis and the analysis of differential drug response were conducted for three compounds derived from PRISM data. ***P < 0.001.

order to gain a deeper understanding of the biological traits and clinical importance of CRGs in LUAD, as well as their potential relevance for LAUD treatments.

In this study, we aim to analyze the complete CRGs as comprehensively as possible. Therefore, we identified 34 DECRGs after collecting 322 CRGs from the HPA database, and subsequently found extensive genomic alterations in these DECRGs through multi-omics data analysis. Univariate cox analysis was conducted using these genes to identify potential prognostic CRGs for LUAD. Subsequently, we incorporated prognostic DECRGs into building a prognostic model for forecasting patient outcomes and performing a patient classification analysis. Based on the prognostic DECRGs expression profile of the TCGA training set, a total of 101 combinations were generated using 10 different machine learning algorithms. Additional assessment in three GEO testing sets demonstrated that the Cov-2S, which was the most suitable model, consisted of the combination of RFS. The Cov-2S demonstrated satisfactory performance in predicting OS in both TCGA and GEO datasets. The Cov-2S demonstrated superior clinical application potential compared to other clinical variables, as indicated by higher values of ROC AUC and C-index in various datasets. Interestingly, compared to the vast majority of previously reported prediction models, the predictive performance of Cov-2S remains superior. Additionally, additional examination indicated that Cov-2S acts as a separate determinant of the OS of patients with LUAD. Then, the median Cov-2S was utilized to classify both groups of participants into high and low Cov-2S groups. In both the TCGA training and GEO testing sets, it was observed that individuals with low Cov-2S had a longer survival time, suggesting that Cov-2S could serve as an unfavorable prognostic indicator.

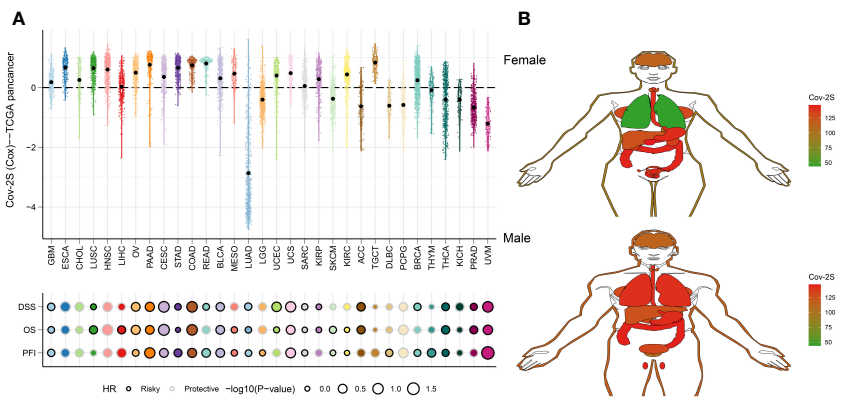

FIGURE 10
Predictive accuracy of the Cov-2S in the TCGA-pancancer set. **(A)** Distribution and predictive value of Cov-2S in solid tumors in the TCGA-pancancer set. **(B)** Differences in the distribution of Cov-2S in tumor tissues in different organs.

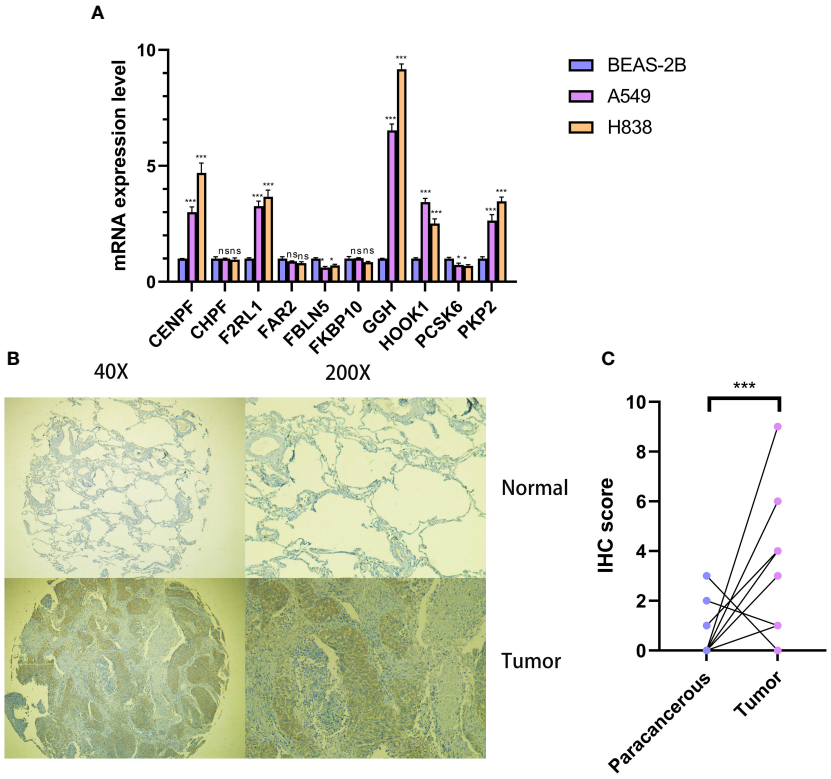

FIGURE 11
Cellular and histological and validation candidate gene expression changes. **(A)** Cov-2S genes expression in cancer and normal cell lines. beta-actin was used as the internal reference gene and experiment was performed in triplicate and at least three times. **(B, C)** IHC analysis of GGH in 10 LUAD and 10 adjacent tissues. ns, not significant. *P < 0.05, ***P < 0.001.

"Hot" and "cold" tumors are an informal concept that represents the immunogenicity of tumors, with the former showing a high infiltration rate (41). On the contrary, "cold" tumors are distinguished by the absence or limited occurrence of lymphocytes in the TME, leading to a lack of response to ICIs therapy (42). Hence, recent research has focused on the potential and reality of transforming cold tumors into hot tumors, revealing the fluctuating alterations in the TME, with the aim of improving the effectiveness of ICIs treatment (43). Significantly, individuals with low Cov-2S exhibited elevated stromal and immune scores, along with reduced tumor purity in comparison to those with high Cov-2S. The interaction between immune cells and tumors was highly intricate, with distinct immune cells performing diverse functions. According to recent research, it has been demonstrated that Th2 cells possess the ability to promote tumors in LC and even in primary NSCLC tumors in humans (44). Current evidence indicates that B cells infiltrating tumors are involved in nearly every phase of LC (45). Cytotoxic cells, known as CD8+ T cells, stimulate antitumor responses by generating IFN-gamma (46). In line with the aforementioned discoveries, we observed that the low Cov-2S group exhibited increased levels of B cells and CD8+ T cells, as well as decreased levels of Th2 cells. These findings provide some insight into the improved OS of LUAD patients in the low Cov-2S group. Furthermore, the levels of immune checkpoints expression and the activities of the anti-tumor immunity cycles were notably increased in the low Cov-2S group. Several hallmarks associated with cancer, such as cell growth, genetic mending, and oxygen deprivation, exhibited greater activity in the high Cov-2S group. Further, this study found that the Cov-2S correlated with many immune-related and metabolic pathways. The collected evidence suggests that Cov-2S potentially plays a role in the progression of LUAD through the regulation of tumor immunity and metabolism. Additionally, patients with low Cov-2S exhibit signs of immune activity within the TME.

Earlier research suggested the comparison of tumors to "hot" and "cold" to explain their responsiveness to immunotherapy (41, 47). Tumors in this category, which have high TME scores, may be better suited for immunotherapy due to their increased presence of activated immunocytes and cells associated with inflammation. Hence, we hypothesized that individuals belonging to the low Cov-2S category might exhibit heightened responsiveness to immunotherapy, leading to extended periods of survival. In order to confirm our hypothesis, we will now examine how Cov-2S performs in terms of prognosis and its response to immunotherapy across different algorithms and datasets that have been treated with ICIs. TIDE has the potential to forecast the result of cancer patients who undergo treatment with initial anti-PD1 or anti-CTLA4 medications (31, 48). A higher TIDE score suggested a

10.3389/fimmu.2024.1366928

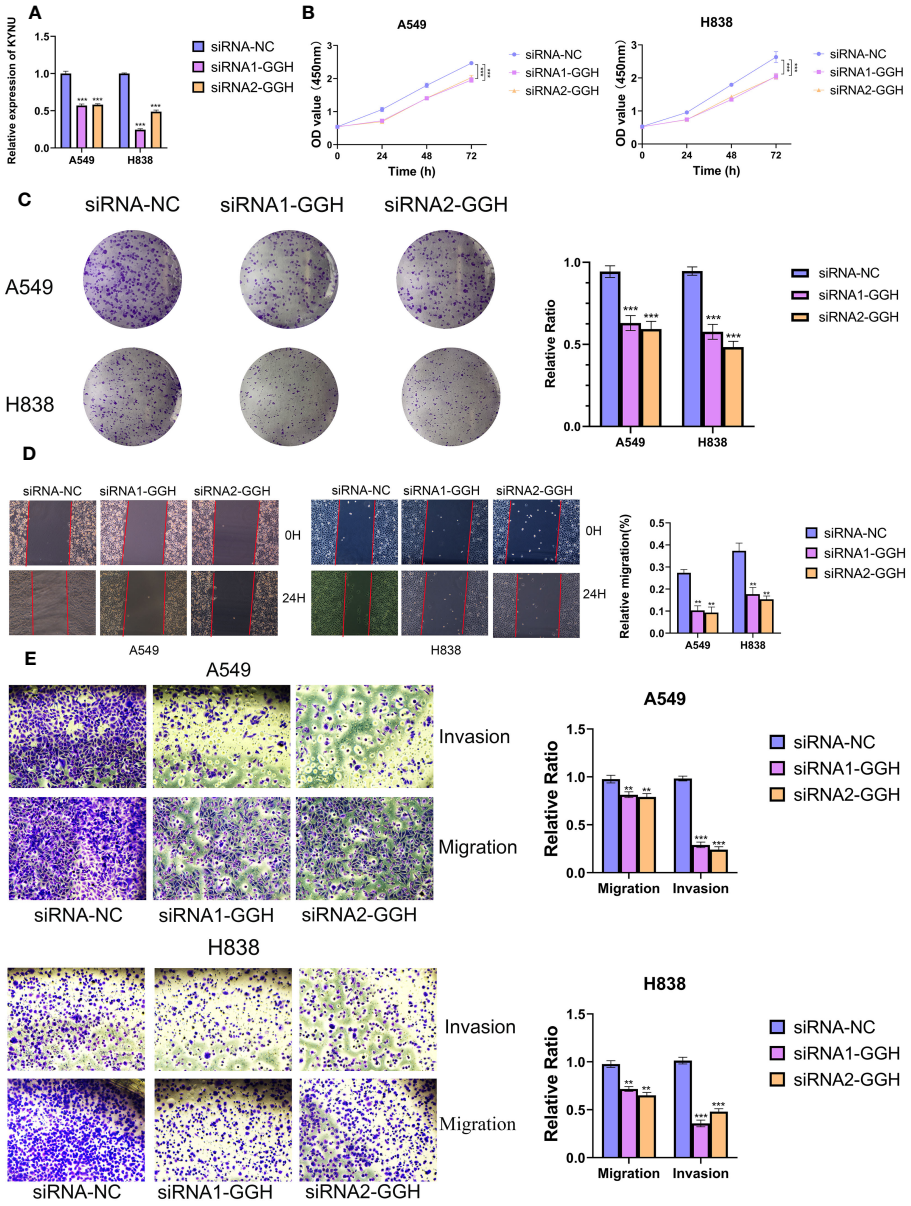

FIGURE 12
GGH promoted proliferation, migration, invasion and inhibited apoptosis of LUAD cell lines. **(A, B)** Knockdown of GGH was confirmed by qRT-PCR. **(C, D)** CCK8 and clone formation assays were performed to assess cell viability and proliferation of A549 and H838 cells. **(E)** Transwell assay was performed to assess cell migration and invasion of A549 and H838 cells. **P < 0.01, ***P < 0.001.

more favorable reaction to immunotherapy. The algorithm is utilized to assess the similarity in gene expression patterns between patients in distinct molecular subtypes and those with metastatic melanoma who received ICIs, facilitating submap analysis (32). The results of submap and TIDE analysis suggested that low Cov-2S was more promising for PD1 and CTLA4 treatment. The Cov-2S exhibited a significant decrease in patients who responded, as observed in the GSE78220, NIHMS1611472, and IMvigor210 datasets, in comparison to patients who did not respond. The performance of Cov-2S in prognosis and predicting immunotherapeutic response was indicated by all these indicators. Since chemotherapy is considered a crucial treatment for LUAD, we additionally examined the IC50 value of typical medications for each LUAD patients. Consequently, LUAD patients with high Cov-2S exhibited lower IC50 values for paclitaxel, SB-743921, ispinesib, epothilone-b, and cabazitaxel, indicating a potential higher susceptibility to chemotherapy in these individuals. Hence, implementing various approaches could enhance the clinical result for individuals. For example, tumors that were considered "hot" were advised to undergo therapy specifically targeting T-cells (49, 50). The sensitivity of "cold" tumors can be improved by combining chemotherapy with T cell enhancement or stimulatory signals (51). Considering the TME score when selecting LUAD treatment could enhance the survival outcome of patients.

In our research, we developed a Cov-2S signature composed of 10 CRGs, which emerged as a promising prognostic predictor for LUAD. Notably, the majority of these genes have been previously reported to be involved in the onset and progression of LC, underscoring their relevance in the disease's pathology. PKP2 is a member of the plaque-bound plakophilins family and is extensively present in epithelial cells (52). PKP2 is overexpressed in LUAD tissues and its high expression correlates with poor outcome of patients. PKP2 overexpression enhances proliferation and invasion of LUAD cells, and this effect is potentiated by EGFR activation (53). Cheng et al. discovered that inhibiting PKP2 methylation reduces its binding affinity to β-catenin, thereby overcoming the radioresistance in LUAD cells (54). CENPF functions as a component of the centromere-kinetochore complex and as an element of the nuclear matrix during G2 phase of interphase (55). CENPF was overexpressed in LUAD tissues and cell lines (56). The progression of LUAD is influenced by both CENPF and ERβ2/5, and inhibiting the expression of ER2/5 can impede the advancement of LUAD through the knockdown of CENPF (57). CHPF, a 775 amino acid type II transmembrane protein belonging to the chondroitin synthase family, was found overexpressed in LC tissues, correlating with reduced OS (58). *In vitro* experiments revealed that CHPF stimulated the proliferation, migration, and invasion of LC cells, as well as induced tumorigenesis *in vivo* (59). FKBP10, an endoplasmic reticulum chaperone with four PPIase domains, exhibits an expression inversely related to the survival of LC patients (60). Through its PPIase activity, FKBP10 mechanistically enhances both cancer growth and stemness. Also, FKBP10 is involved in interactions with ribosomes. The downregulation of FKBP10 has been shown to lead to a reduction in translation elongation, particularly at the start of open reading frames (61). FBLN5, a newly discovered member of the fibulin family, has the ability to inhibit angiogenesis in a manner that relies on the presence of RGD (62). Activation of the ERK pathway induces MMP-7 expression, facilitating LC invasion and metastasis, by promoting epigenetic suppression of FBLN5 (63). F2RL1 belongs to the extensively researched G protein-coupled receptor family, recognized as significant targets in drug development (64). The inhibition of F2RL1 significantly increased the effectiveness of gefitinib in regulating EGFR transactivation, cell survival, movement, and programmed cell death in LC cells (65). Moreover, inhibiting F2RL1 could restrict ERK-induced epithelial-mesenchymal transition (EMT) and immune checkpoints, thereby reducing EGFR transactivation and reactivating osimertinib (66). We conducted qRT-PCR to evaluate the expression of 10 CRGs in LUAD cells, ultimately selecting GGH for experimental validation due to its markedly differential expression and lack of prior reporting in LUAD. IHC assay further confirmed high expression of GGH protein in LUAD tissues. The functional trials revealed that the robust inhibition of LUAD cell growth, proliferation, migration, and invasion was observed when siRNA induced GGH silencing, indicating a potential oncogenic function of GGH in LUAD.

Apart from the encouraging results of this work, we were also aware of the limitations of the present study. Although our research has the merit of using large cohorts from multiple databases for the generation and verification of the Cov-2S, the present study is still retrospective in nature. There is a need for a prospective set study to further validate the utility of the Cov-2S. We conducted preliminary validation of the expression levels and biological functions of key genes in the Cov-2S only in LUAD cells and tissues, further validation in clinical samples and further mechanistic investigation are needed.

Conclusion

In conclusion, the Cov-2S identified in this research is an innovative prognostic indicator that reveals fresh targets for therapy and new theoretical principles for assessing the prognosis and personalized treatment of LUAD. Furthermore, our experiments validated that GGH functioned as a cancer-causing gene that could potentially enhance the advancement of LUAD.

Data availability statement

The datasets presented in this study can be found in online repositories. The names of the repository/repositories and accession number(s) can be found in the article/Supplementary Material.

Ethics statement

The studies involving humans were approved by ethics committee and institutional review board of the Outdo Biotech. Co., Ltd. (SHYJS-CP-1804018). The studies were conducted in accordance with the local legislation and institutional requirements. The participants provided their written informed consent to participate in this study.

Author contributions

YW: Formal analysis, Investigation, Writing – original draft. YX: Writing – original draft, Formal analysis, Validation, Writing – review & editing, Supervision. YD: Formal analysis, Investigation, Writing – original draft. LY: Resources, Writing – review & editing. DW: Visualization, Writing – review & editing. ZY: Writing – review & editing. YZ: Conceptualization, Project administration, Supervision, Writing – review & editing.

Funding

The author(s) declare financial support was received for the research, authorship, and/or publication of this article. This research was funded by the incubated thesis capital of the People's Hospital of Deyang City (Grant number FHS202401).

Conflict of interest

The authors declare that the research was conducted in the absence of any commercial or financial relationships that could be construed as a potential conflict of interest.

Publisher's note

All claims expressed in this article are solely those of the authors and do not necessarily represent those of their affiliated organizations, or those of the publisher, the editors and the reviewers. Any product that may be evaluated in this article, or claim that may be made by its manufacturer, is not guaranteed or endorsed by the publisher.

Supplementary material

The Supplementary Material for this article can be found online at: https://www.frontiersin.org/articles/10.3389/fimmu.2024.1366928/full#supplementary-material

References

1. Bray F, Ferlay J, Soerjomataram I, Siegel RL, Torre LA, Jemal A. Global cancer statistics 2018: GLOBOCAN estimates of incidence and mortality worldwide for 36 cancers in 185 countries. *CA Cancer J Clin*. (2018) 68:394–424. doi: 10.3322/caac.21492

2. Basu A, Bodycombe NE, Cheah JH, Price EV, Liu K, Schaefer GI, et al. An interactive resource to identify cancer genetic and lineage dependencies targeted by small molecules. *Cell*. (2013) 154:1151–61. doi: 10.1016/j.cell.2013.08.003

3. Siegel RL, Miller KD, Wagle NS, Jemal A. Cancer statistics, 2023. *CA Cancer J Clin*. (2023) 73:17–48. doi: 10.3322/caac.21763

4. Thai AA, Solomon BJ, Sequist LV, Gainor JF, Heist RS. Lung cancer. *Lancet*. (2021) 398:535–54. doi: 10.1016/s0140-6736(21)00312-3

5. Duma N, Santana-Davila R, Molina JR. Non-small cell lung cancer: epidemiology, screening, diagnosis, and treatment. *Mayo Clin Proc*. (2019) 94:1623–40. doi: 10.1016/j.mayocp.2019.01.013

6. Sholl LM. Biomarkers in lung adenocarcinoma: a decade of progress. *Arch Pathol Lab Med*. (2015) 139:469–80. doi: 10.5858/arpa.2014-0128-RA

7. Tavernari D, Battistello E, Dheilly E, Petruzzella AS, Mina M, Sordet-Dessimoz J, et al. Nongenetic evolution drives lung adenocarcinoma spatial heterogeneity and progression. *Cancer Discovery*. (2021) 11:1490–507. doi: 10.1158/2159-8290.Cd-20-1274

8. Zhang C, Zhang J, Xu FP, Wang YG, Xie Z, Su J, et al. Genomic landscape and immune microenvironment features of preinvasive and early invasive lung adenocarcinoma. *J Thorac Oncol*. (2019) 14:1912–23. doi: 10.1016/j.jtho.2019.07.031

9. Safiabadi Tali SH, LeBlanc JJ, Sadiq Z, Oyewunmi OD, Camargo C, Nikpour B, et al. Tools and techniques for severe acute respiratory syndrome coronavirus 2 (SARS-coV-2)/COVID-19 detection. *Clin Microbiol Rev*. (2021) 34(3):e00228-20. doi: 10.1128/cmr.00228-20

10. Dai M, Liu D, Liu M, Zhou F, Li G, Chen Z, et al. Patients with cancer appear more vulnerable to SARS-coV-2: A multicenter study during the COVID-19 outbreak. *Cancer Discovery*. (2020) 10:783–91. doi: 10.1158/2159-8290.Cd-20-0422

11. Liang W, Guan W, Chen R, Wang W, Li J, Xu K, et al. Cancer patients in SARS-CoV-2 infection: a nationwide analysis in China. *Lancet Oncol*. (2020) 21:335–7. doi: 10.1016/s1470-2045(20)30096-6

12. White MK, Pagano JS, Khalili K. Viruses and human cancers: a long road of discovery of molecular paradigms. *Clin Microbiol Rev*. (2014) 27:463–81. doi: 10.1128/cmr.00124-13

13. Müller-Coan BG, Caetano BFR, Pagano JS, Elgui de Oliveira D. Cancer progression goes viral: the role of oncoviruses in aggressiveness of Malignancies. *Trends Cancer*. (2018) 4:485–98. doi: 10.1016/j.trecan.2018.04.006

14. Mesri EA, Feitelson MA, Munger K. Human viral oncogenesis: a cancer hallmarks analysis. *Cell Host Microbe*. (2014) 15:266–82. doi: 10.1016/j.chom.2014.02.011

15. Krump NA, You J. Molecular mechanisms of viral oncogenesis in humans. *Nat Rev Microbiol*. (2018) 16:684–98. doi: 10.1038/s41579-018-0064-6

16. Su S, Wong G, Shi W, Liu J, Lai ACK, Zhou J, et al. Epidemiology, genetic recombination, and pathogenesis of coronaviruses. *Trends Microbiol*. (2016) 24:490–502. doi: 10.1016/j.tim.2016.03.003

17. Geisslinger F, Vollmar AM, Bartel K. Cancer patients have a higher risk regarding COVID-19 - and vice versa? *Pharm (Basel)*. (2020) 13(7):143. doi: 10.3390/ph13070143

18. Song D, Jia X, Liu X, Hu L, Lin K, Xiao T, et al. Identification of the receptor of oncolytic virus M1 as a therapeutic predictor for multiple solid tumors. *Signal Transduct Target Ther*. (2022) 7:100. doi: 10.1038/s41392-022-00921-3

19. Jiang F, Lu DF, Zhan Z, Yuan GQ, Liu GJ, Gu JY, et al. SARS-coV-2 pattern provides a new scoring system and predicts the prognosis and immune therapeutic response in glioma. *Cells*. (2022) 11(24):3997. doi: 10.3390/cells11243997

20. Wang Z, Yuan Q, Chen X, Luo F, Shi X, Guo F, et al. A prospective prognostic signature for pancreatic adenocarcinoma based on ubiquitination-related mRNA-lncRNA with experimental validation in *vitro* and vivo. *Funct Integr Genomics*. (2023) 23:263. doi: 10.1007/s10142-023-01158-1

21. Subramanian A, Tamayo P, Mootha VK, Mukherjee S, Ebert BL, Gillette MA, et al. Gene set enrichment analysis: a knowledge-based approach for interpreting genome-wide expression profiles. *Proc Natl Acad Sci USA*. (2005) 102:15545–50. doi: 10.1073/pnas.0506580102

22. Liu Z, Liu L, Weng S, Guo C, Dang Q, Xu H, et al. Machine learning-based integration develops an immune-derived lncRNA signature for improving outcomes in colorectal cancer. *Nat Commun*. (2022) 13:816. doi: 10.1038/s41467-022-28421-6

23. Heagerty PJ, Lumley T, Pepe MS. Time-dependent ROC curves for censored survival data and a diagnostic marker. *Biometrics*. (2000) 56:337–44. doi: 10.1111/j.0006-341X.2000.00337.x

24. Wilkerson MD, Hayes DN. ConsensusClusterPlus: a class discovery tool with confidence assessments and item tracking. *Bioinformatics*. (2010) 26:1572–3. doi: 10.1093/bioinformatics/btq170

25. Reich M, Liefeld T, Gould J, Lerner J, Tamayo P, Mesirov JP. GenePattern 2.0. *Nat Genet*. (2006) 38:500–1. doi: 10.1038/ng0506-500

26. Xu L, Deng C, Pang B, Zhang X, Liu W, Liao G, et al. TIP: A web server for resolving tumor immunophenotype profiling. *Cancer Res*. (2018) 78:6575–80. doi: 10.1158/0008-5472.Can-18-0689

27. Yoshihara K, Shahmoradgoli M, Martínez E, Vegesna R, Kim H, Torres-Garcia W, et al. Inferring tumour purity and stromal and immune cell admixture from expression data. *Nat Commun*. (2013) 4:2612. doi: 10.1038/ncomms3612

28. Li T, Fan J, Wang B, Traugh N, Chen Q, Liu JS, et al. TIMER: A web server for comprehensive analysis of tumor-infiltrating immune cells. *Cancer Res*. (2017) 77:e108–10. doi: 10.1158/0008-5472.Can-17-0307

29. Becht E, Giraldo NA, Lacroix L, Buttard B, Elarouci N, Petitprez F, et al. Estimating the population abundance of tissue-infiltrating immune and stromal cell populations using gene expression. *Genome Biol*. (2016) 17:218. doi: 10.1186/s13059-016-1070-5

30. Yi M, Nissley DV, McCormick F, Stephens RM. ssGSEA score-based Ras dependency indexes derived from gene expression data reveal potential Ras addiction mechanisms with possible clinical implications. *Sci Rep*. (2020) 10:10258. doi: 10.1038/s41598-020-66986-8

31. Jiang P, Gu S, Pan D, Fu J, Sahu A, Hu X, et al. Signatures of T cell dysfunction and exclusion predict cancer immunotherapy response. *Nat Med*. (2018) 24:1550–8. doi: 10.1038/s41591-018-0136-1

32. Hoshida Y, Brunet JP, Tamayo P, Golub TR, Mesirov JP. Subclass mapping: identifying common subtypes in independent disease data sets. *PloS One*. (2007) 2:e1195. doi: 10.1371/journal.pone.0001195

33. Seashore-Ludlow B, Rees MG, Cheah JH, Cokol M, Price EV, Coletti ME, et al. Harnessing connectivity in a large-scale small-molecule sensitivity dataset. *Cancer Discovery*. (2015) 5:1210–23. doi: 10.1158/2159-8290.Cd-15-0235

34. Anghel CV, Quon G, Haider S, Nguyen F, Deshwar AG, Morris QD, et al. ISOpureR: an R implementation of a computational purification algorithm of mixed tumour profiles. *BMC Bioinf*. (2015) 16:156. doi: 10.1186/s12859-015-0597-x

35. Geeleher P, Cox N, Huang RS. pRRophetic: an R package for prediction of clinical chemotherapeutic response from tumor gene expression levels. *PloS One*. (2014) 9:e107468. doi: 10.1371/journal.pone.0107468

36. Zhang Y, Wang Y, Chen J, Xia Y, Huang Y. A programmed cell death-related model based on machine learning for predicting prognosis and immunotherapy responses in patients with lung adenocarcinoma. *Front Immunol*. (2023) 14:1183230. doi: 10.3389/fimmu.2023.1183230

37. Liu S, Tian W, Ma Y, Li J, Yang J, Li B. Serum exosomal proteomics analysis of lung adenocarcinoma to discover new tumor markers. *BMC Cancer*. (2022) 22:279. doi: 10.1186/s12885-022-09366-x

38. Bade BC, Dela Cruz CS. Lung cancer 2020: epidemiology, etiology, and prevention. *Clin Chest Med*. (2020) 41:1–24. doi: 10.1016/j.ccm.2019.10.001

39. Kim D, Maharjan S, Kim J, Park S, Park JA, Park BK, et al. MUC1-C influences cell survival in lung adenocarcinoma Calu-3 cells after SARS-CoV-2 infection. *BMB Rep*. (2021) 54:425–30. doi: 10.5483/BMBRep.2021.54.8.018

40. Kim MJ, Kim JY, Shin JH, Son J, Kang Y, Jeong SK, et al. The SARS-CoV-2 spike protein induces lung cancer migration and invasion in a TLR2-dependent manner. *Cancer Commun (Lond)*. (2023) 44(2):273–277. doi: 10.1002/cac2.12485

41. Galon J, Bruni D. Approaches to treat immune hot, altered and cold tumours with combination immunotherapies. *Nat Rev Drug Discovery*. (2019) 18:197–218. doi: 10.1038/s41573-018-0007-y

42. Ochoa de Olza M, Navarro Rodrigo B, Zimmermann S, Coukos G. Turning up the heat on non-immunoreactive tumours: opportunities for clinical development. *Lancet Oncol*. (2020) 21:e419–30. doi: 10.1016/s1470-2045(20)30234-5

43. Hu R, Han Q, Zhang J. STAT3: A key signaling molecule for converting cold to hot tumors. *Cancer Lett*. (2020) 489:29–40. doi: 10.1016/j.canlet.2020.05.035

44. Zhong R, Zhang Y, Chen D, Cao S, Han B, Zhong H. Single-cell RNA sequencing reveals cellular and molecular immune profile in a Pembrolizumab-responsive PD-L1-negative lung cancer patient. *Cancer Immunol Immunother*. (2021) 70:2261–74. doi: 10.1007/s00262-021-02848-0

45. Wang SS, Liu W, Ly D, Xu H, Qu L, Zhang L. Tumor-infiltrating B cells: their role and application in anti-tumor immunity in lung cancer. *Cell Mol Immunol*. (2019) 16:6–18. doi: 10.1038/s41423-018-0027-x

46. St Paul M, Ohashi PS. The roles of CD8(+) T cell subsets in antitumor immunity. *Trends Cell Biol*. (2020) 30:695–704. doi: 10.1016/j.tcb.2020.06.003

47. Galon J, Costes A, Sanchez-Cabo F, Kirilovsky A, Mlecnik B, Lagorce-Pagès C, et al. Type, density, and location of immune cells within human colorectal tumors predict clinical outcome. *Science*. (2006) 313:1960–4. doi: 10.1126/science.1129139

48. Fu J, Li K, Zhang W, Wan C, Zhang J, Jiang P, et al. Large-scale public data reuse to model immunotherapy response and resistance. *Genome Med*. (2020) 12:21. doi: 10.1186/s13073-020-0721-z

49. Buchbinder EI, Desai A. CTLA-4 and PD-1 pathways: similarities, differences, and implications of their inhibition. *Am J Clin Oncol*. (2016) 39:98–106. doi: 10.1097/coc.0000000000000239

50. Hellmann MD, Friedman CF, Wolchok JD. Combinatorial cancer immunotherapies. *Adv Immunol*. (2016) 130:251–77. doi: 10.1016/bs.ai.2015.12.005

51. Whiteside TL, Demaria S, Rodriguez-Ruiz ME, Zarour HM, Melero I. Emerging opportunities and challenges in cancer immunotherapy. *Clin Cancer Res*. (2016) 22:1845–55. doi: 10.1158/1078-0432.Ccr-16-0049

52. Bass-Zubek AE, Godsel LM, Delmar M, Green KJ. Plakophilins: multifunctional scaffolds for adhesion and signaling. *Curr Opin Cell Biol*. (2009) 21:708–16. doi: 10.1016/j.ceb.2009.07.002

53. Hao XL, Tian Z, Han F, Chen JP, Gao LY, Liu JY. Plakophilin-2 accelerates cell proliferation and migration through activating EGFR signaling in lung adenocarcinoma. *Pathol Res Pract*. (2019) 215:152438. doi: 10.1016/j.prp.2019.152438

54. Cheng C, Pei X, Li SW, Yang J, Li C, Tang J, et al. CRISPR/Cas9 library screening uncovered methylated PKP2 as a critical driver of lung cancer radioresistance by stabilizing β-catenin. *Oncogene*. (2021) 40:2842–57. doi: 10.1038/s41388-021-01692-x

55. Liao H, Winkfein RJ, Mack G, Rattner JB, Yen TJ. CENP-F is a protein of the nuclear matrix that assembles onto kinetochores at late G2 and is rapidly degraded after mitosis. *J Cell Biol*. (1995) 130:507–18. doi: 10.1083/jcb.130.3.507

56. Li MX, Zhang MY, Dong HH, Li AJ, Teng HF, Liu AL, et al. Overexpression of CENPF is associated with progression and poor prognosis of lung adenocarcinoma. *Int J Med Sci*. (2021) 18:494–504. doi: 10.7150/ijms.49041

57. Hexiao T, Yuquan B, Lecai X, Yanhong W, Li S, Weidong H, et al. Knockdown of CENPF inhibits the progression of lung adenocarcinoma mediated by ERβ2/5 pathway. *Aging (Albany NY)*. (2021) 13:2604–25. doi: 10.18632/aging.202303

58. Siebert JR, Conta Steencken A, Osterhout DJ. Chondroitin sulfate proteoglycans in the nervous system: inhibitors to repair. *BioMed Res Int*. (2014) 2014:845323. doi: 10.1155/2014/845323

59. Cao C, Liu Y, Wang Q, Zhao J, Shi M, Zheng J. Expression of CHPF modulates cell proliferation and invasion in lung cancer. *Braz J Med Biol Res*. (2020) 53:e9021. doi: 10.1590/1414-431x20209021

60. Chen Y, Terajima M, Banerjee P, Guo H, Liu X, Yu J, et al. FKBP65-dependent peptidyl-prolyl isomerase activity potentiates the lysyl hydroxylase 2-driven collagen cross-link switch. *Sci Rep*. (2017) 7:46021. doi: 10.1038/srep46021

61. Ramadori G, Ioris RM, Villanyi Z, Firnkes R, Panasenko OO, Allen G, et al. FKBP10 regulates protein translation to sustain lung cancer growth. *Cell Rep*. (2020) 30:3851–3863.e6. doi: 10.1016/j.celrep.2020.02.082

62. Albig AR, Neil JR, Schiemann WP. Fibulins 3 and 5 antagonize tumor angiogenesis in *vivo*. *Cancer Res*. (2006) 66:2621–9. doi: 10.1158/0008-5472.Can-04-4096

63. Yue W, Sun Q, Landreneau R, Wu C, Siegfried JM, Yu J, et al. Fibulin-5 suppresses lung cancer invasion by inhibiting matrix metalloproteinase-7 expression. *Cancer Res*. (2009) 69:6339–46. doi: 10.1158/0008-5472.Can-09-0398

64. Pawar NR, Buzza MS, Antalis TM. Membrane-anchored serine proteases and protease-activated receptor-2-mediated signaling: co-conspirators in cancer progression. *Cancer Res*. (2019) 79:301–10. doi: 10.1158/0008-5472.Can-18-1745

65. Jiang Y, Zhuo X, Fu X, Wu Y, Mao C. Targeting PAR2 overcomes gefitinib resistance in non-small-cell lung cancer cells through inhibition of EGFR transactivation. *Front Pharmacol*. (2021) 12:625289. doi: 10.3389/fphar.2021.625289

66. Jiang Y, Zhuo X, Wu Y, Fu X, Mao C. PAR2 blockade reverses osimertinib resistance in non-small-cell lung cancer cells via attenuating ERK-mediated EMT and PD-L1 expression. *Biochim Biophys Acta Mol Cell Res*. (2022) 1869:119144. doi: 10.1016/j.bbamcr.2021.119144

frontiers | Frontiers in Immunology

TYPE Original Research
PUBLISHED 02 April 2024
DOI 10.3389/fimmu.2024.1362970

OPEN ACCESS

EDITED BY
Takaji Matsutani,
Maruho, Japan

REVIEWED BY
Yan Lv,
Capital Medical University, China
Ling Xu,
Jinan University, China

*CORRESPONDENCE
Youwen Deng
drywdeng@163.com
Renfeng Liu
524412608@qq.com
Xiaofang Zang
xy3zxf@yeah.net

†These authors have contributed equally to this work and share first authorship

RECEIVED 29 December 2023
ACCEPTED 18 March 2024
PUBLISHED 02 April 2024

CITATION
Fan Q, Wang Y, Cheng J, Pan B, Zang X, Liu R and Deng Y (2024) Single-cell RNA-seq reveals T cell exhaustion and immune response landscape in osteosarcoma. *Front. Immunol.* 15:1362970. doi: 10.3389/fimmu.2024.1362970

Single-cell RNA-seq reveals T cell exhaustion and immune response landscape in osteosarcoma

Qizhi Fan[1†], Yiyan Wang[1†], Jun Cheng[1], Boyu Pan[2], Xiaofang Zang[1*], Renfeng Liu[1*] and Youwen Deng[1*]

[1]Department of Spine Surgery, Third Xiangya Hospital, Central South University, Changsha, China, [2]Department of Orthopedics, Third Hospital of Changsha, Changsha, China

Background: T cell exhaustion in the tumor microenvironment has been demonstrated as a substantial contributor to tumor immunosuppression and progression. However, the correlation between T cell exhaustion and osteosarcoma (OS) remains unclear.

Methods: In our present study, single-cell RNA-seq data for OS from the GEO database was analysed to identify CD8+ T cells and discern CD8+ T cell subsets objectively. Subgroup differentiation trajectory was then used to pinpoint genes altered in response to T cell exhaustion. Subsequently, six machine learning algorithms were applied to develop a prognostic model linked with T cell exhaustion. This model was subsequently validated in the TARGETs and Meta cohorts. Finally, we examined disparities in immune cell infiltration, immune checkpoints, immune-related pathways, and the efficacy of immunotherapy between high and low TEX score groups.

Results: The findings unveiled differential exhaustion in CD8+ T cells within the OS microenvironment. Three genes related to T cell exhaustion (RAD23A, SAC3D1, PSIP1) were identified and employed to formulate a T cell exhaustion model. This model exhibited robust predictive capabilities for OS prognosis, with patients in the low TEX score group demonstrating a more favorable prognosis, increased immune cell infiltration, and heightened responsiveness to treatment compared to those in the high TEX score group.

Conclusion: In summary, our research elucidates the role of T cell exhaustion in the immunotherapy and progression of OS, the prognostic model constructed based on T cell exhaustion-related genes holds promise as a potential method for prognostication in the management and treatment of OS patients.

KEYWORDS

osteosarcoma, T cell exhaustion, tumor immune microenvironment, prognosis, immunotherapy

1 Introduction

Osteosarcoma (OS) is the most prevalent aggressive bone tumor occurring in children and adolescents, constituting the majority of all bone tumor cases (1). The conventional approach to OS entails a blend of surgery and rigorous multi-agent chemotherapy. However, the prognosis for OS patients remains exceedingly grim, primarily attributed to delayed diagnosis and early-stage distant metastasis (2). Therefore, it is crucial to explore innovative and efficacious therapies aimed at enhancing the prognosis of OS patients.

Immunotherapy holds significant promise in the treatment of malignant tumors in humans, numerous recent studies have highlighted its considerable potential in tumor therapy, with preclinical trials providing robust support (3). Immune checkpoint inhibitors (ICIs) exhibit considerable potential for immunotherapy in OS. They can navigate the genomic complexity of OS, leading to enhanced overall outcomes (4). Although immunotherapy for OS has demonstrated promising therapeutic effects in some studies, it has yet to substantially improve patient prognosis (5, 6). In clinical trials of OS, the response to ICIs has not been favorable and trial results are not yet satisfactory (7). This may be attributed to the immune microenvironment in OS, which suppresses T cell function (8). Immune cells constitute the cellular foundation of immunotherapy, of which $CD8^+$ T cells serving as a pivotal component of cancer immunotherapy (9). Activated $CD8^+$ T cells mature into cytotoxic T lymphocytes (CTLs) and represent a key component of the immune system's antitumor response, CTLs are associated with increased survival rates in various types of cancer and play a crucial role in immune surveillance, targeting and eliminating cancer cells (10). The optimal approach for achieving tumor eradication will likely entail a combination of therapies that promote immune activation and T cell initiation, counteract immunosuppressive signals in the tumor microenvironment, and sustain the presence of T cells in cancerous tissue.

T cell exhaustion entails a progressive, hierarchical, and negatively regulatory process affecting T cells within the tumor microenvironment (11). Classical inhibitors targeting PD-1 and CTLA-4 largely exert their anti-tumor effects by mitigating functional exhaustion (12). However, the precise underlying mechanisms of these inhibitors necessitate further investigation. The recent advancement of biomarkers unveiled potential molecular regulatory targets for $CD8^+$ T cells in the intricate tumor heterogeneity of OS. Moreover, the potential correlation between alterations in exhaustion expression profiles and immune checkpoints has presented avenues for research (13).

In this study, we aim to delve into potential molecular regulatory targets and core regulatory genes associated with T cell exhaustion in the intricate tumor heterogeneity of OS. We developed a multi-biomarker model based on genes linked to T cell exhaustion, which functions in evaluating the tumor microenvironment, predicting immunotherapy response, and forecasting the prognosis of diverse OS patients. It has great potential to play a vital role in guiding clinical practice in the future.

2 Methods

2.1 Obtaining the raw data

The single-cell sequencing data (GSE162454), along with microarray data (GSE16091 and GSE21257) pertaining to OS, were acquired from the GEO database (http://www.ncbi.nlm.nih.gov/geo). Additionally, data from 84 distinct OS patients' samples were retrieved from the TARGETs database. All datasets were accompanied by clinical and prognostic information, which was employed for subsequent analyses.

2.2 Data processing of single-cell RNA sequence

Data analysis and quality assessment were conducted using the R package "Seurat" (version 4.3.0; http://satijalab.org/seurat/). Cells with expression of fewer than 250 genes or with a percentage of mitochondrial genes exceeding 20% of the total expressed genes were excluded from the analysis. Additionally, cells with unique molecular identifiers (UMI) resulting in log10(UMI) > 0.80 were also removed. Subsequently, potential doublets were identified and eliminated using the R package "DoubletDecon" (version 1.1.6; http://EDePasquale/DoubletDecon).

2.3 Data integration and dimensionality reduction

The feature counts for each cell underwent a transformation, involving division by the total counts for that cell, followed by multiplication by 10,000. Subsequently, the results were logarithmically transformed and then normalized by adding 1, thus preventing the computation of the logarithm of 0. Before proceeding with the normalization of the expression matrix, the top 2000 highly variable genes (HVGs) were identified, centered, and scaled. Subsequent to this, a principal component analysis (PCA) was conducted based on these HVGs. Following that, the R package "Harmony" (https://github.com/immunogenomics/Harmony) was employed to integrate the cellular data from six samples and mitigate any potential batch effects.

2.4 Cell-clustering and annotation

The clustering analysis relied on the embedding of the Harmony algorithm, executed through the "FindNeighbors" and "FindClusters" functions within the "Seurat" package. The resulting clusters were visualized on a two-dimensional plot generated via the UMAP method. For subcluster analysis, akin procedures were applied, encompassing variable gene identification, dimensionality reduction, Harmony for cell integration, and cluster identification

for the distinct clusters derived from the overall analysis. The annotation of clusters was performed using established cellular markers drawn from the literature. Detailed information regarding the cellular markers can be found in the Supplementary Tables.

2.5 Identification and analysis of $CD8^+$ T cell subtypes

$CD8^+$ T cells were isolated and subsequently re-clustered using the "Seurat" package in R. Single-cell pseudotime trajectories were constructed employing the "Monocle2" package in R. Following this, a weighted correlation network analysis (WGCNA) was conducted to identify the core gene sets within $CD8^+$ T cellular clusters using the "hdWGCNA" package in R. To explore intercellular communication between all cell clusters, the R package "Cellchat" was utilized. The levels of immune checkpoint molecules between clusters were assessed based on the immune checkpoint expression profile. Differential functional status regarding Gene Ontology (GO) and KEGG pathways for each $CD8^+$ T cell cluster were analyzed using the "ClusterProfiler" R package. Additionally, the GSEA pathways obtained from MSigDB (gsea-msigdb.org) were evaluated using the "fgsea" R package. Furthermore, differences in HALLMARK pathways between the clusters were determined through gene set variation analysis (GSVA) using the "GSVA" R package.

2.6 Construction and validation of the T cell exhaustion signature

The $CD8^+$ T cell exhaustion genes with prognostic potential in the TARGETs dataset were identified through Univariate Cox regression analysis ($P<0.05$). Subsequently, a combination of six machine learning algorithms was employed, which included the least absolute shrinkage and selection operator (LASSO) Cox regression algorithm (14), Boruta feature selection algorithm (15), survival support vector machine (survival-SVM) based on 10-fold cross-validation (16), Boosting in Cox regression (Cox-boost) (17), Extreme Gradient Boosting(XG-boost) (18), and generalized boosted regression modeling (GBM) (19), to further refine the valuable T cell exhaustion signature. In constructing the model, the output of the biomarkers from the machine learning models was intersected, followed by the utilization of multiple Cox regression to calculate the weight of each gene. The TEX-score formula is as follows:

$$\begin{aligned} \text{TEX} - \text{Score} = \text{X1}(&\text{coefficient} \quad \text{of} \quad \text{multi} \\ &- \text{COX} \quad \text{of} \quad \text{gene1}) * \text{Y1}(\text{expression} \\ &- \text{level} \quad \text{of} \quad \text{gene1}) + \text{X2} * \text{Y2} + \text{X3} * \text{Y3} \end{aligned}$$

Based on the median value of the TEX-score, patients in the OS TARGETs cohort and the meta-cohort (formed by combining data from GSE21257 and GSE16091 using the R package "Combat") were stratified into high and low TEX-score groups. Subsequently, Kaplan-Meier survival analysis and receiver operator characteristic curves (ROC) between these two groups were conducted using the "survminer", "survival", "rms", and "timeROC" R packages.

2.7 Clinical characteristic and nomogram establishment

Uni-Cox and multi-Cox regression analyses were employed to assess the correlation and independence of the TEX-score in conjunction with clinical parameters in the meta-cohort. In order to delineate disparities between patient subgroups, a nomogram was developed. This nomogram is capable of accurately forecasting an individual's probability of encountering an event in a clinical setting, incorporating independent clinical prognostic factors like age, gender, metastasis, and TEX-score. The performance of the nomogram in prognostic prediction was subsequently evaluated using calibration and ROC curves, validating its predictive capability for prognosis (20).

2.8 Evaluation of immune-related characteristics for the TEX-signature

The immune cell components in each sample were computed using the Tumor Immune Estimation Resource (TIMER), single sample gene set enrichment analysis (ssGSEA), and Microenvironment Cell Populations-counter (MCP-counter) algorithm (21). Additionally, the "ESTIMATE" package was utilized to estimate both stromal and immune scores, enabling the quantification of the Tumor Microenvironment (TME) in malignant tumors (22). The cancer immune cycle, encompassing seven distinct steps (TIP, hrbmu.edu.cn), as well as various immune indicators calculated by the "easier" package, were used to gauge the immune capacity of the TME (23). Furthermore, an examination was conducted into the expression levels of co-stimulatory, co-inhibitory, and HLA molecules. Parameters including T cell-inflamed gene expression profile (GEP), cytotoxic activity (CYT), and IFN-γ were computed in accordance with previously established methodologies (21, 24, 25). TME signatures, independently developed by Kobayashi, were gathered and computed utilizing Gene Set Variation Analysis (GSVA) (26).

2.9 Prediction of immunotherapy

The immunotherapy data was sourced from several datasets, namely GSE91061 (melanoma), GSE126044 (lung adenocarcinoma), Nathon (melanoma), and Mel-ucla (2016, metastatic-melanoma), which were utilized to forecast the response to immunotherapy (27, 28). Additionally, GSE79671 (glioblastoma) and GSE61676 (non-small cell lung cancer) were employed to assess the effectiveness of antivascular drugs within high and low TEX-score groups (29, 30). The TEX-score was calculated independently for each dataset. Subsequently, drug screening was conducted for patients with differing TEX-scores using the "oncopredict" package.

2.10 Quantitative real-time polymerase chain reaction

Ethical approval was obtained from the Medical Ethics Committee for tissue specimens acquired from the Third Xiangya Hospital of Central South University (Approval No. fast-23816). These specimens were stored at a temperature of -80°C. A total of three pairs of samples were collected from OS patients who underwent tumor resection, including tumor tissue and paratumor tissue. Total RNA from tissues was isolated using the TRIzol reagent by Thermo Fisher Scientific, based in Waltham, MA, USA. The cDNA was synthesized from 2μg of RNA utilizing the RevertAid^{TM} First Strand cDNA Synthesis Kit (Thermo Fisher Scientific). Quantitative real-time polymerase chain reaction (qRT-PCR) was performed using SYBR Green Master Mix (Q111-02, Vazyme). The quantification of relative gene expression levels was conducted using the $2^{-\triangle\triangle CT}$ method. The primer sequences are shown in Supplementary Table 1.

2.11 Western blot analysis and Immunofluorescence

Protein samples were collected using RIPA buffer (Beyotime, China) and the protein concentration was determined using a bicinchoninic acid (BCA) assay kit (Chinese Biotechnology Company). A total of 20 μg of protein was separated by 12% SDS-PAGE and transferred onto PVDF membranes (Bio-Rad). After blocking with 5% non-fat milk at room temperature for one hour, the membranes were incubated overnight with antibodies diluted in antibody solutions against RAD23A (Immunoway), SAC3D1 (Immunoway), GAPDH (Immunoway), and PSIP1 (Proteintech). Following washing, the membranes were then incubated with ananti-rabbit IgG solution at room temperature for one hour, followed by additional washing and visualization. For histological analysis, the specimens were fixed in 4% paraformaldehyde after removal, and the fixed tissues were embedded in paraffin for sectioning and subsequent staining. The antibodies used for immunofluorescence staining were as follows: anti-human CD8 (Abcam); anti-human RAD23A (Immunoway); anti-human SAC3D1(Immunoway), anti-human PSIP1 (Proteintech), Alexa 546-conjugated anti-rabbit IgG (Invitrogen). Cell nuclei were counterstained with DAPI (Sigma Aldrich). Imaging was performed using a Zeiss Axio Observer Z1 LSM 710 BiG confocal microscope (Carl Zeiss), and fluorescence images were captured using Zen 2012 software (Carl Zeiss). Images were pseudocolored for overlay, cropping, resizing, and enhancing contrast and brightness using Photoshop and Illustrator (Adobe Systems) or ImageJ (NIH).

2.12 Statistical analysis

The statistical analyses were performed using R (version 4.2.2) and RStudio. A prognostic model for OS was developed employing Combined LASSO regression, Boruta, survival-SVM, Cox-boost, XG-boost, and GBM. For survival analysis and assessing the diagnostic value of the TEX-signature, Kaplan-Meier curves and the Area Under the Curve (AUC) of the Receiver Operating Characteristic (ROC) were employed, respectively. In cases of normally distributed variables, significant quantitative differences between and among groups were determined using a two-tailed t-test or one-way ANOVA, as applicable. Conversely, for non-normally distributed variables, significant quantitative differences were assessed using a Wilcoxon test. A statistical P-value<0.05 was considered to be statistically significant.

3 Results

3.1 Single-cell analysis explored cell subtypes in OS

After controlling data quality and curating single-cell sequencing data from 6 OS patients, a total of 31,398 cells were screened and visualized through uniform manifold approximation and projection (Supplementary Figures S1 and 2A). The optimal number of cell populations was determined using the Seurat package, resulting in the differentiation of all cells into 13 distinct clusters (Figure 1A). Using the differential expression of genes between these 13 major clusters, combined with corrections for cell-specific cell markers for all subpopulations, an annotated classification of each cellular subpopulation within the osteosarcoma tumor microenvironment was performed. This included both immune (such as myeloid cells, NK/T cells, and B cells) and non-immune cells (such as osteoblastic OS cells, endothelial cells, OCs, and CAFs) (Figure 1B, C and Supplementary Figures 2B-H). After a comprehensive examination of the landscape and dynamics of immune cells, all groups of immune cells were re-grouped and annotated (Figures 1D, E). The NK/T cells underwent a similar process, while $CD8^+$ T cells were specifically singled out for subsequent research (Figures 1F-H). Additionally, we observed a low expression level of CD4 within the T cell subpopulation (Figure 1H).

3.2 Analysis of $CD8^+$ T cell site differentiation, cell population communication, and functional enrichment

The pseudo-time series analysis revealed the differentiation status among distinct clusters of $CD8^+$ T cells and the rearrangement of cell types within the Tumor Microenvironment (TME) of OS (Figures 2A, B). Subsequently, we delved into the communication network among cell populations and found that $CD8^+$ T cell cluster one exhibited a more active interaction status and weight compared to $CD8^+$ T cell cluster two (Figure 2C). Classical inflammatory activation pathways such as TNF, OSM, and IFN-II signaling pathways displayed heightened activity in $CD8^+$ T cell cluster one and Myeloid cells. Similarly, we investigated the signaling pattern and weight of cytokine families like IL-1, IL-2, IL-

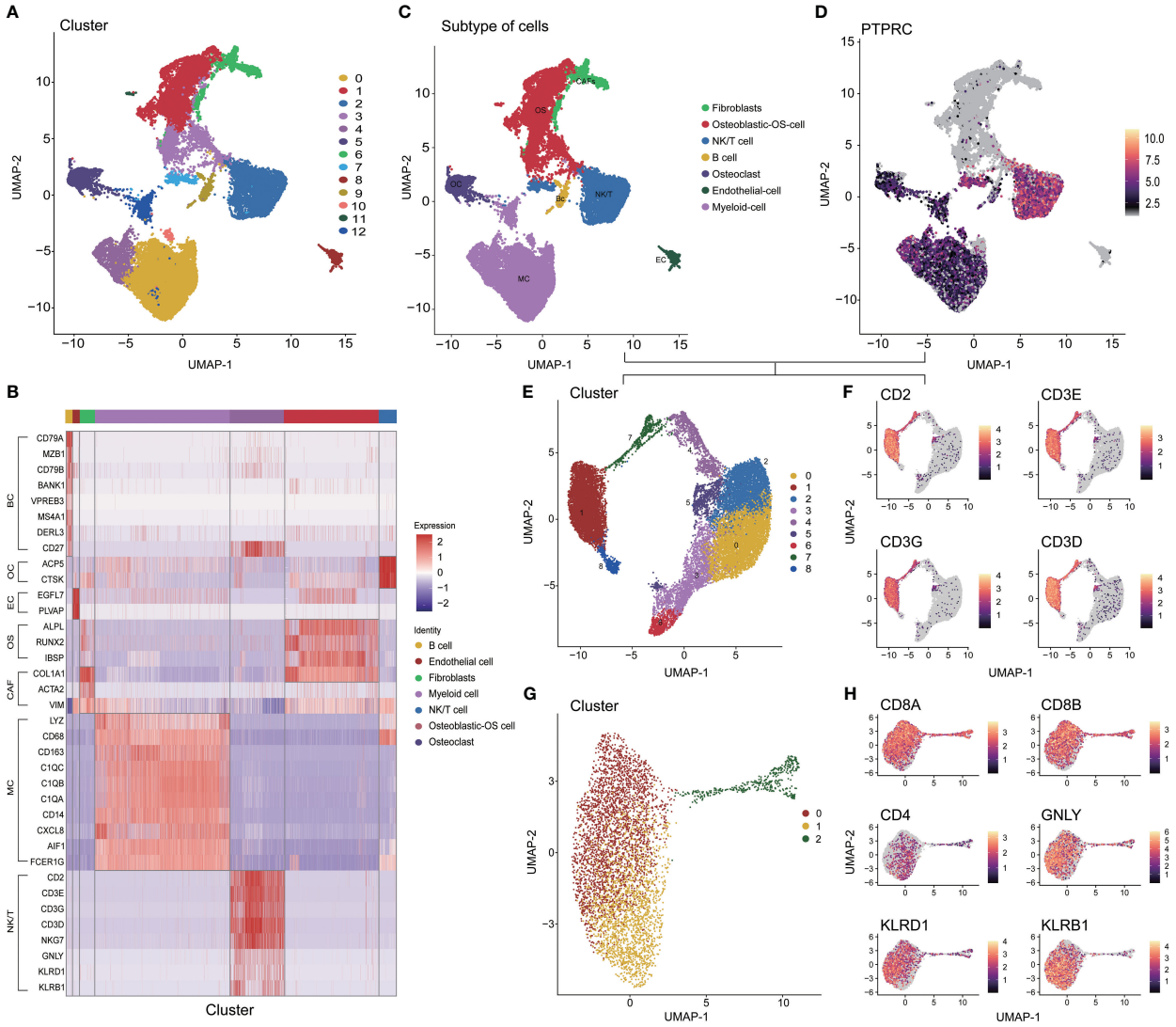

FIGURE 1
Different cell clustering in single cell sequencing data of osteosarcoma. **(A)** Identification 13 types of cells in single cell sequencing data. **(B)** Co-heatmap of marker genes for different cell types. **(C)** The 7 cell types were identified by marker genes. **(D, E)** Extraction, recombination and annotation of immune cells. **(F-H)** Screening of CD8+ T cell and NK/NKT cell cluster. OS: Osteoblastic-OS cell, EC: Endothelial cell, OC: Osteoclast, CAF: Fibroblasts, MC: Myeloid cell, NK/T: NK/NKT/T cell.

4, and IL-6 pathways, along with signaling pathways including TGF-beta, CCL, CD40, complement, and TRAIL in clusters (Figure 2D, E and Supplementary Figure 3A). In summary, $CD8^+$ T cell cluster one demonstrated more pronounced advantages than cluster two across most inflammatory and immune activation pathways. Further visualization of the ligand interaction signal intensity revealed that the ligand interaction between $CD8^+$ T cell cluster two and others was relatively attenuated in comparison to $CD8^+$ T cell cluster one (Figure 2F). Furthermore, gene enrichment analysis was conducted between the two subtypes of $CD8^+$ T cells to validate our hypothesis. The GSVA results of KEGG terms demonstrated a strong association of cluster one with cytokine, JAK-STAT, and T cell receptor signaling pathways (Figure 2G). Additionally, KEGG analysis was carried out by evaluating the up- and down-regulated differentially expressed genes in subgroup one of $CD8^+$ T cells. It revealed that major pathways in cytotoxicity mediated by NK cells, necroptosis, TNF, and NOD signaling were positively enriched (Figure 2H). As for GO terms, a plethora of immune processes exhibited significant enrichment in cluster one, including inflammatory response, lymphocyte migration, proliferation and activation, as well as T cell differentiation and activation regulation (Figure 2I). Furthermore, the hallmark pathways of GSEA in cluster one indicated that molecules and pathways associated with immune function were highly activated (Figure 2J). In contrast, cluster two exhibited greater enrichment in metabolism-related pathways and lacked immune activation in GO, KEGG, and GSEA analyses (Figure 2H, Supplementary Figures 3B, C). Finally, the overall expression status of co-stimulatory and co-inhibitory molecules was compared between the two clusters (Figure 2K). Combining these findings with our previous results, we propose a process of functional exhaustion in the differentiation of $CD8^+$ T cells between the two subsets.

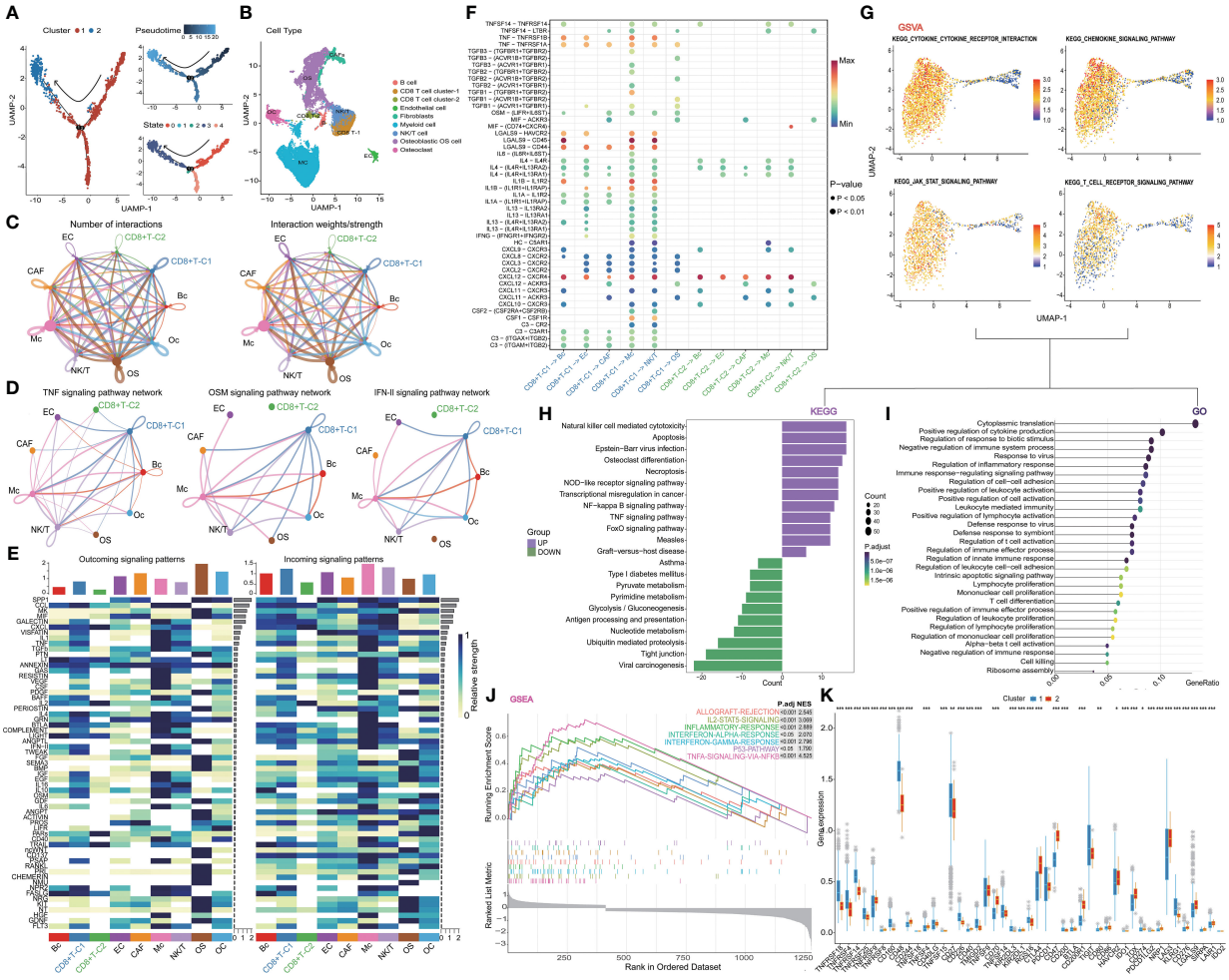

FIGURE 2
Further analysis of CD8+ T cell. **(A)** Trajectory plots showing different clusters in CD8+ T cells. **(B)** Rearrangement of cell types in TIME **(C)** The number and weights/strength of interactions in the cell-cell communication network. **(D)** Weight of classical inflammatory activation pathways. **(E)** Signal pattern and weight of the cytokine family **(F)** Visualization of the signal intensity of ligand interaction. **(G)** GSVA analysis of CD8+ T cells. **(H-J)** The outstanding enrichment of GO, KEGG, and GSEA terms in cluster 1. **(K)** Box plots comparing co-stimulatory and co-inhibitory molecules between two clusters. CD8+T-C1: CD8+T cell cluster 1, CD8+T-C2: CD8+t cell cluster 2.

3.3 Exploring the genetic changes associated with exhaustion phenotype

We delved into the core gene-level alterations within the differentiation trajectory of $CD8^+$ T cell subpopulations and found that there were noteworthy disparities in core genes between different clusters (Figures 3A, B). We utilized the hd-WGCNA algorithm to compute the gene expression profiles of the two $CD8^+$ T cell subsets, and then categorized the core genes between these subsets into distinct gene modules to identify the core gene sets. Finally, we verified the correlation between genes and modules in the network. By setting β to 14, we achieved an R-squared value of 0.85, which established a scale-free network (Figure 3C). The genes were segregated into respective modules via hierarchical clustering, and a gene similarity heatmap was generated based on the topological overlap matrix (Figures 3D-F). The core genes were predominantly concentrated in the turquoise module, with a remarkably high correlation of 96% (Figure 3G). Further analysis revealed a strong correlation between genes within the block and the block (Figure 3H).

3.4 Machine learning to build TEX-signature

In our initial investigation into the biomarkers of T cell exhaustion, which have prognostic significance for patients with OS, we identified 668 genes that were commonly present in both cohorts (Figure 4A). Following univariate analysis of these exhausted core genes, feature selection was performed using six machine learning algorithms, including LASSO, XGboost, GBM, Boruta, CoxBoost, and survival-SVM (Figure 4B, Supplementary Figure 4A). The C-index values for all the algorithms exceeded 0.8, indicating the strong performance of each model (Figure 4C). Subsequently, we selected the intersection of the biomarkers obtained from the machine learning model to construct a refined

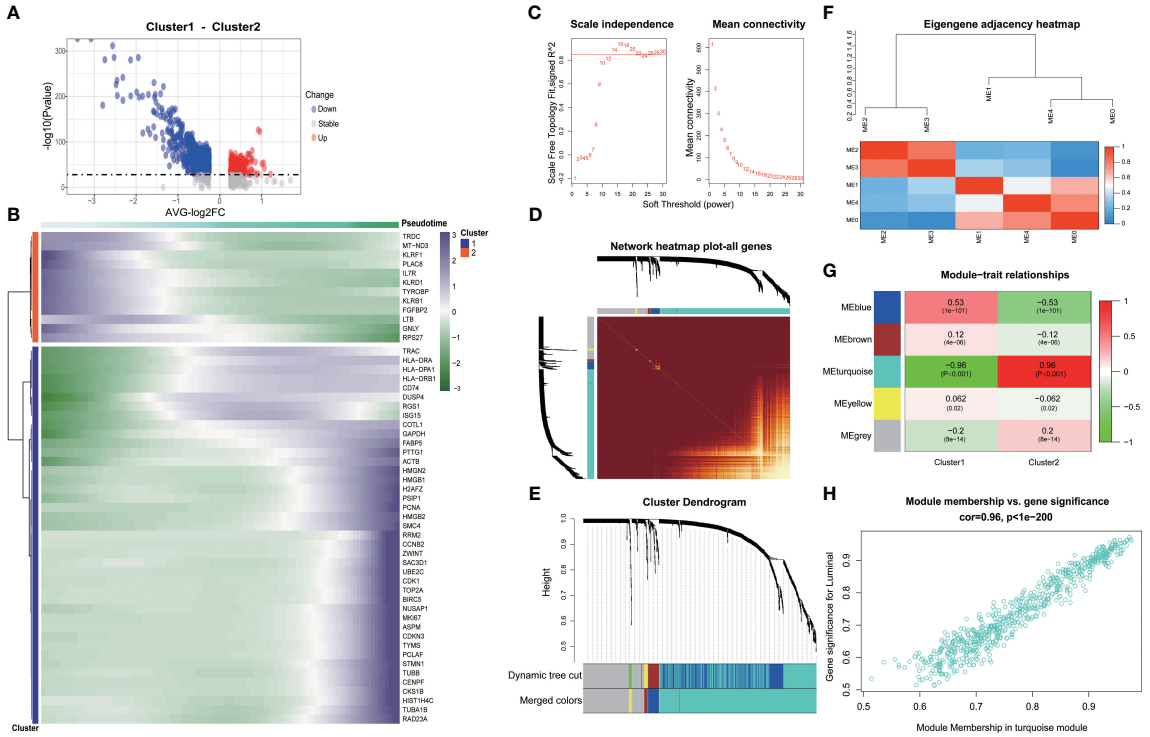

FIGURE 3
Exploring the genetic changes associated with exhaustion phenotype. **(A)** Volcano map of differentially expressed genes in CD8+ T cell clusters. **(B)** Heat map of differentially expressed genes in CD8+ T cell clusters. **(C)** Scale independence and average connectivity. **(D)** Network heatmap plot of all genes. **(E)** Cluster dendrogram. **(F)** Eigengene adjacency heatmap. **(G)** Heatmap of module−trait correlations. **(H)** Correlation between gene significance and module membership.

model (Figure 4D). Three target genes, RAD23A, SAC3D1, and PSIP1, were screened along with their corresponding coefficients calculated through multivariate analysis (Figure 4E). Expression of target genes between the two cell clusters was also visualized (Figure 4F). Moreover, we defined the TEX-score as the sum of the product of the expression values and the correlation coefficients of these three genes separately. Comparisons of the prognostic status of patients with high TEX-scores against those with low TEX-scores revealed that in both the TARGETs cohort and the meta-cohort, patients with high TEX-scores exhibited worse clinical outcomes, while those with low TEX-scores demonstrated better outcomes (Figures 4G, H). Additionally, the area under the ROC curve demonstrated the excellent diagnostic efficacy and predictive ability of the model at 1, 2, 3, 5, and 10 years in both the TARGETs cohort and the meta-cohort (Figures 4I, J).

3.5 Construction of a nomogram and clinical characteristic subgroup analysis

We developed a nomogram that incorporated age, gender, metastasis, and TEX-scores for clinical prediction (Figure 5A, Supplementary Figures 4B–E). The AUC values for 1-, 2-, 3-, 5-, and 10-year Overall Survival (OS) for the nomogram were 0.96, 0.89, 0.82, 0.79, and 0.79, respectively, indicating that our model exhibited strong and consistent predictive capability (Figure 5B). Furthermore, the calibration plots illustrated the level of agreement between the predicted OS and the actual OS (Figure 5C). To further underscore the predictive potential of the TEX-signature, we conducted subgroup analyses based on available clinical features in the TARGETs and GSE21257 databases. The signature demonstrated accurate and robust performance across these subgroups. According to Kaplan-Meier survival analysis, the low TEX-score group consistently exhibited a superior prognosis compared to the high TEX-score group within subgroups stratified by OS type, gender, age, or metastasis (Figures 5D–L and Supplementary Figures 4F–J). In addition, there is a tendency for the TEX-score to decrease with age, suggesting to some extent that they may be generalizable (Supplementary Figures 4K-L).

3.6 Immune characteristics related to the TEX-signature

We investigated the association between TEX-signature and immune cell infiltration as well as immunomodulators in both the TARGETs cohort and the meta-cohort to evaluate the impact of TEX-signature in OS. Patients with high TEX-scores displayed a strong correlation with tumor purity, whereas the low TEX-score group exhibited a more favorable immune microenvironment and matrix score (Figure 6A and Supplementary Figure 5A). Moreover, we discovered that the low TEX-score group had positive associations

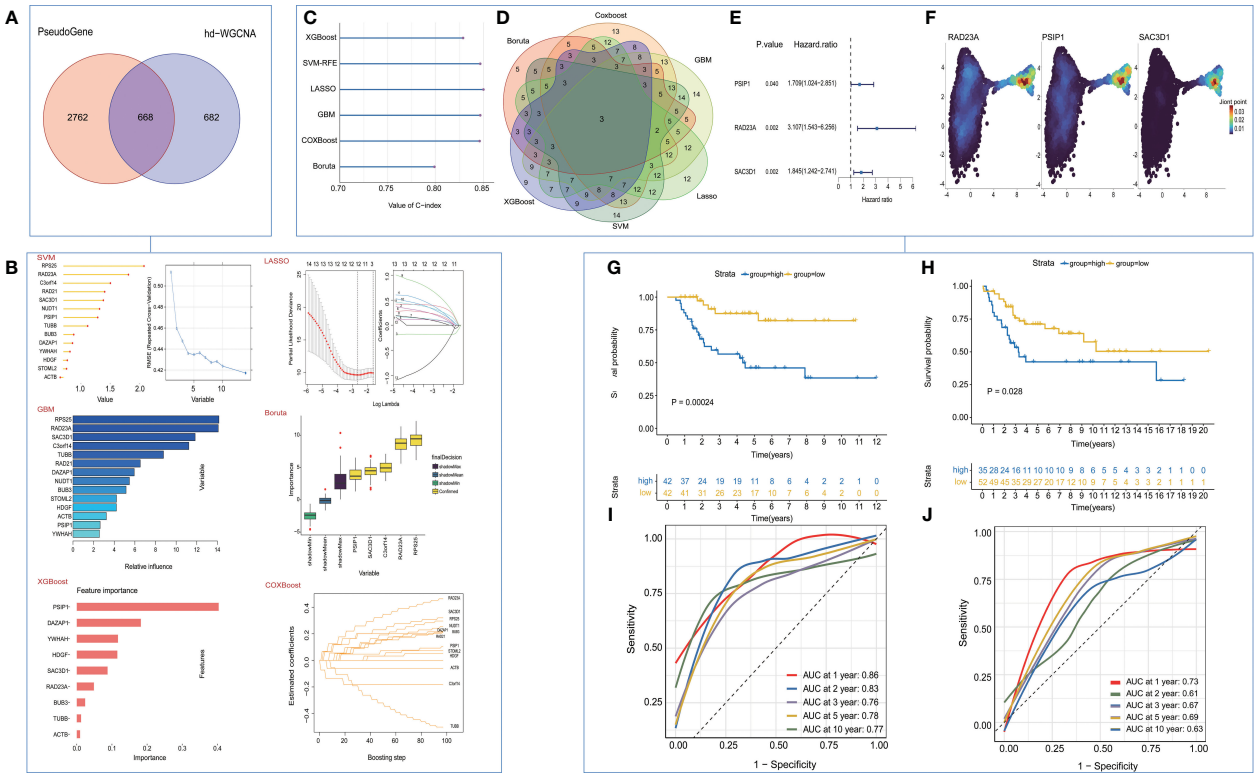

FIGURE 4
Construction and validation of the TEX-Signature. **(A)** Venn diagram of exhausted genes and core genes of the turquoise module. **(B)** machine learning for valuable models. **(C)** The C-index of various algorithms. **(D)** Venn plot showing the intersection of valuable TEX-genes based on six machine learning algorithms. **(E)** coefficient of three target genes calculated by multivariate analysis **(F)** Density plots of gene expression intensity for target genes. **(G)** Kaplan-Meier survival curve of OS between patients with a relative high score of TEX-Signature and a low score of TEX-Signature in the TARGETs cohort. **(H)** Kaplan-Meier survival curve of OS between patients with a high score of TEX-Signature and a low score of TEX-Signature in the meta-cohort. **(I)** Time-dependent ROC curve at 1, 2, 3, 5, and 10 years in the TARGETs cohort. **(J)** Time-dependent ROC curve at 1, 2, 3, 5, and 10 years in the meta-cohort.

with immune cells such as $CD8^+$ T cells, macrophages, natural killer cells (NK cells), NK T cells, B cells, and central and effector memory T cells, all of which play important roles in positive immune regulation and immune-mediated killing utilizing multiple algorithms including ESTIMATE, TIMER, MCP-counter, and ssGSEA (Figure 6A, Supplementary Figures 5B–D). However, myeloid-derived suppressor cells (MDSC) were also more enriched in the low TEX-score group (Figure 6A and Supplementary Figures 5B-D). Additionally, the TEX-score exhibited negative correlations with most immune modulators, classified as antigen presentation, co-stimulatory, co-inhibitory, receptor, and others in the TARGETs cohort. The expression status of all immune checkpoint molecules was also depicted (Figures 6B, C). Furthermore, we confirmed the expression levels of co-stimulatory, co-inhibitory, and HLA molecules in the meta-cohort (Supplementary Figures 5E, F). Finally, we explored several immunotherapy indices in both the TARGETs cohort and meta-cohort. High levels of GEP, CYT, and IFN-γ were significantly associated with a low TEX-score, all of which are determinants of a potentially improved immunotherapy response (Figures 6D-F and Supplementary Figures 5G-I). Interestingly, there was no statistically significant difference in IFN in the TARGETs cohort, although our validation in the meta-cohort indicated that the results were still meaningful. Our results showed a clear intrinsic correlation between the immune microenvironment and TEX-scores, with the low TEX-score patients having an “immune-heat response phenotype” reflecting a better immunotherapeutic potential, whereas the high TEX-score group showed an “immune-poor state”.

3.7 Potential biological process related to TEX-signature

We examined the immunity cycle of cancer to elucidate the relationship between immune processes and TEX-score across the entire dataset, several steps of the immune cycle were found to be more activated in the low TEX-score group in our study. They included cancer antigen presentation, recruitment of T cells, $CD8^+$ T cells, Th1 cells, NK cells, macrophages, B cells, infiltration of immune cells into tumors, and killing of cancer cells (Figure 7A). Moreover, we gathered various indices, including the T cell inflammatory microenvironment signature (T-cell-inflamed), which is based on the combined potential of IFN-γ and T-cell-associated inflammatory genes in predicting the response to PD-1 blockade, as well as the immunological characteristics of Roh (Roh-IS) associated with immune activation related to tumor rejection, and the immunological characteristics of Davoli (Davoli-IS), defined by the

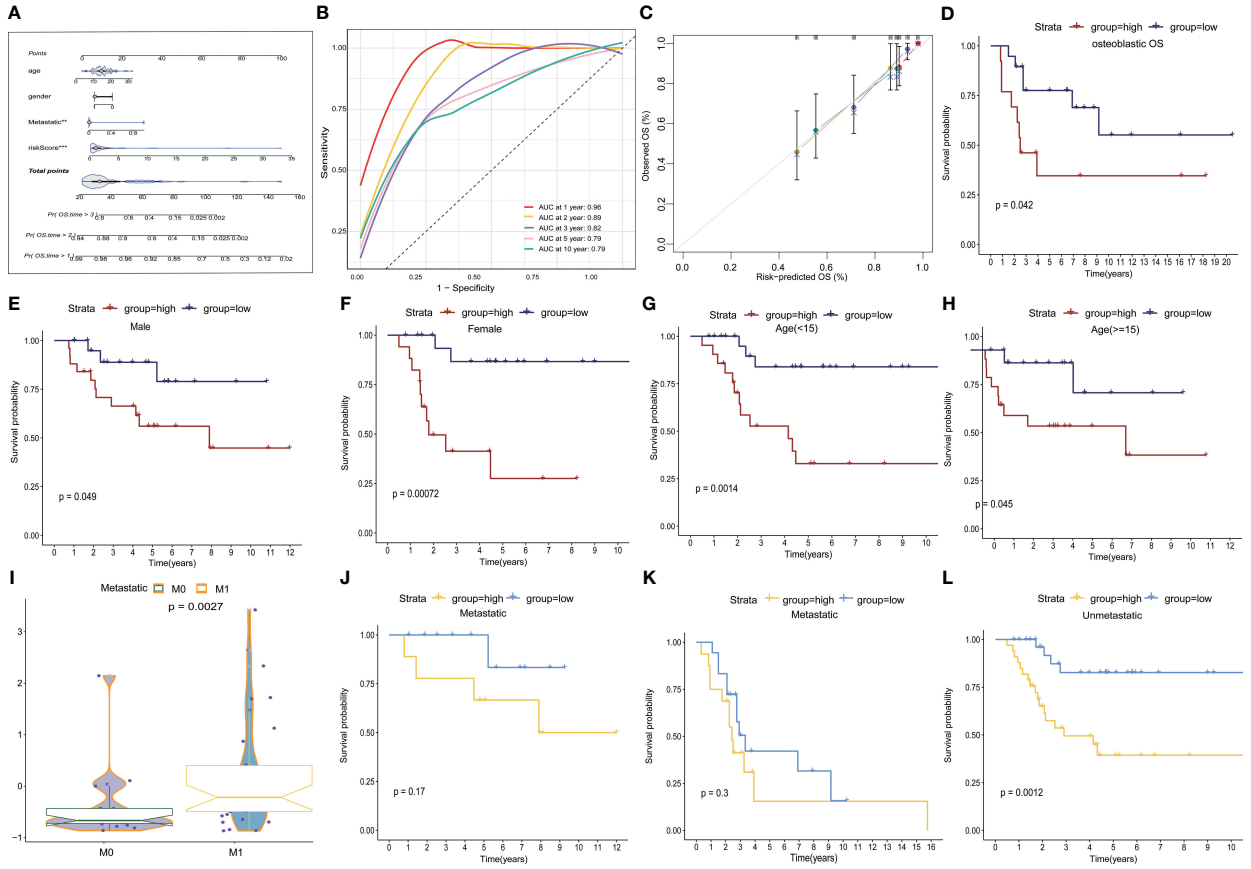

FIGURE 5
Construction of a nomogram and subgroup analysis. **(A)** Nomogram based on gender, age, metastasis and the TEX-score. **(B)** ROC curves for predicting 1-, 2-, 3-, 5- and 10-year survival in the TARGETs database. **(C)** The calibration plot for the probability of 1-, 2-, 3- and 5- year overall survival of OS patients. **(D-H)** Kaplan–Meier survival analysis for OS patients with diverse clinical characteristics of osteosarcoma type **(D)**, gender **(E, F)**, age **(G, H)** in TARGETs cohort. **(I)** Boxplot of TEX scores between metastatic and non-metastatic patients in the GSE21257 dataset **(J-L)** Kaplan-Meier survival analysis of metastatic and non-metastatic patients in the TARGETs **(J)** and the GSE21257 dataset **(K-L)**.

expression of cytotoxic $CD8^+$ T cell, NK cell markers, and immuno-expanded label (Ayers-expIS), which is produced by genes highly associated with IFN-γ signature genes. All of these scores were highly significant in the low TEX-score group (Figure 7B). The immune resistance program (resF-down, resF-up, and resF) represents the efficacy of immune resistance in the tumor microenvironment, with patients in the high TEX-score group exhibiting stronger immune resistance (resF, resF-up), while lower levels of immune resistance (resF-down) were present in the low TEX-score group (Figure 7B). Furthermore, we examined the signatures developed by Kobayashi in the TARGETs cohort, where a low TEX-score was associated with higher levels of recognition of tumor cells, innate immunity, T cells, IFN-γ response, Tregs, and MDSCs, while proliferation levels were positively correlated with TEX-scores (Figure 7C). Additionally, we found that transcription factors associated with inflammation and tumor suppression, such as USF1, USF2, RFX5, TP53, ETS1, SPI1, GATA, and STAT1, were highly expressed in the low TEX-score group. Factors that play a bidirectional role in proliferation and immunity, including NF-κB, STAT5B, and STAT6, were also highly expressed in the low TEX-score group. Other major potential tumor growth factors, such as POU2F2, RUNX1, ERG, REL, and JUN, were also relatively increased in the low TEX-score group. Except for FOXO1, KLF4, and SMAD4, the highly expressed transcription factors promoted OS proliferation, metastasis, and drug resistance in the high TEX-score group, including the E2F family, MYC, TFDP1, ZEB1, TFAP2C, LEF1, FOSL1, TCF7L2, TWIST1, GLI2, and FOXO3 (Figure 7D).

3.8 Function enrichment and metabolism of TEX-signature

We examined the similarities and differences between TEX-score subgroups at the level of specific biological functions and pathways. The GO analysis of biological processes primarily encompassed positive reactions of leukocytes, such as immune migration, adhesion, activation, and phagocytosis in the low TEX-score group. This specifically included the activation and differentiation of $CD8^+$ T cells, B cells, and myeloid cell-mediated immunity (Figure 8A). The cellular components identified in the GO analysis were associated with membrane and filopodium components. Molecular functions included IgG binding, immunoglobulin binding, immune receptor activity, and serine-type peptidase activity (Figure 8B). The GO analysis results for the high TEX-score group were also notable. There was enrichment

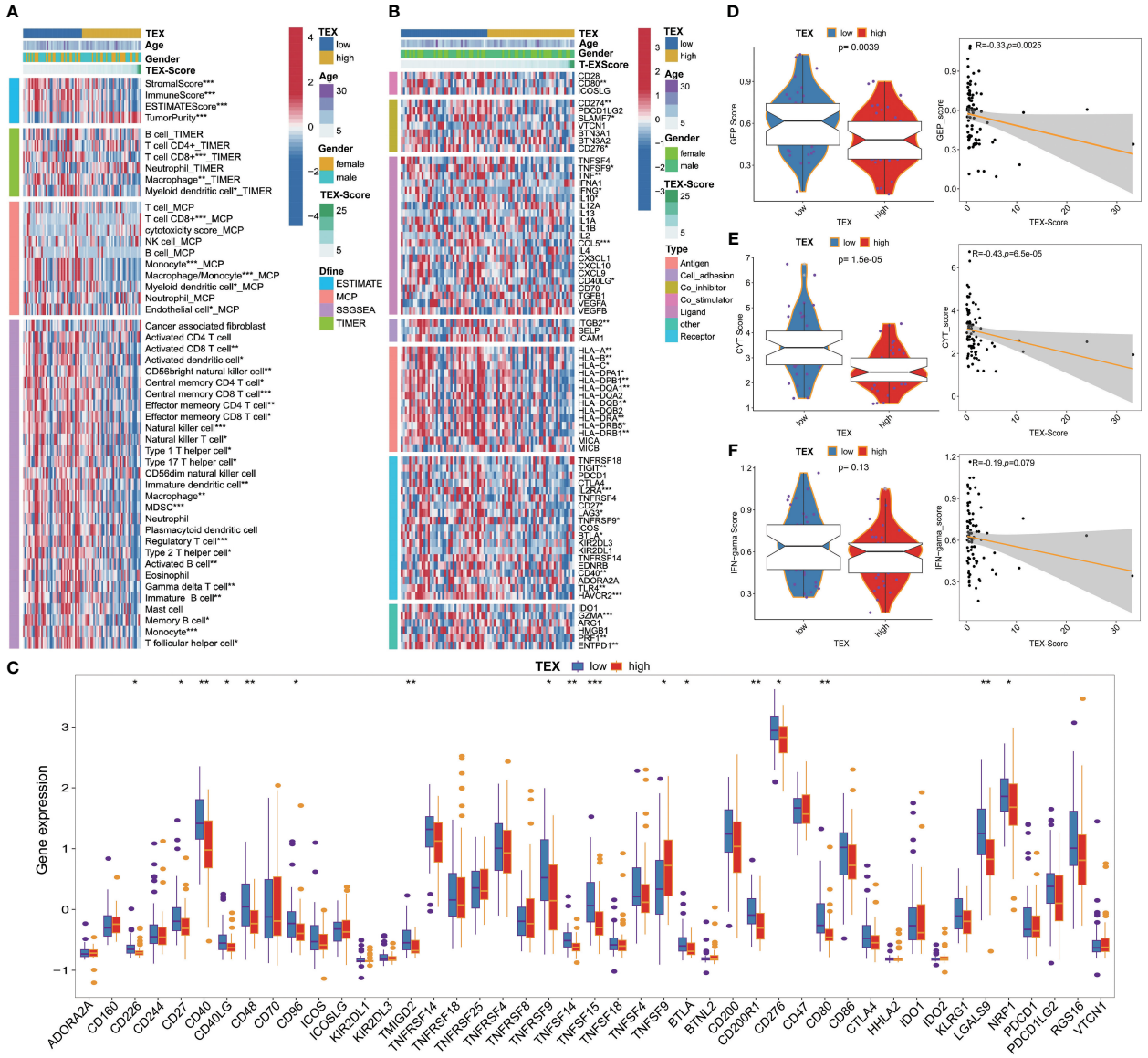

FIGURE 6
Immune-related characteristics of TEX-signature in TARGETs and Meta-cohort. **(A)** Heatmap showing the correlation between TEX-score and immune infiltrating. **(B)** Heatmap showing the correlation between TEX-score and immune modulators. **(C)** Box plots comparing the expression status of all immune checkpoint molecules between low and high TEX-score groups. **(D-F)** Boxplot and scatter plot displaying the levels of GEP, CYT, and IFN-γ between low and high TEX-score groups. *p<0.05, **p<0.01, ***p<0.001.

related to ion channels, both voltage-dependent and independent in biological processes. Terms like transporter complex and channel complex were enriched for cellular components. Bone morphogenesis and ossification were significantly enriched in terms of molecular functions (Supplementary Figure 6A). Additionally, we conducted a KEGG analysis that showed a significant enrichment in the low TEX-score group. We visually compared the enrichment status of the corresponding pathways in the two subgroups. Pathways including the Toll-like receptor, T cell receptor, NOD-like receptor, leukocyte trans-endothelial migration, Fc-γ receptor-mediated phagocytosis, cytokine-cytokine receptor interaction, chemokine signaling pathway, and B cell receptor, all of which were involved in immune processes, were significantly associated with the low TEX-score group (Figure 8C). Furthermore, numerous Hallmark signaling pathways of GSVA correlated with the low TEX-score, included complement, IL6-JAK-STAT3, and IL2-STAT5 signaling pathway, inflammatory response, IFN-α and IFN-γ response, and TNFα-NF-kB signaling pathway. As for the high TEX-score group, the results were consistent with what we obtained previously (Figure 8D).

3.9 Predictive efficacy of TEX-signature for therapy

To further investigate the potential value of the TEX-signature in therapy response, we proceeded to validate its efficacy in multiple published therapy datasets. The predictive capacity of the TEX-signature was well-evidenced by Disease Control Rate (DCR) in the

10.3389/fimmu.2024.1362970

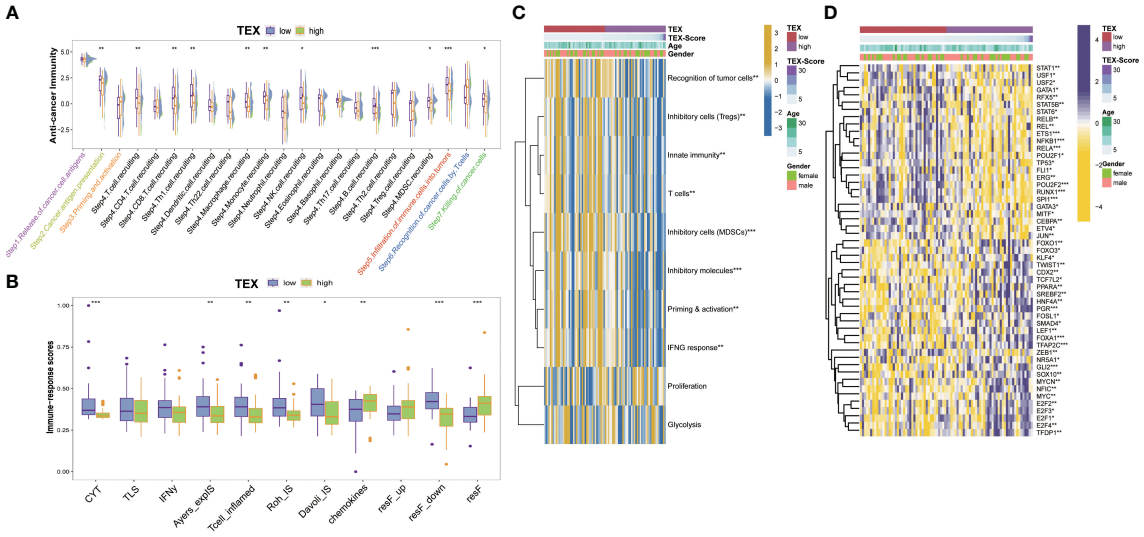

FIGURE 7
Potential biological process of the TEX-signature. **(A)** Boxplot showing the differences in the cancer immunity cycle between low and high TEX-score groups. **(B)** The differences in immune-related indexes collected from the "easier" package in groups. **(C)** Heatmap showing the correlation between TEX-score and immune level developed by Kobayashi. **(D)** Heatmap showing the correlation between the TEX-score and transcription factors. *p<0.05, **p<0.01, ***p<0.001.

context of immunotherapy. Patients with low TEX-scores in the GSE91061 cohort exhibited significantly improved DCR compared to patients with high TEX-scores, and the ROC curve confirmed the robustness of the TEX-score in predicting therapy response (Figure 9A). Similarly, patients with low TEX-scores in the GSE126044 dataset demonstrated a higher likelihood of responding positively to immunotherapy (Figure 9B). Patients with low TEX-scores in the Nanthon dataset experienced extended survival times and were more inclined to respond to immunotherapy (Figure 9C). Patients with low TEX-scores in the Mel-ucla dataset exhibited a superior DCR (Figure 9D). Turning to anti-angiogenic therapy, patients with low TEX-scores in the GSE79671 dataset were more prone to positive responses to anti-angiogenic therapy (Figure 9E). Likewise, in the GSE61676 dataset, patients with low TEX-scores demonstrated prolonged survival times and were more likely to respond favorably to anti-angiogenic therapy (Figure 9F). In addition, we verified the predictive value of the TEX-signature for chemotherapies. As shown, the TEX-score showed a significant correlation with major chemotherapeutic agents, including docetaxel-tanespimycin, regorafenib, sorafenib, topotecan, pazopanib, and paclitaxel. Patients with high TEX-scores appeared to be more likely to respond positively to chemotherapies (Figures 9G, H and Supplementary Figures 6B-E). Taken together, our research revealed that patients with low TEX-scores could potentially benefit more from certain treatment options.

3.10 The validation of TEX-related gene expression

To validate the expression patterns of TEX-related genes in osteosarcoma (OS) patients, we performed RT-PCR and Western Blot analyses on tumor tissues and adjacent non-tumor tissues from three patients. The results showed that, compared to adjacent non-tumor tissues, the expression of RAD23A, SAC3D1, and PSIP1 was significantly upregulated in OS tissues (Figures 10A, B). Additionally, we characterized the localization expression of the three target genes in CD8 T cells using immunofluorescence in OS tissue (Figure 10C). Therefore, we propose that dysregulated expression of these genes may lead to T-cell exhaustion and promote OS progression.

4 Discussion

Chemotherapy and surgical resection have long been the mainstay of treatment for OS (31). Unfortunately, there has been limited advancement in the treatment of OS over the last three decades, particularly in contrast to the notable progress made in developing novel therapies for other types of cancer (32). This stagnation in innovation has regrettably not translated into improved survival rates for patients dealing with OS. The need for further research and breakthroughs in treatment options for OS remains paramount.

Immunotherapy, an emerging therapeutic approach, has made significant strides in treating various cancer types. However, its impact on OS has been relatively limited (33). Effectively reshaping the immunosuppressive tumor microenvironment is crucial for the success of immunotherapy (34). Nevertheless, the intricate interplay of factors including the complex immune microenvironment, tumor heterogeneity, and individual variations in OS poses formidable challenges to harnessing the full potential of immune-based treatments (35). The core of immunotherapy is the activated T cells, particularly $CD8^+$ T cells, whose functional state closely correlates with immune response effectiveness. However, $CD8^+$ T

10.3389/fimmu.2024.1362970

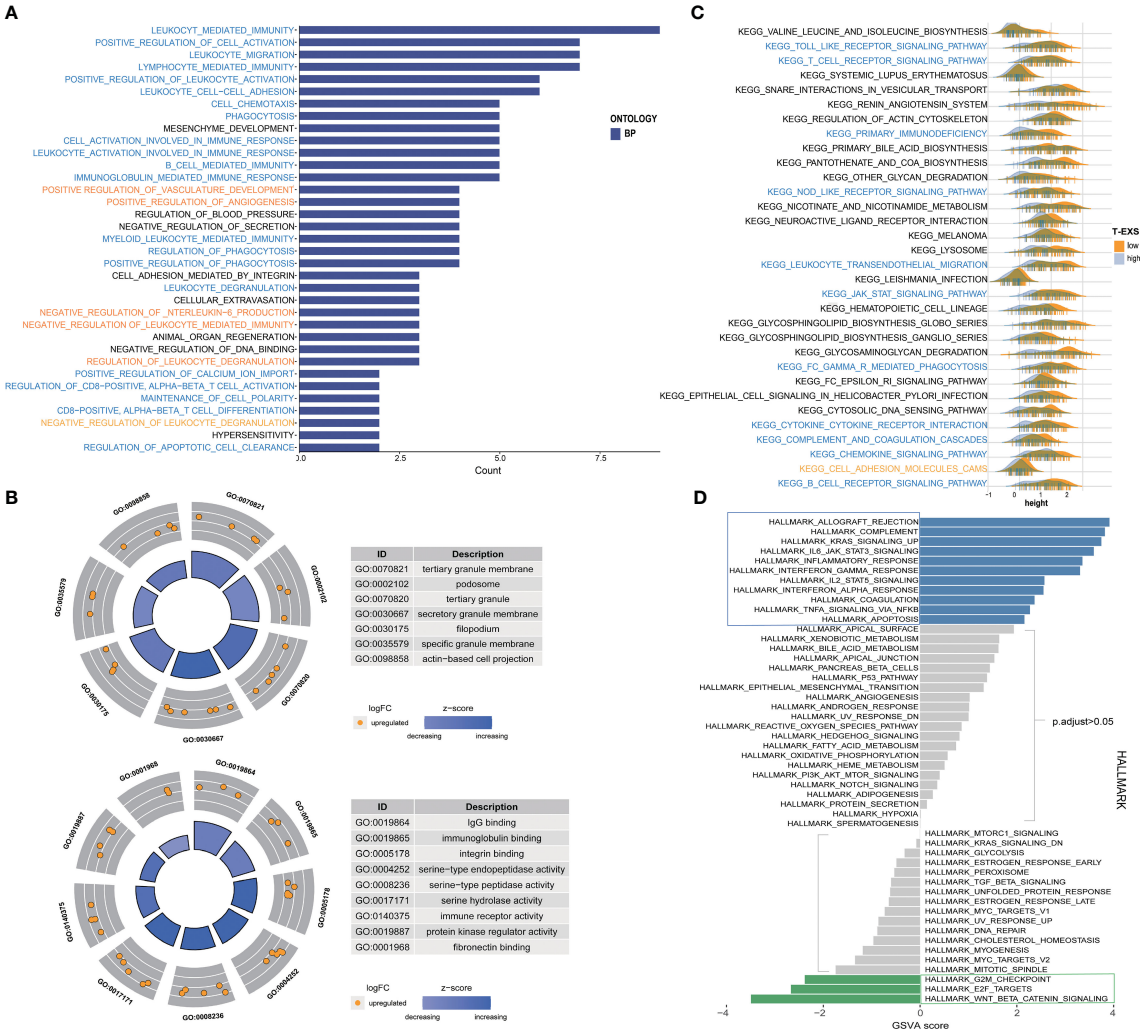

FIGURE 8
Function enrichment and metabolism of the TEX-signature. **(A)** Biological process of GO analysis in the low TEX-score group. **(B)** Cell component and molecular function of GO analysis in the low TEX-score group. **(C)** KEGG analysis in the low TEX-score group. **(D)** GSVA analysis of low and high TEX-score groups.

cells are often altered or exhausted due to prolonged exposure to high levels of persistent antigen and inflammatory stimuli during tumor progression. These exhausted T cells lose their ability to eliminate tumor cells (11, 36). Immune checkpoint inhibitors such as anti-PD-1 antibodies and anti-CTLA-4 antibodies, regulatory cytokines, and metabolic reprogramming targeting the tumor microenvironment work to reverse the exhausted T cell states, restore their functionality, and reactivate immune responses. Previous studies have indicated that the number of tumor-infiltrating lymphocytes (TIL) is significantly higher in OS compared to other sarcomas (37), which suggests that immune checkpoint inhibitors may be able to leverage the abundance of TIL in OS, offering hope for immunotherapy in this context. However, the relationship between T cell exhaustion and OS remains inadequately understood.

$CD8^+$ T cells, originating from CD34 hematopoietic stem cells located in the bone marrow, can be activated by endogenous antigenic peptides presented in MHC class I molecules, thereby exerting anti-tumor immunity (38). When the functionality of $CD8^+$ T cells is compromised, the body's anti-tumor immune capacity diminishes, elevating the risk of tumor growth and cancer metastasis (39). Through an exploration of the molecular and functional attributes of distinct $CD8^+$ T cell subgroups in OS, we observed indications of functional exhaustion within the tumor immune microenvironment. In contrast to relatively exhausted $CD8^+$ T cells, their more active counterparts demonstrated heightened engagement in cellular interactions, with most immune-related pathways exhibiting elevated activity. These pathways encompassed inflammatory activation pathways, TNF family members, complement C3, cytokine family, immune response, cell-cell adhesion, necroptosis, and T cell activation. The relatively exhausted cell subgroup exhibited heightened expression of markers like LAG-3, TOX, CTLA-4, aligning with prior studies elucidating mechanisms associated with $CD8^+$ T cell exhaustion (40). This expression profile may potentially impact the immune response and prognosis of OS patients. These findings

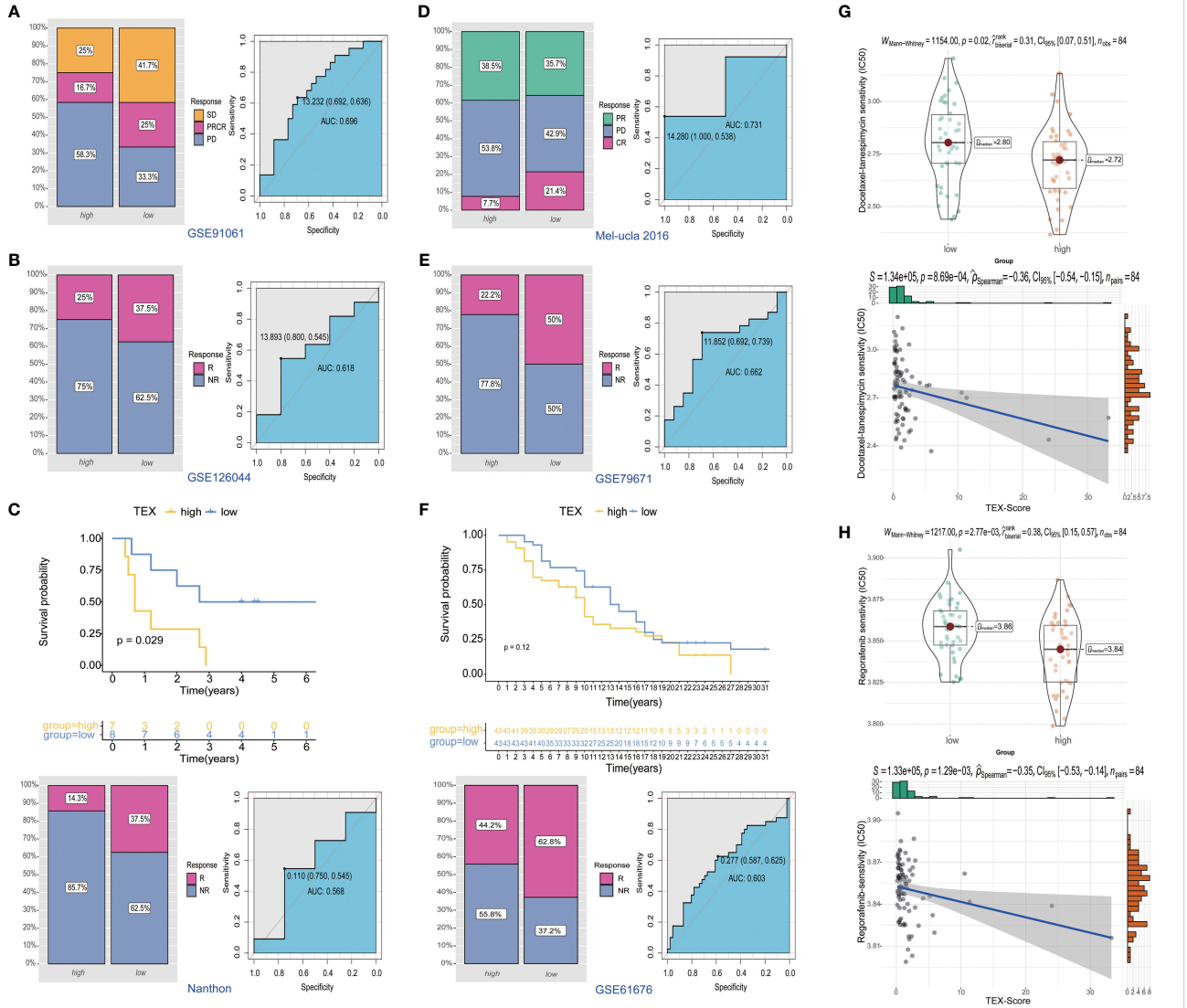

FIGURE 9
Predictive value of TEX-signature in therapy response. **(A-D)** Distribution of immunotherapy responses and ROC curves in the GSE91061 cohort, GSE126044 cohort, Nanthon dataset and Mel-ucla dataset based on the TEX-signature **(E, F)** Distribution of anti-angiogenic therapy responses and the ROC curve between low and high TEX-score groups in the GSE79617 and GSE61676 dataset. **(G, H)** The sensitivity of docetaxel-tanespimycin and regorafenib in two groups.

inspire us to further refine and scrutinize exhaustion models, seeking additional insights to advance immunotherapy for OS.

Following the application of six machine learning algorithms, we identified RAD23A, SAC3D1, and PSIP1 as genes associated with T cell exhaustion, forming the basis for an OS prognostic model. RAD23A, also known as RAD23 or HR23A, is involved in nucleotide excision repair and the regulation of intracellular protein degradation (41). Previous pan-carcinoma analyses have indicated a significant positive correlation of RAD23A in various cancers (42). It participate in processes such as nuclear translocation of AIF during cell death induction and enhances resistance to chemical agents by modulating autophagic response (43). RAD23A may mediate T cell exhaustion through diverse pathways and is recognized as an immune function biomarker, substantiating its inclusion in the prognostic model (44). SAC3D1, or SHD1, is implicated in centrosome duplication and mitotic progression, potentially mediating cell cycle regulation via centrosome amplification (45). SAC3D1 is involved in immune response, as well as its association with metabolism-related signaling pathways, positions it as a key player in T cell exhaustion and provides valuable insights for prognosis and immunotherapy effectiveness in various cancers (46, 47). PSIP1, also known as LEDGF/p75, participates in various biological processes and plays a significant role in lens epithelium differentiation into fiber cell terminals (48). The precise influence of these genes on the occurrence and progression of T cell exhaustion, particularly in relation to $CD8^+$ T cell exhaustion in OS, deserves further exploration. Indeed, understanding the intricate interplay between the tumor immune microenvironment and T cell exhaustion is crucial for unraveling the complexities of cancer progression and devising effective

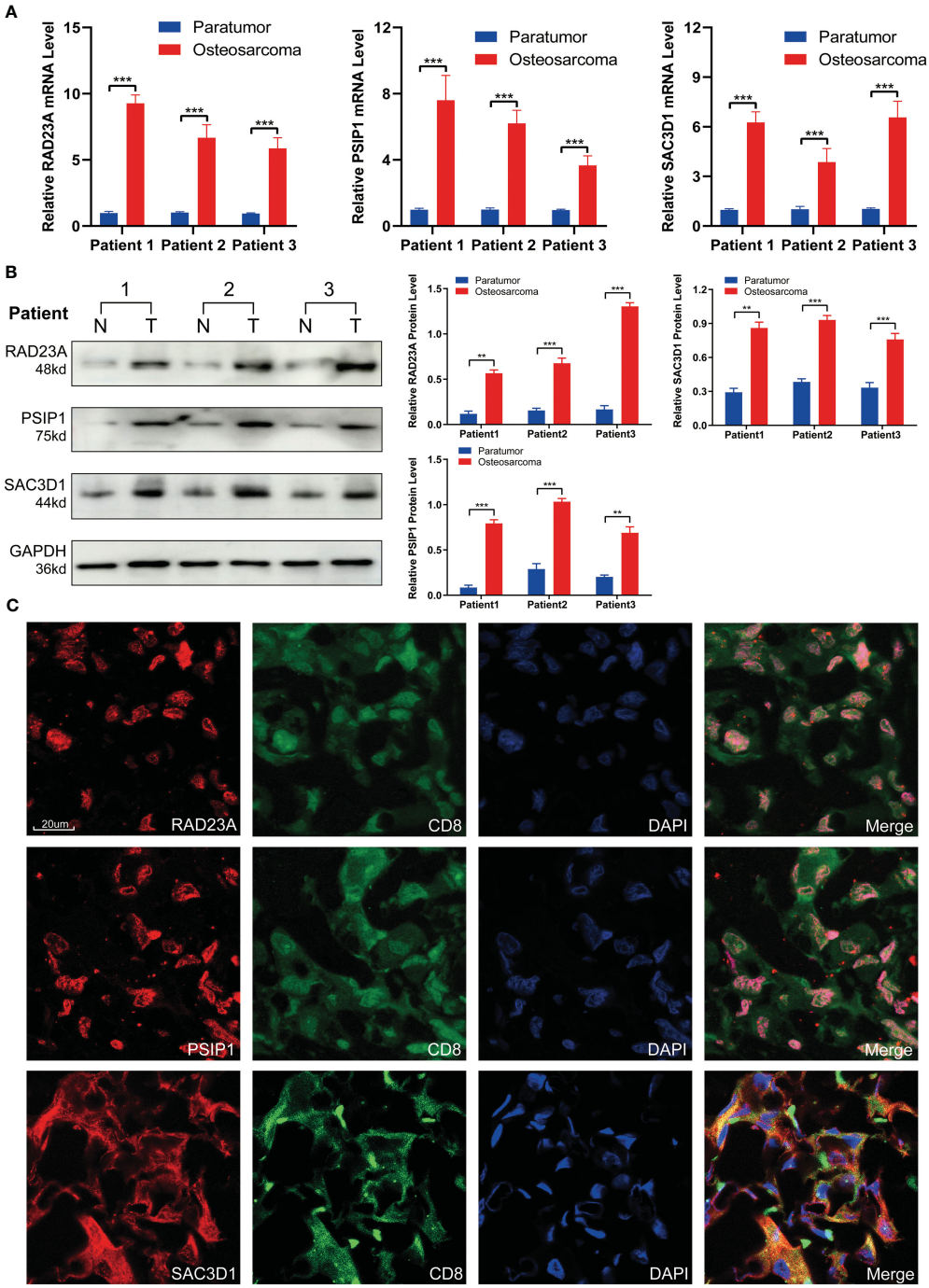

FIGURE 10
Validation of TEX-related gene expression. **(A)** QRT-PCR analysis and **(B)** Western blot analysis of RAD23A, PSIP1, and SAC3D1. **(C)** Immunofluorescence co-localization of CD8 and TEX-related genes was performed under 40x magnification. *P < 0.05, **P < 0.01, ***P < 0.001.

therapeutic strategies (49, 50). The observations made in this study regarding immune cell infiltration and immune checkpoints between individuals with high and low TEX-scores shed light on potential avenues for enhancing immune efficacy. The heightened presence of CD8+ cells, macrophages, NK cells, NK T cells, B cells, and monocyte cells in the low TEX-score group signifies a more active immune response, which aligns with the notion of reduced T cell exhaustion. Moreover, the association of immune pathways with TEX-score subgroups provides valuable insights into the potential effectiveness of immunotherapy in OS. The activation of the WNT/β-catenin signaling pathway in the high TEX-score group is particularly noteworthy, as this pathway is known to play a crucial role in T cell differentiation and effector function (51). Previous studies have demonstrated that the activation of WNT/β-catenin signaling can suppress the effector functions of CD8+ T cells, further emphasizing its relevance in the context of T cell exhaustion (52). The expression of immune checkpoint molecules can originate from various cell types, including tumor cells,

regulatory T cells (Treg), fibroblasts, or their extracellular vesicles. In the low-TEX group, co-stimulatory molecules such as CD40/CD40LG and CD96 were relatively upregulated, accompanied by elevated levels of TNF-α, GZMA, and IFN-α/IFN-γ. Meanwhile, we observed a relative upregulation of some inhibitory immune checkpoints, this may be attributed to heightened antigen presentation stimulation due to high HLA expression and a tumor's self-protective effect induced by sustained inflammatory responses. The upregulation of CD274, IDO1, etc. on the tumor surface by T cell activation and IFN-α/IFN-γ stimulation has been demonstrated (53, 54). Furthermore, the Meta-dataset's high-TEX group showed increased expression of TOX and VCTN1, and the relationship between immune checkpoint regulation and immune infiltration was more intricate than we had first thought. Patients with elevated immune checkpoint levels may also exhibit higher levels of immune activation, and this group of patients may experience better clinical benefit from combination immunotherapy (55). This highlights the potential for interventions aimed at reversing the state of immune exhaustion in the tumor microenvironment, a development that could have far-reaching implications for cancer therapy. Reassuringly, recent clinical successes in reversing T cell exhaustion underscore the promising potential of such approaches (56).

As we know, T cell exhaustion is a prolonged and persistent process characterized by the upregulation of various immune inhibitory factors and impaired functionality, such as compromised release of IFN-γ and granzymes, within the tumor immune microenvironment (TIME) under inflammatory stimuli. Despite being the mainstay of immunotherapy, classical immune inhibitors like Anti-PD1 and Anti-CTLA4, represented by immune checkpoint blockade (ICB), unfortunately, fail to provide long-term benefits for a significant proportion of patients (57). The restoration of exhausted T cell functions is often limited, and they can rapidly revert to their pre-treatment state. Current research has identified CD8+ and Th1-type T cell markers, including IFN-γ, PRF1, and TAP1, to be significantly correlated with patients' responses to immunotherapy (58). Additionally, scholars have found that early PD-1 blockade combined with CAR-T therapy can achieve better prognosis improvement (59). Therefore, for patients with relatively low tumor heterogeneity, high immune infiltration, and limited exhaustion, immunotherapy may attain better long-term efficacy (60). In our research cohort, besides the significant correlation of important indicators such as GEP, IFN-γ, and CYT with low exhaustion levels, the consistent performance of scores like Roh-is, Davoli-is, and RIR further supports our hypothesis, affirming the favorable prognosis of low TEX and providing support for our hypothesis. The validation of this model in multiple therapy datasets across different tumor types further strengthens its predictive efficiency. The findings regarding the sensitivity of patients to anti-angiogenic drugs and conventional chemotherapy drugs for OS highlight the potential clinical utility of the TEX-signature in guiding treatment decisions. However, it's important to acknowledge the need for further validation and clinical implementation. This study sets a promising foundation for future research and potential advancements in the treatment of OS.

It should be mentioned that there are a few of restrictions. Firstly, due to tumor heterogeneity and limited sample size, the study's findings are based on single-cell sequencing data from a relatively small sample number, which may not fully capture the heterogeneity present in osteosarcoma. Further validation in larger cohorts would provide more robust and generalizable results. Second, while the study identifies core genes in the TEX-signature, further molecular experiments are necessary to elucidate the functional roles of these genes and understand the underlying molecular mechanisms of $CD8^+$ T cell exhaustion. Finally, the study did not specifically address the prediction of metastasis in osteosarcoma. It's important to acknowledge that the model's performance in this regard remains uncertain, because we were unable to get reliable metastasis-related data.

In conclusion, our study aims to analyze the immune microenvironment and tumor heterogeneity in OS using single-cell sequencing data, identifying distinct differentiation trajectories of $CD8^+$ T cells in different individuals, and conducting a thorough evaluation of $CD8^+$ T cells, which holds promise in shedding light on new avenues for OS immunotherapy.

Data availability statement

The datasets presented in this study can be found in online repositories. The names of the repository/repositories and accession number(s) can be found in the article/Supplementary Material.

Ethics statement

The animal study was approved by the Medical Ethics Committee of the Third Xiangya Hospital of Central South University. The study was conducted in accordance with the local legislation and institutional requirements.

Author contributions

QF: Conceptualization, Funding acquisition, Investigation, Writing – original draft, Data curation, Validation, Visualization. YW: Funding acquisition, Software, Conceptualization, Data curation, Investigation, Project administration, Visualization, Writing – original draft. JC: Data curation, Formal analysis, Methodology, Supervision, Writing – review & editing. BP: Methodology, Funding acquisition, Investigation, Validation, Writing – original draft. XZ: Validation, Funding acquisition, Writing – review & editing. RL: Investigation, Writing – original draft, Conceptualization, Data curation, Formal analysis. YD: Funding acquisition, Resources, Software, Supervision, Writing – review & editing.

Funding

The author(s) declare financial support was received for the research, authorship, and/or publication of this article. This work was supported by Natural Science Foundation of Hunan Province

(2023JJ30855), Changsha Natural Science Foundation (kq2208364) and the Fundamental Research Funds for the Central Universities of Central South University (CX20220313).

Conflict of interest

The authors declare that the research was conducted in the absence of any commercial or financial relationships that could be construed as a potential conflict of interest.

Publisher's note

All claims expressed in this article are solely those of the authors and do not necessarily represent those of their affiliated organizations, or those of the publisher, the editors and the reviewers. Any product that may be evaluated in this article, or claim that may be made by its manufacturer, is not guaranteed or endorsed by the publisher.

Supplementary material

The Supplementary Material for this article can be found online at: https://www.frontiersin.org/articles/10.3389/fimmu.2024.1362970/full#supplementary-material

SUPPLEMENTARY FIGURE 1
(A) Density plot of transcript counts detected in each sample as a proportion of cell number. **(B)** Total number of genes detected in each sample. **(C)** Distribution of the percentage of mitochondrial genes in each sample. **(D)** Correlation analysis of total transcript number with mitochondrial genes, total gene number and PCA clustering analysis of all cells.

SUPPLEMENTARY FIGURE 2
(A) Two-dimensional visualization of cell distribution across samples. **(B-H)** The "umap" visualization of cell subpopulation-specific marker expression levels.

SUPPLEMENTARY FIGURE 3
(A) Communication networks among cell populations of multiple signaling pathways in cluster 2. **(B)** The enrichment of GO and GSEA terms in cluster 2.

SUPPLEMENTARY FIGURE 4
(A) Risk coefficients for potential TEX-related genes calculated by univariate analysis. **(B-E)** The risk correlation analysis for each clinical characteristic and TEX-score in **(B-C)** The TARGETs and **(D-E)** the GSE21257 dataset. **(F)** Comparison of TEX scores of metastatic patients in the TARGETs cohort. **(G-J)** Kaplan–Meier survival analysis for OS patients with diverse clinical characteristics of age **(G, H)**, and gender **(I, J)** in the GSE21257 dataset. **(K-L)** Distribution of TEX scores for all patients by age.

SUPPLEMENTARY FIGURE 5
(A-C) Immune characteristics related to the TEX-signature. **(D)** Heatmap showing the correlation between TEX-score and immune infiltrating. **(E-F)** The expression status of immune checkpoint and antigen-presenting molecules between low and high TEX-score groups. **(G-I)** The levels of CYT, IFN-γ and GEP between low and high TEX-score groups.

SUPPLEMENTARY FIGURE 6
(A) Function enrichment and metabolism of the high TEX-score. **(B-E)** The sensitivity of Sorafenib, Topotecan, Pazopanib, and Paclitaxel between low and high TEX-score.

References

1. Matsuoka K, Bakiri L, Wolff LI, Linder M, Mikels-Vigdal A, Patiño-García A, et al. Wnt signaling and Loxl2 promote aggressive osteosarcoma. *Cell Res*. (2020) 30:885–901. doi: 10.1038/s41422-020-0370-1

2. Isakoff MS, Bielack SS, Meltzer P, Gorlick R. Osteosarcoma: current treatment and a collaborative pathway to success. *J Clin Oncol*. (2015) 33:3029–35. doi: 10.1200/JCO.2014.59.4895

3. Kciuk M, Yahya EB, Mohamed Ibrahim Mohamed M, Rashid S, Iqbal MO, Kontek R, et al. Recent advances in molecular mechanisms of cancer immunotherapy. *Cancers (Basel)*. (2023) 15. doi: 10.3390/cancers15102721

4. Wedekind MF, Wagner LM, Cripe TP. Immunotherapy for osteosarcoma: Where do we go from here? *Pediatr Blood Cancer*. (2018) 65:e27227. doi: 10.1002/pbc.27227

5. Bielack SS, Smeland S, Whelan JS, Marina N, Jovic G, Hook JM, et al. Methotrexate, doxorubicin, and cisplatin (MAP) plus maintenance pegylated interferon alfa-2b versus MAP alone in patients with resectable high-grade osteosarcoma and good histologic response to preoperative MAP: first results of the EURAMOS-1 good response randomized controlled trial. *J Clin Oncol*. (2015) 33:2279–87. doi: 10.1200/JCO.2014.60.0734

6. Tawbi HA, Burgess M, Bolejack V, Van Tine BA, Schuetze SM, Hu J, et al. Pembrolizumab in advanced soft-tissue sarcoma and bone sarcoma (SARC028): a multicentre, two-cohort, single-arm, open-label, phase 2 trial. *Lancet Oncol*. (2017) 18:1493–501. doi: 10.1016/S1470-2045(17)30624-1

7. Somaiah N, Conley AP, Parra ER, Lin H, Amini B, Solis Soto L, et al. Durvalumab plus tremelimumab in advanced or metastatic soft tissue and bone sarcomas: a single-centre phase 2 trial. *Lancet Oncol*. (2022) 23:1156–66. doi: 10.1016/S1470-2045(22)00392-8

8. Kawano M, Itonaga I, Iwasaki T, Tsumura H. Enhancement of antitumor immunity by combining anti-cytotoxic T lymphocyte antigen-4 antibodies and cryotreated tumor lysate-pulsed dendritic cells in murine osteosarcoma. *Oncol Rep*. (2013) 29:1001–6. doi: 10.3892/or.2013.2224

9. Sun L, Su Y, Jiao A, Wang X, Zhang B. T cells in health and disease. *Signal Transduct Target Ther*. (2023) 8:235. doi: 10.1038/s41392-023-01471-y

10. Russell JH, Ley TJ. Lymphocyte-mediated cytotoxicity. *Annu Rev Immunol*. (2002) 20:323–70. doi: 10.1146/annurev.immunol.20.100201.131730

11. Wherry EJ. T cell exhaustion. *Nat Immunol*. (2011) 12:492–9. doi: 10.1038/ni.2035

12. Nakamoto N, Cho H, Shaked A, Olthoff K, Valiga ME, Kaminski M, et al. Synergistic reversal of intrahepatic HCV-specific CD8 T cell exhaustion by combined PD-1/CTLA-4 blockade. *PloS Pathog*. (2009) 5:e1000313. doi: 10.1371/journal.ppat.1000313

13. Bi J, Jin X, Zheng C, Huang C, Zhong C, Zheng X, et al. Checkpoint TIPE2 limits the helper functions of NK cells in supporting antitumor CD8+ T cells. *Adv Sci (Weinh)*. (2023) 10:e2207499. doi: 10.1002/advs.202207499

14. Van Calster B, Van Smeden M, De Cock B, Steyerberg EW. Regression shrinkage methods for clinical prediction models do not guarantee improved performance: Simulation study. *Stat Methods Med Res*. (2020) 29:3166–78. doi: 10.1177/0962280220921415

15. Kursa MB, Jankowski A, Rudnicki WR. Boruta - A system for feature selection. *Fundamenta Informaticae*. (2010) 101:271–86. doi: 10.3233/FI-2010-288

16. Van Belle V, Van Calster B, Van Huffel S, Suykens JAK, Lisboa P. Explaining support vector machines: A color based nomogram. *PloS One*. (2016) 11:e0164568. doi: 10.1371/journal.pone.0164568

17. Tutz G, Binder H. Generalized additive modeling with implicit variable selection by likelihood-based boosting. *Biometrics*. (2006) 62:961–71. doi: 10.1111/j.1541-0420.2006.00578.x

18. Ester M, Kriegel HP, Xu X. XGBoost: A scalable tree boosting system. In Proceedings of the 22Nd ACM SIGKDD International Conference on Knowledge Discovery and Data Mining. *Geographical Anal*. (2022), 785. doi: 10.1111/gean.12315

19. Cham H, West SG. Propensity score analysis with missing data. *Psychol Methods*. (2016) 21:427–45. doi: 10.1037/met0000076

20. Wang W, Xiang M, Liu H, Chu X, Sun Z, Feng L, et al. A prognostic risk model based on DNA methylation levels of genes and lncRNAs in lung squamous cell carcinoma. *PeerJ*. (2022) 10:e13057. doi: 10.7717/peerj.13057

21. Charoentong P, Finotello F, Angelova M, Mayer C, Efremova M, Rieder D, et al. Pan-cancer immunogenomic analyses reveal genotype-immunophenotype relationships and predictors of response to checkpoint blockade. *Cell Rep*. (2017) 18:248–62. doi: 10.1016/j.celrep.2016.12.019

22. Yoshihara K, Shahmoradgoli M, Martínez E, Vegesna R, Kim H, Torres-Garcia W, et al. Inferring tumour purity and stromal and immune cell admixture from expression data. *Nat Commun*. (2013) 4:2612. doi: 10.1038/ncomms3612

23. Chen DS, Mellman I. Oncology meets immunology: the cancer-immunity cycle. *Immunity*. (2013) 39. doi: 10.1016/j.immuni.2013.07.012

24. Roh W, Chen P-L, Reuben A, Spencer CN, Prieto PA, Miller JP, et al. Integrated molecular analysis of tumor biopsies on sequential CTLA-4 and PD-1 blockade reveals markers of response and resistance. *Sci Transl Med*. (2017) 9. doi: 10.1126/scitranslmed.aah3560

25. Ayers M, Lunceford J, Nebozhyn M, Murphy E, Loboda A, Kaufman DR, et al. IFN-γ-related mRNA profile predicts clinical response to PD-1 blockade. *J Clin Invest*. (2017) 127:2930–40. doi: 10.1172/JCI91190

26. Kobayashi Y, Kushihara Y, Saito N, Yamaguchi S, Kakimi K. A novel scoring method based on RNA-Seq immunograms describing individual cancer-immunity interactions. *Cancer Sci*. (2020) 111:4031–40. doi: 10.1111/cas.14621

27. Yang L, Wei S, Zhang J, Hu Q, Hu W, Cao M, et al. Construction of a predictive model for immunotherapy efficacy in lung squamous cell carcinoma based on the degree of tumor-infiltrating immune cells and molecular typing. *J Transl Med*. (2022) 20:364. doi: 10.1186/s12967-022-03565-7

28. Nathanson T, Ahuja A, Rubinsteyn A, Aksoy BA, Hellmann MD, Miao D, et al. Somatic mutations and neoepitope homology in melanomas treated with CTLA-4 blockade. *Cancer Immunol Res*. (2017) 5:84–91. doi: 10.1158/2326-6066.CIR-16-0019

29. Urup T, Staunstrup LM, Michaelsen SR, Vitting-Seerup K, Bennedbæk M, Toft A, et al. Transcriptional changes induced by bevacizumab combination therapy in responding and non-responding recurrent glioblastoma patients. *BMC Cancer*. (2017) 17:278. doi: 10.1186/s12885-017-3251-3

30. Baty F, Joerger M, Früh M, Klingbiel D, Zappa F, Brutsche M. 24h-gene variation effect of combined bevacizumab/erlotinib in advanced non-squamous non-small cell lung cancer using exon array blood profiling. *J Transl Med*. (2017) 15:66. doi: 10.1186/s12967-017-1174-z

31. Strauss SJ, Frezza AM, Abecassis N, Bajpai J, Bauer S, Biagini R. Bone sarcomas: ESMO-EURACAN-GENTURIS-ERN PaedCan Clinical Practice Guideline for diagnosis, treatment and follow-up. *Ann Oncol*. (2021) 32:1520–36. doi: 10.1016/j.annonc.2021.08.1995

32. Cole S, Gianferante DM, Zhu B, Mirabello L. Osteosarcoma: A Surveillance, Epidemiology, and End Results program-based analysis from 1975 to 2017. *Cancer*. (2022) 128:2107–18. doi: 10.1002/cncr.34163

33. Evdokimova V, Gassmann H, Radvanyi L, Burdach SEG. Current state of immunotherapy and mechanisms of immune evasion in ewing sarcoma and osteosarcoma. *Cancers (Basel)*. (2022) 15. doi: 10.3390/cancers15010272

34. Bedognetti D, Ceccarelli M, Galluzzi L, Lu R, Palucka K, Samayoa J, et al. Toward a comprehensive view of cancer immune responsiveness: a synopsis from the SITC workshop. *J Immunother Cancer*. (2019) 7:131. doi: 10.1186/s40425-019-0602-4

35. Zhang N, Bevan MJ. CD8(+) T cells: foot soldiers of the immune system. *Immunity*. (2011) 35:161–8. doi: 10.1016/j.immuni.2011.07.010

36. Franco F, Jaccard A, Romero P, Yu YR, Ho PC. Metabolic and epigenetic regulation of T-cell exhaustion. *Nat Metab*. (2020) 2:1001–12. doi: 10.1038/s42255-020-00280-9

37. Van Erp AEM, Versleijen-Jonkers YMH, Hillebrandt-Roeffen MHS, Houdt L, Gorris Mark A J, Van Dam LS. Expression and clinical association of programmed cell death-1, programmed death-ligand-1 and CD8+ lymphocytes in primary sarcomas is subtype dependent. *Oncotarget*. (2017) 8:71371–84. doi: 10.18632/oncotarget.v8i41

38. Gascoigne NRJ. Do T cells need endogenous peptides for activation? *Nat Rev Immunol*. (2008) 8:895–900. doi: 10.1038/nri2431

39. Gonzalez SM, Taborda NA, Rugeles MT. Role of different subpopulations of CD8+ T cells during HIV exposure and infection. *Front Immunol*. (2017) 8:936. doi: 10.3389/fimmu.2017.00936

40. Scott AC, Dündar F, Zumbo P, Chandran SS, Klebanoff CA, Shakiba M. TOX is a critical regulator of tumour-specific T cell differentiation. *Nature*. (2019) 571:270–4. doi: 10.1038/s41586-019-1324-y

41. Schauber C, Chen L, Tongaonkar P , Madura K. Rad23 links DNA repair to the ubiquitin/proteasome pathway. *Nature*. (1998) 391:715–8. doi: 10.1038/35661

42. Zhao S, Wu Y, Wei Y, Wei Y, Xu X, Zheng J. Identification of biomarkers associated with CD8+ T cells in coronary artery disease and their pan-cancer analysis. *Front Immunol*. (2022) 13:876616. doi: 10.3389/fimmu.2022.876616

43. Tan X, Wang H-C, Liang R-Y, Chuang SM. Human Rad23A plays a regulatory role in autophagy. *Biochem Biophys Res Commun*. (2016) 478:1772–9. doi: 10.1016/j.bbrc.2016.09.025

44. Park S, So M-K, Huh J. Methylation of DNA repair genes as a prognostic biomarker in AML of a TCGA-LAML cohort. *Clin Lab*. (2022) 68. doi: 10.7754/Clin.Lab.2021.211025

45. Liu Y, He M, Ke X, Chen Y, Zhu J, Tan Z, et al. Centrosome amplification-related signature correlated with immune microenvironment and treatment response predicts prognosis and improves diagnosis of hepatocellular carcinoma by integrating machine learning and single-cell analyses. *Hepatol Int*. (2023). doi: 10.1007/s12072-023-10538-5

46. Nakajima H, Tamura T, Ito M, Shibata F, Kuroda K, Fukuchi Y, et al. SHD1 is a novel cytokine-inducible, negative feedback regulator of STAT5-dependent transcription. *Blood*. (2009) 113:1027–36. doi: 10.1182/blood-2008-01-133405

47. Lu W, Huang J, Shen Q, Li J. Identification of diagnostic biomarkers for idiopathic pulmonary hypertension with metabolic syndrome by bioinformatics and machine learning. *Sci Rep*. (2023) 13:615. doi: 10.1038/s41598-023-27435-4

48. Singh DP, Ohguro N, Kikuchi T, Sueno T, Reddy VN, Yuge K, et al. Lens epithelium-derived growth factor: effects on growth and survival of lens epithelial cells, keratinocytes, and fibroblasts. *Biochem Biophys Res Commun*. (2000) 267:373–81. doi: 10.1006/bbrc.1999.1979

49. Van Der Heide V, Humblin E, Vaidya A, Kamphorst AO. Advancing beyond the twists and turns of T cell exhaustion in cancer. *Sci Transl Med*. (2022) 14:eabo4997. doi: 10.1126/scitranslmed.abo4997

50. Babar Q, Saeed A, Tabish TA, Sarwar M, Thorat ND. Targeting the tumor microenvironment: Potential strategy for cancer therapeutics. *Biochim Biophys Acta Mol Basis Dis*. (2023) 1869:166746. doi: 10.1016/j.bbadis.2023.166746

51. Gattinoni L, Ji Y, Restifo NP. Wnt/beta-catenin signaling in T-cell immunity and cancer immunotherapy. *Clin Cancer Res*. (2010) 16:4695–701. doi: 10.1158/1078-0432.CCR-10-0356

52. Li X, Xiang Y, Li F, Yin C, Li B, Ke X. WNT/β-catenin signaling pathway regulating T cell-inflammation in the tumor microenvironment. *Front Immunol*. (2019) 10:2293. doi: 10.3389/fimmu.2019.02293

53. Dong H, Strome SE, Salomao DR, Tamura H, Hirano F, Flies DB, et al. Tumor-associated B7-H1 promotes T-cell apoptosis: a potential mechanism of immune evasion. *Nat Med*. (2002) 8:793–800. doi: 10.1038/nm730

54. Mclane LM, Abdel-Hakeem MS, Wherry EJ. CD8 T cell exhaustion during chronic viral infection and cancer. *Annu Rev Immunol*. (2019) 37:457–95. doi: 10.1146/annurev-immunol-041015-055318

55. Liu L, Liu Z, Gao J, Liu X, Weng S, Guo C, et al. CD8+ T cell trajectory subtypes decode tumor heterogeneity and provide treatment recommendations for hepatocellular carcinoma. *Front Immunol*. (2022) 13:964190. doi: 10.3389/fimmu.2022.964190

56. Dall'olio FG, Marabelle A, Caramella C, Garcia C, Aldea M, Chapu N, et al. Tumour burden and efficacy of immune-checkpoint inhibitors. *Nat Rev Clin Oncol*. (2022) 19:75–90. doi: 10.1038/s41571-021-00564-3

57. Davoli T, Uno H, Wooten EC, Elledge SJ. Tumor aneuploidy correlates with markers of immune evasion and with reduced response to immunotherapy. *Science*. (2017) 355. doi: 10.1126/science.aaf8399

58. Papatriantafyllou M. Regulatory T cells: distilling regulatory T cell inducers. *Nat Rev Immunol*. (2013) 13:546. doi: 10.1038/nri3506

59. Sznol M, Chen L. Antagonist antibodies to PD-1 and B7-H1 (PD-L1) in the treatment of advanced human cancer. *Clin Cancer Res*. (2013) 19:1021–34. doi: 10.1158/1078-0432.CCR-12-2063

60. Vitale I, Shema E, Loi S, Galluzzi S. Intratumoral heterogeneity in cancer progression and response to immunotherapy. *Nat Med*. (2021) 27:212–24. doi: 10.1038/s41591-021-01233-9

frontiers | Frontiers in Oncology

TYPE Original Research
PUBLISHED 02 May 2024
DOI 10.3389/fonc.2024.1342262

OPEN ACCESS

EDITED BY
Takaji Matsutani,
Maruho, Japan

REVIEWED BY
LianCheng Zhu,
China Medical University, China
Yingcheng Wu,
Fudan University, China

*CORRESPONDENCE
Daoke Yang
15903650068@163.com

†These authors have contributed equally to this work

RECEIVED 21 November 2023
ACCEPTED 08 April 2024
PUBLISHED 02 May 2024

CITATION
Shi S, Wang Y, Wu J, Zha B, Li P, Liu Y, Yang Y, Kong J, Gao S, Cui H, Huangfu L, Sun X, Li Z, Liang T, Zheng Y and Yang D (2024) Predictive value of PD-L1 and TMB for short-term efficacy prognosis in non-small cell lung cancer and construction of prediction models.
Front. Oncol. 14:1342262.
doi: 10.3389/fonc.2024.1342262

Predictive value of PD-L1 and TMB for short-term efficacy prognosis in non-small cell lung cancer and construction of prediction models

Shuling Shi[1†], Yingyi Wang[1†], Jingjing Wu[1], Boya Zha[1], Peihong Li[1], Yukun Liu[1], Yuchuan Yang[1], Jinglin Kong[1], Shibo Gao[1], Haiyang Cui[1], Linkuan Huangfu[1], Xiaocong Sun[1], Zhikai Li[1], Tiansong Liang[1], Yingjuan Zheng[1,2] and Daoke Yang[1,2*]

[1]Department of Radiation Oncology, The First Affiliated Hospital of Zhengzhou University, Zhengzhou, Henan, China, [2]Institute of Radiotherapy and Critical Care Oncology, Zhengzhou University, Zhengzhou, Henan, China

Objective: To investigate the correlation between programmed death ligand 1 (PD-L1), tumor mutation burden (TMB) and the short-term efficacy and clinical characteristics of anti-PD-1 immune checkpoint inhibitor combination chemotherapy in NSCLC patients. The efficacy of the prediction model was evaluated.

Methods: A total of 220 NSCLC patients receiving first-line treatment with anti-PD-1 immune checkpoint inhibitor combined with chemotherapy were retrospectively collected. The primary endpoint was short-term efficacy ORR. The correlation between short-term efficacy, PD-L1, TMB, and clinical characteristics using $\chi 2$ test or t-test was evaluated. Screen the independent prognostic factors using univariate and multivariate logistic regression analyses, and construct a nomogram prediction model using the "rms" package in R software. Using receiver operating characteristic (ROC) curve analysis to evaluate the independent Prognostic factors and the prediction model. Using decision curve analysis (DCA) to verify the superiority of the prediction model.

Results: The mean values of PD-L1, TMB, neutrophils, lymphocytes, neutrophil-to-lymphocyte ratio, and albumin were the highest in the ORR group, PD-L1 expression and TMB correlated with epidermal growth factor receptor expression. Multivariate analyses showed that PD-L1, TMB, and neutrophil were independent prognostic factors for ORR. The area under the ROC curve (AUC) values of the ROC constructed based on these three indicators were 0.7104, 0.7139, and 0.7131, respectively. The AUC value under the ROC of the nomogram model was 0.813. The DCA of the model showed that all three indicators used together to build the prediction model of the net return were higher than those of the single indicator prediction model.

Conclusion: PD-L1, TMB, and neutrophils are independent prognostic factors for short-term efficacy. The nomogram prediction model constructed using these three indicators can further improve predictive efficacy of ICIs in patients with NSCLC.

KEYWORDS

non-small cell lung cancer, PD-L1, tumor mutation burden, objective response rate, nomogram model

1 Introduction

Lung cancer is the leading cause of cancer-related deaths, and non-small cell lung cancer (NSCLC) is the most common type of lung cancer. Most lung cancer patients are diagnosed when the disease has progressed to the middle or late stages; however, traditional chemoradiotherapy has a low cure rate and high adverse effects, and the 5-year survival rate is less than 22% (1). Therefore, new therapeutic modalities are urgently needed to improve disease control and prolong OS in patients with lung cancer.

Among new therapeutic modalities, targeted therapies have the best efficacy for NSCLC patients, especially those carrying epidermal growth factor receptor (EGFR) mutations (2, 3), However, targeted therapies inevitably generate drug resistance, posing a challenge for the follow-up of NSCLC patients. Meanwhile, immunotherapy using immune checkpoint inhibitors (ICI) has brought new hope for patients with Solid tumor. ICIs are based on the tumor cell immune escape (4)mechanism which regulates the immune microenvironment around tumor cells and restores their antitumor function of immune cells (5). ICIs have been applied to various cancers, such as melanoma, renal cell carcinoma, bladder cancer, and mismatch repair-deficient solid tumors (6–9), and have achieved good clinical efficacy.

The main ICIs currently in clinical use for NSCLC are anti- PD-1/PD-L1 ICIs. PD-1 and PD-L1 are usually highly expressed on the surface of activated lymphocytes and tumor cells, respectively, and the combination of the two down-regulates TCR signaling and reduces the production of TNF-α, IFN-γ, and IL-2 (10), which inhibits the tumor-killing function of immune cells. Anti-PD-1/PD-L1 ICIs are novel therapeutic modalities that restore immune killing functions by blocking this pathway. A large number of studies have confirmed that anti-PD-1/PD-L1 ICIs produce better clinical therapeutic effects in patients with NSCLC, increasing the objective response and survival rates, and improving the quality of patient survival (11, 12).

According to the 2023 CSCO guidelines for the diagnosis and treatment of NSCLC, ICIs have been used as first- and second-line treatments for advanced NSCLC. However, as ICIs are widely used in patients with NSCLC, the resistance and immune-related adverse events (irAEs) they generate have become the main factors limiting the clinical application of ICIs (13). In this context, finding accurate predictive markers has become the main research focus to solve this problem.

At present, PD-1/PD-L1 expression levels, and tumor mutation burden have become the main detection biomarkers before clinical immunotherapy, with the aim of screening patients with NSCLC who are suitable for individualized immunotherapy. However, for many patients with advanced NSCLC, obtaining sufficient tumor samples is a significant limiting factor. Therefore, this study aimed to investigate the predictive value of PD-L1 and TMB on the short-term efficacy of first-line treatment with ICIs in combination with chemotherapy in patients with locally advanced NSCLC and to provide a theoretical basis for the clinical development of individualized treatment.

2 Materials and methods

2.1 Clinical data

This study retrospectively collected data from 220 patients with NSCLC who visited the First Affiliated Hospital of Zhengzhou University from September 2021 to September 2023 and received first-line treatment with anti-PD-1 ICIs combined with chemotherapy. The inclusion criteria were as follows: (1) pathological type of NSCLC; (2) stage III or IV according to TNM staging; (3) patients with primary diagnosis; (4) patients receiving anti-PD-1 immune checkpoint inhibitor therapy as first-line treatment; (5) patients with KPS score >70 before treatment; (6) patients aged 18–80 years (7) with at least one measurable lesion. The exclusion criteria were as follows: (1) previous history of malignant tumors or current diagnosis of dual primary tumors; (2) incomplete clinical data; and (3) combined immune-related diseases. All patients underwent complete blood routine, liver and

Abbreviations: NSCLC, non-small cell lung cancer; ORR, objective response rate; PD-L1, programmed death ligand 1; TMB, tumor mutation burden; PD-1, programmed death receptor 1; ICIs, immune checkpoint inhibitors; Neut, neutrophil; NLR, Neutrophil-to-lymphocyte ratio; LYM, lymphocytes; Alb, Albumin; ROC, receiver operating characteristic; DCA, Decision curve analysis; EGFR, epidermal growth factor receptor.

kidney function, chest MRI/CT abdominal CT, brain MRI, whole-body bone ECT, and other related examinations. This study was approved by the Ethics Committee of the First Affiliated Hospital of Zhengzhou University.

2.2 Treatment

All the patients are treated with a chemotherapy + anti-PD-1 immune checkpoint inhibitor regimen. nab-PP regimen was adopted for synchronous chemotherapy (albumin paclitaxel 100 mg/m^2, ivgtt d1, 8, 15 + cisplatin 75 mg/m^2/carboplatin area under the receiver operating characteristic (ROC) curve (AUC) = 5-6, ivgtt d1), AP regimen (pemetrexed 500 mg/m^2, ivgtt d1 + cisplatin 75 mg/m^2, ivgtt d1/carboplatin AUC = 5–6, ivgtt d1), GP regimen (gemcitabine 1,000 mg/m^2, ivgtt d1,8 + nedaplatin 80 mg/m^2 ivgtt d1), DP regimen (docetaxel 70 mg/m^2 ivgtt d1 + carboplatin AUC = 5–6, ivgtt d1). Immunotherapy was administered via an intravenous drip of camrelizumab/sintilimab/tislelizumab/pembrolizumab 200 mg. The first day was used, and the course of treatment was 21 days. Some patients were followed-up with immune checkpoint inhibitor consolidation therapy.

2.3 Indicators

Immunohistochemical PD-L1 detection index: specimen, tumor tissue section of the patient; detection reagent, monoclonal mouse anti-human PD-L1; evaluation method: TPS, number of PD-L1 staining positive tumor cells/total number of live tumor cells * 100%; cut-off value for judging the test results: <1% was negative, 1%–49% was low expression, and ≥50% was high expression. TMB was defined as the total number of somatic mutations detected per million bases (muts per Mb unit, muts/Mb). Specimen: tumor tissue FFPE; detection reagent: DNA extraction kit (OMEGA); Detection method: DNA-based probe capture library building method high-throughput sequencing (NGS); evaluation method: according to the current clinical research data, TMB > 10 muts/Mb was considered high. The absolute value of neutrophils (Neut) was defined as the number of neutrophils in the white blood cell count, with a normal reference range of 1.8 − 6.3 * 10 ^ 9/L. The absolute value of lymphocytes (LYM) refers to the specific number of lymphocytes in the blood, with a normal reference range of 1.1 − 3.2 * 10 ^ 9/L. Neutrophil-to-lymphocyte ratio (NLR) was defined as the ratio of routine neutrophil-to-lymphocyte counts. Albumin (Alb), a major protein in human plasma, was also used as an indicator.

2.4 the evaluation of curative effect

All first-line treatment patients were evaluated for short-term efficacy 3 months after the first course of treatment. The evaluation criteria were response evaluation criteria in solid tumors (RECIST). The evaluation indexes were complete response (CR), partial response (PR), stable disease (SD), and progressive disease (PD). The objective response rate (ORR) was defined as the proportion of patients whose tumor volume shrank to a predetermined value and could be maintained in the minimum time limit, as the sum of the proportion of CR + PR; non-ORR was defined as the sum of the proportion of SD + PD. Efficacy was evaluated every 6 weeks, and CT, MRI, and other related examinations showed improvement.

2.5 Statistical processing

Statistical analyses were performed using SPSS 23.0, and GraphPad Prism 8 software was used for plotting. The diagnostic efficacy of the different indicators was evaluated using the ROC. Count data were expressed as the number of cases and the rate (%); the $\chi 2$ test or Fisher's exact probability method was used for the qualitative data of the general clinical data and treatment results of the patients included in the study, and the t-test was used for the quantitative data. Prognostic factors were evaluated using univariate and multivariate logistic regression analyses, and the independent prognostic variables in the logistic regression analyses were used to construct a nomogram prediction model using the "rms" package in R software. ROC analysis was used to evaluate the predictive efficacy of the prognostic factors and nomogram prediction model, and decision curve analysis (DCA) was used to verify the superiority of the prediction of this model. the nomogram construction flowchart as shown in Figure 1.

3 Results

3.1 General data

A total of 220 patients were enrolled: 127 in the ORR group and 93 in the non-ORR group. A comparison of the general data of the two groups is presented in Table 1. Immunotherapy efficacy was not related to alcohol consumption history, hypertension history, diabetes history, T stage, N stage, M stage, TNM stage. The ORR was the highest in men, age ≥60 years, history of smoking, and patients with squamous carcinoma. The mean values of PD-L1, Neut, LYM, and NLR in the ORR group were greater than those in the non-ORR group, whereas the mean value of Alb was relatively higher in the non-ORR group, and the differences were all statistically significant ($P < 0.05$).

3.2 Correlation analysis of PD-L1, TMB and clinical features

PD-L1 and TMB were grouped according to clinical study data. PD-L1 high expression group: PD-L1 ≥50%, low expression group: PD-L1 <50%; TMB high expression group: TMB ≥10 muts/Mb; low expression group: TMB <10 muts/Mb. The relationship between PDL1, TMB, and the clinical characteristics of patients with NSCLC is shown in Table 2. The PD-L1 score was significantly correlated with EGFR drive type and TMB, whereas the TMB score was correlated with sex, smoking history, drinking history, and T stage.

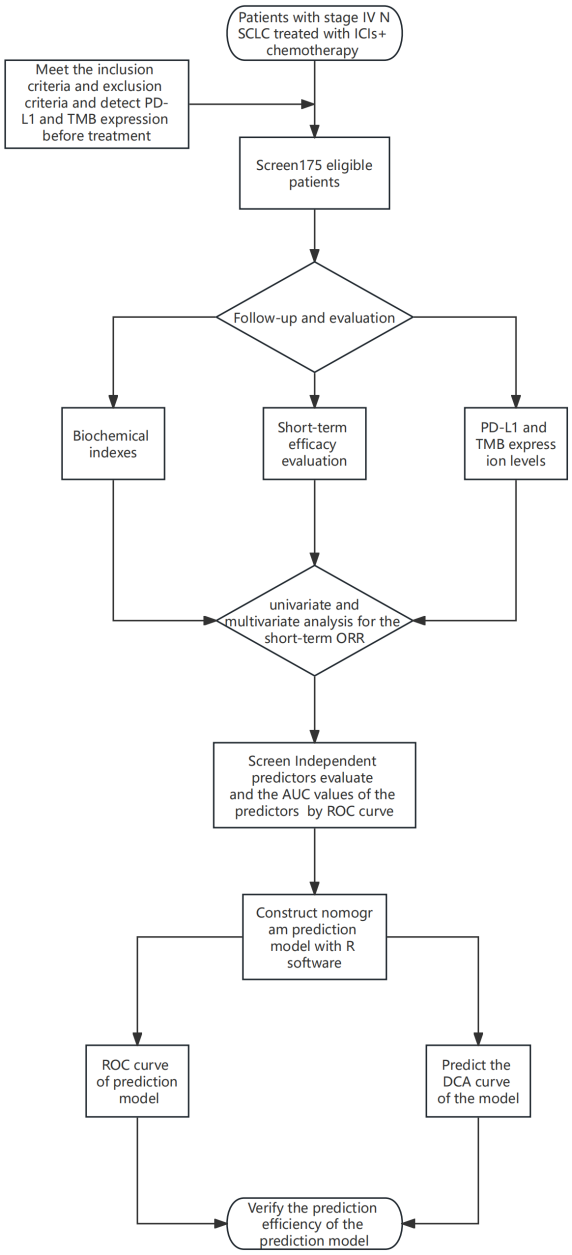

FIGURE 1
The nomogram construction flowchart.

3.3 Univariate analysis of ORR

The results of the univariate analysis of ORR are shown in Table 3. Sex, age, smoking history, pathologic staging, PD-L1, TMB, neutrophils, and NLR were significantly associated with ORR in NSCLC ($P < 0.05$). There were no significant correlations among drinking history, hypertension history, diabetes history, T staging, N staging, M staging, TNM staging, lymphocytes, albumin, or ORR.

3.4 Multivariate analysis results of ORR

The results of the multivariate analysis of ORR are shown in Table 4. Eight significant results from the univariate analysis were included in the multivariate analysis. The results showed that PD-L1 expression ($P < 0.001$), TMB ($P < 0.001$), and neutrophils ($P < 0.001$) were independent prognostic factors for ORR in patients with NSCLC. Sex, smoking history, age, pathological classification, and NLR were not independent prognostic factors for the ORR in patients with NSCLC.

3.5 ROC for different indicators

According to the results of the multivariate analysis, the ROC curves of three independent prognostic factors, PD-L1, TMB, and neutrophils, of the ORR in patients with NSCLC were drawn. As

TABLE 1 General data of the two groups of patients.

clinical characteristic	ORR127	non-ORR93	*P*
Sex			<0.001
Man	109	59	
Women	18	34	
age(years)			0.005
≥60	94	52	
<60	33	41	
smoking history			0.008
Yes	65	31	
No	62	62	
Alcohol consumption history			0.250
Yes	36	20	
No	91	73	
Hypertension history			0.646
Yes	32	26	
No	95	67	
Diabetes history			0.156
Yes	19	8	
No	108	85	
T staging			0.388
T1~T2	73	48	
T3~T4	54	45	
N staging			0.649
N0~N2	87	61	
N3	40	32	
M staging			0.636
M0	56	44	
M1	71	49	
TNM staging			0.842
III	57	43	
IV	70	50	
Pathological classification			0.014
squamous carcinoma	69	35	
Adenocarcinoma	58	58	
PD-L1(%)	67.34 ± 0.32	58.02 ± 0.57	<0.001
TMB (muts/Mb)	15.28 ± 0.20	9.59 ± 0.17	<0.001
Neut(*10^9/L)	6.48 ± 0.11	5.15 ± 0.12	<0.001
LYM(*10^9/L)	3.43 ± 0.35	1.78 ± 0.05	<0.001
NLR	8.50 ± 0.44	4.09 ± 0.17	<0.001
Alb(g/L)	39.47 ± 0.08	39.85 ± 0.07	<0.001

shown in Figure 2, the AUC of the ROC curves of PD-L1, TMB, and neutrophils were 0.7104, 0.7139, and 0.7131 respectively, and were statistically significant ($P < 0.001$). When the sensitivity was 74.0% and the specificity was 61.2%, the best cut-off value for the Yoden index was 4.205 * 10 ^ 9/L.

3.6 Construction of nomogram prediction model

According to the results of the ORR multivariate analysis and evaluation of the prediction efficiency of ROC, a line chart (nomogram) model based on PD-L1, TMB, and neutrophils was drawn using the nomogram function in the rms package, as shown in Figure 3. Neut expression range from 0*10^9/L to 20*10^9/L corresponds to the score threshold between 0 and 100 points, and PD-L1 expression range from 0% to 100% corresponds to the score threshold between 12 and 38 points. The TMB expression range ranges from 0muts/Mb to 35muts/Mb and the corresponding score threshold ranges from 0 to 88 points. Neutrophils and TMB had the widest range of risk scores and the most significant impact on prognosis. The points corresponding to the three indicators were added to the total points, which corresponded to the ORR risk value. The ROC curve drawn according to the model is shown in Figure 4. The AUC was 0.813, indicating medium accuracy. This shows that the model performs well in predicting the ORR in NSCLC.

3.7 The decision curve analysis

Among the factors of the nomogram prediction model, the DCA analysis of the complex model constructed using the three factors of "PD-L1," "TMB," and "neutrophils" and the simple model constructed using the three indexes individually is shown in Figure 5. The complex model had a higher net benefit ratio than the simple model for all thresholds in the range of 0.1–0.6.

4 Discussion

As tumors have entered the era of immunotherapy, both preclinical and clinical studies on the application of ICIs to patients with NSCLC have achieved good efficacy; however, with the wide application of ICIs in the clinic, especially for advanced NSCLC patients, only 15%–30% of patients can benefit from immunotherapy and survive for a long period of time, and even immune hyperprogression occurs (14). Therefore, there is an urgent need to identify suitable predictive biomarkers for precise tumor therapy. Extensively studied predictors of tumor immunotherapy include PD-L1, TMB, microsatellite instability (MSI), EGFR, and tumor-infiltrating lymphocytes (TILs). However, most of them have not been applied for detection before clinical immunization treatment, and based on the results of many studies, it is currently difficult for a single marker to achieve satisfactory

TABLE 2 Correlation analysis of PD-L1, TMB and clinical features.

clinical characteristic	PD-L1		*P1*	TMB		*P2*
	≥50%	<50%		≥10 muts/Mb	<10 muts/Mb	
Sex			0.141			0.004
Man	64	104		83	85	
Women	14	38		14	38	
age(years)			0.118			0.184
≥60	57	89		69	77	
<60	21	53		28	46	
smoking history			0.158			0.003
Yes	39	57		53	43	
No	39	85		44	80	
Alcohol consumption history			0.488			0.023
Yes	22	34		32	24	
No	56	108		65	99	
Hypertension history			0.436			0.895
Yes	23	35		26	32	
No	55	107		71	91	
Diabetes history			0.540			0.708
Yes	11	16		11	16	
No	67	126		86	107	
T staging			0.067			0.001
T1~T2	44	77		65	56	
T3~T4	34	65		67	32	
N staging			0.458			0.717
N0~N2	50	98		64	84	
N3	28	44		33	39	
M staging			0.471			0.603
M0	38	62		46	54	
M1	40	80		51	69	
TNM staging			0.471			0.804
III	38	62		45	55	
IV	40	80		52	68	
Pathological classification			0.274			0.560
squamous carcinoma	33	71		48	56	
Adenocarcinoma	45	71		49	67	
PD-L1(%)				30.31 ± 3.39	29.96 ± 2.90	0.937
TMB (muts/Mb)	10.81 ± 0.91	8.20 ± 0.43	0.004			
Neut(*10^9/L)	5.28 ± 0.25	4.87 ± 0.19	0.193	5.01 ± 0.17	5.02 ± 0.23	0.967
LYM(*10^9/L)	1.87 ± 0.24	1.54 ± 0.05	0.09	1.81 ± 0.20	1.54 ± 0.06	0.139
NLR	3.88 ± 0.55	3.47 ± 0.20	0.396	3.27 ± 0.23	3.89 ± 0.38	0.186
Alb(g/L)	39.01 ± 0.63	39.12 ± 0.34	0.866	39.58 ± 0.52	38.69 ± 0.38	0.160

TABLE 3 Univariate analysis of ORR in NSCLC patients.

clinical characteristic	B	OR	95%CI	*P*
genders(Man vs Women)	-1.250	0.287	0.149~0.551	<0.001
age(years)(<60 vs≥60)	0.840	2.316	1.306~4.180	0.004
smoking history(yes vs no)	0.740	2.097	1.205~3.649	0.009
Alcohol consumption history(yes vs no)	0.367	1.444	0.771~2.704	0.251
Hypertension history(yes vs no)	-0.142	0.868	0.474~1.589	0.646
Diabetes history(yes vs no)	0.626	1.869	0.780~4.478	0.160
T staging (T1~2 vs T3~4)	-0.237	0.789	0.461~1.351	0.388
N staging(N0~2 vs N3)	-0.132	0.876	0.496~1.547	0.649
M staging(M0 vs M1)	0.130	0.636	0.665~1.948	0.636
TNM staging(IIIvs IV)	0.055	1.056	0.617~1.807	0.842
Pathological classification(squamous carcinoma vs Adenocarcinoma)	-0.679	0.507	0.294~0.875	0.015
PD-L1(%)	0.025	1.026	1.016~1.036	<0.001
TMB (muts/Mb)	0.157	1.170	1.101~1.243	<0.001
Neut(*10^9/L)	1.511	4.533	2.437~8.429	<0.001
LYM(*10^9/L)	0.154	1.166	0.830~1.639	0.375
NLR	0.143	1.154	1.008~1.321	0.038
Alb (g/L)	0.027	0.973	0.918~1.032	0.364

predictive efficiency. The combination of multiple predictive markers to build a predictive model may be more effective in predicting the efficacy of ICIs.

The treatment regimen used in this study was a combination of anti-PD-1 ICIs and chemotherapy, which has become the standard first-line treatment for advanced NSCLC without EGFR mutations or high PD-L1 expression. Early studies (15) also showed that chemotherapy can improve tumor immunogenicity by inducing immunogenic cell death and new antigen release. Additionally both radiotherapy (16) and targeted therapy (17) have synergistic effects on ICIs. In the study of the correlation between short-term efficacy in patients with NSCLC and patient clinical characteristics, the results showed that male sex, age <60 years, history of smoking, and squamous carcinoma were the highest in the ORR group, and the differences were all statistically significant ($P < 0.05$). In addition, PD-L1, TMB, neutrophils, lymphocytes, NLR, and albumin were significantly correlated with ORR ($P < 0.001$). PD-L1 can be expressed on the surface of many types of tumor cells, and PD-L1 detected by immunohistochemistry (IHC) has become the first predictive biomarker for ICIs treatment approved by the Food and Drug Administration (FDA). Theoretically, the higher the expression level, the better the antitumor effect of ICIs. The results of this study showed that the mean value of PD-L1 was the highest in patients in the ORR group, which was also confirmed by many studies (18, 19). However, some studies (20) showed that even if ICIs were applied to patients with PD-L1 >50%, they performed poorer than chemotherapy. Bradley et al. (21) showed that patients with NSCLC with low PD-L1 expression had higher

TABLE 4 Multifactorial analysis of ORR in NSCLC patients.

clinical characteristic	B	OR	95%CI	*P*
sex(Man vs Women)	-0.250	0.779	0.309~1.964	0.596
smoking history(yes vs no)	-0.080	0.923	0.423~2.013	0.923
age(years)(<60 vs≥60)	0.448	1.565	0.768~3.189	0.218
Pathological classification(squamous carcinoma vs Adenocarcinoma)	-0.690	0.502	0.245~1.026	0.059
PD-L1(%)	0.025	1.025	1.013~1.037	<0.001
TMB (muts/Mb)	0.152	1.165	1.082~1.254	<0.001
Neut(*10^9/L)	1.353	3.869	1.766~8.477	0.001
NLR	0.098	1.103	0.958~1.271	0.172

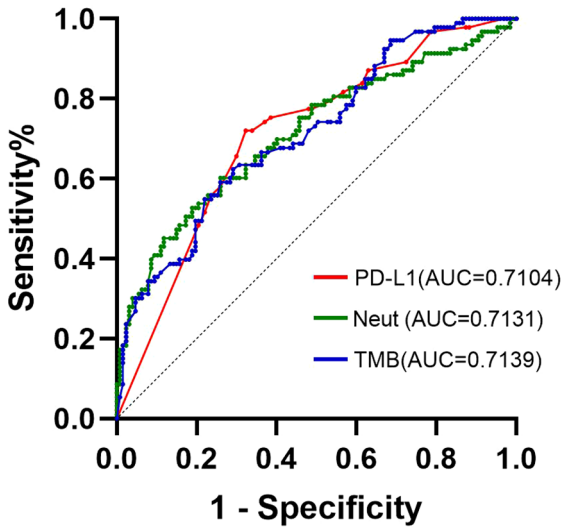

FIGURE 2
ROC curve of ORR group predicted by PD-L1, TMB, and neutrophils for patients with NSCLC.

OS with ICIs than with chemotherapy. These studies have extended the application of ICIs to patients with low PD-L1 expression. Therefore, there is still great controversy regarding the criteria for PD-L1 expression in NSCLC. The second predictor included in this study was TMB. TMB represents the number of mutations per Megabyte (Mut/Mb) of DNA sequenced in a specific cancer (22), and the FDA approved a TMB score of ≥10 mut/Mb as the threshold for Pembrolizumab treatment of solid tumors, but the suitability of TMB-H needs to be demonstrated by further clinical studies. Similar to PD-L1, the higher the level of TMB expression in the tumor tissue, the more likely it is to benefit from immunotherapy. The results of this study showed that the mean value of TMB was the highest in the patients in the ORR group, as described previously. A number of studies (23, 24) have confirmed this. For example, Marabelle et al (25) studied the efficacy comparison between ICIs first-line immunotherapy and chemotherapy drugs in patients with advanced NSCLC, and found that ORR, PFS and OS in the immunotherapy group were relatively better than those in the chemotherapy group. But McGrail et al (26) studied the relationship between TMB and ICIs therapeutic efficacy in more than 10,000 solid tumors, and found that [for some tumors, such as breast cancer and prostate cancer, tumors with high TMB expression had lower ORR, which also indicated that TMB could not be completely used as a predictor of tumor immunotherapy. Future studies are needed to analyze the differences between different cancer types and establish TMB cutoff values in order to create a more standardized approach to the clinical use of TMB. Therefore, these limitations should be overcome before TMB can be widely used in the clinic, making TMB one of the promising predictive markers for immunotherapy.

Analysis of the correlation between PD-L1, TMB, and clinical features showed that there was a correlation between PD-L1 and EGFR, which was consistent with the results of Azuma et al. (27), whereas the results of Jiang et al. (28) clearly indicated that there was a negative correlation between EGFR mutation and PD-L1 expression. Therefore, it is suggested that expression of PD-L1 may be related to the mechanism of drug resistance to EGFR-TKIs. One study (29) found that in patients with NSCLC treated with EGFR-

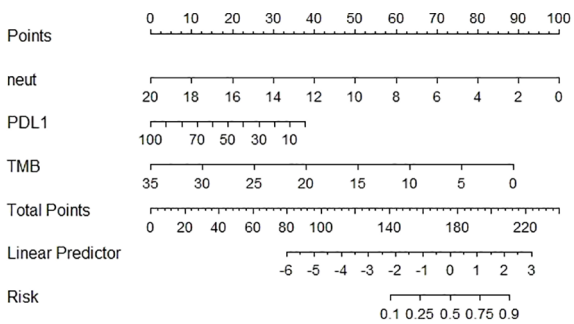

FIGURE 3
Construction of nomogram prediction model for NSCLC based on PD-L1, TMB, neutrophils.

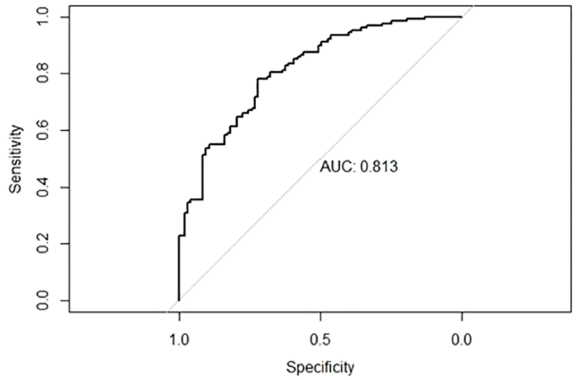

FIGURE 4
ROC curve for nomogram prediction model with AUC of 0.813.

TKI, PD-L1-negative patients had a longer median progression-free survival (mPFS), which confirmed this idea. It has also been suggested (30) that EGFR-TKI treatment can downregulate PD-L1 expression and indirectly enhance antitumor immunity. Therefore, whether anti-PD-1/PD-L1 ICIs can be applied to EGFR-TKI-sensitive patients, especially in EGFR-TKI-resistant NSCLC patients, remains to be further studied. TMB grouping with 10 muts/Mb as the threshold correlated with sex, smoking history, drinking history, T stage, and EGFR. In a study of the relationship between tobacco and TMB, some experimental results showed that smoking can increase TMB (26, 31), and high TMB expression can increase the efficacy of immunotherapy, which explains why smokers are more sensitive to ICIs therapy. The results of this study also showed that more patients in the ORR group had a history of smoking. The results of this study showed a correlation between EGFR mutation type and TMB ($P = 0.047$). The results of this study (32) investigating the relationship between gene mutations and TMB. The results showed that low TMB expression was usually enriched in EGFR-mutant tumors, which is consistent with the results of this study. The results of the present study were inconsistent regarding the relationship between PD-L1 expression and TMB. The results of PD-L1 grouping with a 50% threshold and TMB numerical t-test showed a strong correlation ($P = 0.004$). However, there was no significant correlation between TMB grouping with 10 muts/Mb as the threshold and PD-L1 numerical t-test results ($P = 0.937$). Most studies have shown no significant correlation between them (20, 24, 33). Matthew et al. (24) showed that the progression-free survival time of first-line ICIs therapy was longer than that of chemotherapy in NSCLC patients with high TMB expression, regardless of PD-L1 expression level. This further suggests that the TMB is a beneficial biomarker for ICIs at all PD-L1 expression levels. Although this study showed no significant correlation between TMB and PD-L1 expression, both had similar predictive values. One study (32) investigated the efficacy of immunotherapy in NSCLC patients grouped according to TMB and PD-L1 expression; it found that patients with higher TMB and PD-L1 ≥50% had an ORR of up to 57% with anti-PD-1/PD-L1 ICIs, so the inclusion of TMB and PD-L1 expression in multivariate prediction models should yield great predictive power.

In the present study, the value of peripheral blood cells in predicting the short-term efficacy of immunotherapy was unexpected. Compared to those in the non-ORR group, the average values of neutrophils, lymphocytes, and NLR in the ORR group were relatively higher, and the differences were statistically significant. From the current studies on peripheral blood cells, most studies show that low neutrophil and high lymphocyte counts are positively correlated with the prognosis of tumors (34–37), which is not consistent with the results of this study. The high neutrophil

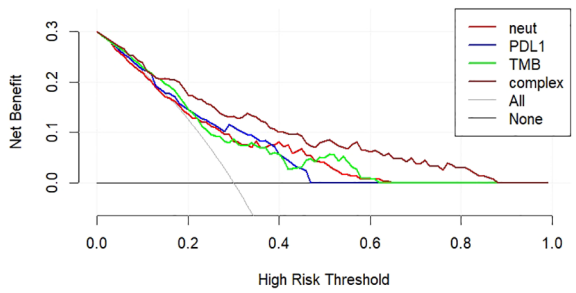

FIGURE 5
DCA curves for nomogram prediction models.

count in this study positively correlated with short-term effects ($P < 0.001$). In humans, Neutrophils are the most abundant immune cells, accounting for 50%-70% of all white blood cells (38). Neutrophils participate in the composition of the tumor microenvironment and secrete chemokines that promote tumor proliferation, invasion, and angiogenesis, which are closely related to the occurrence and development of tumors. However, the number of neutrophils required to determine its effect on tumor immune efficacy is not completely convincing. A previous study (39) has proposed that the infiltrating neutrophils in the tumor have two sides; the phenotype of promoting tumor growth and metastasis, and the phenotype of inhibiting tumor growth. Moreover, the heterogeneity of tumor-associated neutrophils (TAN) was strong. According to phenotypic and functional differences, the most common neutrophils were mainly N1 and N2. N1 cells were anti-tumor neutrophils, while N2 cells showed the function of promoting tumor progression (40, 41). It has been proposed that infiltrating neutrophils in tumors can enhance their anti-tumor activity by recruiting immune cells (42). The role of neutrophil heterogeneity in immunotherapy has been widely studied (43). According to their surface marker molecules, some promote tumor growth, while others inhibit tumor progression. Therefore, for different neutrophil phenotypes, some studies targeting neutrophils have become the focus of research (44). Wang et al. (45) found that CD300ld expressed on neutrophils is a key immunosuppressive factor in the TME. Targeting CD3001d provides a new direction for tumor immunotherapy. Most studies have focused on the measurement of neutrophils, lymphocytes, and NLR before immunotherapy. Immunotherapy can also induce neutrophil responses and increase the number of neutrophils infiltrating tumors. Therefore, it is important to infer the dynamic changes in neutrophil numbers to predict the efficacy of immunotherapy. Most studies have investigated the relationship between neutrophils and the long-term prognosis of ICIs treatment, very few studies have investigated their relationship with the short-term efficacy of ICIs has. Moreover, studies (46) have shown that neutrophils can stimulate T cell response and increase anti-tumor response in the early stage of immunotherapy. In addition, there exists a heterogeneity of neutrophils and complex responses in the tumor immune microenvironment. Thus, more studies are needed to confirm the role of neutrophils in immunotherapy and to conclusively demonstrate that neutrophils are positively correlated with immunologic efficacy.

In this study, through univariate and multivariate analyses of ORR, it was determined that PD-L1, TMB, and neutrophils were independent prognostic factors of ORR in patients with NSCLC, and the AUC values of the ROC curves based on the three indices were 0.7104, 0.7139, and 0.7131, respectively, indicating that the three have good predictive efficiency. The line chart (nomogram) model drawn according to these three indicators showed good predictive ability, and the results showed that neutrophils and TMB had the widest range of risk scores and the most significant impact on prognosis. The AUC value under the ROC curve for the predictive model was 0.813. According to the DCA curve, the net return of the prediction model constructed using the three indicators was higher than that of the single-index prediction model, which again proved its prediction efficiency. From these results, it can be seen that the nomogram model constructed by the expression level of PD-L1 and TMB combined with other characteristics has a good predictive effect on the immune efficacy of patients with advanced NSCLC. Sun et al. (47) constructed a classification model based on PD-L1 and TILs and found that this model was significant for the choice of ICI treatment. This study provides feasibility for the predictive efficacy of PD-L1, TMB and neutrophil models in NSCLC patients. But few studies have been conducted on multiple variables to construct an ICI predictive model. Therefore, we need to study more predictive factors, build a more comprehensive prognostic model to predict the prognosis of patients with NSCLC, and formulate more individualized treatment strategies.

The current study has a few limitations. Firstly, the results of PD-L1 and TMB testing were affected by different testing platforms and the lack of uniform standards for diagnostic results. In addition, the heterogeneity of PD-L1 and TMB expression affected the test results. Furthermore, differences were noted in the PD-L1 expression levels between primary lung lesions and metastatic brain tissues in NSCLC patients. Regarding the detection of TMB, some studies (48) have shown that the detection success rate of TMB in peripheral blood is higher than that in tumor tissue TMB; however, this conclusion needs to be further confirmed. Secondly, many factors influence the routine clinical blood index, which cannot guarantee the accuracy of its influence on the results. Finally, this was a single-center, retrospective study with a relatively small sample size.

5 Conclusion

PD-L1, TMB, and neutrophils are prognostic factors for the short-term efficacy of anti-PD-1 combined chemotherapy in NSCLC. A predictive model constructed using these three indicators could further improve the predictive efficiency of ICIs efficacy.

Data availability statement

The original contributions presented in the study are included in the article/supplementary material. Further inquiries can be directed to the corresponding author.

Ethics statement

The studies involving humans were approved by the Ethics Committee of the First Affiliated Hospital of Zhengzhou University. Ethical number: 2023-KY-1063-001. The studies were conducted in accordance with the local legislation and institutional requirements. The participants provided their written informed consent to participate in this study. Written informed consent was obtained from the individual(s) for the publication of any potentially identifiable images or data included in this article.

Author contributions

SS: Writing – original draft. YW: Writing – original draft. YL: Writing – review & editing. YY: Conceptualization, Writing – review & editing. JK: Data curation, Writing – review & editing. SG: Formal analysis, Writing – review & editing. HC: Investigation, Writing – review & editing. LH: Methodology, Writing – review & editing. XS: Project administration, Writing – review & editing. ZL: Software, Writing – review & editing. TL: Writing – review & editing, Resources. JW: Resources, Writing – review & editing. BZ: Supervision, Writing – review & editing. PL: Validation, Writing – review & editing. YZ: Visualization, Writing – review & editing. DY: Supervision, Writing – review & editing.

Funding

The author(s) declare financial support was received for the research, authorship, and/or publication of this article. This study was supported by Provincial-Ministry Joint Project of Medical Science and Technology Tackling Programme in Henan Province (SB201901037).

Conflict of interest

The authors declare that the research was conducted in the absence of any commercial or financial relationships that could be construed as a potential conflict of interest.

Publisher's note

References

1. Siegel RL, Miller KD, Fuchs HE, Jemal A. Cancer statistics, 2022. *CA: Cancer J Clin*. (2022) 72:7–33. doi: 10.3322/caac.21708

2. Noronha V, Patil VM, Joshi A, Menon N, Chougule A, Mahajan A, et al. Gefitinib versus gefitinib plus pemetrexed and carboplatin chemotherapy in EGFR -mutated lung cancer. *J Clin Oncol*. (2020) 38:124–36. doi: 10.1200/JCO.19.01154

3. Elamin YY, Robichaux JP, Carter BW, Altan M, Tran H, Gibbons D, et al. Poziotinib for EGFR exon 20-mutant NSCLC: Clinical efficacy, resistance mechanisms, and impact of insertion location on drug sensitivity. *Cancer Cell*. (2022) 40:754–67.e6. doi: 10.1016/j.ccell.2022.06.006

4. Jhunjhunwala S, Hammer C, Delamarre L. Antigen presentation in cancer: insights into tumour immunogenicity and immune evasion. *Nat Rev Cancer*. (2021) 21:298–312. doi: 10.1038/s41568-021-00339-z

5. Sanmamed MF, Chen L. A paradigm shift in cancer immunotherapy: from enhancement to normalization. *Cell*. (2019) 176:677. doi: 10.1016/j.cell.2019.01.008

6. Eroglu Z, Zaretsky JM, Hu-Lieskovan S, Kim DW, Algazi A, Johnson DB, et al. High response rate to PD-1 blockade in desmoplastic melanomas. *Nature*. (2018) 553:347–50. doi: 10.1038/nature25187

7. Lee C-H, Shah AY, Rasco D, Rao A, Taylor MH, Simone CD, et al. Lenvatinib plus pembrolizumab in patients with either treatment-naive or previously treated metastatic renal cell carcinoma (Study 111/KEYNOTE-146): a phase 1b/2 study. *Lancet Oncol*. (2021) 22:946–58. doi: 10.1016/S1470-2045(21)00241-2

8. André T, Shiu K-K, Kim TW, Jensen BV, Jensen LH, Punt C, et al. Pembrolizumab in microsatellite-instability–high advanced colorectal cancer. *New Engl J Med*. (2020) 383:2207–18. doi: 10.1056/NEJMoa2017699

9. Li J, Deng Y, Zhang W, Zhou A-P, Gou W, Yang J, et al. Subcutaneous envafolimab monotherapy in patients with advanced defective mismatch repair/microsatellite instability high solid tumors. *J Hematol Oncol*. (2021) 14:95. doi: 10.1186/s13045-021-01095-1

10. Li X, Shao C, Shi Y, et al. Lessons learned from the blockade of immune checkpoints in cancer immunotherapy. *J Hematol Oncol*. (2018) 11:31. doi: 10.1186/s13045-018-0578-4

11. Ettinger DS, Wood DE, Aisner DL, Akerley W, Bauman JR, Bharat A, et al. NCCN guidelines® Insights: non–small cell lung cancer, version 2.2023: featured updates to the NCCN guidelines. *J Natl Compr Cancer Network*. (2023) 21:340–50. doi: 10.6004/jnccn.2023.0020

12. Gogishvili M, Melkadze T, Makharadze T, Giorgadze D, Dvorkin M, Penkov K, et al. Cemiplimab plus chemotherapy versus chemotherapy alone in non-small cell lung cancer: a randomized, controlled, double-blind phase 3 trial. *Nat Med*. (2022) 28:2374–80. doi: 10.1038/s41591-022-01977-y

13. Schoenfeld AJ, Antonia SJ, Awad MM, Felip E, Gainor J, Gettinger SE, et al. Clinical definition of acquired resistance to immunotherapy in patients with metastatic non-small-cell lung cancer. *Ann Oncol*. (2021) 32:1597–607. doi: 10.1016/j.annonc.2021.08.2151

14. Kim CG, Kim C, Yoon SE, Kim KH, Choi SJ, Kang B, et al. Hyperprogressive disease during PD-1 blockade in patients with advanced hepatocellular carcinoma. *J Hepatol*. (2021) 74:350–9. doi: 10.1016/j.jhep.2020.08.010

15. Bezu L, Gomes-de-Silva LC, Dewitte H, Breckpot K, Fucikova J, Spisek R, et al. Combinatorial strategies for the induction of immunogenic cell death. *Front Immunol*. (2015) 6:187. doi: 10.3389/fimmu.2015.00187

16. Gong X, Li X, Jiang T, Xie H, Zhu Z, Zhou C, et al. Combined radiotherapy and anti-PD-L1 antibody synergistically enhances antitumor effect in non-small cell lung cancer. *J Thorac Oncol*. (2017) 12:1085–97. doi: 10.1016/j.jtho.2017.04.014

17. Yang JC-H, Gadgeel SM, Sequist LV, Wu C-L, Papadimitrakopoulou V, Su W-C, et al. Pembrolizumab in combination with erlotinib or gefitinib as first-line therapy for advanced NSCLC with sensitizing EGFR mutation. *J Thorac Oncol*. (2019) 14:553–9. doi: 10.1016/j.jtho.2018.11.028

18. Garon EB, Rizvi NA, Hui R, Leighl N, Balmanoukian AS, Eder JP, et al. Pembrolizumab for the treatment of non-small-cell lung cancer. *New Engl J Med*. (2015) 372:2018–28. doi: 10.1056/NEJMoa1501824

19. Leighl NB, Hellmann MD, Hui R, Carcereny E, Felip E, Ahn M-J, et al. Pembrolizumab in patients with advanced non-small-cell lung cancer (KEYNOTE-001): 3-year results from an open-label, phase 1 study. *Lancet Respir Med*. (2019) 7:347–57. doi: 10.1016/S2213-2600(18)30500-9

20. Carbone DP, Reck M, Paz-Ares L, Creelan B, Horn L, Steins M, et , et al. First-line nivolumab in stage IV or recurrent non-small-cell lung cancer. *New Engl J Med*. (2017) 376:2415–26. doi: 10.1056/NEJMoa1613493

21. Bradley CA. Pembrolizumab improves OS across PD-L1 subgroups. *Nat Rev Clin Oncol*. (2019) 16:403. doi: 10.1038/s41571-019-0213-5

22. Addeo A, Friedlaender A, Banna GL, Weiss G. TMB or not TMB as a biomarker: that is the question. *Crit Rev Oncology/Hematology*. (2021) 163:103374. doi: 10.1016/j.critrevonc.2021.103374

23. Valero C, Lee M, Hoen D, Wang J, Nadeem Z, Patel N, et al. The association between tumor mutational burden and prognosis is dependent on treatment context. *Nat Genet*. (2021) 53:11–5. doi: 10.1038/s41588-020-00752-4

24. Hellmann MD, Ciuleanu T-E, Pluzanski A, Lee JS, Otterson JA, Audigier-Valette C, et al. Nivolumab plus ipilimumab in lung cancer with a high tumor mutational burden. *New Engl J Med*. (2018) 378:2093–104. doi: 10.1056/NEJMoa1801946

25. Galvano A, Gristina V, Malapelle U, Pisapia P, Pepe F, Barraco N, et al. The prognostic impact of tumor mutational burden (TMB) in the first-line management of advanced non-oncogene addicted non-small-cell lung cancer (NSCLC): a systematic review and meta-analysis of randomized controlled trials. *ESMO Open*. (2021) 6:100124. doi: 10.1016/j.esmoop.2021.100124

26. McGrail DJ, Pilié PG, Rashid NU, Voorwerk L, Slagter M, Kok M, et al. High tumor mutation burden fails to predict immune checkpoint blockade response across all cancer types. *Ann Oncol*. (2021) 32:661–72. doi: 10.1016/j.annonc.2021.02.006

27. Azuma K, Ota K, Kawahara A, Hattori S, Iwama E, Harada T, et al. Association of PD-L1 overexpression with activating EGFR mutations in surgically resected nonsmall-cell lung cancer. *Ann Oncol*. (2014) 25:1935–40. doi: 10.1093/annonc/mdu242

28. Jiang L, Lin Z, Li N, Jiang J, Lu C, Du S, et al. [Correlation study on expression of PD-1 and PD-L1 in non-small cell lung cancer and epidermal growth factor receptor mutations]. *Zhongguo Fei Ai Za Zhi = Chin J Lung Cancer*. (2021) 24:623–31. doi: 10.3779/j.issn.1009-3419.2021.102.31

29. Chen R, Gao X, Xu F, Zhang S, Ma L, Hu B, et al. [A real-world study on the expression characteristics of PD-L1 in patients with advanced EGFR positive NSCLC and its relationship with the Therapeutic efficacy of EGFR-TKIs]. *Zhongguo Fei Ai Za Zhi = Chin J Lung Cancer*. (2023) 26:217–27. doi: 10.3779/j.issn.1009-3419.2023.101.09

30. Chen N, Fang W, Zhan J, Hong S, Tang Y, Kang S, et al. Upregulation of PD-L1 by EGFR activation mediates the immune escape in EGFR-driven NSCLC: implication for optional immune targeted therapy for NSCLC patients with EGFR mutation. *J Thorac Oncol*. (2015) 10:910–23. doi: 10.1097/JTO.0000000000000500

31. Gibbons DL, Byers LA, Kurie JM. Smoking, p53 mutation, and lung cancer. *Mol Cancer research: MCR*. (2014) 12:3–13. doi: 10.1158/1541-7786.MCR-13-0539

32. Ricciuti B, Wang X, Alessi JV, Rizvi H, Mahadevan NR, Li YY, et al. Association of high tumor mutation burden in non-small cell lung cancers with increased immune infiltration and improved clinical outcomes of PD-L1 blockade across PD-L1 expression levels. *JAMA Oncol*. (2022) 8:1160–8. doi: 10.1001/jamaoncol.2022.1981

33. Rizvi H, Sanchez-Vega F, La K, Chatila W, Jonsson P, Halpenny D, et al. Molecular determinants of response to anti-programmed cell death (PD)-1 and anti-programmed death-ligand 1 (PD-L1) blockade in patients with non-small-cell lung cancer profiled with targeted next-generation sequencing. *J Clin Oncol*. (2018) 36:633–41. doi: 10.1200/JCO.2017.75.3384

34. Wu Y, Yang S, Ma J, Chen Z, Song G, Rao D, et al. Spatiotemporal immune landscape of colorectal cancer liver metastasis at single-cell level. *Cancer Discovery*. (2022) 12:134–53. doi: 10.1158/2159-8290.CD-21-0316

35. Yang S, Sun Z, Zhou Q, Wang W, Wang G, Song J, et al. MicroRNAs, long noncoding RNAs, and circular RNAs: potential tumor biomarkers and targets for colorectal cancer. *Cancer Manage Res*. (2018) 10:2249–57. doi: 10.2147/CMAR

36. Diem S, Schmid S, Krapf M, et al. Neutrophil-to-Lymphocyte ratio (NLR) and Platelet-to-Lymphocyte ratio (PLR) as prognostic markers in patients with non-small cell lung cancer (NSCLC) treated with nivolumab. *Lung Cancer (Amsterdam Netherlands)*. (2017) 111:176–81. doi: 10.1016/j.lungcan.2017.07.024

37. Ameratunga M, Chénard-Poirier M, Moreno Candilejo I, Pedregal M, Lui A, Dolling D, et al. Neutrophil-lymphocyte ratio kinetics in patients with advanced solid tumours on phase I trials of PD-1/PD-L1 inhibitors. *Eur J Cancer (Oxford England: 1990)*. (2018) 89:56–63. doi: 10.1016/j.ejca.2017.11.012

38. Coffelt SB, Wellenstein MD, De Visser KE. Neutrophils in cancer: neutral no more. *Nat Rev Cancer*. (2016) 16:431–46. doi: 10.1038/nrc.2016.52

39. Dumitru CA, Lang S, Brandau S. Modulation of neutrophil granulocytes in the tumor microenvironment: mechanisms and consequences for tumor progression. *Semin Cancer Biol*. (2013) 23:141–8. doi: 10.1016/j.semcancer.2013.02.005

40. Gershkovitz M, Caspi Y, Fainsod-Levi T, Katz B, Michaeli J, Khawaled S, et al. TRPM2 mediates neutrophil killing of disseminated tumor cells. *Cancer Res*. (2018) 78:2680–90. doi: 10.1158/0008-5472.CAN-17-3614

41. Das A, Monteiro M, Barai A, Kumar S, Sen S, et al. MMP proteolytic activity regulates cancer invasiveness by modulating integrins. *Sci Rep*. (2017) 7:14219. doi: 10.1038/s41598-017-14340-w

42. Sica A, Porta C, Morlacchi S, Banfi S, Strauss L, Rimoldi M, et al. Origin and functions of tumor-associated myeloid cells (TAMCs). *Cancer Microenviron*. (2012) 5:133–49. doi: 10.1007/s12307-011-0091-6

43. Gungabeesoon J, Gort-Freitas NA, Kiss M, Bolli E, Messemaker M, Siwicki M, et al. A neutrophil response linked to tumor control in immunotherapy. *Cell*. (2023) 186:1448–64.e20. doi: 10.1016/j.cell.2023.02.032

44. Yang S, Jia J, Wang F, Wang Y, Fang Y, Yang Y, et al. Targeting neutrophils: Mechanism and advances in cancer therapy. *Clin Trans Med*. (2024) 14:e1599. doi: 10.1002/ctm2.1599

45. Wang C, Zheng X, Zhang J, Jiang X, Wang J, Li Y, et al. CD300ld on neutrophils is required for tumour-driven immune suppression. *Nature*. (2023) 621:830–9. doi: 10.1038/s41586-023-06511-9

46. Zhou J, Jiang S, Wang W, Liu R. [Research progress of tumor-associated neutrophils and lung cancer]. *Zhongguo Fei Ai Za Zhi = Chin J Lung Cancer*. (2019) 22:727–31. doi: 10.3779/j.issn.1009-3419.2019.11.07

47. Sun D, Liu J, Zhou H, Sun J, Zhao S, Chen G, et al. Classification of tumor immune microenvironment according to programmed death-ligand 1 expression and immune infiltration predicts response to immunotherapy plus chemotherapy in advanced patients with NSCLC. *J Thorac Oncol*. (2023) 18:869–81. doi: 10.1016/j.jtho.2023.03.012

48. Si H, Kuziora M, Quinn KJ, Helman E, Ye J, Liu F, et al. A blood-based assay for assessment of tumor mutational burden in first-line metastatic NSCLC treatment: results from the MYSTIC study. *Clin Cancer Res*. (2021) 27:1631–40. doi: 10.1158/1078-0432.CCR-20-3771

frontiers | Frontiers in Immunology

TYPE Original Research
PUBLISHED 07 May 2024
DOI 10.3389/fimmu.2024.1381061

OPEN ACCESS

EDITED BY
Takaji Matsutani,
Maruho, Japan

REVIEWED BY
Tingting Zhang,
Shanxi Medical University, China
Christopher Alan Muir,
St. Vincent's Hospital Sydney, Australia

*CORRESPONDENCE
Zhanjun Guo
zjguo5886@aliyun.com

RECEIVED 02 February 2024
ACCEPTED 22 April 2024
PUBLISHED 07 May 2024

CITATION
Xing N, Liu J, Hou L, Zhao Y, Ma H, Wang F and Guo Z (2024) Clinical biomarkers for thyroid immune-related adverse events in patients with stage III and IV gastrointestinal tumors. *Front. Immunol.* 15:1381061. doi: 10.3389/fimmu.2024.1381061

Clinical biomarkers for thyroid immune-related adverse events in patients with stage III and IV gastrointestinal tumors

Na Xing[1,2], Jing Liu[3], Lin Hou[2], Yue Zhao[4], Hongfang Ma[2], Fujun Wang[2] and Zhanjun Guo[1*]

[1]Department of Rheumatology and Immunology, The Fourth Hospital of Hebei Medical University, Shijiazhuang, China, [2]Department of Endocrinology, The Fourth Hospital of Hebei Medical University, Shijiazhuang, China, [3]Department of Cardiology, The Fourth Hospital of Hebei Medical University, Shijiazhuang, China, [4]Department of Gastroenterology, The Fourth Hospital of Hebei Medical University, Shijiazhuang, China

Background: Thyroid immune-related adverse events (irAEs) associated with immune checkpoint inhibitor (ICI) treatment appear to correlate with a better prognosis. We aimed to investigate clinical biomarkers associated with thyroid irAEs.

Methods: We retrospectively analyzed data from 129 patients receiving programmed cell death protein 1 (PD-1) inhibitors for stage III and IV gastrointestinal tumors. Patients were divided into two groups: "thyroid irAEs" group and "no thyroid irAEs" group. We compared continuous variables using Mann–Whitney U and Kruskal–Wallis tests and categorical variables using Pearson's chi–square test. Survival curves were generated using the Kaplan–Meier method, and associations between clinical features and thyroid irAEs were assessed using univariate and multivariate logistic regression models. Associations for thyroid irAEs and outcomes [progression-free survival (PFS), overall survival (OS)] of the patients were performed with a Cox proportional hazard model.

Results: A total of 129 patients, including 66 gastric cancer, 30 esophageal squamous cell carcinoma, and 33 hepatocellular carcinoma (HCC), were involved in this analysis with 47 cases of thyroid irAEs occurrence. The Cox proportional hazard model analysis confirmed the extended PFS [hazard rate (HR) = 0.447, 95% confidence interval (CI): 0.215 to 0.931, p = 0.031] and OS (HR = 0.424, 95% CI: 0.201 to 0.893, p = 0.024) for thyroid irAEs group when compared with those of the no thyroid irAEs group. Association between thyroid irAEs and clinical characteristics at baseline was analyzed subsequently by univariate analysis. Higher body mass index (p = 0.005), increased eosinophil count (p = 0.014), increased lactate dehydrogenase (p = 0.008), higher baseline thyroid stimulating hormone (TSH) (p = 0.001), HCC (p = 0.001) and increased adenosine deaminase (ADA) (p = 0.001) were linked with thyroid irAEs occurrence. The multivariable logistic regression model indicated that ADA [odds rate (OR) = 4.756, 95% CI: 1.147 to 19.729, p = 0.032] was independently associated with thyroid irAEs occurrence.

Conclusions: Increased baseline level of ADA was associated with thyroid irAEs occurrence in patients with advanced gastrointestinal tumors who received ICI treatment. In the case of abnormal ADA, attention should be paid to the risk of thyroid irAEs.

KEYWORDS

thyroid, immune related adverse events, programmed cell death protein 1 inhibitors, adenosine deaminase, clinical biomarkers

1 Introduction

The global incidence and mortality rates of gastrointestinal tumors in China have reached approximately 50% (1), indicating the necessity for increased attention toward their prevention, diagnosis, and treatment. Since 2011, immune checkpoint inhibitors (ICIs), which promote the anti-tumor immune response of activated T cells by blocking the inhibitory signal, including cytotoxic T-lymphocyte associated protein 4 inhibitors, programmed cell death protein 1 (PD-1) inhibitors, and programmed cell death ligand 1 inhibitors, have been used as a treatment method for unresectable or metastatic melanoma, lung cancer, breast cancer, and gastrointestinal tumors with monotherapy or combined therapy (2). Immune-related adverse events (irAEs) occur owing to the overactivation of the immune system following ICI treatment. This overactivation triggers enhanced T cell activity towards antigens found in both tumor and normal tissues, inducing an inflammatory response and alterations in the autoimmune environment, thereby initiating the incidence of irAEs (3, 4). IrAEs appear to be associated with a favorable prognosis for ICI treatment, however, severe adverse reactions may necessitate discontinuation of medication and can even be life-threatening (2).

IrAEs can affect various organs and systems, causing dysfunction; thyroid dysfunction is a common endocrine irAE with a widely range of incidence rates in different reports (5–7). The mean incidence rate in phase III clinical trials is 10.8%, especially in patients using anti-PD1 drugs (8). Thyroid dysfunction includes primary hyperthyroidism, primary hypothyroidism, central hypothyroidism, and biphasic thyroiditis that transitions from transient hyperthyroidism to hypothyroidism with severe grade in rare cases (6). Thyroid dysfunction as an irAE has been associated with prolonged survival in various cancers, including caseds of non-small cell lung carcinoma (NSCLC), malignant melanoma, renal cell carcinoma, head and neck cancer, and gastric cancer (4–6). However, thyroid dysfunction can lead to metabolic abnormalities affecting the overall treatment effectiveness.

Few studies have focused on clinical biomarkers for the occurrence and timely monitoring of thyroid dysfunction as an irAE (5). High baseline levels of thyroid stimulating hormone (TSH) and positive thyroid related antibodies were associated with the occurrence of thyroid irAEs, but others biomarkers didn't reach consensus. This study is aimed to investigate clinical biomarkers for earlier diagnosis and follow-up of thyroid irAEs. Adenosine deaminase (ADA) is associated with the immune status in patients with solid tumors, with alterations observed during thyroid dysfunction occurred. ADA is a key enzyme regulating purine metabolism by degrading adenosine, thereby reducing its inhibitory effects on the immune system. Currently, no research has focused on the role of ADA in the occurrence of irAEs. In this study, we aimed to identify clinical biomarkers for the occurrence of thyroid irAEs.

2 Materials and methods

2.1 Patients

Patients diagnosed with stage III and IV gastrointestinal tumors and undergoing treatment with anti-PD-1 antibody monotherapy or combined therapy (chemotherapy or targeted therapy) at The Fourth Hospital of Hebei Medical University from November 2018 and November 2021 were included in this study. The inclusion criteria were: (1) any cancer type treated with a minimum of two courses of ICIs; (2) availability of serum thyroid hormone evaluation at baseline; and (3) availability of at least two different serum thyroid hormone evaluations during ICI treatment. The exclusion criteria were: (1) a surgical history of thyroid disease; (2) a history of head and neck radiotherapy; (3) a history of pituitary disease; (4) abnormal baseline thyroid hormone, and (5) a history of treatment with amiodarone. Clinical information, including age, sex, body mass index (BMI), cancer type, Eastern Cooperative Oncology Group Performance Status (ECOG PS), TNM stage, treatment lines, treatment regimen, irAEs, baseline peripheral blood markers, baseline thyroid function tests, and posttreatment thyroid function tests, was obtained from electronic medical records. The National Cancer Institute Common Terminology Criteria for Adverse Events ver. 4.03 (https://ctep.cancer.gov/protocolDevelopment/electronic_applications/ctc.htm#ctc 40) were used for irAE assessment.

All procedures were approved by the Ethics Committee of the Fourth Hospital of Hebei Medical University. This retrospective study analyzed existing data, and the requirement for informed consent was waived.

2.2 Treatment and assessment

Patients received standard anti-PD-1 antibodies (sintilimab, camrelizumab, pembrolizumab, toripalimab, and tisleizumab) every 3 weeks as monotherapy or combined therapy (targeted therapy/chemotherapy) until disease progression, clinical worsening, unacceptable toxicity, or patient refusal. No cytotoxic T lymphocyte-associated antigen-4 inhibitor was used in these patients. Clinical and laboratory tests were performed during each cycle before dosing. Body computed tomography or magnetic resonance imaging scans were performed every 2–3 cycles. Progression-free survival (PFS) was defined as the time from the first administration of anti-PD-1 therapy to disease progression, death, or the study cutoff; overall survival (OS) was defined as the time from the commencement of anti-PD-1 therapy to death or the study cutoff values. PFS and OS were evaluated using the Response Evaluation Criteria in Solid Tumors version 1.1 as the study endpoints.

Patients were divided into two groups based on thyroid function outcomes: the "thyroid irAEs" group and the "no thyroid irAEs" group. Thyrotoxicosis was defined as a TSH level <0.34 mIU/L, with free thyroxine (FT4) or total thyroxine (TT4) levels within or above the reference range. Hypothyroidism was characterized by a TSH level above the upper reference range, with FT4 or TT4 levels within or below the lower reference interval. Biphasic thyroiditis indicated transient thyrotoxicosis transitioning into hypothyroidism during follow-up. Thyroid function was measured using established reference ranges: TSH, 0.34–5.6 mIU/L; FT4, 7.98–16.02 pmol/L; free triiodothyronine, 3.53–7.37 pmol/L; TT4, 69.71–163.95 nmol/L; total triiodothyronine, 0.92–2.38 nmol/L; anti-thyroid peroxidase antibodies (TPOAb), <9 IU/mL; and thyroglobulin antibody (TGAb), <4 IU/mL.

2.3 Statistical analysis

Continuous variables were compared using Mann–Whitney U and Kruskal–Wallis tests, while categorical variables were analyzed using Pearson's chi–square test. Survival curves were drawn using the Kaplan–Meier method. The associations between clinical features and thyroid irAEs were assessed using univariate and multivariate logistic regression models. The association between the clinical features and survival was analyzed using the log-rank test. The associations between thyroid irAEs and outcomes (PFS, OS) of the patients were performed with a COX proportional hazard model. The receiver operating characteristic (ROC) curve analysis determined the best cutoff value. All results were considered statistically significant at p <0.05. Statistical analysis was performed using SPSS version 25.0 software (IBM Corp, Armonk, NY, USA), and figures were generated using GraphPad Prism version 9 (GraphPad Software, San Diego, CA, USA).

3 Results

3.1 Clinical characteristics analysis for thyroid irAEs and no-irAEs groups

In the cohort, 129 inpatients including 60 females and 69 males were involved in this study, with a median age of 63 years [interquartile range (IQR) 56–69 years], a median PFS of 146 days [95% confidence interval (CI): 181.44–241.21 days] and a median OS of 239 days (95% CI: 260.78–322.32 days). Gastric cancer was the most common type of tumor (n = 66, 51.2%), while 33 patients had hepatocellular carcinoma (HCC), and 30 patients had esophageal squamous cell carcinoma. Thyroid irAEs were observed in 47 patients (11 thyrotoxicosis, 27 hypothyroidism, 9 biphasic thyroiditis), with a median of 3 (IQR 2–5) cycles of treatment. Patients with HCC were more prone to thyroid irAEs compared with other cancer types. The baseline information is shown in Table 1.

3.2 Thyroid irAEs associated with disease control rate, PFS and OS

As shown in Table 1, BMI, tumor type, ADA level, lactate dehydrogenase (LDH) level, and baseline TSH level differed between the thyroid irAEs and no thyroid irAEs groups, demonstrating that the baseline status of these indicators affected the occurrence of thyroid irAEs. The distribution frequency of thyroid irAEs incidence was not different for these 5 antibodies (p = 0.867). In Table 2, the disease control rate (DCR) between the two groups was significantly different (p= 0.002), which was observed 85.1% (95%CI:74.9% to 95.3%) in the thyroid irAEs group and 61.0% (95%CI:50.4% to 71.5%) in the no thyroid irAEs group.

The Kaplan–Meier curves of PFS and OS between the two groups are shown in Figure 1. The PFS analysis displayed a differentiated trend without statistical difference, while the median PFS in the thyroid irAEs group (559 [95% CI: 348–1142] days) was higher than that in the no-irAEs group (360 [95% CI: 247–441] days) (p = 0.052). The median OS in the no- irAEs group was 408 (95% CI: 235–499) days, which was lower than that (611 days [95% CI: 367–1123) days) in the thyroid irAEs group (p = 0.013). Univariate and multivariate analysis were performed for these clinical characteristics and outcomes (PFS and OS) in these patients. In Table 3, the multivariate analysis indicated the thyroid irAEs group [hazard rate (HR) = 0.447, 95%CI: 0.215 to 0.931, p = 0.031 for PFS; HR = 0.424, 95%CI: 0.201 to 0.893, p = 0.024 for OS] and treatment line (>2) (HR = 3.360, 95%CI: 1.592 to 7.092, p = 0.001 for PFS; HR = 2.137, 95%CI: 1.037 to 4.405, p = 0.040 for OS) were linked with outcome of these patients with gastrointestinal cancer. Higher level of neutrophil: lymphocyte ratio (NLR) was associated with a shorter OS at statistical levels (HR =

10.3389/fimmu.2024.1381061

TABLE 1 Characteristics of patients with and without thyroid immune-related adverse events (irAEs).

	Total N (%)	No thyroid irAEs No. (%)	Thyroid irAEs No. (%)	*p*
Total N	120 (100)	82 (63.6)	47 (36.4)	
Sex				
female	60 (46.5)	37 (45.1)	23 (48.9)	0.676
male	69 (53.5)	45 (54.9)	24 (51.1)	
Age(years)				
≤60	51 (39.5)	29 (35.4)	22 (46.8)	0.201
>60	78 (60.5)	53 (64.6)	25 (53.2)	
BMI (kg/m^2)				
≤21.06	54 (41.9)	42 (51.2)	12 (25.5)	0.004
>21.06	75 (58.1)	40 (48.8)	35 (74.5)	
ECOG PS				
≤1	60 (46.5)	36 (43.9)	24 (51.1)	0.433
>1	69 (53.5)	46 (56.1)	23 (48.9)	
Treatment Line				
≤2	100 (77.5)	61 (74.4)	39 (83.0)	0.261
>2	29 (22.5)	21 (25.6)	8 (17.0)	
Anti-PD-1 antibodies				
Sintilimab	31(24.0)	20(24.4)	11(23.4)	0.867
Camrelizumab	51(39.5)	31(37.8)	20(42.6)	
Pembrolizumab	19(14.7)	11(13.4)	8(17.0)	
Toripalimab	6(4.7)	4(4.9)	2(4.3)	
Tisleizumab	22(17.1)	16(19.5)	6(12.8)	
Disease Status				
III	47 (36.4)	30 (36.6)	17 (36.2)	0.962
IV	82 (63.6)	52 (63.4)	30 (63.8)	
Tumor Types				
HCC	33 (25.6)	12 (14.6)	21 (44.7)	0.001
Esophageal squamous cell carcinoma	30 (23.3)	19 (23.2)	11 (23.4)	
Gastric cancer	66 (51.2)	51 (62.2)	15 (31.9)	
Concurrent therapy				
Chemotherapy drugs	55 (42.6)	40 (48.8)	15 (31.9)	0.062
Targeted drugs	74 (57.4)	42 (51.2)	32 (68.1)	
Other irAEs				
No	111 (86.0)	71 (86.6)	40 (85.1)	0.816
Yes	18 (14.0)	11 (13.4)	7 (14.9)	
TPOAb				
Negative	84 (80.0)	58 (85.3)	26 (70.33)	0.066
Positive	21 (20.0)	10 (14.7)	10 (29.7)	

(Continued)

TABLE 1 Continued

	Total N (%)	No thyroid irAEs No. (%)	Thyroid irAEs No. (%)	*p*
TGAb				
Negative	84 (80.0)	56 (82.4)	28 (75.7)	0.414
Positive	21 (20.0)	12 (17.6)	9 (24.3)	
Clinical Baseline Value[Median (IQR)]				
NLR	3.47 (2.90)	3.24 (2.70)	3.57 (3.57)	0.391
PLR	181.15 (140.43)	181.36 (135.39)	177.91 (164.39)	0.483
Eosinophil count ($\times 10^9$/L)	0.08 (0.13)	0.08 (0.11)	0.09 (0.19)	0.145
ADA(U/L)	11.90 (7.55)	10.90 (5.10)	14.20 (11.28)	0.005
LDH(U/L)	182.00 (82.68)	175.00 (67.50)	192.30 (135.00)	0.004
Baseline TSH (mIU/L)	1.67 (1.37)	1.48 (1.05)	2.24 (1.44)	0.001

IQR, interquartile range; NLR, neutrophil-to-lymphocyte ratio; PLR, platelet-to-lymphocyte ratio; ADA, adenosine deaminase; LDH, lactate dehydrogenase.

2.265, 95%CI: 1.138 to 4.508, $p = 0.020$). These data indicate that thyroid irAEs were associated with a better prognosis for these cancer patients after ICI treatment.

3.3 The association analysis for clinical characteristics and thyroid irAEs

The thyroid irAEs identified in this study were mild (grade 1–2). The association between thyroid irAEs and clinical characteristics at baseline was analyzed subsequently by univariate analysis. Higher BMI ($p = 0.005$), increased eosinophil count ($p = 0.014$), increased LDH ($p = 0.008$), higher TSH ($p = 0.001$), HCC ($p = 0.001$) and increased ADA ($p = 0.001$) were linked with thyroid irAEs occurrence. The multivariate analysis, shown in Table 4, indicated that higher BMI [odds rate (OR) = 5.095, 95%CI: 1.316 to 19.730, $p = 0.018$], increased eosinophil count (OR = 7.553, 95%CI: 1.940 to 29.400, $p = 0.004$), increased ADA (OR = 4.756, 95%CI: 1.147 to 19.729, $p = 0.032$), higher TSH (OR = 3.540, 95%CI: 1.007 to 12.440, $p = 0.049$), lower ECOG PS level (OR = 0.221, 95%CI: 0.054 to 0.899, $p = 0.035$), and positive TPOAb (OR = 11.326, 95%CI: 1.637 to 78.355, $p = 0.014$) were independently associated with the occurrence of thyroid irAEs.

4 Discussion

Thyroid irAEs were the most prevalent PD-1 inhibitors related irAEs including hypothyroidism, hyperthyroidism, biphasic thyroiditis, and central hypothyroidism, with hypothyroidism comprises the majority (9). Our study revealed thyroid irAEs in 47 out of 129 patients (36.4%), which is comparable to previous reports (42%) (4). Despite the occurrence of thyroid irAEs, most patients exhibited a low fatality rate and manifested symptoms, such as arrhythmia, myxedema, and marasmus (10). Timely monitoring of thyroid function is crucial to prevent thyroid dysfunction in cancer patients receiving the ICI treatment and maintain sustained therapeutic effects. Patients with thyroid irAEs tended to a longer OS and a trend of longer PFS than those without thyroid dysfunction, which was also comparable to the previous reports (6).

Patients with HCC were more prone to thyroid thyroid irAEs compared with other cancer types, although this conclusion needs to be validated in a larger population. The liver is the site for thyroid hormone synthesis and metabolism, HCC can initiate more synthesis and secretion of thyroxine binding globulin, which contributes to the occurrence of hypothyroidism by augmented thyroxine binding globulin-T4 binding (11, 12). In addition, signaling pathways, such

TABLE 2 Effect of thyroid immune-related adverse events (irAEs) on immune checkpoint inhibitor (ICI) efficacy.

	Total	No thyroid irAEs	Thyroid irAEs	*p*
PD	38	32	6	–
SD	59	34	25	–
PR	300	16	14	–
CR	2	0	2	–
ORR	24.8% (16.5–30.6%)	19.5% (10.9–28.1%)	34.0% (20.5–47.6%)	0.066
DCR	69.8% (61.6–76.9%)	61.0% (50.4–71.5%)	85.1% (74.9–95.3%)	0.004

SD, stable disease; PR, partial response; PD, progressive disease; CR, complete response; ORR, objective response rate; DCR, disease control rate.

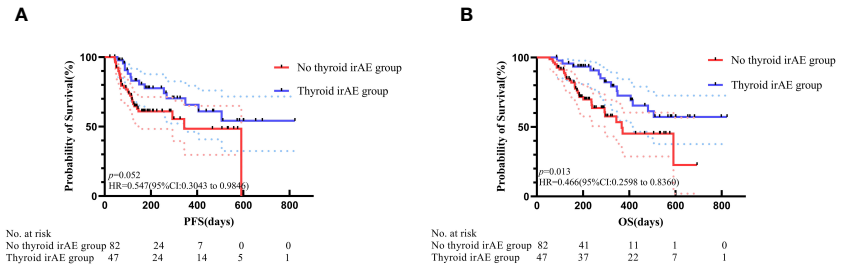

FIGURE 1
Association of thyroid irAEs with patient prognosis. **(A)** Kaplan–Meier curve showing PFS; **(B)** Kaplan-Meier curve illustrating OS.

as TGF-β, Wnt, and Hedgehog, midiate inflammation and fibrosis of HCC, which can regulate the metabolism of thyroid hormones. Liver abnormalities are more likely to induce the abnormalities of thyroid hormone metabolism, which may be one of the reasons why patients with HCC are more prone to thyroid irAEs (13).

Our investigation identified a higher baseline level of ADA (>14.05 U/L) as an independent biomarker associated with thyroid irAEs. ADA, a key enzyme involved in purine metabolism and immune system regulation, has been associated with thyroid autoimmune diseases at the transcriptional level (14). It can activate T lymphocytes (15) as well as alleviate immunosuppressive effects by degrading adenosine (16). The adenosine receptors on the dendritic cells (DCs) can interact with CD26 on the surface of T cells to mediate the CD4+ T cell differentiation (17), DCs deliver antigens to CD4+ T cells so as to stimulate the production of thyroid related antibodies, thereby destroying the thyroid follicular

TABLE 3 Multivariate analysis of PFS and OS with COX regression models.

	PFS			OS		
	HR	95%CI	*p*	HR	95%CI	*p*
Age (years)						
≤60 >60	Reference 1.080	0.552-2.114	0.822	Reference 1.441	0.746-2.783	0.277
BMI (kg/m2)						
≤21.06	Reference		0.191	Reference		0.158
>21.06	0.645	0.334-1.244		0.626	0.326-1.201	
ECOG PS						
≤1 >1	Reference 1.577	0.778-3.189	0.207	Reference 1.587	0.785-3.206	0.198
Treatment Line						
≤2	Reference		0.001	Reference		0.040
>2	3.360	1.592-7.092		2.137	1.037-4.405	
Tumor Types						
HCC	Reference			Reference		
Esophageal squamous cell carcinoma	0.431	0.143-1.298	0.135	0.574	0.200-1.643	0.301
Gastric cancer	0.515	0.218-1.221	0.132	0.744	0.273-2.026	0.563
NLR						
≤3.26 >3.26	Reference 1.637	0.841-3.189	0.147	Reference 2.265	1.138-4.508	0.020
Thyroid irAEs						
No	Reference		0.031	Reference		0.024
Yes	0.447	0.215-0.931		0.424	0.201-0.893	

NLR, neutrophil: lymphocyte ratio.

10.3389/fimmu.2024.1381061

TABLE 4 Univariate and multivariate analysis of thyroid immune-related adverse events (irAEs) with Logistic regression models.

	Univariate analysis			Multivariate analysis		
	OR	95% CI	*p*	OR	95% CI	*p*
Sex						
female	Reference		0.676	Reference		0.455
male	0.858	0.418-1.7760		1.698	0.423-6.809	
Age (years)						
≤60	Reference		0.202	Reference		0.833
>60	0.622	0.300-1.291		0.878	0.263-2.936	
BMI (kg/m^2)						
≤21.06	Reference		0.005	Reference		0.018
>21.06	3.062	1.396-6.719		5.095	1.316-19.730	
ECOG PS						
≤1	Reference		0.433	Reference		0.035
>1	0.750	0.365-1.540		0.221	0.054-0.899	
Tumor Types						
Gastric Cance	Reference			Reference		
HCC	5.950	2.387-14.833	0.001	5.467	0.884-33.824	0.068
Esophageal squamous cell carcinoma	0.968	0.769-5.037	0.158	0.816	0.128-5.218	0.830
TPOAb						
Negative	Reference		0.071	Reference		0.014
Positive	2.454	0.927-6.495		11.326	1.637-78.355	
TGAb						
Negative	Reference		0.416	Reference		0.451
Positive	1.500	0.565-3.981		0.458	0.060-3.484	
NLR						
≤3.26	Reference		0.100	Reference		0.711
>3.26	1.853	0.888-3.868		1.288	0.338-4.906	
PLR						
≤286.48	Reference		0.383	Reference		0.076
>286.48	1.484	0.611-3.603		3.999	0.863-18.528	
Eosinophil count)						
≤0.20 × 10^9/L	Reference		0.014	Reference		0.004
>0.20 × 10^9/L	3.026	1.251-7.315		7.553	1.940-29.400	
ADA (U/L)						
≤14.05	Reference		0.001	Reference		0.032
>14.05	4.304	1.952-9.492		4.756	1.147-19.729	
LDH (U/L)						
≤173.50	Reference		0.008	Reference		0.513
>173.50	3.042	1.336-6.927		1.552	0.416-5.792	

(Continued)

TABLE 4 Continued

	Univariate analysis			Multivariate analysis		
	OR	95% CI	*p*	OR	95% CI	*p*
Baseline TSH (mIU/L)						
≤2.205	Reference		0.001	Reference		0.049
>2.205	4.040	1.860-8.776		3.540	1.007-12.440	

cells (18). In addition, the number of DCs increased significantly when thyroid autoimmune response occurred to aggravate the immune response (19). ADA might modify the thyroid irAEs by stimulating DCs and T cells through the adenosine receptors on DCs. The increasing of ADA after ICI treatment especially in thyroid irAEs patients reminds us to pay attention to the change of thyroid function.

We identified BMI (>21.06 kg/m^2), ECOG PS (≤1) and eosinophil count (>0.20 × 10^9/L) as associated factors for thyroid irAEs. Consistent report demonstrated that a higher BMI is associated with increased incidence of irAEs and improved outcomes in various cancers such as NSCLC, melanoma, renal cell carcinoma, head and neck tumors, and epithelial urothelial carcinoma (20, 21). Additionally, a study involving approximately 19% of patients with gastrointestinal tumors suggested a correlation between higher BMI and increased risk of overt thyroid dysfunction in ICI-treated cancers (21). Our study corroborated these findings, demonstrating that patients with gastrointestinal tumors and higher BMI are more susceptible to thyroid irAEs. One plausible explanation for this association is that obesity induces systemic inflammation and compromises immune response through modulation of leptin secretion, which is known to correlate with PD-1 expression in CD8+ T cells (22).

In our previous study, we observed that a lower ECOG PS was associated with a better prognosis (23). However, the relationship between ECOG PS and irAEs remains contentious due to the limited data. While ECOG PS (≤1) was identified as an independent risk factor for irAEs in patients with NSCLC who received ICI treatment (24), however, another study found no significant association between ECOG PS and irAEs for patients with metastatic renal cell carcinoma who received ICI treatment (25). This potential association between ECOG PS and thyroid irAEs should be re-evaluated in a larger population.

Additionally, higher eosinophil count (>0.20 × 10^9/L), higher level of TSH (>2.205mIU/L) and positivie TPOAb were identified as baseline factors for thyroid irAEs association in gastrointestinal tumors, which was also consistent with previous findings in solid tumors (26–28).

5 Conclusions

Increased baseline level of ADA was associated with thyroid irAEs occurrence in patients with advanced gastrointestinal tumors who received ICI treatment. In the case of abnormal ADA, attention should be paid to the risk of thyroid irAEs.

Data availability statement

The original contributions presented in the study are included in the article/supplementary materials, further inquiries can be directed to the corresponding author/s.

Ethics statement

The studies involving humans were approved by The Ethics Committee of The Fourth Hospital of Hebei Medical University. The studies were conducted in accordance with the local legislation and institutional requirements. The ethics committee/institutional review board waived the requirement of written informed consent for participation from the participants or the participants' legal guardians/next of kin because This study was retrospective and analyzed by existing data, waiver of informed consent was applied for the patient.

Author contributions

NX: Conceptualization, Funding acquisition, Methodology, Validation, Writing – original draft, Writing – review & editing. JL: Data curation, Formal analysis, Investigation, Software, Writing – review & editing. LH: Formal analysis, Project administration, Validation, Visualization, Writing – review & editing. YZ: Resources, Supervision, Visualization, Writing – review & editing. HM: Data curation, Resources, Writing – review & editing. FW: Conceptualization, Supervision, Writing – review & editing. ZG: Conceptualization, Funding acquisition, Resources, Supervision, Validation, Writing – review & editing.

Funding

The author(s) declare financial support was received for the research, authorship, and/or publication of this article. This work was supported by the Key Research and Development Projects of Hebei Province (No. 20230895).

Conflict of interest

The authors declare that the research was conducted in the absence of any commercial or financial relationships that could be construed as a potential conflict of interest.

Publisher's note

References

1. Qiu H, Cao S, Xu R. Cancer incidence, mortality, and burden in China: a time-trend analysis and comparison with the United States and United Kingdom based on the global epidemiological data released in 2020. *Cancer Commun (Lond)*. (2021) 41:1037–48. doi: 10.1002/cac2.12197

2. Khoja L, Day D, Wei-Wu Chen T, Siu LL, Hansen AR. Tumour- and class-specific patterns of immune-related adverse events of immune checkpoint inhibitors: a systematic review. *Ann Oncol*. (2017) 28:2377–85. doi: 10.1093/annonc/mdx286

3. Chennamadhavuni A, Abushahin L, Jin N, Presley CJ, Manne A. Risk factors and biomarkers for immune-related adverse events: A practical guide to identifying high-risk patients and rechallenging immune checkpoint inhibitors. *Front Immunol*. (2022) 13:779691. doi: 10.3389/fimmu.2022.779691

4. Passat T, Touchefeu Y, Gervois N, Jarry A, Bossard C, Bennouna J. [Physiopathological mechanisms of immune-related adverse events induced by anti-CTLA-4, anti-PD-1 and anti-PD-L1 antibodies in cancer treatment]. *Bull Cancer*. (2018) 105:1033–41. doi: 10.1016/j.bulcan.2018.07.005

5. Muir CA, Clifton-Bligh RJ, Long GV, Scolyer RA, Lo SN, Carlino MS, et al. Thyroid immune-related adverse events following immune checkpoint inhibitor treatment. *J Clin Endocrinol Metab*. (2021) 106:e3704–3704e3713. doi: 10.1210/clinem/dgab263

6. Lima Ferreira J, Costa C, Marques B, Castro S, Victor M, Oliveira J, et al. Improved survival in patients with thyroid function test abnormalities secondary to immune-checkpoint inhibitors. *Cancer Immunol Immunother*. (2021) 70:299–309. doi: 10.1007/s00262-020-02664-y

7. Zhou Y, Xia R, Xiao H, Pu D, Long Y, Ding Z, et al. Thyroid function abnormality induced by PD-1 inhibitors have a positive impact on survival in patients with non-small cell lung cancer. *Int Immunopharmacol*. (2021) 91:107296. doi: 10.1016/j.intimp.2020.107296

8. Muir CA, Menzies AM, Clifton-Bligh R, Tsang V. Thyroid toxicity following immune checkpoint inhibitor treatment in advanced cancer. *Thyroid*. (2020) 30:1458–69. doi: 10.1089/thy.2020.0032

9. Lu Y, Li Q, Xu L, Zheng Y, Wang Y, Liu Y, et al. Thyroid dysfunction induced by anti-PD-1 therapy is associated with a better progression-free survival in patients with advanced carcinoma. *J Cancer Res Clin Oncol*. (2023) 149:16501–10. doi: 10.1007/s00432-023-05364-z

10. Wang DY, Salem JE, Cohen JV, Chandra S, Menzer C, Ye F, et al. Fatal toxic effects associated with immune checkpoint inhibitors: A systematic review and meta-analysis. *JAMA Oncol*. (2018) 4:1721–8. doi: 10.1001/jamaoncol.2018.3923

11. Burra P. Liver abnormalities and endocrine diseases. *Best Pract Res Clin Gastroenterol*. (2013) 27:553–63. doi: 10.1016/j.bpg.2013.06.014

12. Duan J, Kang J, Deng T, Yang X, Chen M. Exposure to DBP and high iodine aggravates autoimmune thyroid disease through increasing the levels of IL-17 and thyroid-binding globulin in wistar rats. *Toxicol Sci*. (2018) 163:196–205. doi: 10.1093/toxsci/kfy019

13. Manka P, Coombes JD, Boosman R, Gauthier K, Papa S, Syn WK. Thyroid hormone in the regulation of hepatocellular carcinoma and its microenvironment. *Cancer Lett*. (2018) 419:175–86. doi: 10.1016/j.canlet.2018.01.055

14. Karbownik M, Brzeziańska E, Zasada K, Lewiński A. Expression of genes for certain enzymes of pyrimidine and purine salvage pathway in peripheral blood leukocytes collected from patients with Graves' or Hashimoto's disease. *J Cell Biochem*. (2003) 89:550–5. doi: 10.1002/jcb.10533

15. Van der Weyden MB, Kelley WN. Human adenosine deaminase. Distribution and properties. *J Biol Chem*. (1976) 251:5448–56. doi: 10.1016/S0021-9258(17)33080-6

16. Qu Y, Dunn ZS, Chen X, MacMullan M, Cinay G, Wang HY, et al. Adenosine deaminase 1 overexpression enhances the antitumor efficacy of chimeric antigen receptor-engineered T cells. *Hum Gene Ther*. (2022) 33:223–36. doi: 10.1089/hum.2021.050

17. Martinez-Navio JM, Casanova V, Pacheco R, Naval-Macabuhay I, Climent N, Garcia F, et al. Adenosine deaminase potentiates the generation of effector, memory, and regulatory CD4+ T cells. *J Leukoc Biol*. (2011) 89:127–36. doi: 10.1189/jlb.1009696

18. Wang Q, Shi BM, Xie F, Fu ZY, Chen YJ, An JN, et al. Enhancement of CD4(+) T cell response and survival via coexpressed OX40/OX40L in Graves' disease. *Mol Cell Endocrinol*. (2016) 430:115–24. doi: 10.1016/j.mce.2016.04.008

19. Vasu C, Holterman MJ, Prabhakar BS. Modulation of dendritic cell function and cytokine production to prevent thyroid autoimmunity. *Autoimmunity*. (2003) 36:389–96. doi: 10.1080/0891693031000160373

20. Rogado J, Romero-Laorden N, Sanchez-Torres JM, Ramos-Levi AM, Pacheco-Barcia V, Ballesteros AI, et al. Effect of excess weight and immune-related adverse events on the efficacy of cancer immunotherapy with anti-PD-1 antibodies. *Oncoimmunology*. (2020) 9:1751548. doi: 10.1080/2162402X.2020.1751548

21. Gülave B, Hew MN, de Groot JS, Rodwell L, Teerenstra S, Fabriek BO. High body mass index and pre-existing autoimmune disease are associated with an increased risk of immune-related adverse events in cancer patients treated with PD-(L)1 inhibitors across different solid tumors. *ESMO Open*. (2021) 6:100107. doi: 10.1016/j.esmoop.2021.100107

22. Wang Z, Aguilar EG, Luna JI, Dunai C, Khuat LT, Le CT, et al. Paradoxical effects of obesity on T cell function during tumor progression and PD-1 checkpoint blockade. *Nat Med*. (2019) 25:141–51. doi: 10.1038/s41591-018-0221-5

23. Wang Y, Zhang S, Zhang F, Wang L, Wu C, Zhang X, et al. Young patients show poor efficacy for immune checkpoint inhibitor combined therapy in metastatic gastrointestinal cancers. *Front Oncol*. (2023) 13:1155019. doi: 10.3389/fonc.2023.1155019

24. Gao W, Liu Q, Zhou Y, Yang M, Yu Y. The predictive model construction for immune-related adverse events in non-small cell lung cancer patients receiving immunotherapy. *Technol Cancer Res Treat*. (2023) 22:15330338231206705. doi: 10.1177/15330338231206705

25. Desai k RL, Nizam A WL, Allman K MA, Calabrese C. Retrospective analysis of immune-related adverse events (irAE) in metastatic renal cell carcinoma (mRCC) patients treated with first-line ipilimumab and nivolumab (I N). *J Clin Oncol* (2020) 38 (15):e17094–17094e17094. doi: 10.1200/jco.2020.38.15_suppl.e17094

26. Sakakida T, Ishikawa T, Uchino J, Chihara Y, Komori S, Asai J, et al. Clinical features of immune-related thyroid dysfunction and its association with outcomes in patients with advanced Malignancies treated by PD-1 blockade. *Oncol Lett*. (2019) 18:2140–7. doi: 10.3892/ol.2019.10466

27. Iwama S, Kobayashi T, Yasuda Y, Okuji T, Ito M, Ando M, et al. Increased risk of thyroid dysfunction by PD-1 and CTLA-4 blockade in patients without thyroid autoantibodies at baseline. *J Clin Endocrinol Metab*. (2022) 107:e1620–1620e1630. doi: 10.1210/clinem/dgab829

28. Kobayashi T, Iwama S, Yamagami A, Yasuda Y, Okuji T, Ito M, et al. Elevated TSH level, tgAb, and prior use of ramucirumab or TKIs as risk factors for thyroid dysfunction in PD-L1 blockade. *J Clin Endocrinol Metab*. (2022) 107:e4115–4115e4123. doi: 10.1210/clinem/dgac467

frontiers | Frontiers in Immunology

TYPE Original Research
PUBLISHED 17 June 2024
DOI 10.3389/fimmu.2024.1425873

OPEN ACCESS

EDITED BY
Takaji Matsutani,
Maruho, Japan

REVIEWED BY
Sreeram Vallabhaneni,
Harvard Medical School, United States
Jiexian Ma,
Fudan University, China

*CORRESPONDENCE
Danke Su
sudanke33@sina.com

†These authors have contributed equally to this work

RECEIVED 30 April 2024
ACCEPTED 04 June 2024
PUBLISHED 17 June 2024

CITATION
Fang X, Huang X, Lu J and Su D (2024) Causal role of immune cells in thyroid cancer: a bidirectional Mendelian randomization study. *Front. Immunol.* 15:1425873. doi: 10.3389/fimmu.2024.1425873

Causal role of immune cells in thyroid cancer: a bidirectional Mendelian randomization study

Xianliu Fang[1†], Xiaoxiao Huang[2†], Jianhua Lu[1] and Danke Su[1*]

[1]Department of Medical Imaging Center, Guangxi Medical University Cancer Hospital, Nanning, Guangxi, China, [2]Rehabilitation Medicine Department, The First Affiliated Hospital of Guangxi Medical University, Nanning, Guangxi, China

Background: The immune system plays an important role in the development and treatment of thyroid cancer(THCA).However, the correlation between immune cells and THCA has not been systematically studied.

Methods: This study used a two-sample Mendelian randomization (MR) study to determine the causal relationship between immune cell characteristics and THCA. Based on a large sample of publicly available genetic data, we explored the causal relationship between 731 immune cell characteristics and THCA risk. The 731 immunophenotypes were divided into 7 groups, including B cell panel (n=190),cDC panel(n=64),Maturation stages of T cell panel(n=79),Monocyte panel(n=43),Myeloid cell panel(n=64),TBNK panel(n=124),and Treg panel (n=167). The sensitivity of the results was analyzed, and heterogeneity and horizontal pleiotropy were excluded.

Results: After FDR correction, the effect of immunophenotype on THCA was not statistically significant. It is worth mentioning, however, that there are some unadjusted low P-values phenotypes. The odds ratio (OR) of CD62L on monocyte on THCA risk was estimated to be 0.953 (95% CI=0.930~0.976, P=1.005×10^{-4}),and which was estimated to be 0.975(95% CI=0.961–0.989, P=7.984×10^{-4}) for Resting Treg%CD4 on THCA risk. Furthermore, THCA was associated with a reduced risk of 5 immunophenotype:CD25 on CD39+ CD4 on Treg (OR=0.871, 95% CI=0.812~0.935, P=1.274×10^{-4}), activated Treg AC (OR=0.884, 95% CI=0.820~0.953, P=0.001), activated & resting Treg % CD4 Treg (OR=0.872, 95%CI=0.811~0.937,P=2.109×10^{-4}),CD28- CD25++ CD8br AC(OR=0.867,95% CI=0.809~0.930,P=6.09×10^{-5}),CD28-CD127-CD25++CD8brAC(OR=0.875,95% CI=0.814~0.942,P=3.619×10^{-4}).THCA was associated with an increased risk of Secreting Treg % CD4 Treg (OR=1.143, 95% CI=1.064~1.229, P=2.779×10^{-4}) and CD19 on IgD+ CD24+ (OR=1.118, 95% CI=1.041~1.120, P=0.002).

Conclusions: These findings suggest the causal associations between immune cells and THCA by genetic means. Our results may have the potential to provide guidance for future clinical research.

KEYWORDS

immunophenotypes, causal inference, Mendelian randomization study, thyroid cancer, immunotherapy

1 Introduction

Thyroid cancer (THCA) is the most common malignancy of the endocrine system. The incidence of THCA has been increasing over the past few decades (1). According to the GLOBOCAN 2020 Cancer Incidence and Mortality database of the World Health Organization's International Agency for Research on Cancer, thyroid cancer ranks ninth in the global incidence of cancer (2, 3). Thyroid cancer has become the most common malignancy among adolescents and adults aged 16–33 years (4). Although most patients with THCA are cured by 131I or surgery, a small percentage die from metastasis or recurrence (5). One study showed that 28% of THCA patients relapsed and 9% of THCA patients died (6). Part of the reason is that in the process of tumor development, the interaction and collective action between the tumor and the surrounding immune microenvironment promote immune tolerance, and then develop into immune escape, resulting in the inability of the body to completely clear the tumor. In recent years, important progress has been made in the treatment of tumor immune-related regulation (7, 8). Studies have shown that, the immune system plays a key role in the occurrence and development of tumor. Tumor cells are recognized and eliminated by various immune cells in the body (9). Mantovani A et al. found that both innate and acquired immune responses can promote cancer initiation and tumor growth, or have anticancer effects (10). Previous studies have found that macrophage-targeted therapy can be used for invasive THCA, especially for THCA with high tumor-associated macrophage (TAM) content. Despite immunotherapy, including tumor vaccine therapy, immune checkpoints Inhibitor therapy, adoptive immune cell therapy, monoclonal antibody therapy and immunoregulatory cell targeting therapy have been widely used in the clinical treatment of thyroid cancer (8), but the correlation between immune cells and THCA has not been systematically studied.

Recently, Mendelian randomization (MR) studies based on whole genome sequencing data have been an effective and powerful statistical method to uncover causality by using genetic variation as an instrumental variable (IVs) (11). MR analysis makes use of the fixed nature and heredity of genes, that is, when meiosis gametes are formed, alleles of parents are randomly assigned to offspring, and the relationship between genes and outcome is not interfered by common confounding factors such as postnatal environment, behavioral habits, and social economy, so the causal relationship derived from this is reasonable (12).

In this study, we performed a comprehensive two-sample MR analysis to determine the causal association between immunophenotypes and THCA.

2 Materials and methods

2.1 Study design

Through a two-sample MR Analysis, we analyzed the causal relationship between 731 immune cell characteristics (7 groups) and THCA. MR analysis uses genetic variation as a working variable to estimate the causal relationship between the exposure factor of interest and the outcome of concern. Therefore, the effective instrumental variables (IVs) in MR Analysis must satisfy three key assumptions:(1) The association hypothesis: genetic variation needs to have a strong correlation with exposure factors, and if weak IVs are used, the results are prone to bias; (2) Independence hypothesis: genetic variation cannot be associated with possible confounders; (3) Exclusivity hypothesis: genetic variation can only affect outcomes through exposure, but not through other factors. Data for analysis included in our study were obtained with the approval of the relevant institutional review boards, and study participants provided informed consent.

2.2 Data sources

The genetic variation of each immune trait was obtained from the GWAS catalog (registration numbers GCST0001391 to GCST0002121) (13), which is the largest GWAS published so far on peripheral blood immune phenotypes. The total of 731 immunophenotypes were divided into 7 groups, including B cell panel(n=190),cDC panel(n=64),Maturation stages of T cell panel (n=79),Monocyte panel(n=43),Myeloid cell panel(n=64),TBNK panel(n=124),and Treg panel(n=167).

The initial immune characteristics of GWAS were analyzed using data from 3757 Europeans (57% female) without overlapping cohorts. About 22 million single nucleotide polymorphisms(SNPs) genotyped using high-density arrays were estimated using a reference panel based on Sardinian sequences and tested the correlation after adjusting for covariates (i.e.sex, age) (14). GWAS summary statistics for THCA were obtained from a GWAS, which was downloaded at FinnGen consortiums, including 491,974 European individuals (N_{case} = 1,054, $N_{control}$ = 490,920), with approximately 24.2 million variants analyzed after quality control and imputation.

2.3 Selection of instrumental variables

In this study, IVs were selected according to the following selection criteria:(1)SNPs strongly associated with exposure factors were selected ($p<1\times10^{-5}$); (2)Linkage disequilibrium(LD) was removed using r^2 <0.1 within 500 KB distance; (3)Instrumental variable correlation assessment: select F>10 to avoid bias caused by weak tools; (4) When palindromic SNPs exist, the allele frequency information is used to infer the front chain allele.

2.4 Statistical analysis

We used the following statistical methods to make causal inference of MR Analysis to evaluate the causal relationship between 731 immunophenotypes and THCA:(1)Inverse variance weighting (IVW) (15) was used as the main analysis; (2)Cochran's Q statistic and MR pleiotropy residual sum and outlier (MR-PRESSO) (16) were used to analyze the heterogeneity of SNPs.

(3)MR-Egger (17) and Leave-one-out method were used to analyze the sensitivity of the results. (4) The significant association between immunophenotype and THCA was corrected for false discovery rate (FDR) to control for the proportion of false positives in multiple tests. In addition, according to the IVs generated by THCA GWAS statistical data, reverse MR analysis was conducted to determine whether there was a causal relationship between THCA and immune traits. $P<0.05$ indicates the potential causal relationship in MR analysis, which is statistically significant. All statistical analyses were conducted using the "Two-Sample MR" package in R 4.3.1 software (http://www.Rproject.org).

3 Results

3.1 Exploration of the causal effect of THCA onset on immunophenotypes

Using two-sample MR analysis to explore the causal effects of THCA onset on immunophenotypes. After a variety of tests and adjustments using the FDR method, 7 immune traits were identified with a difference of 0.05, including 6 in the Treg group and 1 in the B cell group. We found that THCA onset could decrease the level of CD25 on CD39+ CD4 on Treg (OR=0.871, 95% CI=0.812~0.935, $P=1.274\times10^{-4}$, *P*FDR= 0.01, Table 1). Activated Treg AC were decreased in THCA patients (OR=0.884, 95% CI=0.820~0.953, $P=0.001$, *P*FDR =0.03, Table 1). Activated & resting Treg % CD4 Treg was also found to be decreased (OR=0.872, 95% CI=0.811~0.937,$P=2.109\times10^{-4}$, *P*FDR = 0.013, Table 1). Similar associations were found for CD28- CD25++ CD8br AC (OR=0.867, 95% CI=0.809~0.930, $P=6.09\times10^{-5}$, *P*FDR = 0.006, Table 1), and CD28- CD127- CD25++ CD8br AC (OR=0.875, 95% CI=0.814~0.942,$P=3.619\times10^{-4}$, *P*FDR = 0.017, Table 1). By contrary, We found that THCA onset could increase the level of Secreting Treg % CD4 Treg (OR=1.143, 95% CI=1.064~1.229, $P=2.779\times10^{-4}$, *P*FDR=0.016, Table 1), and CD19 on IgD+ CD24+ (OR=1.118, 95% CI=1.041~1.120, $P=0.002$, *P*FDR = 0.048, Table 1). The MR effect of THCA onset on immunophenotypes in different MR method was showed in Figure 1. Visual inspection of funnel plots (Figure 2) and leave-one-out plots (Figure 3) did not reveal any obvious directional pleiotropy.

3.2 Exploration of the causal effect of immunophenotypes on THCA

After multiple experimental adjustments based on the FDR method, no immune characteristics at a significance of 0.05 were found. At a significance of 0.20, we detected two immune traits as protective effects against THCA: CD62L on monocyte(cDC panel), with the odds ratio(OR) being estimated to be 0.953 (95% CI=0.930~0.976, $P=1.005\times10^{-4}$, PFDR=0.073, Table 2), and Resting Treg%CD4 (Treg panel),with the odds ratio(OR) being estimated to be 0.975(95% CI=0.961–0.989,$P=7.984\times10^{-4}$, *P*FDR=0.195, Table 2).The MR effect of each exposure on THCA in different MR method was showed in Figure 4. Visual inspection of funnel plots (Figure 5) and leave-one-out plots (Figure 6) did not reveal any obvious directional pleiotropy.

4 Discussion

The relationship between the immune system and THCA has always been a research hotspot. THCA is a malignant tumor that occurs in thyroid tissue, and the immune system plays an important role in the development and treatment of THCA. In THCA, immune cell interactions or interactions with cancer cells can exert anti-tumor and pro-tumor functions. In addition, various soluble factors released by immune cells (such as chemokines, cytokines, angiogenic factors, etc.) can also mediate the pro-tumor and anti-tumor effects of immune cells in cancer.

Galdiero et al. proposed that the immune system may be involved in the occurrence of THCA (18). Previous meta-analyses and systematic reviews of observational studies have also demonstrated an association between THCA and certain immune factors (e.g., neutrophils, Natural killer T cells, γδ T cells and innate lymphoid cells) (9, 19). However, observational studies may introduce confounding factors, and they cannot always differentiate between symptoms and etiology. Using genetically predicted causal effects of immunophenotypes on THCA, our results do not align with the previous findings.

It is well known that inflammation helps tumor development (20), and the immune system may prevent tumor growth by eliminating infections in a timely manner. Willimsky G et al. found that the immune system seems to have little effect on the onset of tumors, with some parts of the immune system showing a clear protective effect (21). Similarly, in our results, both CD62L on monocyte and Resting Treg %CD4 had protective effects on THCA,and no immune factors were found to contribute to the onset of THCA. CD62L is a cell adhesion molecule and type I transmembrane glycoprotein expressed on most circulating white blood cells. It is widely described as a bound/rolling receptor that plays a role in regulating monocyte protrusion during transendothelial migration (TEM). In adult humans, monocytes account for 2–8% of all circulating white blood cells and classic monocytes express high levels of L-selectin, i.e. CD62L on monocyte. During TEM of monocyte, the detachment of CD62L domains is crucial for establishing pre- and post cell polarity and achieving chemotaxis towards the site of injury (22), which can exert anti-tumor immune effects. The anti-tumor ability of CD4+ T cells has been widely demonstrated in mouse models and humans (23). By activating the immune system, CD4+ T cells can enhance the recognition and elimination of tumor cells, thereby inhibiting tumor growth and spread. Our results show that both CD62L on monocyte and Resting Treg %CD4 have a protective effect on THCA. Enhancing the activity of CD62L on monocyte and resting Treg% CD4 cells in tumor immunotherapy is expected to improve the therapeutic effect and may become an important part of future tumor immunotherapy strategies.

Jena D et al. found that the type of immune response produced by THCA was associated with disease severity (24). Many studies have proved that tumors have strong immunosuppressive ability. Regulatory

10.3389/fimmu.2024.1425873

TABLE 1 MR estimates for the causal effect of THCA onset on immunophenotypes.

traits (outcome)	MR method	No. of SNP	F-statistic	OR	95% CI	*P*-value
CD25 on CD39+ CD4 Treg	IVW	34	63.4	0.871	0.812~0.935,	1.274×10^{-4}
	MR-Egger	34	63.4	0.747	0.547–1.019	0.075
	Weighted median	34	63.4	0.840	0.751–0.938	0.002
	Weighted mode	34	63.4	0.825	0.709–0.959	0.017
	Simple mode	34	63.4	0.962	0.769–1.202	0.733
Activated Treg AC	IVW	34	63.4	0.884	0.820–0.953	0.001
	MR-Egger	34	63.4	1.092	0.794–1.502	0.591
	Weighted median	34	63.4	0.923	0.821–1.039	0.184
	Weighted mode	34	63.4	0.972	0.804–1.174	0.767
	Simple mode	34	63.4	0.905	0.721–1.136	0.395
Activated & resting Treg % CD4 Treg	IVW	34	63.4	0.8716	0.811–0.937	2.109×10^{-4}
	MR-Egger	34	63.4	0.800	0.585–1.093	0.170
	Weighted median	34	63.4	0.876	0.784–0.979	0.019
	Weighted mode	34	63.4	0.874	0.755–1.011	0.079
	Simple mode	34	63.4	0.850	0.707–1.022	0.093
Secreting Treg % CD4 Treg	IVW	34	63.4	1.143	1.064–1.229	2.779×10^{-4}
	MR-Egger	34	63.4	1.256	0.921–1.714	0.160
	Weighted median	34	63.4	1.126	1.010–1.256	0.033
	Weighted mode	34	63.4	1.137	0.985–1.313	0.090
	Simple mode	34	63.4	1.168	0.975–1.400	0.101
CD28- CD25++ CD8br AC	IVW	33	63.6	0.867	0.809–0.930	6.09×10^{-5}
	MR-Egger	33	63.6	0.899	0.670–1.205	0.480
	Weighted median	33	63.6	0.885	0.796–0.983	0.022
	Weighted mode	33	63.6	0.925	0.772–1.110	0.409
	Simple mode	33	63.6	0.950	0.774–1.167	0.630
CD19 on IgD+ CD24+	IVW	34	63.4	1.118	1.041–1.200	0.002
	MR-Egger	34	63.4	1.184	0.887–1.583	0.261
	Weighted median	34	63.4	1.054	0.950–1.169	0.324
	Weighted mode	34	63.4	1.030	0.890–1.191	0.698
	Simple mode	34	63.4	1.037	0.867–1.240	0.691
CD28- CD127- CD25++ CD8br AC	IVW	33	63.6	0.875	0.814–0.942	3.619×10^{-4}
	MR-Egger	33	63.6	0.876	0.665–1.155	0.355
	Weighted median	33	63.6	0.883	0.794–0.983	0.023
	Weighted mode	33	63.6	0.887	0.759–1.037	0.141
	Simple mode	33	63.6	0.829	0.694–0.990	0.047

MR, Mendelian randomization; SNP, single nucleotide polymorphism; OR, odds ratio; CI, confidence interval; IVW, inverse variance weighted.

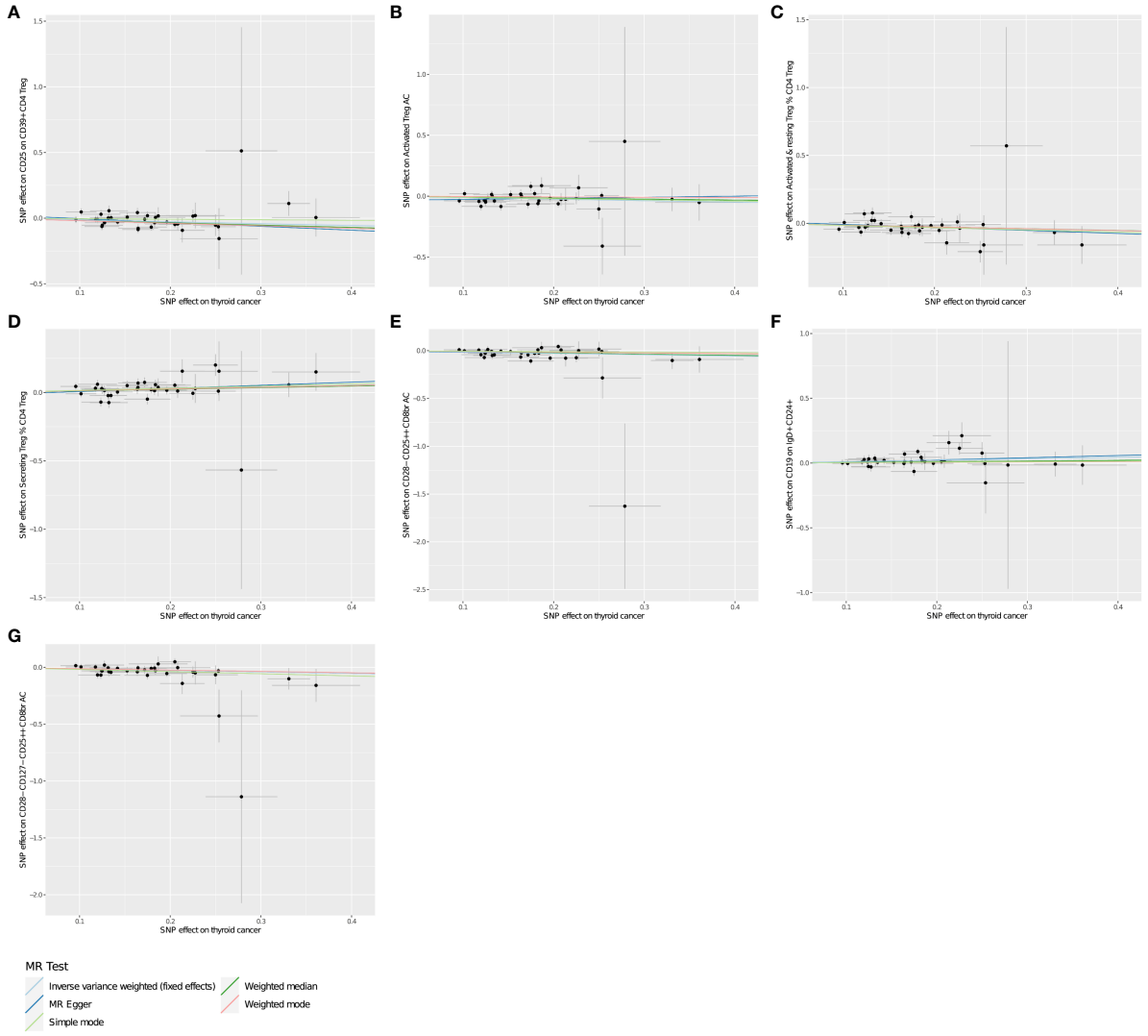

FIGURE 1
(A–G) Scatter plots show the MR effect of THCA onset on immunophenotypes in different MR methods.

T cells (Tregs) are a subset of T cells that inhibit the function of many immune cells. Tregs usually accumulate in cancer foci, draining lymph nodes, and peripheral blood (25–27). It is reported that the poor prognosis of many cancers is related to the increase of Tregs, such as breast cancer, ovarian cancer and lymphoma (28–30), and the invasiveness of THCA is related to the increase of Tregs. The analysis of specific lymphocyte indicates that Tregs are consistently present in THCA lesions and peripheral blood, and their increase is correlated with the severity of the disease (23). Our results show that Secreting Treg % CD4 Tregs are significantly elevated in THCA, substantiating previous studies at the genetic level. Although further research is needed to clarify the exact mechanisms of action of Tregs in THCA, the clear elevation of Secreting Treg % CD4 Treg in THCA provides new avenues for future diagnostics and therapeutics.

Regulatory B cells (Bregs) promote tumor immune escape by secreting cytokines such as IL-10, TGF-β1, IL-35, PD-L1 and so on. Recently, it has been found that PD-1+Breg is abundant in thyroid cancer tissue and peripheral blood, and inhibits T cell viability and proliferation in an IL-10-independent manner (31). CD19 molecule is a differentiation antigen on the surface of Breg and one of the characteristic markers on the cell membrane. CD19 can participate in the activation and proliferation of Breg, and is widely expressed in tumors related to the B lymphatic system, but not in plasma cells, T cells, and other tissues. It does not disappear or decay during Breg activation (32). In this study, we performed MR Analysis based on recently published GWAS data, showing that CD19 on IgD+ CD24+ is significantly elevated in Thachik supports previous studies.

Additionally, it was noteworthy that the presence of THCA is related to the reduction of the level of 5 immunophenotypes in Treg group, including CD25 on CD39+ CD4 Treg, Activated Treg AC, Activated & resting Treg % CD4 Treg, CD28- CD25++ CD8br AC, and CD28- CD127- CD25++ CD8br AC. Cancer can stimulate the body's specific immunity against tumors. However, due to the highly immunosuppressive nature of the tumor microenvironment and the suppression of tumor-associated antigen-specific T cells, the body is unable to eliminate cancer cells. This immunosuppressive

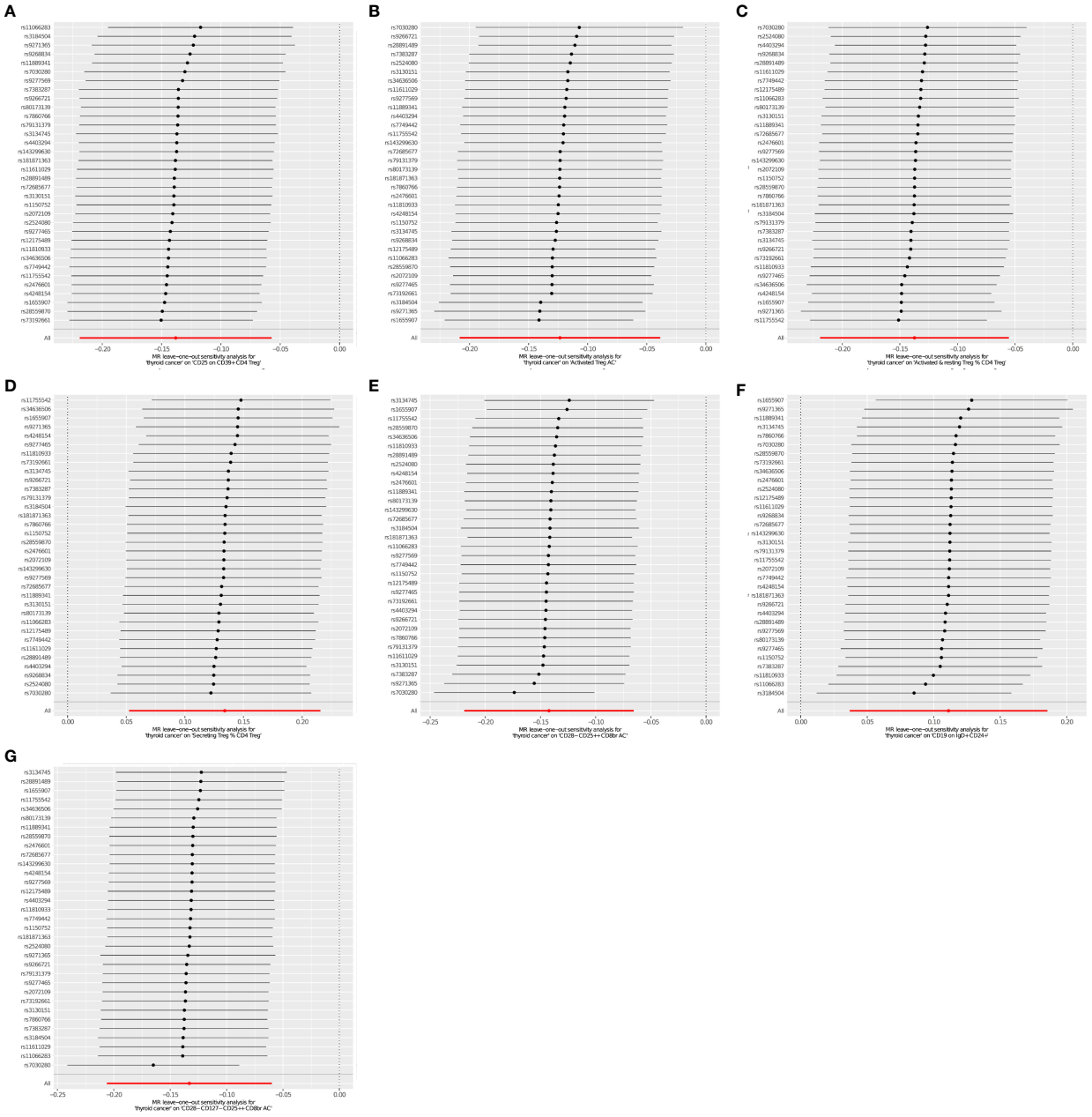

FIGURE 2
(A–G) Leave-one-out plots for the causal effect of THCA onset on immunophenotypes.

microenvironment promotes the growth of cancer cells, leading to tumor recurrence and poor prognosis.

This study conducted a two sample MR analysis on the causal relationship between immunophenotypes and THCA, with a sample size of about 24.2 million individuals, indicating a high statistical effect. Multiple MR analysis methods were used in this study to infer causal relationships between genetic instrumental variables, and there was no heterogeneity or horizontal pleiotropy among IVs, resulting in robust results. However, there are some limitations to this study that should be noted. First, population stratification cannot be performed because the data is not raw and specific personal data cannot be seen. Second, to obtain more IVs for horizontal pleiotropy testing and multiple sensitivity analysis, we did not use the traditional GWAS significance threshold ($p < 5 \times 10^{-8}$). Third, because the GWAS data for this study came from a European database, the conclusions cannot be generalized to non-European ethnic groups. Finally, since we used a more lenient threshold to evaluate the results, this may have increased some false positive rates while being able to assess the association between immune cell signatures and THCA more fully.

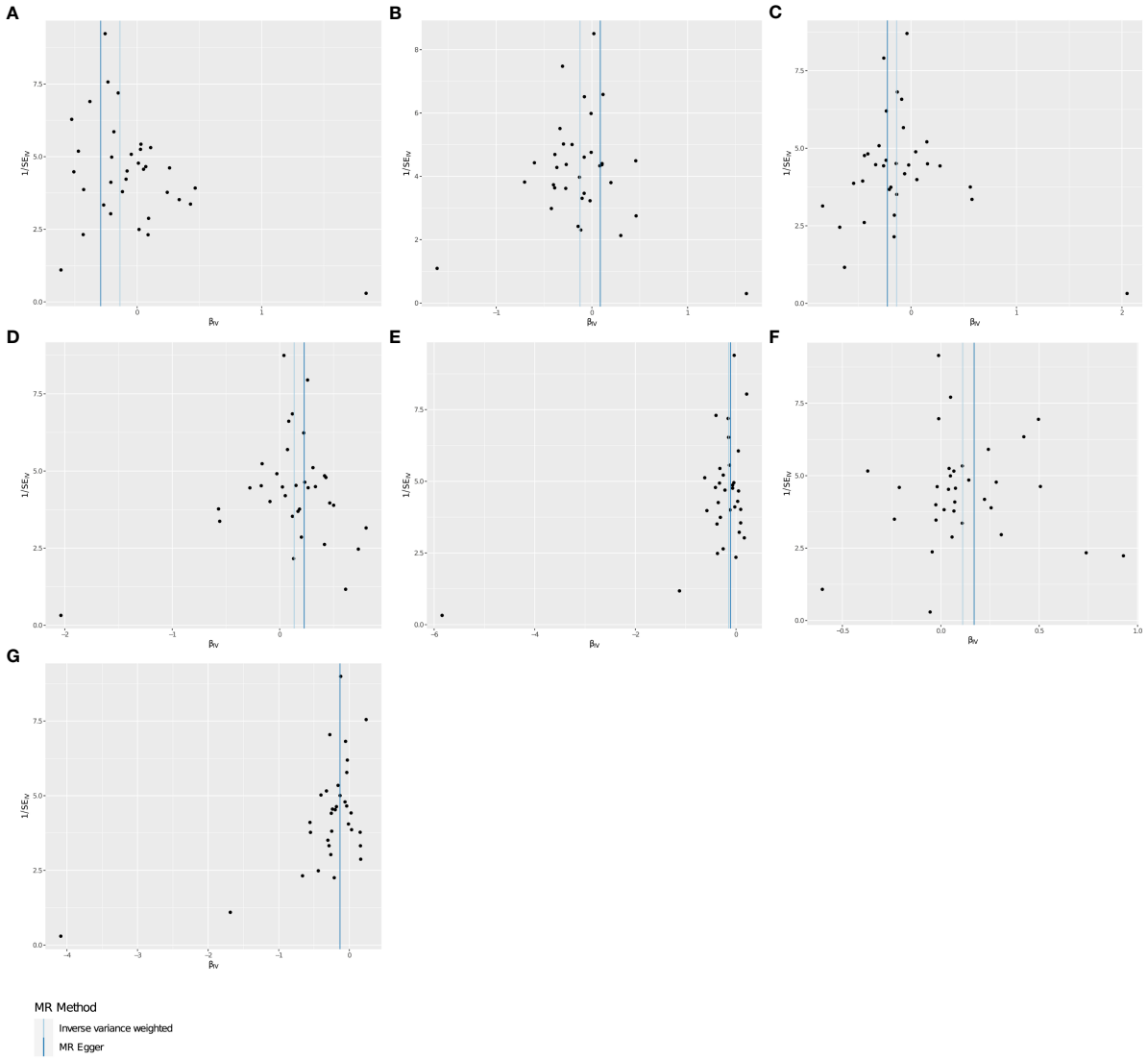

FIGURE 3
(A–G) Funnel plots for the causal effect of THCA onset on immunophenotypes.

TABLE 2 MR estimates for the causal effect of immunophenotypes on THCA.

traits (exposure)	MR method	No. of SNP	F-statistic	OR	95% CI	*P*-value
CD62L on monocyte	IVW	41	31.3	0.953	0.930~0.976	1.005×10^{-4}
	MR-Egger	41	31.3	0.971	0.935–1.009	0.137
	Weighted median	41	31.3	0.970	0.930–1.010	0.143
	Weighted mode	41	31.3	0.972	0.938–1.006	0.112
	Simple mode	41	31.3	0.982	0.918–1.050	0.591
Resting Treg %CD4	IVW	71	35.9	0.975	0.961–0.989	7.984×10^{-4}
	MR-Egger	71	35.9	0.978	0.959–0.998	0.031
	Weighted median	71	35.9	0.971	0.950–0.993	0.011
	Weighted mode	71	35.9	0.978	0.961–0.996	0.018
	Simple mode	71	35.9	0.966	0.925–1.009	0.127

MR, Mendelian randomization; SNP, single nucleotide polymorphism; OR, odds ratio; CI, confidence interval; IVW, inverse variance weighted.

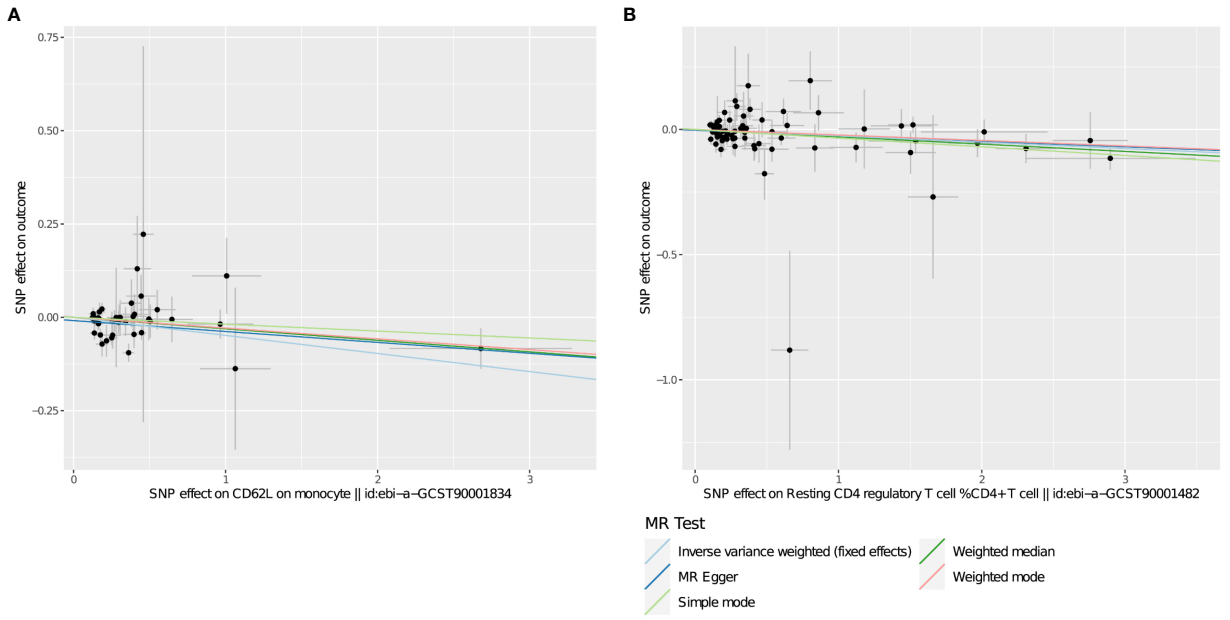

FIGURE 4
(A, B) Scatter plots show the MR effect of immunophenotypes on THCA in different MR methods.

5 Conclusions

In conclusion, we explored the causal relationship between 731 immunophenotypes and THCA through MR analysis, providing new insights into the potential relationship between the immune system and THCA, providing direction and investment rationale for confirmatory experiments, and generating new hypotheses on the etiology and immunotherapy of THCA.

In addition, as long as the necessary genetic data, exposure and outcome variable data are available, it is possible to analyze the positive and negative causality of exposure and outcome without the inevitable confounders, this kind of research may carry on the low-cost, the random research to the biological pathology

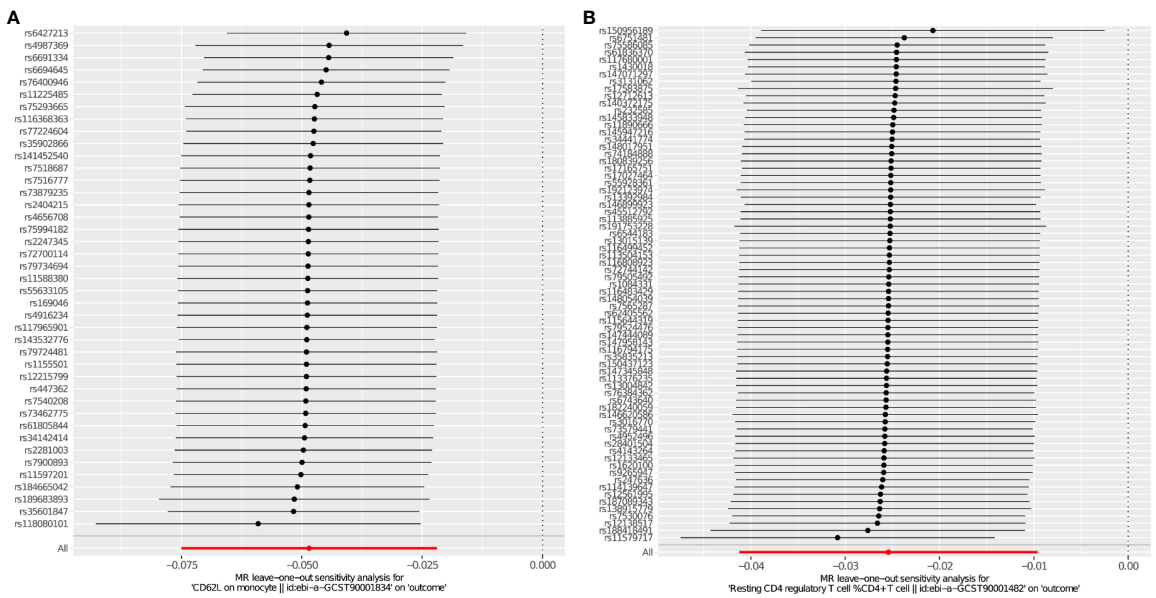

FIGURE 5
(A, B) Leave-one-out plots for the causal effect of immunophenotypes on THCA.

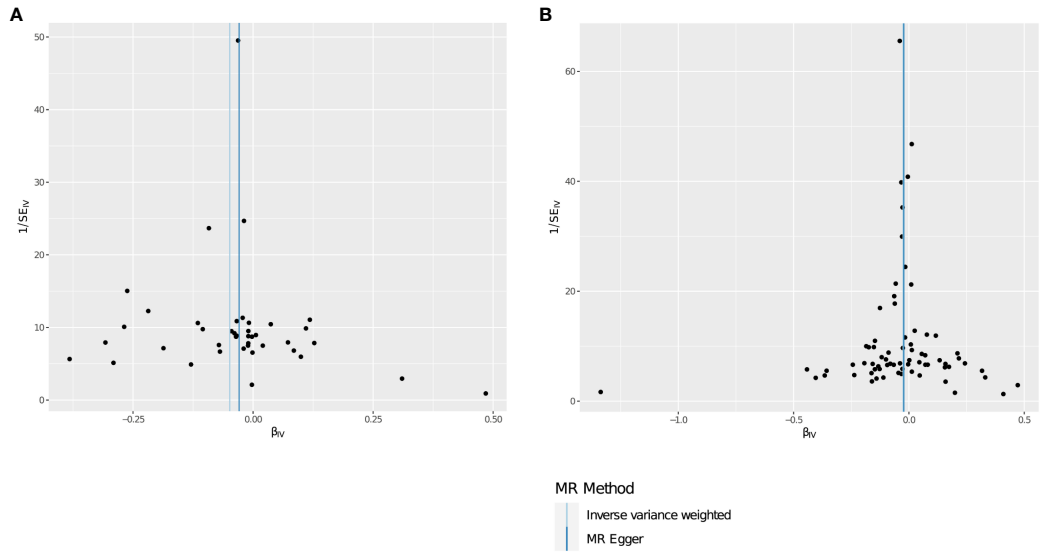

FIGURE 6
(A, B) Funnel plots for the causal effect of immunophenotypes on THCA.

mechanism without outside interference. This approach can help researchers and institutions optimize the allocation of resources for expensive and resource-intensive clinical trials.

Data availability statement

Publicly available datasets were analyzed in this study. This data can be found here: https://gwas.mrcieu.ac.uk/datasets/ebi-a-GCST90018929/.

Ethics statement

Ethical approval was not required for the study involving humans in accordance with the local legislation and institutional requirements. Written informed consent to participate in this study was not required from the participants or the participants' legal guardians/next of kin in accordance with the national legislation and the institutional requirements. Ethical approval was not required for the studies on animals in accordance with the local legislation and institutional requirements because only commercially available established cell lines were used.

Author contributions

XF: Data curation, Writing – original draft. XH: Data curation, Formal analysis, Writing – original draft. JL: Data curation, Writing – original draft. DS: Writing – review & editing.

Funding

The author(s) declare that no financial support was received for the research, authorship, and/or publication of this article.

Acknowledgments

We would like to thank all of the GWASs for making their summary data available to the public, and all of the investigators and participants who contributed to these studies. In addition, we want to acknowledge the participants and investigators of the GWAS catalog and FinnGen study.

Conflict of interest

The authors declare that the research was conducted in the absence of any commercial or financial relationships that could be construed as a potential conflict of interest.

Publisher's note

References

1. Gubbi S, Araque KA, Klubo-Gwiezdzinska J. Updates on the management of thyroid cancer. *Hormone Metab Res*. (2020) 52:562–77. doi: 10.1055/a-1089-7870

2. Sung H, Ferlay J, Siegel RL, Laversanne M, Soerjomataram I, Jemal A, et al. Global cancer statistics 2020: GLOBOCAN estimates of incidence and mortality worldwide for 36 cancers in 185 countries. *CA Cancer J Clin*. (2021) 71:209–49. doi: 10.3322/caac.21660

3. Pizzato M, Li MM, Vignat J, Laversanne M, Singh D, La Vecchia C, et al. The epidemiological landscape of thyroid cancer worldwide: GLOBOCAN estimates for incidence and mortality rates in 2020. *Lancet Diabetes Endocrinol*. (2022) 10:264–72. doi: 10.1016/S2213-8587(22)00035-3

4. Massimino M, Evans DB, Podda M, Spinelli C, Collini P, Pizzi N, et al. Thyroid cancer in adolescents and young adults. *Pediatr Blood Cancer*. (2018) 65. doi: 10.1002/pbc.27025

5. Albero A, Lopéz JE, Torres A, de la Cruz L, Martín T. Effectiveness of chemotherapy in advanced differentiated thyroid cancer: a systematic review. *Endocrine-Related Cancer*. (2016) 23:R71–84. doi: 10.1530/ERC-15-0194

6. Hay ID, Grogan RH, Duh QY. A study of recurrence and death from papillary thyroid cancer with 27 years of median follow-up. *Surgery*. (2013) 154:1446–7. doi: 10.1016/j.surg.2013.07.008

7. Angell TE, Lechner MG, Jang JK, LoPresti JS, Epstein AL. MHC class I loss is a frequent mechanism of immune escape in papillary thyroid cancer that is reversed by interferon and selumetinib treatment *in vitro*. *Clin Cancer Res*. (2014) 20:6034–44. doi: 10.1158/1078-0432.CCR-14-0879

8. Prete A, de Souza PB, Censi S, Muzza M, Nucci N, Sponziello M. Update on fundamental mechanisms of thyroid cancer. *Front Endocrinol*. (2020) 11. doi: 10.3389/fendo.2020.00102

9. Ferrari SM, Fallahi P, Galdiero MR, Ruffilli I, Elia G, Ragusa F, et al. Immune and inflammatory cells in thyroid cancer microenvironment. *Int J Mol Sci*. (2019) 20. doi: 10.3390/ijms20184413

10. Mantovani A, Romero P, Palucka AK, Marincola FM. Tumour immunity: effector response to tumour and role of the microenvironment. *Lancet*. (2008) 371:771–83. doi: 10.1016/S0140-6736(08)60241-X

11. Burgess S, Butterworth A, Thompson SG. Mendelian randomization analysis with multiple genetic variants using summarized data. *Genet Epidemiol*. (2013) 37:658–65. doi: 10.1002/gepi.21758

12. Lawlor DA, Harbord RM, Sterne JAC, Timpson N, Smith GD. Mendelian randomization: Using genes as instruments for making causal inferences in epidemiology. *Stat Med*. (2008) 27:1133–63. doi: 10.1002/sim.3034

13. Orrù V, Steri M, Sidore C, Marongiu M, Serra V, Olla S, et al. Complex genetic signatures in immune cells underlie autoimmunity and inform therapy. *Nat Genet*. (2020) 52:1266–6. doi: 10.1038/s41588-020-00718-6

14. Sidore C, Busonero F, Maschio A, Porcu E, Naitza S, Zoledziewska M, et al. Genome sequencing elucidates Sardinian genetic architecture and augments association analyses for lipid and blood inflammatory markers. *Nat Genet*. (2015) 47:1272–+. doi: 10.1038/ng.3368

15. Burgess S, Small DS, Thompson SG. A review of instrumental variable estimators for Mendelian randomization. *Stat Methods Med Res*. (2017) 26:2333–55. doi: 10.1177/0962280215597579

16. Verbanck M, Chen CY, Neale B, Do R. Detection of widespread horizontal pleiotropy in causal relationships inferred from Mendelian randomization between complex traits and diseases. *Nat Genet*. (2018) 50:1196–6. doi: 10.1038/s41588-018-0164-2

17. Burgess S, Thompson SG. Interpreting findings from Mendelian randomization using the MR-Egger method. *Eur J Epidemiol*. (2017) 32:391–2. doi: 10.1007/s10654-017-0276-5

18. Galdiero MR, Varricchi G, Loffredo S, Bellevicine C, Lansione T, Ferrara AL, et al. Potential involvement of neutrophils in human thyroid cancer. *PloS One*. (2018) 13:e0199740. doi: 10.1371/journal.pone.0199740

19. Dias Lopes NM, Mendonca Lens HH, Armani A, Marinello PC, Cecchini AL. Thyroid cancer and thyroid autoimmune disease: A review of molecular aspects and clinical outcomes. *Pathol Res Pract*. (2020) 216:153098. doi: 10.1016/j.prp.2020.153098

20. Singh N, Baby D, Rajguru J, Patil P, Thakkannavar S, Pujari V. Inflammation and cancer. *Ann Afr Med*. (2019) 18:121–6. doi: 10.4103/aam.aam_56_18

21. Willimsky G, Blankenstein T. Sporadic immunogenic tumours avoid destruction by inducing T-cell tolerance. *Nature*. (2005) 437:141–6. doi: 10.1038/nature03954

22. Ivetic A, Green HLH, Hart SJ. L-selectin: A major regulator of leukocyte adhesion, migration and signaling. *Front Immunol*. (2019) 10. doi: 10.3389/fimmu.2019.01068

23. Galdiero MR, Varricchi G, Marone G. The immune network in thyroid cancer. *Oncoimmunology*. (2016) 5:e1168556. doi: 10.1080/2162402X.2016.1168556

24. French JD, Kotnis GR, Said S, Raeburn CD, McIntyre RC, Klopper JP, et al. Programmed death-1+ T cells and regulatory T cells are enriched in tumor-involved lymph nodes and associated with aggressive features in papillary thyroid cancer. *J Clin Endocrinol Metab*. (2012) 97:E934–43. doi: 10.1210/jc.2011-3428

25. Curiel TJ, Coukos G, Zou LH, Alvarez X, Cheng P, Mottram P, et al. Specific recruitment of regulatory T cells in ovarian carcinoma fosters immune privilege and predicts reduced survival. *Nat Med*. (2004) 10:942–9. doi: 10.1038/nm1093

26. Wolf D, Wolf AM, Rumpold H, Fiegl H, Zeimet AG, Muller-Holzner E, et al. The expression of the regulatory T cell-specific forkhead box transcription factor FoxP3 is associated with poor prognosis in ovarian cancer. *Clin Cancer Res*. (2005) 11:8326–31. doi: 10.1158/1078-0432.CCR-05-1244

27. Jandus C, Bioley G, Cerottini JC, Speiser DE, Romero P. Selective accumulation of differentiated FOXP3(+) CD4 (+) T cells in metastatic tumor lesions from melanoma patients compared to peripheral blood. *Swiss Med Weekly*. (2007) 137:38S–S. doi: 10.1007/s00262-008-0507-4

28. Bates GJ, Fox SB, Han C, Leek RD, Garcia JF, Harris AL, et al. Quantification of regulatory T cells enables the identification of high-risk breast cancer patients and those at risk of late relapse. *J Clin Oncol*. (2006) 24:5373–80. doi: 10.1200/JCO.2006.05.9584

29. Barnett B, Kryczek I, Cheng P, Zou WP, Curiel TJ. Regulatory T cells in ovarian cancer: Biology and therapeutic potential. *Am J Reprod Immunol*. (2005) 54:369–77. doi: 10.1111/j.1600-0897.2005.00330.x

30. Alvaro T, Lejeune M, Salvadó MT, Bosch R, García JF, Jaén J, et al. Outcome in Hodgkin's lymphoma can be predicted from the presence of accompanying cytotoxic and regulatory T cells. *Clin Cancer Res*. (2005) 11:1467–73. doi: 10.1158/1078-0432.CCR-04-1869

31. Wang XF, Wang GQ, Wang ZH, Liu B, Han N, Li J, et al. PD-1-expressing B cells suppress CD4+ and CD8+ T cells via PD-1/PD-L1-dependent pathway. *Mol Immunol*. (2019) 109:20–6. doi: 10.1016/j.molimm.2019.02.009

32. Anderson KC, Bates MP, Slaughenhoupt BL, Pinkus GS, Schlossman SF, Nadler LM. Expression of human B cell-associated antigens on leukemias and lymphomas: a model of human B cell differentiation. *Blood*. (1984) 63:1424–33. doi: 10.1182/blood.V63.6.1424.1424

frontiers | Frontiers in Immunology

TYPE Systematic Review
PUBLISHED 15 August 2024
DOI 10.3389/fimmu.2024.1416068

OPEN ACCESS

EDITED BY
Takaji Matsutani,
Maruho, Japan

REVIEWED BY
Abbas Karimi,
Tabriz University of Medical Sciences, Iran
Zhenzhen Han,
Anhui Medical University, China

*CORRESPONDENCE
Ziwei Jiang
jiang75312024@163.com

RECEIVED 11 April 2024
ACCEPTED 29 July 2024
PUBLISHED 15 August 2024

CITATION
Wang X, Wu Z, Zhang Z and Jiang Z (2024) Prognostic and clinicopathological value of systemic immune-inflammation index in patients with osteosarcoma: a meta-analysis. *Front. Immunol.* 15:1416068. doi: 10.3389/fimmu.2024.1416068

Prognostic and clinicopathological value of systemic immune-inflammation index in patients with osteosarcoma: a meta-analysis

Xiaoyan Wang[1], Zhong Wu[2], Zongxin Zhang[1] and Ziwei Jiang[3]*

[1]Clinical Laboratory, Huzhou Central Hospital, Affiliated Central Hospital of Huzhou University, Huzhou, Zhejiang, China, [2]Clinical Laboratory, Nanxun District Hospital of Traditional Chinese Medicine, Huzhou, Zhejiang, China, [3]Clinical Laboratory, People's Hospital of Anji, Huzhou, Zhejiang, China

Background: The efficiency of systemic immune-inflammation index (SII) in predicting prognosis of osteosarcoma (OSA) patients has been extensively analyzed, but no consistent findings are obtained. Therefore, this meta-analysis focused on identifying the precise prognostic value of SII for OSA.

Methods: We comprehensively searched electronic databases of PubMed, Embase, Web of Science, Cochrane Library, and China National Knowledge Infrastructure (CNKI) from inception to 24 February, 2024. Meanwhile, the efficiency of SII in predicting prognosis of OSA was evaluated by calculating pooled hazard ratios (HRs) as well as 95% confidence intervals (CIs). Additionally, the correlation of SII with the OSA clinicopathological characteristics was analyzed based on pooled odds ratios (ORs) and 95%CIs.

Results: Six studies with 1015 cases were enrolled into this work. According to the combined data, the higher SII was markedly related to poor overall survival (OS) (HR=2.01, 95%CI=1.30-3.09, p=0.002) and Enneking stage III (OR=2.21, 95% CI=1.11-4.39, p=0.024) of patients with OSA. Nonetheless, SII was not significantly related to gender, age, pathological fracture, tumor size, tumor location, tumor differentiation, and metastasis in patients with OSA.

Conclusions: In summary, the higher SII is markedly related to poor OS and advanced Enneking stage in OSA patients.

Systematic review registration: https://inplasy.com/inplasy-2024-7-0107/, identifier INPLASY202470107.

KEYWORDS

systemic immune-inflammation index, meta-analysis, osteosarcoma, evidence-based medicine, prognosis

Abbreviations: SII, systemic immune-inflammation index; OSA, osteosarcoma; CNKI, China National Knowledge Infrastructure; HR, hazard ratio; CI, confidence interval; OR, odds ratio; OS, overall survival; PNI, prognostic nutritional index; PRISMA, Preferred Reporting Items for Systematic Reviews and Meta-Analyses; NOS, Newcastle–Ottawa scale; EMT, epithelial-mesenchymal transition; TME, tumor microenvironment; TILs, tumor-infiltrating lymphocytes; RFS, recurrence–free survival; PFS, progression-free survival.

Introduction

Osteosarcoma (OSA) shows the highest morbidity among primary malignant bone tumor among children and young adults (1). It exhibits the typical feature of formation of immature osteoid by tumor cells (2). All OSA patients have a median age of 20 years. The incidence of OSA in children and young adults worldwide varies between 2-3 per million, accounting for about 20%-30% of all primary bone tumors (3). In the past several decades, OSA patients have been treated by multiple strategies like surgery, radiotherapy, chemotherapy, gene therapy and immunotherapy (4). In spite of this, the prognosis of OSA remains poor. The 5-year survival rate in patients with localized OSA is about 60%, but that is only 20% in those developing metastases or recurrent disease (5). Around 10-15% of newly diagnosed OSA cases develop metastases, usually located in the lung (6). Therefore, it is of urgent necessary to develop novel and creditable markers for predicting prognosis of patients with OSA.

It has been widely reported that cancer-related inflammation and immune system have a critical effect on carcinogenesis, tumor growth, progression and metastasis (7, 8). Many hematological parameters including platelet-to-lymphocyte ratio (9), lymphocyte-to-monocyte ratio (10), prognostic nutritional index (PNI) (11), neutrophil-to-lymphocyte ratio (12), and systemic immune-inflammation index (SII) (13), are identified as efficient markers for predicting prognosis of various cancers. SII was developed in 2014 and reflects the general immune status of the body as an easy-to-access inflammatory parameter (14). SII is calculated as follows: SII= platelet number* neutrophil number/ lymphocyte number (14). Notably, SII is previously reported to be significant for predicting prognosis of diverse solid tumors including rectal cancer (15), non-small cell lung cancer (16), breast cancer (17), renal cell carcinoma (18), and pancreatic neuroendocrine tumors (19). Meanwhile, the efficiency of SII in predicting prognosis of OSA patients is widely analyzed in numerous studies, but no consistent findings are obtained (20–25). For example, in some studies, the higher SII significantly predicted the prognosis of OSA patients (21, 22, 24, 25). Whereas in others, SII is not markedly related to the prognosis of OSA patients (23). Consequently, the present work was performed for identifying the accurate role of SII in predicting prognosis of OSA patients. Moreover, we investigated the correlation of SII with the OSA clinicopathological factors.

Materials and methods

Study guideline

The present work was conducted following the Preferred Reporting Items for Systematic Reviews and Meta-Analyses (PRISMA) guideline (26). This meta-analysis was registered in INPLASY under the registration number INPLASY202470107. This protocol can be available at https://inplasy.com/inplasy-2024-7-0107/.

Ethics statement

Ethical approval and informed consent were waived since the present work was conducted using previously published data.

Literature search

PubMed, Embase, Web of Science, Cochrane Library, and China National Knowledge Infrastructure (CNKI) databases were thoroughly retrieved between inception and 24 February, 2024 using the following search strategies (systemic immune-inflammatory index OR systemic-immune-inflammation index OR systemic immune-inflammation index) AND (osteosarcoma OR osteogenic sarcoma OR bone sarcoma). There was no limitation to publication language. The detailed search strategies for each database were shown in Supplementary File 1. Besides, we manually screened references in enrolled articles to identify more eligible studies.

Eligibility criteria

Studies conforming to criteria below were included: (1) the diagnosis of OSA was made pathologically; (2) the relation of SII with prognosis of OSA was reported; (3) hazard ratios (HRs) and 95% confidence intervals (CIs) were available or calculable using Tierney's method (27); (4) the SII threshold was provided; and (5) there was no restriction of publication language. Studies below were excluded: (1) meeting abstracts, reviews, case reports, comments, and letters; (2) those did not provide survival data; and (3) animal studies.

Data collection and quality evaluation

Data were collected from qualified articles by two researchers (ZW and ZZ). Any disagreement between them was settled through discussion with a third researcher (ZJ) to reach a consensus. Data below were collected: first author, year, country, sample size, gender, age, study duration, study design, study center, Enneking stage, treatment, SII threshold, survival endpoints, survival analysis types, follow-up, and HRs with 95%CIs. Two independent reviewers (XW and ZZ) used Newcastle–Ottawa scale (NOS) to evaluate study quality (28). Notably, NOS evaluates study quality from 3 domains, selection, comparability, and outcome ascertainment. The total NOS score is 0-9 points, with ≥6 points indicating high-quality studies.

Statistical analysis

The value of SII in predicting prognosis of OSA was analyzed by calculating combined HRs and 95%CIs. Moreover, the heterogeneity degree among enrolled studies was quantified by Cochran's Q-test and Higgins I^2 statistic. In the presence of

obvious heterogeneity (I^2>50% or p<0.010), we utilized a random-effects model; or else, we adopted a fixed-effects model. Additionally, the significance of SII for predicting prognosis of different subgroup OSA populations was explored by subgroup analysis. The correlation between SII and the OSA clinicopathological factors was investigated through pooling odds ratios (ORs) and 95%CIs. In the meantime, sensitivity analysis was also conducted for comparing the pooled effect when each study was excluded individually to determine whether a particular study is responsible for heterogeneity and to ensure results are stable. Publication bias was evaluated by using Begg's funnel plot and Egger's test. Stata version 12.0 (Statacorp, College Station, TX, USA) was employed for statistical analysis. p<0.05 stood for statistical significance.

Results

Process of literature search

Initially, 24 studies were obtained through primary retrieval, among which, 12 were maintained when duplicates were eliminated (Figure 1). By title and abstract screening, we discarded three articles due to irrelevance. Full-texts of the rest 9 studies were examined, among which, three were eliminated due to irrelevance of SII (n=2) and unavailable survival data (n=1). Finally, six studies with 1015 patients (20–25) were enrolled into this work (Figure 1; Table 1).

Enrolled study features

Table 1 displays basic study features (20–25). These studies were published during 2019-2023 and were all conducted in China. There were four (20–23) and two (24, 25) studies published in English and Chinese separately. All included studies were of retrospective design (20–25). The sample size was 77-487 (median, 116.5). There were four single center studies (20, 21, 23, 25) and two multicenter studies (22, 24). Five articles enrolled OSA patients of Enneking stage I-III (20–22, 24, 25), while one included those of Enneking stage II-III (23). All studies treated patients with mixed treatments including surgery, chemotherapy, and radiotherapy (20–25). The median SII threshold was 639.48 (range, 384.9-869.04). Each of our enrolled articles mentioned the relation of SII with overall survival (OS) in patients with OSA. In four articles, the HRs and 95%CIs were obtained through multivariate analysis (20, 22, 23, 25), while in another two articles, they were acquired through univariate analysis (21, 24). NOS scores ranged from 7 to 9, suggesting high-quality studies (Table 1).

SII and OS

The six articles involving 1015 patients (20–25) reported the value of SII in predicting OS of OSA patients. Due to obvious heterogeneity (I^2 = 79.1%, p<0.001), we used the random-effects model. HR=2.01, 95%CI=1.30-3.09, and p=0.002 were obtained from

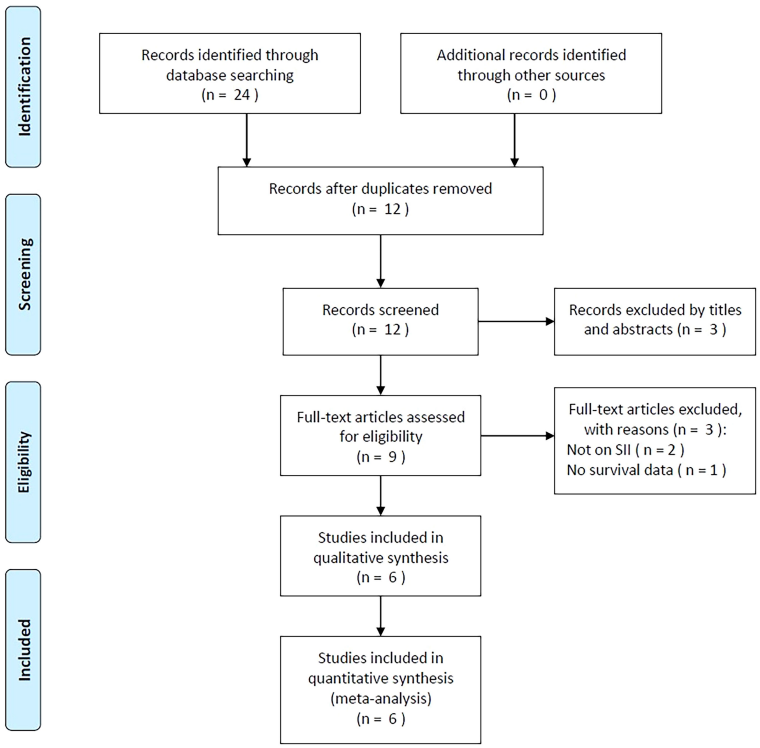

FIGURE 1
Flow diagram of study selection.

TABLE 1 Basic characteristics of included studies in this meta-analysis.

Study	Year	Country	Sample size	Gender (M/F)	Age (years) Median (range)	Study period	Study center	Enneking stage	Treatment	Survival outcomes	Survival analysis	Follow-up (months) Median(range)	NOS
Huang, X.	2019	China	126	78/48	30(6-72)	2012-2018	Single center	I-III	Mixed	OS	Multivariate	44(7-81)	7
Yang, S.	2020	China	77	43/34	19(7-66)	2010-2013	Single center	I-III	Mixed	OS	Univariate	1-100	7
Ma, C.	2022	China	125	84/41	31(6-80)	2012-2019	Multicenter	I-III	Mixed	OS	Multivariate	1-120	9
Yang, Y.	2022	China	487	283/204	20	2008-2018	Single center	II-III	Mixed	OS	Multivariate	To Dec 2020	7
He, H.	2023	China	92	51/41	28(11-66)	2000-2018	Multicenter	I-III	Mixed	OS	Univariate	58(37-66)	8
Wu, Y.	2023	China	108	61/47	34(9-67)	2012-2017	Single center	I-III	Mixed	OS	Multivariate	62(4-132)	8

M, male; F, female; OS, overall survival; NOS, Newcastle-Ottawa Scale.

pooled results, suggesting that the higher SII was markedly related to dismal OS of OSA patients (Table 2; Figure 2). Upon subgroup analysis, SII still significantly predicted OS of OSA patients, irrespective of study center, threshold, and survival analysis types ($p<0.02$; Table 2). Additionally, SII was significantly related to dismal OS of OSA in subgroups below: sample size <120 ($p<0.001$) and patients with Enneking stage I-III ($p=0.002$) (Table 2).

The association of SII with the OSA clinicopathological features

Four studies with 436 patients (20–22, 25) provided the data on association of SII with the OSA clinicopathological characteristics. According to pooled data, an elevated SII was remarkably related to Enneking stage III in patients with OSA (OR=2.21, 95%CI=1.11-4.39, p=0.024; Table 3; Figure 3). However, SII was not significantly related to gender (OR=1.56, 95%CI=0.66-3.71, p=0.315), age (OR=1.34, 95%CI=0.91-1.99, p=0.141), pathological fracture (OR=1.38, 95%CI=0.85-2.24, p=0.189), tumor location (OR=1.81, 95%CI=0.91-3.62, p=0.092), tumor size (OR=2.18, 95%CI=0.88-5.37, p=0.092), tumor differentiation (OR=2.50, 95%CI=0.93-6.70, p=0.069), and metastasis (OR=2.44, 95%CI=0.69-8.59, p=0.164) of OSA patients (Table 3; Figures 3, 4).

Sensitivity analysis

Sensitivity analysis suggested that the observed effect size for the relationship of SII with OS was not affected by any single study (Figure 5), which indicated the stability of the results in this work.

Publication bias

We employed Begg's test and Egger's test for evaluating the possible publication bias. From Figure 6, funnel plots showed symmetry. Moreover, the results (p=0.124 and 0.178 upon Begg's and Egger's tests separately) demonstrated the absence of significant publication bias (Figure 6).

Discussion

According to prior reports, the effect of SII on predicting prognosis of OSA patients remains controversial. In this work, information was synthesized in six articles involving 1015 patients for identifying the precise effect of SII on predicting OSA prognosis. In this meta-analysis, an elevated SII significantly predicted OS of OSA patients. Moreover, the higher SII was markedly related to advanced Enneking stage in OSA. SII served as the cheap and reliable prognostic marker for OSA patients. As far as we know, this meta-analysis is the first to investigate the effect of SII on predicting OSA prognosis.

The higher SII is the result of higher platelet number, higher neutrophil number, and/or lower lymphocyte number. The precise

10.3389/fimmu.2024.1416068

TABLE 2 Subgroup analysis of the prognostic value of SII for OS in patients with osteosarcoma.

Subgroups	No. of studies	No. of patients	Effects model	HR (95%CI)	p	Heterogeneity	
						I2(%)	Ph
Total	6	1015	Random	2.01(1.30-3.09)	0.002	79.1	<0.001
Sample size							
<120	3	277	Fixed	2.86(1.95-4.19)	<0.001	25.7	0.260
≥120	3	738	Random	1.39(0.96-2.00)	0.080	61.3	0.075
Study center							
Single center	4	798	Random	1.78(1.05-3.02)	0.032	79.1	0.002
Multicenter	2	217	Fixed	2.55(1.68-3.87)	<0.001	0	0.796
Enneking stage							
I-III	5	528	Random	2.36(1.37-4.06)	0.002	82.7	<0.001
II-III	1	487	–	1.11(0.67-1.82)	0.685	–	–
Cut-off value							
<650	3	359	Random	2.33(1.01-5.36)	0.047	84.6	0.002
≥650	3	656	Random	1.92(1.08-3.42)	0.027	70.4	0.034
Survival analysis							
Univariate	2	169	Fixed	2.58(1.72-3.85)	<0.001	0	0.839
Multivariate	4	846	Random	1.76(1.04-2.95)	0.034	77.4	0.004

mechanisms of the association between SII and prognosis of OSA are not fully elucidated yet. Notably, the value of SII in predicting OSA prognosis is interpreted from several aspects. First, several studies have reported that platelets may protect cancer cells from the immune system's cytotoxicity (29). In tumor cells, cytokines may stimulate megakaryocytes to produce platelets, resulting in an increase in platelet count (30). Platelets can also facilitate epithelial-mesenchymal transition (EMT) in cancer cells by directly contacting them or indirectly secreting prostaglandin E2 and growth factors (29). Second, during tumorigenesis, neutrophils contribute to the proliferation, invasion, and migration of tumor cells as well as tumor immunosuppression (31). Through the

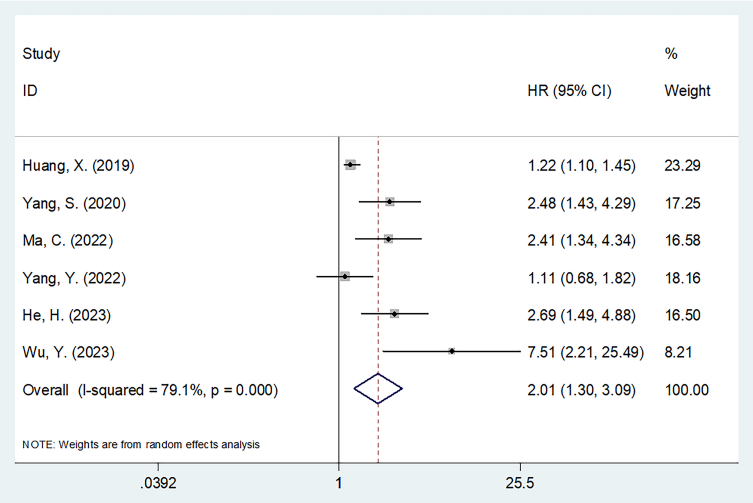

FIGURE 2
Forest plot for the prognostic value of SII for overall survival in patients with OSA.

TABLE 3 The association between SII and clinicopathological features in patients with osteosarcoma.

Factors	No. of studies	No. of patients	Effects model	OR (95%CI)	p	Heterogeneity	
						I^2(%)	Ph
Gender (male vs female)	4	436	Random	1.56(0.66-3.71)	0.315	71.1	0.015
Age (years) (≥20 vs <20)	4	436	Fixed	1.34(0.91-1.99)	0.141	0	0.552
Enneking stage (III vs I-II)	4	436	Random	2.21(1.11-4.39)	0.024	52.1	0.099
Pathological fracture (yes vs no)	4	436	Fixed	1.38(0.85-2.24)	0.189	0	0.902
Tumor location (non-extremities vs extremities)	4	436	Random	1.81(0.91-3.62)	0.092	52.2	0.099
Tumor size (cm) (≥5 vs <5)	3	359	Random	2.18(0.88-5.37)	0.092	68.2	0.043
Tumor differentiation (poor vs well)	3	359	Random	2.50(0.93-6.70)	0.069	79.7	0.007
Metastasis (yes vs no)	3	359	Random	2.44(0.69-8.59)	0.164	76.1	0.015

secretion of chemokines and cytokines, neutrophils are able to directly affect tumor cells or have an indirect effect on other tumor microenvironment (TME) components (32). These include vascular endothelial growth factor, transforming growth factor-beta, matrix metalloproteinases, interleukin-6 (IL-6), and IL-8 (33). Third, lymphocytes are crucial to anti-tumor cell-mediated responses. Lymphocytes can migrate into the TME and evolve into tumor-infiltrating lymphocytes (TILs), which can suppress the proliferation and migration of tumors through apoptosis (34, 35). Therefore, a higher SII can serve as the reasonable marker for predicting OSA prognosis.

Recently, SII is widely reported in meta-analysis with significant value in predicting prognosis of different solid tumors (36–40). According to Yang et al. in their meta-analysis involving 30 studies, the higher SII levels before treatment were related to poor OS and recurrence–free survival (RFS) of gastric cancer (36). Zhang and colleagues reported in their meta-analysis with 3464 patients that the higher SII was remarkably related to poor OS and DFS, low differentiation degree and advanced stage of oral squamous cell carcinoma (37). As mentioned in one meta-analysis enrolling 8133 patients with prostate cancer, a high SII was dramatically associated with poor OS, and worse progression-free survival/biochemical

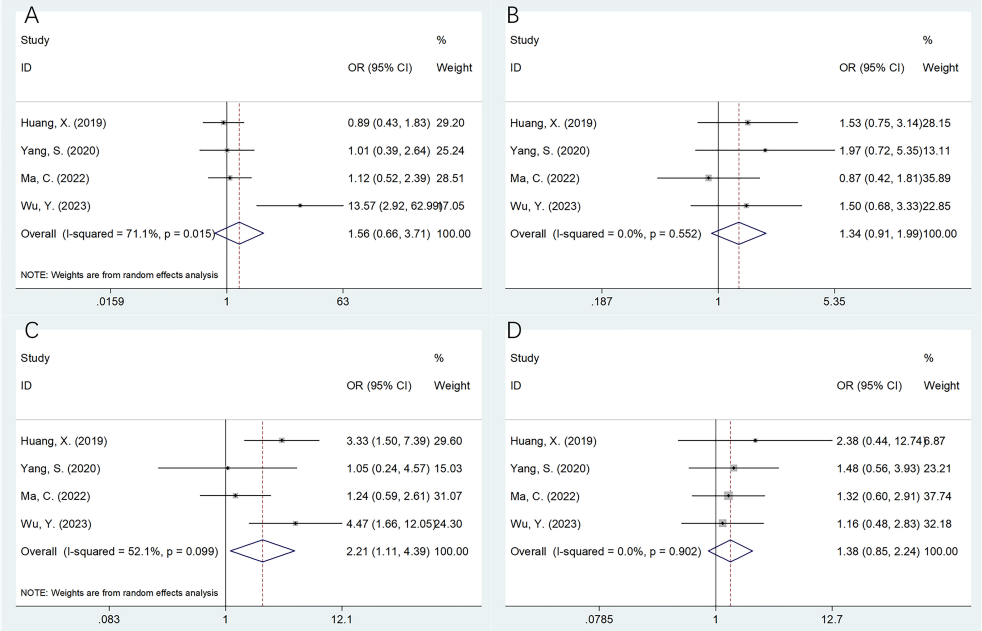

FIGURE 3
Forest plots assessing the relationship between the SII and clinicopathological factors in OSA. **(A)** Gender (male vs female); **(B)** Age (years) (≥20 vs <20); **(C)** Enneking stage (III vs I-II); and **(D)** Pathological fracture (yes vs no).

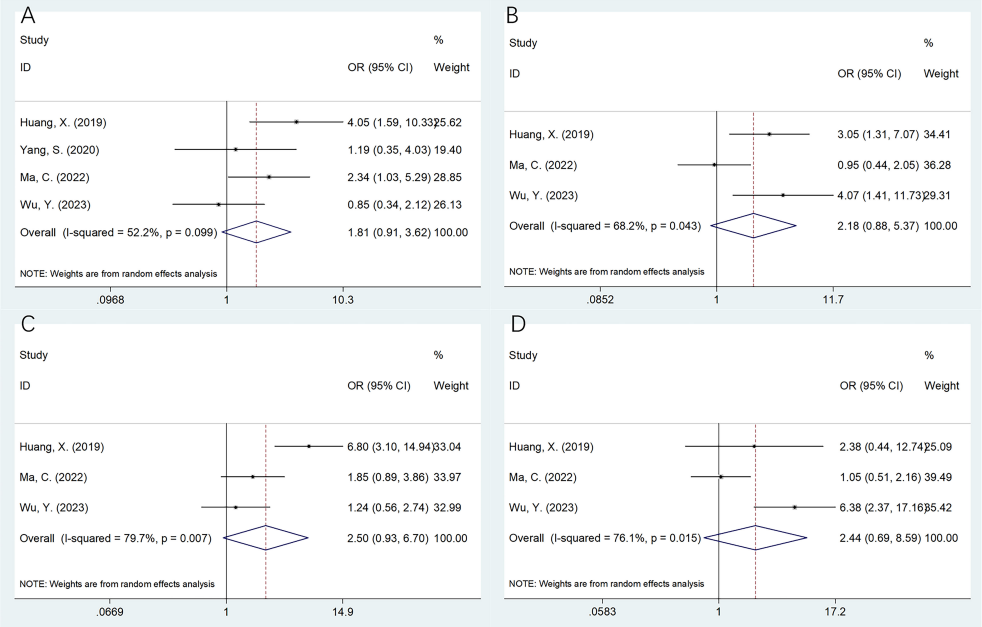

FIGURE 4
Forest plots assessing the relationship between the SII and clinicopathological factors in OSA. **(A)** Tumor location (non-extremities vs extremities); **(B)** Tumor size (cm) (≥5 vs <5); **(C)** Tumor differentiation (poor vs well); and **(D)** Metastasis (yes vs no).

recurrence-free survival (PFS/bRFS) (38). In the meta-analysis comprising 2169 patients, Zeng et al. reported that the higher SII served as the effective marker to predict OS and PFS of nasopharyngeal carcinoma (39). Based on a meta-analysis with 1402 patients, the high SII was related to dismal OS of cholangiocarcinoma patients undergoing invasive surgery (40). Our meta-analysis findings were consistent with those in other cancer types. Notably, tumor necrosis rate is an important index for cancer treatment in patients with OSA (41, 42). A tumor necrosis rate > 90% usually indicates necrosis of tumor tissue, which showed inhibition of the blood supply to tumor tissue (41). In this meta-analysis, the association between SII and tumor necrosis rate was not analyzed due to limited information in included studies. The relationship between SII and tumor necrosis rate should be explored in future studies.

There were some limitations in the present work. First, this study had a small sample size. We just recruited six studies with 1015 patients, although we searched the most recent literature and

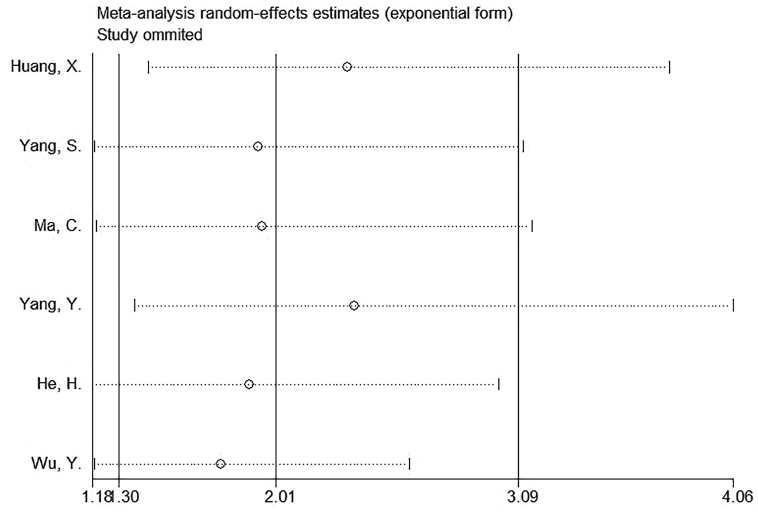

FIGURE 5
Sensitivity analysis for OS.

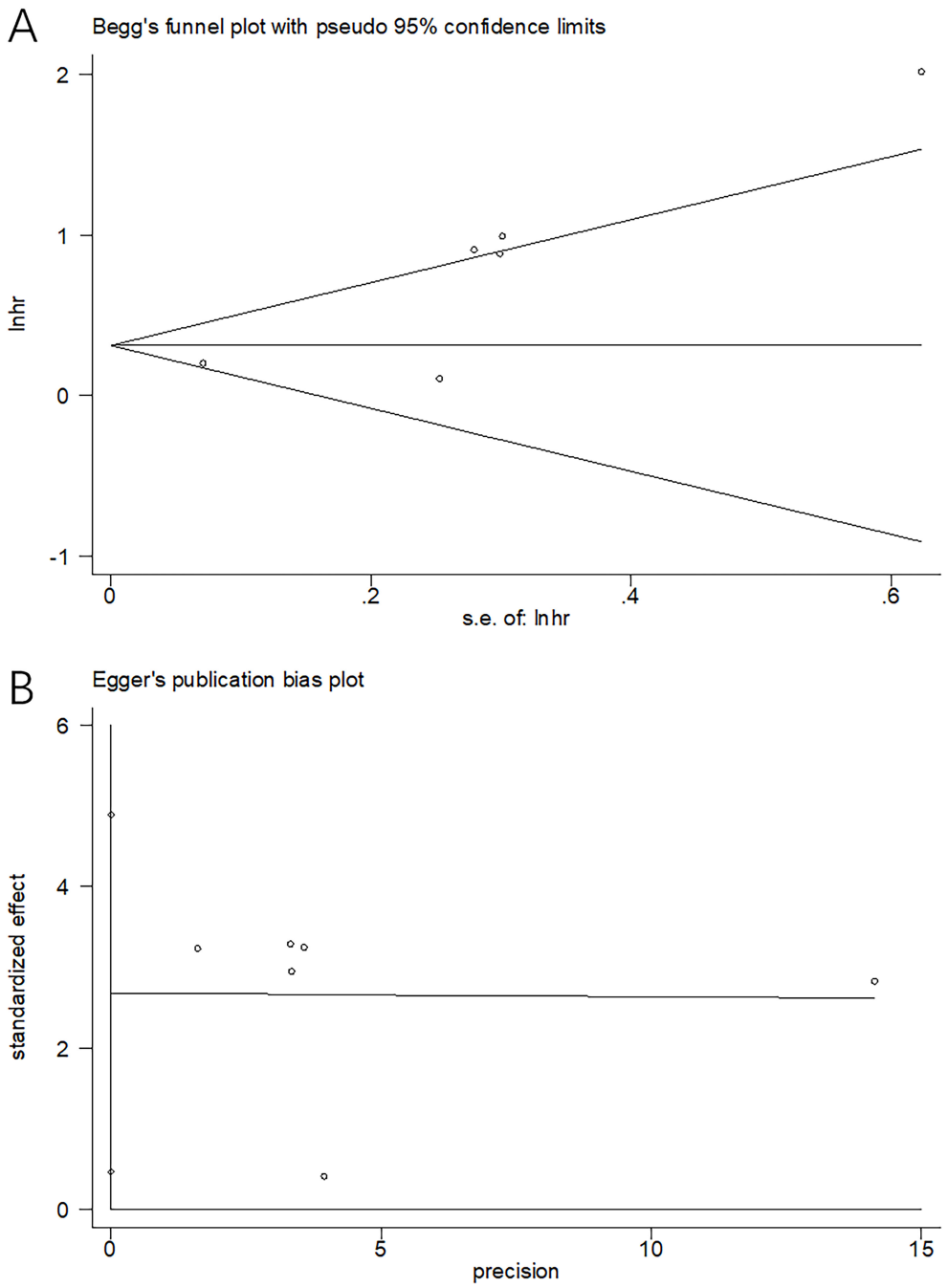

FIGURE 6
Publication bias tests. **(A)** Begg's test for OS, p=0.124; **(B)** Egger's test for OS, p=0.178.

did not restrict publication language. Second, all included studies were from China. In this regard, the findings in this work are more applicable for Chinese OSA populations. While the value of SII in the prognosis of OSA in other regions needs to be explored. Third, only retrospective studies were enrolled, which might lead to selection bias. Fourth, we only analyzed the prognostic value of SII for OS in this meta-analysis. The association between SII and other survival endpoints such as RFS, PFS, and DFS etc. was not investigated for OSA patients. We actually did not exclude RFS, PFS, and DFS in eligibility criteria, they were not included because of limited data provided in eligible studies. The correlation between SII and RFS, PFS, and DFS in OSA needs to be explored in future studies. Considering the above limitations, large-scale multi-regional prospective studies should be conducted for validation.

Conclusions

In summary, according to our meta-analysis results, the higher SII is remarkably related to poor OS of OSA patients.

Additionally, the elevated SII is also significantly related to advanced Enneking stage in OSA. SII is the candidate prognostic marker of OSA.

Data availability statement

The original contributions presented in the study are included in the article/Supplementary Material. Further inquiries can be directed to the corresponding author.

Author contributions

XW: Conceptualization, Data curation, Formal analysis, Investigation, Project administration, Resources, Software, Supervision, Validation, Visualization, Writing – original draft. ZW: Conceptualization, Data curation, Formal analysis, Investigation, Methodology, Project administration, Resources, Supervision, Validation, Visualization, Writing – original draft. ZZ: Conceptualization, Data curation, Formal Analysis, Investigation, Methodology, Project administration, Resources, Validation, Visualization, Writing – original draft. ZJ: Conceptualization, Data curation, Formal analysis, Investigation, Methodology, Project administration, Resources, Visualization, Writing – review & editing.

Funding

The author(s) declare that no financial support was received for the research, authorship, and/or publication of this article.

Conflict of interest

The authors declare that the research was conducted in the absence of any commercial or financial relationships that could be construed as a potential conflict of interest.

Publisher's note

Supplementary material

The Supplementary Material for this article can be found online at: https://www.frontiersin.org/articles/10.3389/fimmu.2024.1416068/full#supplementary-material

References

1. Sadykova LR, Ntekim AI, Muyangwa-Semenova M, Rutland CS, Jeyapalan JN, Blatt N, et al. Epidemiology and risk factors of osteosarcoma. *Cancer Invest*. (2020) 38:259–69. doi: 10.1080/07357907.2020.1768401

2. Belayneh R, Fourman MS, Bhogal S, Weiss KR. Update on osteosarcoma. *Curr Oncol Rep*. (2021) 23:71. doi: 10.1007/s11912-021-01053-7

3. Smeland S, Bielack SS, Whelan J, Bernstein M, Hogendoorn P, Krailo MD, et al. Survival and prognosis with osteosarcoma: outcomes in more than 2000 patients in the EURAMOS-1 (European and American Osteosarcoma Study) cohort. *Eur J Cancer (Oxford England: 1990)*. (2019) 109:36–50. doi: 10.1016/j.ejca.2018.11.027

4. Zhao X, Wu Q, Gong X, Liu J, Ma Y. Osteosarcoma: a review of current and future therapeutic approaches. *BioMed Eng Online*. (2021) 20:24. doi: 10.1186/s12938-021-00860-0

5. Gorlick R, Janeway K, Lessnick S, Randall RL, Marina N. Children's Oncology Group's 2013 blueprint for research: bone tumors. *Pediatr Blood Cancer*. (2013) 60:1009–15. doi: 10.1002/pbc.24429

6. Meltzer PS, Helman LJ. New horizons in the treatment of osteosarcoma. *New Engl J Med*. (2021) 385:2066–76. doi: 10.1056/NEJMra2103423

7. Grivennikov SI, Greten FR, Karin M. Immunity, inflammation, and cancer. *Cell*. (2010) 140:883–99. doi: 10.1016/j.cell.2010.01.025

8. Diakos CI, Charles KA, McMillan DC, Clarke SJ. Cancer-related inflammation and treatment effectiveness. *Lancet Oncol*. (2014) 15:e493–503. doi: 10.1016/S1470-2045(14)70263-3

9. Kim EY, Lee JW, Yoo HM, Park CH, Song KY. The platelet-to-lymphocyte ratio versus neutrophil-to-lymphocyte ratio: which is better as a prognostic factor in gastric cancer? *Ann Surg Oncol*. (2015) 22:4363–70. doi: 10.1245/s10434-015-4518-z

10. Lin ZX, Ruan DY, Li Y, Wu DH, Ma XK, Chen J, et al. Lymphocyte-to-monocyte ratio predicts survival of patients with hepatocellular carcinoma after curative resection. *World J Gastroenterol*. (2015) 21:10898–906. doi: 10.3748/wjg.v21.i38.10898

11. Feng Z, Wen H, Ju X, Bi R, Chen X, Yang W, et al. The preoperative prognostic nutritional index is a predictive and prognostic factor of high-grade serous ovarian cancer. *BMC Cancer*. (2018) 18:883. doi: 10.1186/s12885-018-4732-8

12. Nakaya A, Kurata T, Yoshioka H, Takeyasu Y, Niki M, Kibata K, et al. Neutrophil-to-lymphocyte ratio as an early marker of outcomes in patients with advanced non-small-cell lung cancer treated with nivolumab. *Int J Clin Oncol*. (2018) 23:634–40. doi: 10.1007/s10147-018-1250-2

13. He K, Si L, Pan X, Sun L, Wang Y, Lu J, et al. Preoperative systemic immune-inflammation index (SII) as a superior predictor of long-term survival outcome in patients with stage I-II gastric cancer after radical surgery. *Front Oncol*. (2022) 12:829689. doi: 10.3389/fonc.2022.829689

14. Hu B, Yang XR, Xu Y, Sun YF, Sun C, Guo W, et al. Systemic immune-inflammation index predicts prognosis of patients after curative resection for hepatocellular carcinoma. *Clin Cancer Res*. (2014) 20:6212–22. doi: 10.1158/1078-0432.CCR-14-0442

15. Yu X, Jiang W, Dong X, Yan B, Xu S, Lin Z, et al. Nomograms integrating the collagen signature and systemic immune-inflammation index for predicting prognosis in rectal cancer patients. *BJS Open*. (2024) 8(2):zrae014. doi: 10.1093/bjsopen/zrae014

16. Wei B, Zhang Y, Shi K, Jin X, Qian K, Zhang P, et al. Predictive value of systemic immune-inflammation index in the high-grade subtypes components of small-sized lung adenocarcinoma. *J Cardiothorac Surg*. (2024) 19:39. doi: 10.1186/s13019-024-02528-x

17. Pang J, Ding N, Yin N, Xiao Z. Systemic immune-inflammation index as a prognostic marker in HER2-positive breast cancer patients undergoing trastuzumab therapy. *Sci Rep*. (2024) 14:6578. doi: 10.1038/s41598-024-57343-0

18. Monteiro FSM, Fiala O, Massari F, Myint ZW, Kopecky J, Kucharz J, et al. Systemic immune-inflammation index in patients treated with first-line immune combinations for metastatic renal cell carcinoma: insights from the ARON-1 study. *Clin genitourinary Cancer*. (2024) 22:305–14.e3. doi: 10.1016/j.clgc.2023.11.013

19. Chen G, Liu L, Tan C, Tan Q, Chen Y, An X, et al. Prognostic significance of systemic immune-inflammation index in patients with nonfunction pancreatic neuroendocrine tumor undergoing surgical resection. *Cancer Med*. (2024) 13:e7114. doi: 10.1002/cam4.7114

20. Huang X, Hu H, Zhang W, Shao Z. Prognostic value of prognostic nutritional index and systemic immune-inflammation index in patients with osteosarcoma. *J Cell Physiol*. (2019) 234:18408–14. doi: 10.1002/jcp.28476

21. Yang S, Wu C, Wang L, Shan D, Chen B. Pretreatment inflammatory indexes as prognostic predictors for survival in osteosarcoma patients. *Int J Clin Exp Pathol*. (2020) 13:515–24.

22. Ma C, Yu R, Li J, Guo J, Xu J, Wang X, et al. Preoperative prognostic nutritional index and systemic immune-inflammation index predict survival outcomes in osteosarcoma: A comparison between young and elderly patients. *J Surg Oncol*. (2022) 125:754–65. doi: 10.1002/jso.26757

23. Yang Y, Zhou C, Ma X. Use of nomogram on nutritional assessment indicators to predict clinical outcomes in patients undergoing surgical resection for high-grade osteosarcoma. *Nutr Cancer*. (2022) 74:3564–73. doi: 10.1080/01635581.2022.2081342

24. He H, Liu Y, Zhang R, Li J, Peng G. Value of controlling nutritional status score and related indicators in predicting the prognosis of osteosarcoma patients. *Electron J Metab Nutr Cancer*. (2023) 10:813–9. doi: 10.16689/j.cnki.cn11-9349/r.2023.06.018

25. Wu Y, Chen X, Shi T. Relationship between systemic immune inflammation index and prognosis of osteosarcoma patients and construction of prediction model. *West China Med J*. (2023) 38:1468–73. doi: 10.7507/1002-0179.202308074

26. Moher D, Liberati A, Tetzlaff J, Altman DG, Grp P. Preferred reporting items for systematic reviews and meta-analyses: the PRISMA statement. *J Clin Epidemiol*. (2009) 62:1006–12. doi: 10.1016/j.jclinepi.2009.06.005

27. Tierney JF, Stewart LA, Ghersi D, Burdett S, Sydes MR. Practical methods for incorporating summary time-to-event data into meta-analysis. *Trials*. (2007) 8:16. doi: 10.1186/1745-6215-8-16

28. Stang A. Critical evaluation of the Newcastle-Ottawa scale for the assessment of the quality of nonrandomized studies in meta-analyses. *Eur J Epidemiol*. (2010) 25:603–5. doi: 10.1007/s10654-010-9491-z

29. Labelle M, Begum S, Hynes RO. Direct signaling between platelets and cancer cells induces an epithelial-mesenchymal-like transition and promotes metastasis. *Cancer Cell*. (2011) 20:576–90. doi: 10.1016/j.ccr.2011.09.009

30. Gay LJ, Felding-Habermann B. Contribution of platelets to tumour metastasis. *Nat Rev Cancer*. (2011) 11:123–34. doi: 10.1038/nrc3004

31. Kolaczkowska E, Kubes P. Neutrophil recruitment and function in health and inflammation. *Nat Rev Immunol*. (2013) 13:159–75. doi: 10.1038/nri3399

32. Treffers LW, Hiemstra IH, Kuijpers TW, van den Berg TK, Matlung HL. Neutrophils in cancer. *Immunol Rev*. (2016) 273:312–28. doi: 10.1111/imr.12444

33. Liang W, Ferrara N. The complex role of neutrophils in tumor angiogenesis and metastasis. *Cancer Immunol Res*. (2016) 4:83–91. doi: 10.1158/2326-6066.CIR-15-0313

34. Dunn GP, Old LJ, Schreiber RD. The immunobiology of cancer immunosurveillance and immunoediting. *Immunity*. (2004) 21:137–48. doi: 10.1016/j.immuni.2004.07.017

35. Santoiemma PP, Powell DJ Jr. Tumor infiltrating lymphocytes in ovarian cancer. *Cancer Biol Ther*. (2015) 16:807–20. doi: 10.1080/15384047.2015.1040960

36. Yang X, Wu C. Systemic immune inflammation index and gastric cancer prognosis: A systematic review and meta–analysis. *Exp Ther Med*. (2024) 27:122. doi: 10.3892/etm.2024.12410

37. Zhang J, Dai S. Prognostic and clinicopathological role of pretreatment systemic immune-inflammation index in patients with oral squamous cell carcinoma: a meta-analysis. *Front Oncol*. (2023) 13:1303132. doi: 10.3389/fonc.2023.1303132

38. Zhang B, Xu T. Prognostic significance of pretreatment systemic immune-inflammation index in patients with prostate cancer: a meta-analysis. *World J Surg Oncol*. (2023) 21:2. doi: 10.1186/s12957-022-02878-7

39. Zeng Z, Xu S, Wang D, Qin G. Prognostic significance of systemic immune-inflammation index in patients with nasopharyngeal carcinoma: a meta-analysis. *Syst Rev*. (2022) 11:247. doi: 10.1186/s13643-022-02123-y

40. Liu XC, Jiang YP, Sun XG, Zhao JJ, Zhang LY, Jing X. Prognostic significance of the systemic immune-inflammation index in patients with cholangiocarcinoma: A meta-analysis. *Front Oncol*. (2022) 12:938549. doi: 10.3389/fonc.2022.938549

41. Yang Y, Li Y, Niu X, Liu W. Imaging evaluation of blood supply changes after chemotherapy of osteosarcoma and its correlation with tumor necrosis rate. *J Bone Oncol*. (2023) 41:100492. doi: 10.1016/j.jbo.2023.100492

42. Fidan AK, Uçmak G, Demirel BB, Efetürk H, Öztürk İ, Demirtaş Şenlik S, et al. The relation between staging fluorine-18 fluorodeoxyglucose positron emission tomography/computed tomography metabolic parameters and tumor necrosis rate in pediatric osteosarcoma patients. *Turk J Med Sci*. (2021) 51:1115–22. doi: 10.3906/sag-2004-358

frontiers | Frontiers in Immunology

TYPE Original Research
PUBLISHED 17 September 2024
DOI 10.3389/fimmu.2024.1452946

OPEN ACCESS

EDITED BY
Eyad Elkord,
Xi'an Jiaotong-Liverpool University, China

REVIEWED BY
Dipanjan Ghosh,
National Institute of Pharmaceutical Education and Research, Kolkata, India
Eleni Anastasiadou,
Sapienza University of Rome, Italy

*CORRESPONDENCE
Hailun Zhou
apm70allen@126.com
Yijia Chen
742886487@qq.com

†These authors have contributed equally to this work and share first authorship

RECEIVED 21 June 2024
ACCEPTED 26 August 2024
PUBLISHED 17 September 2024

CITATION
Xu W, Sang S, Wang J, Guo S, Zhang X, Zhou H and Chen Y (2024) Identification of telomere-related lncRNAs and immunological analysis in ovarian cancer. *Front. Immunol.* 15:1452946. doi: 10.3389/fimmu.2024.1452946

Identification of telomere-related lncRNAs and immunological analysis in ovarian cancer

Weina Xu[1†], Shuliu Sang[2†], Jun Wang[1], Shanshan Guo[3], Xiao Zhang[3], Hailun Zhou[2*] and Yijia Chen[3*]

[1]Department of TCM, Zhoujiadu Community Health Service of Shanghai Pudong New Area, Shanghai, China, [2]Department of Oncology, Yueyang Hospital of Integrated Traditional Chinese and Western Medicine, Shanghai University of Traditional Chinese Medicine, Shanghai, China, [3]Department of Gynecology, Longhua Hospital affiliated to Shanghai University of Traditional Chinese Medicine, Shanghai, China

Background: Ovarian cancer (OC) is a global malignancy characterized by metastatic invasiveness and recurrence. Long non-coding RNAs (lncRNAs) and Telomeres are closely connected with several cancers, but their potential as practical prognostic markers in OC is less well-defined.

Methods: Relevant mRNA and clinical data for OC were sourced from The Cancer Genome Atlas (TCGA) database. The telomere-related lncRNAs (TRLs) prognostic model was established by univariate/LASSO/multivariate regression analyses. The effectiveness of the TRLs model was evaluated and measured via the nomogram. Additionally, immune infiltration, tumor mutational load (TMB), and drug sensitivity were evaluated. We validated the expression levels of prognostic genes. Subsequently, PTPRD-AS1 knockdown was utilized to perform the CCK8 assay, colony formation assay, transwell assay, and wound healing assay of CAOV3 cells.

Results: A six-TRLs prognostic model (PTPRD-AS1, SPAG5-AS1, CHRM3-AS2, AC074286.1, FAM27E3, and AC018647.3) was established, which can effectively predict patient survival rates and was successfully validated using external datasets. According to the nomogram, the model could effectively predict prognosis. Furthermore, we detected the levels of regulatory T cells and M_2 macrophages were comparatively higher in the high-risk TRLs group, but the levels of activated CD8 T cells and monocytes were the opposite. Finally, the low-risk group was more sensitive to anti-cancer drugs. The mRNA levels of PTPRD-AS1, SPAG5-AS1, FAM27E3, and AC018647.3 were significantly over-expressed in OC cell lines (SKOV3, A2780, CAOV3) in comparison to normal IOSE-80 cells. AC074286.1 were over-expressed in A2780 and CAOV3 cells and CHRM3-AS2 only in A2780 cells. PTPRD-AS1 knockdown decreased the proliferation, cloning, and migration of CAOV3 cells.

Conclusion: Our study identified potential biomarkers for the six-TRLs model related to the prognosis of OC.

KEYWORDS

ovarian cancer, prognosis, telomere, immune, lncRNA

Introduction

Ovarian cancer (OC) is the fifth most prevalent cancer globally (1, 2). Epithelial OC, accounting for the majority of cases, includes serous, endometrioid, mucinous, and clear cell subtypes, each with varying degrees of differentiation (3). The International Federation of Gynecology and Obstetrics (FIGO) classifies OC into five stages, ranging from stage 0 to extensive stage IV metastasis (4). Currently, targeted therapies, such as poly (ADP-ribose) polymerase inhibitors, and other treatments like surgery, radiation, immunotherapy, nanomedicine technology, and combinatorial therapies, have made rapid progress in improving outcomes for OC patients (5, 6). However, most OC patients still develop resistance, recurrence, metastasis, and the potential development of multi-system complications (7, 8). Hence, it is urgent to pinpoint novel biomarkers that can serve as predictors for clinical outcomes in OC.

Telomeres are special complexes crucial for protecting the ends of eukaryotic chromosomes (9). Abnormal telomeres can result in cancer and age-related pathologies which are related to the integrity of the DNA damage response (10). Notably, short telomeres contribute to genomic instability, which promotes cancer progression. Nevertheless, long telomeres may enhance the risk of cancer (11). It reported that telomerase is highly expressed in ovaries (12). Additionally, a multicenter study shows that the length of telomeres serves as the biomarker in elderly patients with OC (13).

Long non-coding RNAs (lncRNAs) with a length surpassing 200 nucleotides contribute to the modulation of chromatin dynamics, cellular growth, gene expression, differentiation, and developmental processes (14). Compared to mRNAs, lncRNAs are often less abundant in cells, exhibit more specialized tissue-specific expression, and can have a shorter lifespan (15). To fulfill their diverse biological roles, lncRNAs engage in intricate gene regulatory networks through interactions with mRNAs (16). Research has revealed that analyzing lncRNA-mRNA co-expression networks is instrumental for elucidating the involvement of lncRNAs in platinum resistance and for uncovering those with prognostic significance and therapeutic potential in OC (17, 18). Moreover, lncRNAs can modulate immune responses and serve as crucial prognostic biomarkers and diagnostic markers in OC (19, 20). Previous research revealed that certain lncRNAs, including TERC, TERRA, and GUARDIN, have been implicated in the intricate mechanisms of DNA damage response integration, safeguarding of telomere termini, and regulation of telomere length (21, 22). Indeed, emerging evidence suggests that telomere-related lncRNAs (TRLs) are associated with the prognosis of kidney renal clear cell carcinoma prognosis (23). However, the molecular underpinnings of how lncRNAs contribute to telomere homeostasis remain largely uncharted territory. We found that prior research has concentrated on the length and significance of telomeres in cancer prognosis, leaving the correlation of TRLs with OC unexplored. Recognizing the importance of both telomeres and lncRNAs, combining the two to improve prognosis in OC patients may be a viable strategy.

In the present study, we formulated TRLs from The Cancer Genome Atlas (TCGA) dataset to predict OC outcomes. Additionally, we probed the connection between the TRLs model and the immune and delved into the potential impact of TRLs on therapeutic drug selection. This study introduces novel perspectives and targets for treating OC.

Methods

Data collection

The transcriptome data, clinical information, and tumor mutational burden (TMB) information of 429 OC patients were from the TCGA (https://portal.gdc.cancer.gov/) database. Normal sample data (88 samples) were from the GTEx (http://commonfund.nih.gov/GTEx/) database. The annotation information was from the Ensembl database (https://www.ensembl.org) (24) to identify lncRNAs. The inclusion criteria for our study were strictly defined: (1) patients diagnosed with primary ovarian serous cystadenocarcinoma, (2) Samples with complete survival time and outcomes. After matching, a total of 370 OC samples were enrolled in the subsequent study and randomly divided into two groups (7:3 ratio), with 259 cases used for training and 111 cases for testing. The clinical baseline information of the patients is presented in Supplementary Table 1.

Determination of TRLs

The 2093 telomere-related genes (TRGs) were downloaded from TelNet (http://www.cancertelsys.org/telnet/) database (25). The differentially expressed TRGs were pinpointed using the criteria of $|\log_2 FC| \geq 3$ and FDR < 0.05 (23) with the "limma" package. We performed the Pearson correlation analysis to calculate the correlation coefficient between differentially expressed TRGs and lncRNAs expression using the "linkET" package. LncRNAs meeting $P < 0.001$ and $|R| > 0.7$ (18) screening criteria were designated as TRLs.

Establishment and validation of the prognostic model

To identify potential prognostic TRLs in OC patients, the univariate Cox analysis was utilized to integrate the TRLs expression information with survival information using the "survival" package. The least absolute shrinkage and selection operator (LASSO) analysis could mitigate the impact of multicollinearity among the numerous genetic variables (26). This approach, when synergized with the Cox model, can refine the screening of potential biomarkers (27). In the training cohort, we conducted a LASSO analysis to filtrate the prognostic TRLs ulteriorly using the "glmnet" package. The LASSO-selected data applied the multivariate Cox analysis to identify which TRLs emerged as independent prognostic factors for OC patients (28–

31). Subsequently, Kaplan-Meier (KM) analysis was utilized to contrast the high- and low-risk groups, divided by the median risk score. The KM method generated a survival curve with time depicted on the x-axis and the cumulative survival probability represented on the y-axis, offering a visual representation of the proportion of individuals surviving over the study period. If the log-rank test p-value is less than 0.05, there is a statistically significant difference between survival curves (32). Additionally, Receiver Operating Characteristic (ROC) analysis was applied to observe the predictive value of the TRLs prognostic model using the "timeROC" package. The ROC curve was plotted with the false positive rate on the x-axis and the true positive rate on the y-axis, featuring a 95% confidence interval indicated by dotted lines. The area under the ROC curve (AUC) quantified the model's discriminatory ability, the AUC value closer to 1.0 signified superior model performance and generalization capabilities (33, 34). To assess the independence of risk scores derived from the signature, we performed the Cox regression analyses. Subsequently, we verified the prediction performance using testing and entire sets. Ultimately, the integrated nomogram was constructed, encompassing all independent prognostic parameters using the "rms" package, to provide a qualitative prediction of the overall survival (OS) for OC patients within the entire set.

Go and KEGG analysis

To explore the functional mechanisms associated with the model, we determined the differentially expressed genes between low- and high-risk TRLs groups ($|\log_2 FC| > 1$ and FDR < 0.05) using the "limma" package. Subsequently, we conducted GO and KEGG analyses on the above genes. $P < 0.05$ was considered significant.

Immune profile analysis

To delve into the connection between risk score and immune infiltration, the ESTIMATE algorithm was employed to compute the abundance of stromal and immune components. Patients were stratified into two groups according to the median values of risk score levels. Then, the abundance of 28 immune-cell types in two groups was determined by the ssGSEA. Utilizing the CIBERSORT algorithm, we estimated the abundance of 22 distinct immune cell subtypes in patients. The distribution pattern of the two groups was visualized by PCA analysis. To investigate the correlation between immune cells and prognostic TRLs, the results were performed by the Pearson correlation analysis and visualized utilizing the "ggplot2" package.

Tumor mutation analysis

The TMB data was computed in low- and high-TMB groups, categorized by the median TMB value of OC patients. Subsequently, the mutational landscape was depicted in a waterfall plot using the "maftool" package. Furthermore, comparative and survival analyses were executed to explore disparities in somatic mutations between the two groups.

Prediction of potential drug sensitivity

The "oncoPredict" package was employed to forecast drugs IC_{50} values. The IC_{50}, indicative of tolerance capacity, was computed, with higher IC_{50} values signifying increased resistance of cells to the drugs. Subsequently, the disparity in sensitivity scores between the two groups was analyzed.

Cell culture

OC cell lines (SKOV3, A2780, CAOV3) and IOSE-80 cells were sourced from the Cell Bank of the Chinese Academy of Sciences. SKOV3 cells were grown in McCoy's 5A medium (Servicebio Technology Co., Ltd., China, G4541-500ML) with 10% fetal bovine serum. A2780 cells and IOSE-80 cells were grown in RPMI-1640 medium (Servicebio Technology Co., Ltd., China, G4535-500ML) with 10% fetal bovine serum. CAOV3 cells were grown in DMEM medium (Servicebio Technology Co., Ltd., China, G4515-500ML) with 10% fetal bovine serum. Then, the cells were cultivated in a 37°C incubator with 5% CO_2.

qRT-PCR validation

Total RNA was extracted from the cells using an RNA extraction solution (Servicebio Technology Co., Ltd., China, G3013-100ML). For the conversion of RNA to cDNA, we utilized a cDNA Synthesis kit ((TransGen, China, AU341-02) to carry out the reverse transcription process. The quantification of lncRNA levels was determined using the $2^{-\Delta\Delta Cq}$ method, with the results being normalized against the expression levels of the GAPDH. The TRLs sequences are shown in Table 1.

Transfection

CAOV3 cells, in the exponential growth phase, were seeded in a six-well plate at a density of 4×10^4 cells per well to achieve 70–80% confluency. Subsequently, CAOV3 cells were transfected with small interfering RNA targeting PTPRD-AS1 (si-PTPRD-AS1) and a non-targeting siRNA as a negative control (siNC) using the Lipofectamine 2000 reagent (Thermo Fisher Scientific, USA, 11668-027). The PTPRD-AS1 siRNAs, siNC, and Lipofectamine 2000 were prepared by dilution in Opti-MEM serum-free medium (Gibco, USA, 31985-070), then combined and allowed to incubate for 20 minutes to form the transfection complex. This mixture was subsequently introduced into CAOV3 cells for transfection. After a 6-hour incubation period, the medium was replaced with the fresh complete growth medium.

TABLE 1 The TRLs sequences.

Gene Name	Forward sequence (5′-3′)	Reverse sequence (5′-3′)
PTPRD-AS1	CTATTCATCATCACCTCCACATTC	AATTATGCACTAGAGGGGGTAGTG
SPAG5-AS1	CTCTCAGATCACCACATTGTTTTC	TAAGTCTGATGACACAGCAGAACA
CHRM3-AS2	GAGTCTAGCATCTTGCATCTTCCT	TGTTGAGGATAGAACTAGCACAGC
AC074286.1	CCACTGCCAGTTAGAAGACCTATT	AGATCAGCACCACATACACCTAAA
FAM27E3	CACTTGAGAAACAGACCGTATTGT	CTAGGATCAAGATGAACACACTGC
AC018647.3	AGTATACACTGCACCCTGTTTGTG	ACCTGGATGAGACTGGAGACTATT
GAPDH	TGACAACTTTGGTATCGTGGAAGG	AGGCAGGGATGATGTTCTGGAGAG

The CAOV3 cells were then collected 48 h post-transfection for further analysis. To confirm the knockdown efficiency, qRT-PCR analysis was conducted post-transfection. The sequences of siRNAs are shown in Table 2.

CCK8 and colony formation assay

The CCK8 assay and the colony formation assay were utilized to determine the effect of PTPRD-AS1 knockdown on the proliferation of CAOV3 cells. 4,000 CAOV3 cells transfected with si-NC or si-PTPRD-AS1 per well were seeded into 96-well plates and grown for 48 h. Subsequently, the optical density (OD) values were measured at 450 nm within 1-4 h after the addition of 10 μL/well of the CCK-8 reagent (Beyotime Inc., China, C0038). For colony formation, a total of 1,000 CAOV3 cells transfected with si-NC or si-PTPRD-AS1 per well were dispensed into 6-well plates and cultured for 2 weeks. Upon the emergence of visible colonies, the cells were processed for staining using crystal violet (Beyotime Inc., China, C0121).

Transwell assay

Upper transwell chambers coated with matrigel (Corning, USA, 354234) were utilized to assess the invasive capacity of PTPRD-AS1 knockdown. 2×10^4 CAOV3 cells transfected with si-NC or si-PTPRD-AS1 were plated in the upper chambers with DMEM medium devoid of FBS. The lower chambers were filled with DMEM supplemented with 10% FBS. Subsequently, the cells were fixed using a 4% paraformaldehyde solution for 30 minutes and stained with crystal violet for an additional 30 minutes to facilitate the quantification of invasive cells.

Wound healing assay

The assessment of cell migration was conducted using a wound healing assay. CAOV3 cells transfected with si-NC or si-PTPRD-AS1 were plated in 6-well plates to achieve 80% confluence. A standardized scratch wound was created across the well using a 10 μL pipette tip to generate a uniform gap and photographed after 24 h.

Statistical analysis

All statistical analyses were carried out through R software (version 4.3.1) and GraphPad Prism 8.0 software. Two Group differences were statistically evaluated using the Student's t-test. For the analysis of multiple groups, One-way ANOVA was the procedure followed. $P < 0.05$ was considered significant.

Results

Determination of TRLs

We obtained the expression information of 2093 TRGs. 79 differentially expressed TRGs, including 31 down-regulated and 48 up-regulated genes (Figure 1A), and 1,6901 lncRNAs were determined. Finally, 77 TRGs were reserved, and 381 lncRNAs were determined as TRLs ($|R| > 0.7$ and $P < 0.001$).

Establishment of TRLs prognostic model

A total of 10 TLRs of 381 TRLs were observably connected with OS via the univariate analysis (Supplementary Table 2). LASSO

TABLE 2 The PTPRD-AS1 gene siRNA sequence.

Gene Name	Sense(5′-3′)	Antisense(5′-3′)
PTPRD-AS1 si-NC	UUCUCCGAAGGUGUCACGUTT	UUCUCCGAAGGUGUCACGUTT
PTPRD-AS1 si-1	GCUCUAACAUUCUGUGAUATT	UAUCACAGAAUGUUAGAGCTT
PTPRD-AS1 si-2	CGAUGACAAUAAUAGUAAUTT	AUUACUAUUAUUGUCAUCGTT

analysis was performed according to the 10 TRLs, and no genes were screened for incompatibility (Figures 1B, C). Subsequently, we performed the multivariate Cox regression analysis and identified six key TLRs (Figure 1D). The risk score for prognostic-related TRLs = (0.941293163 × PTPRD-AS1) + (0.893391681 × SPAG5-AS1) + (-7.750446273 × CHRM3-AS2) + (1.50190086 × AC074286.1) + (-0.57365439 × FAM27E3)+ (-3.094785104 × AC018647.3). Notably, CHRM3-AS2, FAM27E3, and AC018647.3 were protective factors with HR < 1 in OC patients. Nevertheless, PTPRD-AS1, SPAG5-AS1, and AC074286.1 were risk factors with HR > 1. The findings indicated that PTPRD-AS1, CHRM3-AS2, AC074286.1, and AC018647.3 were independent prognostic factors of OC patients (P< 0.05). The coefficient results of six TRLs are shown in Figure 1E. The expression levels of six TLRs in tumor cases in comparison to normal cases are shown in Figure 1F.

Validation of the TRLs prognostic model

The low- and high-risk groups were categorized by the median score in the training, testing, and entire cohorts (Figures 2A–C). Analysis of survival status distributions indicated a higher mortality rate in the high-risk group (Figures 2D–F). The six TRLs in two groups were visually depicted through heat maps (Figures 2G–I). In the high-risk group, PTPRD-AS1, SPAG5-AS1, and AC074286.1 demonstrated comparatively elevated expression levels, while three protective lncRNAs (PTPRD-AS1, SPAG5-AS1, and AC074286.1) displayed the opposite trend. Additionally, the low-risk group experienced a higher OS rate (Figures 3A–C). The precision of the TRLs prognostic model was assessed by ROC analysis, revealing that the TRLs prognostic signature demonstrated potential in predicting OS (training cohort: 5-year AUC = 0.691, test cohort: 5-year AUC = 0.666, and entire cohort: 5-year AUC = 0.68) (Figures 3D–F). Furthermore, the risk score demonstrated superior prognostic prediction for OC patients compared to other clinical variables (Figures 3G–I). PCA analysis was employed to distinct distribution patterns between the two risk groups in the training, testing, and overall sets (Supplementary Figure 1). The two risk groups tended to diverge along two paths. These results underscored the robust predictive capability of this signature.

Identification of TRLs prognostic model independence

In the training cohort, univariate analysis showed risk score was related to patient survival (Figure 4A). Furthermore, the multivariate analysis suggested that risk score was the independent prognostic factor for OC patients (Figure 4B). The analysis results for both the testing set (Figures 4C, D) and the overall set (Figures 4E, F) were consistent. Subsequently, a nomogram was conducted by combining the risk score with clinical features (Figure 4G). The calibration curves proved the dependability of the six TRLs prognostic model (Figure 4H).

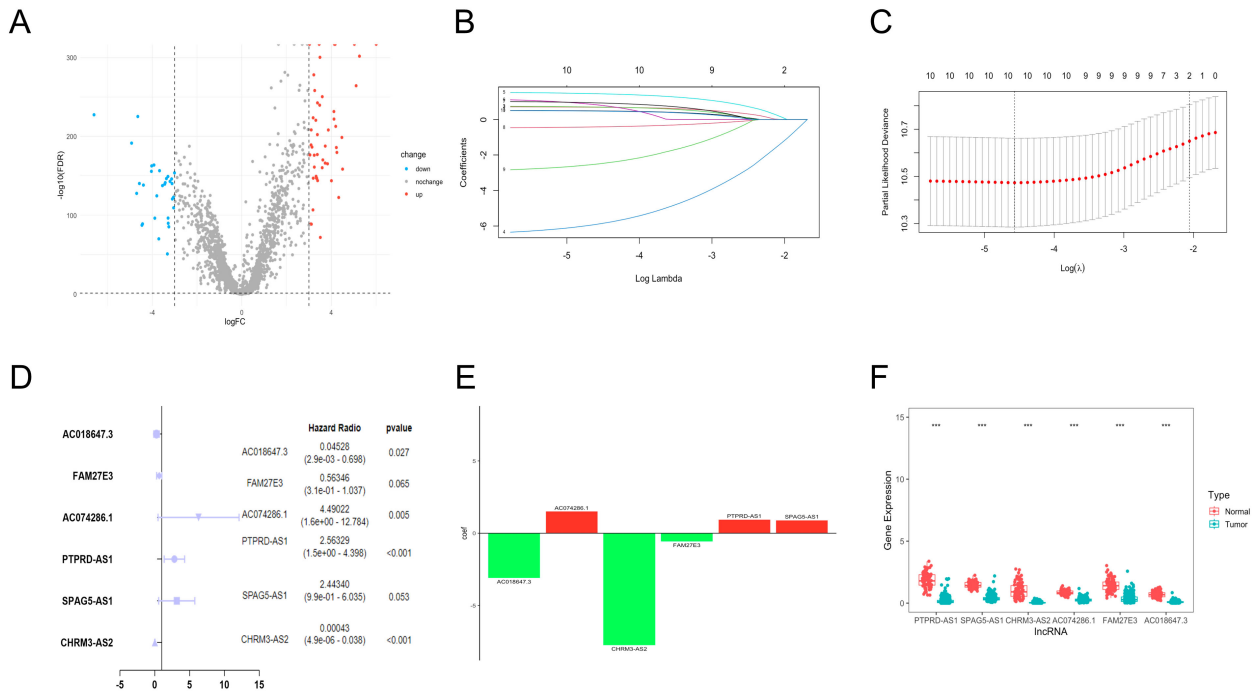

FIGURE 1
Establishment of TRLs prognostic model in OC. **(A)** The differentially expressed TRGs between normal and OC samples. **(B)** The distribution of lambda values in LASSO analysis. **(C)** The deviance diagram of LASSO analysis. **(D)** The six prognostic TRLs by multivariate analysis. **(E)** The coefficient distributions of six prognostic TRLs. **(F)** The expression of six prognostic TRLs between normal and OC tissues. *** P < 0.001.

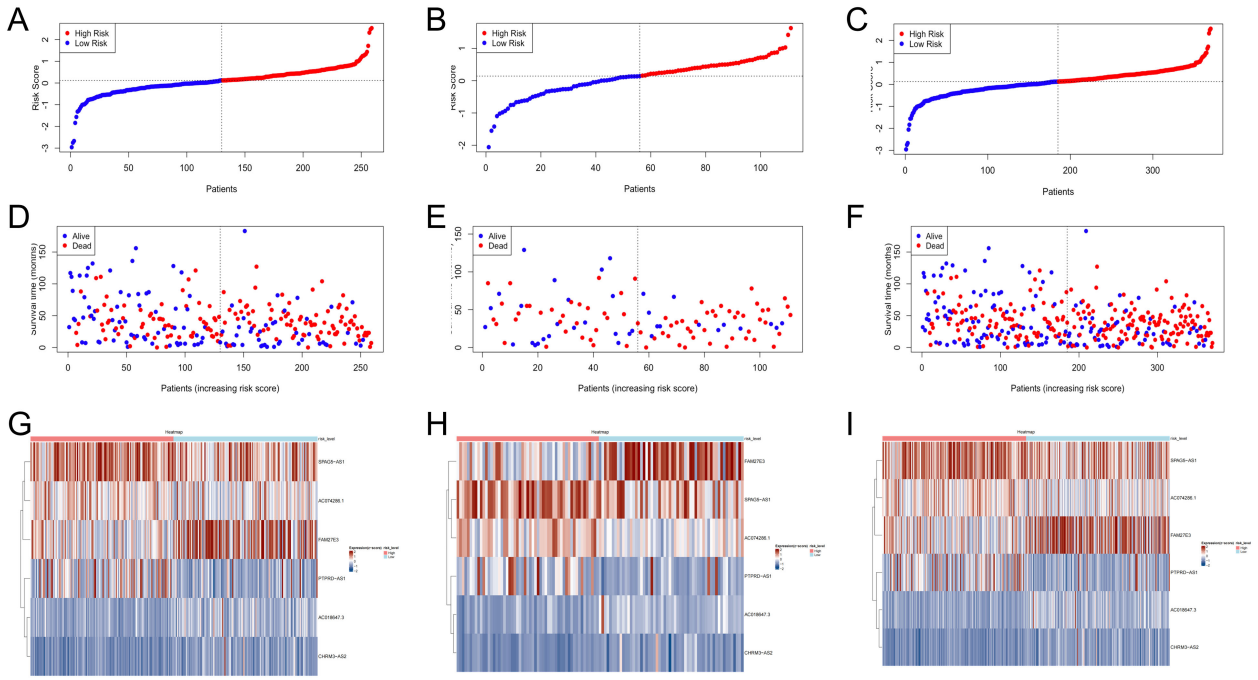

FIGURE 2
Verification of prognostic model in the training, testing, and overall sets. **(A–C)** The risk scores. **(D–F)** The survival status. **(G–I)** Heatmaps of 6 TRLs expression.

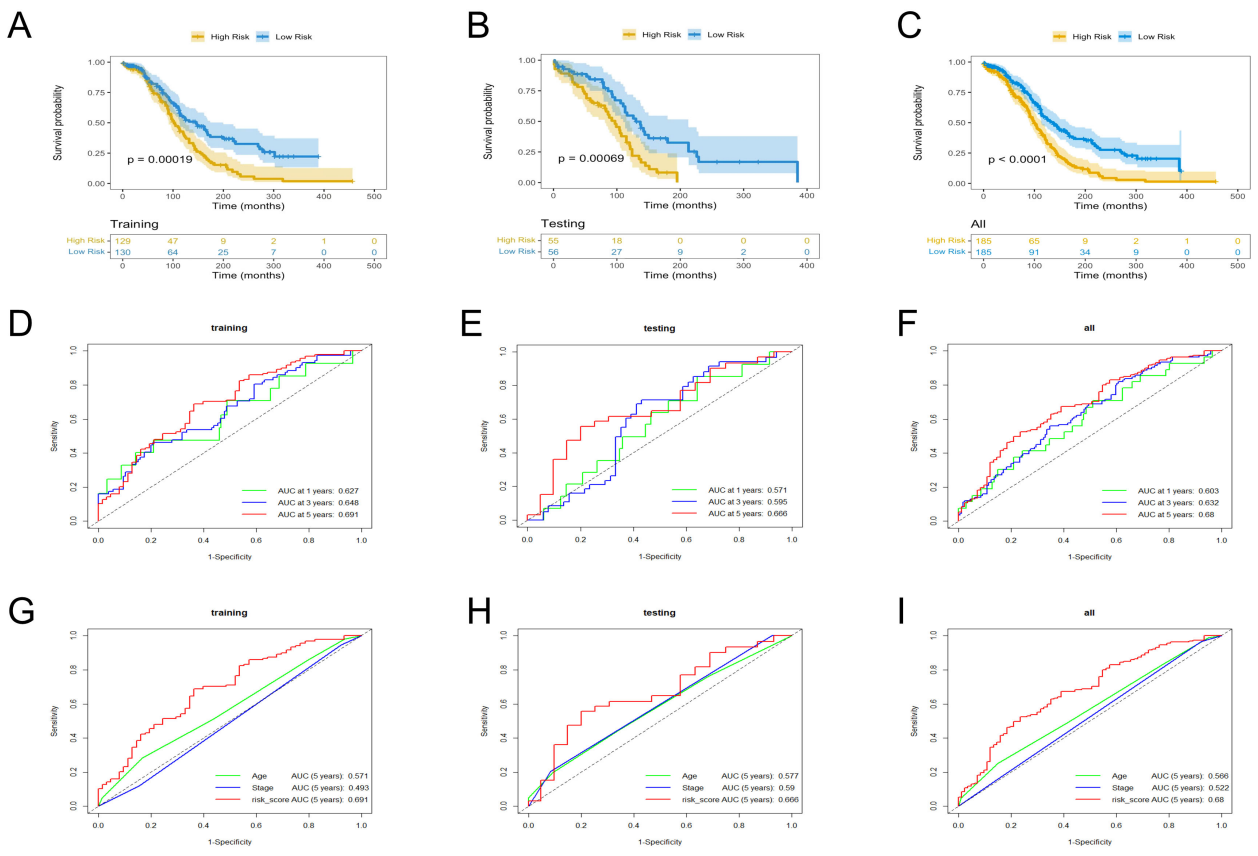

FIGURE 3
KM and ROC curves analysis in the training, testing, and overall sets. **(A–C)** OS rates. **(D–F)** ROC curves for the prognostic model. **(G–I)** ROC curves for the six TRLs risk scores and clinical factors.

Enrichment analysis

To study the potential biological function between the two groups, relevant enrichment analyses were carried out with 12 genes of differential expression between the two groups. GO terms showed that 12 genes were related to fibrillar collagen trimer and collagen fibrill organization (Figures 5A–C), while the KEGG pathway contained proteoglycans in cancer and PI3K-Akt signaling pathway, etc. (Figure 5D). Moreover, the cnetplots were used for the specific GO terms and KEGG categories (Figures 5E–H). These biological processes and pathways likely contribute to the high-risk group towards poorer clinical prognosis.

Immune infiltration analysis

The levels of stromal score were significantly lower in the low-risk group (Figure 6A). ssGSEA analysis demonstrated that the abundance of regulatory T cells was comparatively higher in the high-risk group, and the abundance of activated CD8 T cells and monocytes was the opposite (Figure 6B). CIBERSORT analysis revealed that the high-risk group had significantly higher levels of M_2 macrophages (Figure 6C). PCA plot demonstrated the marked classification of immune cells in two groups (Figure 6D). Moreover, the correlation analysis indicated that PTPRD-AS1, SPAG5-AS1, CHRM3-AS2, AC074286.1, FAM27E3 and AC018647.3 were strongly associated with 28 immune cells (Figures 6E–J). In summary, these findings reveal the obvious differences between the two groups in the immune cells and are closely related to PTPRD-AS1, SPAG5-AS1, CHRM3-AS2, AC074286.1, FAM27E3, and AC018647.3.

Tumor mutation analysis

In the analysis of TMB in OC patients, individual TMB values were determined. The probability of TMB in the high- and low-risk groups was 99.28% and 99.29%, respectively (Figures 7A, B). Nevertheless, the TMB values between the two groups were no significant difference (Figure 7C). Subsequent survival analyses were conducted across different TMB and risk groups. Notably, the high-TMB group exhibited the favorable OS, and the high-TMB combined with the low-risk group demonstrated the highest OS rate (Figures 7D, E).

Sensitivity of potential drugs

To assess the efficacy of the TRLs prognostic model for predicting several drugs in OC, we calculated the IC_{50} value of

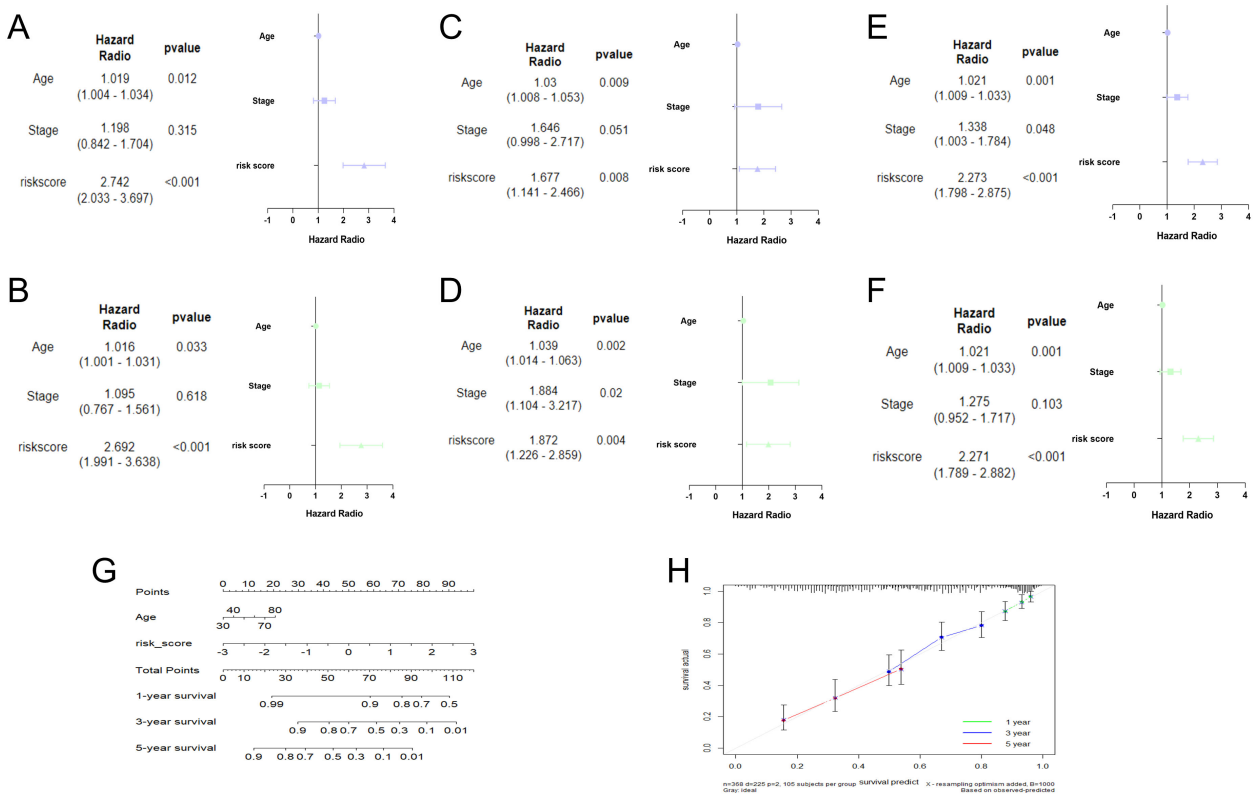

FIGURE 4
Establishment of nomogram. Univariate and multivariate analysis in the training **(A, B)**, testing **(C, D)**, and overall **(E, F)** sets. **(G)** Nomogram analysis in OC patients. **(H)** The calibration curves of the nomogram.

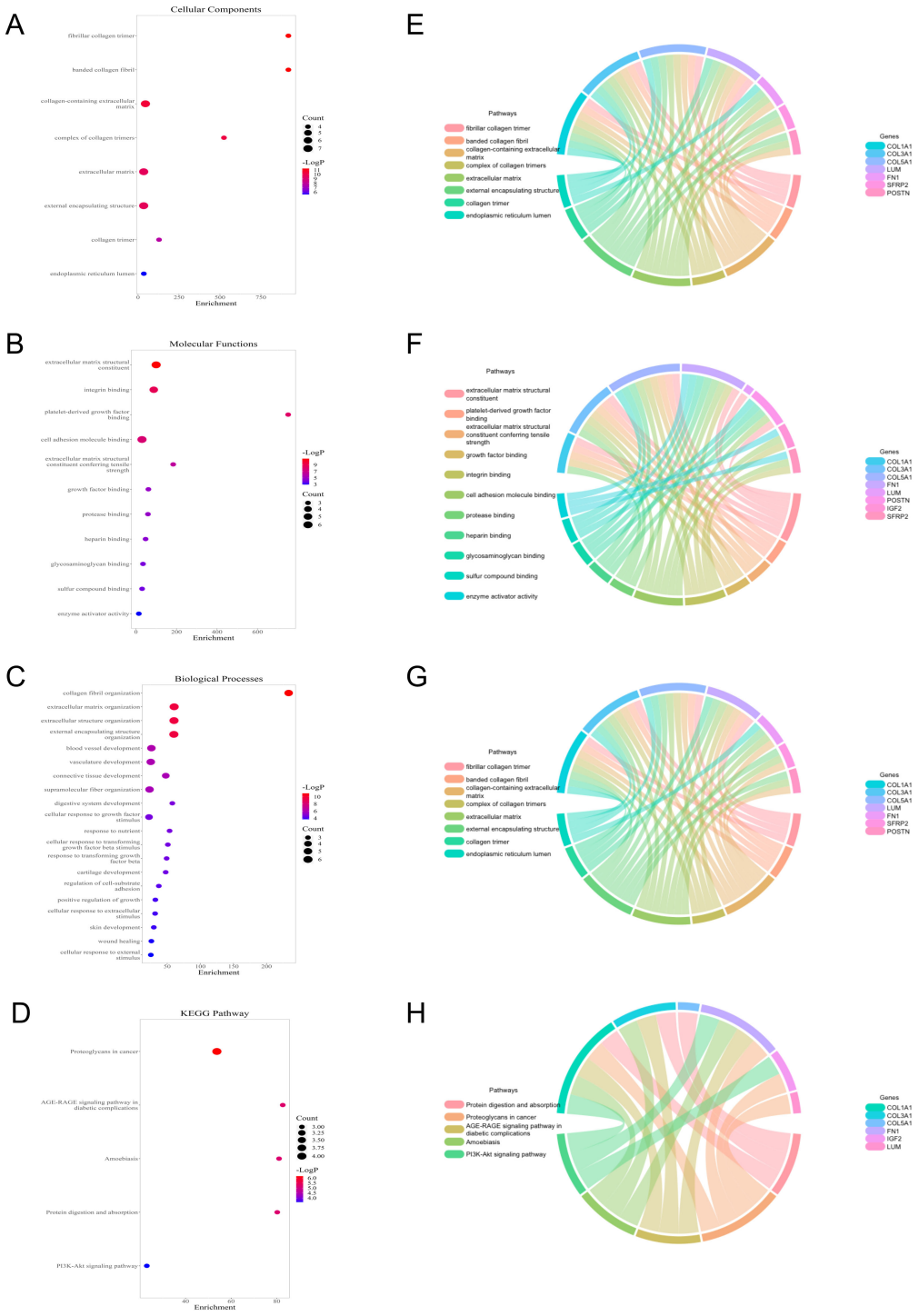

FIGURE 5
Functional analysis of 12 genes with differential expression between low- and high-risk groups. **(A–C)** GO terms analysis. **(D)** KEGG pathways analysis. **(E–H)** Specific genes related to the GO terms and pathways.

the anti-cancer drugs in two groups of OC patients. The low-risk group had the low IC_{50} value of the anti-cancer drugs, which means that the above drugs were more sensitive to the low-risk group (Figure 8).

PTPRD-AS1 associated with OC prognosis

We performed qRT-PCR, and the result demonstrated that PTPRD-AS1, SPAG5-AS1, FAM27E3, and AC018647.3 were

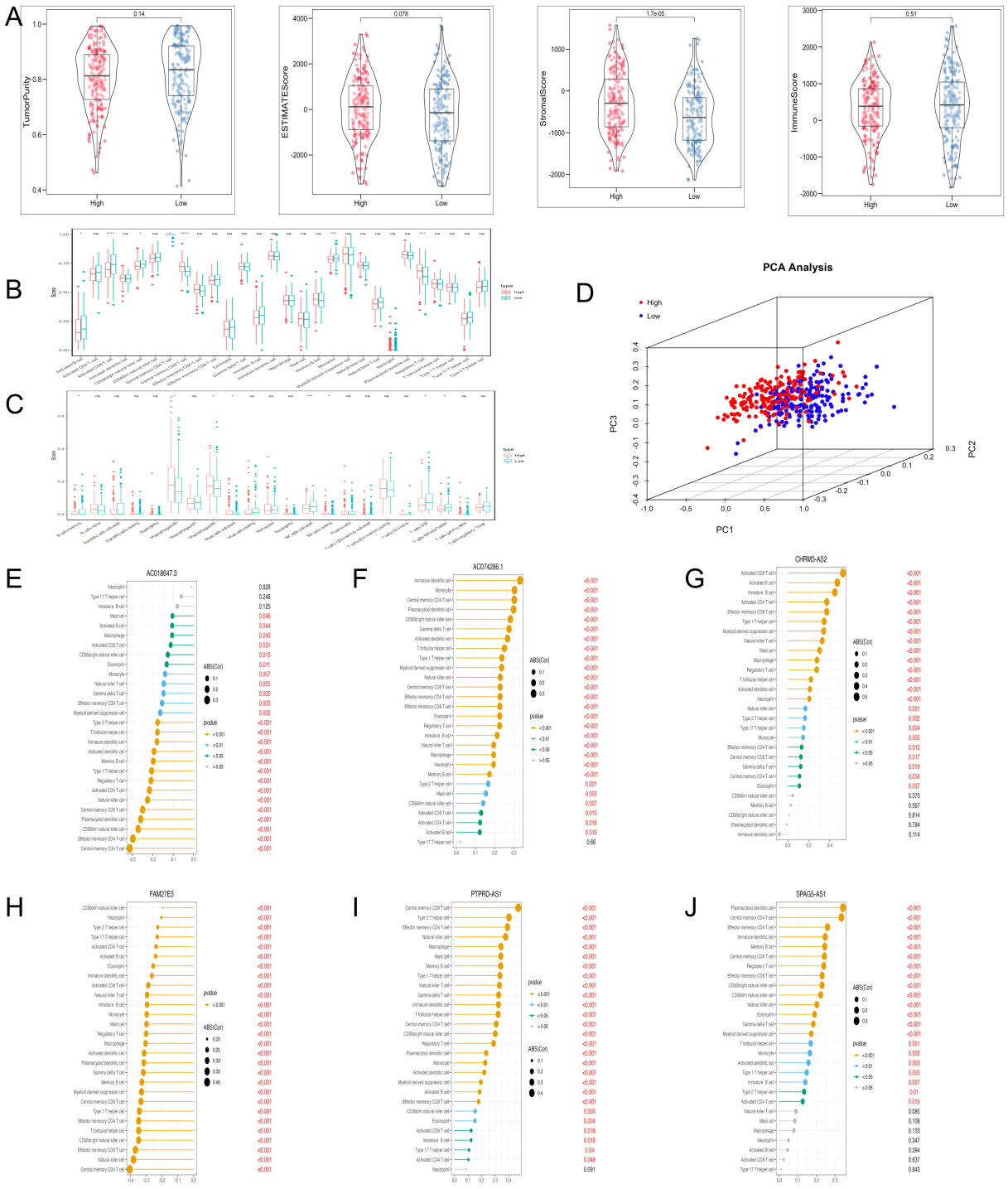

FIGURE 6
Immune cell infiltration analysis with TRLs risk group. **(A)** The ESTIMATE score, Immune score, and Stromal score diagrams. **(B)** The 28 type immune cells in two risk groups by ssGSEA. **(C)** The level of 22 immune cell infiltration in two risk groups by the CIBERSORT algorithm. **(D)** PCA analysis of immune cells between two groups. **(E–J)** Correlation analysis of six prognostic biomarkers (PTPRD-AS1, SPAG5-AS1, CHRM3-AS2, AC074286.1, FAM27E3, and AC018647.3) and immune cells. * $P < 0.05$, ** $P < 0.01$, **** $P < 0.0001$, ns, not significant.

significantly over-expressed in OC cell lines (SKOV3, A2780, CAOV3) in comparison to normal IOSE-80 cells ($P < 0.05$). AC074286.1 were over-expressed in A2780 and CAOV3 cells and CHRM3-AS2 only in A2780 cells ($P < 0.05$) (Figure 9A). FAM27E3 had the highest expression in OC cell lines. We found that high expression of FAM27E3 was associated with a good prognosis ($P = 0.036$). Moreover, the levels of FAM27E3 were increased in stages III and grade III in OC. However, there was no significant difference among different stages and grades (Supplementary Figure 2). Among them, PTPRD-AS1, CHRM3-AS2, AC074286.1, and

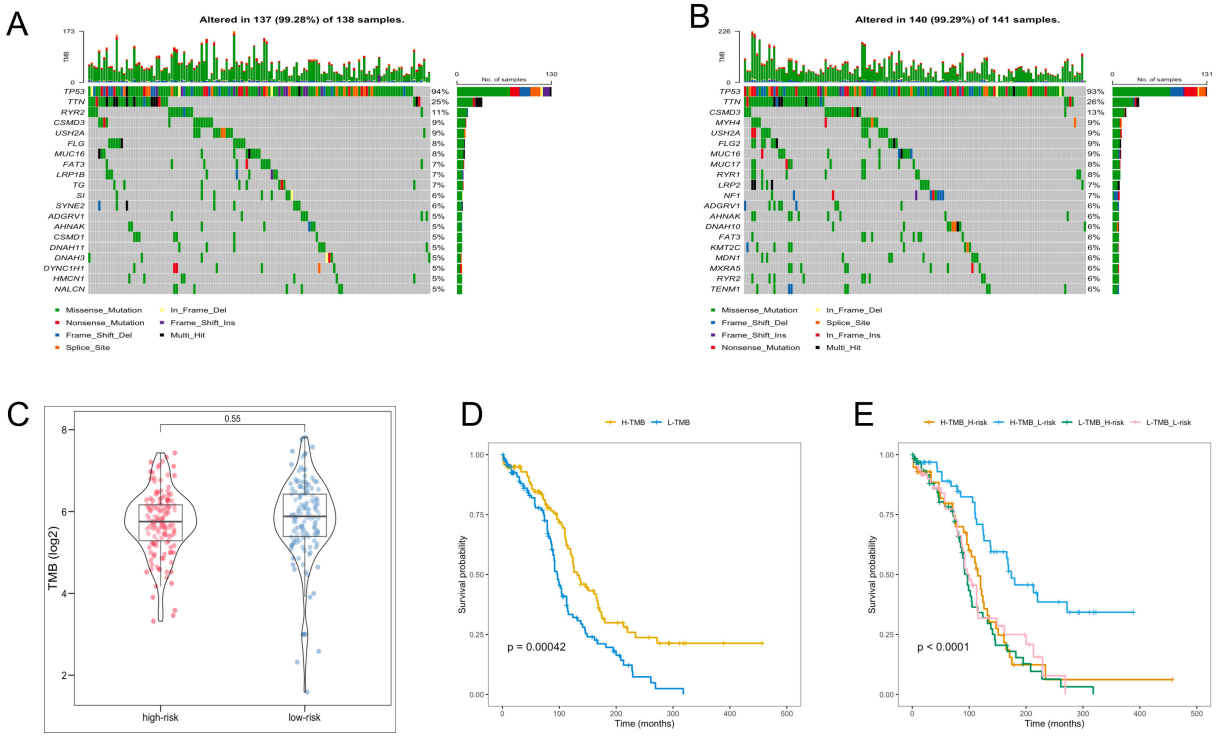

FIGURE 7
TMB analysis. **(A, B)** The waterfall plot of the frequency of TMB in two risk groups. **(C)** TMB levels between the two risk groups. **(D)** KM analysis of TCGA-OV patients in the low- and high-TMB groups. **(E)** KM analysis of TCGA-OV patients in the two risk groups combining the TMB groups.

AC018647.3 were independent prognostic factors of OC patients. PTPRD-AS1 was strongly associated with the immune cells. In addition, high expression levels of PTPRD-AS1 have been proven to be associated with shorter survival of OC (35). But there is no further experimental evidence. Thus, we selected PTPRD-AS1 for more in-depth analysis. We utilized OS as the outcome measure to evaluate its effect on prognostic outcomes. Our results demonstrated a significant correlation between elevated PTPRD-AS1 expression and a poorer prognosis ($P = 0.036$, Supplementary Figure 3A), which was consistent with the previous research. Concurrently, we appraised the anti-cancer drugs sensitivity analysis. Patients exhibiting high levels of PTPRD-AS1 showed a

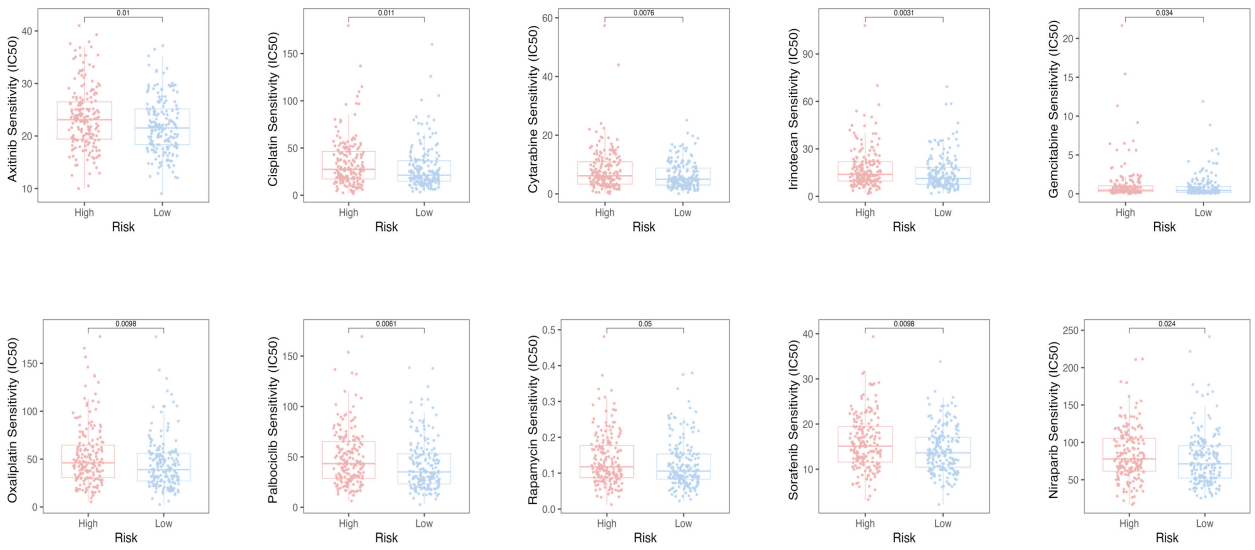

FIGURE 8
The oncoPredict algorithm predicted the IC_{50} values for ten anti-cancer drugs.

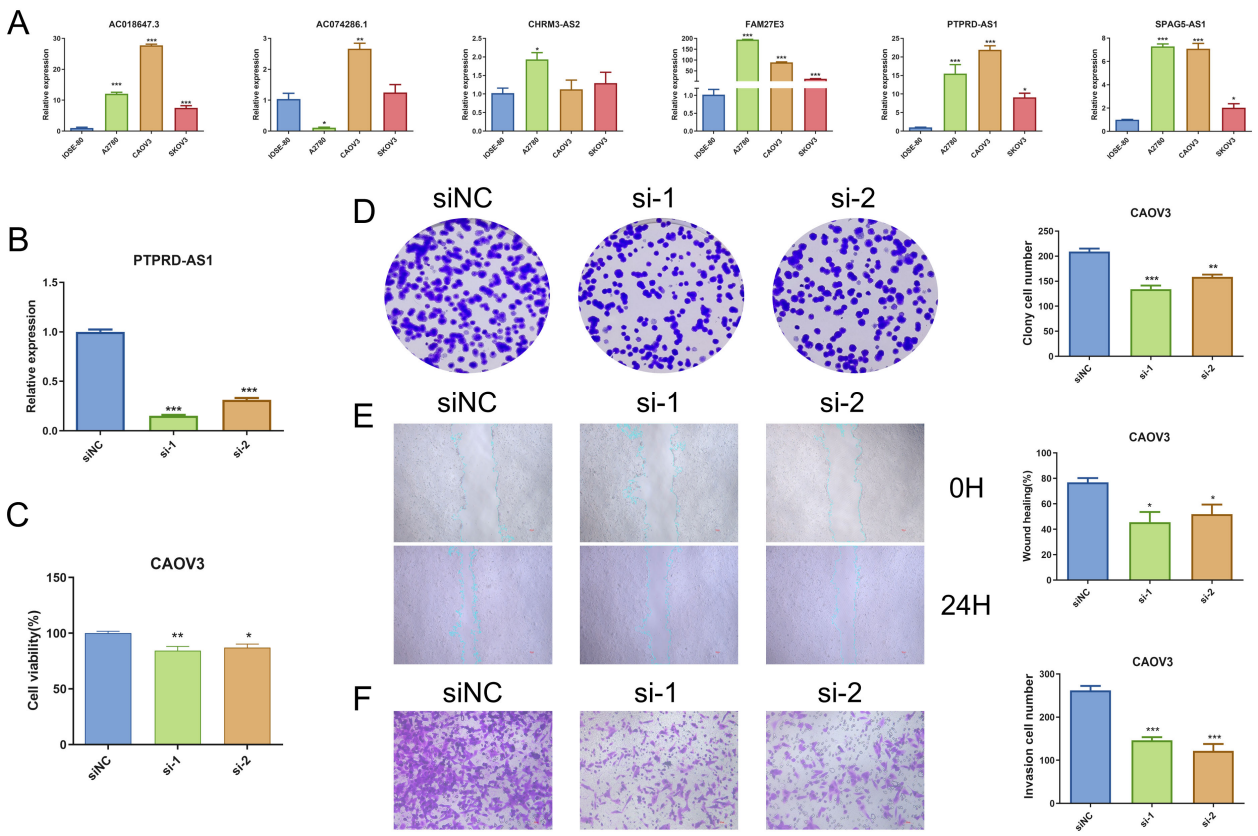

FIGURE 9
Analysis of PTPRD-AS1 mRNA Levels in OC. **(A)** Comparative expression levels of six prognostic genes in OC cell lines (SKOV3, A2780, CAOV3) and normal IOSE-80 cells by qRT-PCR. **(B)** Expression levels of PTPRD-AS1 in CAOV3 cells transduced with siRNA by qRT-PCR. **(C–F)** CCK8 assay, colony formation assay, wound healing assay, and transwell assay in transduced CAOV3 cells. The experiments were repeated at least three times. The One-way ANOVA was applied for statistical significance, * $P < 0.05$, ** $P < 0.01$, *** $P < 0.001$.

more favorable response to the drugs Rapamycin and Dasatinib (Supplementary Figures 3B–F).

PTPRD-AS1 inhibition suppresses CAOV3 cells proliferation, migration, and invasion

PTPRD-AS1 exhibited the highest mRNA expression levels in CAOV3 cells compared to other OC cell lines. Consequently, CAOV3 cells were chosen for further functional analysis. We achieved successful knockdown of PTPRD-AS1 in CAOV3 cells through transfection with Si-PTPRD-AS1 (Figure 9B). Importantly, the CCK8 assay and colony formation assay demonstrated a reduction in the proliferative capacity of CAOV3 cells after the knockdown of PTPRD-AS1, respectively (Figures 9C, D). Additionally, our findings indicated that the suppression of PTPRD-AS1 significantly impeded the metastatic and invasive properties of CAOV3 cells (Figures 9E, F). Notably, qPCR experiments revealed a significant downregulation of MMP2 and MMP9 upon PTPRD-AS1 knockdown (Supplementary Figure 4). Collectively, these results imply that the knockdown of PTPRD-AS1 exerts an inhibitory effect on the proliferation, migration, and invasion of CAOV3 cells.

Discussion

OC remains a global malignancy characterized by metastatic invasiveness and recurrence (36). Notably, prognosis models based on lncRNAs have demonstrated accurate predictions for OC patient outcomes (37, 38). Although the clinical application of lncRNAs as predictive biomarkers is not yet fully understood, they offer distinct advantages over protein and mRNA biomarkers due to their tissue and stage-specific expression (39). This calls for more research to identify similar biomarkers for OC. Telomeres play a crucial role in preserving genomic integrity by safeguarding chromosome ends (40). Interestingly, anomalies in telomeric structures have been associated with various cancer types, underscoring their impact on oncogenesis and tumor progression. However, few studies explore the links between telomeres and lncRNAs in OC.

In this study, 79 TRGs were initially screened for differential expression between normal samples and OC samples. Through univariate Cox regression analysis, 10 TRLs were identified. Subsequently, based on LASSO and multivariate analysis, the prognostic model comprising 6 TRLs (PTPRD-AS1, SPAG5-AS1, CHRM3-AS2, AC074286.1, FAM27E3, and AC018647.3) was constructed. Among them, PTPRD-AS1 has been recognized as an effective biomarker for predicting the prognosis of breast cancer

patients and OC patients (41). SPAG5-AS1 can promote apoptosis to improve and alleviate podocyte injury (42). CHRM3-AS2 was highly expressed in glioma cells, and silencing of CHRM3-AS2 expression could inhibit glioma growth (43). AC074286.1 had been proven as a protective lncRNA in glioma, and its high expression showed a favorable prognosis (44). The expression of FAM27E3 was up-regulated in thyroid cancer, and the high expressions of FAM27E3 suggested poor prognosis (45). However, the role of AC018647.3 remains unexplored in the literature, so future studies will necessitate investigations to unravel its functions and mechanisms.

To evaluate the prognostic utility of the model for OC patients, the OC patients were allocated into two risk groups. KM analysis revealed the low-risk group had the higher OS. ROC analysis demonstrated that the TRLs prognostic signature demonstrated potential in predicting OS. Subsequently, we confirmed the risk scores were the adverse prognostic factor. In addition, the nomogram enhanced the applicability of the prognostic model in clinical practice. The enrichment analysis was used to explore the mechanisms of prognostic TRLs. GO terms revealed these genes were observably related to fibrillar collagen trimer and collagen fibrill organization. The KEGG pathway contained proteoglycans in cancer and PI3K-Akt signaling pathway, etc. These biological processes and pathways likely contribute to the high-risk group towards poorer clinical OS.

We investigated the association between the characteristics of OC tumors and immune infiltration. The high-risk group had higher stromal score and estimate score, which might mean the activation of diverse biological behavior within the tumor microenvironment (46, 47). In addition, we find the levels of regulatory T cells (Tregs) were comparatively higher in the high-risk group, while the abundance of activated CD8 T cells and monocytes was the opposite by ssGESA. CIBERSORT analysis revealed that the high-risk group had significantly higher levels of M_2 macrophages. Tregs are connected with dampening excessive immune activation and preserving immune homeostasis (48). Excessive activity of Tregs has the potential to promote the development of tumors (49). The strategic targeting of Tregs to restore a pro-inflammatory and immunogenic tumor microenvironment has gained increasing attention as an attractive approach for cancer treatment (50). CD8 T cells are the primary effector cells crucial for anti-tumor responses in immunotherapy. The phenomenon of CD8 T cell "exhaustion" frequently results in the loss of control and advancement of tumors (51). Monocytes, integral components of the mononuclear phagocyte system within the innate immune system, are crucial regulators of cancer initiation and progression. Distinct subsets of monocytes undertake diverse functions, contributing to both pro-tumoral and anti-tumoral immune responses (52). The expression of M_2 macrophages is associated with a poor prognosis of OC (53). The study revealed that M_2 macrophages stimulated the proliferation of OC cells, a process associated with the elevated expression of MMP9 (54). We observed discrepancies between the outcomes of ssGSEA and CIBERSORT analyses, which may point to contradictions. The varying levels of immune activity could potentially account for the poor prognosis observed in high-risk OC patients. It is noteworthy that the connection between the risk stratification of TRLs and immune response has not yet been verified. Elucidating the underlying mechanisms of this association is a valuable area for future investigation.

TMB is a critical measure of the tumor's mutational load, which is translated into antigens that are presented to T cells. An elevated TMB can lead to the production of a greater number of neoantigens, increasing the chances of T cell recognition. This increased recognition may, in turn, enhance the efficacy of treatments involving immune checkpoint inhibitors by bolstering the immune system's response against the tumor (55, 56). TMB levels are becoming widely acknowledged as a sensitive indicator predicting clinical responses to immunotherapy across diverse cancer types (57). Overall, TMB levels serve as a reflection of effective immune activation, with research indicating that higher TMB levels are associated with a greater likelihood of benefiting from immunotherapy (58). To investigate the essential roles of TMB in OC through somatic mutation analysis, we identified somatic mutations in 247 patients, with 137 (99.28%) in the high-risk group and 140 (99.29%) in the low-risk group. Consistent with findings from other studies, the TP53 gene had the highest mutation frequency (59). Moreover, The high-TMB group exhibited superior survival rates in OC, corroborating findings from the previous study (60). Interestingly, the high-TMB combined with the low-risk group demonstrated the highest OS rate, demonstrating that the low-risk group might derive more significant benefits from immunotherapy.

Additionally, we looked at patients' responses to drug sensitivity, assessed through IC_{50} values. It is noteworthy that the above anti-tumor drugs were more sensitive to the low-risk group. In our subsequent analysis, we explored the correlation between PTPRD-AS1 expression and the sensitivity to the above anti-tumor drugs. Our findings indicated that patients with elevated PTPRD-AS1 levels exhibited a significantly better therapeutic response to Rapamycin and Dasatinib compared to those with lower levels. Rapamycin, a multifaceted immunosuppressant, has demonstrated therapeutic potential in the treatment of OC. Its antitumor activity is mediated through the inhibition of the mTOR signaling pathway, a critical cellular regulator of growth and proliferation (61, 62). Dasatinib, a potent tyrosine kinase inhibitor, has exhibited antitumor effects against OC (63). Collectively, these results indicate that patients with elevated levels of PTPRD-AS1 may respond more favorably to the therapeutic effects of Rapamycin and Dasatinib.

We verified six prognostic genes by qRT-PCR. The PTPRD-AS1, SPAG5-AS1, CHRM3-AS2, AC074286.1, FAM27E3 and AC018647.3 expression levels were significantly over-expressed in OC cell lines (SKOV3, A2780, CAOV3) in comparison to normal IOSE-80 cells. Notably, PTPRD-AS1 knockdown decreased cell proliferation, migration, and invasion in OC. In addition, we found a significant correlation between elevated PTPRD-AS1 expression and a poorer prognosis. And, PTPRD-AS1 was closely

related to the immune cells. These results demonstrate that PTPRD-AS1 might serve as an efficient biomarker in OC.

Our study holds distinctive advantages. First, our prognostic model allows for a more nuanced understanding of the interactions between TRLs and patient outcomes. The risk of disease progression and prognosis for patients is evaluated by integrating clinical data with the expression levels of TRLs. Second, our model proposes a high-low risk stratification of patients and assesses their susceptibility to anti-cancer drugs as well as the efficacy of immunotherapy, which can facilitate more accurate treatment approaches and follow-up plans, providing the basis for personalized management and treatment strategies. Furthermore, our research has uncovered a novel biomarker for OC, PTPRD-AS1, which could be instrumental in identifying high-risk populations. It has the potential to enhance both the sensitivity and specificity of early diagnostic approaches, thereby improving the detection rate among at-risk individuals.

There are still some limitations to our study. First, aside from PTPRD-AS1, the remaining 5 TRLs need further experimental verification to confirm their roles. Second, our analysis was confined to the TCGA database, which means that our TRLs prognostic model needs to be validated using external datasets and ideally tested to test the predictive power of the model in a multicenter, large-scale clinical trial. In addition, achieving personalized precision studies depends on the integration of varied datasets, including clinical and multi-omics study data. Undoubtedly, our future research will be conducted in subsequent papers, including *in vitro* and *in vivo* experimental studies to better determine the capabilities of TRLs and mitigate the development of OC. We also need to collect blood and tissue samples from OC patients and integrate metabolomics and proteomics for comprehensive detection and analysis. This study is the first to verify the therapeutic potential of PTPRD-AS1 in OC. However, the precise mechanism by which PTPRD-AS1 influences prognosis, particularly its relationship with immune cell infiltration, remains to be elucidated. To explore this, We plan to examine the transcriptional effects of PTPRD-AS1 by conducting an RNA sequencing (RNA-seq) analysis. This will be complemented by the GO analysis to identify and characterize the functional roles of differentially expressed TRGs, providing insights into the mechanism of PTPRD-AS1. We will conduct flow cytometry assays to evaluate the impact of PTPRD-AS1 knockdown on the expression of OC cell surface markers. Additionally, we will co-culture these cells with peripheral blood mononuclear cells (PBMCs) or tumor-specific T cells to measure cytotoxic effects and the proliferation of immune cells. Immunohistochemical staining will be utilized to examine the spatial distribution and concentration of immune cells within tumor tissues, including CD8 + T cells, Monocytes, and Tregs. It is important to note that this study does not include drug-related validation. Consequently, future research will focus on pharmacokinetic studies to assess drug delivery, distribution, and accumulation of Rapamycin and Dasatinib in OC tissues.

Data availability statement

The original contributions presented in the study are included in the article/Supplementary Material. Further inquiries can be directed to the corresponding authors.

Author contributions

WX: Investigation, Writing – original draft. SS: Validation, Writing – original draft. JW: Methodology, Writing – original draft. SG: Data curation, Writing – original draft. XZ: Methodology, Writing – original draft. HZ: Validation, Writing – original draft. YC: Funding acquisition, Writing – review & editing.

Funding

The author(s) declare financial support was received for the research, authorship, and/or publication of this article. The study was supported by the National Nature Science Foundation of China (No. 82004313), Natural Science Foundation of Minhang District, Shanghai (2023MHZ038), Medicine Foundation project of Longhua Hospital Affiliated to Shanghai University of Traditional Chinese Medicine (YM2021006) and Health Research Project of Shanghai Pudong New Area Health Commission (PKJ2021-Y101).

Conflict of interest

The authors declare that the research was conducted in the absence of any commercial or financial relationships that could be construed as a potential conflict of interest.

Publisher's note

Supplementary material

The Supplementary Material for this article can be found online at: https://www.frontiersin.org/articles/10.3389/fimmu.2024.1452946/full#supplementary-material

References

1. Siegel RL, Miller KD, Wagle NS, Jemal A. Cancer statistics, 2023. *CA Cancer J Clin*. (2023) 73:17–48. doi: 10.3322/caac.21763

2. Vang R, Shih I, Kurman RJ. Ovarian low-grade and high-grade serous carcinoma: pathogenesis, clinicopathologic and molecular biologic features, and diagnostic problems. *Adv Anat Pathol*. (2009) 16:267–82. doi: 10.1097/PAP.0b013e3181b4fffa

3. Testa U, Petrucci E, Pasquini L, Castelli G, Pelosi E. Ovarian cancers: genetic abnormalities, tumor heterogeneity and progression, clonal evolution and cancer stem cells. *Medicines (Basel)*. (2018) 5:16. doi: 10.3390/medicines5010016

4. Prat J. Figo's staging classification for cancer of the ovary, fallopian tube, and peritoneum: abridged republication. *J Gynecol Oncol*. (2015) 26:87–9. doi: 10.3802/jgo.2015.26.2.87

5. Anastasiadou E, Messina E, Sanavia T, Labruna V, Ceccarelli S, Megiorni F, et al. Calcineurin gamma catalytic subunit ppp3cc inhibition by mir-200c-3p affects apoptosis in epithelial ovarian cancer. *Genes (Basel)*. (2021) 12:1400. doi: 10.3390/genes12091400

6. Anastasiadou E, Messina E, Sanavia T, Mundo L, Farinella F, Lazzi S, et al. Mir-200c-3p contrasts pd-l1 induction by combinatorial therapies and slows proliferation of epithelial ovarian cancer through downregulation of β-catenin and c-myc. *Cells*. (2021) 10:519. doi: 10.3390/cells10030519

7. Hennessy BT, Coleman RL, Markman M. Ovarian cancer. *Lancet*. (2009) 374:1371–82. doi: 10.1016/S0140-6736(09)61338-6

8. Konstantinopoulos PA, Matulonis UA. Clinical and translational advances in ovarian cancer therapy. *Nat Cancer*. (2023) 4:1239–57. doi: 10.1038/s43018-023-00617-9

9. Blackburn EH. Switching and signaling at the telomere. *Cell*. (2001) 106:661–73. doi: 10.1016/s0092-8674(01)00492-5

10. Martínez P, Blasco MA. Telomeric and extra-telomeric roles for telomerase and the telomere-binding proteins. *Nat Rev Cancer*. (2011) 11:161–76. doi: 10.1038/nrc3025

11. Aviv A, Anderson JJ, Shay JW. Mutations, cancer and the telomere length paradox. *Trends Cancer*. (2017) 3:253–8. doi: 10.1016/j.trecan.2017.02.005

12. Toupance S, Fattet AJ, Thornton SN, Benetos A, Guéant JL, Koscinski I. Ovarian telomerase and female fertility. *Biomedicines*. (2021) 9:842. doi: 10.3390/biomedicines9070842

13. Falandry C, Horard B, Bruyas A, Legouffe E, Cretin J, Meunier J, et al. Telomere length is a prognostic biomarker in elderly advanced ovarian cancer patients: a multicenter gineco study. *Aging (Albany NY)*. (2015) 7:1066–76. doi: 10.18632/aging.100840

14. Bhan A, Mandal SS. Lncrna hotair: a master regulator of chromatin dynamics and cancer. *Biochim Biophys Acta*. (2015) 1856:151–64. doi: 10.1016/j.bbcan.2015.07.001

15. Yunusov D, Anderson L, DaSilva LF, Wysocka J, Ezashi T, Roberts RM, et al. Hipstr and thousands of lncrnas are heterogeneously expressed in human embryos, primordial germ cells and stable cell lines. *Sci Rep*. (2016) 6:32753. doi: 10.1038/srep32753

16. Entezari M, Taheriazam A, Orouei S, Fallah S, Sanaei A, Hejazi ES, et al. Lncrna-mirna axis in tumor progression and therapy response: an emphasis on molecular interactions and therapeutic interventions. *BioMed Pharmacother*. (2022) 154:113609. doi: 10.1016/j.biopha.2022.113609

17. Xiao Q, Luo J, Liang C, Li G, Cai J, Ding P, et al. Identifying lncrna and mrna co-expression modules from matched expression data in ovarian cancer. *IEEE/ACM Trans Comput Biol Bioinform*. (2020) 17:623–34. doi: 10.1109/TCBB.2018.2864129

18. Fang L, Wang H, Li P. Systematic analysis reveals a lncrna-mrna co-expression network associated with platinum resistance in high-grade serous ovarian cancer. *Invest New Drugs*. (2018) 36:187–94. doi: 10.1007/s10637-017-0523-3

19. Fu LL, Li CJ, Xu Y, Li LY, Zhou X, Li DD, et al. Role of lncrnas as novel biomarkers and therapeutic targets in ovarian cancer. *Crit Rev Eukaryot Gene Expr*. (2017) 27:183–95. doi: 10.1615/CritRevEukaryotGeneExpr.v27.i2

20. Wang X, Wang Y, Sun F, Xu Y, Zhang Z, Yang C, et al. Novel lncrna zfhx4-as1 as a potential prognostic biomarker that affects the immune microenvironment in ovarian cancer. *Front Oncol*. (2022) 12:945518. doi: 10.3389/fonc.2022.945518

21. Rossi M, Gorospe M. Noncoding rnas controlling telomere homeostasis in senescence and aging. *Trends Mol Med*. (2020) 26:422–33. doi: 10.1016/j.molmed.2020.01.010

22. Oliva-Rico D, Herrera LA. Regulated expression of the lncrna terra and its impact on telomere biology. *Mech Ageing Dev*. (2017) 167:16–23. doi: 10.1016/j.mad.2017.09.001

23. Chen J, Zhang D, Ren X, Wang P. A comprehensive prognostic and immunological analysis of telomere-related lncrnas in kidney renal clear cell carcinoma. *Aging (Albany NY)*. (2023) 15:11012–32. doi: 10.18632/aging.205056

24. Martin FJ, Amode MR, Aneja A, Austine-Orimoloye O, Azov AG, Barnes I, et al. Ensembl 2023. *Nucleic Acids Res*. (2023) 51:D933–41. doi: 10.1093/nar/gkac958

25. Braun DM, Chung I, Kepper N, Deeg KI, Rippe K. Telnet - a database for human and yeast genes involved in telomere maintenance. *BMC Genet*. (2018) 19:32. doi: 10.1186/s12863-018-0617-8

26. Zhang G, Feng Z, Zeng Q, Huang P. Exploring cancer dependency map genes and immune subtypes in colon cancer, in which tigd1 contributes to colon cancer progression. *Aging (Albany NY)*. (2023) 15:6400–28. doi: 10.18632/aging.204859

27. Feng J, Yu Y, Yin W, Qian S. Development and verification of a 7-lncrna prognostic model based on tumor immunity for patients with ovarian cancer. *J Ovarian Res*. (2023) 16:31. doi: 10.1186/s13048-023-01099-0

28. Li XY, Zhao ZJ, Wang JB, Shao YH, Liu H, You JX, et al. M7g methylation-related genes as biomarkers for predicting overall survival outcomes for hepatocellular carcinoma. *Front Bioeng Biotechnol*. (2022) 10:849756. doi: 10.3389/fbioe.2022.849756

29. Zou J, Lin Z, Jiao W, Chen J, Lin L, Zhang F, et al. A multi-omics-based investigation of the prognostic and immunological impact of necroptosis-related mrna in patients with cervical squamous carcinoma and adenocarcinoma. *Sci Rep*. (2022) 12:16773. doi: 10.1038/s41598-022-20566-0

30. Lin Z, Zou J, Sui X, Yao S, Lin L, Wang J, et al. Necroptosis-related lncrna signature predicts prognosis and immune response for cervical squamous cell carcinoma and endocervical adenocarcinomas. *Sci Rep*. (2022) 12:16285. doi: 10.1038/s41598-022-20858-5

31. Zhao J, Zou J, Jiao W, Lin L, Wang J, Lin Z. Construction of n-7 methylguanine-related mrna prognostic model in uterine corpus endometrial carcinoma based on multi-omics data and immune-related analysis. *Sci Rep*. (2022) 12:18813. doi: 10.1038/s41598-022-22879-6

32. Marengo E, Robotti E. Biomarkers for pancreatic cancer: recent achievements in proteomics and genomics through classical and multivariate statistical methods. *World J Gastroenterol*. (2014) 20:13325–42. doi: 10.3748/wjg.v20.i37.13325

33. Ferri C, Hernández-Orallo J, Flach PA. A coherent interpretation of auc as a measure of aggregated classification performance. *Proceedings of the 28th International Conference on Machine Learning (ICML-11)* (2011), 657–64.

34. Xiao J, Wang R, Cai X, Ye Z. Coupling of co-expression network analysis and machine learning validation unearthed potential key genes involved in rheumatoid arthritis. *Front Genet*. (2021) 12:604714. doi: 10.3389/fgene.2021.604714

35. Zhou M, Sun Y, Sun Y, Xu W, Zhang Z, Zhao H, et al. Comprehensive analysis of lncrna expression profiles reveals a novel lncrna signature to discriminate nonequivalent outcomes in patients with ovarian cancer. *Oncotarget*. (2016) 7:32433–48. doi: 10.18632/oncotarget.8653

36. Schoutrop E, Moyano-Galceran L, Lheureux S, Mattsson J, Lehti K, Dahlstrand H, et al. Molecular, cellular and systemic aspects of epithelial ovarian cancer and its tumor microenvironment. *Semin Cancer Biol*. (2022) 86:207–23. doi: 10.1016/j.semcancer.2022.03.027

37. Chen Y, Bi F, An Y, Yang Q. Identification of pathological grade and prognosis-associated lncrna for ovarian cancer. *J Cell Biochem*. (2019) 120:14444–54. doi: 10.1002/jcb.28704

38. Zheng M, Hu Y, Gou R, Nie X, Li X, Liu J, et al. Identification three lncrna prognostic signature of ovarian cancer based on genome-wide copy number variation. *BioMed Pharmacother*. (2020) 124:109810. doi: 10.1016/j.biopha.2019.109810

39. Jin H, Du W, Huang W, Yan J, Tang Q, Chen Y, et al. Lncrna and breast cancer: progress from identifying mechanisms to challenges and opportunities of clinical treatment. *Mol Ther Nucleic Acids*. (2021) 25:613–37. doi: 10.1016/j.omtn.2021.08.005

40. Maciejowski J, de Lange T. Telomeres in cancer: tumour suppression and genome instability. *Nat Rev Mol Cell Biol*. (2017) 18:175–86. doi: 10.1038/nrm.2016.171

41. Wu Y, Zhang L, He S, Guan B, He A, Yang K, et al. Identification of immune-related lncrna for predicting prognosis and immunotherapeutic response in bladder cancer. *Aging (Albany NY)*. (2020) 12:23306–25. doi: 10.18632/aging.104115

42. Gao X, Zhang S, Chen Y, Wen X, Chen M, Wang S, et al. Development of a novel six-long noncoding rna signature predicting survival of patients with bladder urothelial carcinoma. *J Cell Biochem*. (2019) 120:19796–809. doi: 10.1002/jcb.29285

43. Wang D, Chen Q, Liu J, Liao Y, Jiang Q. Silencing of lncrna chrm3-as2 expression exerts anti-tumour effects against glioma via targeting microrna-370-5p/klf4. *Front Oncol*. (2022) 12:856381. doi: 10.3389/fonc.2022.856381

44. Duan WW, Yang LT, Liu J, Dai ZY, Wang ZY, Zhang H, et al. A TGF-β signaling-related lncRNA signature for prediction of glioma prognosis, immune microenvironment, and immunotherapy response. *CNS Neurosci Ther*. (2024) 30:e14489. doi: 10.1111/cns.14489

45. Zhang D, Xiang KF, Xiang C, Wu Y, Wang L. Construction of novel 7 integrin-related gene signatures in thyroid cancer construction of model based on integrin genes. *Med (Baltimore)*. (2023) 102:e36412. doi: 10.1097/MD.0000000000036412

46. Liu Y, Wang Y, Li C, Feng H, Liu Y, Ma L. An effective prognostic model in colon adenocarcinoma composed of cuproptosis-related epigenetic regulators. *Front Pharmacol*. (2023) 14:1254918. doi: 10.3389/fphar.2023.1254918

47. Anderson NM, Simon MC. The tumor microenvironment. *Curr Biol*. (2020) 30:R921–5. doi: 10.1016/j.cub.2020.06.081

48. Ferreira L, Muller YD, Bluestone JA, Tang Q. Next-generation regulatory t cell therapy. *Nat Rev Drug Discovery*. (2019) 18:749–69. doi: 10.1038/s41573-019-0041-4

49. Dees S, Ganesan R, Singh S, Grewal IS. Regulatory t cell targeting in cancer: emerging strategies in immunotherapy. *Eur J Immunol*. (2021) 51:280–91. doi: 10.1002/eji.202048992

50. Yan Y, Huang L, Liu Y, Yi M, Chu Q, Jiao D, et al. Metabolic profiles of regulatory t cells and their adaptations to the tumor microenvironment: implications for antitumor immunity. *J Hematol Oncol*. (2022) 15:104. doi: 10.1186/s13045-022-01322-3

51. Wang Q, Qin Y, Li B. Cd8(+) t cell exhaustion and cancer immunotherapy. *Cancer Lett*. (2023) 559:216043. doi: 10.1016/j.canlet.2022.216043

52. Olingy CE, Dinh HQ, Hedrick CC. Monocyte heterogeneity and functions in cancer. *J Leukoc Biol*. (2019) 106:309–22. doi: 10.1002/JLB.4RI0818-311R

53. Hensler M, Kasikova L, Fiser K, Rakova J, Skapa P, Laco J, et al. M2-like macrophages dictate clinically relevant immunosuppression in metastatic ovarian cancer. *J Immunother Cancer*. (2020) 8:e000979. doi: 10.1136/jitc-2020-000979

54. Carroll MJ, Kapur A, Felder M, Patankar MS, Kreeger PK. M2 macrophages induce ovarian cancer cell proliferation via a heparin binding epidermal growth factor/matrix metalloproteinase 9 intercellular feedback loop. *Oncotarget*. (2016) 7:86608–20. doi: 10.18632/oncotarget.13474

55. Jardim DL, Goodman A, de Melo GD, Kurzrock R. The challenges of tumor mutational burden as an immunotherapy biomarker. *Cancer Cell*. (2021) 39:154–73. doi: 10.1016/j.ccell.2020.10.001

56. Li ZH, Li JY, Wu ZT, Zhu YJ, Zhuo T, Nong JS, et al. Upregulation of poc1a in lung adenocarcinoma promotes tumour progression and predicts poor prognosis. *J Cell Mol Med*. (2024) 28:e18135. doi: 10.1111/jcmm.18135

57. Samstein RM, Lee CH, Shoushtari AN, Hellmann MD, Shen R, Janjigian YY, et al. Tumor mutational load predicts survival after immunotherapy across multiple cancer types. *Nat Genet*. (2019) 51:202–6. doi: 10.1038/s41588-018-0312-8

58. Nie S, Ni N, Chen N, Gong M, Feng E, Liu J, et al. Development of a necroptosis-related gene signature and the immune landscape in ovarian cancer. *J Ovarian Res*. (2023) 16:82. doi: 10.1186/s13048-023-01155-9

59. Zhao S, Zhang X, Gao F, Chi H, Zhang J, Xia Z, et al. Identification of copper metabolism-related subtypes and establishment of the prognostic model in ovarian cancer. *Front Endocrinol (Lausanne)*. (2023) 14:1145797. doi: 10.3389/fendo.2023.1145797

60. Wang H, Liu J, Yang J, Wang Z, Zhang Z, Peng J, et al. A novel tumor mutational burden-based risk model predicts prognosis and correlates with immune infiltration in ovarian cancer. *Front Immunol*. (2022) 13:943389. doi: 10.3389/fimmu.2022.943389

61. Huynh H, Teo CC, Soo KC. Bevacizumab and rapamycin inhibit tumor growth in peritoneal model of human ovarian cancer. *Mol Cancer Ther*. (2007) 6:2959–66. doi: 10.1158/1535-7163.MCT-07-0237

62. Schlosshauer PW, Li W, Lin KT, Chan JL, Wang LH. Rapamycin by itself and additively in combination with carboplatin inhibits the growth of ovarian cancer cells. *Gynecol Oncol*. (2009) 114:516–22. doi: 10.1016/j.ygyno.2009.06.002

63. Xiao J, Xu M, Hou T, Huang Y, Yang C, Li J. Dasatinib enhances antitumor activity of paclitaxel in ovarian cancer through src signaling. *Mol Med Rep*. (2015) 12:3249–56. doi: 10.3892/mmr.2015.3784

frontiers | Frontiers in Immunology

TYPE Original Research
PUBLISHED 20 September 2024
DOI 10.3389/fimmu.2024.1453232

OPEN ACCESS

EDITED BY
Takaji Matsutani,
Maruho, Japan

REVIEWED BY
Yong Ren,
Sun Yat-sen University, China
Hao Zhang,
The Affiliated Hospital of Xuzhou Medical University, China

*CORRESPONDENCE
Wei Huang
alvinbird@126.com
Shaoyu Hao
hshaoyu1985@126.com

†These authors have contributed equally to this work and share first authorship

RECEIVED 22 June 2024
ACCEPTED 27 August 2024
PUBLISHED 20 September 2024

CITATION
Han D, Li H, Zheng X, Fu S, Wei R, Zhao Q, Liu C, Wang Z, Huang W and Hao S (2024) Whole slide image-based weakly supervised deep learning for predicting major pathological response in non-small cell lung cancer following neoadjuvant chemoimmunotherapy: a multicenter, retrospective, cohort study.
Front. Immunol. 15:1453232.
doi: 10.3389/fimmu.2024.1453232

Whole slide image-based weakly supervised deep learning for predicting major pathological response in non-small cell lung cancer following neoadjuvant chemoimmunotherapy: a multicenter, retrospective, cohort study

Dan Han[1,2†], Hao Li[3,4†], Xin Zheng[5], Shenbo Fu[6], Ran Wei[7], Qian Zhao[2], Chengxin Liu[2], Zhongtang Wang[2], Wei Huang[1,2*] and Shaoyu Hao[8,9*]

[1]Department of Radiation Oncology, Shandong University Cancer Center, Jinan, Shandong, China, [2]Department of Radiation Oncology, Shandong Cancer Hospital and Institute, Shandong First Medical University and Shandong Academy of Medical Sciences, Jinan, Shandong, China, [3]Department of Radiology, Shandong Provincial Qianfoshan Hospital, Shandong University, Jinan, Shandong, China, [4]Department of Radiation Oncology and Shandong Provincial Key Laboratory of Radiation Oncology, Shandong Cancer Hospital and Institute, Shandong First Medical University and Shandong Academy of Medical Sciences, Jinan, Shandong, China, [5]Department of Traditional Chinese Medicine, Qingdao Hospital of Traditional Chinese Medicine (Qingdao Hiser Hospital), Qingdao, China, [6]Department of Radiation Oncology, Shanxi Provincial Tumor Hospital, Xi'an, Shanxi, China, [7]Department of Radiology, Jining No.1 People's Hospital, Jining, Shandong, China, [8]Department of Thoracic Surgery, Shandong University Cancer Center, Jinan, Shandong, China, [9]Department of Thoracic Surgery, Shandong Cancer Hospital and Institute, Shandong First Medical University, and Shandong Academy of Medical Sciences, Jinan, Shandong, China

Objective: Develop a predictive model utilizing weakly supervised deep learning techniques to accurately forecast major pathological response (MPR) in patients with resectable non-small cell lung cancer (NSCLC) undergoing neoadjuvant chemoimmunotherapy (NICT), by leveraging whole slide images (WSIs).

Methods: This retrospective study examined pre-treatment WSIs from 186 patients with non-small cell lung cancer (NSCLC), using a weakly supervised learning framework. We employed advanced deep learning architectures, including DenseNet121, ResNet50, and Inception V3, to analyze WSIs on both micro (patch) and macro (slide) levels. The training process incorporated innovative data augmentation and normalization techniques to bolster the robustness of the models. We evaluated the performance of these models against traditional clinical predictors and integrated them with a novel pathomics signature, which was developed using multi-instance learning algorithms that facilitate feature aggregation from patch-level probability distributions.

Results: Univariate and multivariable analyses confirmed histology as a statistically significant prognostic factor for MPR (*P*-value< 0.05). In patch model evaluations, DenseNet121 led in the validation set with an area under the curve (AUC) of 0.656, surpassing ResNet50 (AUC = 0.626) and Inception V3 (AUC = 0.654), and showed strong generalization in external testing (AUC = 0.611). Further evaluation through visual inspection of patch-level data integration into WSIs revealed XGBoost's superior class differentiation and generalization, achieving the highest AUCs of 0.998 in training and robust scores of 0.818 in validation and 0.805 in testing. Integrating pathomics features with clinical data into a nomogram yielded AUC of 0.819 in validation and 0.820 in testing, enhancing discriminative accuracy. Gradient-weighted Class Activation Mapping (Grad-CAM) and feature aggregation methods notably boosted the model's interpretability and feature modeling.

Conclusion: The application of weakly supervised deep learning to WSIs offers a powerful tool for predicting MPR in NSCLC patients treated with NICT.

KEYWORDS

non-small cell lung cancer, major pathological response, neoadjuvant chemoimmunotherapy, whole slide image, weakly supervised learning

Introduction

The employment of neoadjuvant chemoimmunotherapy (NICT) has risen as an effective method for managing resectable non-small cell lung cancer (NSCLC). A number of research has explored its viability and efficacy, showcasing that this strategy can enhance pathological response rates and complete tumor removal. Furthermore, it assists in managing microscopically invisible metastases, thus favorably influencing patient outcomes (1–6).

In many trials focusing on neoadjuvant immunotherapy for NSCLC, major pathological response (MPR) is considered a key predictor for overall survival (OS) and disease-free survival (DFS). However, the rates of MPR observed in current clinical research on NICT display a wide variance, ranging from 18% to 83% (1, 3–5, 7–14). This disparity underscores that not all patients derive benefit from NICT; indeed, ineffective treatment may lead to delays in surgical intervention and an increased likelihood of immune-related side effects. Consequently, crafting a dependable predictive model for MPR response to NICT in patients with resectable NSCLC is crucial, offering the potential to tailor treatments more effectively and enhance patient outcomes.

Tissue specimens stained with Hematoxylin and Eosin (H&E) contain a wealth of useful information for routine histopathological analysis. Artificial intelligence (AI) is increasingly used to analyze H&E stained histopathological images for differential diagnosis and prognosis prediction in NSCLC studies, enhancing the evaluation of conventional histological slides (15–22). This approach holds immense potential for disease research, as AI algorithms can assist clinicians and pathologists in their decision-making by analyzing whole slide images (WSIs).

Weakly supervised learning has garnered widespread attention due to its significant advantage in reducing the workload of manual annotation and has been gradually applied in the field of pathological image analysis (23–25). The classic patch-based weakly supervised method provides a specific workflow for processing histological images. Due to the expansive dimensions of WSIs, segmentation into smaller tiles is necessary for processing, with an averaging method subsequently aggregating the tile-level predictions for each slide (26). This approach has introduced a new level of flexibility and application prospects in the realm of weakly supervised learning for pathological image analysis.

In this study, we developed a weakly supervised deep learning model utilizing pre-treatment WSIs to predict MPR in patients undergoing NICT for NSCLC. The model's predictions can serve as a reference for physicians to enhance treatment planning.

Materials and methods

Data collection

The flowchart illustrating the cohort selection process for this study is presented in Figure 1. This study initially enrolled 302 patients who received NICT followed by surgical intervention from November 24, 2020, to March 10, 2024. However, 116 patients were subsequently excluded based on predefined criteria. All pre-treatment

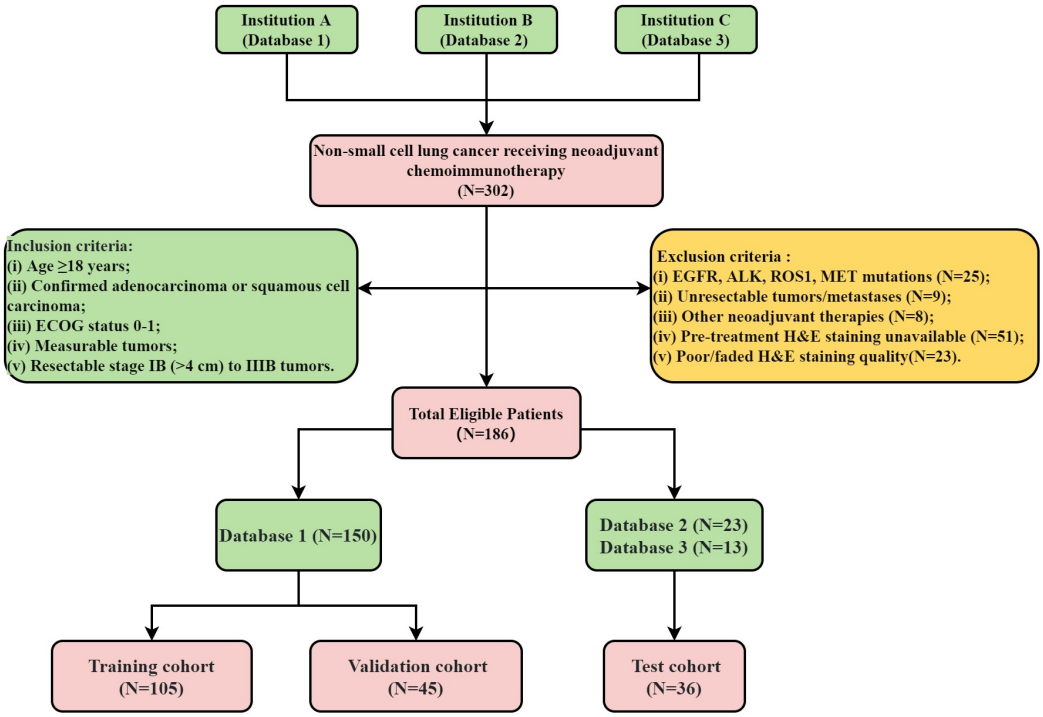

FIGURE 1
Flowchart of the cohorts used in this study.

H&E-stained slides were digitized into WSIs using a WISLEAP scanner and then converted to NDPI format via NDPView2 software. Ultimately, 186 patients contributing 212 WSIs diagnosed with NSCLC were retrospectively selected from three institutions. The allocation of patients across these institutions was as follows: 150 from Shandong Cancer Hospital (Database 1), 23 from Shanxi Cancer Hospital (Database 2), and 13 from the First People's Hospital of Jining City (Database 3). Within the training cohort, samples were apportioned into a training subset and an internal validation subset at a 7:3 ratio. Due to sample size constraints, data from Databases 2 and 3 were amalgamated to constitute the test datasets.

Full details regarding the treatment protocols can be found in Supplementary Data Sheet 2. This study was conducted in accordance with the 8th edition of the American Joint Committee on Cancer (AJCC) Tumor, Node, Metastasis (TNM) staging system. MPR was defined as the presence of less than 10% viable tumor cells in the pathological examination of the surgical specimen (27). The conduct of this study was in strict compliance with the principles of the Declaration of Helsinki and received ethical clearance from the institutional review board (number: SDTHEC2024002010). This study, which was retrospectively registered with the ResearchRegistry (registration ID: researchregistry10216). Additionally, the study received further ethical approvals from the Institutional Review Board of the First People's Hospital of Jining City (approval number: JNRM-2024-KY-037) and the Medical Ethics Committee of Shaanxi Cancer Hospital [approval number: Ethics Review No. 39 (2024)]. Owing to its retrospective design and the absence of any risk to participants, the need for informed consent was duly waived. Figure 2 depicts the comprehensive workflow of our study.

Data processing

In processing the WSIs, which typically span dimensions of approximately 100,000 x 50,000 pixels, we utilized a 20x magnification to capture these images, resulting in a pixel resolution of about 0.5 μm/pixel. The WSIs were subsequently divided into smaller segments of 512x512 pixels each. By employing a series of image processing techniques, including grayscale conversion, Otsu's thresholding, and morphological operations for background removal, we efficiently eliminated all white backgrounds from these patches. This process resulted in over 17,000 distinct, non-overlapping tiles.

During the model's training phase, we incorporated online data augmentation strategies to increase the dataset's variability. This included random horizontal and vertical flips of the image patches. To maintain a standardized input size, we meticulously performed center cropping to adjust the dimensions to 224 x 224 pixels, and specifically to 299 x 299 pixels for the Inception V3 architecture. Additionally, Z-score normalization was applied to the RGB channels to normalize the distribution of pixel values.

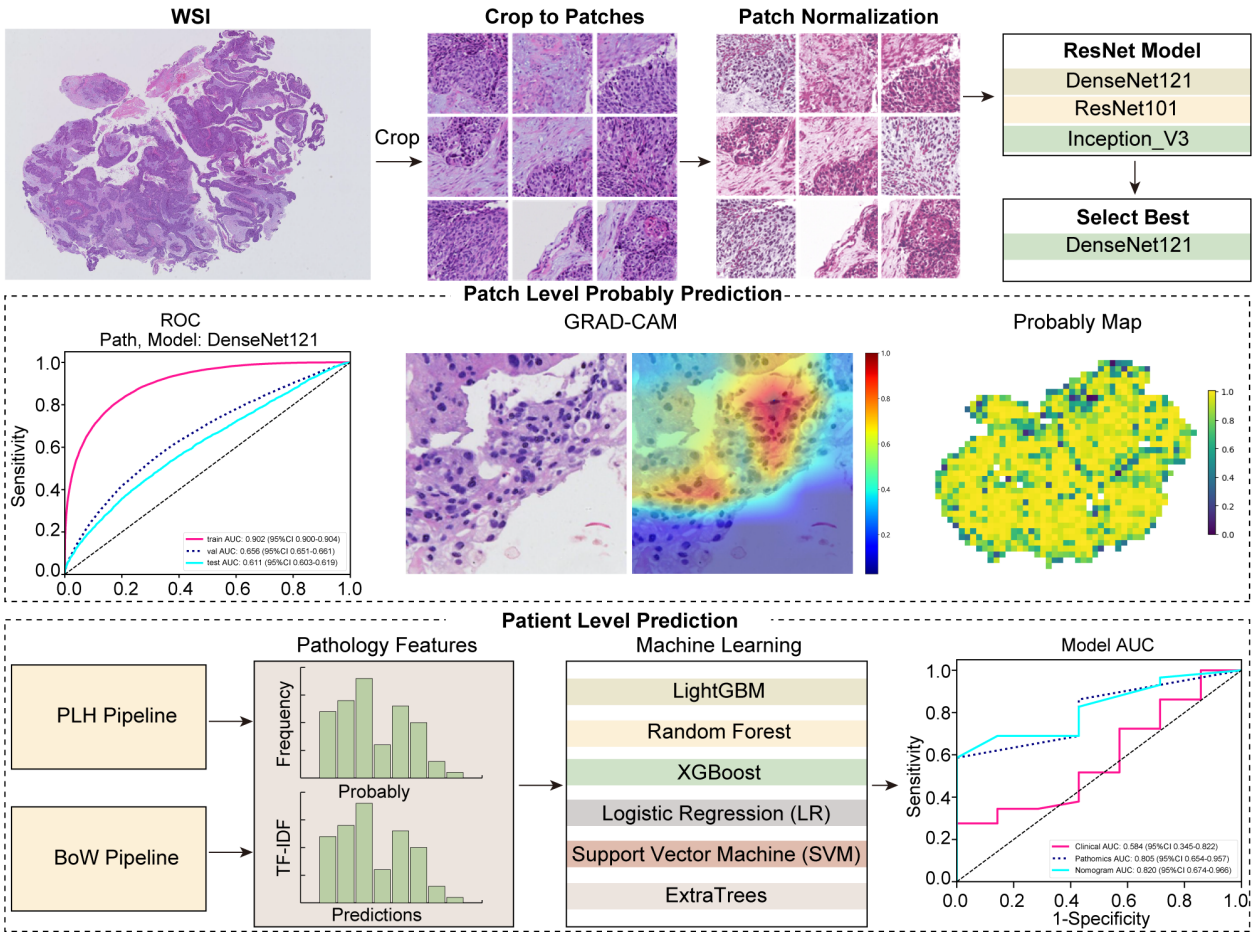

FIGURE 2
Overall workflow of the study.

Weakly supervised learning

In our study, we employed deep learning algorithms to facilitate predictive analysis at both the micro (patch) and macro (WSI) levels. The segmentation of WSIs into smaller, discrete patches was undertaken, ensuring that each patch from a single specimen uniformly bore the same MPR designation. To predict outcomes at the patch level, we meticulously evaluated three prominent neural network architectures: DenseNet121, ResNet50, and Inception V3. The objective was to ascertain the precision with which each patch could be classified into a category mirroring its overarching WSI classification.

To improve the generalizability of our pathology model, we optimized the learning rate employing a cosine decay algorithm, ensuring a refined and effective adjustment over the training period. This approach is characterized as follows:

$$\eta_t = \eta_{min}^i + \frac{1}{2}(\eta_{max}^i - \eta_{min}^i)\left(1 + \cos\left(\frac{T_{cur}}{T_i}\pi\right)\right)$$

In this formulation, $\eta^i_{min} = 0$ sets the minimum learning rate, $\eta^i_{max} = 0.01$ establishes the maximum learning rate, and $T_i = 50$ denotes the number of epochs in the iterative training process. This learning rate schedule employs a gradual diminution strategy, enabling precise model refinement throughout the training phase.

For further refinement of the training approach and to increase predictive accuracy, we utilized stochastic gradient descent as the optimization technique. Additionally, softmax cross-entropy served as the loss function, aiding in calculating the probability distribution over the intended target classes.

Multi-instance learning for WSI integration

Upon completing the training of our deep learning model, we directed our efforts towards predicting labels and corresponding probabilities for individual patches. Subsequently, these probabilities were aggregated through a classifier to formulate predictions at the WSI level. In our study, we employed the densenet121 model to predict labels and obtain corresponding probabilities for each patch, denoted as $Patch_{prob}$ and $Patch_{pred}$, respectively. The prediction probabilities were precisely rounded to two decimal places.

In our study, we developed two machine learning strategies for integrating patch-level probabilities. Firstly, employing histogram

feature aggregation for the Probability Label Heatmap (PLH), we categorized each unique numerical value as a "bin," monitoring the occurrence of data types within these bins. We specifically tallied the frequencies of $Patch_{prob}$ and $Patch_{pred}$ in each bin and applied min-max normalization across all features. This process culminated in the generation of $Histo_{prob}$ and $Histo_{pred}$, enhancing data interpretability. Secondly, we implemented the Bag of Words (BoW) feature aggregation method, initiating with a comprehensive dictionary comprising unique dataset elements. Each patch was vectorized according to the presence of these elements, with further refinement via term frequency-inverse document frequency (TF-IDF) transformation, emphasizing the significance of unique, informative features. This approach yielded a BoW feature representation for each patch, effectively encapsulating feature presence and relevance. The final BoW features, denoted as BoW_{prob} and BoW_{pred} offered a comprehensive, weighted overview, priming them for advanced analytical applications.

In the final phase of our feature fusion approach, based on multi-instance learning, we integrated previously derived features: $Histo_{prob}$, $Histo_{pred}$, Bow_{prob}, and Bow_{pred}. To accomplish this integration, we employed a feature concatenation method symbolized by $\oplus$, effectively merging these distinct feature sets into a single, comprehensive feature vector. The specific formula for this concatenation is as follows:

$$feature_{fusion} = Histo_{prob} \oplus Histo_{pred} \oplus Bow_{prob} \oplus Bow_{pred}$$

Pathomics signature

In our study, we developed a nuanced pathomics signature by integrating patch-level predictions, probability histograms, and TF-IDF features to create individualized patient profiles. To refine feature selection, we employed the Pearson correlation coefficient, retaining only one feature from each pair with a correlation exceeding 0.9. The model integrates a diverse array of machine learning methodologies, encompassing Logistic Regression (LR), Support Vector Machine (SVM), Random Forest, LightGBM, ExtraTrees, and XGBoost. Together, these techniques form what is termed the pathomics signature.

Model evaluation and statistical analysis

Model accuracy was evaluated through receiver operating characteristic (ROC) curves. Statistical analyses, comprising independent sample t-tests for continuous variables and χ^2 tests for discrete variables, were performed to evaluate differences in patients' clinical characteristics. Univariate and multivariate logistic regression analyses were utilized to examine clinical characteristics, retaining those with P-values< 0.05 in the combined model for further use. For practical clinical application, we integrated significant clinical characteristics with the pathomics signature into a combined model, which is visualized through a nomogram for ease of interpretation.

All selected patients were regularly followed up through outpatient visits and telephone check-ins. During the follow-up period, they underwent routine physical examinations and chest-enhanced computed tomography (CT) scans, with additional tests such as positron emission tomography-computed tomography (PET-CT), ultrasound, bronchoscopy, magnetic resonance imaging (MRI), or whole-body bone scans as necessary. For patients with more than one month since the last recorded entry in the case system, we conducted telephone follow-ups to assess their condition and survival status. The last follow-up for all patients was conducted on August 18, 2024, with a median follow-up time of 21 months (range: 3-44 months). In our study, DFS was defined as the interval from the date of curative lung cancer resection to the first occurrence of recurrence, metastasis, death from any cause, or the last follow-up. OS was defined as the time from the initiation of treatment to death from any cause or the last follow-up. Kaplan-Meier analysis was used to estimate DFS and OS, and comparisons between groups were performed using the log-rank test.

The deep learning models in this study were trained on robust hardware, including an Intel i9-14900k CPU, 64GB of RAM, and an NVIDIA RTX 4090 GPU. For our analysis, we employed a blend of software tools alongside custom scripts to achieve precise and efficient processing. Medical image segmentation and processing were facilitated using ITK-SNAP v3.8.0. Our computational work, spanning from modeling to data analysis, was primarily executed in Python v3.7.12, leveraging essential libraries such as PyTorch v1.8.0 for deep learning algorithms, scikit-learn v1.0.2 for machine learning.

Results

Patients data and clinical features

Table 1 summarizes the baseline characteristics of our study cohort. Notably, the MPR rate was 63.4%(118/186). The cohort predominantly consisted of male patients, representing 89.2%(166/186), with the majority undergoing 2 to 3 cycles of neoadjuvant therapy, which accounted for 89.8%(167/186). Squamous cell carcinoma emerged as the leading histological type, comprising 72.6%(135/186) of cases, and most patients were classified under clinical TNM stage III (136/186, 73.1%). Through detailed univariate and multivariable analysis of clinical features, histology was identified as an independent prognostic factor for MPR, showing statistical significance with a P-value below 0.05, as illustrated in Table 2.

The performance of the clinical model, assessed using the area under the curve (AUC) metric, revealed distinct levels of discrimination capability across various machine learning algorithms and datasets. LR exhibited modest effectiveness in the training set (AUC = 0.735), but its performance significantly declined in the validation set (AUC = 0.484), highlighting a notable reduction in its discriminative power. The SVM algorithm demonstrated superior discrimination in the training set (AUC = 0.871), though it achieved only moderate results in the validation set (AUC = 0.585).

10.3389/fimmu.2024.1453232

TABLE 1 Baseline characteristics of all cohorts.

Characteristics	Training cohort(n=105)			Validation cohort(n=45)			Test cohort(n=36)		
	Non-MPR (n=47)	MPR (n=58)	*P* value	Non-MPR (n=14)	MPR (n=31)	*P* value	Non-MPR (n=7)	MPR (n=29)	*P* value
Age			0.642			0.421			1.0
≥60	15(31.91)	15(25.86)		7(50.00)	10(32.26)		2(28.57)	9(31.03)	
<60	32(68.09)	43(74.14)		7(50.00)	21(67.74)		5(71.43)	20(68.97)	
Gender			0.099			0.547			0.838
Female	8(17.02)	3(5.17)		1(7.14)	6(19.35)		1(14.29)	1(3.45)	
Male	39(82.98)	55(94.83)		13(92.86)	25(80.65)		6(85.71)	28(96.55)	
Smoking status			0.339			0.948			1.0
No	18(38.30)	16(27.59)		5(35.71)	13(41.94)		1(14.29)	4(13.79)	
Yes	29(61.70)	42(72.41)		9(64.29)	18(58.06)		6(85.71)	25(86.21)	
Alcohol status			0.119			1.0			1.0
No	36(76.60)	35(60.34)		10(71.43)	22(70.97)		4(57.14)	19(65.52)	
Yes	11(23.40)	23(39.66)		4(28.57)	9(29.03)		3(42.86)	10(34.48)	
Histology			0.004			0.549			0.049
Adenocarcinoma	24(51.06)	13(22.41)		3(21.43)	3(9.68)		4(57.14)	4(13.79)	
SCC	23(48.94)	45(77.59)		11(78.57)	28(90.32)		3(42.86)	25(86.21)	
Surgical approach			0.383			1.0			0.808
Thoracotomy	30(63.83)	31(53.45)		8(57.14)	18(58.06)		1(14.29)	8(27.59)	
VATS	17(36.17)	27(46.55)		6(42.86)	13(41.94)		6(85.71)	21(72.41)	
Neoadjuvant therapy cycle			0.583			0.053			0.634
1	1(2.13)	0		1(7.14)	0		1(14.29)	1(3.45)	
2	24(51.06)	35(60.34)		5(35.71)	20(64.52)		3(42.86)	12(41.38)	
3	17(36.17)	18(31.03)		8(57.14)	8(25.81)		3(42.86)	14(48.28)	
4	5(10.64)	5(8.62)		0	3(9.68)		0	2(6.90)	
Clinical T stage			0.839			0.819			0.591
1	3(6.38)	2(3.45)		2(14.29)	2(6.45)		2(28.57)	5(17.24)	
2	22(46.81)	26(44.83)		5(35.71)	12(38.71)		2(28.57)	16(55.17)	
3	11(23.40)	17(29.31)		4(28.57)	8(25.81)		2(28.57)	4(13.79)	
4	11(23.40)	13(22.41)		3(21.43)	9(29.03)		1(14.29)	4(13.79)	
Clinical N stage			0.277			0.19			0.447
0	10(21.28)	9(15.52)		2(14.29)	13(41.94)		0	5(17.24)	
1	9(19.15)	19(32.76)		4(28.57)	6(19.35)		2(28.57)	9(31.03)	
2	28(59.57)	30(51.72)		8(57.14)	12(38.71)		5(71.43)	15(51.72)	
Clinical TNM stage			0.13			0.571			0.285
I	2(4.26)	1(1.72)		0	1(3.23)		0	0	
II	7(14.89)	18(31.03)		3(21.43)	10(32.26)		0	8(27.59)	
III	38(80.85)	39(67.24)		11(78.57)	20(64.52)		7(100.00)	21(72.41)	
Surgical procedure			0.242			0.445			0.087

(Continued)

TABLE 1 Continued

Characteristics	Training cohort(n=105)			Validation cohort(n=45)			Test cohort(n=36)		
	Non-MPR (n=47)	MPR (n=58)	*P* value	Non-MPR (n=14)	MPR (n=31)	*P* value	Non-MPR (n=7)	MPR (n=29)	*P* value
Bilobectomy	6(12.77)	5(8.62)		3(21.43)	3(9.68)		0	3(10.34)	
Lobectomy	36(76.60)	51(87.93)		10(71.43)	27(87.10)		6(85.71)	26(89.66)	
Pneumonectomy	5(10.64)	2(3.45)		1(7.14)	1(3.23)		1(14.29)	0	

MPR, major pathologic response; Non-MPR, non-major pathologic response; SCC, Squamous cell carcinoma; VATS, video-assisted thoracic surgery.

TABLE 2 Univariable and multivariable analysis for predicting major pathological response in non-small cell lung cancer after neoadjuvant chemoimmunotherapy.

Variables	Univariate Analysis		Multivariate Analysis	
	OR(95% CI)	*P* value	OR(95% CI)	*P* value
Age (<60)	1.255 (0.661, 2.380)	0.487		
Smoking status (No)	1.455 (0.766, 2.760)	0.252		
Alcohol status (No)	1.485 (0.769, 2.868)	0.239		
Gender (Female)	1.912 (0.752, 4.862)	0.173		
Histology (Adenocarcinoma)	3.784 (1.929, 7.423)	<0.001	3.784(1.929,7.423)	<0.001
Surgical approach (Thoracotomy)	1.378 (0.755, 2.517)	0.297		
Neoadjuvant therapy cycle				
1	Reference			
2	6.281 (0.628, 62.780)	0.118		
3	4.556 (0.450, 46.113)	0.199		
4	6.000 (0.490, 73.455)	0.161		
Clinical T stage				
1	Reference			
2	1.117 (0.369, 3.384)	0.845		
3	1.024 (0.316, 3.318)	0.969		
4	1.040 (0.315, 3.436)	0.949		
Clinical N stage				
0	Reference			
1	1.007 (0.405, 2.507)	0.987		
2	0.644 (0.292, 1.420)	0.276		
Clinical TNM stage				
I	Reference			
II	3.600 (0.449, 28.858)	0.228		
III	1.473 (0.201, 10.770)	0.703		
Surgical procedure				
Bilobectomy	Reference			
Lobectomy	1.684 (0.656, 4.322)	0.278		
Pneumonectomy	0.351 (0.070, 1.761)	0.203		

OR, odds ratio; CI, confidence interval; SCC, squamous cell carcinoma; VATS, video-assisted thoracic surgery.

Both Random Forest and ExtraTrees algorithms displayed commendable results in the training set (AUC = 0.799 and 0.810, respectively), yet their efficacy was moderate to modest in the validation and test sets. XGBoost demonstrated consistent performance with good results in both the training (AUC = 0.722) and test sets (AUC = 0.714), but it exhibited suboptimal performance in the validation set (AUC = 0.492). LightGBM presented moderate performance across all datasets, with AUC scores of 0.674, 0.563, and 0.667 for the training, validation, and test sets, respectively (Supplementary Figure 1).

Pathomics signature

Our pathology models' ability to discern regional features was rigorously evaluated using ROC curves at the patch level. DenseNet121, among the models assessed, distinguished itself in the validation set, achieving an AUC of 0.656 (95% CI: 0.651-0.661), thereby surpassing both ResNet50 (AUC = 0.626, 95% CI: 0.621-0.631) and Inception V3 (AUC = 0.654, 95% CI: 0.649-0.660). Additionally, DenseNet121 demonstrated commendable generalization with an AUC of 0.611 (95% CI: 0.603-0.619) in the external test set. The comparative analysis of these models is illustrated in Figures 3A–C.

To further evaluate our model's effectiveness, we visually inspected the amalgamation of patch-level data into WSIs. Among the machine learning techniques assessed, XGBoost outperformed others, delivering the highest AUC scores in the training and testing phases. With an AUC of 0.998 in the training phase, XGBoost demonstrated exemplary discriminative prowess. In the validation phase, it achieved a robust AUC of 0.818 and maintained a strong AUC of 0.805 in the testing phase, indicating reliable performance. XGBoost's consistent AUC superiority reveals its remarkable capacity for class differentiation and generalization to unseen data (Figures 3D–F).

Gradient-weighted class activation mapping (Grad-CAM) generates visual maps by tracing gradients in the network's final convolutional layer, preserving key spatial details relevant to the classification task, details that are often lost in fully connected layers. This technique seamlessly fits into existing neural architectures without necessitating any model modifications or retraining. Figure 4 demonstrates this, by providing a clear depiction of the last convolutional layer's contribution in the model's predictive response, enhancing interpretability of the model's decision-making. Predictive label and probability heatmaps were obtained to assist in the evaluation. As depicted in Figure 5, the prediction heatmap vividly showcases our pathological model's high accuracy when assessing regional tiles. The results indicate that feature modeling has been notably improved following aggregation via the BoW and PLH processes. This signifies the efficacy of our feature aggregation methodology.

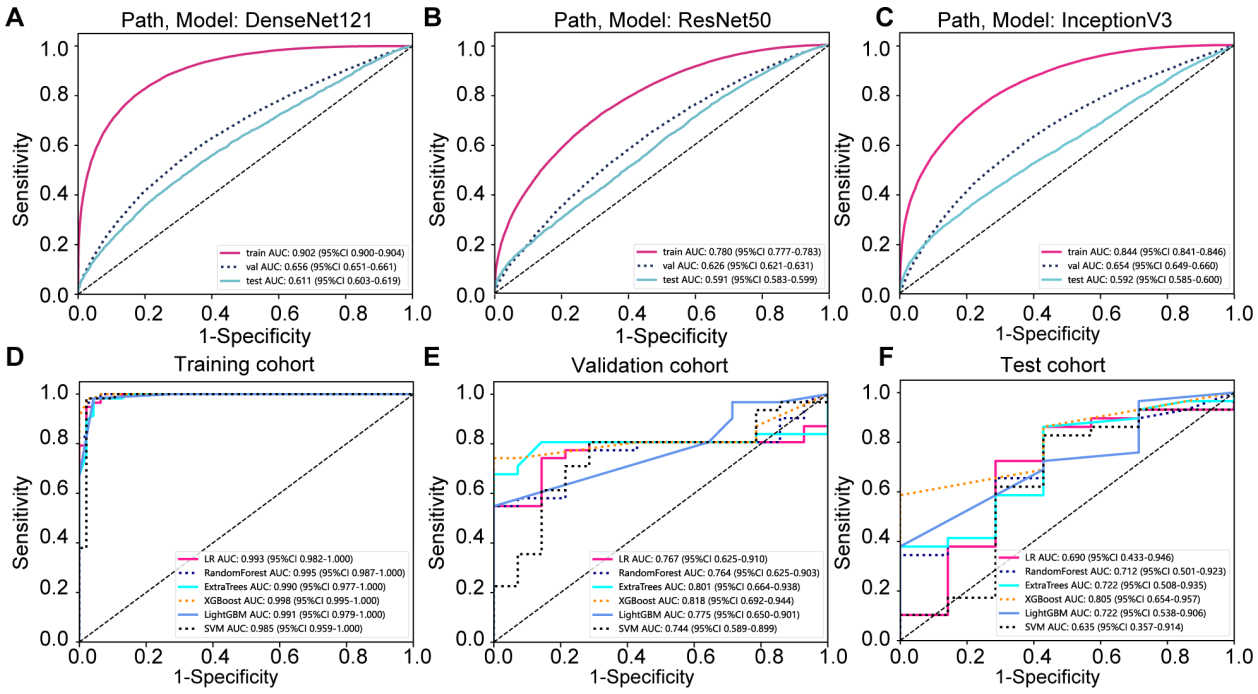

FIGURE 3
Prediction model evaluation. **(A)** Patch-level area under the curve (AUC) for the DenseNet121 prediction model across cohorts; **(B)** Patch-level AUC for the Resnet50 prediction model; **(C)** Patch-level AUC for the Inception v3 prediction model; **(D)** whole slide image (WSI)-level AUC for the prediction model in the training cohort; **(E)** WSI-level AUC for the prediction model in the validation cohort; **(F)** WSI-level AUC for the prediction model in the testing cohort.

10.3389/fimmu.2024.1453232

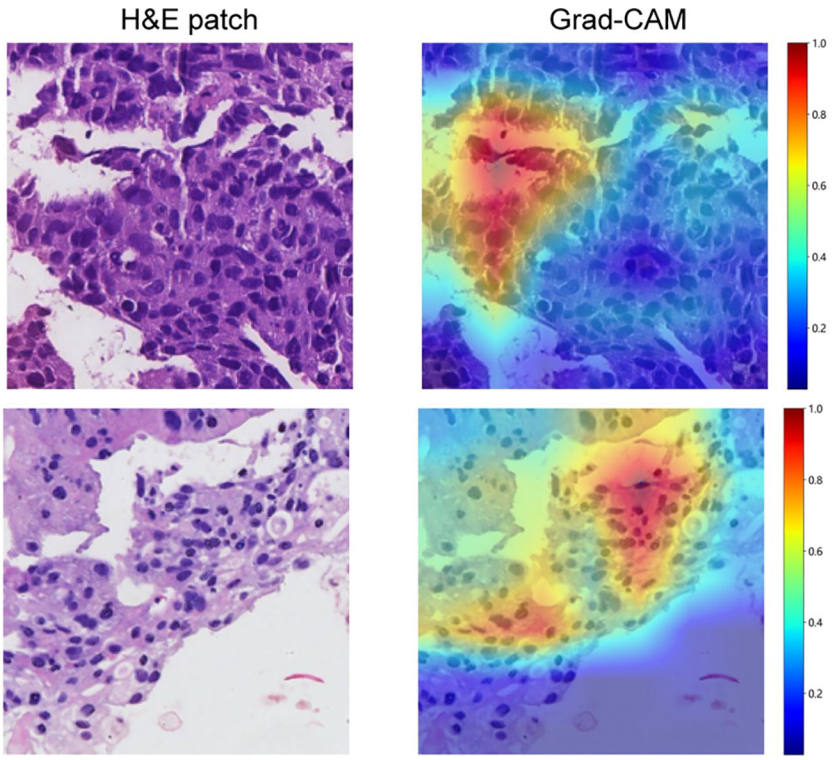

FIGURE 4
Use of Grad-CAM to illustrate activation in the final convolutional layer of the prediction model.

Model fusion and performance

The nomogram, an integrative tool combining clinical and pathomics information, is effectively illustrated in Figure 6. The assessment of AUC scores for clinical, pathomics, and nomogram signatures indicates that the nomogram consistently secures marginally higher AUC values than the pathomics signature on its own, observed in both validation and test datasets. Notably, the nomogram records an AUC of 0.819 in the validation group and 0.820 in the test group, reflecting an effective amalgamation of

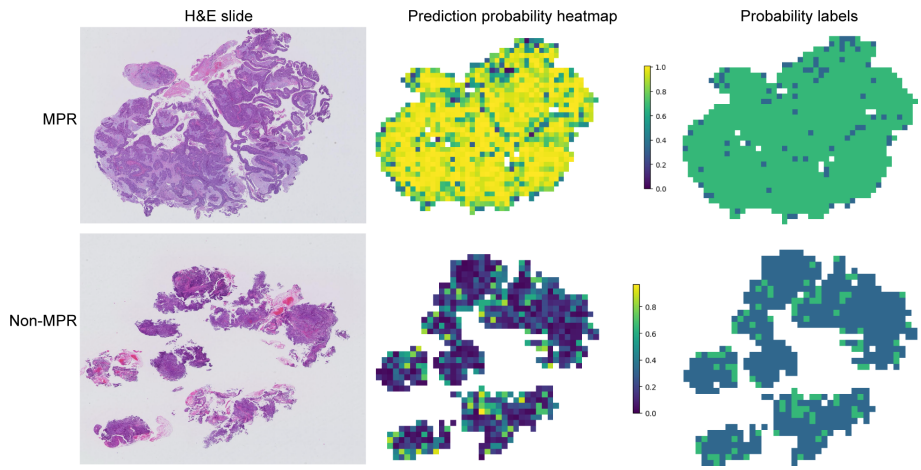

FIGURE 5
Probability and prediction heatmap of the prediction model. This image displays the whole slide image (WSI)-level hematoxylin and eosin slide (left), a heatmap of the prediction probabilities for each patch (middle), and the result prediction map for the WSI (right). Major pathological response (MPR) is primarily predicted with a probability label of 1, whereas non-major pathological response (Non-MPR) is predominantly predicted with a probability label of 0.

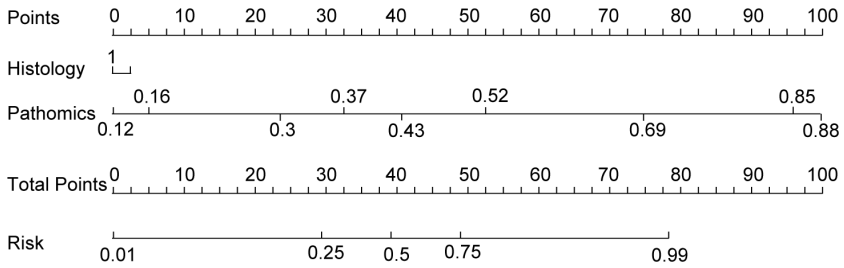

FIGURE 6
Clinical nomogram to predict major pathological response in non-small cell lung cancer patients post-neoadjuvant chemoimmunotherapy.

features for refined discriminative accuracy. The pathomics signature alone exhibits formidable discriminative strength across all datasets, with an almost perfect AUC of 0.998 in training. The clinical signature, however, reveals a descending trajectory in discriminative capacity, with an AUC drop from 0.799 in training to 0.613 in validation and further to 0.584 in testing, thereby emphasizing the incremental benefit of pathomics feature integration in enhancing model efficacy (Supplementary Table 1, Figure 7A). Utilizing the DeLong test for statistical comparison, the nomogram, which synthesizes clinical and pathomics attributes, demonstrated augmented predictive superiority. The performance elevation of the nomogram over the clinical-only model was statistically significant, registering a *P*-value less than 0.05, hence confirming the added value of integrating pathomics insights into clinical predictions (Figure 7B).

Clinical outcomes

Figures 8A, B present the DFS and OS curves for patients treated with NICT, comparing the MPR group to the Non-MPR group. The analysis reveals that the MPR group exhibited significantly improved DFS and OS outcomes, with statistically significant differences between the two cohorts.

Discussion

In this study, our objective was to develop an accurate predictive model for MPR in NSCLC patients undergoing NICT. By integrating machine learning analyses of clinical data, we established a clinical signature grounded in machine learning

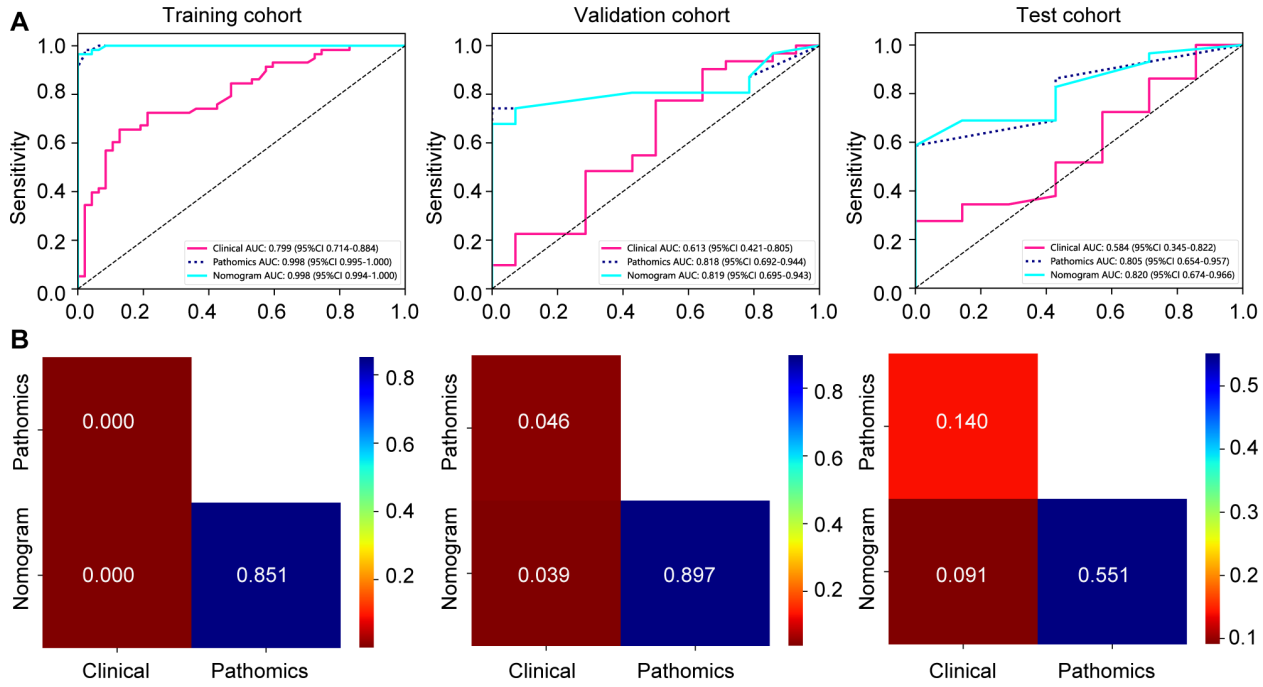

FIGURE 7
Assessment of model efficacy in forecasting major pathological responses to neoadjuvant chemoimmunotherapy in training, validation, and test cohorts. **(A)** receiver operating characteristic curves depicting prediction accuracy of signatures; **(B)** DeLong test comparisons among various signatures.

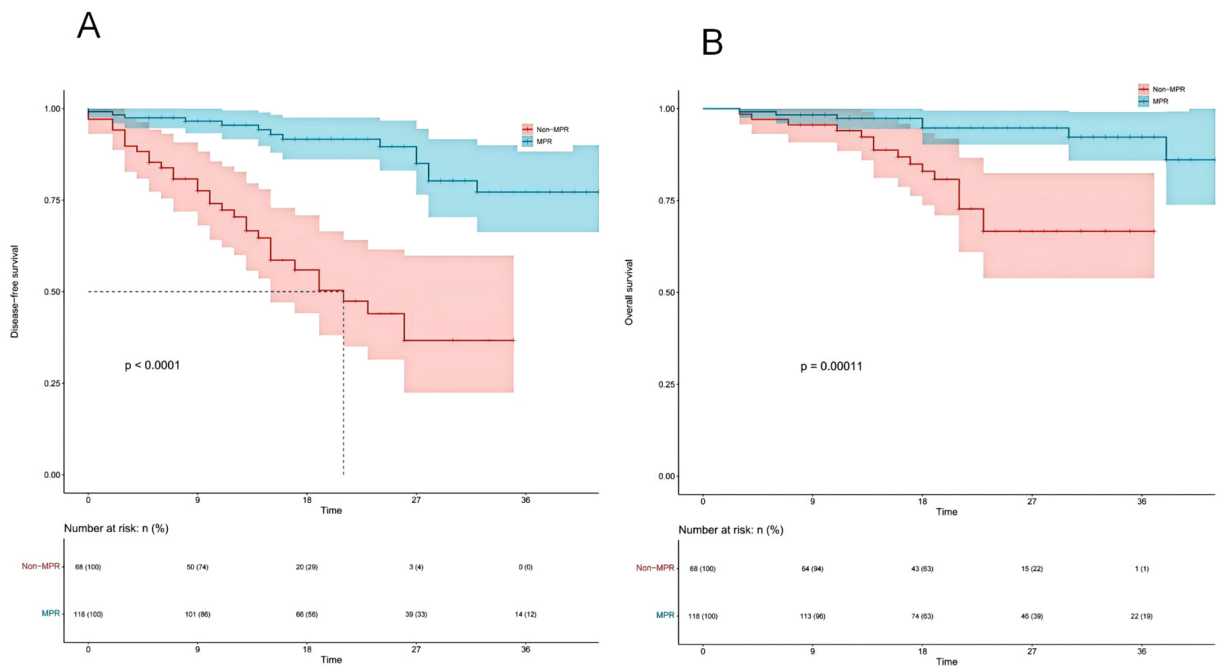

FIGURE 8
Kaplan-Meier survival analysis of disease-free survival (DFS) **(A)** and overall survival (OS) **(B)** between major pathological response (MPR) and non-major pathological response (Non-MPR) groups.

principles. Moreover, we assessed the predictive value of pathomics data on MPR outcomes. Leveraging a weakly supervised deep learning framework trained on WSIs with multi-instance aggregation, we achieved precise predictions of MPR at the patient level, culminating in the establishment of a pathomics signature. The pinnacle of our study involved merging the derived clinical features with the pathomics signature into a unified nomogram, crafted for extensive interpretability and detailed examination, offering a methodology for MPR prediction in NSCLC patients receiving NICT. This integrated approach represents a significant fusion of clinical insights with advanced machine learning techniques and, to our knowledge, it pioneers the use of WSI for the first-time prediction of MPR in NSCLC patients treated with NICT, setting a new benchmark in the field.

MPR is gaining recognition as a pivotal prognostic marker in resectable NSCLC, particularly when considering the context of NICT. The capability of MPR to accurately mirror the tumor's response to therapeutic interventions is essential for predicting patient outcomes effectively. Research demonstrates MPR's link to improved long-term OS among NSCLC patients who receive neoadjuvant chemotherapy, underscoring its significance as both a surrogate endpoint for survival and a critical measure for evaluating neoadjuvant therapy in clinical trials (28). Additionally, comprehensive studies exploring the prognostic relevance of MPR in NSCLC patients undergoing NICT have found a strong correlation with enhanced DFS and OS, supporting the use of MPR as a surrogate marker for survival outcomes in the evaluation of NICT's effectiveness (2, 4, 6, 29, 30). Our research, in conjunction with these findings, accentuates the crucial role of MPR in assessing the success of neoadjuvant treatment approaches in NSCLC, thereby validating our decision to use MPR as a predictor of NICT's efficacy in this clinical setting.

In the field of deep learning model development, access to large datasets and high-quality annotations is crucial for training high-performance models. However, the high resolution of WSI presents significant challenges for detailed annotation. Consequently, researchers have developed a new training method using limited annotations, known as weak supervision (31, 32). In the realm of WSI classification under weak supervision, a significant portion of research has predominantly concentrated on employing multiple instance learning (MIL) techniques (33–36). The MIL approach identifies the relative importance of each image patch for model prediction by analyzing histopathological images, allowing the model to autonomously learn to recognize morphological features of diseases without the need for manual annotations. In this research, we applied a weakly supervised learning framework using MIL on pre-treatment WSIs to forecast MPR in NSCLC patients post-NICT, achieving an AUC of 0.998 in training, and demonstrating robust performance with AUCs of 0.818 in validation and 0.805 in testing phases. Additionally, we enhanced our model's interpretability in decision-making by utilizing GradCAM localization mapping, which facilitated the evaluation through predictive labels and probability heatmaps. GradCAM uniquely enables target localization in models trained using only image labels by incorporating guided backpropagation, precisely determining pixel-level importance in predictive areas, thus offering significant benefits for applications like cancer subtype classification (37–39).

This study has several limitations, including a small sample size and reliance on a retrospective cohort, which may affect the generalizability of our findings. To validate our results and

strengthen the conclusions drawn, future research with a larger sample size and a prospective design is essential. Furthermore, the developed model focuses on pathological images and clinical features without incorporating conventional imaging data, such as CT scans, or molecular information like genetic and protein expressions. Acknowledging the dynamic nature of AI models, future iterations will aim to incorporate multidimensional patient data to enhance the performance of model predictions.

Moving forward, our research will focus on several key areas. First, we plan to conduct prospective studies to validate our findings and evaluate the model's applicability across diverse populations and clinical settings. Additionally, we aim to develop advanced visualization and interpretation tools to improve model transparency and facilitate its use by clinicians in decision-making processes. Finally, we will explore strategies for integrating the predictive model into existing clinical workflows, with an emphasis on feasibility, usability, and acceptance in real-world clinical environments.

Conclusion

The utilization of weakly supervised deep learning for analyzing WSIs provides a potent predictive tool for MPR in NSCLC patients undergoing NICT. By enhancing treatment precision, this model promises not only to improve patient outcomes but also to refine therapeutic strategies. Future work will aim to incorporate extensive multimodal data, further improving the predictive accuracy and robustness of our models.

Data availability statement

The raw data supporting the conclusions of this article will be made available by the authors, without undue reservation.

Ethics statement

The studies involving humans were approved by Shandong First Medical University Affiliated Cancer Hospital Ethics Committee. The studies were conducted in accordance with the local legislation and institutional requirements. The ethics committee/institutional review board waived the requirement of written informed consent for participation from the participants or the participants' legal guardians/next of kin because Patient consent was waived due to the retrospective nature of this research.

Author contributions

DH: Conceptualization, Writing – original draft, Writing – review & editing. HL: Conceptualization, Writing – original draft, Writing – review & editing. XZ: Data curation, Formal analysis, Funding acquisition, Writing – review & editing. SF: Data curation, Formal analysis, Writing – review & editing. RW: Investigation, Resources, Software, Visualization, Writing – review & editing. QZ: Investigation, Resources, Software, Visualization, Writing – review & editing. CL: Data curation, Writing – review & editing. ZW: Data curation, Writing – original draft. WH: Project administration, Supervision, Writing – review & editing. SH: Project administration, Supervision, Writing – review & editing.

Funding

The author(s) declare financial support was received for the research, authorship, and/or publication of this article. This research was supported by the Shandong Provincial Natural Science Foundation -General Project (No. ZR202103040386) in 2021.

Conflict of interest

The authors declare that this research was conducted without any commercial or financial relationships that could be interpreted as potential conflicts of interest.

Publisher's note

Supplementary material

The Supplementary Material for this article can be found online at: https://www.frontiersin.org/articles/10.3389/fimmu.2024.1453232/full#supplementary-material

References

1. Cascone T, Leung CH, Weissferdt A, Pataer A, Carter BW, Godoy MCB, et al. Neoadjuvant chemotherapy plus nivolumab with or without ipilimumab in operable non-small cell lung cancer: the phase 2 platform neostar trial. *Nat Med*. (2023) 29:593–604. doi: 10.1038/s41591-022-02189-0

2. Chen Y, Qin J, Wu Y, Lin Q, Wang J, Zhang W, et al. Does major pathological response after neoadjuvant immunotherapy in resectable nonsmall-cell lung cancers predict prognosis? A systematic review and meta-analysis. *Int J Surg*. (2023) 109:2794–807. doi: 10.1097/JS9.0000000000000496

3. Forde PM, Spicer J, Lu S, Provencio M, Mitsudomi T, Awad MM, et al. Neoadjuvant nivolumab plus chemotherapy in resectable lung cancer. *N Engl J Med*. (2022) 386:1973–85. doi: 10.1056/NEJMoa2202170

4. Provencio M, Nadal E, Insa A, Garcia-Campelo MR, Casal-Rubio J, Domine M, et al. Neoadjuvant chemotherapy and nivolumab in resectable non-small-cell lung cancer (Nadim): an open-label, multicenter, single-arm, phase 2 trial. *Lancet Oncol*. (2020) 21:1413–22. doi: 10.1016/S1470-2045(20)30453-8

5. Shu CA, Gainor JF, Awad MM, Chiuzan C, Grigg CM, Pabani A, et al. Neoadjuvant atezolizumab and chemotherapy in patients with resectable non-small-cell lung cancer: an open-label, multicenter, single-arm, phase 2 trial. *Lancet Oncol*. (2020) 21:786–95. doi: 10.1016/S1470-2045(20)30140-6

6. Zhao J, Hao S, Li Y, Liu X, Liu Z, Zheng C, et al. Comparative efficacy and safety of neoadjuvant immunotherapy with chemotherapy versus chemotherapy alone in non-small cell lung cancer: A propensity score and inverse probability treatment weighting analysis. *Immunotargets Ther*. (2023) 12:113–33. doi: 10.2147/ITT.S437911

7. Heymach JV, Mitsudomi T, Harpole D, Aperghis M, Jones S, Mann H, et al. Design and rationale for a phase iii, double-blind, placebo-controlled study of neoadjuvant durvalumab+ Chemotherapy followed by adjuvant durvalumab for the treatment of patients with resectable stages ii and iii non-small-cell lung cancer: the aegean trial. *Clin Lung Cancer*. (2022) 23:e247–e51. doi: 10.1016/j.cllc.2021.09.010

8. Lu S, Wu L, Zhang W, Zhang P, Wang W, Fang W, et al. Perioperative toripalimab + Platinum-doublet chemotherapy vs chemotherapy in resectable stage II/III non-small cell lung cancer (Nsclc): interim event-free survival (Efs) analysis of the phase iii neotorch study. *J Clin Oncol*. (2023) 41:425126. doi: 10.1200/JCO.2023.41.36_suppl.425126

9. Qiu F, Fan J, Shao M, Yao J, Zhao L, Zhu L, et al. Two cycles versus three cycles of neoadjuvant sintilimab plus platinum-doublet chemotherapy in patients with resectable non-small-cell lung cancer (Neoscore): A randomized, single center, two-arm phase ii trial. *J Clin Oncol*. (2022) 40:8500. doi: 10.1200/JCO.2022.40.16_suppl.8500

10. Rothschild SI, Zippelius A, Eboulet EI, Savic Prince S, Betticher D, Bettini A, et al. Sakk 16/14: durvalumab in addition to neoadjuvant chemotherapy in patients with stage IIIa(N2) non-small-cell lung cancer-a multicenter single-arm phase II trial. *J Clin Oncol*. (2021) 39:2872–80. doi: 10.1200/JCO.21.00276

11. Wakelee H, Liberman M, Kato T, Tsuboi M, Lee S-H, Gao S, et al. Perioperative pembrolizumab for early-stage non–small-cell lung cancer. *N Engl J Med*. (2023) 389:491–503. doi: 10.1056/NEJMoa2302983

12. Yan W, Zhong WZ, Liu YH, Chen Q, Xing W, Zhang Q, et al. Adebrelimab (Shr-1316) in combination with chemotherapy as perioperative treatment in patients with resectable stage II to III nsclcs: an open-label, multicenter, phase 1b trial. *J Thorac Oncol*. (2022) 18:194–203. doi: 10.1016/j.jtho.2022.09.222

13. Zhao Z, Chen S, Qi H, Yang CP, Lin YB, Jin JT, et al. Phase ii trial of toripalimab plus chemotherapy as neoadjuvant treatment in resectable stage iii non-small cell lung cancer (Neotpd01 study). *J Clin Oncol*. (2021) 39:8541. doi: 10.1080/2162402X.2021.1996000

14. Zhao ZR, Yang CP, Chen S, Yu H, Lin YB, Lin YB, et al. Phase 2 trial of neoadjuvant toripalimab with chemotherapy for resectable stage III non-small-cell lung cancer. *Oncoimmunology*. (2021) 10:1996000. doi: 10.1080/2162402X.2021.1996000

15. Huang Z, Chen L, Lv L, Fu CC, Jin Y, Zheng Q, et al. A new ai-assisted scoring system for pd-L1 expression in nsclc. *Comput Methods Programs BioMed*. (2022) 221:106829. doi: 10.1016/j.cmpb.2022.106829

16. Pan Y, Sheng W, Shi L, Jing D, Jiang W, Chen JC, et al. Whole slide imaging-based deep learning to predict the treatment response of patients with non-small cell lung cancer. *Quant Imaging Med Surg*. (2023) 13:3547–55. doi: 10.21037/qims-22-1098

17. Park J, Cho HG, Park J, Lee G, Kim HS, Paeng K, et al. Artificial intelligence-powered hematoxylin and eosin analyzer reveals distinct immunologic and mutational profiles among immune phenotypes in non-small-cell lung cancer. *Am J Pathol*. (2022) 192:701–11. doi: 10.1016/j.ajpath.2022.01.006

18. Park S, Ock C-Y, Kim H, Pereira S, Park S, Ma M, et al. Artificial intelligence–powered spatial analysis of tumor-infiltrating lymphocytes as complementary biomarker for immune checkpoint inhibition in non–small-cell lung cancer. *J Clin Oncol*. (2022) 40:1916–28. doi: 10.1200/jco.21.02010

19. Prelaj A, Miskovic V, Zanitti M, Trovo F, Genova C, Viscardi G, et al. Artificial intelligence for predictive biomarker discovery in immuno-oncology: A systematic review. *Ann Oncol*. (2024) 35:29–65. doi: 10.1016/j.annonc.2023.10.125

20. Wang S, Yu H, Gan Y, Wu Z, Li E, Li X, et al. Mining whole-lung information by artificial intelligence for predicting egfr genotype and targeted therapy response in lung cancer: A multicohort study. *Lancet Digit Health*. (2022) 4:e309–e19. doi: 10.1016/S2589-7500(22)00024-3

21. Wu J, Liu C, Liu X, Sun W, Li L, Gao N, et al. Artificial intelligence-assisted system for precision diagnosis of pd-L1 expression in non-small cell lung cancer. *Mod Pathol*. (2022) 35:403–11. doi: 10.1038/s41379-021-00904-9

22. Zhao L, Xu X, Hou R, Zhao W, Zhong H, Teng H, et al. Lung cancer subtype classification using histopathological images based on weakly supervised multi-instance learning. *Phys Med Biol*. (2021) 66(23):10.1088/1361-6560/ac3b32. doi: 10.1088/1361-6560/ac3b32

23. Fu Y, Jung AW, Torne RV, Gonzalez S, Vohringer H, Shmatko A, et al. Pan-cancer computational histopathology reveals mutations, tumor composition and prognosis. *Nat Cancer*. (2020) 1:800–10. doi: 10.1038/s43018-020-0085-8

24. Kather JN, Heij LR, Grabsch HI, Loeffler C, Echle A, Muti HS, et al. Pan-cancer image-based detection of clinically actionable genetic alterations. *Nat Cancer*. (2020) 1:789–99. doi: 10.1038/s43018-020-0087-6

25. Muti HS, Heij LR, Keller G, Kohlruss M, Langer R, Dislich B, et al. Development and validation of deep learning classifiers to detect epstein-barr virus and microsatellite instability status in gastric cancer: A retrospective multicenter cohort study. *Lancet Digit Health*. (2021) 3:e654–e64. doi: 10.1016/S2589-7500(21)00133-3

26. Coudray N, Ocampo PS, Sakellaropoulos T, Narula N, Snuderl M, Fenyo D, et al. Classification and mutation prediction from non-small cell lung cancer histopathology images using deep learning. *Nat Med*. (2018) 24:1559–67. doi: 10.1038/s41591-018-0177-5

27. Dacic S, Travis W, Redman M, Saqi A, Cooper WA, Borczuk A, et al. International association for the study of lung cancer study of reproducibility in assessment of pathologic response in resected lung cancers after neoadjuvant therapy. *J Thorac Oncol*. (2023) 18:1290–302. doi: 10.1016/j.jtho.2023.07.017

28. Weissferdt A, Pataer A, Vaporciyan AA, Correa AM, Sepesi B, Moran CA, et al. Agreement on major pathological response in nsclc patients receiving neoadjuvant chemotherapy. *Clin Lung Cancer*. (2020) 21:341–8. doi: 10.1016/j.cllc.2019.11.003

29. Liu Y, Xiong L, Chen Y, Cai R, Xu X, Wang T, et al. Complete pathological remission and tertiary lymphoid structures are associated with the efficacy of resectable nsclc receiving neoadjuvant chemoimmunotherapy: A double-center retrospective study. *Hum Vaccin Immunother*. (2023) 19:2285902. doi: 10.1080/21645515.2023.2285902

30. Zhang B, Xiao H, Pu X, Zhou C, Yang D, Li X, et al. A real-world comparison between neoadjuvant chemoimmunotherapy and chemotherapy alone for resectable non-small cell lung cancer. *Cancer Med*. (2023) 12:274–86. doi: 10.1002/cam4.4889

31. Campanella G, Hanna MG, Geneslaw L, Miraflor A, Werneck Krauss Silva V, Busam KJ, et al. Clinical-grade computational pathology using weakly supervised deep learning on whole slide images. *Nat Med*. (2019) 25:1301–9. doi: 10.1038/s41591-019-0508-1

32. Qu H, Wu P, Huang Q, Yi J, Yan Z, Li K, et al. Weakly supervised deep nuclei segmentation using partial points annotation in histopathology images. *IEEE Trans Med Imaging*. (2020) 39:3655–66. doi: 10.1109/TMI.2020.3002244

33. Lu MY, Williamson DFK, Chen TY, Chen RJ, Barbieri M, Mahmood F. Data-efficient and weakly supervised computational pathology on whole-slide images. *Nat BioMed Eng*. (2021) 5:555–70. doi: 10.1038/s41551-020-00682-w

34. Gadermayr M, Tschuchnig M. Multiple instance learning for digital pathology: A review of the state-of-the-art, limitations & Future potential. *Comput Med Imaging Graph*. (2024) 112:102337. doi: 10.1016/j.compmedimag.2024.102337

35. Zhou Y, Che S, Lu F, Liu S, Yan Z, Wei J, et al. Iterative multiple instance learning for weakly annotated whole slide image classification. *Phys Med Biol*. (2023) 68 (23):10.1088/1361-6560/ac3b32. doi: 10.1088/1361-6560/acde3f

36. Dov D, Kovalsky SZ, Assaad S, Cohen J, Range DE, Pendse AA, et al. Weakly supervised instance learning for thyroid Malignancy prediction from whole slide cytopathology images. *Med Image Anal*. (2021) 67:101814. doi: 10.1016/j.media.2020.101814

37. Selvaraju RR, Das A, Vedantam R, Cogswell M, Parikh D, Batra D. Grad-cam: why did you say that? *arXiv preprint arXiv:161107450*. (2016).

38. Zhang H, Ogasawara K. Grad-cam-based explainable artificial intelligence related to medical text processing. *Bioengineering (Basel)*. (2023) 10:1070. doi: 10.3390/bioengineering10091070

39. Lipkova J, Chen RJ, Chen B, Lu MY, Barbieri M, Shao D, et al. Artificial intelligence for multimodal data integration in oncology. *Cancer Cell*. (2022) 40:1095–110. doi: 10.1016/j.ccell.2022.09.012

frontiers | Frontiers in Immunology

TYPE Original Research
PUBLISHED 25 November 2024
DOI 10.3389/fimmu.2024.1456150

OPEN ACCESS

EDITED BY
Takaji Matsutani,
Maruho, Japan

REVIEWED BY
Daniel Souza Monteiro De Araújo,
University of Florence, Italy
Yingcheng Charles Wu,
Fudan University, China

*CORRESPONDENCE
Haibo Zhang
haibozh@gzucm.edu.cn
Yihan He
yihanhe@gzucm.edu.cn

†These authors have contributed equally to this work

RECEIVED 28 June 2024
ACCEPTED 30 October 2024
PUBLISHED 25 November 2024

CITATION
Zhang Z, Zhao W, Lv C, Wu Z, Liu W, Chang X, Yu Y, Xiao Z, He Y and Zhang H (2024) Unraveling impact and potential mechanisms of baseline pain on efficacy of immunotherapy in lung cancer patients: a retrospective and bioinformatic analysis. *Front. Immunol.* 15:1456150. doi: 10.3389/fimmu.2024.1456150

Unraveling impact and potential mechanisms of baseline pain on efficacy of immunotherapy in lung cancer patients: a retrospective and bioinformatic analysis

Zexin Zhang[1†], Wenjie Zhao[1†], Chang Lv[1], Zexia Wu[1], Wenhao Liu[2], Xuesong Chang[3,4], Yaya Yu[3,4], Zhenzhen Xiao[3,4], Yihan He[3,4*] and Haibo Zhang[3,4,5,6,7*]

[1]The Second Clinical School of Guangzhou University of Chinese Medicine, Guangzhou, China, [2]Clinical Medical College of Acupuncture Moxibustion and Rehabilitation, Guangzhou University of Chinese Medicine, Guangzhou, China, [3]Deparment of Oncology, Guangdong Province Hospital of Chinese Medicine, Guangzhou, China, [4]The Second Affiliated Hospital of Guangzhou University of Chinese Medicine, Guangzhou, China, [5]Guangdong Provincial Key Laboratory of Clinical Research on Traditional Chinese Medicine Syndrome, Guangzhou, China, [6]Guangdong-Hong Kong-Macau Joint Lab on Chinese Medicine and Immune Disease Research, Guangzhou University of Chinese Medicine, Guangzhou, China, [7]State Key Laboratory of Dampness Syndrome of Chinese Medicine, The Second Affiliated Hospital of Guangzhou University of Chinese Medicine, Guangzhou, China

Objective: Pain is a prevalent discomfort symptom associated with cancer, yet the correlations and potential mechanisms between pain and the efficacy of cancer immunotherapy remain uncertain.

Methods: Non-small cell lung cancer (NSCLC) patients who received immune checkpoint inhibitors (ICIs) in the inpatient department of Guangdong Provincial Hospital of Chinese Medicine from January 1, 2018, to December 31, 2021, were retrospectively enrolled. Through cox regression analysis, prognostic factors and independent prognostic factors affecting the efficacy of ICIs were identified, and a nomogram model was constructed. Hub cancer-related pain genes (CRPGs) were identified through bioinformatic analysis. Finally, the expression levels of hub CRPGs were detected using an enzyme-linked immunosorbent assay (ELISA).

Results: Before PSM, a total of 222 patients were enrolled in this study. Univariate and multivariate cox analysis indicated that bone metastasis and NRS scores were independent prognostic factors for the efficacy of ICIs. After PSM, a total of 94 people were enrolled in this study. Univariate cox analysis and multivariate cox analysis indicated that age, platelets, Dnlr, liver metastasis, bone metastasis, and NRS scores were independent prognostic factors for the efficacy of ICIs. A nomogram was constructed based on 6 independent prognostic factors with AUC values of 0.80 for 1-year, 0.73 for 2-year, and 0.80 for 3-year survival. ELISA assay results indicated that the level of CXCL12 significantly decreased compared to baseline after pain was relieved.

Conclusion: Baseline pain is an independent prognostic factor affecting the efficacy of ICIs in lung cancer, potentially through CXCL12-mediated inflammation promotion and immunosuppression.

KEYWORDS

baseline pain, immunotherapy, lung cancer, prognostic model, peripheral inflammatory cells, C-X-C motif chemokine ligand 12

Background

Pain is a prevalent complication of cancer, with an estimated incidence of approximately 44.5% among cancer patients (1). Inadequate management of pain have profound effects on physical and emotional well-being, exacerbating anxiety, anger, and depression, and significantly diminishing quality of life (2–4). Furthermore, pain has been shown to suppress immune responses and facilitate tumor growth (5). Refractory cancer pain significantly diminishes the quality of life for individuals with cancer and is intricately linked to a decline in overall survival (OS) (6). Among patients with lung cancer, as many as 50% will endure pain that detrimentally impacts the efficacy of tumor therapies and their prospects for survival (7).

Tumor immune microenvironment (TME) is a complex component and tumor cells can evade the killing effect of various therapies through reprogramming metabolism (8), angiogenesis and other methods. In recent years, immunotherapy has emerged as a crucial component in the treatment of tumors (9). The effect of this treatment is closely related to the complex composition of the tumor immune infiltrating microenvironment (10, 11). Though some patients may experience long-term survival benefits from ICIs treatment, particularly those in late-stage, the response rate was limited to approximately 23% (12). Furthermore, as high as to 80% patients still exhibit primary drug resistance (13). This resistance persists even in patients with high PD-L1 expression levels, with approximately 50% of these patients showing resistance to ICIs treatment (14). Many studies have indicated that baseline characteristics including age, gender, and brain metastasis can impact the effectiveness of ICIs in lung cancer (15). Nevertheless, there is limited understanding regarding the potential impact of baseline pain on survival outcomes in lung cancer patients undergoing treatment with ICIs.

Certain studies have found that the significance of pain persisted even after accounting for various clinical variables such as age, gender, performance status, and disease stage in multivariable analysis (15, 16). A preliminary investigation into the prognostic value of Patient-Reported Outcomes (PRO) and performance status in forecasting survival among patients with metastatic lung cancer undergoing chemoimmunotherapy indicated that pain levels reported in PRO can be a valuable predictor of OS and progression-free survival (PFS) (17).

Cancer related pain is characterized by a combination of nociceptive and neuropathic components, with evidence suggesting that tumor-infiltrating neutrophils play a role in the development of cancer-related inflammation and neuropathic pain (18, 19). A recent study indicated that neutrophils was demonstrated remarkable complexity, and was characterized by 10 distinct states encompassing inflammation, angiogenesis, and antigen presentation (11). Neutrophil infiltration within the tumor microenvironment (TME) has been shown to potentially elevate peripheral neutrophil levels, which could impede the trafficking of anti-cancer T cells (20). The enumeration of diverse leukocytes and soluble factors in peripheral blood can serve as an indirect indicator of the immune profile of the cancer, with neutrophils and lymphocytes frequently representing the predominant subtypes (21). In accordance with the findings of numerous studies, an elevated baseline neutrophil-to-lymphocyte ratio (NLR) typically correlates with an unfavorable prognosis (22). This adverse association extends to patients undergoing treatment with ICIs. In a comprehensive pan-cancer study, elevated NLR was correlated with decreased OS, PFS, and objective response rate (ORR) (23). Kargl et al. discovered a negative correlation between tumor-infiltrating neutrophils and CD8-expressing T cells in NSCLC specimens (24), with further investigations revealing a connection between intratumoral NLR and reduced effectiveness of ICIs (25). Using a mouse model of lung cancer, the researchers demonstrated that antagonizing neutrophils restored the infiltration of tumor CD8 T cells and improved the efficacy of anti-PD1 treatment (25). In the pathogenesis of nociceptive pain associated with another type of cancer, calcitonin gene-related peptide (CGRP) serves as a crucial signaling molecule that can induce hyperalgesia and impact the tumor microenvironment (26). Cancer cells interact with nociceptor neurons and stimulate the release of CGRP, leading to increased exhaustion of cytotoxic CD8 T cells (27), which in turn hinders their ability to eliminate tumors and diminishes the effectiveness of ICIs (28).

Therefore, we conducted a retrospective analysis to determine whether baseline pain is an independent prognostic factor for ICIs. We also performed a bioinformatics analysis to elucidate the underlying possible mechanisms. Finally, the expression level of hub CRPGs were detected using enzyme linked immunosorbent assay.

Methods and materials

Study oversight

In this retrospective cohort study, lung cancer patients who received ICIs treatment were recruited from the inpatient department of Guangdong Provincial Hospital of Chinese Medicine from January 1, 2018, to December 31, 2021. Data collected was performed by medical record system and telephone follow-up. The sample used to detect the expression level of hub CRPGs in ELISA assay comes from a prospective study. This study conformed to the Helsinki Declaration and was approved by the Ethics Committee of Guangdong Provincial Hospital of Chinese Medicine. The ethical batch number are ZE2024-027-01 and BF2020-277-02, respectively.

Participants

The inclusion criteria for patients were as follows: 1. Patients diagnosed with lung cancer by histological or cytological pathological examination; 2. Patients aged 18 years or older; 3. Patients received at least one course of ICIs treatment, whether alone or in combination; 4. Baseline NRS scores were recorded. The exclusion criteria for patients were as follow: 1. Unidentified pathological types, non-primary lesions, or more than two pathological types; 2. Patients with multiple organ primary cancers; 3. Missing follow-up data; 4. Completely missing clinical and laboratory data.

Intervention

All enrolled lung cancer patients received at least one course of ICIs treatment, either alone or in combination with chemotherapy or targeted therapy. There were no restrictions on the types of ICIs. The determination of whether patients received ICIs treatment was obtained from the medical records system.

Comparisons

According to NRS scores, the patients were divided into a Pain group (NRS scores > 0) and a Non-Pain group (NRS scores = 0). By comparing the clinical factors between the two groups, we identified key factors affecting the efficacy of ICIs mediated by pain. Kaplan-Meier (KM) survival analysis was used to evaluate the survival differences between the two groups. A P-value of the log-rank test less than 0.05 was considered significant. All tests were two-sided, with an α of 0.05.

Outcome measures

The main outcome measure is overall survival (OS), defined as the time from the start of ICIs treatment to the occurrence of death.

Propensity score matching

To mitigate differences between the Pain group and the Non-Pain group, we employed Propensity Score Matching (PSM) analysis. Even with only one confounding variable, we included all variables in the PSM analysis to ensure more reliable results. Nearest neighbor matching was utilized as the matching method, with a caliper value set to 0.05, and a 1:1 ratio of the target group to the control group.

Cox regression analysis and nomogram construction

Univariate cox analysis was used to identify the prognostic factors affecting the efficacy of ICIs, and multivariate cox analysis was used to identify the independent prognostic risk factors affecting the efficacy of ICIs. The P value of log rank test <0.05 was considered to be significantly different. For the prognostic factors with significant differences in multivariate cox analysis, it was further used to construct nomogram for prognosis evaluation of patients. According to the risk score of the model, KM survival analysis was used to evaluate the difference between them. Finally, ROC curve was used to evaluate the reliability of the model.

Construction of cancer-related pain matrix

The chip data GSE93157 and platform annotation files GPL19965 of patients with NSCLC receiving ICIs treatment were obtained from the GEO database. This data was published by Prat A et al. in Cancer Research in 2017. The authors utilized the PanCancer 730-Immune Panel to analyze tumor samples from 65 patients treated with anti-PD-1 therapy for melanoma, lung cancer, and head and neck cancer on the nCounter system (29). Among them, there were 13 cases of squamous cell carcinoma and 22 cases of non-small cell non-squamous cell carcinoma, totaling 35 cases. The patients were treated with either NIVOLUMAB or PEMBROLIZUMAB. The targets of cancer-related pain were identified by searching the GeneCards database using the keyword “cancer related pain” and intersecting with genes in the GSE93157 chip. Subsequently, the expression levels of these targets were extracted to create the NSCLC Cancer Related Pain Matrix.

Consistency cluster analysis and differential expression analysis

Unsupervised learning was conducted utilizing the K-means consensus clustering method to partition the NSCLC Cancer Related Pain Matrix into distinct modules, based on the coherence of internal pain gene expression. Subsequently, the limma package was employed to conduct differential expression analysis between modules, with the threshold set at log |FC (Fold Change)| > 1 and a P value < 0.05.

GO and KEGG functional enrichment analysis

For the gene set functional enrichment analysis, the KEGG REST API was utilized to access the most recent KEGG Pathway gene annotations and genes in the org.Hs.eg.db. The GO annotation served as the background for the analysis, with DEGs being mapped to this background set. Enrichment analysis was then conducted using the R software package clusterProfiler to determine gene set enrichment outcomes. The minimum gene set size was established at 5, while the maximum gene set size was set at 5000. Significance was determined by a P value of < 0.05 and a false discovery rate (FDR) of < 0.1.

PPI network construction and correlation analysis

The cancer-related pain genes (CRPGs) from the core KEGG pathway were imported into the STRING database, with Homo sapiens selected as the sample. A correlation coefficient of 0.900 was observed, followed by the utilization of the MCC algorithm within the cytoHubba plug-in of Cytoscape 3.8.2 software to determine the top 10 targets within the core. To further clarify the regulatory relationship between these 10 cytokines, analysis was performed using Pearson correlation analysis.

Survival analysis

In order to study the survival difference of the top 10 CRPGs in lung cancer patients, the top 10 targets were divided into high and low groups according to their median expression levels. The GEPIA database was used to perform KM survival analysis on LUAD and LUSC respectively. In addition, we used the GEO database lung cancer cohort to externally validate the results in TCGA. Log rank P value <0.05 was considered significant differences.

Tumor immune dysfunction and exclusion (TIDE) algorithm

In order to predict whether the survival related CRPGs affect the efficacy of immunotherapy for lung cancer, we divided them into two groups, high and low, based on the expression of CRPGs, and used the TIDE algorithm to analyze the effectiveness of ICIs treatment between different groups.

Correlation analysis between survival related CRPGs, immune cells, and inflammatory pathways

In order to further clarify the immune cells and pathways regulated by survival related CRPGs, the CIBERSORT algorithm and Pearson correlation analysis were used to conduct correlation analysis among the three.

ELISA assay

The expression levels of hub CRPGs were detected using an enzyme-linked immunosorbent assay (ELISA). ELISA assay was performed using the kit from Lianke Biotechnology (EK1119-AW1). Briefly, 20ul of sample and 80ul of detection buffer were added to the sample well. The subsequent steps were consistent with the instructions. Finally, the OD values at 450nm and 630nm was measured by microplate reader. The CXCL12 content in each sample was calculated from the standard curve.

Statistical analysis

All data were entered using by WPS Office or Excel, and data analysis and visualization were conducted by R language software 4.2.1 and SPSS version 26.0. Measurement data were assessed for normal distribution and described using the mean standard deviation. For data that did not follow a normal distribution, the median, lower quartile (Q1), upper quartile (Q3), minimum value, and maximum value were reported. The measurement data conform to normal distribution and homogeneity of variance by T test, and those that do not conform to normal distribution or homogeneity of variance by Mann Whitney U test. Counting data were presented as composition ratio and ratio. Chi-square test or Fisher exact probability method was used for analyzing counting data.

For variables with less than 20% missing data, the mice package in R language 4.2.0 was used for data interpolation, and the data interpolation was carried out by setting the number of random seeds. Variables with more than 20% missing data are eliminated.

Univariate Cox analysis was employed to identify prognostic factors associated with ICIs treatment, and multivariate Cox analysis to identify independent prognostic factors associated with ICIs treatment. Independent prognostic factors were utilized to construct a nomogram, and ROC curve analysis was employed to assess the reliability of the model. Additionally, Spearman correlation analysis was used to evaluate the regulatory relationship between NRS and circulating inflammatory cells.

Results

Patient characteristics

The study workflow was shown in Figure 1. Before PSM, a total of 222 patients with lung cancer treated with ICIs were enrolled. Patients were divided into Pain group and Non-Pain group according to NRS scores. There were 112 cases in Pain group and 110 cases in Non-Pain group. The difference analysis between groups showed that PLR, HBV, M stage, Bone metastasis and pleural metastasis in Pain group were significantly higher than

those in Non-Pain group. The detail of baseline before PSM was shown in Table 1.

After PSM, a total of 94 patients with lung cancer treated with ICIs were enrolled. There were 47 cases in Pain Group and 47 cases in Non-Pain group. PSM eliminated the confounding factors between groups, and there was no significant difference in all included clinical indexes. The detail of baseline after PSM was shown in Table 2.

Univariate cox analysis

Before PSM, univariate cox analysis suggested that Dnlr (HR: 1.10, 95% CI: 1.01 - 1.21, p value: 0.027), PLR (HR: 1.01, 95% CI: 1.01 - 1.01, p value: 0.002), Systemic inflammation index (SII) (HR: 1.01, 95% CI: 1.01 - 1.01, p value: 0.014), Eastern Cooperative Oncology Group (ECOG) scores (HR: 13.55, 95% CI: 3.18 - 57.68, p value < 0.001, 4 vs 0), M stage (HR: 1.52, 95% CI: 1.03 - 2.24, p value: 0.033), Lung metastasis (HR: 1.47, 95% CI: 1.08 - 2.00, p value: 0.015), Bone metastasis (HR: 1.76, 95% CI: 1.30 - 2.38, p value < 0.001), Adrenal metastasis (HR: 1.51, 95% CI: 1.04 - 2.19, p value: 0.031) and NRS score (HR: 1.65, 95% CI: 1.21 - 2.23, p value: 0.001) were risk factors of ICIs. Table 3.

After PSM, univariate cox analysis suggested that Age (HR: 1.04, 95% CI: 1.01 - 1.07, p value: 0.012), NLR (HR: 1.09, 95% CI: 1.03 - 1.17, p value: 0.006), Derived neutrophil lymphocyte ratio (Dnlr) (HR: 1.18, 95% CI: 1.03 - 1.36, p value: 0.017), PLR (HR: 1.01, 95% CI: 1.01 - 1.01, p value: 0.030), SII (HR: 1.01, 95% CI: 1.01 - 1.01, p value: 0.009), Bone metastasis (HR: 1.98, 95% CI: 1.21 - 3.24, p value: 0.006) were risk factors of ICIs. Table 4.

Multivariate cox analysis

Before PSM, Multivariate cox analysis suggested that Bone metastasis (HR: 1.63, 95% CI: 1.05 - 2.51, p value: 0.028) and NRS scores (HR: 1.56, 95% CI: 1.06 - 2.30, p value: 0.023) were independent prognostic factors for the efficacy of ICIs. Table 3.

After PSM, Multivariate cox analysis suggested that Age (HR: 1.08, 95% CI: 1.03 - 1.13, p value< 0.001), Platelets (HR: 1.01, 95% CI: 1.01 - 1.02, p value: 0.006), Dnlr (HR: 3.27, 95% CI: 1.33 - 8.04, p value: 0.010), Liver metastasis (HR: 3.88, 95% CI: 1.22 - 12.34, p value: 0.022), Bone metastasis (HR: 3.66, 95% CI: 1.47 - 9.16, p value: 0.005) and NRS score (HR: 2.66, 95% CI: 1.32 - 5.37, p value: 0.006) were independent prognostic factors for the efficacy of ICIs. Table 4.

Prognostic model construction and evaluation

Before PSM, based on bone metastasis and NRS scores, we established nomogram for prognosis evaluation of patients Figure 2A. It can be seen that patients with lung cancer complicated with Bone metastasis and pain have poor effect and prognosis after receiving ICIs treatment. The survival of lung cancer patients with low risk score is significantly better than that with

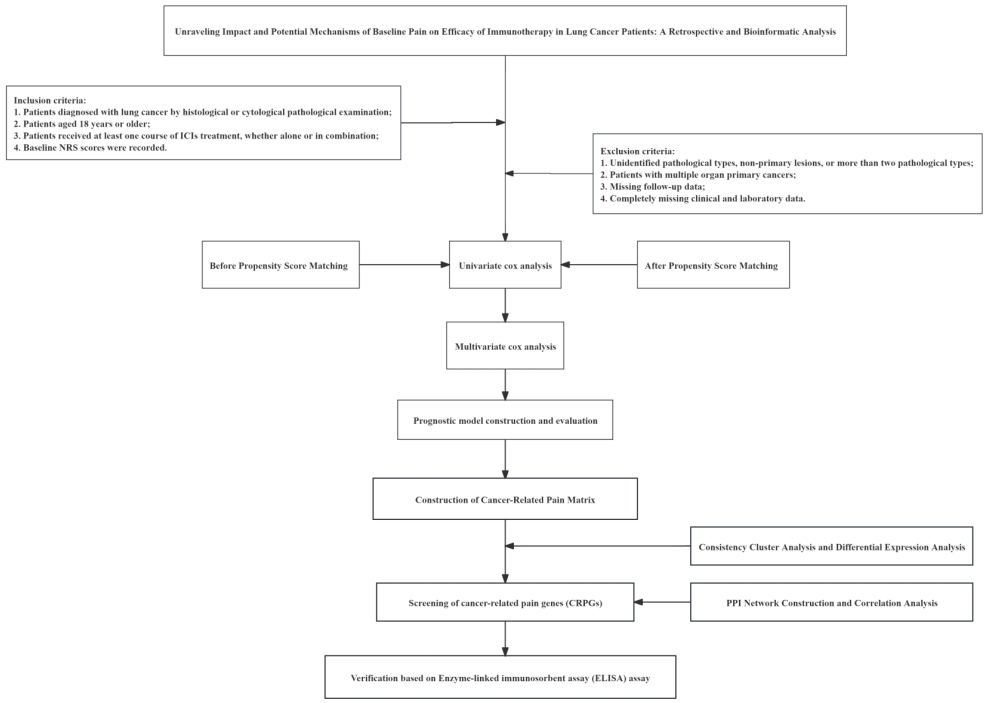

FIGURE 1
The study workflow.

10.3389/fimmu.2024.1456150

High risk score. The median OS was 740 days and 418 days respectively, HR=1.73,95CI% (1.26, 2.38), and P value: 5.8e-4. Figure 2B. Nomogram's predictive efficiency was good with AUC under roc curve 1-year 0.69, 2-year 0.62 and 3-year 0.62 Figure 2C.

After PSM, based on age, platelets, dNLR, liver metastasis, bone metastasis and NRS Scores, we established nomogram for prognosis evaluation of patients Figure 2D. It can be seen that patients with liver metastasis and bone metastasis, high platelet and dNLR, and pain have a poor prognosis after receiving ICIs treatment. The survival of lung cancer patients with Low risk score is significantly better than that with High risk score. The median OS was 753 days and 316 days respectively, HR=2.41,95CI%(1.51,3.86), and P value: 1.6e-4 Figure 2E. Nomogram's predictive efficiency was good with AUC under roc curve 1-year 0.80, 2-year 0.73 and 3-year 0.80 Figure 2F. Whether before or after PSM, the risk score showed significant different between with or without bone metastasis and pain group Supplementary Figures 1A–D. And with the increasing of age and dNLR, the risk scores was also increased Supplementary Figures 1E, F.

Spearman correlation analysis among NRS scores and peripheral circulating inflammatory cells

Spearman correlation analysis suggested that NRS had positive regulation on monocytes (cor: 0.08), neutrophils (cor: 0.07), leukocytes (cor: 0.04) and platelets (cor: 0.09), and negative regulation on lymphocytes (cor: -0.04). The results was showed in Figure 2G.

TABLE 1 The detail of baseline before PSM.

Variable	Total (n = 222)	Group		Statistic		
		Non-Pain (n = 110)	Pain (n = 112)	Z	P	SMD
Age, M (Q_1, Q_3)	62.00 (56.00, 67.00)	63.00 (56.25, 67.75)	62.00 (56.00, 67.00)	Z=-1.337	0.181	-0.205
Weight, M (Q_1, Q_3)	58.00 (52.00, 65.00)	58.00 (52.00, 64.00)	58.00 (51.75, 65.75)	Z=-0.100	0.920	0.047
Height, M (Q_1, Q_3)	165.00 (160.00, 170.00)	165.00 (160.00, 170.00)	165.00 (160.00, 170.00)	Z=-0.569	0.570	0.077
BSA, M (Q_1, Q_3)	1.63 (1.55, 1.73)	1.63 (1.56, 1.74)	1.62 (1.55, 1.72)	Z=-0.074	0.941	0.040
Neutrophils, M (Q_1, Q_3)	5.10 (3.82, 6.86)	5.11 (3.82, 6.44)	5.08 (3.80, 6.89)	Z=-0.077	0.938	0.059
Lymphocytes, M (Q_1, Q_3)	1.37 (1.02, 1.81)	1.43 (1.10, 1.81)	1.31 (0.93, 1.80)	Z=-1.401	0.161	-0.112
Leukocytes, M (Q_1, Q_3)	7.45 (5.89, 9.70)	7.54 (6.13, 9.46)	7.39 (5.74, 10.02)	Z=-0.524	0.601	0.029
Platelets, M (Q_1, Q_3)	279.50 (216.50, 348.25)	276.50 (214.00, 324.75)	286.50 (223.00, 358.25)	Z=-1.101	0.271	0.176
Monocytes, M (Q_1, Q_3)	0.56 (0.39, 0.81)	0.54 (0.41, 0.76)	0.57 (0.38, 0.86)	Z=-0.474	0.635	0.112
NLR, M (Q_1, Q_3)	3.80 (2.62, 6.12)	3.62 (2.53, 5.46)	4.01 (2.64, 6.26)	Z=-1.003	0.316	-1.267
Dnlr, M (Q_1, Q_3)	2.33 (1.75, 3.16)	2.25 (1.76, 2.92)	2.44 (1.75, 3.35)	Z=-1.329	0.184	0.167
PLR, M (Q_1, Q_3)	203.56 (150.05, 295.17)	185.00 (148.36, 231.87)	213.02 (156.47, 321.33)	Z=-2.419	**0.016**	0.295
LMR, M (Q_1, Q_3)	2.36 (1.63, 3.35)	2.46 (1.64, 3.45)	2.27 (1.61, 3.16)	Z=-0.807	0.420	-0.011
SII, M (Q_1, Q_3)	1036.97 (625.13, 1621.41)	922.05 (600.19, 1555.31)	1113.73 (728.34, 1695.25)	Z=-1.717	0.086	0.166
Gender, n (%)				χ^2=0.197	0.657	
1	179 (80.63)	90 (81.82)	89 (79.46)			-0.058
2	43 (19.37)	20 (18.18)	23 (20.54)			0.058
Alcohol, n (%)				χ^2=1.763	0.184	
0	168 (75.68)	79 (71.82)	89 (79.46)			0.189
1	54 (24.32)	31 (28.18)	23 (20.54)			-0.189
ECOG, n (%)				-	0.137	
0	100 (45.05)	57 (51.82)	43 (38.39)			-0.276
1	100 (45.05)	45 (40.91)	55 (49.11)			0.164
2	12 (5.41)	6 (5.45)	6 (5.36)			-0.004
3	8 (3.6)	2 (1.82)	6 (5.36)			0.157

(Continued)

10.3389/fimmu.2024.1456150

TABLE 1 Continued

Variable	Total (n = 222)	Group		Statistic		
		Non-Pain (n = 110)	Pain (n = 112)	Z	P	SMD
4	2 (0.9)	0 (0.00)	2 (1.79)			0.135
Smoke, n (%)				χ^2=0.681	0.409	
0	60 (27.03)	27 (24.55)	33 (29.46)			0.108
1	162 (72.97)	83 (75.45)	79 (70.54)			-0.108
HBV, n (%)				χ^2=4.487	**0.034**	
0	203 (91.44)	105 (95.45)	98 (87.50)			-0.241
1	19 (8.56)	5 (4.55)	14 (12.50)			0.241
Tumor, n (%)				χ^2=0.889	0.346	
1	200 (90.09)	97 (88.18)	103 (91.96)			0.139
2	22 (9.91)	13 (11.82)	9 (8.04)			-0.139
Pathology, n (%)				χ^2=1.971	0.373	
1	125 (56.31)	57 (51.82)	68 (60.71)			0.182
2	55 (24.77)	29 (26.36)	26 (23.21)			-0.075
3	42 (18.92)	24 (21.82)	18 (16.07)			-0.156
T, n (%)				χ^2=4.341	0.362	
0	30 (13.51)	17 (15.45)	13 (11.61)			-0.120
1	25 (11.26)	10 (9.09)	15 (13.39)			0.126
2	36 (16.22)	16 (14.55)	20 (17.86)			0.086
3	30 (13.51)	19 (17.27)	11 (9.82)			-0.250
4	101 (45.5)	48 (43.64)	53 (47.32)			0.074
N, n (%)				-	0.958	
0	40 (18.02)	19 (17.27)	21 (18.75)			0.038
1	3 (1.35)	2 (1.82)	1 (0.89)			-0.098
2	85 (38.29)	43 (39.09)	42 (37.50)			-0.033
3	94 (42.34)	46 (41.82)	48 (42.86)			0.021
M, n (%)				χ^2=14.810	**<.001**	
0	47 (21.17)	35 (31.82)	12 (10.71)			-0.682
1	175 (78.83)	75 (68.18)	100 (89.29)			0.682
Lung metastasis, n (%)				χ^2=1.020	0.313	
0	140 (63.06)	73 (66.36)	67 (59.82)			-0.133
1	82 (36.94)	37 (33.64)	45 (40.18)			0.133
Liver metastasis, n (%)				χ^2=1.801	0.180	
0	193 (86.94)	99 (90.00)	94 (83.93)			-0.165
1	29 (13.06)	11 (10.00)	18 (16.07)			0.165
Bone metastasis, n (%)				χ^2=36.352	**<.001**	
0	131 (59.01)	87 (79.09)	44 (39.29)			-0.815

(Continued)

TABLE 1 Continued

Variable	Total (n = 222)	Group		Statistic		
		Non-Pain (n = 110)	Pain (n = 112)	Z	P	SMD
1	91 (40.99)	23 (20.91)	68 (60.71)			0.815
Brain metastasis, n (%)				χ^2=3.681	0.055	
0	176 (79.28)	93 (84.55)	83 (74.11)			-0.238
1	46 (20.72)	17 (15.45)	29 (25.89)			0.238
Adrenal metastasis, n (%)				χ^2=0.004	0.950	
0	182 (81.98)	90 (81.82)	92 (82.14)			0.008
1	40 (18.02)	20 (18.18)	20 (17.86)			-0.008
Other Lymph node metastasis, n (%)				χ^2=0.744	0.388	
0	187 (84.23)	95 (86.36)	92 (82.14)			-0.110
1	35 (15.77)	15 (13.64)	20 (17.86)			0.110
Pleura metastasis, n (%)				χ^2=6.242	**0.012**	
0	172 (77.48)	93 (84.55)	79 (70.54)			-0.307
1	50 (22.52)	17 (15.45)	33 (29.46)			0.307
Meningeal metastasis, n (%)				χ^2=0.000	1.000	
0	213 (95.95)	106 (96.36)	107 (95.54)			-0.040
1	9 (4.05)	4 (3.64)	5 (4.46)			0.040

Bold values: P value<0.05.

TABLE 2 The detail of baseline after PSM.

Variable	Total (n = 94)	Group		Statistic		
		Non-Pain (n = 47)	Pain (n = 47)	Z	P	SMD
Age, M (Q_1, Q_3)	62.00 (54.00, 66.00)	61.00 (53.00, 67.00)	62.00 (56.00, 66.00)	Z=-0.413	0.680	0.002
Weight, M (Q_1, Q_3)	59.00 (54.00, 65.00)	58.50 (52.00, 65.75)	59.50 (56.00, 64.50)	Z=-0.908	0.364	0.181
Height, M (Q_1, Q_3)	168.00 (160.00, 170.00)	165.00 (159.00, 170.00)	168.00 (160.50, 170.50)	Z=-0.921	0.357	0.174
BSA, M (Q_1, Q_3)	1.65 (1.57, 1.74)	1.63 (1.56, 1.76)	1.66 (1.57, 1.73)	Z=-0.969	0.333	0.282
Neutrophils, M (Q_1, Q_3)	4.66 (3.30, 6.46)	5.01 (3.72, 6.75)	4.49 (3.05, 6.37)	Z=-0.866	0.387	-0.084
Lymphocytes, M (Q_1, Q_3)	1.44 (1.10, 1.84)	1.40 (1.11, 1.75)	1.53 (1.09, 1.93)	Z=-0.609	0.543	0.209
Leukocytes, M (Q_1, Q_3)	7.21 (5.38, 9.32)	7.25 (5.62, 9.64)	6.77 (5.04, 8.73)	Z=-0.650	0.515	-0.001
Platelets, M (Q_1, Q_3)	272.50 (213.25, 321.75)	266.00 (213.50, 322.00)	281.00 (217.00, 321.50)	Z=-0.386	0.700	0.089
Monocytes, M (Q_1, Q_3)	0.54 (0.37, 0.72)	0.54 (0.36, 0.68)	0.55 (0.38, 0.83)	Z=-0.495	0.620	0.114
NLR, M (Q_1, Q_3)	3.56 (2.28, 5.43)	3.89 (2.35, 5.46)	3.38 (2.25, 5.06)	Z=-0.873	0.382	-0.304
Dnlr, M (Q_1, Q_3)	2.12 (1.56, 3.04)	2.26 (1.65, 3.06)	1.98 (1.60, 2.82)	Z=-0.945	0.345	-0.335
PLR, M (Q_1, Q_3)	189.09 (146.99, 233.83)	194.44 (151.81, 259.75)	188.89 (138.38, 227.18)	Z=-1.157	0.247	-0.176
LMR, M (Q_1, Q_3)	2.54 (1.74, 3.53)	2.50 (1.71, 3.38)	2.54 (1.80, 3.69)	Z=-0.635	0.525	0.071
SII, M (Q_1, Q_3)	870.69 (581.38, 1465.57)	988.13 (592.40, 1605.02)	820.99 (571.88, 1411.20)	Z=-0.873	0.382	-0.074
Gender, n (%)				χ^2=0.275	0.600	

(Continued)

TABLE 2 Continued

Variable	Total (n = 94)	Group		Statistic		
		Non-Pain (n = 47)	Pain (n = 47)	Z	P	SMD
1	76 (80.85)	39 (82.98)	37 (78.72)			-0.104
2	18 (19.15)	8 (17.02)	10 (21.28)			0.104
Alcohol, n (%)				χ^2=2.014	0.156	
0	70 (74.47)	32 (68.09)	38 (80.85)			0.324
1	24 (25.53)	15 (31.91)	9 (19.15)			-0.324
ECOG, n (%)				-	0.180	
0	44 (46.81)	23 (48.94)	21 (44.68)			-0.086
1	43 (45.74)	18 (38.30)	25 (53.19)			0.298
2	5 (5.32)	4 (8.51)	1 (2.13)			-0.442
3	2 (2.13)	2 (4.26)	0 (0.00)			-0.298
Smoke, n (%)				χ^2=0.203	0.652	
0	28 (29.79)	13 (27.66)	15 (31.91)			0.091
1	66 (70.21)	34 (72.34)	32 (68.09)			-0.091
HBV, n (%)				χ^2=0.261	0.609	
0	90 (95.74)	44 (93.62)	46 (97.87)			0.295
1	4 (4.26)	3 (6.38)	1 (2.13)			-0.295
Tumor, n (%)				χ^2=0.103	0.748	
1	83 (88.3)	41 (87.23)	42 (89.36)			0.069
2	11 (11.7)	6 (12.77)	5 (10.64)			-0.069
Pathology, n (%)				χ^2=1.554	0.460	
1	46 (48.94)	20 (42.55)	26 (55.32)			0.257
2	28 (29.79)	16 (34.04)	12 (25.53)			-0.195
3	20 (21.28)	11 (23.40)	9 (19.15)			-0.108
T, n (%)				χ^2=1.022	0.907	
0	18 (19.15)	9 (19.15)	9 (19.15)			0.000
1	9 (9.57)	5 (10.64)	4 (8.51)			-0.076
2	15 (15.96)	6 (12.77)	9 (19.15)			0.162
3	11 (11.7)	5 (10.64)	6 (12.77)			0.064
4	41 (43.62)	22 (46.81)	19 (40.43)			-0.130
N, n (%)				χ^2=0.377	0.828	
0	14 (14.89)	6 (12.77)	8 (17.02)			0.113
2	36 (38.3)	18 (38.30)	18 (38.30)			0.000
3	44 (46.81)	23 (48.94)	21 (44.68)			-0.086
M, n (%)				χ^2=0.072	0.789	
0	17 (18.09)	8 (17.02)	9 (19.15)			0.054
1	77 (81.91)	39 (82.98)	38 (80.85)			-0.054
Lung metastasis, n (%)				χ^2=0.720	0.396	

(Continued)

TABLE 2 Continued

Variable	Total (n = 94)	Group		Statistic		
		Non-Pain (n = 47)	Pain (n = 47)	Z	P	SMD
0	58 (61.7)	27 (57.45)	31 (65.96)			0.180
1	36 (38.3)	20 (42.55)	16 (34.04)			-0.180
Liver metastasis, n (%)				χ^2=2.574	0.109	
0	83 (88.3)	39 (82.98)	44 (93.62)			0.435
1	11 (11.7)	8 (17.02)	3 (6.38)			-0.435
Bone metastasis, n (%)				χ^2=0.048	0.826	
0	63 (67.02)	32 (68.09)	31 (65.96)			-0.045
1	31 (32.98)	15 (31.91)	16 (34.04)			0.045
Brain metastasis, n (%)				χ^2=0.066	0.797	
0	75 (79.79)	38 (80.85)	37 (78.72)			-0.052
1	19 (20.21)	9 (19.15)	10 (21.28)			0.052
Adrenal metastasis, n (%)				χ^2=0.072	0.789	
0	77 (81.91)	39 (82.98)	38 (80.85)			-0.054
1	17 (18.09)	8 (17.02)	9 (19.15)			0.054
Other Lymph node metastasis, n (%)				χ^2=0.000	1.000	
0	76 (80.85)	38 (80.85)	38 (80.85)			0.000
1	18 (19.15)	9 (19.15)	9 (19.15)			0.000
Pleura metastasis, n (%)				χ^2=0.066	0.797	
0	75 (79.79)	37 (78.72)	38 (80.85)			0.054
1	19 (20.21)	10 (21.28)	9 (19.15)			-0.054
Meningeal metastasis, n (%)				χ^2=0.000	1.000	
0	92 (97.87)	46 (97.87)	46 (97.87)			0.000
1	2 (2.13)	1 (2.13)	1 (2.13)			0.000

Bold values: P value<0.05.

Construction of cancer-related pain matrix

A total of 725 genes were obtained from GSE93157. A total of 12,098 targets were obtained from the GeneCards database. After the intersection of the two, a total of 662 cancer-related pain genes (CRPGs) were obtained. The expression levels of these 662 CRPGs were further extracted and the NSCLC Cancer-Related Pain Matrix was constructed.

Consistency cluster analysis and differential expression analysis

The K-means consistency clustering method was used for unsupervised learning, and the pain gene expression consistency within the NSCLC Cancer-Related Pain Matrix was divided into two modules, C2 and C1. There is a clear boundary between the two modules C1 and C2 Figure 3A. When consensus matrix k=2, the internal consistency performed best Figures 3B, C. Consensus scores of all samples were displayed Figure 3D. Principal component analysis indicated that when consensus matrix k=2, the samples can be well distinguished Figure 3E. Among them, 23 patients were classified into C2 and 12 patients were classified into C1 module. The limma package was used to perform differential expression analysis between C2 and C1, and a total of 420 differentially expressed genes (DEGs) were obtained. Among them, 398 were up-regulated and 22 were down-regulated Figures 4A, B.

GO and KEGG functional enrichment analysis

GO and KEGG functional enrichment analysis of 420 DEGs showed that the interaction between cytokines and cytokine receptors is the main signaling pathway that mediates pain,

10.3389/fimmu.2024.1456150

TABLE 3 Univariate cox analysis and Multivariate cox analysis before PSM.

Variables	Beta	S.E	Z	P	HR (95%CI)	m_Beta	m_S.E	m_Z	aP	aHR (95%CI)
Age	0.01	0.01	0.87	0.387	1.01 (0.99 - 1.03)	0.01	0.01	0.67	0.500	1.01 (0.99 - 1.03)
Weight	-0.01	0.01	-1.49	0.137	0.99 (0.97 - 1.00)	-0.04	0.05	-0.93	0.353	0.96 (0.88 - 1.05)
Height	0.01	0.01	0.77	0.443	1.01 (0.99 - 1.03)	0.00	0.03	0.03	0.973	1.00 (0.94 - 1.07)
BSA	-0.55	0.57	-0.97	0.334	0.58 (0.19 - 1.76)	2.43	3.84	0.63	0.527	11.36 (0.01 - 21151.82)
Neutrophils	0.03	0.03	1.00	0.317	1.03 (0.98 - 1.08)	-0.26	0.33	-0.79	0.431	0.77 (0.40 - 1.47)
Lymphocytes	-0.23	0.12	-1.91	0.057	0.80 (0.63 - 1.01)	-0.09	0.35	-0.26	0.794	0.91 (0.46 - 1.82)
Leukocyte	0.01	0.02	0.54	0.592	1.01 (0.97 - 1.06)	0.16	0.30	0.53	0.594	1.17 (0.65 - 2.10)
Platelets	0.00	0.00	1.20	0.229	1.00 (1.00 - 1.00)	0.00	0.00	0.14	0.887	1.00 (1.00 - 1.00)
Monocytes	0.30	0.24	1.26	0.208	1.35 (0.85 - 2.16)	0.73	0.52	1.41	0.160	2.08 (0.75 - 5.79)
NLR	0.00	0.00	1.74	0.082	1.00 (1.00 - 1.01)	0.00	0.00	1.02	0.310	1.00 (1.00 - 1.01)
Dnlr	0.10	0.05	2.20	**0.027**	1.10 (1.01 - 1.21)	0.19	0.15	1.24	0.215	1.21 (0.90 - 1.62)
PLR	0.01	0.00	3.02	**0.002**	1.01 (1.01 - 1.01)	0.00	0.00	0.56	0.574	1.00 (1.00 - 1.00)
LMR	-0.06	0.04	-1.51	0.131	0.94 (0.88 - 1.02)	0.02	0.05	0.43	0.670	1.02 (0.92 - 1.13)
SII	0.01	0.00	2.45	**0.014**	1.01 (1.01 - 1.01)	0.00	0.00	0.09	0.928	1.00 (1.00 - 1.00)
Gender										
1					Ref					Ref
2	0.11	0.19	0.57	0.566	1.11 (0.77 - 1.61)	0.54	0.37	1.46	0.145	1.72 (0.83 - 3.55)
Alcohol										
0					Ref					Ref
1	-0.32	0.19	-1.72	0.086	0.73 (0.50 - 1.05)	-0.13	0.24	-0.53	0.593	0.88 (0.55 - 1.41)
ECOG										
0					Ref					Ref
1	0.10	0.16	0.59	0.556	1.10 (0.80 - 1.51)	-0.00	0.20	-0.01	0.995	1.00 (0.68 - 1.47)
2	0.32	0.35	0.91	0.361	1.38 (0.69 - 2.76)	0.03	0.43	0.07	0.941	1.03 (0.45 - 2.38)
3	0.76	0.40	1.91	0.056	2.14 (0.98 - 4.65)	0.29	0.61	0.48	0.634	1.34 (0.40 - 4.42)
4	2.61	0.74	3.53	**<.001**	13.55 (3.18 - 57.68)	1.34	1.02	1.31	0.189	3.83 (0.52 - 28.41)
Smoke										
0					Ref					Ref
1	-0.13	0.17	-0.76	0.450	0.88 (0.63 - 1.23)	-0.04	0.30	-0.12	0.904	0.96 (0.53 - 1.75)
HBV										
0					Ref					Ref
1	0.06	0.26	0.23	0.815	1.06 (0.64 - 1.76)	-0.21	0.32	-0.64	0.521	0.81 (0.43 - 1.53)
Tumor										
1					Ref					Ref
2	0.36	0.26	1.41	0.158	1.44 (0.87 - 2.38)	0.40	0.41	0.97	0.331	1.49 (0.66 - 3.36)
Lung pathology										
1					Ref					Ref

(Continued)

10.3389/fimmu.2024.1456150

TABLE 3 Continued

Variables	Beta	S.E	Z	P	HR (95%CI)	m_Beta	m_S.E	m_Z	aP	aHR (95%CI)
Lung pathology										
2	0.08	0.19	0.44	0.663	1.09 (0.75 - 1.57)	0.45	0.24	1.89	0.059	1.57 (0.98 - 2.50)
3	0.25	0.20	1.26	0.208	1.29 (0.87 - 1.90)	0.29	0.29	0.98	0.328	1.33 (0.75 - 2.37)
T										
0					Ref					Ref
1	-0.48	0.32	-1.47	0.141	0.62 (0.33 - 1.17)	-0.50	0.38	-1.31	0.189	0.60 (0.28 - 1.28)
2	-0.01	0.28	-0.03	0.975	0.99 (0.57 - 1.71)	-0.16	0.37	-0.42	0.672	0.86 (0.42 - 1.76)
3	-0.02	0.30	-0.06	0.949	0.98 (0.55 - 1.75)	0.09	0.39	0.23	0.816	1.10 (0.51 - 2.35)
4	0.06	0.23	0.25	0.802	1.06 (0.67 - 1.68)	0.01	0.30	0.03	0.975	1.01 (0.56 - 1.82)
N										
0					Ref					Ref
1	-0.23	0.73	-0.32	0.749	0.79 (0.19 - 3.32)	-0.22	0.82	-0.27	0.788	0.80 (0.16 - 3.98)
2	0.02	0.22	0.08	0.935	1.02 (0.66 - 1.58)	-0.07	0.27	-0.25	0.802	0.93 (0.55 - 1.60)
3	0.13	0.22	0.59	0.556	1.14 (0.74 - 1.75)	-0.02	0.28	-0.05	0.956	0.98 (0.57 - 1.71)
M										
0					Ref					Ref
1	0.42	0.20	2.13	**0.033**	1.52 (1.03 - 2.24)	-0.07	0.28	-0.23	0.816	0.94 (0.54 - 1.63)
Lung metastasis										
0					Ref					Ref
1	0.38	0.16	2.43	**0.015**	1.47 (1.08 - 2.00)	0.35	0.21	1.67	0.095	1.41 (0.94 - 2.12)
Liver metastasis										
0					Ref					Ref
1	0.27	0.22	1.25	0.213	1.31 (0.86 - 2.01)	0.25	0.30	0.84	0.398	1.28 (0.72 - 2.29)
Bone metastasis										
0					Ref					Ref
1	0.56	0.16	3.62	**<.001**	1.76 (1.30 - 2.38)	0.49	0.22	2.20	**0.028**	1.63 (1.05 - 2.51)
Brain metastasis										
0					Ref					Ref
1	0.17	0.18	0.94	0.348	1.19 (0.83 - 1.71)	-0.11	0.24	-0.46	0.648	0.90 (0.56 - 1.44)
Adrenal metastasis										
0					Ref					Ref
1	0.41	0.19	2.15	**0.031**	1.51 (1.04 - 2.19)	0.27	0.25	1.07	0.283	1.31 (0.80 - 2.16)
Other Lymph node metastasis										
0					Ref					Ref
1	0.17	0.21	0.82	0.414	1.19 (0.79 - 1.78)	-0.05	0.28	-0.18	0.855	0.95 (0.54 - 1.65)
Pleura metastasis										
0					Ref					Ref
1	0.36	0.18	1.96	0.050	1.43 (1.01 - 2.04)	0.16	0.25	0.64	0.522	1.17 (0.72 - 1.91)

(Continued)

10.3389/fimmu.2024.1456150

TABLE 3 Continued

Variables	Beta	S.E	Z	P	HR (95%CI)	m_Beta	m_S.E	m_Z	aP	aHR (95%CI)
Meningeal metastasis										
0					Ref					Ref
1	-0.21	0.42	-0.50	0.614	0.81 (0.36 - 1.83)	-0.23	0.55	-0.43	0.668	0.79 (0.27 - 2.31)
NRS										
0					Ref					Ref
1	0.50	0.16	3.20	**0.001**	1.65 (1.21 - 2.23)	0.45	0.20	2.27	**0.023**	1.56 (1.06 - 2.30)

Bold values: P value<0.05.

TABLE 4 Univariate cox analysis and Multivariate cox analysis after PSM.

Variables	Univariate					Multivariate				
	β	S. E	t	P	HR (95%CI)	β	S. E	t	P	HR (95%CI)
Age	0.04	0.01	2.52	**0.012**	1.04 (1.01 - 1.07)	0.08	0.02	3.35	**<.001**	1.08 (1.03 - 1.13)
Weight	-0.02	0.01	-1.28	0.201	0.98 (0.96 - 1.01)	-0.04	0.12	-0.31	0.759	0.96 (0.77 - 1.21)
Height	0.02	0.02	0.97	0.331	1.02 (0.98 - 1.05)	0.01	0.07	0.10	0.917	1.01 (0.88 - 1.15)
BSA	-0.38	0.87	-0.44	0.661	0.68 (0.13 - 3.73)	4.50	9.10	0.49	0.621	89.62 (0.00 - 4947835799.89)
Neutrophils	0.03	0.03	0.84	0.400	1.03 (0.96 - 1.10)	-1.22	0.72	-1.70	0.089	0.30 (0.07 - 1.20)
Lymphocytes	-0.27	0.18	-1.49	0.135	0.77 (0.54 - 1.09)	-1.94	1.00	-1.93	0.054	0.14 (0.02 - 1.03)
Leukocyte	0.02	0.03	0.57	0.568	1.02 (0.96 - 1.08)	1.09	0.66	1.64	0.100	2.96 (0.81 - 10.84)
Platelets	0.00	0.00	0.95	0.343	1.00 (1.00 - 1.00)	0.01	0.00	2.74	**0.006**	1.01 (1.01 - 1.02)
Monocytes	0.31	0.33	0.94	0.348	1.36 (0.72 - 2.58)	0.79	1.01	0.78	0.438	2.20 (0.30 - 16.05)
NLR	0.09	0.03	2.77	**0.006**	1.09 (1.03 - 1.17)	0.01	0.13	0.09	0.926	1.01 (0.79 - 1.30)
Dnlr	0.17	0.07	2.38	**0.017**	1.18 (1.03 - 1.36)	1.18	0.46	2.57	**0.010**	3.27 (1.33 - 8.04)
PLR	0.01	0.00	2.16	**0.030**	1.01 (1.01 - 1.01)	-0.00	0.01	-0.70	0.484	1.00 (0.99 - 1.01)
LMR	-0.11	0.06	-1.71	0.087	0.90 (0.80 - 1.02)	0.11	0.11	1.01	0.312	1.12 (0.90 - 1.39)
SII	0.01	0.00	2.62	**0.009**	1.01 (1.01 - 1.01)	-0.00	0.00	-1.95	0.051	1.00 (1.00 - 1.00)
Gender										
1					Ref					Ref
2	0.05	0.29	0.16	0.873	1.05 (0.59 - 1.85)	0.53	0.76	0.70	0.486	1.69 (0.38 - 7.47)
Alcohol										
0					Ref					Ref

(Continued)

TABLE 4 Continued

Variables	Univariate					Multivariate				
	β	S. E	t	P	HR (95%CI)	β	S. E	t	P	HR (95%CI)
Alcohol										
1	-0.19	0.27	-0.68	0.495	0.83 (0.49 - 1.42)	0.35	0.53	0.67	0.501	1.43 (0.51 - 4.00)
ECOG										
0					Ref					Ref
1	0.16	0.25	0.63	0.527	1.17 (0.72 - 1.90)	0.49	0.40	1.24	0.215	1.63 (0.75 - 3.54)
2	0.51	0.48	1.06	0.291	1.66 (0.65 - 4.27)	0.58	1.08	0.54	0.592	1.79 (0.21 - 14.89)
3		0.00	NA		NA (NA - NA)		0.00	NA		NA (NA - NA)
Smoke										
0					Ref					Ref
1	-0.00	0.26	-0.00	0.999	1.00 (0.61 - 1.65)	-0.15	0.64	-0.24	0.809	0.86 (0.25 - 3.00)
HBV										
0					Ref					Ref
1	0.10	0.52	0.19	0.849	1.10 (0.40 - 3.03)	0.66	0.73	0.90	0.366	1.93 (0.46 - 8.00)
Tumor										
1					Ref					Ref
2	0.33	0.36	0.93	0.354	1.39 (0.69 - 2.80)	-0.16	0.78	-0.20	0.842	0.86 (0.19 - 3.94)
Pathology										
1					Ref					Ref
2	-0.13	0.28	-0.46	0.645	0.88 (0.51 - 1.52)	0.50	0.46	1.07	0.283	1.64 (0.66 - 4.06)
3	0.28	0.30	0.93	0.350	1.32 (0.74 - 2.35)	0.20	0.58	0.35	0.729	1.22 (0.39 - 3.80)
T										
0					Ref					Ref
1	-0.96	0.52	-1.84	0.066	0.38 (0.14 - 1.07)	-0.31	0.80	-0.38	0.701	0.74 (0.15 - 3.52)
2	-0.26	0.40	-0.64	0.519	0.77 (0.35 - 1.69)	-0.75	0.62	-1.21	0.228	0.47 (0.14 - 1.60)
3	0.05	0.42	0.12	0.907	1.05 (0.46 - 2.40)	0.30	0.63	0.48	0.632	1.35 (0.40 - 4.61)
4	0.00	0.31	0.01	0.990	1.00 (0.54 - 1.85)	-0.01	0.49	-0.02	0.985	0.99 (0.38 - 2.59)
N										
0					Ref					Ref
2	-0.09	0.36	-0.25	0.803	0.91 (0.45 - 1.84)	-0.06	0.56	-0.10	0.921	0.95 (0.32 - 2.82)

(Continued)

10.3389/fimmu.2024.1456150

TABLE 4 Continued

Variables	Univariate					Multivariate				
	β	S. E	t	P	HR (95%CI)	β	S. E	t	P	HR (95%CI)
N										
3	-0.16	0.35	-0.46	0.645	0.85 (0.43 - 1.69)	-0.87	0.61	-1.43	0.152	0.42 (0.13 - 1.38)
M										
0					Ref					Ref
1	0.07	0.31	0.24	0.807	1.08 (0.59 - 1.96)	-0.32	0.53	-0.59	0.552	0.73 (0.26 - 2.07)
Lung metastasis										
0					Ref					Ref
1	0.30	0.24	1.24	0.215	1.34 (0.84 - 2.15)	0.84	0.47	1.76	0.078	2.31 (0.91 - 5.85)
Liver metastasis										
0					Ref					Ref
1	0.19	0.34	0.56	0.577	1.21 (0.62 - 2.36)	1.35	0.59	2.29	**0.022**	3.88 (1.22 - 12.34)
Bone metastasis										
0					Ref					Ref
1	0.68	0.25	2.73	**0.006**	1.98 (1.21 - 3.24)	1.30	0.47	2.78	**0.005**	3.66 (1.47 - 9.16)
Brain metastasis										
0					Ref					Ref
1	0.22	0.29	0.75	0.452	1.24 (0.71 - 2.18)	0.01	0.51	0.03	0.980	1.01 (0.37 - 2.76)
Adrenal metastasis										
0					Ref					Ref
1	0.40	0.29	1.37	0.172	1.49 (0.84 - 2.65)	-0.29	0.50	-0.57	0.567	0.75 (0.28 - 2.01)
Other Lymph node metastasis										
0					Ref					Ref
1	-0.24	0.30	-0.80	0.426	0.78 (0.43 - 1.42)	-0.00	0.50	-0.01	0.995	1.00 (0.37 - 2.66)
Pleura metastasis										
0					Ref					Ref
1	0.40	0.29	1.38	0.167	1.50 (0.84 - 2.65)	0.34	0.45	0.76	0.448	1.40 (0.58 - 3.37)
Meningeal metastasis										
0					Ref					Ref
1	-17.07	3113.62	-0.01	0.996	0.00 (0.00 - Inf)	-17.61	3344.31	-0.01	0.996	0.00 (0.00 - Inf)
NRS										
0					Ref					Ref
1	0.40	0.24	1.68	0.093	1.49 (0.94 - 2.36)	0.98	0.36	2.74	**0.006**	2.66 (1.32 - 5.37)

Bold values: P value<0.05.

Supplementary Figure S2, and these cytokines are mainly located on the cell membrane Supplementary Figure S3.

PPI network construction and correlation analysis

Seventy-three targets involved in the interaction pathway between cytokines and cytokine receptors were imported into the string database, with Homo sapiens selected as the sample. The correlation coefficient was found to be 0.900. Subsequently, the MCC algorithm of the cytoHubba plug-in within the Cytoscape 3.8.2 software was utilized to identify the top 10 core targets. The analysis revealed that CXCL10, CCR2, CXCL9, CCR5, CXCL12, CXCL11, CXCR4, CCR1, CXCL13, and CCL5 were identified as the core top 10 targets Figure 4C. Correlation analysis between 10 hub targets indicated that there was a significant up-regulation relationship among the 10 factors Figure 4D.

Survival analysis

To elucidate the potential association between 10 cytokines and survival in non-small cell lung cancer (NSCLC), a survival analysis was conducted utilizing data from the large-sample The Cancer Genome Atlas (TCGA) database, specifically focusing on the LUSC and LUAD subtypes. The findings revealed a significant correlation between high expression levels of CCR1 and CXCL12 in LUSC and poorer overall survival (OS) outcomes, Figures 4G, H, while in LUAD, high expression levels of CCR2 and CXCR4 were associated with improved OS Figures 4E, F. Additional corhorts from GSE14814, GSE73403 and GSE157010 indicated that high expression of CXCL12 showed potential significant difference correlation with poor prognosis of OS, and significant difference correlation with poor disease-free survival in GSE14814. Supplementary Figure S4.

Tumor immune dysfunction and exclusion (TIDE) algorithm

To elucidate the impact of elevated levels of CCR1, CXCL12, CCR2, and CCR4 on the effectiveness of ICIs in the treatment of lung cancer, the TIDE algorithm was employed for predictive purposes. Figure 5A. The findings indicate that heightened CXCL12 expression is associated with diminished efficacy of immunotherapy in LUSC. Conversely, CCR1, CCR2, and CCR4 levels do not appear to influence the response to ICIs.

Correlation analysis between survival related CRPGs, immune cells, and inflammatory pathways

In order to gain further insight into the potential effects of CXCL12 on immune cell populations, the CIBERSORT algorithm and Pearson correlation analysis were utilized. CXCL12 can significantly up-regulate the expression of macrophages, monocyte cells and T cell regulatory (Tregs), and down-regulate CD8+ T cells and NK cells Figure 5B. CXCL12 significantly up-regulates inflammatory response pathways and tumor inflammation characteristic pathways Figures 5C, D.

ELISA assay

35 patients with cancer pain were prospectively enrolled, all of whom had NRS scores recorded at baseline. Following cancer pain treatment, there was a significant decrease in NRS scores Figure 6A. ELISA detection revealed a significant decrease in serum CXCL12 levels after pain relief Figure 6B.

Discussion

Pain is among the most frequently reported symptoms in individuals diagnosed with cancer (5). A recent systematic review, encompassing studies conducted between 2014 and 2021, determined the overall prevalence of pain in cancer patients to be 44.5%. Furthermore, 30.6% of these patients experienced moderate to severe pain (1). Cancer-related pain (CRP) is consistently linked to a diminished quality of life, attributable to psychological distress and impaired functioning (30). Several studies have suggested that inadequately managed pain may adversely affect survival rates in cancer patients (31, 32). The influence of pain on the effectiveness of immunotherapy remains a subject of debate in contemporary research. A retrospective study by Huan Zhou and colleagues indicated that baseline cancer pain serves as a negative prognostic indicator for lung cancer patients undergoing immunotherapy. Specifically, patients experiencing baseline cancer pain may exhibit poorer survival outcomes if they subsequently develop breakthrough pain (33).

CRP is hypothesized to be partially induced by tissue damage and inflammation within the tumor microenvironment (TME) through mechanisms that are not yet fully understood. Growing evidence indicates that the pathophysiology of chronic pain involves a complex interaction between the nervous and immune systems (34). Circulating immune cells, including neutrophils, monocytes, and T cells, are recruited to sites of tissue damage or inflammation and frequently infiltrate both the peripheral and central nervous systems (35, 36). The activation of these cells leads to the expression of a range of inflammatory mediators, such as cytokines, chemokines, lipids, and proteases. These mediators exert direct effects on peripheral sensory neurons and central second-order neurons, as well as indirect effects on other immune or local cells, thereby modulating pain.

Inflammation and cell-mediated immune function have been identified as factors associated with the efficacy of PD-1 blockade therapies (37, 38). Our study demonstrates that patients exhibiting elevated levels of the Platelet-Lymphocyte Ratio (PLR), Derived

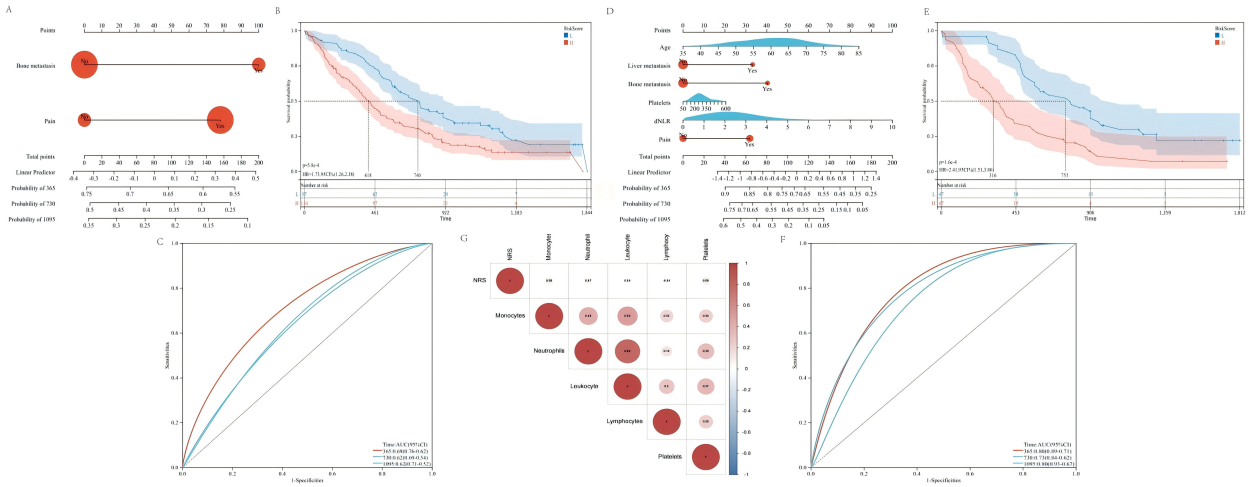

FIGURE 2
Cox regression analysis and correlation analysis indicated that baseline pain was the independent prognostic factor for ICIs treatment. **(A)** Nomogram construction based on bone metastasis and pain before PSM. **(B)** KM survival analysis showed that the prognosis of low risk patients better than high risk patients (HR=1.73, 95%CI: 1.26-2.38, p=5.8e-4). **(C)** The AUC under the ROC curve with 1 year 0.69, 3 year 0.62 and 5year 0.62. **(D)** Nomogram construction based on age, liver metastasis, bone metastasis, platelets, dNLR and pain after PSM. **(E)** KM survival analysis showed that the prognosis of low risk patients better than high risk patients (HR=2.41, 95%CI: 1.51-3.86, p=1.6e-4). **(F)** The AUC under the ROC curve with 1 year 0.80, 3 year 0.73 and 5year 0.80. **(G)** Correlation analysis showed that NRS score was positively correlated with monocytes, neutrophils, leukocytes and platelets, and negatively correlated with lymphocytes.

Neutrophil-Lymphocyte Ratio (dNLR), Systemic Inflammation Index (SII), and bone metastasis experience reduced efficacy of immunotherapy, both prior to and following Propensity Score Matching (PSM). The activation of neutrophils results in the upregulation of various proteins, including damage-associated molecular patterns (DAMPs), chemokines, and cytokines, such as vascular endothelial growth factor (VEGF), which contribute to enhanced tumor angiogenesis and the facilitation of distant metastasis (39). Furthermore, neutrophils can undergo degranulation, a process during which molecules such as defensins, myeloperoxidase, and lysozyme are secreted from intracellular granules into the extracellular environment, leading to tissue damage and promoting tumor metastasis (40, 41). Importantly, neutrophils can exhibit an immunosuppressive function in cancer, facilitating tumor progression primarily by inhibiting the recruitment of other immune cells to the tumor microenvironment (TME). Specifically, neutrophils are capable of releasing reactive oxygen species (ROS) (42), and enzymes such as arginase 1, which suppress the T-cell response within the TME. Notably, the secretion of interleukin-8 (IL-8) by cancer cells can stimulate neutrophils to release arginase into the TME (43). This enzyme degrades extracellular arginine, a crucial amino acid for T-cell activation and proliferation (44), thereby inhibiting the T-cell response.

In addition to the role of neutrophils, platelets typically exert a negative regulatory influence on immune checkpoint inhibitors (ICIs) therapy. Platelets facilitate the survival and proliferation of tumor cells through the secretion of various cytokines, including vascular endothelial growth factor (VEGF), transforming growth factor-β (TGF-β), and platelet-derived growth factor (PDGF) (45).Furthermore, chemokines associated with platelets have the capacity to modulate immune responses within the tumor microenvironment and influence tumor angiogenesis (46). Activated platelets are capable of engaging in both direct and mediated binding interactions with cancer cells. For instance, direct binding can occur between platelet P-selectin and cancer cell CD44. Additionally, fibrinogen can mediate binding between platelet GPIIb-IIIa and integrin αVβ3 on both cancer cells and cancer-associated angiogenic endothelial cells. Furthermore, von Willebrand factor can facilitate binding between platelet GPIbα and GPIbα-like motifs on cancer cells (47–51). These interactions enable activated platelets to effectively "cloak" cancer cells, thereby shielding them from immune surveillance within the circulatory system (49, 52, 53).

The effectiveness of immune checkpoint inhibitors (ICIs) is intricately linked to both the function and quantity of lymphocytes, particularly CD8+ T cells. These CD8+ T cells serve as the primary effector cells capable of infiltrating the tumor microenvironment of immunogenic tumors, thereby augmenting the therapeutic response to ICIs (54). Furthermore, various cytokines secreted by lymphocytes, including interferon-gamma (IFN-γ) and tumor necrosis factor-alpha (TNF-α), contribute to tumor suppression and extend the survival of cancer patients (55).

In addition to the involvement of peripheral blood inflammatory cells, our findings indicate that bone metastases significantly contribute to the limited efficacy of immune checkpoint inhibitors (ICIs) treatment. The skeletal system is frequently affected during metastatic progression, resulting in bone-related complications such

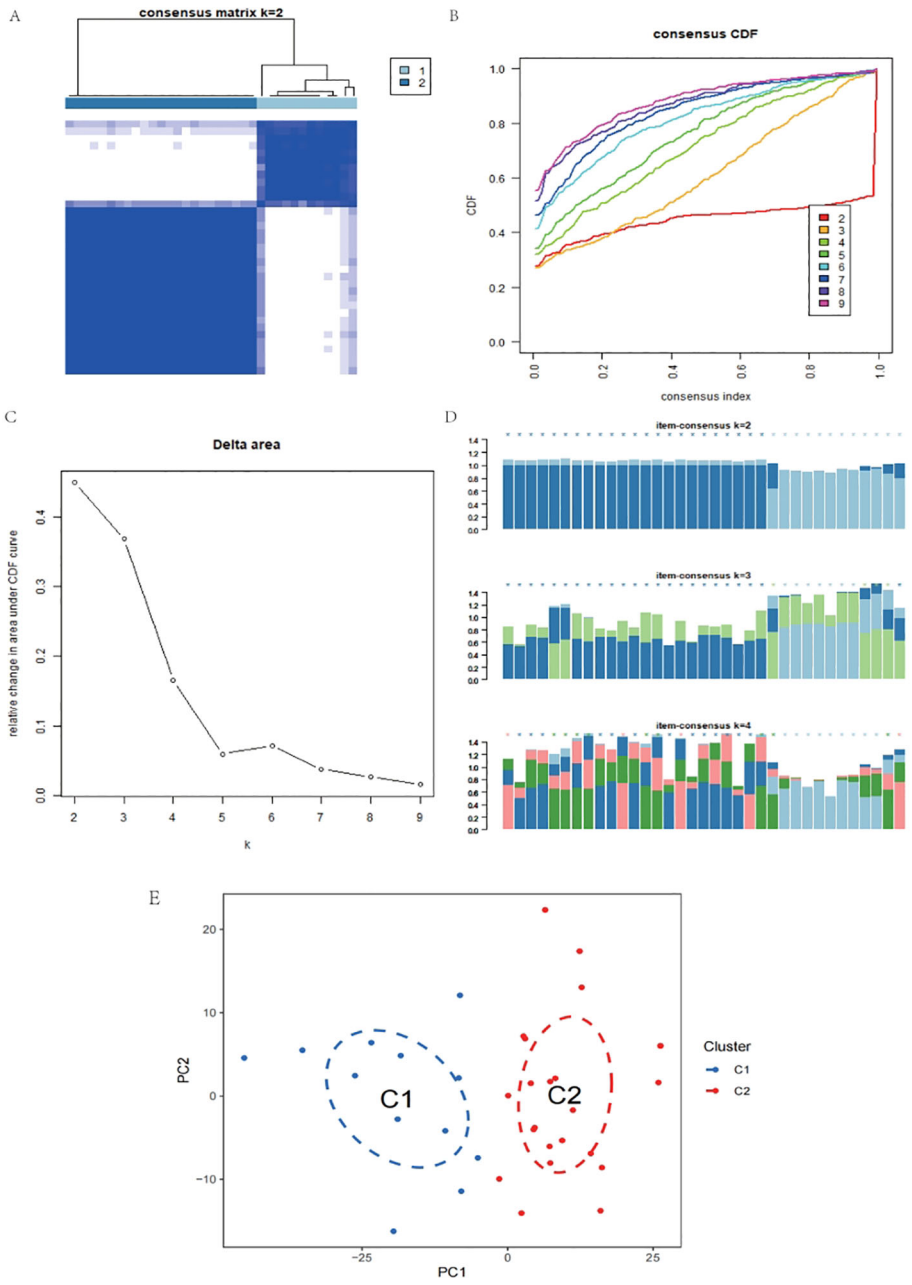

FIGURE 3
Consistency cluster analysis and principal component analysis. **(A)** When consensus matrix k=2, the samples were divided into two modules. **(B, C)** When consensus matrix k=2, the internal consistency performed best. **(D)** When consensus matrix k=2, consensus scores of all samples were displayed. **(E)** Principal component analysis indicated that when consensus matrix k=2, the samples can be well distinguished.

as severe pain, pathological fractures, and hypercalcemia, all of which substantially diminish patients' quality of life (56). Furthermore, the bone microenvironment is characterized by a distinct immunosuppressive milieu (57). Notably, bone marrow-derived suppressor cells (MDSCs) have been implicated in the suboptimal therapeutic outcomes associated with ICIs (58). MDSCs have the capacity to impede the anti-tumor activities of CD8+ T cells and NK cells, thereby exerting a detrimental influence on immune regulation.

Although it was clear in retrospective analysis that pain will lead to poor curative effect of ICIs, the key molecules and mechanisms that played a role were still unclear. We found that CXCL12 played an important role in this process. Through GEO data set, we identified CXCL12, a pain-related core target in patients receiving ICIs treatment. Studies have shown that the activation of CXCL12/CXCR4 signaling pathway can up-regulate the phosphorylation of extracellular signal regulated kinase (ERK) in spinal cord or the

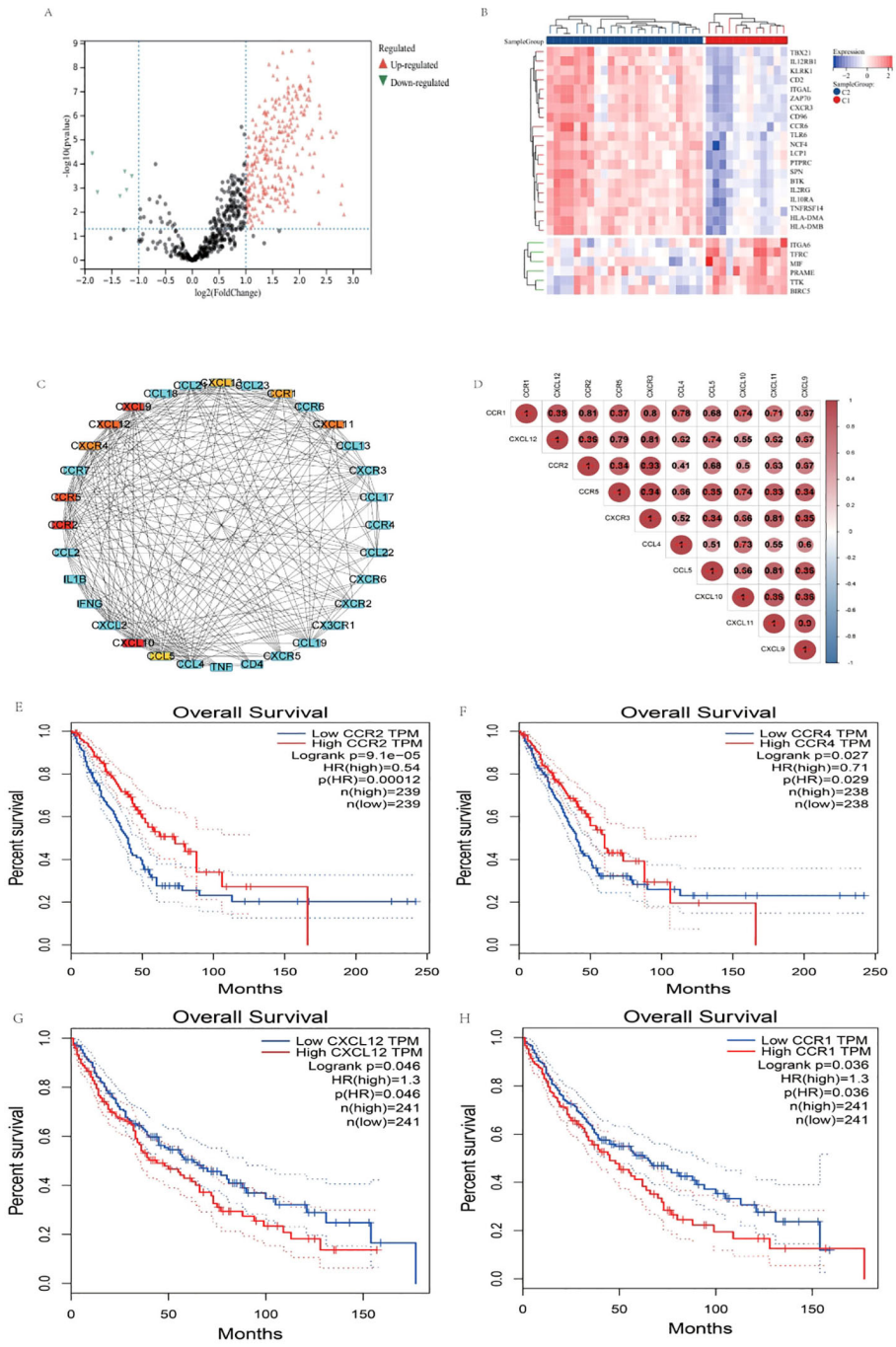

FIGURE 4
Differential expression analysis and survival analysis. **(A)** Volcanic map, red stands for up-regulation and green stands for down-regulation. **(B)** Heat map, red stands for up-regulation and blue stands for down-regulation. **(C)** MCC algorithm identified CXCL10, CCR2, CXCL9, CCR5, CXCL12, CXCL11, CXCR4, CCR1, CXCL13, and CCL5 hub 10 core targets. **(D)** Correlation analysis between 10 hub core targets. **(E)** OS of CCR2 in LUAD. **(F)** OS of CCR4 in LUAD. **(G)** OS of CXCL12 in LUSC. **(H)** OS of CCR1 in LUSC.

phosphorylation and expression level of sodium channel Nav1.8 in DRG, and activate neurons to generate excitement, thus causing chronic pain (59, 60). However, the specific inhibition of CXCL12/CXCR4 signal pathway or the expression of its upstream and downstream channels can inhibit pain sensitization. The activation of CXCL12/CXCR4 axis also plays an important role in the formation of cancer pain. The strong interaction between signal transducer and activator of transcription 3 (STAT3) and p300 leads to the high expression of CXCL12 in dorsal horn neurons, which leads to neuropathic pain induced by anti-tubulin chemotherapy

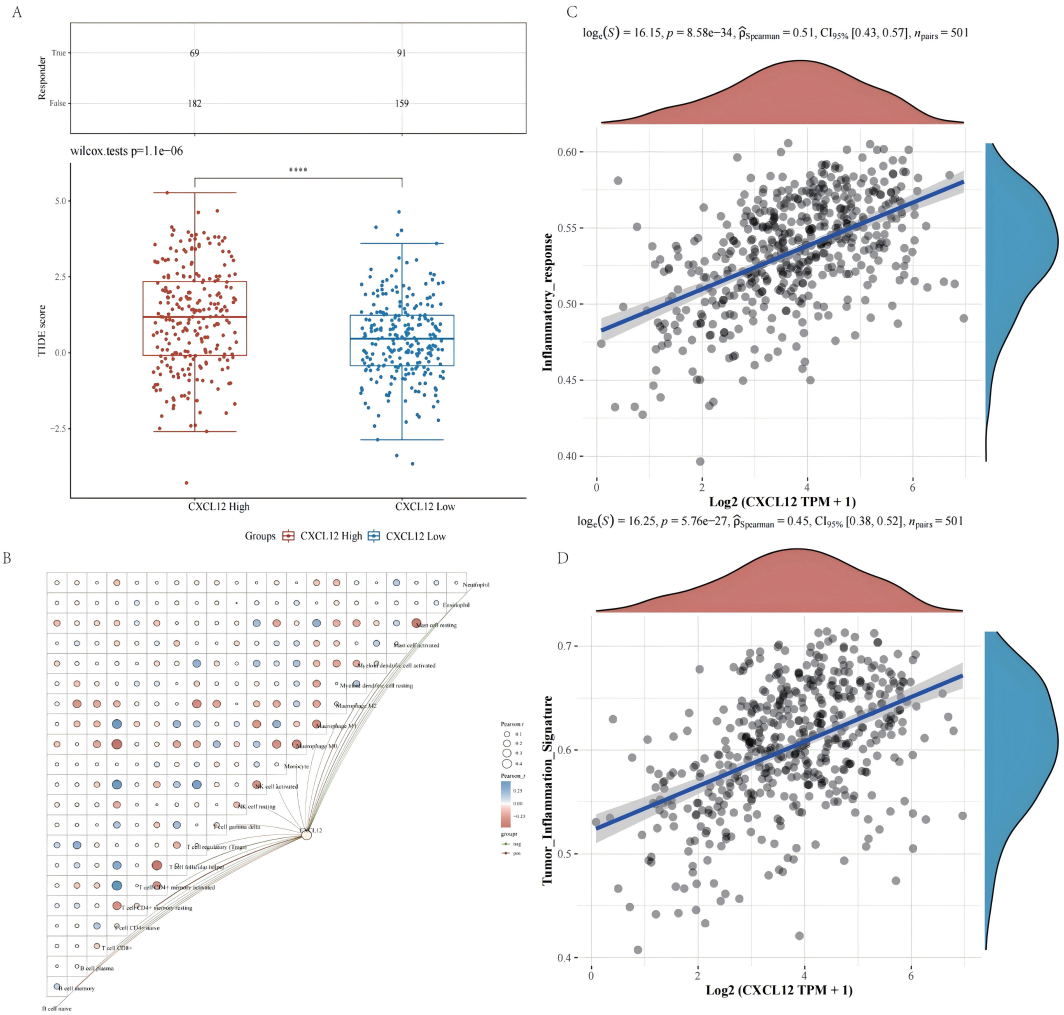

FIGURE 5
Efficacy evaluation of ICIs treatment and correlation analysis between CXCL12, immune cells, and inflammatory pathways. **(A)** Tumor immune dysfunction and exclusion algorithm indicated that high expression of CXCL12 was insensitivity to ICIs treatment. **(B)** CXCL12 can significantly up-regulate the expression of macrophages, monocyte cells and Tregs, and down-regulate CD8+ T cells and NK cells. **(C, D)** CXCL12 can significantly up-regulates inflammatory response pathway and tumor inflammation characteristic pathway.

drugs (such as paclitaxel) (61). CXCL12/CXCR4 signaling pathway activates sensitized neurons, astrocytes and microglia through mitogen-activated protein kinase (MAPK), promotes the release of inflammatory factors, such as IL(interleukin) and TNF, and causes persistent bone cancer pain (62).

Further using TCGA data set, it was found that the prognosis of patients with high expression of CXCL12 in LUSC was significantly worse than that of patients with low expression. CXCL12 promotes tumor angiogenesis by targeting vascular endothelial cells and cooperating with vascular endothelial growth factor (VEGF) (63), and also promotes tumor cell proliferation and survival (64, 65). In addition, CXCL12-CXCR4 signaling pathway is involved in the invasion and metastasis of cancer cells. In many retrospective studies, it was found that CXCR4 is the most widely expressed chemokine receptor in tumor cells, which is responsible for the metastasis of tumor cells to lung, liver and bone marrow, which are the most common metastasis destinations in many cancers (66). On the other hand, CXCL12 has immunosuppressive effect, which will reduce the efficacy of ICIs. CXCL 12/CXCR 4 axis can regulate the recruitment of specific immune cells in TME, and drive the immune cells expressing CXCR 4 to polarize toward immunosuppression phenotype. Previous evidence shows that CXCL12 mediates plasma cell-like DC transport to tumor and Treg cells homing to bone marrow microenvironment (67); In addition, it stimulates antigen-specific T lymphocytes and macrophages to express pro-angiogenic factors by mediating the polarization of T cells to Treg (68, 69) and producing DC with poor function (70).

In melanoma mouse model, high levels of CXCL12 can repel T effector cells expressing CXCR4 (71), limiting their infiltration and killing of tumor cells (72, 73). In clinical specimens, cancer cells in breast, colorectal, and breast cancer appear to be surrounded by CXCL12-KRT19 heterodimers, potentially making them resistant to

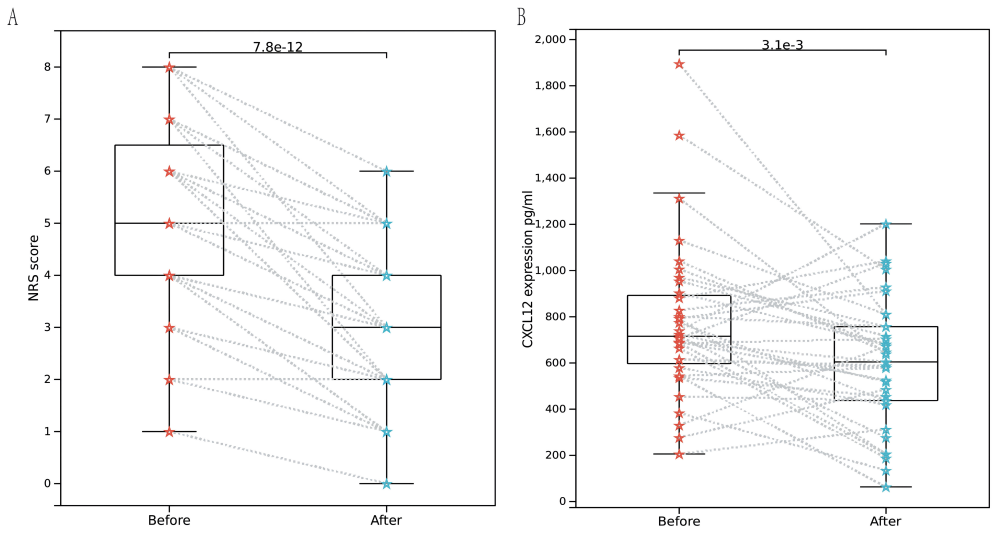

FIGURE 6
Enzyme-linked immunosorbent assay. **(A)** Rank sum test of NRS scores between baseline pain and pain relieved among 35 patients. **(B)** Rank sum test of NRS scores between baseline pain and pain relieved among 35 patients indicated that CXCL12 significantly decreased with p value of 3.1e-3.

immunotherapy (74). A study found that T cells' movement may be affected by CXCL12 dimer inhibiting F-actin polymerization (75). Tumor-related lymphatic vessels control CD8+ T cell migration through CXCL12, and accumulating antigen-specific CD8+ T cells in tumors was crucial for effective immunotherapy (76).

Conclusion

Baseline pain was identified as an independent prognostic risk factor for the diminished efficacy of ICIs in the treatment of NSCLC. Baseline pain has the potential to inhibit the tumor immune micro-environment by increasing the presence of inflammatory cells in the peripheral blood cell counts, specifically neutrophils and monocytes, ultimately leading to reduced responsiveness to ICIs. The chemokine CXCL12 was implicated in both pain modulation and immune regulation, with its up-regulation further contributing to the presence of inflammatory cells in the peripheral blood cell counts, such as monocytes and macrophages, while simultaneously suppressing the activity of NK cells and CD8+ T cells. This phenomenon results in suboptimal therapeutic outcomes with ICIs, particularly in patients with LUSC. However, this study also has some limitations. First, the conclusions based on retrospective analysis were weak in terms of evidence level. Secondly, there are many variables included in this study, but the sample size is relatively insufficient.

Data availability statement

The original contributions presented in the study are included in the article/Supplementary Material. Further inquiries can be directed to the corresponding authors.

Ethics statement

The studies involving humans were approved by Ethics Committee of Guangdong Provincial Hospital of Chinese Medicine. The studies were conducted in accordance with the local legislation and institutional requirements. The participants provided their written informed consent to participate in this study.

Author contributions

ZZ: Conceptualization, Methodology, Writing – original draft. WZ: Investigation, Methodology, Writing – original draft. CL: Writing – original draft. ZW: Writing – original draft. WL: Investigation, Writing – original draft. XC: Investigation, Writing – original draft. YY: Investigation, Writing – original draft. ZX: Investigation, Writing – original draft. YH: Writing – review & editing. HZ: Writing – review & editing.

Funding

The author(s) declare financial support was received for the research, authorship, and/or publication of this article. This work was funded by the National Key Research and Development Program of China (2023YFC3503303), the National Natural Science Foundation of China (NSFC, grant number 82004447), the Major Innovation Technology Construction Project of Synergistic Chinese Medicine and Western Medicine of Guangzhou (grant number 2023-2318), Guangzhou Municipal Science and Technology Bureau, China (grant number 2024A03J0730 and 2023A04J0452) and The Project of

Guangdong Provincial Key Laboratory of Clinical Research on Traditional Chinese Medicine Syndrome (grant number YN2023ZH03).

Conflict of interest

The authors declare that the research was conducted in the absence of any commercial or financial relationships that could be construed as a potential conflict of interest.

Publisher's note

Supplementary material

The Supplementary Material for this article can be found online at: https://www.frontiersin.org/articles/10.3389/fimmu.2024.1456150/full#supplementary-material

SUPPLEMENTARY FIGURE 1
Differential analysis of Risk scores. **(A)** Bone metastasis before PSM. **(B)** Pain before PSM. **(E)** Bone metastasis after PSM. **(D)** Pain after PSM. **(E)** Age after PSM. **(F)** dNLR after PSM.

SUPPLEMENTARY FIGURE 2
KEGG functional enrichment analysis of 420 DEGs showed that the interaction between cytokines and cytokine receptors was the main signaling pathway that mediates pain.

SUPPLEMENTARY FIGURE 3
GO functional enrichment analysis of 420 DEGs showed that these cytokines were mainly located on the cell membrane. They were closely related to biological processes like immune system processes and molecular functions like signaling receptor activity.

SUPPLEMENTARY FIGURE 4
Survival analysis of CXCL12 in external cohorts. **(A)** OS in GSE14814. **(B)** DFS in GSE14814. **(C)** OS in GSE73403. **(D)** OS in 157010.

References

1. Snijders RAH, Brom L, Theunissen M. Update on prevalence of pain in patients with cancer 2022: A systematic literature review and meta-analysis. (2023) 15:591. doi: 10.3390/cancers15030591

2. Kroenke K, Theobald D, Wu J, Loza JK, Carpenter JS, Tu W. The association of depression and pain with health-related quality of life, disability, and health care use in cancer patients. *J Pain Symptom Manage*. (2010) 40:327–41. doi: 10.1016/j.jpainsymman.2009.12.023

3. Ośmiałowska E, Misiąg W. Coping strategies, pain, and quality of life in patients with breast cancer. (2021) 10:4469. doi: 10.3390/jcm10194469

4. Lin CC, Lai YL, Ward SE. Effect of cancer pain on performance status, mood states, and level of hope among Taiwanese cancer patients. *J Pain Symptom Manage*. (2003) 25:29–37. doi: 10.1016/S0885-3924(02)00542-0

5. van den Beuken-van Everdingen MH, Hochstenbach LM, Joosten EA, Tjan-Heijnen VC, Janssen DJ. Update on prevalence of pain in patients with cancer: systematic review and meta-analysis. *J Pain Symptom Manage*. (2016) 51:1070–1090.e1079. doi: 10.1016/j.jpainsymman.2015.12.340

6. Neufeld NJ, Elnahal SM, Alvarez RH. Cancer pain: a review of epidemiology, clinical quality and value impact. *Future Oncol*. (2017) 13:833–41. doi: 10.2217/fon-2016-0423

7. Chen M, Yu H, Yang L, Yang H, Cao H, Lei L, et al. Combined early palliative care for non-small-cell lung cancer patients: a randomized controlled trial in Chongqing, China. *Front Oncol*. (2023) 13:1184961. doi: 10.3389/fonc.2023.1184961

8. Wu Y, Zou Q. Tumor-host cometabolism collaborates to shape cancer immunity. *Cancer Discov*. (2024) 14:653–7. doi: 10.1158/2159-8290.CD-23-1509

9. Bardhan K, Anagnostou T, Boussiotis VA. The PD1:PD-L1/2 pathway from discovery to clinical implementation. *Front Immunol*. (2016) 7:550. doi: 10.3389/fimmu.2016.00550

10. Ma J, Wu Y. A blueprint for tumor-infiltrating B cells across human cancers. (2024) 384:. doi: 10.1126/science.adj4857

11. Wu Y, Ma J, Yang X, Nan F, Zhang T, Ji S, et al. Neutrophil profiling illuminates anti-tumor antigen-presenting potency. *Cell*. (2024) 187:1422–1439.e1424. doi: 10.1016/j.cell.2024.02.005

12. Garon EB, Hellmann MD, Rizvi NA, Carcereny E, Leighl NB, Ahn MJ, et al. Five-year overall survival for patients with advanced non-Small-cell lung cancer treated with pembrolizumab: results from the phase I KEYNOTE-001 study. *J Clin Oncol*. (2019) 37:2518–27. doi: 10.1200/JCO.19.00934

13. Topalian SL, Hodi FS, Brahmer JR, Gettinger SN, Smith DC, McDermott DF, et al. Five-year survival and correlates among patients with advanced melanoma, renal cell carcinoma, or non-small cell lung cancer treated with nivolumab. *JAMA Oncol*. (2019) 5:1411–20. doi: 10.1001/jamaoncol.2019.2187

14. Reck M, Rodríguez-Abreu D, Robinson AG, Hui R, Csőszi T, Fülöp A, et al. Pembrolizumab versus chemotherapy for PD-L1-positive non-small-cell lung cancer. *N Engl J Med*. (2016) 375:1823–33. doi: 10.1056/NEJMoa1606774

15. Xiao Q, Yu X, Shuai Z, Yao T, Yang X, Zhang Y. The influence of baseline characteristics on the efficacy of immune checkpoint inhibitors for advanced lung cancer: A systematic review and meta-analysis. *Front Pharmacol*. (2022) 13:956788. doi: 10.3389/fphar.2022.956788

16. Herndon JE 2nd, Fleishman S, Kornblith AB, Kosty M, Green MR, Holland J. Is quality of life predictive of the survival of patients with advanced nonsmall cell lung carcinoma? *Cancer*. (1999) 85:333–40. doi: 10.1002/(sici)1097-0142(19990115)85:2<333::aid-cncr10>3.0.co;2-q

17. Efficace F, Bottomley A, Smit EF, Lianes P, Legrand C, Debruyne C, et al. Is a patient's self-reported health-related quality of life a prognostic factor for survival in non-small-cell lung cancer patients? A multivariate analysis of prognostic factors of EORTC study 08975. *Ann Oncol*. (2006) 17:1698–704. doi: 10.1093/annonc/mdl183

18. Smeester BA, Al-Gizawiy M, Beitz AJ. Effects of different electroacupuncture scheduling regimens on murine bone tumor-induced hyperalgesia: sex differences and role of inflammation. *Evid Based Complement Alternat Med*. (2012) 2012:671386. doi: 10.1155/2012/671386

19. Bali KK, Kuner R. Therapeutic potential for leukocyte elastase in chronic pain states harboring a neuropathic component. *Pain*. (2017) 158:2243–58. doi: 10.1097/j.pain.0000000000001032

20. Takakura K, Ito Z, Suka M, Kanai T, Matsumoto Y, Odahara S, et al. Comprehensive assessment of the prognosis of pancreatic cancer: peripheral blood neutrophil-lymphocyte ratio and immunohistochemical analyses of the tumour site. *Scand J Gastroenterol*. (2016) 51:610–7. doi: 10.3109/00365521.2015.1121515

21. Andrews MC, Reuben A, Gopalakrishnan V, Wargo JA. Concepts collide: genomic, immune, and microbial influences on the tumor microenvironment and response to cancer therapy. *Front Immunol*. (2018) 9:946. doi: 10.3389/fimmu.2018.00946

22. Cupp MA, Cariolou M, Tzoulaki I, Aune D, Evangelou E, Berlanga-Taylor AJ. Neutrophil to lymphocyte ratio and cancer prognosis: an umbrella review of systematic reviews and meta-analyses of observational studies. *BMC Med*. (2020) 18:360. doi: 10.1186/s12916-020-01817-1

23. Valero C, Lee M, Hoen D, Weiss K, Kelly DW, Adusumilli PS. Pretreatment neutrophil-to-lymphocyte ratio and mutational burden as biomarkers of tumor response to immune checkpoint inhibitors. *Nat Commun*. (2021) 12:729. doi: 10.1038/s41467-021-20935-9

24. Kargl J, Busch SE, Yang GH, Kim KH, Hanke ML, Metz HE, et al. Neutrophils dominate the immune cell composition in non-small cell lung cancer. *Nat Commun*. (2017) 8:14381. doi: 10.1038/ncomms14381

25. Kargl J, Zhu X, Zhang H, Yang GHY, Friesen TJ, Shipley M, et al. Neutrophil content predicts lymphocyte depletion and anti-PD1 treatment failure in NSCLC. *JCI Insight*. (2019) 4. doi: 10.1172/jci.insight.130850

26. Wu M, Zhu A, Shen L. Pancreatic cancer-related pain: mechanism and management. *J Pancreatol*. (2023) 6:202–9. doi: 10.1097/JP9.0000000000000140

27. Balood M, Ahmadi M, Eichwald T, Ahmadi A, Majdoubi A, Roversi K, et al. Nociceptor neurons affect cancer immunosurveillance. *Nature*. (2022) 611:405–12. doi: 10.1038/s41586-022-05374-w

28. Chen W, Teo JMN, Yau SW, Wong MY, Lok CN, Che CM, et al. Chronic type I interferon signaling promotes lipid-peroxidation-driven terminal CD8(+) T cell exhaustion and curtails anti-PD-1 efficacy. *Cell Rep*. (2022) 41:111647. doi: 10.1016/j.celrep.2022.111647

29. Prat A, Navarro A, Paré L, Reguart N, Galván P, Pascual T, et al. Immune-related gene expression profiling after PD-1 blockade in non-small cell lung carcinoma, head and neck squamous cell carcinoma, and melanoma. *Cancer Res*. (2017) 77:3540–50. doi: 10.1158/0008-5472.CAN-16-3556

30. Bennett MI, Kaasa S, Barke A, Korwisi B, Rief W, Treede RD. The IASP classification of chronic pain for ICD-11: chronic cancer-related pain. *Pain*. (2019) 160:38–44. doi: 10.1097/j.pain.0000000000001363

31. Boland JW, Allgar V, Boland EG, Bennett MI, Kaasa S, Hjermstad MJ, et al. The relationship between pain, analgesics and survival in patients with advanced cancer; a secondary data analysis of the international European palliative care Cancer symptom study. *Eur J Clin Pharmacol*. (2020) 76:393–402. doi: 10.1007/s00228-019-02801-2

32. De Groef A, Evenepoel M, Van Dijck S, Dams L, Haenen V, Wiles L, et al. Feasibility and pilot testing of a personalized eHealth intervention for pain science education and self-management for breast cancer survivors with persistent pain: a mixed-method study. *Support Care Cancer*. (2023) 31:119. doi: 10.1007/s00520-022-07557-7

33. Zhou H, Wei J, Sun W, Song Z. Effect of baseline cancer pain on the efficacy of immunotherapy in lung cancer patients. *J Thorac Dis*. (2023) 15:4314–23. doi: 10.21037/jtd-23-375

34. Ji RR, Chamessian A, Zhang YQ. Pain regulation by non-neuronal cells and inflammation. *Science*. (2016) 354:572–7. doi: 10.1126/science.aaf8924

35. Kavelaars A, Heijnen CJ. Immune regulation of pain: Friend and foe. *Sci Transl Med*. (2021) 13:. doi: 10.1126/scitranslmed.abj7152

36. Scholz J, Woolf CJ. The neuropathic pain triad: neurons, immune cells and glia. *Nat Neurosci*. (2007) 10:1361–8. doi: 10.1038/nn1992

37. Kumagai S, Togashi Y. The PD-1 expression balance between effector and regulatory T cells predicts the clinical efficacy of PD-1 blockade therapies. *Nat Immunol*. (2020) 21:1346–58. doi: 10.1038/s41590-020-0769-3

38. Liu CH, Chen Z. Lipopolysaccharide-mediated chronic inflammation promotes tobacco carcinogen-induced lung cancer and determines the efficacy of immunotherapy. *Cancer Res*. (2021) 81:144–57. doi: 10.1158/0008-5472.CAN-20-1994

39. Dvorak HF. Tumor stroma, tumor blood vessels, and antiangiogenesis therapy. *Cancer J*. (2015) 21:237–43. doi: 10.1097/PPO.0000000000000124

40. Paludan SR, Mogensen TH. Innate immunological pathways in COVID-19 pathogenesis. *Sci Immunol*. (2022) 7:. doi: 10.1126/sciimmunol.abm5505

41. Cavalcante-Silva LHA, Carvalho DCM, Lima ÉA, Galvão J, da Silva JSF, Sales-Neto JM, et al. Neutrophils and COVID-19: The road so far. *Int Immunopharmacol*. (2021) 90:107233. doi: 10.1016/j.intimp.2020.107233

42. Güngör N, Knaapen AM, Munnia A, Peluso M, Haenen GR, Chiu RK, et al. Genotoxic effects of neutrophils and hypochlorous acid. *Mutagenesis*. (2010) 25:149–54. doi: 10.1093/mutage/gep053

43. Rotondo R, Barisione G, Mastracci L, Grossi F, Orengo AM, Costa R, et al. IL-8 induces exocytosis of arginase 1 by neutrophil polymorphonuclears in nonsmall cell lung cancer. *Int J Cancer*. (2009) 125:887–93. doi: 10.1002/ijc.v125:4

44. Yachimovich-Cohen N, Even-Ram S, Shufaro Y, Rachmilewitz J, Reubinoff B. Human embryonic stem cells suppress T cell responses via arginase I-dependent mechanism. *J Immunol*. (2010) 184:1300–8. doi: 10.4049/jimmunol.0804261

45. Bambace NM, Holmes CE. The platelet contribution to cancer progression. *J Thromb Haemost*. (2011) 9:237–49. doi: 10.1111/j.1538-7836.2010.04131.x

46. el-Hag A, Clark RA. Immunosuppression by activated human neutrophils. Dependence on the myeloperoxidase system. *J Immunol*. (1987) 139:2406–13. doi: 10.4049/jimmunol.139.7.2406

47. Konstantopoulos K, Thomas SN. Cancer cells in transit: the vascular interactions of tumor cells. *Annu Rev BioMed Eng*. (2009) 11:177–202. doi: 10.1146/annurev-bioeng-061008-124949

48. Labelle M, Begum S, Hynes RO. Direct signaling between platelets and cancer cells induces an epithelial-mesenchymal-like transition and promotes metastasis. *Cancer Cell*. (2011) 20:576–90. doi: 10.1016/j.ccr.2011.09.009

49. Palumbo JS, Talmage KE, Massari JV, La Jeunesse CM, Flick MJ, Kombrinck KW, et al. Platelets and fibrin(ogen) increase metastatic potential by impeding natural killer cell-mediated elimination of tumor cells. *Blood*. (2005) 105:178–85. doi: 10.1182/blood-2004-06-2272

50. Coupland LA, Chong BH, Parish CR. Platelets and P-selectin control tumor cell metastasis in an organ-specific manner and independently of NK cells. *Cancer Res*. (2012) 72:4662–71. doi: 10.1158/0008-5472.CAN-11-4010

51. Suter CM, Hogg PJ, Price JT, Chong BH, Ward RL. Identification and characterisation of a platelet GPIb/V/IX-like complex on human breast cancers: implications for the metastatic process. *Jpn J Cancer Res*. (2001) 92:1082–92. doi: 10.1111/j.1349-7006.2001.tb01063.x

52. Trikha M, Zhou Z, Timar J, Raso E, Kennel M, Emmell E, et al. Multiple roles for platelet GPIIb/IIIa and alphavbeta3 integrins in tumor growth, angiogenesis, and metastasis. *Cancer Res*. (2002) 62:2824–33.

53. Gay LJ, Felding-Habermann B. Contribution of platelets to tumour metastasis. *Nat Rev Cancer*. (2011) 11:123–34. doi: 10.1038/nrc3004

54. Farhood B, Najafi M, Mortezaee K. CD8(+) cytotoxic T lymphocytes in cancer immunotherapy: A review. *J Cell Physiol*. (2019) 234:8509–21. doi: 10.1002/jcp.v234.6

55. Kou J, Huang J, Li J, Wu Z, Ni L. Systemic immune-inflammation index predicts prognosis and responsiveness to immunotherapy in cancer patients: a systematic review and meta–analysis. *Clin Exp Med*. (2023) 23:3895–905. doi: 10.1007/s10238-023-01035-y

56. Coleman RE. Metastatic bone disease: clinical features, pathophysiology and treatment strategies. *Cancer Treat Rev*. (2001) 27:165–76. doi: 10.1053/ctrv.2000.0210

57. Del Conte A, De Carlo E, Bertoli E, Stanzione B. Bone metastasis and immune checkpoint inhibitors in non-small cell lung cancer (NSCLC): microenvironment and possible clinical implications. (2022) 23:6832. doi: 10.3390/ijms23126832

58. Zhao E, Xu H, Wang L, Kryczek I, Wu K, Hu Y, et al. Bone marrow and the control of immunity. *Cell Mol Immunol*. (2012) 9:11–9. doi: 10.1038/cmi.2011.47

59. Bai L, Wang X, Li Z, Kong C, Zhao Y, Qian JL, et al. Upregulation of chemokine CXCL12 in the dorsal root ganglia and spinal cord contributes to the development and maintenance of neuropathic pain following spared nerve injury in rats. *Neurosci Bull*. (2016) 32:27–40. doi: 10.1007/s12264-015-0007-4

60. Jayaraj ND, Bhattacharyya BJ, Belmadani AA, Ren D, Rathwell CA, Hackelberg S, et al. Reducing CXCR4-mediated nociceptor hyperexcitability reverses painful diabetic neuropathy. *J Clin Invest*. (2018) 128:2205–25. doi: 10.1172/JCI92117

61. Xu T, Zhang XL, Ou-Yang HD, Li ZY, Liu CC, Huang ZZ, et al. Epigenetic upregulation of CXCL12 expression mediates antitubulin chemotherapeutics-induced neuropathic pain. *Pain*. (2017) 158:637–48. doi: 10.1097/j.pain.0000000000000805

62. Shen W, Hu XM, Liu YN, Han Y, Chen LP, Wang CC, et al. CXCL12 in astrocytes contributes to bone cancer pain through CXCR4-mediated neuronal sensitization and glial activation in rat spinal cord. *J Neuroinflamm*. (2014) 11:75. doi: 10.1186/1742-2094-11-75

63. Kryczek I, Lange A, Mottram P, Alvarez X, Cheng P, Hogan M, et al. CXCL12 and vascular endothelial growth factor synergistically induce neoangiogenesis in human ovarian cancers. *Cancer Res*. (2005) 65:465–72. doi: 10.1158/0008-5472.465.65.2

64. Scotton CJ, Wilson JL, Milliken D, Stamp G, Balkwill FR. Epithelial cancer cell migration: a role for chemokine receptors? *Cancer Res*. (2001) 61:4961–5.

65. Scotton CJ, Wilson JL, Scott K, Stamp G, Wilbanks GD, Fricker S, et al. Multiple actions of the chemokine CXCL12 on epithelial tumor cells in human ovarian cancer. *Cancer Res*. (2002) 62:5930–8.

66. Zlotnik A, Burkhardt AM, Homey B. Homeostatic chemokine receptors and organ-specific metastasis. *Nat Rev Immunol*. (2011) 11:597–606. doi: 10.1038/nri3049

67. Nagarsheth N, Wicha MS, Zou W. Chemokines in the cancer microenvironment and their relevance in cancer immunotherapy. *Nat Rev Immunol*. (2017) 17:559–72. doi: 10.1038/nri.2017.49

68. Karin N. The multiple faces of CXCL12 (SDF-1alpha) in the regulation of immunity during health and disease. *J Leukoc Biol*. (2010) 88:463–73. doi: 10.1189/jlb.0909602

69. Meiron M, Zohar Y, Anunu R, Wildbaum G, Karin N. CXCL12 (SDF-1alpha) suppresses ongoing experimental autoimmune encephalomyelitis by selecting antigen-specific regulatory T cells. *J Exp Med*. (2008) 205:2643–55. doi: 10.1084/jem.20080730

70. Sánchez-Alcañiz JA, Haege S, Mueller W, Pla R, Mackay F, Schulz S, et al. Cxcr7 controls neuronal migration by regulating chemokine responsiveness. *Neuron*. (2011) 69:77–90. doi: 10.1016/j.neuron.2010.12.006

71. Vianello F, Papeta N, Chen T, Kraft P, White N, Hart WK, et al. Murine B16 melanomas expressing high levels of the chemokine stromal-derived factor-1/CXCL12 induce tumor-specific T cell chemorepulsion and escape from immune control. *J Immunol*. (2006) 176:2902–14. doi: 10.4049/jimmunol.176.5.2902

72. Poznansky MC, Olszak IT, Foxall R, Evans RH, Luster AD, Scadden DT. Active movement of T cells away from a chemokine. *Nat Med*. (2000) 6:543–8. doi: 10.1038/75022

73. Vianello F, Olszak IT, Poznansky MC. Fugetaxis: active movement of leukocytes away from a chemokinetic agent. *J Mol Med (Berl)*. (2005) 83:752–63. doi: 10.1007/s00109-005-0675-z

74. Wang Z, Moresco P, Yan R, Li J, Gao Y, Biasci D, et al. Carcinomas assemble a filamentous CXCL12-keratin-19 coating that suppresses T cell-mediated immune attack. (2022) 119:. doi: 10.1073/pnas.2119463119

75. Drury LJ, Ziarek JJ, Gravel S, Veldkamp CT, Takekoshi T, Hwang ST, et al. Monomeric and dimeric CXCL12 inhibit metastasis through distinct CXCR4 interactions and signaling pathways. *Proc Natl Acad Sci U.S.A*. (2011) 108:17655–60. doi: 10.1073/pnas.1101133108

76. Steele MM, Jaiswal A, Delclaux I, Dryg ID, Murugan D, Femel J. T cell egress via lymphatic vessels is tuned by antigen encounter and limits tumor control. *Nat Immunol*. (2023) 24:664–75. doi: 10.1038/s41590-023-01443-y

frontiers | Frontiers in Immunology

TYPE Original Research
PUBLISHED 10 January 2025
DOI 10.3389/fimmu.2024.1464419

OPEN ACCESS

EDITED BY
Takaji Matsutani,
Maruho, Japan

REVIEWED BY
Dwijendra K. Gupta,
Allahabad University, India
Peng Li,
Max Planck Institute for Demographic Research, Germany

*CORRESPONDENCE
Muneyuki Masuda
mmuneyuki@icloud.com;
masuda.muneyuki.pg@mail.hosp.go.jp

RECEIVED 14 July 2024
ACCEPTED 13 December 2024
PUBLISHED 10 January 2025

CITATION
Sato K, Toh S, Murakami T, Nakano T, Hongo T, Matsuo M, Hashimoto K, Sugasawa M, Yamazaki K, Ueki Y, Nakashima T, Uryu H, Ono T, Umeno H, Ueda T, Kano S, Tsukahara K, Watanabe A, Ota I, Monden N, Iwae S, Maruo T, Asada Y, Hanai N, Sano D, Ozawa H, Asakage T, Fukusumi T and Masuda M (2025) Nationwide multi-centric prospective study for the identification of biomarkers to predict the treatment responses of nivolumab through comprehensive analyses of pretreatment plasma exosome mRNAs from head and neck cancer patients (BIONEXT study). *Front. Immunol.* 15:1464419. doi: 10.3389/fimmu.2024.1464419

Nationwide multi-centric prospective study for the identification of biomarkers to predict the treatment responses of nivolumab through comprehensive analyses of pretreatment plasma exosome mRNAs from head and neck cancer patients (BIONEXT study)

Kuniaki Sato[1], Satoshi Toh[1], Taku Murakami[2], Takafumi Nakano[1], Takahiro Hongo[1], Mioko Matsuo[3], Kazuki Hashimoto[3], Masashi Sugasawa[4], Keisuke Yamazaki[5], Yushi Ueki[5], Torahiko Nakashima[6], Hideoki Uryu[6], Takeharu Ono[7], Hirohito Umeno[7], Tsutomu Ueda[8], Satoshi Kano[9], Kiyoaki Tsukahara[10], Akihito Watanabe[11], Ichiro Ota[12], Nobuya Monden[13], Shigemichi Iwae[14], Takashi Maruo[15], Yukinori Asada[16], Nobuhiro Hanai[17], Daisuke Sano[18], Hiroyuki Ozawa[19], Takahiro Asakage[20], Takahito Fukusumi[21] and Muneyuki Masuda[1*]

[1]Department of Head and Neck Surgery, National Hospital Organization Kyushu Cancer Center, Fukuoka, Fukuoka, Japan, [2]Showa Denko Materials America, R&D Center, Irvine, CA, United States, [3]Department of Otolaryngology, Head and Neck Surgery, Graduate School of Medical Science, Kyushu University, Fukuoka, Fukuoka, Japan, [4]Department of Head & Neck Surgery, International Medical Center, Saitama Medical University, Hidaka, Saitama, Japan, [5]Department of Otolaryngology, Head and Neck Surgery, Niigata University Graduate School of Medical and Dental Sciences, Niigata, Niigata, Japan, [6]Department of Otorhinolaryngology, National Hospital Organization Kyushu Medical Center, Fukuoka, Fukuoka, Japan, [7]Department of Otolaryngology, Head and Neck Surgery, Kurume University School of Medicine, Kurume, Fukuoka, Japan, [8]Department of Otorhinolaryngology, Head and Neck Surgery Graduate School of Biomedical and Health Sciences Hiroshima University, Hiroshima, Hiroshima, Japan, [9]Department of Otolaryngology, Head and Neck Surgery, Faculty of Medicine and Graduate School of Medicine, Hokkaido University, Sapporo, Hokkaido, Japan, [10]Department of Otorhinolaryngology, Head and Neck Surgery, Tokyo Medical University, Tokyo, Japan, [11]Department of Otolaryngology, Head and Neck Surgery, Keiyukai Sapporo Hospital, Sapporo, Hokkaido, Japan, [12]Department of Otolaryngology-Head and Neck Surgery, Nara Medical University, Kashiwara, Nara, Japan, [13]Department of Head and Neck Surgery, National Hospital Organization Shikoku Cancer Center, Matsuyama, Ehime, Japan, [14]Department of Head and Neck Surgery, Hyogo Cancer Center, Akashi, Hyogo, Japan, [15]Department of Otorhinolaryngology, Nagoya University Graduate School of Medicine, Nagoya, Aichi, Japan, [16]Department of Head and Neck Surgery, Miyagi Cancer Center, Natori, Miyagi, Japan, [17]Department of Head and Neck Surgery, Aichi Cancer Center Hospital, Nagoya, Aichi, Japan, [18]Department of Otorhinolaryngology-Head and Neck Surgery, School of Medicine, Yokohama City University, Yokohama, Kanagawa, Japan, [19]Keio University School of Medicine, Otolaryngology, Head and Neck Surgery, Tokyo, Japan, [20]Department of Head and Neck Surgery, Tokyo Medical and Dental University, Tokyo, Japan, [21]Department of Otorhinolaryngology-Head and Neck Surgery, Osaka University Graduate School of Medicine, Suita, Osaka, Japan

Background: Nivolumab paved a new way in the treatment of patients with recurrent or metastatic (RM) head and neck squamous cell carcinoma (RM-HNSCC). However, the limited rates of long-term survivors (< 20%) demand a robust prognostic biomarker. This nationwide multi-centric prospective study aimed to identify a plasma exosome (PEX) mRNA signature, which serves as a companion diagnostic of nivolumab and provides a biological clue to develop effective therapies for a majority of non-survivors.

Methods: Pre-treatment plasmas (*N* = 104) of RM-HNSCC patients were subjected to comprehensive PEX mRNA analyses for prognostic marker discovery and validation. In parallel, paired treatment-naïve tumor and plasma samples (*N* = 20) were assayed to elucidate biological implications of the PEX mRNA signature.

Results: Assays for pre-treatment blood samples (*N* = 104) demonstrated that a combination of 6 candidate PEX mRNAs plus neutrophil-to-lymphocyte ratio precisely distinguished non-survivors from >2-year survivors (2-year OS; 0% vs 57.7%; *P* = 0.000124) with a high hazard ratio of 2.878 (95% CI 1.639-5.055; *P* = 0.0002348). Parallel biological assays demonstrated that in the paired treatment-naïve HNSCC tumor and plasma samples (*N* = 20), PEX *HLA-E* mRNA (a non-survivor-predicting marker) was positively corelated with overexpression of HLA-E protein (*P* = 0.0191) and the dense population of tumor-infiltrating NK cells (*P* = 0.024) in the corresponding tumor, suggesting that the HLA-E-NKG2A immune checkpoint may inhibit the antitumor effect of PD-1blockade.

Conclusion: The PEX mRNA signature could be useful as a companion diagnostic of nivolumab. The combination of an anti-NKG2A antibody (i.e., monalizumab) and nivolumab may serve as a treatment option for non-survivors predicted by a RT-qPCR-based pre-treatment measurement of PEX mRNAs.

KEYWORDS

nivolumab, head and neck cancer, biomarker, exosome, HLA-E

Introduction

The emergence of immune checkpoint inhibitors (ICIs), especially those blocking programmed death-1 (PD-1), such as nivolumab or pembrolizumab, has had a substantial impact on the treatment of patients with recurrent or metastatic (RM) head and neck squamous cell carcinoma (HNSCC) (1). The CheckMate 141 study revealed that nivolumab treatments for selected patients achieved a long-term survival of >2 years for selected patients (2, 3), an unexpected achievement compared with conventional chemotherapeutic regimens. However, only 16.9% of patients experience this long-term survival (3); therefore, a reliable biomarker urgently needs to be established to address socioeconomic issues (4), and more importantly, an effective therapeutic strategy for a majority of non-survivors who don't benefit from nivolumab administration needs to be developed.

The prognostic and predictive ICI biomarkers has been developed by the use of tissue sample-based methods including measurement of PD-L1 expression to determine the tumor proportion score (TPS) or combined positive score (CPS), tumor mutation burden, microsatellite instability, and interferon (IFN)-γ-related signatures (5–8). Overall, these indicators are utilized as a biomarker of pembrolizumab with limited clinical efficacy. In addition, these high cost, labor intensive, and time-consuming methods have insufficient accuracy for the response prediction of nivolumab and, more importantly, are not suitable to timely monitor the ever-changing tumor immune-microenvironment (TIME) of patients. It is necessary to establish a rapid and reliable biopsy-free prognostic biomarker (e.g., a biomarker that can be analyzed in blood) for nivolumab. In this context, exosome mRNA has attracted our attention. Exosomes are small-size (30-150 nm) extracellular vesicles secreted by a variety of cells, including cancer cells (9). Accumulating evidence

indicates that exosomes function as cargos of biological information (i.e., proteins, lipids, DNAs, and RNAs), and significantly affect the milieus and physiological functions of the recipient cells in a context-dependent manner. Notably, exosome mRNAs are transcribed and function in the recipient cells (10). Exosome-mediated-cross-talks between cancer cells and the extracellular matrix and normal cells therein (e.g., immune cells) promote a tumor-specific microenvironment that is advantageous for cancer cells to proliferate, survive, migrate, metastasize, and escape from immune surveillance (10). A recent milestone study demonstrated that exosomes secreted from *TP53*-mutated cancer cells can reprogram neurons into a cancer-promoting phenotype in HNSCC (11). The immune-suppressive effects of exosomes have also been confirmed in a series of HNSCC studies (12, 13). Thus, it is highly expected that the TIME of RM HNSCC, which regulates the response to nivolumab, can be assessed based on the plasma exosome (PEX) status. Due to the technological advancements, quantitative isolation of exosome mRNA from human samples (e.g., blood and urine) is feasible using commercially available high-throughput extraction kits in a couple of days with low cost (14, 15). Therefore, we designed a multicentric prospective study to identify a PEX mRNA signature, which is measurable in clinical practice by reverse transcription-quantitative polymerase chain reaction (RT-qPCR). The main aim of this study is to establish a companion diagnostic for nivolumab that accurately predicts non-survivors and provides a clue for the development of a novel therapeutic strategy for non-survivors.

Methods

Study design

The BIONEXT study is composed of the following two parts (Figure 1).

Part 1: This part included patients with RM HNSCC patients who were treated with nivolumab. Inclusion criteria were age ≧20 years; history of platinum agent administration; pathologically confirmed SCC of the nasal cavity, paranasal sinus, nasopharynx, oropharynx, oral cavity, hypopharynx, or larynx that was recurrent or metastatic and not curable by local therapy; an Eastern Cooperative Oncology Group (ECOG) performance status score of 0 or 1; and at least one tumor lesion measurable per Response Evaluation Criteria in Solid Tumors (RECIST) version 1.1 demonstrated by computed tomography imaging within 28 days of registration. The exclusion criteria were history of ICI therapy or any kind of immunotherapy; and active synchronous or metachronous (within 5 years) cancers except for the carcinoma *in situ* (CIS) and early esophageal cancer curable by endoscopic resection. Enrolled patients were treated with nivolumab (240 mg every 2 weeks or 480 mg every 4 weeks), and their responses were evaluated every 8 weeks until progressive disease (PD) was detected. Clinical data were collected through the Viedec4 electronic data capture system constructed and maintained by the Clinical Research Support Center (CReS) Kyushu. The endpoint of this study was the identification of a PEX mRNA signature that could segregate non-survivors from long-term (> 2-year) survivors.

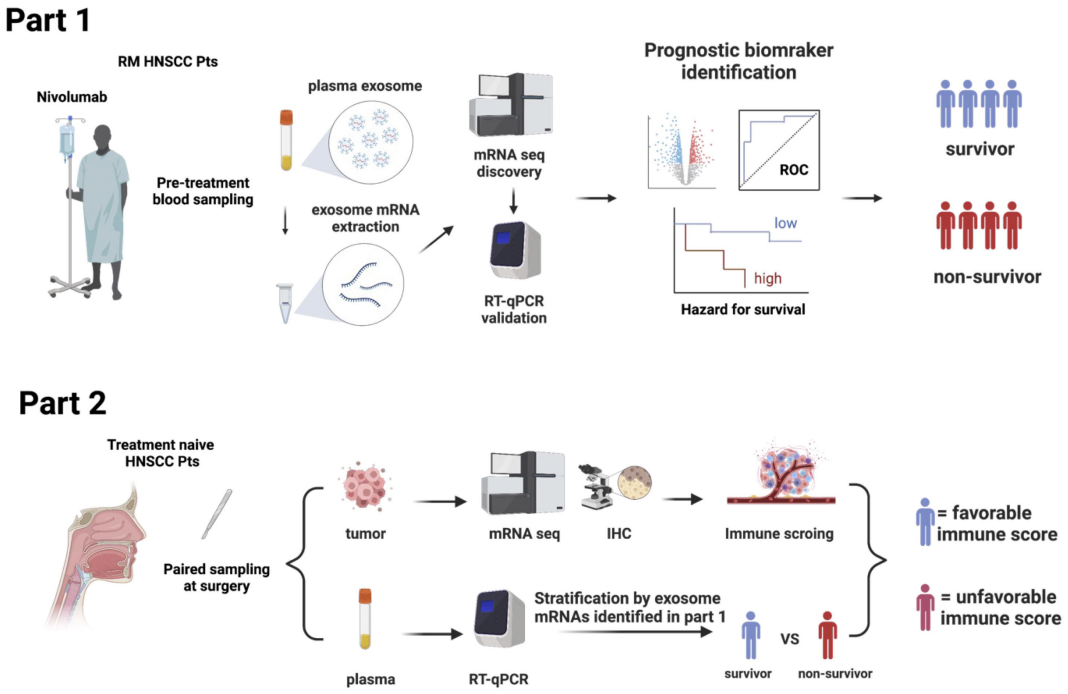

FIGURE 1
Study design.

Pretreatment plasma samples (5 mL), collected from peripheral blood, were preserved at -80°C until assays. Selected pilot samples were subjected to comprehensive RNA-seq analysis for the discovery of candidate PEX mRNA markers, and then the performance of these markers for prognosis prediction was validated by RT-qPCR assays in the entire cohort. All assays were conducted in compliance with the minimal information for studies of extracellular vesicle 2018 protocol (15) in the laboratory of Showa Denko Materials America under strict quality and quantity control anticipating future practical use as a companion diagnostic.

Part 2: This part was designed to confirm that the specific PEX mRNA signature could indeed reflect the TIME of the HNSCC tumors in the identical patient and moreover to elucidate the mechanism of action canceling the effects of nivolumab in non-survivors. Paired tumor and plasma samples were collected from 20 treatment-naïve patients who underwent radical surgery at the National Kyushu Cancer Center. Respective frozen and formalin-fixed paraffin-embedded (FFPE) tumor samples were subjected to mRNA-seq and immunohistochemistry (IHC) to score TIME. Concurrently, the PEX mRNA expression profile of the same patient was evaluated by RT-qPCR in reference to the prognostic biomarker genes established in part 1. Then, patients were stratified into two groups (survivor vs non-survivor signature). Comparing these two cohorts, the TIME score and the biological implication of PEX mRNA signature were investigated.

This study was approved by the Institutional Review Board of the National Kyushu Cancer Center (2019–024), and written informed consent was obtained from all patients before enrolment. This study is registered to the UMIN Clinical Trial Registry: UMIN000037029.

Sample collection

Blood samples, taken within 28 days before nivolumab administration, were immediately centrifuged at 1100xg for 10 minutes and 5 ml of plasma samples were dispensed and snap-frozen at -80°C. Sample collection, preservation, and shipment to Showa Denko America were performed by the SRL Inc. (Tokyo, Japan) under restrict quality and temperature management.

PEX mRNA isolation and sequencing

PEXs were quantitatively isolated from plasma using a high throughput ExoComplete isolation tube kit (Showa Denko Materials, Tokyo, Japan), and total RNA was isolated with a MagMax Total Nucleic Acid Isolation Kit (Thermo Fisher, CA) as previously described unless otherwise noted (14). cDNA libraries were prepared using a TruSeq mRNA stranded library kit (Illumina, CA) and sequenced by paired-end read sequencing on a NovaSeq 6000 (Illumina, CA). The obtained raw reads were mapped against the human genome (GRCh38.p13) by hitsat2 and the read counts were obtained by featureCount on a Linux workstation. Differential gene expression analysis was performed by edgeR.

PEX mRNA RT-qPCR assay

PEX mRNA isolation was conducted as described above. cDNA was synthesized with qScript XLT cDNA SuperMix (Quantabio, MA, USA) following the manufacturer's protocol. qPCR was performed with SsoAdvanced Universal SYBR Green Supermix (Bio-Rad, CA, USA) in a ViiA 7 Real-Time PCR System (Thermo Fisher Scientific, CA, USA) with the following protocol: 95°C for 10 min, followed by 40 cycles of 95°C for 30 s and 65°C for 1 min and a melting curve analysis. The primer sequences are shown in Supplementary Table S1. Threshold cycle (Ct) values of the marker candidates were normalized to that of the reference gene (*GAPDH*) using the delta Ct method.

IHC

Human leukocyte antigen E (HLA-E) and programmed death ligand 1 (PD-L1) protein expression levels in the FFPE tumor samples were analyzed using a Ventana Benchmark Ultra slide processor using antibodies against HLA-E (MEM-E/02; Sant Cruz Biotechnology, Inc.) and PD-L1(22C3; PharmDx). The CPS was calculated according to the standard method (5). HLA-E tumor expression was interpreted as strong when more than half of tumor cells was positive, whereas as low when less than half of cells were positive.

RNA-seq of primary tumor tissues and scoring of the TIME

RNA extracted from the 17 primary tumor tissues was sequenced on a DNBSEQ-G400 sequencer at Beijing Genomics Institutions (Shenzhen, China). The sequenced reads were aligned to the human reference GRCh38 genome by STAR v2.7.9a with Gencode v38 annotations using the supercomputing system SHIROKANE (University of Tokyo). Transcript-per-million (TPM)-normalized read count tables were generated by RSEM. Downstream analyses were conducted using R v4.1.1. (The R Foundation for Statistical Computing). The IFN-g-signature (the original 6 genes and an expanded 18 genes signature) and the proportions of immune cells in primary tumor tissues were estimated according to the methods in previous reports (6, 7) and CIBERSORTx (https://cibersortx.stanford.edu/) (16). The 17 cases were divided into two groups according to *HLA-E* expression levels based on the median value. The difference in the IFN-g-signature and the proportions of immune cells between the *HLA-E* high and low groups were examined by Mann-Whitney U tests. The correlations of the detected marker genes between tissue and PEX-mRNA were examined by Pearson correlation tests.

Statistics

Data analysis was performed using R version 4.1.1 unless otherwise noted. Statistical significance was determined by a *p*-

value of < 5% derived from ANOVA or Welch's t test. The performance of the marker candidates was evaluated by the AUC of ROC analysis by R package pROC. The optimum threshold was obtained based on the point of the ROC curve nearest to the top-left corner and used to calculate sensitivity, specificity, positive predictive value (ppv), and negative predictive value (npv) to characterize the performance of marker candidates. Sparse logistic regression was also employed to further validate the predictive values of the biomarkers (17). Survival endpoints used to analyze the candidate biomarkers were visualized using Kaplan-Meier analysis. The log-rank test was applied to test the differences among survival curves. Cox proportional hazards regression models were used to calculate the HR.

Results

Enrollment and clinical outcomes

Part 1of the study enrolled 111 patients from July 7, 2019, to December 31, 2020, and the clinical data were collected and monitored until July 2022 by CReS Kyushu. Seven patients were excluded due to screening (N = 6) and sampling (N = 1) errors; therefore, the samples and clinical records of 104 patients were utilized for the biomarker assay and survival curve generation. Among them, 7 (6.7%) patients demonstrated a complete response (CR), 12 (12%) had a partial response (PR), 25 (24%) had stable disease (SD), 55 (53%) had progressive disease (PD), and 5 (4.8%) were not evaluated (NE) due to rapid tumor progression. These response rates were similar to those seen in the real world large scale date in Japan (18). The characteristics of the 104 patients are shown in Supplementary Table S2.

Candidate BOR-predicting PEX mRNA discovery

Based on the previous findings that the survival of patients treated by ICI could be stratified by best overall response (BOR) (19), we adopted a standard strategy to initially develop a BOR-predicting biomarker employing receiver operating characteristic (ROC) curve analyses and then to apply this biomarker to prognostic prediction by calculating cumulative survival rates and hazard ratios (HRs) between the marker-selected (i.e., high vs low) cohorts. In preparation for BOR-predicting biomarker exploration, we confirmed the accuracy of BOR for survival prediction in the current cohort (N =104). As shown in Figures 2A, B, the overall survival (OS) rates of patients were well stratified in accordance with BOR; no patients were lost in the CR arm, while extremely poor prognosis was observed in patients with NE, who experienced rapid tumor progression before the first evaluation (Figure 2A). Consequently, a substantial difference was found between the curves of responders (N = 19) and non-responders (N = 85) for 2-year OS (93.3% vs. 12.3%, Log-rank test P = 0.00000339; HR: 0.04; 95% confidence interval [CI]: 0.0055-0.293, P = 0.0015079) (Figure 2B). However, not only responder (CR+PR), non-responder patients demonstrated long-survival; SD patients revealed a 48.7% of OS at 20 months and PD patients a 20.7% of OS at 2 years (Figure 2A), reflecting the fact that a certain portion of patients show durable responses to salvage chemotherapy beyond PD following nivolumab (20). Given that our main goal is to establish an accurate non-survivor-predicting biomarker, these beyond-PD survivors pose a conundrum. This is because, when response-predicting (i.e., responder vs non-responder) biomarkers are applied to survival analyses in this setting, a responder-predicting biomarker with high specificity (score low patients = responders) keeps its power as a survivor-predicting prognostic biomarker, whereas a non-responder predicting biomarker with high sensitivity (score high patients = non-responders) loses its power as a non-survivor-predicting prognostic biomarker, mis-predicting these beyond-PD survivors as non-survivors. Keeping this critical point in mind, we proceeded to the identification of a BOR-predicting PEX mRNA biomarker. We cumulatively collected PEX mRNA sequencing data employing 17 plasma samples of initial phase patients (PR: 6; SD: 5; and PD: 6) when their responses were determined as of November 2020. It is of note that these 6 PR patients were > 2-year survivors (i.e., good responders). Then, we selected candidate BOR-predicting PEX mRNA, adopting a less restricted marker-selecting condition not confining the comparisons of groups between responders and non-responders, thus if they met one of the following criteria: 1) genes that were differentially expressed among the BOR categories (PR vs PD, PR vs SD/PD, and PR/SD vs PD) (P < 0.05), 2) genes with |log (fold change)| > 1.5, 3) genes with high area under the curve (AUC) values (> 0.7) in the ROC analyses for detection of PR vs PD, PR/SD vs PD (AUC1) and PR vs SD/PD (AUC2), or 4) genes identified as potential biomarkers in previous ICI studies (6, 8, 21, 22) or with high |log(fold change)| values in the present study. With these less broad criteria, the top 20 genes, *TAF4B, TESK2, MFSD8, RABL2B, ZNF480, FAM76A, TGIF1, TNFRSF13C, CTSW, LOC283788, SLC25A13, HLA-DQA1, COL10A1, MPIG6B, RPL23AP7, MSH2, CD3D, TCF7, HLA-E, and HLA-DRA* were selected as candidate BOR-predicting biomarkers for further analyses (Figure 2C; Supplementary Table S3).

Response-predicting PEX mRNA biomarker identification

Employing these candidate BOR-predicting PEX mRNAs, their powers for response prediction (i.e., responder vs non-responder) were investigated by RT-qPCR assays in the entire cohort (N = 104). To normalize the PEX mRNA data, two representative reference genes, *ACTB* and *GAPDH*, were added to assays. Interestingly, they demonstrated significantly (*ACTB*, P < 0.001; *GAPDH*, P < 0.05) higher expression (i.e., raw threshold cycle value) in the non-responder than in the responder. Assuming that these increases may reflect the vigorous total exosome production from aggressive cancer cells as confirmed in previous studies (10), we adopted *ACTB*, which had a greater difference, as one of the candidate biomarker PEX mRNAs, and used *GAPDH* as the reference gene. We then compared the expression levels of *GAPDH*-normalized 21

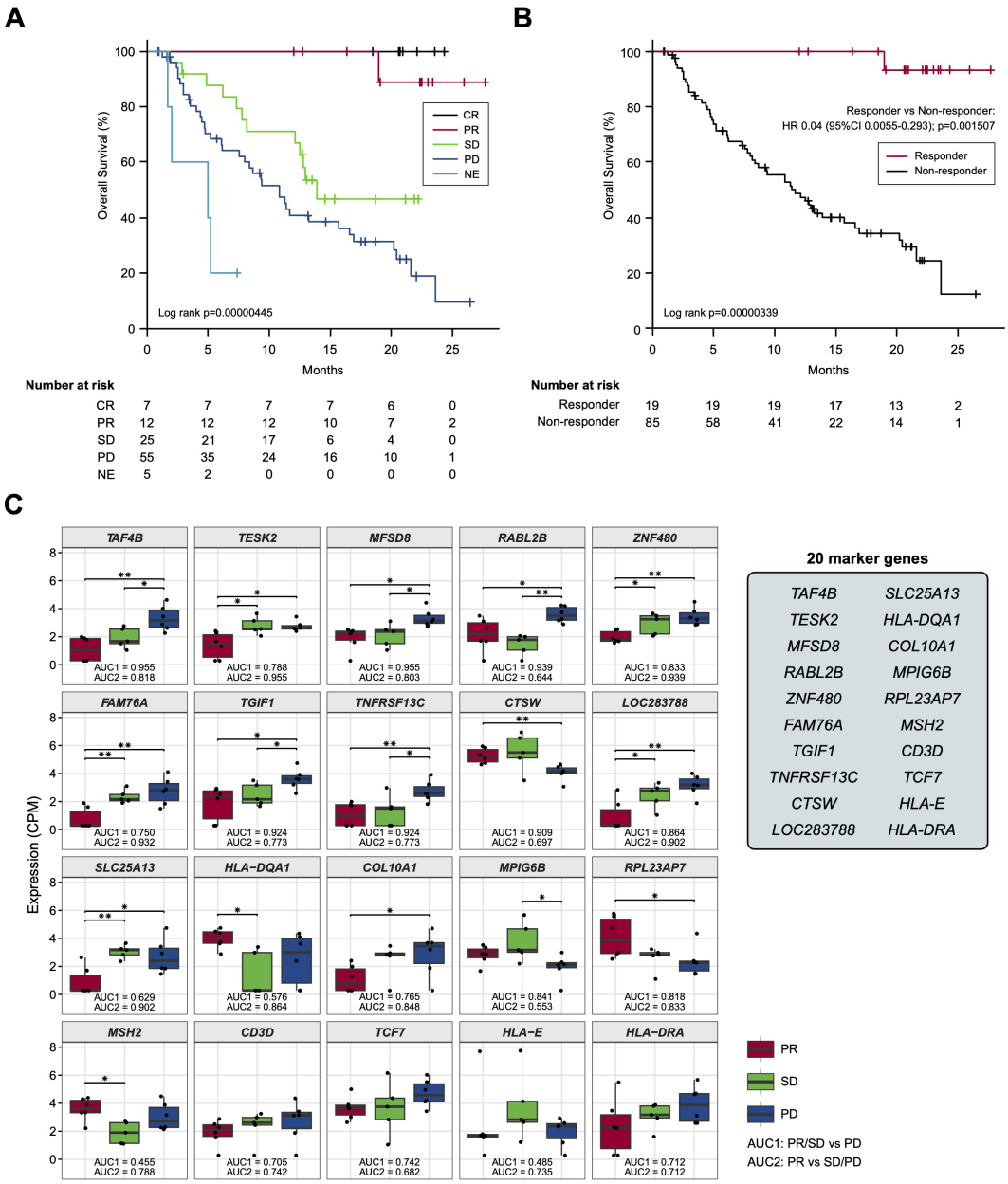

FIGURE 2
(A, B) Kaplan-Meier curves representing the overall survival of patients classified according to the best overall response. **(C)** Box plots representing the expression levels of 20 candidate biomarker genes in patients stratified according to the best overall response. CR, complete response; PR, partial response; SD, stable disease; PD, progressive disease; NE, not evaluated. (*) P <0.05; (**) P <0.005.

PEX mRNAs between responders and non-responders and their response-predicting powers were measured by the values of AUC in the ROC curve analyses and their optima thresholds were determined by the point nearest to the top-left corner on the ROC curve. The top 6 genes with the high AUCs, *HLA-E, ACTB, MPIG6B, RABL2B, TNFRSF13C*, and *ZNF480*, were selected as putative response-predicting biomarkers (Supplementary Table S4). PEX mRNAs that were increased in the non-responders (*HLA-E, ACTB, MPIG6B* and *TNFRSF13*) were considered as non-responder-predicting markers, while those that were increased in the responders (*RABL2B*, and *ZNF480*) were considered as responder-predicting markers (Figure 3A). Of note, the *GAPDH*-normalized *ACTB* PEX mRNA remained significantly higher in non-responders, supporting our hypothesis. The AUC of these PEX mRNAs ranged from 0.593 to 0.729. For comparison, we calculated the AUC of the neutrophil-to-lymphocyte ratio (NLR), a proposed non-responder-predicting biomarker of ICI (23, 24), and found it was 0.591 (Supplementary Table S4; Figure 3A). The performance of individual PEX mRNAs was better than that of the NLR, but the values were not sufficiently high for clinical use. We then employed a simple algorithm to develop a better signature for response prediction by the combination of multiple PEX mRNA markers and the NLR. With the intent to generate non-responder-predicting combinations, we assigned 1 point if the expression of a non-responder-predicting gene or NLR

10.3389/fimmu.2024.1464419

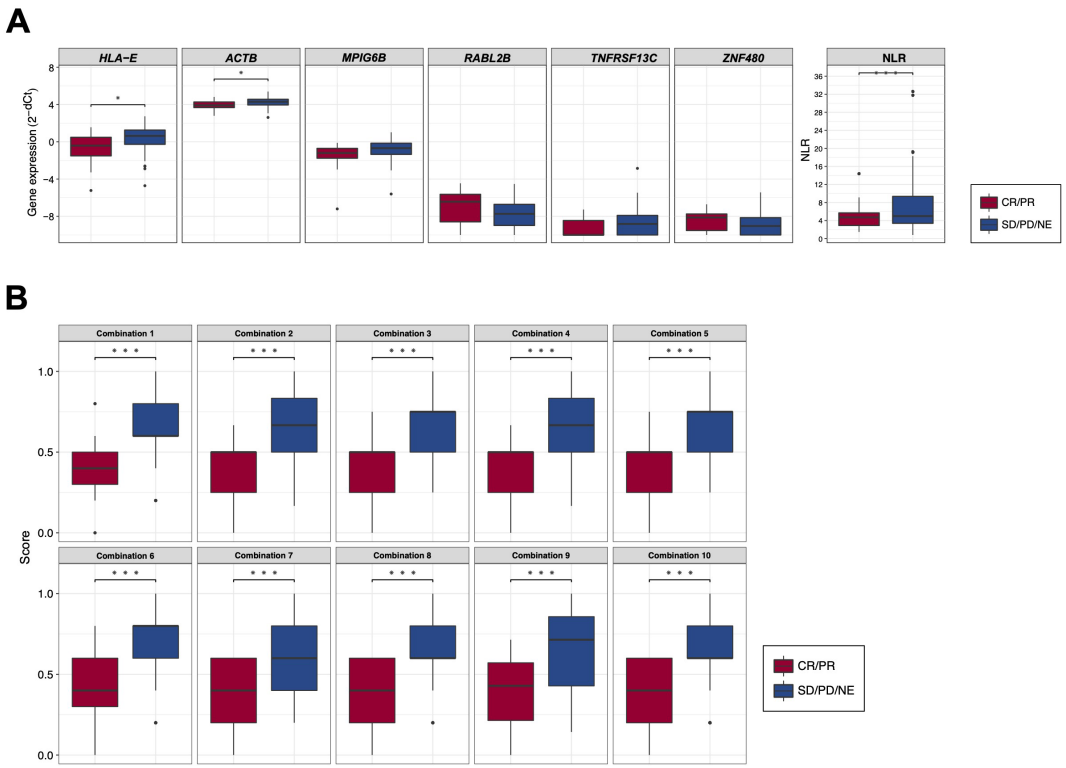

FIGURE 3
(A) Box plots comparing the expression levels of response-predicting biomarker genes and the neutrophil-to-lymphocyte ratios (NLR) between responders (CR/PR) and non-responders (SD/PD/NE). **(B)** Box plots comparing the scores of combinations calculated by biomarker genes and the NLR between responders (CR/PR) and non-responders (SD/PD/NE). (*) P <0.05; (**) P <0.005; (***) P <0.0005.

exceeded the threshold or a responder-predicting gene fall below the threshold using the best threshold value (i.e., the point of the highest sensitivity and specificity) of each marker determined by the ROC curve analysis (Supplementary Table S4), and the points were averaged for various marker combinations. The score ranged between 0 and 1, and a score of 0 indicated that no marker in the combination predicted a non-responder, while a score of 1 indicated that all markers in the combination predicted a non-responder. To obtain the best combination of markers, we tested all the possible combinations of the top 6 markers and the NLR and identified the top 10 combinations with higher AUCs (ranging from 0.793 to 0.812) (Table 1; Figure 3B). In the comparison of responders and non-responders, the scores of these combinations demonstrated more significant differences (P < 0.0005) (Figure 3B) than the mean expression of individual 6 PEX mRNAs and NLR, in which only *HLA-E*, *ACTB* (P < 0.05) and NLR (P < 0.005) demonstrated significant differences (Figure 3A). Notably, all the top 10 combinations included *HLA-E*, which may suggest its importance for response prediction (Table 1).

Prognostic biomarker identification

In our final assay, we investigated whether these non-responder-predicting combinations can serve as prognostic biomarkers for the prediction of non-survivors. Kaplan-Meier curves of patients were generated according to the thresholds of combinations 1-10 (Table 1). In combination 1, 2, 4, 7, 9, and 10, patients with high non-responder scores (above the threshold) demonstrated significantly (P = 0.0002348-0.0238) higher HRs (2.09-2.878) (Figure 4A). Strikingly, in the most promising (i.e., high HR) combinations (9 and 10), the OS of the patients with high non-responder scores demonstrated a sharp drop towards 0% at 2 years (Figure 4B), while that of patients with low non-responder scores demonstrated an approximately 60% 2-year OS and a tendency to plateau after 20 months. Considering the highest HR and the lowest P value, we determined to adopt the combination 9 as a prognostic biomarker of nivolumab.

Correlation of prognostic biomarker combinations with the TIME

In part 1 of our study, we identified a prognostic biomarker combination (*HLA-E, ACTB, MPIG6B, RABL2B, TNFRSF13C, ZNF480* and NLR) that could precisely predict non-survivors treated with nivolumab. We then proceeded to part 2 of the study to confirm that the combination of 6 PEX mRNAs and NLR indeed reflect the TIME and, more importantly, to find a biological clue for the development of novel strategies for non-survivors (Figure 1).

10.3389/fimmu.2024.1464419

TABLE 1 Candidate response-predicting combinations (assessed in responder vs non-responder groups).

	AUC	Threshold	Sensitivity	Specificity	ppv	npv	Markers
Comb 1	0.812 (0.716-0.907)	0.5	0.765	0.737	0.929	0.412	HLA-E RABL2B TNFRSF13C ZNF480 NLR
Comb 2	0.809 (0.722-0.896)	0.583	0.635	0.895	0.964	0.354	HLA-E ACTB RABL2B TNFRSF13C ZNF480 NLR
Comb 3	0.803 (0.714-0.893)	0.625	0.635	0.895	0.964	0.354	HLA-E RABL2B TNFRSF13C ZNF480
Comb 4	0.801 (0.713-0.890)	0.583	0.635	0.895	0.964	0.354	HLA-E MPIG6B RABL2B TNFRSF13C ZNF480 NLR
Comb 5	0.796 (0.702-0.890)	0.625	0.576	0.895	0.961	0.321	HLA-E TNFRSF13C ZNF480 NLR
Comb 6	0.796 (0.702-0.890)	0.5	0.765	0.632	0.903	0.375	HLA-E ACTB RABL2B TNFRSF13C ZNF480
Comb 7	0.795 (0.705-0.885)	0.5	0.729	0.632	0.899	0.343	HLA-E MPIG6B TNFRSF13C ZNF480 NLR
Comb 8	0.795 (0.703-0.887)	0.5	0.753	0.579	0.889	0.344	HLA-E ACTB TNFRSF13C ZNF480 NLR
Comb 9	0.794 (0.700-0.887)	0.643	0.576	0.947	0.98	0.333	HLA-E ACTB MPIG6B RABL2B TNFRSF13C ZNF480 NLR
Comb 10	0.793 (0.700-0.886)	0.5	0.753	0.632	0.901	0.364	HLA-E ACTB RABL2B TNFRSF13C NLR

AUC, area under curve; ppv, positive predictive value; npv, negative predictive value.

For part 2, 20 paired blood, plasma and tumor samples were collected from the treatment-naïve HNSCC patients who underwent radical surgery at National Kyusyu Cancer Center. This is mainly because it is often difficult to obtain appropriate tumor samples from the patients with R/M HNSCC. Blood samples were used for the measurement of NLR. Plasma samples were subjected to PEX mRNA assay and tumor samples were to RNA-seq and IHC. Sufficient tissue amounts for RNA-seq were not obtained for 3 frozen tumor samples; thus, 17 tumor samples were subjected to the mRNA analyses, 20 tumor samples were subjected to the IHC analysis, and 20 plasma samples for PEX mRNA assay. We first measured the expression levels of *GADPH*-normalized 6 PEX mRNAs by RT-qPCR and the levels of mRNAs in the corresponding tumors by RNA-seq to examine their correlations. Consistent with the previous finding that only specific genes demonstrated significant correlations (25), PEX *HLA-E* mRNA showed a near-significant (P = 0.052) correlation with tumor *HLA-E* mRNA among the 6 genes (Figure 5A). In view of this positive tendency, we compared the expression levels of PEX *HLA-E* mRNA and HLA-E protein in the tumors and found a significant association (P = 0.0191) (Figure 5C). Collectively, the high PEX *HLA-E* mRNA expression appears to reflect the high *HLA-E* mRNA transcription and protein translation in the corresponding tumor. We then attempted to stratify the 20 patients into score high candidate non-survivors and score low candidate survivors based on the biomarker combination 9 established in part 1 of the study (Table 1; Figure 1A). However, interestingly, all 20 patients were grouped with survivor signature, because in the blood and plasma samples obtained from the treatment-naïve patients the NLR and the mean PEX mRNA expression levels of 6 PEX mRNAs except for *TNFRSF13C* indicated favorable response patterns compared to the RM samples (Figure 5B); *HLA-E, ACTB*, and *MPIG6B* (non-responder genes) were lower and *RABL2B* and *ZNF480* (responder genes) were higher. This result is consistent with the fact that the TIME of treatment-naïve tumor is more tumor-eliminating compared to the exhausted TIME of RM tumor, warranting the efficacy of this biomarker as a monitor of the TIME. Given the prominent role of HLA-E repeatedly identified in the present study and its importance as a target of immunotherapy (i.e., therapies targeting the HLA-E-NKG2A immune checkpoint) (26, 27), we alternatively utilized the mean value of PEX *HLA-E* mRNA to stratify the 20 patients. We compared the status of immune parameters (PD-L1 CPS score, IFN-γ-related signature score, and CIBERSORT-derived infiltrating immune cell levels) (6, 7, 16) between PEX *HLA-E* mRNA high (N = 10) and low (N = 10) patients. The CPS (P = 0.6242) and IFN-γ-related signature (P = 0.1802) did not show significant correlations with the levels of PEX *HLA-E* mRNA. However, the number of activated natural killer (NK) cells determined by CIBERSORT were significantly (P = 0.024) abundant in the tumors of patients with high PEX *HLA-E* mRNA (Figure 5D). It is known that HNSCC is the most immune-infiltrating cancer types across the solid tumors (28) and these tumor-infiltrating NK cells and $CD8^+$ cytotoxic T lymphocytes (CTL) strongly express NKG2A and PD-1 (27). Considering the positive correlation of PEX *HLA-E* mRNA and HLA-E protein expression confirmed above, the effects of PD-1blockade by nivolumab may be canceled by HLA-E-NKG2A check point in patients with high PEX *HLA-E* mRNA, as illustrated in Figure 5E. Thus, the combination of clinically usable anti-NKG2A antibody (i.e., monalizumab) and nivolumab may be useful for the candidate non-survivors predicted by the pre-treatment biomarker combination indicating high PEX *HLA-E* mRNA.

Discussion

To the best of our knowledge, this is the first prospective study to demonstrate the feasibility of a single pretreatment RT-qPCR-based blood test for predicting the non-survivors with RM HNSCC treated with to nivolumab. In this study, we adopted a standard strategy to apply response-predicting biomarkers identified by the ROC curve to the survival analyses (29). For the development of marker combination, we adopted a simple algorism which is suitable for clinical use after confirming its credibility on a sparse logistic regression algorithm (17) (data not shown). Although the

10.3389/fimmu.2024.1464419

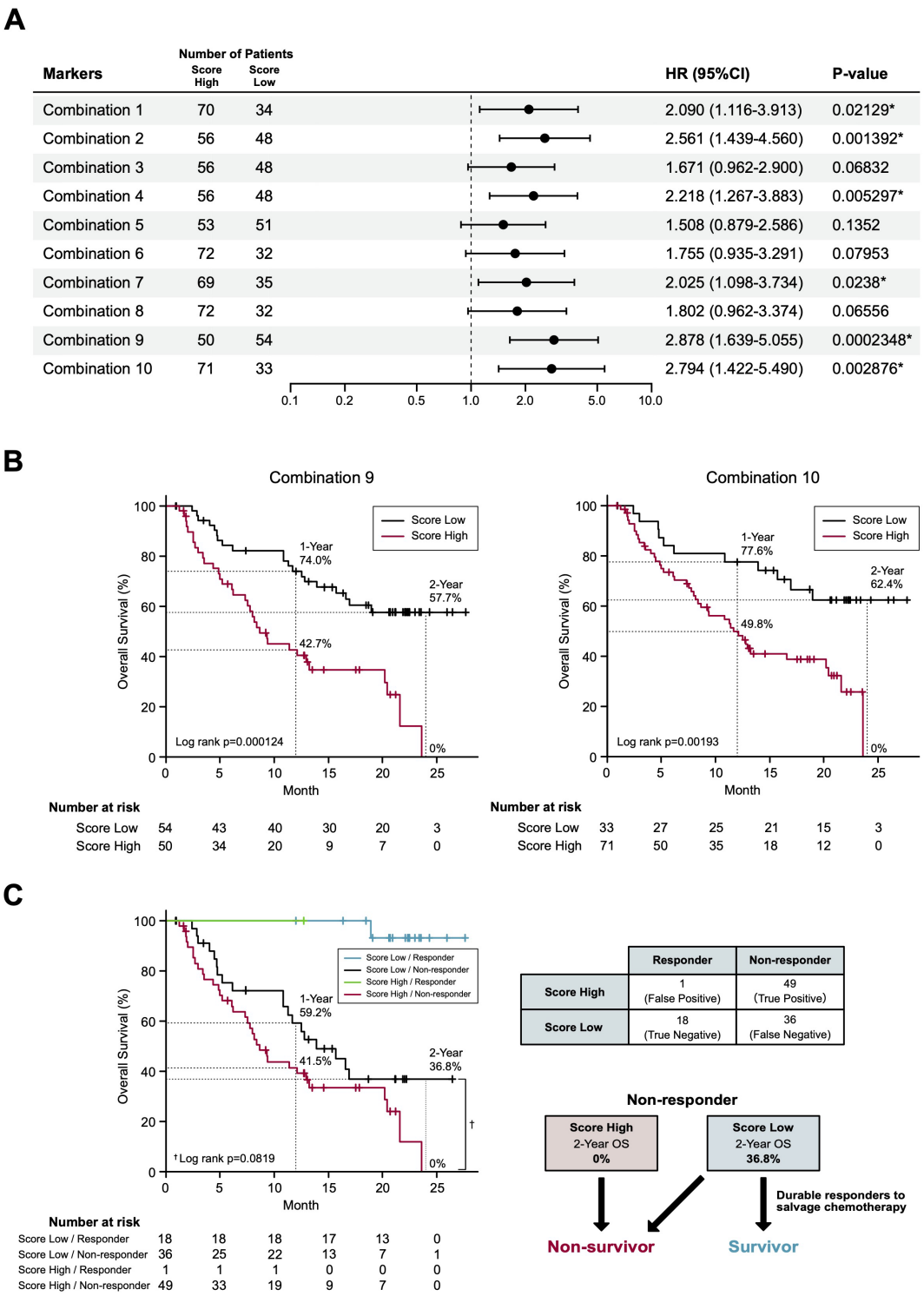

FIGURE 4
Survival prediction based on the identified biomarker combinations. **(A)** Forest plots representing the hazard ratios of the biomarker combinations. HR, hazard ratios; CI, confidence intervals. **(B)** Kaplan-Meier curves representing the overall survival of patients classified according to the score of biomarker combination (left panel, combination 9; right panel, combination 10). **(C)** Kaplan-Meier curves (left panel) representing the overall survival of patients classified according to the 2 x 2 contingency table (right panel). (*) P <0.05.

combination 9 showed a limited sensitivity (0.576) and negative predictive value (0.333) in the response prediction (Table 1), it demonstrated a strong non-survivor predicting power. To explain this mechanism, we disassembled the Kaplan-Meier curve of combination 9 (Figure 4B) based on the distribution of patients divided in the 2 x 2 contingency table (response x combination 9 score) (Figure 4C). Strikingly, in non-responders, combination 9 score precisely segregated non-survivors in the score-high

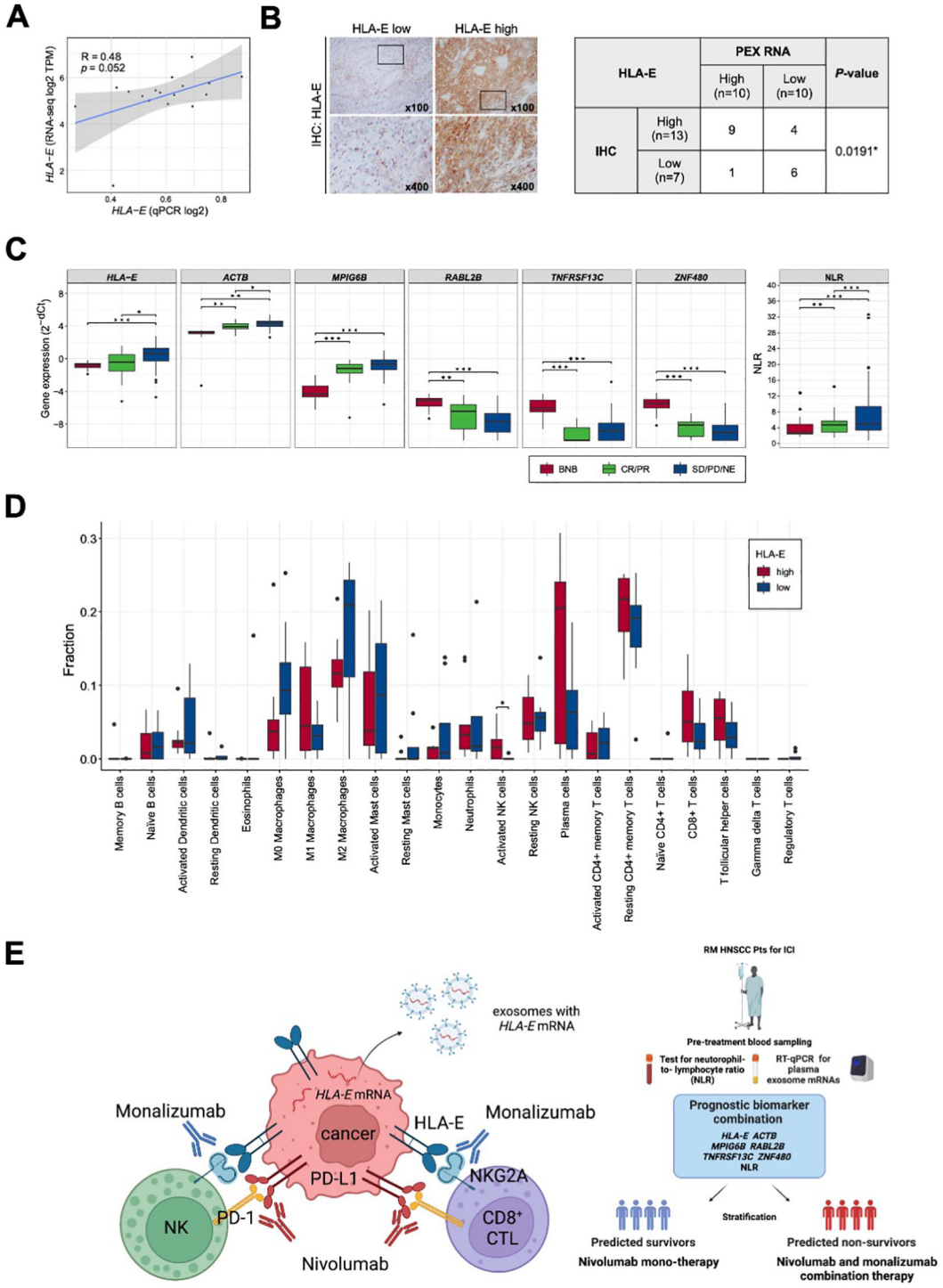

FIGURE 5
Correlation of PEX mRNA and the tumor immune microenvironment. **(A)** Correlation between the *HLA-E* expression levels detected by RNA-seq (vertical axis) and qPCR (horizontal axis) (*N* =17). R represents the Pearson correlation coefficient. **(B)** Representative images of immunohistochemistry staining for HLA-E in tumor tissues; HLA-E low (left) and HLA-E high (right). High-magnification images of the regions indicated by black boxes are shown. The table represents the numbers of cases and the correlation between HLA-E protein and *HLA-E* mRNA expression levels in PEXs (*N* =20). The P-value was calculated by Fisher's exact test. (*) *P* <0.05; (**) *P* <0.005; (***) *P* <0.0005. **(C)** Box plots representing the expression levels of biomarker genes detected by RT-qPCR of exosomes extracted from peripheral blood and the NLR. BNB represents the cohort of part 2 study cohort (*N* =20). CR, complete response; PR, partial response; SD, stable disease; PD, progressive disease; NE, not evaluated. **(D)** Box plots representing the proportion of immune cells estimated by CIBERSORTx in the primary tumor tissues (*N* =17). Patients were classified according to the expression levels of PEX *HLA-E* mRNA (HLA-E high, *N* =9; HLA-E low, *N* =8). P-value was calculated by Mann-Whitney U-tests. (*) *P* <0.05; (**) *P* <0.005; (***) *P* <0.0005. **(E)** Schematic summarizing of our proposed mechanism by which the effect of nivolumab is canceled in the tumor of patient with high PEX HLA-E mRNA (left panel) and a decision-making algorithm for patients (right panel). The high PEX mRNA level reflects the vigorous HLA-E protein production in cancer cells, forming HLA-E/NKG2A checkpoint with NK and CD8+CTL cells. In this setting, administration of nivolumab alone is not effective. Addition of an anti-NKG2A antibody, monalizumab, is expected to restore the cytotoxic effects of NK and CTL cells circumvented by the dual immune checkpoints.

population and exclusively separated the beyond-PD durable responders in the score-low population (2-year OS: 0% vs 36.8%, Log rank P = 0.0819, HR 1.642; 95% confidence interval 0.9335-2.887; P = 0.0852) (Figure 4C). Consequently, a 12.3% of 2-year OS in BOR-determined non-responders (N = 85) (Figure 2A) dropped to 0% (N = 50) in patients with high combination 9 score (Figure 4B). The broad curation of BOR- predicting PEX mRNAs in the discovery cohort might contribute to this improvement.

Currently, an IFN-γ-related signature (the original 6 genes and an expanded 18-gene signature), which was established as a biomarker of pembrolizumab using the tissue-based NanoString platform, is often employed (5, 8) based on its relatively high AUC of 0.75 for response prediction in RM HNSCC (6). However, the power of this biomarker remains unclear when utilized as a prognostic biomarker. The present study revealed that our liquid biomarker combinations consisting of 6 PEX mRNAs and the NLR demonstrated similar AUC of 0.794 for response-prediction and as well showed high performance as a prognostic biomarker. Considering, the accuracy, speed, ease and low cost with which it can be assayed, the pretreatment measurement of NLR by routine blood test and PEX mRNA signature by RT-qPCR may be a novel companion strategy for nivolumab therapy in patients with RM HNSCC.

In addition to serving as a novel companion diagnostic, our biomarker exploration provided evidence for the development of more effective therapeutic strategies for non-survivors. The immune evasive role of HLA-E/NKG2A immune checkpoint is confirmed in a variety of cancers (26, 27, 30). In addition, increasing evidence indicates the frequent formation of dual immune checkpoints (PD-L1/PD1 and HLA-E/NKG2A) in HNSCC (27, 28), accounting for the limited effects of nivolumab. In the UPSTREM (phase II) (31) and the INTERLINK 1 (phase III) (https://yhoo.it/3OPZbGx) study monalizumab alone or in combination with cetuximab (an anti-EGFR antibody) failed to show clinical efficacy for RM HNSSC. It is likely that the effect of targeting one immune checkpoint is canceled by another immune checkpoint. Thus, our strategy to simultaneously target PD-1/PD-L1 and HLA-E/NKG2A immune checkpoints for biomarker-selected patients appears to be more precise and promising (Figure 5E). The safety and efficacy of the combinational administration of durvalumab (an anti-PDL-1 antibody) and monalizumab were confirmed in the Phase II lung cancer study (32). Thus, a prospective clinical study to test our strategy appears to be promising.

Unfavorable markers including *ACTB, MPIG6B, TNFRSF13C*, and the NLR, and favorable markers including *RABL2B*, and *ZNF480*, were also in our prognostic biomarker combination. The levels of PEX *ACTB* mRNA are expected to reflect the total amounts of PEX, as mentioned above, being related to proliferative activity and rapid tumor growth (10). The oncogenic and immunogenic functions of MPIG6B are poorly understood, but a recent study identified that this molecule is essential for the induction of megakaryocytes, which are responsible for myelofibrosis (33). TNFRSF13C is expressed in HNSCC tumor-infiltrating lymphocytes (34), and has been identified as an inducer of regulatory T cells in melanoma (35). The correlation of the NLR with ICI response has been investigated in several reports, including some in HNSCC (23, 24). Overall, the reported predictive value of the pretreatment NLR alone is not sufficient, as confirmed in our study, but its utility in combination with other factors was confirmed. RABL2B is a small RAB GTPase. Interestingly, several members of this family of proteins (e.g., RAB27) are known to regulate exosome biogenesis and to promote melanoma progression (36, 37). However, the physiological and pathological functions of RABL2B remain unclear. The zinc finger protein, ZNF480, is reported to be a core transcription factor required for embryonic stem cell differentiation (38), but its oncogenic function is poorly understood. In summary, the precise roles that make these 6 PEX mRNAs good prognostic biomarkers of nivolumab should be investigated in future studies. However, given the reported and predicted functions of each gene, these molecules likely have functions in the oncogenesis and the immune system, when expressed in PEX mRNA-producing cells (e.g., cancer cells) and recipient cells (e.g., immune cells).

It is obvious that this study includes limitations such as the sample size in both part 1 and 2 and the lack of explanation about the detailed mechanisms by which several specific PEX mRNAs work as a monitor of TIME. However, it seems that the strong prognostic predictive power demonstrated by our biomarker combination compensates these limitations and encourages further validation in a larger-scale study.

In conclusion, this pilot study indicates that it might be possible to predict non-survivors following nivolumab with a single pretreatment blood test. A prospective study that examines the efficacy of simultaneous administration of nivolumab and monalizumab in the candidate non-survivors also appears to be promising.

Data availability statement

The original contributions presented in the study are included in the article/Supplementary Material. Further inquiries can be directed to the corresponding author.

Ethics statement

The studies involving humans were approved by Institutional Review Board of the National Kyushu Cancer Center (2019–024). The studies were conducted in accordance with the local legislation and institutional requirements. The participants provided their written informed consent to participate in this study.

Author contributions

KS: Formal analysis, Methodology, Resources, Software, Validation, Visualization, Writing – review & editing. ST: Conceptualization, Data curation, Formal analysis, Investigation, Methodology, Project administration, Software, Supervision, Validation, Visualization,

Writing – review & editing. TMu: Conceptualization, Data curation, Formal analysis, Investigation, Methodology, Resources, Software, Supervision, Validation, Visualization, Writing – review & editing. TaN: Data curation, Formal analysis, Investigation, Methodology, Software, Validation, Visualization, Writing – review & editing. TH: Data curation, Formal analysis, Methodology, Software, Validation, Visualization, Writing – review & editing. MiM: Data curation, Writing – review & editing. KH: Data curation, Writing – review & editing. MS: Data curation, Writing – review & editing. KY: Data curation, Writing – review & editing. YU: Data curation, Writing – review & editing. ToN: Data curation, Writing – review & editing. HUr: Data curation, Writing – review & editing. TO: Data curation, Writing – review & editing. HUm: Data curation, Writing – review & editing. TU: Data curation, Writing – review & editing. SK: Data curation, Writing – review & editing. KT: Data curation, Writing – review & editing. AW: Data curation, Writing – review & editing. IO: Data curation, Writing – review & editing. NM: Data curation, Writing – review & editing. SI: Data curation, Writing – review & editing. TMa: Data curation, Writing – review & editing. YA: Data curation, Writing – review & editing. NH: Data curation, Writing – review & editing. DS: Data curation, Writing – review & editing. HO: Data curation, Writing – review & editing. TA: Data curation, Writing – review & editing. TF: Data curation, Writing – review & editing. MuM: Conceptualization, Data curation, Formal analysis, Funding acquisition, Investigation, Methodology, Project administration, Resources, Software, Supervision, Validation, Visualization, Writing – original draft, Writing – review & editing.

Funding

The author(s) declare financial support was received for the research, authorship, and/or publication of this article. This study was partly funded by JSPS KAKENHI [Grant number JP 21436707 to MuM] and Sota Memorial Fund to MuM. PEXmRNA analyses were conducted by Showa Denko America Materials. CReS Kyushu organized sample collection and transfer, and conducted clinical data management with funding provided by Ono and Bristol-Myers Squibb. The funders had no role in the study design, data collection and analysis, decision to publish, or preparation of the manuscript.

Acknowledgments

We thank Shoji Tokunaga (Medical Information Center, Kyushu University) for his advice on the study design (e.g., sample size) and statistical analyses and CreS Kyushu for intensive support.

Conflict of interest

The authors declare that the research was conducted in the absence of any commercial or financial relationships that could be construed as a potential conflict of interest.

Publisher's note

Supplementary material

The Supplementary Material for this article can be found online at: https://www.frontiersin.org/articles/10.3389/fimmu.2024.1464419/full#supplementary-material

References

1. Le X, Ferrarotto R, Wise-Draper T, Gillison M. Evolving role of immunotherapy in recurrent metastatic head and neck cancer. *J Natl Compr Cancer Netw.* (2020) 18:899–906. doi: 10.6004/jnccn.2020.7590

2. Ferris RL, Blumenschein G Jr., Fayette J, Guigay J, Colevas AD, Licitra L, et al. Nivolumab for recurrent squamous-cell carcinoma of the head and neck. *N Engl J Med.* (2016) 375:1856–67. doi: 10.1056/NEJMoa1602252

3. Ferris RL, Blumenschein G Jr., Fayette J, Guigay J, Colevas AD, Licitra L, et al. Nivolumab vs investigator's choice in recurrent or metastatic squamous cell carcinoma of the head and neck: 2-year long-term survival update of CheckMate 141 with analyses by tumor PD-L1 expression. *Oral Oncol.* (2018) 81:45–51. doi: 10.1016/j.oraloncology.2018.04.008

4. Tringale KR, Carroll KT, Zakeri K, Sacco AG, Barnachea L, Murphy JD. Cost-effectiveness analysis of nivolumab for treatment of platinum-resistant recurrent or metastatic squamous cell carcinoma of the head and neck. *J Natl Cancer Inst.* (2017). doi: 10.1093/jnci/djx226

5. Gavrielatou N, Doumas S, Economopoulou P, Foukas PG, Psyrri A. Biomarkers for immunotherapy response in head and neck cancer. *Cancer Treat Rev.* (2020) 84:101977. doi: 10.1016/j.ctrv.2020.101977

6. Ayers M, Lunceford J, Nebozhyn M, Murphy E, Loboda A, Kaufman DR, et al. IFN-gamma-related mRNA profile predicts clinical response to PD-1 blockade. *J Clin Invest.* (2017) 127:2930–40. doi: 10.1172/JCI91190

7. Ott PA, Bang YJ, Piha-Paul SA, Razak ARA, Bennouna J, Soria JC, et al. T-cell-inflamed gene-expression profile, programmed death ligand 1 expression, and tumor mutational burden predict efficacy in patients treated with pembrolizumab across 20 cancers: KEYNOTE-028. *J Clin Oncol.* (2019) 37:318–27. doi: 10.1200/jco.2018.78.2276

8. Walk EE, Yohe SL, Beckman A, SChade A, Zutter MM, Pfeifer J, et al. The cancer immunotherapy biomarker testing landscape. *Arch Pathol Lab Med.* (2020) 144:706–24. doi: 10.5858/arpa.2018-0584-CP

9. Möller A, Lobb RJ. The evolving translational potential of small extracellular vesicles in cancer. *Nat Rev Cancer.* (2020) 20:697–709. doi: 10.1038/s41568-020-00299-w

10. Prieto-Vila M, Yoshioka Y, Ochiya T. Biological functions driven by mRNAs carried by extracellular vesicles in cancer. *Front Cell Dev Biol.* (2021) 9:620498. doi: 10.3389/fcell.2021.620498

11. Amit M, Takahashi H, Dragomir MP, Lindemann A, Gleber-Netto FO, Pickering CR, et al. Loss of p53 drives neuron reprogramming in head and neck cancer. *Nature.* (2020) 578:449–54. doi: 10.1038/s41586-020-1996-3

12. Whiteside TL. Exosomes and tumor-mediated immune suppression. *J Clin Invest.* (2016) 126:1216–23. doi: 10.1172/JCI81136

13. Whiteside TL, Diergaarde B, Hong CS. Tumor-derived exosomes (TEX) and their role in immuno-oncology. *Int J Mol Sci.* (2021) 22. doi: 10.3390/ijms22126234

14. Murakami T, Yamamoto CM, Akino T, Tanaka H, Fukuzawa N, Suzuki H, et al. Bladder cancer detection by urinary extracellular vesicle mRNA analysis. *Oncotarget*. (2018) 9:32810–21. doi: 10.18632/oncotarget.25998

15. Thery C, Witwer KW, Aikawa E, Alcaraz MJ, Anderson JD, Andriantsitohaina R, et al. Minimal information for studies of extracellular vesicles 2018 (MISEV2018): a position statement of the International Society for Extracellular Vesicles and update of the MISEV2014 guidelines. *J Extracell Vesicles*. (2018) 7:1535750. doi: 10.1080/20013078.2018.1535750

16. Gentles AJ, Newman AM, Liu CL, Bratman SV, Feng W, Kim D, et al. The prognostic landscape of genes and infiltrating immune cells across human cancers. *Nat Med*. (2015) 21:938–45. doi: 10.1038/nm.3909

17. Friedman J, Hastie T, Tibshirani R. Regularization paths for generalized linear models via coordinate descent. *J Stat Softw*. (2010) 33:1–22. doi: 10.18637/jss.v033.i01

18. Matsuo M, Yasumatsu R, Masuda M, Yamauchi M, Wakasaki T, Hashimoto K, et al. Five-year follow-up of patients with head and neck cancer treated with nivolumab and long-term responders for over two years. *In Vivo*. (2022) 36:1881–6. doi: 10.21873/invivo.12907

19. Licitra L, Ferris RL, Harrington KJ, Guigay J, Blumenschein GJr., Kasper S, et al. Nivolumab vs investigator's choice (IC) in patients with recurrent or metastatic (R/M) squamous cell carcinoma of the head and neck (SCCHN): treatment effect on clinical outcomes by best overall response in checkmate 141. *Ann Oncol*. (2017) 28:377–8. doi: 10.1093/annonc/mdx374

20. Haddad R, Concha-Benavente F, Blumenschein GJr., Fayette J, Guigay J, Colevas AD, et al. Nivolumab treatment beyond RECIST-defined progression in recurrent or metastatic squamous cell carcinoma of the head and neck in CheckMate 141: A subgroup analysis of a randomized phase 3 clinical trial. *Cancer*. (2019) 125:3208–18. doi: 10.1002/cncr.32190

21. Dominguez CX, Muller S, Keerthivasan S, Koeppen H, Hung J, Gierke S, et al. Single-cell RNA sequencing reveals stromal evolution into LRRC15(+) myofibroblasts as a determinant of patient response to cancer immunotherapy. *Cancer Discovery*. (2020) 10:232–53. doi: 10.1158/2159-8290.CD-19-0644

22. Bai R, Lv Z, Xu D, Cui J. Predictive biomarkers for cancer immunotherapy with immune checkpoint inhibitors. *Biomark Res*. (2020) 8:34. doi: 10.1186/s40364-020-00209-0

23. Valero C, Lee M, Hoen D, Weiss K, Kelly DW, Adusumilli PS, et al. Pretreatment neutrophil-to-lymphocyte ratio and mutational burden as biomarkers of tumor response to immune checkpoint inhibitors. *Nat Commun*. (2021) 12:729. doi: 10.1038/s41467-021-20935-9

24. Wakasaki T, Yasumatsu R, Masuda M, Takeuchi T, Manako T, Matsuo M, et al. Prognostic biomarkers of salvage chemotherapy following nivolumab treatment for recurrent and/or metastatic head and neck squamous cell carcinoma. *Cancers (Basel)*. (2020) 12. doi: 10.3390/cancers12082299

25. Skog J, Wurdinger T, van Rijn S, Meijer DH, Gainche L, Sena-Esteves M, et al. Glioblastoma microvesicles transport RNA and proteins that promote tumour growth and provide diagnostic biomarkers. *Nat Cell Biol*. (2008) 10:1470–6. doi: 10.1038/ncb1800

26. Borst L, van der Burg SH, van Hall T. The NKG2A-HLA-E axis as a novel checkpoint in the tumor microenvironment. *Clin Cancer Res*. (2020) 26:5549–56. doi: 10.1158/1078-0432.CCR-19-2095

27. Andre P, Denis C, Soulas C, Bourbon-Caillet C, Lopez J, Arnoux T, et al. Anti-NKG2A mAb is a checkpoint inhibitor that promotes anti-tumor immunity by unleashing both T and NK cells. *Cell*. (2018) 175:1731–43.e13. doi: 10.1016/j.cell.2018.10.014

28. Mandal R, Senbabaoglu Y, Desrichard A, Havel JJ, Dalin MG, Riaz N, et al. The head and neck cancer immune landscape and its immunotherapeutic implications. *JCI Insight*. (2016) 1:e89829. doi: 10.1172/jci.insight.89829

29. Hatae R, Chamoto K, Kim YH, Sonomura K, Taneishi K, Kawaguchi S, et al. Combination of host immune metabolic biomarkers for the PD-1 blockade cancer immunotherapy. *JCI Insight*. (2020) 5. doi: 10.1172/jci.insight.133501

30. Sheffer M, Lowry E, Beelen N, Borah M, Amara SN, Mader CC, et al. Genome-scale screens identify factors regulating tumor cell responses to natural killer cells. *Nat Genet*. (2021) 53:1196–206. doi: 10.1038/s41588-021-00889-w

31. Galot R, Le Tourneau C, Saada-Bouzid E, Daste A, Even C, Debruyne P, et al. A phase II study of monalizumab in patients with recurrent/metastatic squamous cell carcinoma of the head and neck: The I1 cohort of the EORTC-HNCG-1559 UPSTREAM trial. *Eur J Cancer*. (2021) 158:17–26. doi: 10.1016/j.ejca.2021.09.003

32. Herbst RS, Majem M, Barlesi F, Carcereny E, Chu Q, Monnet I, et al. COAST: an open-label, phase II, multidrug platform study of durvalumab alone or in combination with oleclumab or monalizumab in patients with unresectable, stage III non-small-cell lung cancer. *J Clin Oncol*. (2022) Jco2200227. doi: 10.1200/jco.22.00227

33. Psaila B, Wang G, Rodriguez-Meira A, Li R, Heuston EF, Murphy L, et al. Single-cell analyses reveal megakaryocyte-biased hematopoiesis in myelofibrosis and identify mutant clone-specific targets. *Mol Cell*. (2020) 78:477–92.e8. doi: 10.1016/j.molcel.2020.04.008

34. Cillo AR, Kurten CHL, Tabib T, Qi Z, Onkar S, Wang T, et al. Immune landscape of viral- and carcinogen-driven head and neck cancer. *Immunity*. (2020) 52:183–99.e9. doi: 10.1016/j.immuni.2019.11.014

35. Zhang C, Dang D, Cong L, Sun H, Cong X. Pivotal factors associated with the immunosuppressive tumor microenvironment and melanoma metastasis. *Cancer Med*. (2021) 10:4710–20. doi: 10.1002/cam4.3963

36. Stenmark H. Rab GTPases as coordinators of vesicle traffic. *Nat Rev Mol Cell Biol*. (2009) 10:513–25. doi: 10.1038/nrm2728

37. Peinado H, Aleckovic M, Lavotshkin S, Matei I, Costa-Silva B, Moreno-Bueno G, et al. Melanoma exosomes educate bone marrow progenitor cells toward a pro-metastatic phenotype through MET. *Nat Med*. (2012) 18:883–91. doi: 10.1038/nm.2753

38. Zhang C, Li C, Yang L, Leng L, Jovic D, Wang J, et al. The dynamic changes of transcription factors during the development processes of human biparental and uniparental embryos. *Front Cell Dev Biol*. (2021) 9:709498. doi: 10.3389/fcell.2021.709498

frontiers | Frontiers in Immunology

TYPE Original Research
PUBLISHED 13 January 2025
DOI 10.3389/fimmu.2024.1478904

OPEN ACCESS

EDITED BY
Takaji Matsutani,
Maruho, Japan

REVIEWED BY
Shivam Priya,
The Ohio State University, United States
Dmitry Aleksandrovich Zinovkin,
Gomel State Medical University, Belarus
Javier Ismael Altamirano García,
National Institute of Cancerology (INCAN), Mexico

*CORRESPONDENCE
Huang Yuqing
doctorark@163.com
Jin Haigang
jhgwzxshp@163.com
Wang Shaowen
Shawnwang1994@link.cuhk.edu.hk

†These authors have contributed equally to this work

RECEIVED 11 August 2024
ACCEPTED 24 December 2024
PUBLISHED 13 January 2025

CITATION
Pengping L, Kexin Y, Yuwei X, Ke S, Rongguo L, Zhenyu W, Haigang J, Shaowen W and Yuqing H (2025) Construction of an anaplastic thyroid cancer stratification signature to guide immune therapy selection and validation of the pivotal gene HLF through *in vitro* experiments. *Front. Immunol.* 15:1478904. doi: 10.3389/fimmu.2024.1478904

Construction of an anaplastic thyroid cancer stratification signature to guide immune therapy selection and validation of the pivotal gene HLF through *in vitro* experiments

Li Pengping[1†], Yin Kexin[1†], Xie Yuwei[2†], Sun Ke[1], Li Rongguo[1], Wang Zhenyu[1], Jin Haigang[1*], Wang Shaowen[3*] and Huang Yuqing[1*]

[1]Department of Thyroid & Breast Surgery, The First People's Hospital of Xiaoshan District, Xiaoshan Affiliated Hospital of Wenzhou Medical University, Hangzhou, Zhejiang, China, [2]The First Affiliated Hospital of Anhui Medical University, Hefei, Anhui, China, [3]Neuromedicine Center, The University of Hong Kong-Shenzhen Hospital, Shenzhen, Guangdong, China

Introduction: While most thyroid cancer patients have a favorable prognosis, anaplastic thyroid carcinoma (ATC) remains a particularly aggressive form with a median survival time of just five months. Conventional therapies offer limited benefits for this type of thyroid cancer. Our study aims to identify ATC patients who might bene t from immunotherapy.

Methods: Our study uses multiple algorithms by R4.2.0, and gene expression and clinical data are collected from TCGA, GEO and local cohort. In vitro experiments, such as western blot and immunofluorescence staining, are performed.

Results: Using a set of five genes uniquely expressed across various types of thyroid cancer, we developed a machine-learning model to distinguish each type within the GEO dataset of thyroid cancer patients (GSE60542, GSE76039, GSE33630, GSE53157, GSE65144, GSE29265, GSE82208, GSE27155, GSE58545, GSE54958, and GSE32662). These genes allowed us to stratify ATC into three distinct groups, each exhibiting significantly different responses to anti-PD1 therapy as determined by consensus clustering. Through weighted gene co-expression network analysis (WGCNA), we identified 12 differentially expressed genes closely associated with immunotherapy outcomes. This led to the creation of a refined signature for predicting ATC's immune responsiveness to anti-PD1 therapy, which was further validated using thyroid cancer cohorts from TCGA and nine melanoma cohorts from clinical trials. Among the 12 genes, HLF stood out due to its strong association with various cancer hallmarks.

Discussion: Our study revealed that HLF impedes ATC progression by down-regulating the epithelial-to-mesenchymal transition (EMT) pathway, reducing T cell exhaustion, and increasing sensitivity to sorafenib, as demonstrated through our *in-vitro* experiments.

KEYWORDS

anaplastic thyroid cancer (ATC), T cell immunity, machine learning, prediction, model

1 Introduction

Although the prognosis for most thyroid cancer patients is favorable, anaplastic thyroid carcinoma (ATC) remains a notably aggressive form with a median survival time of only five months (1, 2). ATC comprises only 2% of all types of thyroid cancers but accounts for a disproportionate 14% to 39% of deaths associated with this cancer (3). For patients who outlive the median survival time, conventional therapies such as chemotherapy and radiotherapy offer limited benefits (4, 5). Besides, early diagnosis of ATC presents another significant challenge. Thus, detecting ATC in its initial stages and finding other effective therapies are both crucial for improving patient outcomes.

It has been reported that resistance to chemotherapy and radiotherapy is the main reason for poor survival. For some patients carrying the BRAF and MEK gene mutation, the combination of dabrafenib and trametinib has shown promise in extending the effective treatment period (6). For those patients without these mutations, immunotherapy (anti-PD-1 and anti-PD-L1) has manifested a 1-year survival rate of approximately 40%, making it the most promising known therapy (7). However, more research is still urgently needed to identify the subgroup of patients who can benefit from the immunotherapy.

Our study endeavors to identify ATC patients who could potentially benefit from immunotherapy. Leveraging a set of five uniquely expressed genes across various types of thyroid cancer, our research has developed a machine-learning model capable of distinguishing each type within the GEO dataset of thyroid cancer patients (GSE60542, GSE76039, GSE33630, GSE53157, GSE65144, GSE29265, GSE82208, GSE27155, GSE58545, GSE54958, and GSE32662). Utilizing these genes, we have stratified ATC into three distinct groups, each demonstrating significantly different responses to anti-PD1 therapy. Additionally, we employed weighted gene co-expression network analysis (WGCNA) to identify 12 differentially expressed genes intimately associated with both the grouping and immunotherapy outcomes. This led to the creation of a refined signature that could more accurately predict ATC's immune responsiveness to anti-PD1 therapy, which was further corroborated using thyroid cancer cohorts and 9 melanoma cohorts from the clinical trial. Among the 12 genes analyzed, HLF emerged as significantly associated with various cancer hallmarks. Our study elucidated the mechanism by which HLF impeded anaplastic thyroid carcinoma (ATC) progression. Specifically, HLF down-regulated the epithelial-to-mesenchymal transition (EMT) pathway, reduced T cell exhaustion, and increased sensitivity to sorafenib, as demonstrated by our *in-vitro* experiments.

2 Methods

2.1 Data collection

Gene expression profiles and clinical characteristics of thyroid cancer were collected from the cancer genome atlas (TCGA, https://portal.gdc.cancer.gov) and gene expression omnibus (GEO, https://www.ncbi.nlm.nih.gov/geo/). A total of 506 samples with follow-up data were collected from TCGA, and 715 samples were collected from GEO datasets GSE27155, GSE58545, GSE76039, GSE82208, GSE60542, GSE29265, GSE33630, GSE65144, GSE53157, GSE54958, and GSE32662. Among these, 114 samples were thyroid non-cancerous tissue (TNC), 78 samples were anaplastic thyroid carcinoma (ATC), 225 samples were papillary thyroid carcinoma (PTC), 40 samples were follicular thyroid carcinoma (FTC), and 54 samples were medullary thyroid carcinoma (MTC). Verified cohorts of clinical trials (anti-PD1) were collected from GSE115821 (N=37), GSE78220 (N=28), GSE91061 (N=109), Nathanson_2017 (N=24), phs000452 (N=153), and PRJEB23709 (N=91).

2.2 Bioinformatic analysis

2.2.1 Subgrouping signature construction

GEO cohorts of thyroid cancer (TC) were used to identify differentially expressed genes (DEGs) in ATC using R4.2.0 (package: DESeq2). The ConsensusClusterPlus package in R4.2.0 was employed to perform consensus clustering analysis based on the 5 DEGs (BCL2, BHLHE40, MICAL2, TGM2, TPO) (parameters: maxK=10, reps=50). The consensus cumulative density function (CDF) and delta area indicated that a 3-subgroup division was the optimal outcome.

2.2.2 Subtype identification model construction

Decision curve analysis (DCA) was used to evaluate the value of the 5-DEGs in identifying ATC or other subgroups of TC using the ggDCA package in R4.2.0. The DALEX, randomForest, kernlab, xgboost, caret, and pROC packages were applied to construct identification models.

2.2.3 Tumor immune index calculation

Infiltration immune cell fractions were predicted using CIBERSORT, ssGSEA (single sample GSEA), and Pompimol Charoentong's algorithm in R4.2.0. The immune score was predicted using the estimate package in R4.0. Tumor Immune Dysfunction and Exclusion (TIDE) and anti-PD1 response were predicted using the online tool (http://tide.dfci.harvard.edu). To assess MeTIL characteristics, the individual methylation values of MeTIL markers were converted to MeTIL scores using principal component analysis (PCA). The data were converted to a unit-free Z-Score by applying the formula $(x-\mu)/\sigma$. According to the median value of PDCD1, the samples were divided into high and low-expression groups. Wilcoxon Rank Sum Tests were used to compare the MeTIL scores between the two groups (8).

TIP (Tracking Tumor Immunophenotype) was a meta-server that systematically integrates two existing third-party methods, "ssGSEA" and "CIBERSORT", for tracking, analyzing, and visualizing the anti-cancer immune state and the proportion of immune-infiltrating cells in the seven steps of the cancer immune cycle using RNA-seq or microarray data. Spearman correlation between genes and TIP scores, as well as the autocorrelation between TIP scores, were calculated, and the linkET package was used for visualization (8). The red and green lines represented positive and negative correlations, respectively, while the gray lines indicated no significance. The thickness of the lines represented the absolute value of the correlation coefficient. The correlation in the triangular region was represented by the color depth and size of the square: red/blue indicated a positive/negative correlation, with darker colors signifying more significant P-values, and larger squares representing greater absolute values of the correlation coefficient. Easier was a tool for predicting biomarker-based immunotherapies (Cytolytic score, CYT; Tertiary lymphoid structures, TLS; IFNy, T cell-inflamed, Chemokines) based on cancer-specific immune response models, aiming to predict anti-tumor immune responses from RNA-seq data. The CYT level of TCGA-BLCA was calculated using the Easier package to evaluate CYT characteristics. According to the median value of PDCD1, the samples were divided into high and low-expression groups (9). Wilcoxon Rank Sum Tests were used to compare the CYT scores between the two groups.

2.2.4 Cell signaling score calculation

The CancerSEA database collated 14 different functional states of tumor cells (10). The Z-score algorithm, proposed by Lee et al. (11), integrated characteristic gene expression to reflect the activity of a given pathway. Fourteen functional state gene sets were calculated using the Z-score algorithm in the R-package GSVA. The values of each gene set were enumerated separately as Z-scores. Pearson correlations between genes and the Z-scores of each gene set were then calculated.

2.2.5 Pan-cancer analysis of HLF expression

The expression level of HLF in pan-cancer was calculated by R4.2.0 (TCGA cohorts).

2.2.6 The 12-gene signature construction

Firstly, WGCNA (Weighted Gene Co-Expression Network Analysis) was applied to screen out hub genes using the WGCNA package in R4.2.0. The most correlated gene sets (both negative and positive) were collected for subsequent machine learning. AI modeling for ATC subgroup stratification was developed using six AI functions: extreme gradient boosting (XGboost, xgboost package in R4.2.0), support vector machine (SVM, e1071 packages in R4.2.0), multi-logistic (nnet packages in R4.2.0), random forest (RF, randomForest package in R4.2.0), deep learning (DL, h2o package in R4.2.0), and K-Nearest Neighbor (KNN, kknn package in R4.2.0). During model construction, 75% of the data was randomly selected as the training cohort, and 25% was randomly selected as the testing cohort. Gene expression values were standardized to range from 0 to 1 using the preProcess function (caret and tidyverse packages).

2.3 Biological experiments

2.3.1 Clinical sample collection

Twenty-two thyroid cancer samples were collected from 2021-12-01 to 2022-08-01. All experiments were approved by the Medical Ethics Committee of The First People's Hospital of Xiaoshan District, Xiaoshan Affiliated Hospital of Wenzhou Medical University. All patients with ATC were confirmed by at least two pathologists.

2.3.2 Multiple immune fluorescence staining

The procedures for paraffin embedding, tissue sectioning, and immunohistochemistry for HLF, CD8, and PD1 expression levels were performed as previously described (PMID: 23200678 and 20571492). The working concentrations of antibodies against HLF (Proteintech, Wuhan, China), CD8 (Abcam, Shanghai), and PD1 (Proteintech, Wuhan, China) were 1:150. The protein expression levels were assessed by Mean of Integrated Option Density (IOD) with Image-Pro Plus. Briefly, the area of interest (AOI) was detected to gain the Mean of IOD (IOD/AOI, MI).

2.3.3 Reagents

Sorafenib was purchased from CSNpharm (A316727) and dissolved in PBS. Antibodies against beta-actin (AF7018, Affinity), CD8 (GB15068, Servicebio), HLF (DF7892, Affinity), N-cadherin (AF5239, Affinity), E-cadherin (BF0219, Affinity), Vimentin (BF8008, Affinity), Twist1 (AF4009, Affinity), Snail1 (AF6032, Affinity), PD-L1 (BF8035, Affinity), phosphorylated-JAK3 (p-JAK3, AF8160, Affinity), JAK3 (AF0008, Affinity), p-STAT3 (AF3293, Affinity), and STAT3 (BF6294, Affinity) were used for western blot.

2.3.4 Cell culture

ATC cell lines (CAL62, TCO1) were obtained from the cell bank of the Chinese Academy of Science in 2022 with STR matching analysis. The culture media for both ATC cell lines were DMEM with 10% fetal calf serum and 100 units/mL penicillin and streptomycin.

2.3.5 Small interfering RNA experiments

5 × 10^5 ATC cells were transplanted into 6-well plates for 24 hours and then transfected with three different sequences of HLF siRNA (GenePharma, Shanghai, China) for 48, 72, and 96 hours using Lipofectamine 3000 reagent (Invitrogen, USA) and Opti-MEM (Life Technologies, USA), according to the manufacturer's instructions for optimal transfection efficiency. The three siRNA sequences for HLF were as follows:

Sequence-1
Forward (5′-3′): TGCAAAATGTTCAAAATTGAA
Reverse (5′-3′): CAATTTTGACATTTTGCTAA

Sequence-2
Forward (5′-3′): ATTAAAAAAAAACTTTTCGGGTC
Reverse (5′-3′): CGAAAGTTTTTTTTTAATAT

Sequence-3
Forward (5′-3′): AAATGTTGCTGAGCTTTTCCT
Reverse (5′-3′): GAAAGCTCAGCAACTTTTA

2.3.6 Western blot

Total protein extraction: Cells were harvested using a cytology brush and lysed with RIPA lysis buffer (Sigma, USA) supplemented with phosphorylase and protease inhibitor mixture (Thermo, USA), and quantified by the BCA assay. Cytoplasmic and nuclear protein extraction: Cells were harvested using trypsin (Invitrogen), then cytoplasmic and nuclear proteins were extracted using the Cytoplasmic and Nuclear Protein Extraction Kit (Thermo Scientific, USA) according to the protocol, and quantified by the BCA assay. Protein samples were separated by SDS-PAGE (EpiZyme, China, PG113) and transferred to a 0.45 μm or 0.20 μm pore-sized PVDF membrane (Millipore, USA). The membranes were blocked with Tris-buffered saline containing 5% skim milk powder (Biosharp, BS102-500 g, China) at room temperature for 1 hour, followed by incubation with primary antibodies at 4°C overnight. The next day, after three washes with TBST solution, the membranes were incubated with secondary antibodies at room temperature for 60 minutes. Finally, immunoreactive bands were detected using an enhanced chemiluminescence kit (Biosharp, BL520B, China). The conjugation yield was calculated via gel band quantification using Image J software (12).

2.3.7 Migration ability assays

For trans-well assays, 50,000 cells, with or without special treatments, were transplanted into trans-well plates (24-well, 8.0μm, Corning Incorporated, Corning, NY, USA) with a 10% gradient of fetal calf serum for 48 hours. After 24 hours of incubation, the cells that had migrated to the lower surface of the filter were fixed with 4% paraformaldehyde and stained with hematoxylin and eosin. The stained cells were then observed and photographed using a light microscope. Quantification of the passed cell area was performed using Image-Pro Plus (13).

2.3.8 Live & dead cell staining

Live and dead cell staining was carried out using Calcein AM/PI staining. After being seeded in a 24-well plate and cultured for 24 hours, ATC cells were treated with DMSO or 5μM GEM for another 48 hours. Then, all cells were co-cultured with Calcein AM and PI and observed at 480 nm and 525 nm, respectively.

2.3.9 PBMCs extraction

Simply, PBMCs were isolated via Ficoll-Paque density gradient centrifugation: 5 mL of peripheral blood was collected from healthy female volunteers, diluted with PBS at a 1:1 ratio, followed by gentle mixing. Add 10 mL of the diluted blood to 2 mL of Ficoll liquid (density 1.077). The clear stratification of blood and Ficoll liquid confirmed success. Carefully transferred the sample to the centrifuge and spin at 500 g for 15 minutes. Removed the centrifuge tube with care, aspirate the white thin film layer in the middle, representing individual nucleated cells. Wash the isolated nucleated cells with 10 mL of PBS, centrifuge at 250 g for 10 minutes, and discarded the supernatant. Repeat the washing step once and the suspended cells were frozen in vials at 100 million cells/mL in HI FBS with 5% DMSO after washing. Stored in liquid nitrogen, they were revived gradually and washed in pre-warmed RPMI with FBS and pen/strep. Following a 4-5 hour incubation at 37°C, viability was assessed using Trypan blue (0.1%).

2.3.10 Flow cytometry

The co-cultured PBMC were stained with Fixable Viability Stain (Thermo, L34965) and Fc receptor blocking reagent [Ultra-LEAF™ Purified anti-mouse CD16/32 (101320, BioLegend)]. Next, they were stained with CD-3 (BD 557943), PD-1 (BD 561273), and CD8 antibody (thermo, A15448). The prepared single-cell suspensions were filtered through 40-μm nylon meshes (352340, Corning). Results were then acquired using BD Calibur, BD Fortessa, or Miltenyi MACSQuant systems. Data were analyzed with FlowJo_V10 software (TreeStar).

2.4 Statistical analysis

All data analyses were performed in R4.2.0. Pearson's test was used to calculate the correlation between different genes. Wilcox rank sum test and Kruskal-Wallis rank sum test were used to assess differences in continuous variables. Univariate Cox regression was performed to calculate the hazard ratio (HR), and the log-rank test was used to compare survival differences. Heatmaps were generated using the pheatmap package in R4.2.0. Receiver operating characteristic (ROC) curves and AUC values were generated using the pROC package in R4.2.0. GO and KEGG analyses were performed using the clusterProfiler package in R4.2.0. $P<0.05$ was considered to indicate a statistically significant difference.

3 Results

3.1 Five distinct genes were expressed significantly between any pair of thyroid cancer subtypes

The main available gene expression data of 537 thyroid cancer samples from GEO database (GSE60542, GSE76039, GSE33630, GSE53157, GSE65144, GSE29265, GSE82208, GSE27155, GSE58545, GSE54958, and GSE32662) were extracted for analysis of differentially expressed genes between different subtypes of thyroid cancer (Figure 1A). Multiple comparisons between each group identified five genes (BCL2, BHLHE40, MICAL2, TGM2, TPO) that are significantly differentially expressed (P value > 0.05 and a fold change (|FC|) > 2) in any pair of all the subtypes (thyroid carcinoma (TCA), differentiated thyroid carcinoma (DTC), anaplastic thyroid carcinoma (ATC), papillary thyroid carcinoma (PTC), medullary thyroid carcinoma (MTC), follicular thyroid carcinoma (FTC), thyroid non-cancerous tissues (TNC) (Figures 1B–F).

3.2 The model based on the 5 genes by machine learning can distinguish each subtype well

BCL2, BHLHE40, MICAL2, TGM2, and TPO were further employed to make a model to differentially diagnose TCA from TNC (Figures 2A–C), ATC from DTC (Figures 2D–F), MTC from DTC (Figures 2G–I), and FTC from DTC (Figures 2J–L). Different machine learning algorithms, for instance, Random Forest (RF), Support Vector Machine (SVM), eXtreme Gradient Boosting (XGB), Generalized Linear Model (GLM), Gradient Boosting Machine (GBM), Kernel k-Nearest Neighbors (KKNN), Neural Network (NNET), Least Absolute Shrinkage and Selection Operator (LASSO) were used to select the best model. With six of eight AUC values more than 0.9 (Figures 2B, E, H, K, I, L), the model based on RF was validated as the best one in both TCGA and GEO databases.

3.3 The immune cell infiltration varied significantly among the ATC subgroups C1, C2, and C3

The immune cell infiltration between TNC and ATC, calculated by three methods (Pompimol Charoentong's algorithm, ssGSEA and CIBERSORT), was presented in a heatmap. A majority of immune cell types could infiltrate the tumor microenvironment in ATC (Figure 3A). Consensus clustering based on the previous 5 genes was harnessed to categorize ATC into three distinct groups: C1, C2, and C3 (Figure 3B). The immune cell infiltration in the three ATC subgroups was further calculated using three well-recognized methods. Approximately 85% of the immune cell types, including activated CD4 T cells, central memory CD8 T cells, effector memory CD8 T cells, dendritic cells, and macrophages, exhibited differential infiltration among C1-C3. Significant differences in activated CD8 T cell infiltration were observed in the results from the first two methods (Figures 3C–E).

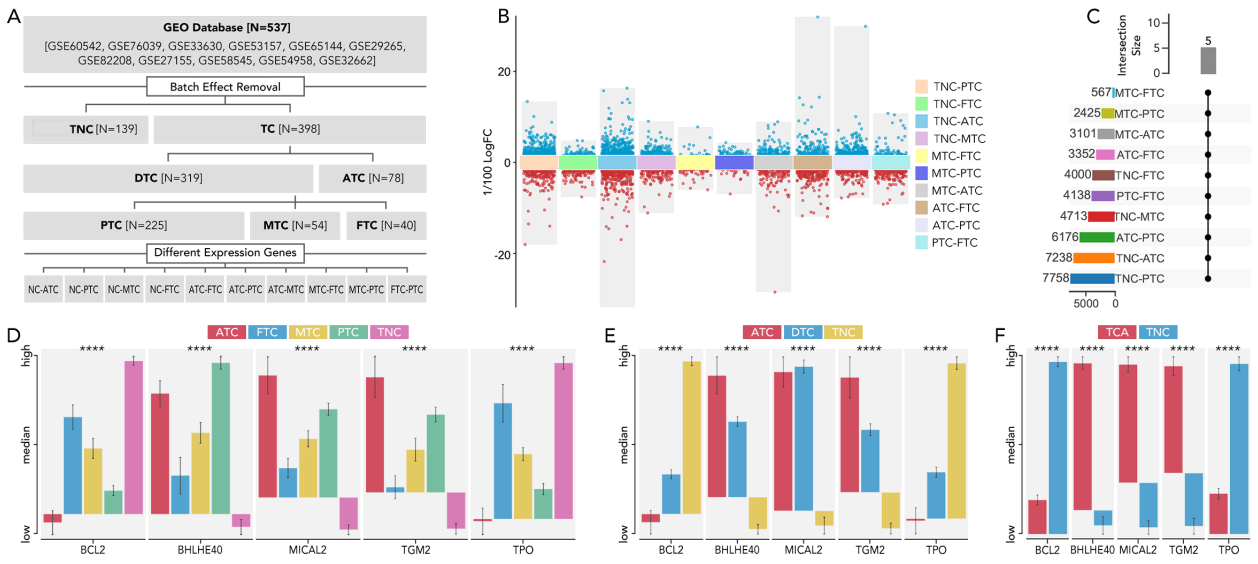

FIGURE 1
The 5 distinct genes were expressed differently in each type of thyroid cancer. **(A)** Flow chart illustrating the thyroid dataset acquisition and comparison strategies in TCA. **(B)** The analysis of differentially expressed genes was conducted between various thyroid cancer subtypes and NC. The comparisons included TNC vs. PTC, TNC vs. FTC, TNC vs. ATC, TNC vs. MTC, MTC vs. FTC, MTC vs. PTC, MTC vs. ATC, ATC vs. FTC, ATC vs. PTC, and PTC vs. FTC. The criteria for significance were set at a P value > 0.05 and a fold change (|FC|) > 2. **(C)** The number of differentially expressed genes in each comparison was listed, with 5 genes consistently differentially expressed across all comparisons. **(D)** The expression levels of these five genes were compared among ATC, FTC, MTC, PTC, and TNC. **(E)** The expression levels of these five genes were compared among ATC, DTC, and TNC. **(F)** The expression levels of these five genes were compared among ATC, DTC, and TNC thyroid carcinoma (TCA), differentiated thyroid carcinoma (DTC), anaplastic thyroid carcinoma (ATC), papillary thyroid carcinoma (PTC), medullary thyroid carcinoma (MTC), follicular thyroid carcinoma (FTC), thyroid non-cancerous tissues (TNC), fold change (FC) P value < 0.0001 (****).

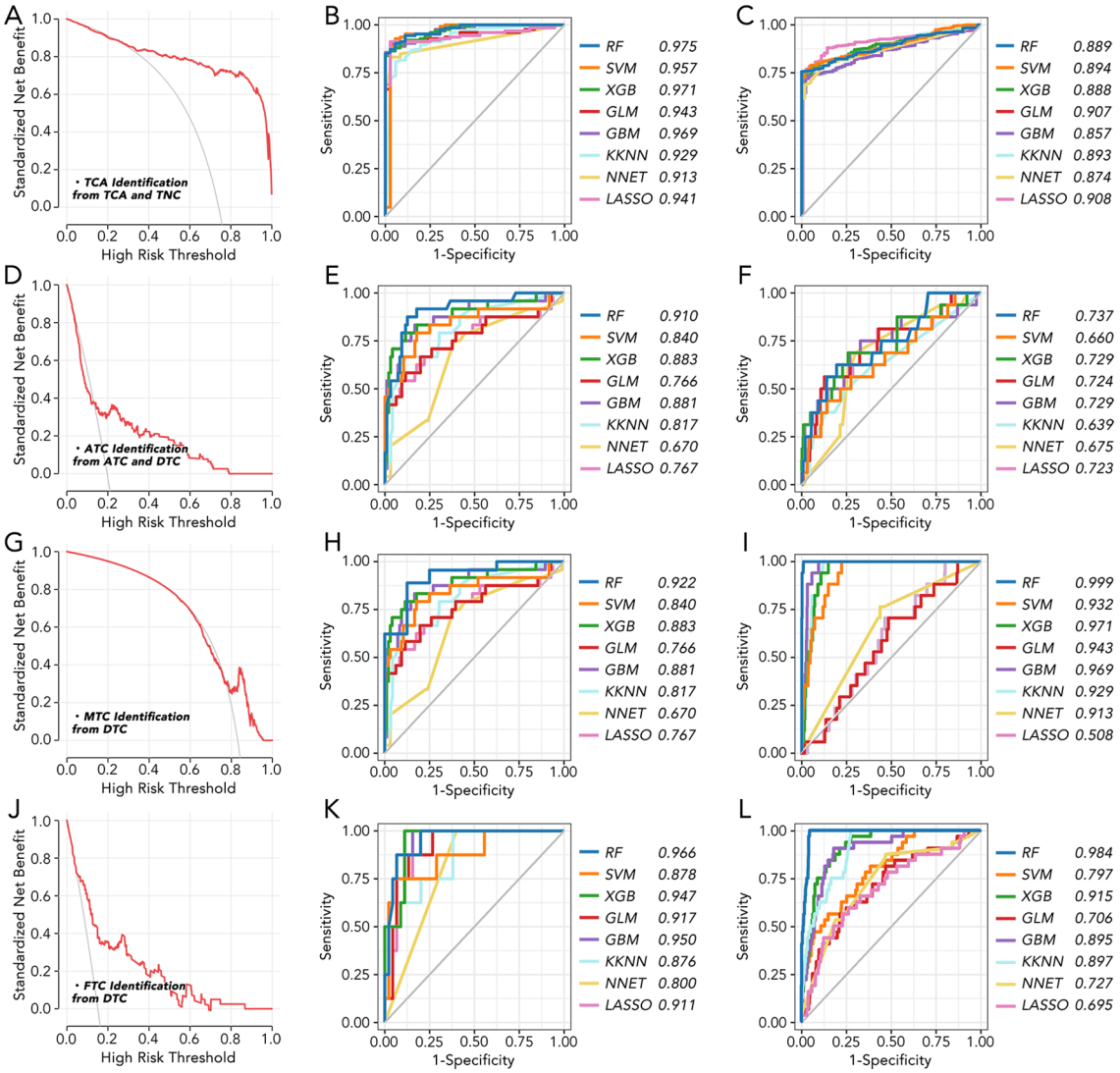

FIGURE 2
The machine learning model for thyroid cancer classification based on 5 key genes **(A)** The standardized net benefit and high-risk threshold were calculated between TCA and TNC. **(B)** Machine learning model to distinguish TCA from TNC in GEO datasets based on 5 key genes. **(C)** Machine learning model to distinguish TCA from TNC in TCGA based on 5 key genes. **(D)** The standardized net benefit and high-risk threshold were calculated between ATC and DTC. **(E)** Machine learning model to distinguish ATC from DTC in GEO datasets based on 5 key genes. **(F)** Machine learning model to distinguish ATC from DTC in TCGA based on 5 key genes. **(G)** The standardized net benefit and high-risk threshold were calculated between MTC and DTC. **(H)** Machine learning model to distinguish MTC from DTC in GEO datasets based on 5 key genes. **(I)** Machine learning model to distinguish MTC from DTC in TCGA based on 5 key genes. **(J)** The standardized net benefit and high-risk threshold were calculated between FTC and DTC. **(K)** Machine learning model to distinguish FTC from DTC in GEO datasets based on 5 key genes. **(L)** Machine learning model to distinguish FTC from DTC in TCGA based on 5 key genes. RF, Random Forest; SVM, Support Vector Machine; XGB, eXtreme Gradient Boosting; GLM, Generalized Linear Model; GBM, Gradient Boosting Machine; KKN, Kernel k-Nearest Neighbors; NNET, Neural Network; LASSO, Least Absolute Shrinkage and Selection Operator.

3.4 The predicted immunotherapy response differed among the ATC subgroups C1, C2, and C3

The expression of key immune checkpoints was compared among the three groups (Figure 4A). CTLA4, CD80, and CD86 (CTLA4 system) were most highly expressed in the C2 group and least expressed in the C1 group (Figure 4B). LAG3 and FGL1 exhibited a similar expression pattern to the CTLA4 system (Figure 4C). Inhibitory markers of CD8 T cells, including T cell exhaustion (TEX) and regulatory T cells (Treg), were more highly expressed in the C2 and C3 groups, while markers of T cells in a stress response state (T sr) were relatively higher in the C1 and C2 groups (Figure 4D). Activating markers of CD8 T cells, such as the cGAS-STING score and CD8 effector T cells (Teff), showed a similar expression pattern to TEX and Treg (Figure 4E). Other immune markers, including IFN-gamma, CD80, and dysfunction score, were also enriched in the C2 and C3 groups (Figure 4F). According to the Tumor Immune Dysfunction and Exclusion (TIDE) analysis, patients in the C1 group may benefit from anti-PD1 therapy, whereas those in the C2 and C3 groups may be more suitable for cytotoxic T lymphocyte (CTL) therapy (Figure 4G).

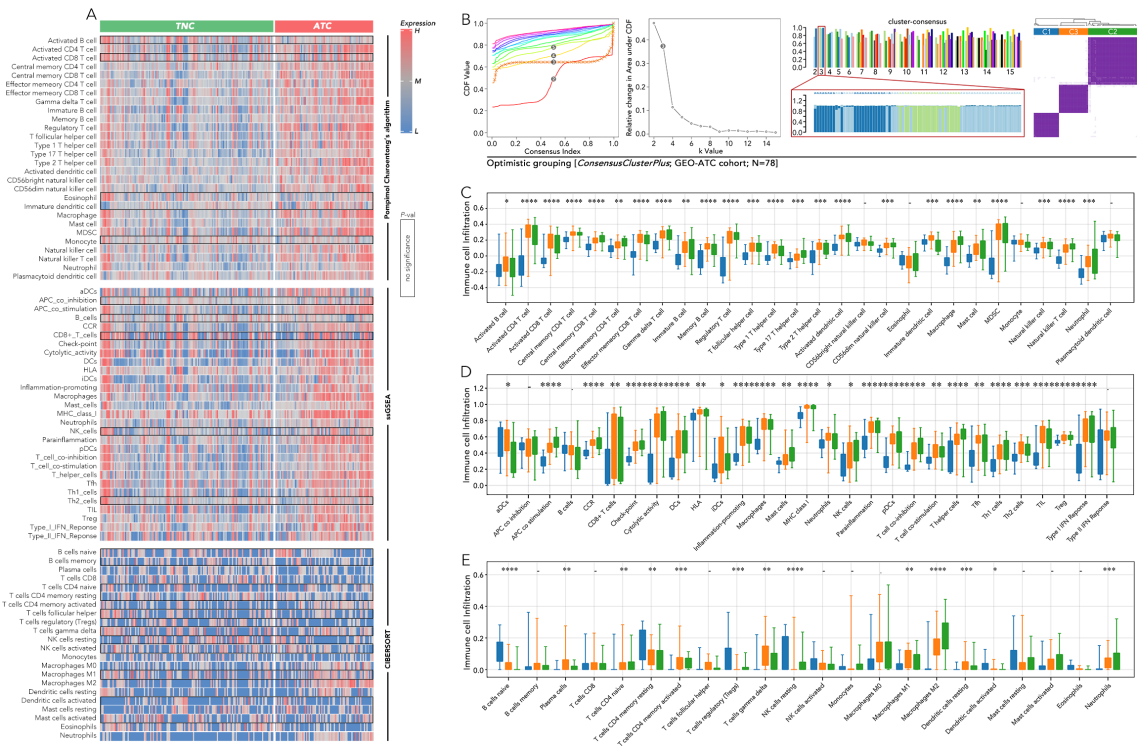

FIGURE 3
Immune cell infiltration analysis among anaplastic thyroid cancer (ATC) subgroups based on 5 key genes. **(A)** Immune cell infiltration was calculated by Pompimol Charoentong's algorithm, ssGSEA, and CIBERSORT compared in TNC and ATC. **(B)** Consensus clustering based on the previous 5 genes divided the ATC into 3 three subgroups (C1, C2, C3). **(C)** Immune cell infiltration calculated by Pompimol Charoentong's algorithm was compared among C1, C2, and C3. **(D)** Immune cell infiltration calculated by ssGSEA was compared among C1, C2, and C3. **(E)** Immune cell infiltration calculated by CIBERSORT was compared among C1, C2, and C3. SsGSEA (single sample GSEA) P value < 0.05 (*), P value < 0.01 (**), P value < 0.001 (***), P value < 0.0001 (****).

3.5 12 innovative genes identified by WGCNA effectively distinguished C1-C3 groups using machine learning

Based on the weighted gene co-expression network analysis (WGCNA), the purple gene module was most negatively correlated with the grouping, TEX, CTLA-4, LAG-3, PD-L1, and immune dysfunction score, while the yellow module was most positively correlated with these markers (Figures 5A–D). Further analysis, overlapping the differentially expressed genes between each pair of C1-C3 groups (P value > 0.05 and a fold change (|FC|) > 2) with the combined gene set of both the yellow and purple modules, identified 12 genes (HLF, BCL2, HHEX, LRP2, FOXE1, FAM189A2, TSHR, EPB41L4B, OCLN, NEBL, ATP8A1, and TMEM30B) that may play an important role in the immune therapy of ATC (Figure 5E). The expression of these 12 genes showed consistent patterns within the C1-C3 groups (high in C1, intermediate in C2, and low in C3) (Figure 5F). Moreover, the individual expression of these 12 genes was positively related to TEX (Figure 5G). The subgrouping model by SVM, based on these 12 genes, effectively distinguished the C1-C3 groups with an AUC over 0.9 (Figures 5H–K).

3.6 Grouping based on the 12 genes across 9 melanoma cohorts receiving anti-PD1 therapy revealed significantly different response rates

The grouping model based on the 12 innovative genes was validated in available clinical trial cohorts. Except in the melanoma-PRJEB23709 cohort, the actual response rates to anti-PD1 therapy in the C2 and C3 groups were much lower than in the C1 group, consistent with our results (Figures 4G; 6A–D). The correlation of individual gene expression with the predicted response rate to anti-PD1 therapy, as determined by TIDE, was further analyzed (Figure 7A). HLF, ATP8A1, and NEBL stood out due to their correlation coefficients over 0.4 and AUC values over 0.75 (Figures 7B, C). All components of the 12-gene signature were down-regulated in the TCGA thyroid cancer samples compared to the non-cancer samples (Figure 7D). Of the three genes, only HLF was of prognostic significance in the disease-free interval (DFI) of TCGA thyroid carcinoma (THCA) patients (Figure 7E). More importantly, its pro-survival role in prognosis was further corroborated in overall survival (OS) from three head and neck squamous cell carcinoma (HNSC) cohorts (GSE41613, GSE65858,

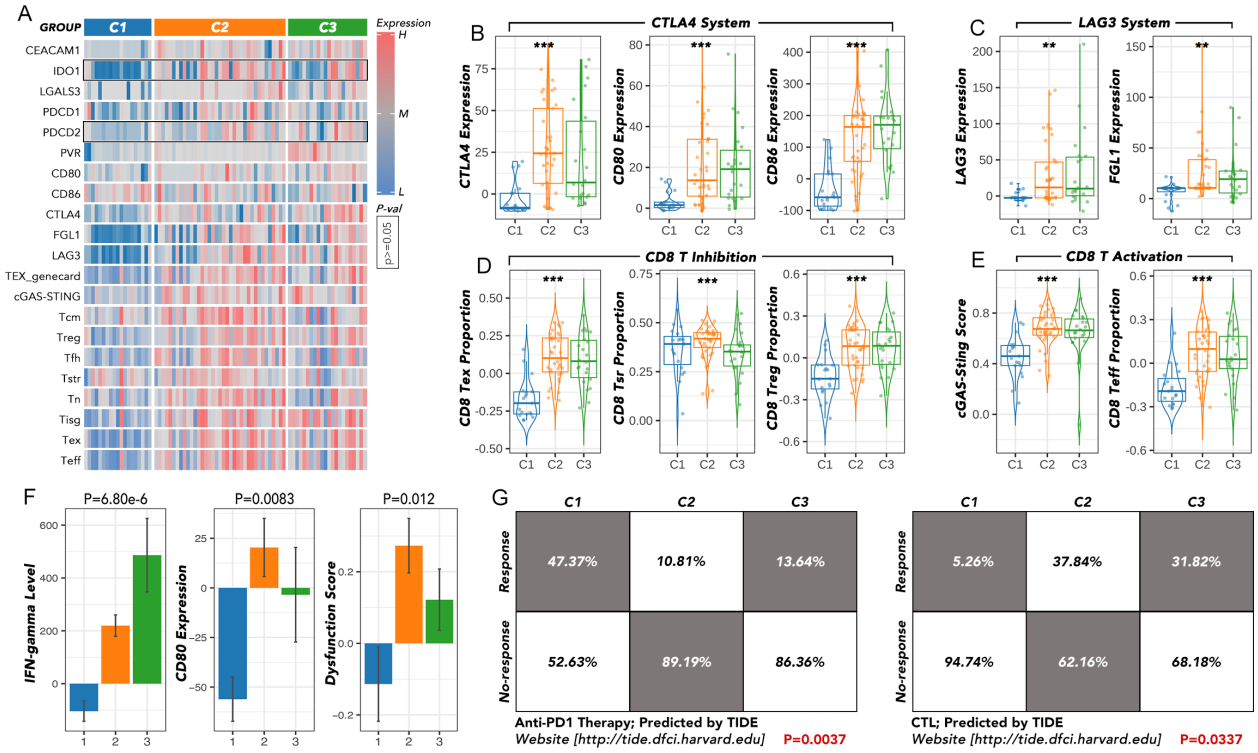

FIGURE 4
The immunotherapy response analysis among the ATC subgroups. **(A)** The expression of key immune checkpoints was compared among C1, C2, and C3. **(B)** The expression of the CTLA4 system was compared among C1, C2 and C3. **(C)** The expression of the LAG3 system was compared among C1, C2 and C3. **(D)** The expression of the CD8 T inhibition family was compared among C1, C2, and C3. **(E)** The expression of the CD8 T activation family was compared among C1, C2 and C3. **(F)** The IFN-gamma level, CD80 expression, and dysfunction score were compared among C1, C2, and C3. **(G)** The response rates to anti-PD1 or CTL therapy were predicted by TIDE. TEX, T cell exhaustion; T cm, central memory T cell; Treg, regulatory T cells; T fh, T follicular helper cells; T sr, T cells in a stress response state; T n, naïve T cell; T isg, IFN stimulated regulator T cell; T eff, effective T cell; TIDE, Tumor Immune Dysfunction and Exclusion; CTL, cytotoxic T lymphocyte. **p<0.01, ***p<0.001.

TCGA). Its role was also validated in disease-specific survival (DSS) and progression-free interval (PFI) in the TCGA-HNSC cohort (Figure 7F).

3.7 HLF was a tumor suppressor in pan-cancer and could promote T-cell infiltration in ATC

Comparative analysis between cancerous (CA) and non-cancerous (NC) tissues revealed that HLF expression was generally lower in CA, observed in 17 out of 20 types (Figure 8A). The expression of HLF was negatively related to markers of apoptosis, cell cycle regulation, differentiation, DNA damage and repair, epithelial-mesenchymal transition (EMT), hypoxia, inflammation, invasion, metastasis, proliferation, and quiescence in TCGA-THCA patients (Figure 8B). Significant differences were also observed in the methylation status of genes in tumor-infiltrating lymphocytes (MeTIL), cytolytic activity (CYT), tertiary lymphoid structures (TLS), human leukocyte antigen (HLA), immunoinhibitor family, immunostimulator family, immune cell recruitment, and other immune markers between HLF high-expression and low-expression groups (Figures 8C–E).

Knockdown of HLF in ATC cell line CAL62 could greatly increase the migration of this cell line. A similar trend was also observed in the treatment of sorafenib in the lower layer (4μM) (Figure 9A). Dead/live cell staining using PI and calcein AM, proliferation staining by EDU, along with apoptosis detection demonstrated that HLF-knockdown CAL62 cells exhibited a lower proportion of dead cells, a higher proportion of live cells, an increased proliferation rate, and enhanced resistance to sorafenib (Figures 9B–E). The EMT pathway was upregulated in HLF-knockdown CAL62 cells (Figures 10A, B). Co-culturing CAL62 (in the lower layer) with peripheral blood mononuclear cells (PBMCs) (in the upper layer) using transwells indicated that HLF knockdown in CAL62 induced more PD1+ CD8 T cells (Figures 11A, B). Further co-culturing of CAL62/TCO1 ATC cells (in the lower layer) with Jurkat T cells (in the upper layer) showed that T cell recruitment decreased following HLF knockdown in the ATC cell line (Figure 11C). Finally, in 22 ATC clinical samples from our hospital, CD8 T cells and PD-L1/CD274 were detected, revealing an increase in PD-L1 and a decrease in CD8 T cells in the HLF low-expression samples (Figure 12).

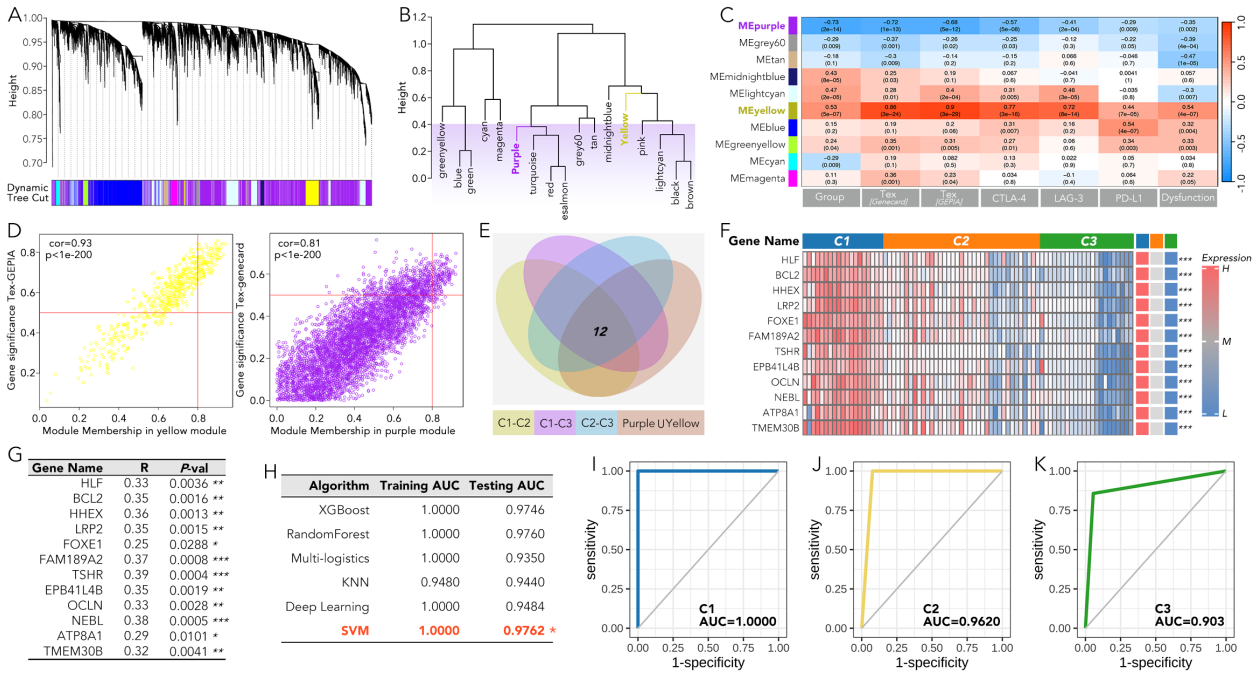

FIGURE 5
A machine-learning grouping model for anaplastic thyroid cancer (ATC) based on the 12 genes most related to the ATC grouping and immune pathways in WGCNA. **(A-D)** The WGCNA results were presented based on the grouping, TEX, CTLA-4, LAG-3, PD-L1, and immune dysfunction score. **(E)** 12 genes in the purple or yellow module were expressed differently (P value > 0.05 and a fold change (|FC|) > 2) between any pair in the C1, C2, and C3 group. **(F)** The expression of the 12 genes in C1-C3 groups was shown by heatmap. **(G)** The correlation coefficients were calculated between the individual level of the 12 genes and the TEX. **(H-K)** A machine learning model based on SVM was used to distinguish C1, C2, and C3 on these 12 genes. T cell exhaustion (TEX). *P<0.05, **p<0.01, ***p<0.001.

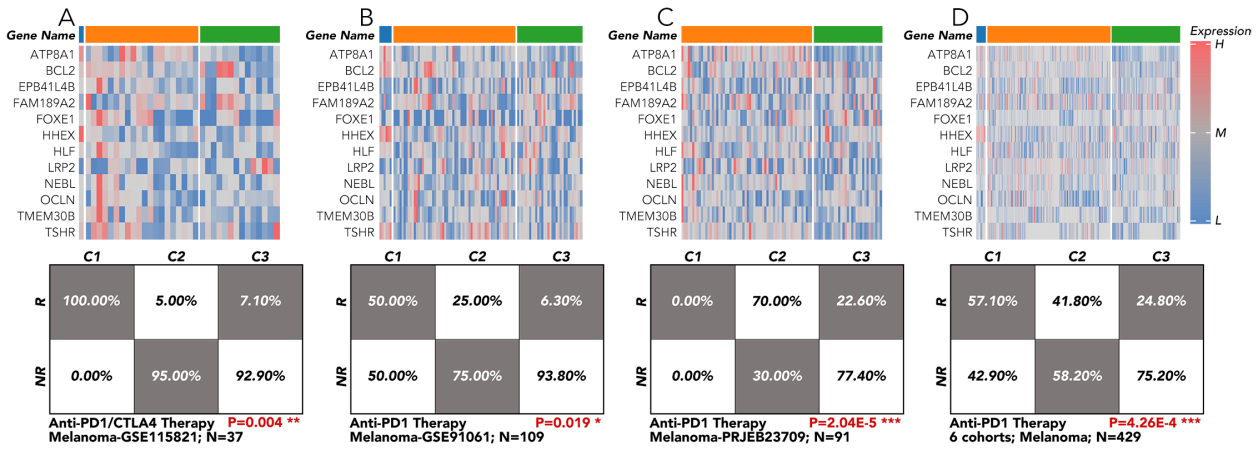

FIGURE 6
Immunotherapy response validation by the 12-gene grouping model in TCGA-THCA and clinical cohort of melanoma. **(A)** The 12-gene signature was applied in the melanoma cohort from GSE115821 to test the response rate to anti-PD1/CTLA4 therapy. **(B)** The 12-gene signature was applied in the melanoma cohort from GSE91061 to test the response rate to anti-PD1 therapy. **(C)** The 12-gene signature was applied in the melanoma cohort from PRJEB23709 to test the response rate to anti-PD1 therapy. **(D)** The 12-gene signature was applied in the 6 melanoma cohorts to test the response rate to anti-PD1 therapy. All the data of the melanoma cohorts were downloaded from the website (http://tide.dfci.harvard.edu/login/). *P<0.05, **p<0.01, ***p<0.001.

4 Discussion

To uncover the most distinct genes in different thyroid cancer subtypes, we screened BCL2, BHLHE40, MICAL2, TGM2, and TPO by comparing each pair of existing subtypes (Figure 1). BCL-2 (B-cell lymphoma 2) is a protein that plays a crucial role in regulating apoptosis (14, 15). Some researchers have found that BCL-2 might help thyroid cancer evade apoptosis, making it a suitable target for

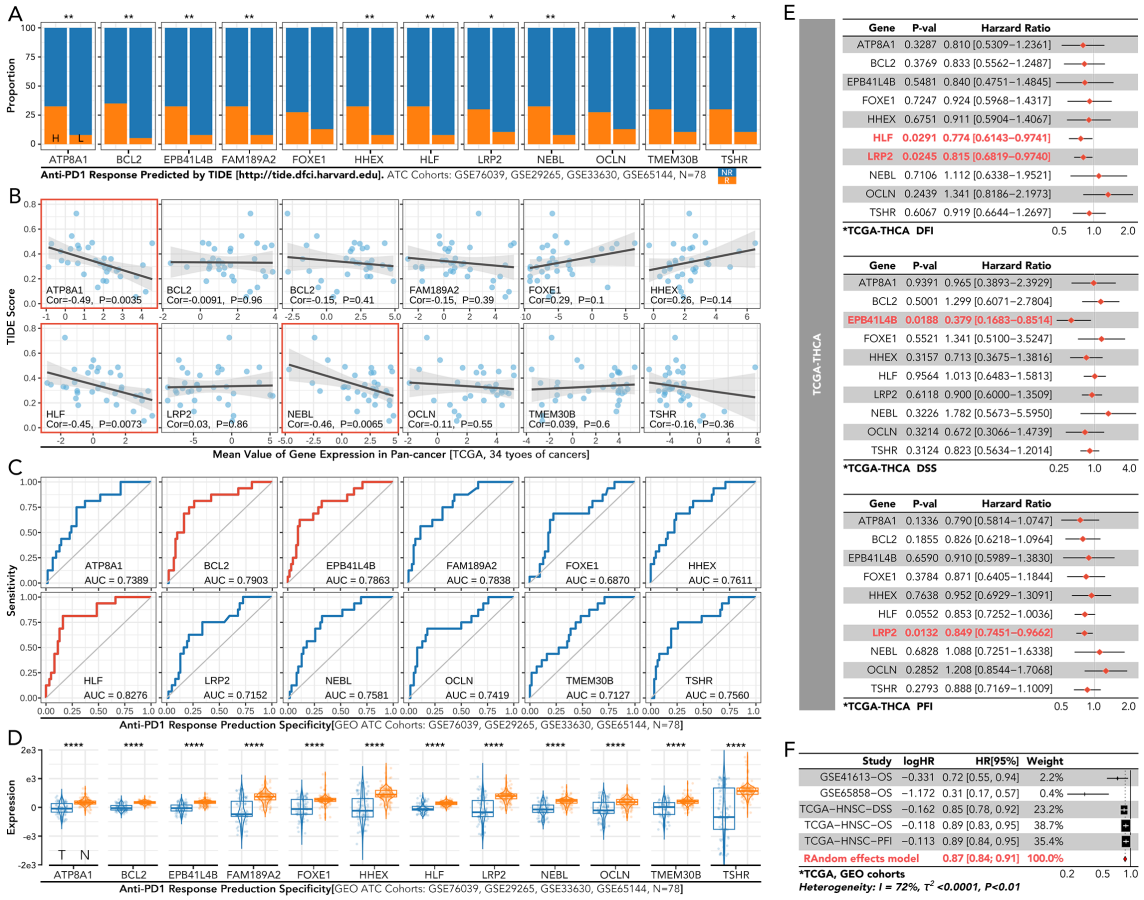

FIGURE 7
Immune response and prognosis analysis of the individual gene from the 12-gene signature in thyroid cancer. **(A)** Predicted response rates to anti-PD1 therapy, calculated by TIDE, were compared between high-expression (left) and low-expression (right) groups for each gene in the 12-gene signature. **(B)** The correlation between the TIDE score and the expression of the individual gene in the 12-gene signature. **(C)** ROC curves for predicting anti-PD1 therapy response based on each gene. **(D)** Comparison of each gene's expression between cancerous **(CA)** and non-cancerous (NC) thyroid tissues in the GEO dataset. **(E)** Cox regression of each gene for DFI/DSS/PFI in TCGA-THCA **(F)** Cox regression analysis of each gene for OS in GSE41613, GSE65858, and TCGA-HNSC, and for DSS and PFI in TCGA-HNSC. NR, No response; ROC, receiver operating characteristic; CA, cancerous; NC, non-cancerous; DFI, disease-free interval; DSS, disease-specific survival; PFI, progression-free interval; TCGA-THCA, the cancer genome atlas-thyroid cancer; OS, overall survival; TCGA-HNSC, the cancer genome atlas-head and neck squamous cell carcinoma. *P<0.05, **p<0.01.

therapy (16–18). In our study, BCL-2 levels were relatively lower in ATC but higher in TNC, suggesting it may not be a promising target for ATC. BHLHE40 has been reported to be involved in the aggressiveness of various cancers, including colorectal, pancreatic, and endometrial cancers (19–22). One study focusing on ATC revealed that the lncRNA/H19-miR-454-3p/BHLHE40 axis could potentiate the progression of ATC (23). Consistent with this, BHLHE40 expression was significantly higher in TCA compared to TNC, and its expression in ATC was the second highest among all subtypes. MICAL2 is known as an oncogene in many cancers, such as pancreatic, ovarian, and gastric cancers (24–26), while there is no related research on thyroid cancer. Our results indicated that MICAL2 may also play a role in ATC. A similar phenomenon was observed with TGM2, which has been proven to be an oncogene with little research on ATC (27, 28). TPO has been reported to predict higher metastasis and recurrence in PTC (29). It was nearly unexpressed in ATC in our results. Our findings revealed that BCL2, BHLHE40, MICAL2, TGM2, and TPO were expressed differently in ATC, FTC, MTC, PTC, and TNC. This inspired us to construct a signature based on these genes to help differentiate the subtypes. The model using the RF machine learning method worked precisely in differentiating TCA from TNC, ATC from DTC, MTC from DTC, and FTC from DTC (Figure 2). However, the mechanisms by which these genes differentiate the subtypes and their roles in ATC, especially MICAL2, still require further research.

Since the five genes were so distinct, we continued to divide the most aggressive type, ATC, into more subtypes by consensus clustering, which may provide clues for specific therapy selection. The great variation of immune cell infiltration in the three subgroups indicated that immune therapy selection may differ among them. Further prediction by TIDE implied that the C1 group could more likely benefit from anti-PD1 therapy, while the C2 and C3 groups may be more suitable for CTL therapy (Figures 3, 4). Until now, immunotherapy (anti-PD-1 and anti-PD-L1) has shown the most

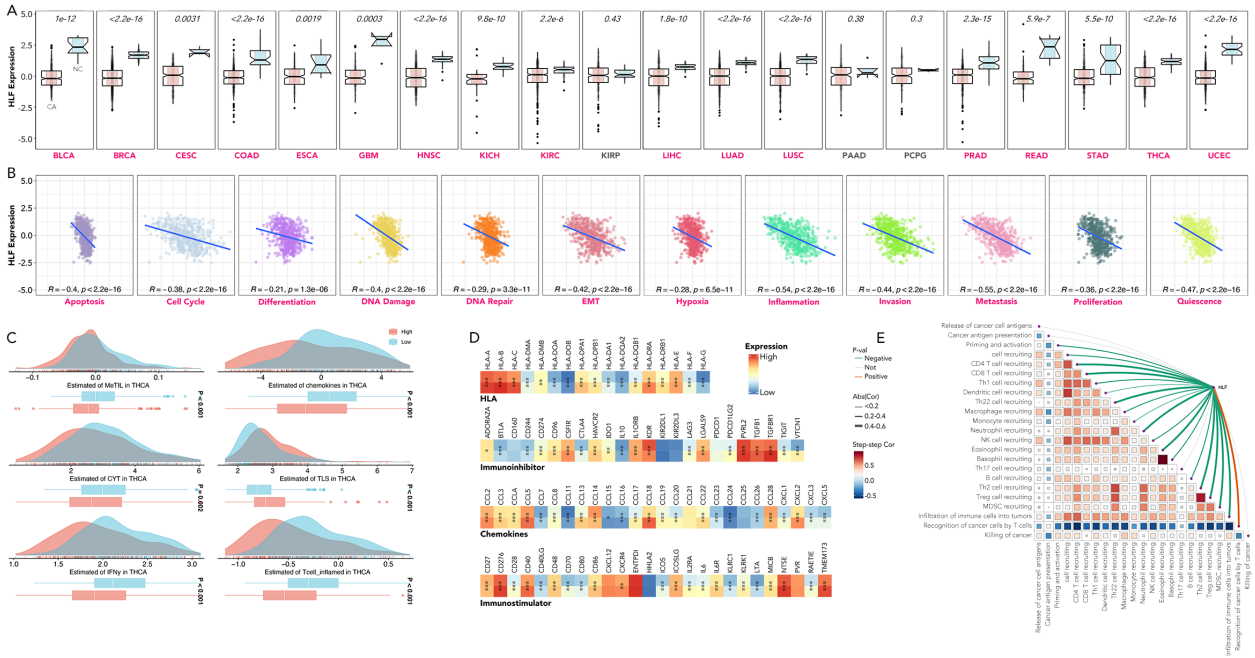

FIGURE 8
Dissection of HLF's relation with cancer hallmarks in pan-cancer. **(A)** HLF expression in CA versus NC tissues across BLCA, BRCA, CESC, COAD, ESCA, GBM, HNSC, KICH, KIRC, KIRP, LIHC, LUAD, LUSC, PAAD, PCPG, PRAD, READ, STAD, THCA, and UCEC. **(B)** Correlation between HLF expression and apoptosis, cell cycle regulation, differentiation, DNA damage and repair, EMT, hypoxia, inflammation, invasion, metastasis, proliferation, and quiescence in TCGA-THCA. **(C)** Comparison of MeTIL, chemokines, CYT, TLS, IFN-gamma, and inflamed T cells between HLF low-expression and high-expression ATC. **(D)** Comparison of HLA, immunoinhibitor family, chemokines, and immunostimulator family between HLF low-expression and high-expression ATC. **(E)** Correlation between HLF expression and recruitment of various types of immune cells in TCGA-THCA. CA, Cancerous; NC, non-cancerous; BLCA, bladder urothelial carcinoma; BRCA, breast invasive carcinoma; CESC, cervical squamous cell carcinoma, endocervical adenocarcinoma; COAD, colon adenocarcinoma; ESCA, esophageal carcinoma; GBM, glioblastoma multiforme; HNSC, head and neck squamous cell carcinoma; KICH, kidney chromophobe; KIRC, kidney renal clear cell carcinoma; KIRP, kidney renal papillary cell carcinoma; LIHC, liver hepatocellular carcinoma; LUAD, lung adenocarcinoma; LUSC, lung squamous cell carcinoma; PAAD, pancreatic adenocarcinoma; PCPG, pheochromocytoma and paraganglioma; PRAD, prostate adenocarcinoma; READ, rectum adenocarcinoma; STAD, stomach adenocarcinoma; THCA, thyroid carcinoma; UCEC, uterine corpus endometrial carcinoma; EMT, epithelial-mesenchymal transition; CYT, cytolytic activity; MeTIL, methylation status of genes in tumor-infiltrating lymphocytes; TLS, tertiary lymphoid structures; HLA, human leukocyte antigen. *P<0.05, **p<0.01, ***p<0.001.

promising 1-year survival rate of approximately 40% for ATC patients without BRAF and MEK gene mutations (7). There is no CTL therapy for ATC patients in clinical trials. Our findings imply that grouping ATC patients may maximize the efficacy of immune therapy. More real-world clinical data are still needed to test this hypothesis.

To further characterize the gene expression patterns among C1, C2, and C3 groups in ATC, WGCNA was used to identify the most associated gene modules. Twelve genes (HLF, BCL2, HHEX, LRP2, FOXE1, FAM189A2, TSHR, EPB41L4B, OCLN, NEBL, ATP8A1, and TMEM30B) were selected from the most related modules due to their distinct expression among the three subgroups. A more precise model based on these 12 genes was created to replace the previous 5-gene signature. More importantly, when the new model was retrospectively applied to the available real-world melanoma clinical cohort, it validated that the C1 group was more suitable for anti-PD1 therapy (Figures 5, 6). However, we must acknowledge that one result from the nine cohorts did not comply with our conclusion. In the future, we hope to test the model using data from ATC patients receiving anti-PD1 therapy or CTL therapy.

HLF was chosen from the 12 genes for final experimental validation because it performed well in both immune therapy response prediction and prognosis prediction in external cohorts (Figure 7). As a transcriptional activator, HLF has been validated as a tumor suppressor in triple-negative breast cancer and ovarian cancer (30, 31). However, one study indicated that it could promote the development of hepatocellular carcinoma and resistance to sorafenib (32). No research on HLF has been found in ATC. Our study indicated that the knockdown of HLF could promote the migration, proliferation, survival and sorafenib resistance of ATC cell lines (Figure 9). The up-regulation of EMT pathway in the HLF-knockdown group may explain its role as a tumor suppressor in ATC (Figure 10). The increased T-cell exhaustion, indicated by up-regulated PD-1 after 48 hours, and the dampened T-cell recruitment were also observed following the decrease in HLF expression in ATC cell lines (Figures 11, 12). More interestingly, PD-L1/CD274 was also up-regulated in the HLF-low-expression group (Figures 10, 12). These results suggest that HLF may be necessary for immune cells to function normally in the ATC tumor environment. Although further research is needed to explore HLF's role in the ATC microenvironment, to our knowledge, this study is the first to investigate HLF in ATC. We will continue to explore this in our future studies.

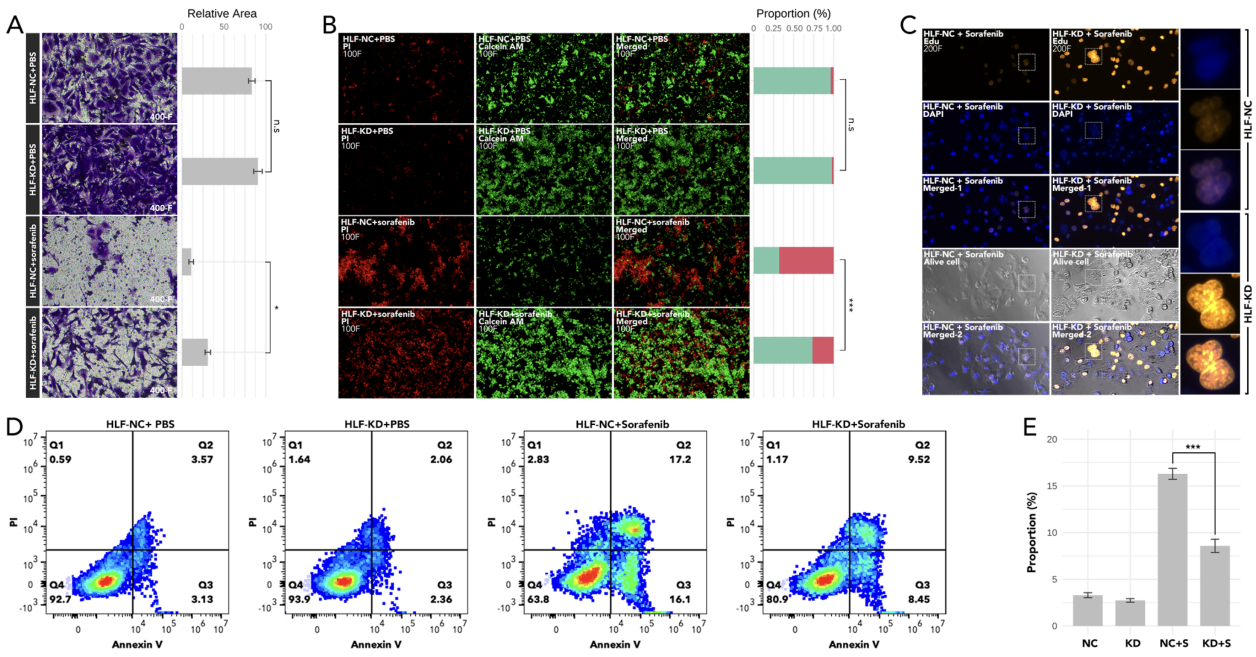

FIGURE 9
Analysis of cell migration, viability, proliferation, and apoptosis following HLF knockdown in ATC cell line CAL62. **(A)** Cell migration assay comparing CAL62 vs. HLF-KD CAL62 and CAL62 treated with sorafenib (4μM) vs. HLF-KD CAL62 treated with sorafenib (4μM). **(B)** Dead (PI)/live staining (calcein AM) detection comparing CAL62 vs. HLF-KD CAL62 and CAL62 treated with sorafenib (4μM) vs. HLF-KD CAL62 treated with sorafenib (4μM). **(C)** Proliferation assay (Edu staining) comparing CAL62 treated with sorafenib (4μM) and HLF-KD CAL62 treated with sorafenib (4μM). **(D)** Apoptosis detection in CAL62 vs. HLF-KD CAL62, and CAL62 treated with sorafenib (4μM) vs. HLF-KD CAL62 treated with sorafenib (4μM). **(E)** Comparison of early apoptosis as shown in **(D)**. HLF-KD indicates HLF knockdown by siRNA. *P<0.05, ***p<0.001.

5 Conclusion

In summary, our study identified five genes with distinct expression patterns across all subtypes of thyroid cancer. A signature based on these five genes can precisely distinguish between the subtypes. Additionally, our group developed a 12-gene signature in ATC that can predict the response to anti-PD1 therapy to some extent. The tumor suppressor role of HLF was validated in ATC cell lines through *in vitro* experiments.

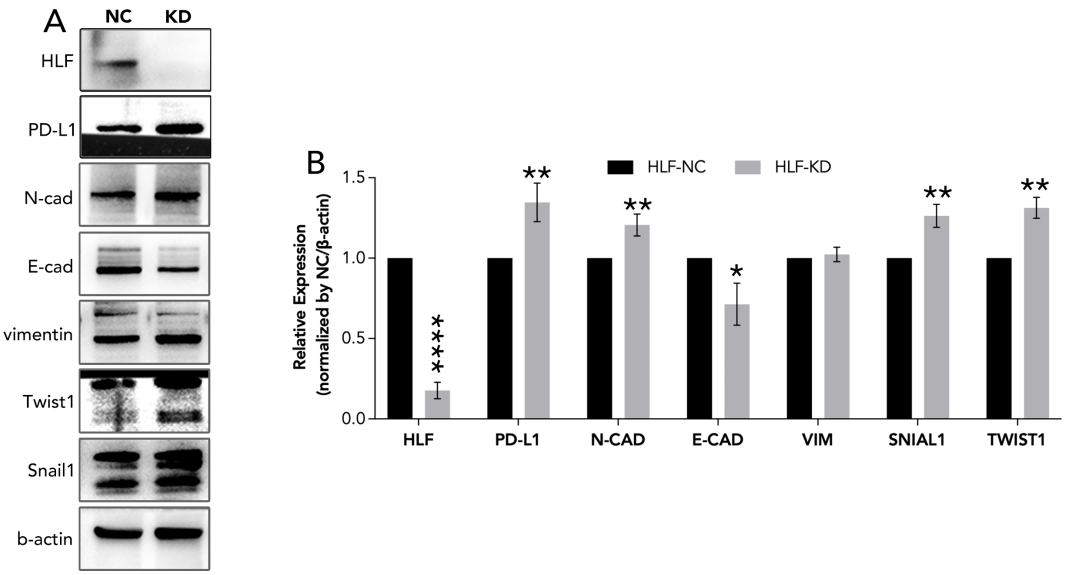

FIGURE 10
EMT pathway detection following HLF knockdown in ATC cell line CAL62. **(A)** EMT pathway detection after HLF knockdown in CAL62. **(B)** Quantitative analysis of protein expression as shown in **(A)**. EMT, Epithelial-mesenchymal transition. *P<0.05, **p<0.01.

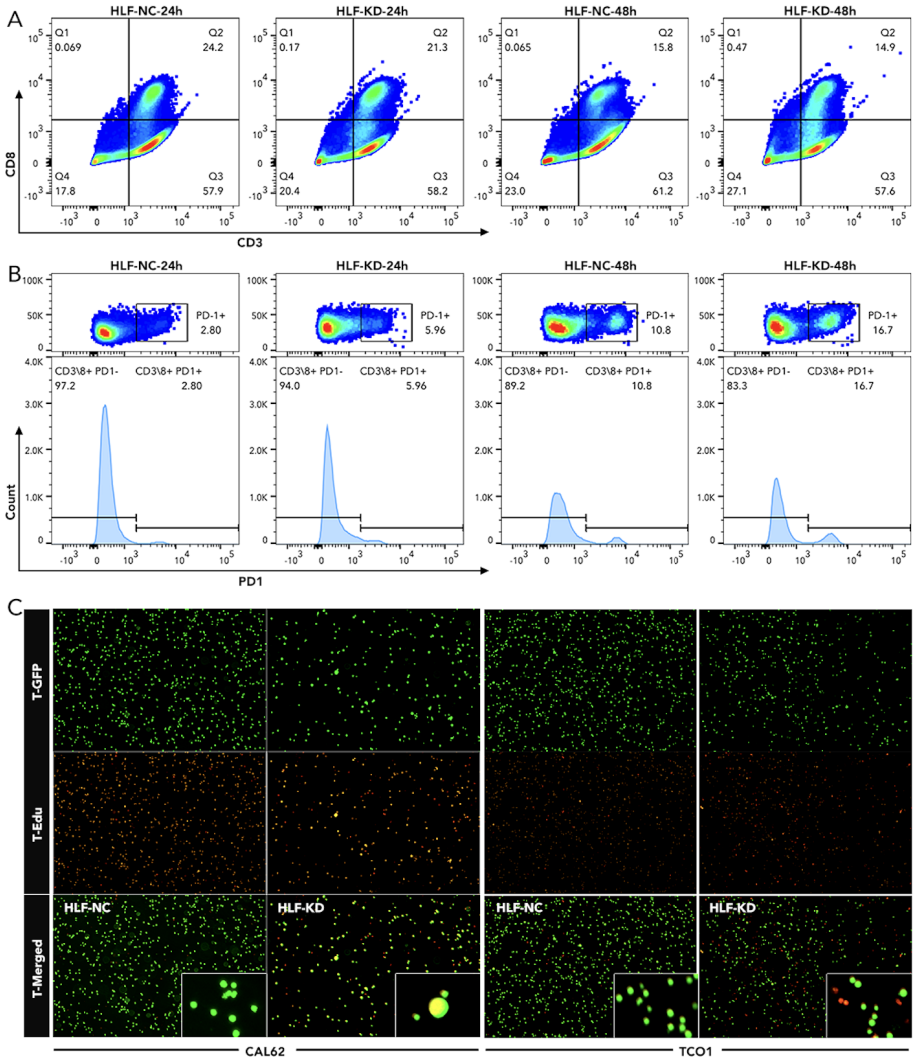

FIGURE 11
Detection of T-cell exhaustion and chemotaxis following HLF knockdown in ATC cell lines **(A)** Detection of CD8 T cells in PBMC co-cultured with CAL62 for 24 hours or 48 hours. **(B)** Detection of PD1 in CD8 T cells as shown in Q2 of **(A)**. **(C)** T-cell (Jurkat cells) chemotaxis assay following HLF knockdown in ATC cell line CAL62 and TCO1. EMT, Epithelial-mesenchymal transition; PBMC, peripheral blood mononuclear cell.

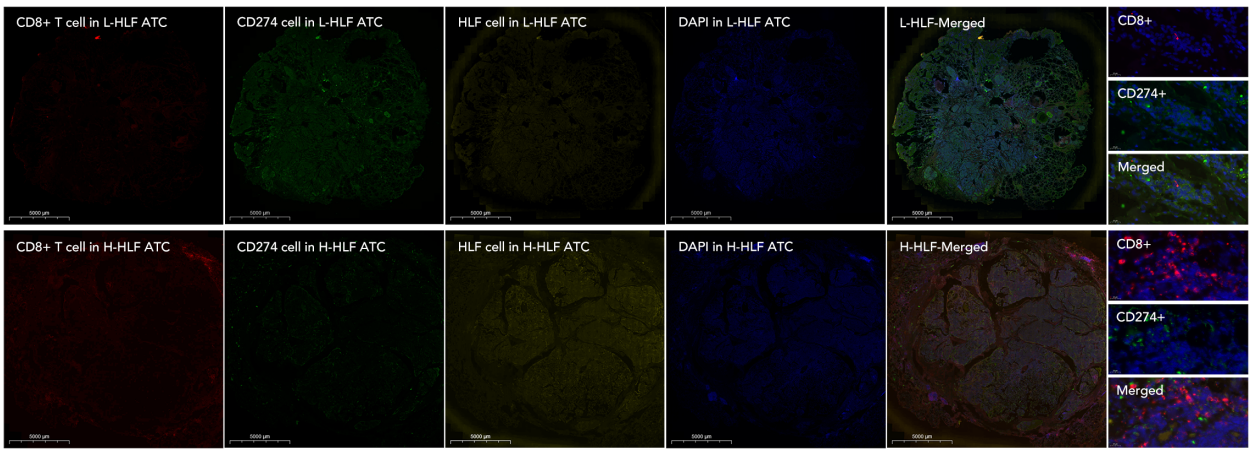

FIGURE 12
T cell infiltration detection in HLF low-expression and high-expression ATC samples. The immunofluorescence intensity of CD8, CD274/PD-L1, HLF, and DAPI was compared between L-HLF and H-HLF ATC. L-HLF, HLF low-expression; H-HLF, HLF high expression.

Data availability statement

The original contributions presented in the study are included in the article/supplementary materials, further inquiries can be directed to the corresponding author/s.

Ethics statement

The studies involving humans were approved by Medical Ethics Committee of The First People's Hospital of Xiaoshan District. The studies were conducted in accordance with the local legislation and institutional requirements. The participants provided their written informed consent to participate in this study. Written informed consent was obtained from the individual (s) for the publication of any potentially identifiable images or data included in this article.

Author contributions

LP: Investigation, Resources, Software, Writing – original draft. YK: Data curation, Formal analysis, Investigation, Resources, Writing – original draft. XY: Formal analysis, Methodology, Validation, Writing – original draft. SK: Methodology, Resources, Validation, Writing – original draft. LR: Resources, Supervision, Visualization, Writing – original draft. WZ: Conceptualization, Data curation, Validation, Writing – original draft. JH: Project administration, Resources, Writing – original draft, Writing – review & editing. WS: Investigation, Methodology, Project administration, Writing – original draft, Writing – review & editing. HY: Funding acquisition, Project administration, Resources, Validation, Writing – review & editing.

Funding

The author(s) declare financial support was received for the research, authorship, and/or publication of this article. All works of this paper are supported by "High-level Talent Research Fund of Xiaoshan District" from WZ-Y, ZW-J, and LP-P, and supported by Hangzhou Municipal Health Commission General Projects (No. B20210264 and B20210311), which are performed by YQ-H, PP-L, ZY-W ect.

Acknowledgments

We would like to extend our sincere gratitude to The First People's Hospital of Xiaoshan District and to Dean Yao Xiao-Cong and Wang Yunchao for encouragement and support to young doctors in performing this research.

Conflict of interest

The authors declare that the research was conducted in the absence of any commercial or financial relationships that could be construed as a potential conflict of interest.

Publisher's note

References

1. Jannin A, Escande A, Al Ghuzlan A, Blanchard P, Hartl D, Chevalier B, et al. Anaplastic thyroid carcinoma: an update. *Cancers (Basel)*. (2022) 14. doi: 10.3390/cancers14041061

2. de Ridder M, Nieveen van Dijkum E, Engelsman A, Kapiteijn E, Klümpen HJ, Rasch CRN. Anaplastic thyroid carcinoma: a nationwide cohort study on incidence, treatment and survival in the Netherlands over 3 decades. *Eur J Endocrinol*. (2020) 183:203–9. doi: 10.1530/EJE-20-0080

3. Sehgal K, Serritella A, Liu M, ON A, Nangia C, Pappa T, et al. A phase I/II trial of sapanisertib in advanced anaplastic and radioiodine refractory differentiated thyroid carcinoma. *J Clin Endocrinol Metab*. (2024). doi: 10.1210/clinem/dgae443

4. Araque KA, Gubbi S, Klubo-Gwiezdzinska J. Updates on the management of thyroid cancer. *Horm Metab Res*. (2020) 52:562–77. doi: 10.1055/a-1089-7870

5. Tiedje V, Stuschke M, Weber F, Dralle H, Moss L, Führer D. Anaplastic thyroid carcinoma: review of treatment protocols. *Endocr Relat Cancer*. (2018) 25:R153–r61. doi: 10.1530/ERC-17-0435

6. Ocanto A, Torres L, Couñago F. Current status of anaplastic thyroid carcinoma. *World J Clin Oncol*. (2024) 15:684–6. doi: 10.5306/wjco.v15.i6.684

7. Pavlidis ET, Galanis IN, Pavlidis TE. Update on current diagnosis and management of anaplastic thyroid carcinoma. *World J Clin Oncol*. (2023) 14:570–83. doi: 10.5306/wjco.v14.i12.570

8. Jeschke J, Bizet M, Desmedt C, Calonne E, Dedeurwaerder S, Garaud S, et al. DNA methylation-based immune response signature improves patient diagnosis in multiple cancers. *J Clin Invest*. (2017) 127:3090–102. doi: 10.1172/JCI91095

9. Lapuente-Santana Ó, van Genderen M, Hilbers PAJ, Finotello F, Eduati F. Interpretable systems biomarkers predict response to immune-checkpoint inhibitors. *Patterns (N Y)*. (2021) 2:100293. doi: 10.1016/j.patter.2021.100293

10. Yuan H, Yan M, Zhang G, Liu W, Deng C, Liao G, et al. CancerSEA: a cancer single-cell state atlas. *Nucleic Acids Res*. (2019) 47:D900–d8. doi: 10.1093/nar/gky939

11. Lee E, Chuang HY, Kim JW, Ideker T, Lee D. Inferring pathway activity toward precise disease classification. *PloS Comput Biol*. (2008) 4:e1000217. doi: 10.1371/journal.pcbi.1000217

12. Cao G, Li P, He X, Jin M, Li M, Chen S, et al. FHL3 contributes to EMT and chemotherapy resistance through up-regulation of slug and activation of TGFβ/smad-independent pathways in gastric cancer. *Front Oncol*. (2021) 11:649029. doi: 10.3389/fonc.2021.649029

13. Li P, Cao G, Zhang Y, Shi J, Cai K, Zhen L, et al. FHL3 promotes pancreatic cancer invasion and metastasis through preventing the ubiquitination degradation of EMT associated transcription factors. *Aging (Albany NY)*. (2020) 12:53–69. doi: 10.18632/aging.102564

14. Zhang C, Bo C, Guo L, Yu P, Miao S, Gu X. BCL2 and hsa-miR-181a-5p are potential biomarkers associated with papillary thyroid cancer based on bioinformatics analysis. *World J Surg Oncol*. (2019) 17:221. doi: 10.1186/s12957-019-1755-9

15. Gunda V, Sarosiek KA, Brauner E, Kim YS, Amin S, Zhou Z, et al. Inhibition of MAPKinase pathway sensitizes thyroid cancer cells to ABT-737 induced apoptosis. *Cancer Lett*. (2017) 395:1–10. doi: 10.1016/j.canlet.2017.02.028

16. Champa D, Russo MA, Liao XH, Refetoff S, Ghossein RA, Di Cristofano A. Obatoclax overcomes resistance to cell death in aggressive thyroid carcinomas by countering Bcl2a1 and Mcl1 overexpression. *Endocr Relat Cancer*. (2014) 21:755–67. doi: 10.1530/ERC-14-0268

17. Kaloni D, Diepstraten ST, Strasser A, Kelly GL. BCL-2 protein family: attractive targets for cancer therapy. *Apoptosis*. (2023) 28:20–38. doi: 10.1007/s10495-022-01780-7

18. Mitsiades CS, Hayden P, Kotoula V, McMillin DW, McMullan C, Negri J, et al. Bcl-2 overexpression in thyroid carcinoma cells increases sensitivity to Bcl-2 homology 3 domain inhibition. *J Clin Endocrinol Metab*. (2007) 92:4845–52. doi: 10.1210/jc.2007-0942

19. Asanoma K, Yagi H, Onoyama I, Cui L, Hori E, Kawakami M, et al. The BHLHE40–PPM1F–AMPK pathway regulates energy metabolism and is associated with the aggressiveness of endometrial cancer. *J Biol Chem*. (2024) 300:105695. doi: 10.1016/j.jbc.2024.105695

20. Ji A, Li H, Fu X, Zhang Y, Liu Y. Long non-coding RNA NEAT1 induced by BHLHE40 activates Wnt/β-catenin signaling and potentiates colorectal cancer progression. *Cell Div*. (2024) 19:25. doi: 10.1186/s13008-024-00129-7

21. Yang S, Zhang D, Sun Q, Nie H, Zhang Y, Wang X, et al. Single-cell and spatial transcriptome profiling identifies the transcription factor BHLHE40 as a driver of EMT in metastatic colorectal cancer. *Cancer Res*. (2024) 84:2202–17. doi: 10.1158/0008-5472.CAN-23-3264

22. Cao Y, Wang X, Liu Y, Liu P, Qin J, Zhu Y, et al. BHLHE40 inhibits ferroptosis in pancreatic cancer cells via upregulating SREBF1. *Adv Sci (Weinh)*. (2024) 11:e2306298. doi: 10.1002/advs.202306298

23. Wu Y, Yang J, Zhang H, Cheng J, Lei P, Huang J. LncRNA H19 Influences Cellular Activities via the miR-454-3p/BHLHE40 Axis in Anaplastic Thyroid Carcinoma. *Horm Metab Res*. (2024) 56:392–9. doi: 10.1055/a-2196-3511

24. Garg B, Khan S, Babu DS, Mose E, Gulay K, Sharma S, et al. MICAL2 is a super enhancer associated gene that promotes pancreatic cancer growth and metastasis. *bioRxiv*. (2024). doi: 10.1101/2024.06.26.600548

25. Liu Z, Sun B, Xu A, Tang J, Zhang H, Gao J, et al. MICAL2 implies immunosuppressive features and acts as an independent and adverse prognostic biomarker in pancreatic cancer. *Sci Rep*. (2024) 14:3177. doi: 10.1038/s41598-024-52729-6

26. Xia T, Ye F, Zhao W, Min P, Qi C, Wang Q, et al. Comprehensive analysis of MICALL2 reveals its potential roles in EGFR stabilization and ovarian cancer cell invasion. *Int J Mol Sci*. (2023) 25. doi: 10.3390/ijms25010518

27. Chang W, Gao W, Liu D, Luo B, Li H, Zhong L, et al. The upregulation of TGM2 is associated with poor prognosis and the shaping of the inflammatory tumor microenvironment in lung squamous cell carcinoma. *Am J Cancer Res*. (2024) 14:2823–38. doi: 10.62347/OBES4130

28. Zhang N, Gao S, Peng H, Wu J, Li H, Gibson C, et al. Chemical proteomic profiling of protein dopaminylation in colorectal cancer cells. *J Proteome Res*. (2024) 23:2651–60. doi: 10.1021/acs.jproteome.4c00379

29. Li X, Cheng R. TPO as an indicator of lymph node metastasis and recurrence in papillary thyroid carcinoma. *Sci Rep*. (2023) 13:10848. doi: 10.1038/s41598-023-37932-1

30. Han T, Chen T, Chen L, Li K, Xiang D, Dou L, et al. HLF promotes ovarian cancer progression and chemoresistance via regulating Hippo signaling pathway. *Cell Death Dis*. (2023) 14:606. doi: 10.1038/s41419-023-06076-5

31. Li H, Yang P, Wang J, Zhang J, Ma Q, Jiang Y, et al. HLF regulates ferroptosis, development and chemoresistance of triple-negative breast cancer by activating tumor cell-macrophage crosstalk. *J Hematol Oncol*. (2022) 15:2. doi: 10.1186/s13045-021-01223-x

32. Xiang DM, Sun W, Zhou T, Zhang C, Cheng Z, Li SC, et al. Oncofetal HLF transactivates c-Jun to promote hepatocellular carcinoma development and sorafenib resistance. *Gut*. (2019) 68:1858–71. doi: 10.1136/gutjnl-2018-317440

frontiers | Frontiers in Immunology

TYPE Original Research
PUBLISHED 15 January 2025
DOI 10.3389/fimmu.2024.1473897

OPEN ACCESS

EDITED BY
Takaji Matsutani,
Maruho, Japan

REVIEWED BY
Sebastian Zahnreich,
Johannes Gutenberg University Mainz, Germany
Anna Fialová,
SOTIO a.s., Czechia
Christoph Schultheiß,
University Hospital of Basel, Switzerland

*CORRESPONDENCE
Gunnar Wichmann
Gunnar.Wichmann@medizin.uni-leipzig.de

†These authors have contributed equally to this work and share senior authorship

RECEIVED 31 July 2024
ACCEPTED 19 December 2024
PUBLISHED 15 January 2025

CITATION
Wellhausen J, Röhl L, Berszin M, Krücken I, Zebralla V, Pirlich M, Stoehr M, Wiegand S, Dietz A, Wald T and Wichmann G (2025) Suppression of MCP-1, IFN-γ and IL-6 production of HNSCC *ex vivo* by pembrolizumab added to docetaxel and cisplatin (TP) exceeding those of TP alone is linked to improved survival. *Front. Immunol.* 15:1473897. doi: 10.3389/fimmu.2024.1473897

Suppression of MCP-1, IFN-γ and IL-6 production of HNSCC *ex vivo* by pembrolizumab added to docetaxel and cisplatin (TP) exceeding those of TP alone is linked to improved survival

Jana Wellhausen[1], Louisa Röhl[1], Michael Berszin[1], Irene Krücken[2,3], Veit Zebralla[1,3], Markus Pirlich[1,3], Matthaeus Stoehr[1,3], Susanne Wiegand[1,3,4], Andreas Dietz[1,3], Theresa Wald[1,3†] and Gunnar Wichmann[1,3*†]

[1]Department of Otorhinolaryngology, Head and Neck surgery, University Hospital Leipzig, Leipzig, Germany, [2]Institute of Pathology, University Hospital Leipzig, Leipzig, Germany, [3]The Comprehensive Cancer Center Central Germany, Leipzig University Hospital, Leipzig, Germany, [4]Department of Otorhinolaryngology, Head and Neck Surgery, Christian-Albrechts-University Kiel, Kiel, Germany

Background: Adding pembrolizumab, an anti-PD-1 antibody approved for treatment of head and neck squamous cell carcinoma (HNSCC) to neoadjuvant (induction-) chemotherapy utilizing docetaxel and cisplatin (TP) followed by radiotherapy may improve outcome in larynx organ-preservation (LOP) that is investigated in the European Larynx-Organ preservation Study (ELOS). As biomarkers for response to TP and pembrolizumab +TP are missing but may include cytokines, this work aims on determining cytokines potentially linked to outcome as prognostic markers sufficient to predict and/or monitor response to successful LOP.

Methods: Collagenase IV digests were generated from 47 histopathological confirmed HNSCC tumor samples and seeded in 96-well plates containing pembrolizumab, docetaxel, cisplatin either solely or in binary or ternary combination. According to the FLAVINO protocol, supernatants were collected after 3 days, adherent cells fixed using ethanol, air-dried and pan-cytokeratin positive epithelial cells counted using fluorescence microscopy. The cytokines IL-6, IL-8, IFN-γ, IP-10, MCP-1, TNF-α, and VEGF in the supernatant were quantified by sandwich ELISA.

Results: The mode of interaction between pembrolizumab and TP was assessed and correlated to outcome (overall, disease-specific and progression-free survival of patients). Suppression of MCP-1, IFN-γ and IL-6 production by pembrolizumab + TP exceeding the suppressive effect of TP was detected in the majority of samples and linked to improved survival. Multivariate Cox proportional hazard regression modeling revealed MCP-1, IFN-γ and IL-6 as independent outcome predictors.

Conclusions: Comparing response to TP vs. pembrolizumab vs. TP + pembrolizumab may allow for identification of patients with superior outcome independent from treatment applied.

KEYWORDS

PD-1:PD-L1 immune-checkpoint inhibitor (ICI) pembrolizumab, local and locoregional advanced head and neck squamous cell carcinoma (HNSCC), neoadjuvant (induction) chemotherapy, predictive assay for chemoresponse-evaluation, biomarker research, monocyte chemoattractant protein 1 (MCP-1, CCL2)

Introduction

Head and neck squamous cell carcinoma (HNSCC) are a group of cancer emerging from the epithelia of the upper aerodigestive tract. While early stages can be cured through monomodal therapies, either surgical resection or radiotherapy, local and locoregional advanced (LA) HNSCC can be cured in sufficiently high frequencies only by combining treatment modalities, for instance surgery followed by post-operative radiotherapy (Op+PORT) or radio-chemotherapy (Op +PORCT) or concurrent radio-chemotherapy (CRT). Ablative surgery can be very devastating for health-related quality of life (QoL), and larynx organ preservation (LOP) in LA laryngeal and hypopharyngeal squamous cell carcinoma (LA-LHSCC) that can only be surgically treated by total laryngectomy (TL) is therefore very desirable. Two alternative multimodal LOP approaches, either induction chemotherapy (IC) followed by radiotherapy (IC+RT) or platinum-based concurrent radio-chemotherapy (CRT), are possible LOP options. Although IC+RT is already recommended in the German guideline on diagnosis, treatment, and follow-up of laryngeal cancer for only by total laryngectomy resectable advanced laryngeal and/or hypopharyngeal cancer responding to IC (1), LOP through IC+RT still remains experimental and is furthermore investigated in clinical LOP trials (2–6). LOP approaches are often discussed as being potentially more harmful for the patient compared to most early TL (without neoadjuvant treatment) followed by either postoperative radiotherapy (TL+PORT) or platinum-based radio-chemotherapy (TL+PORCT). However, using propensity score (PS) matched analyses we recently demonstrated that IC+RT according to DeLOS-II utilizing IC with docetaxel and cisplatin (TP) improves overall (OS), disease-specific (DSS), and event-free survival (EFS) compared to TL+PORT, TL+PORCT and CRT (6). The aim of the ELOS trial is to go one step further by analyzing if addition of the immune-checkpoint inhibitor (ICI) pembrolizumab to TP results in even more improved LOP according to laryngectomy-free survival, increased OS and EFS of LA-LHSCC otherwise amenable for TL (7, 8).

In recent years, significant progress has been made in the treatment of R/M HNSCC with therapeutic approaches in the field of immune checkpoint inhibitors (ICI). The KEYNOTE-048 was a phase-III RCT comparing pembrolizumab monotherapy, pembrolizumab with chemotherapy (cisplatin and 5-fluorouracil), and cetuximab with chemotherapy (cisplatin and 5-fluorouracil) (ClinicalTrials.gov, number NCT02358031). The KEYNOTE-048 study led to the approval of pembrolizumab as monotherapy or in combination with chemotherapy with platinum and 5-fluorouracil (5-FU) for first-line treatment for PD-L1-positive R/M HNSCC with CPS ≥ 1 (9).

Immunomodulation by ICI targeting PD-1 has also been used in the curative setting, *e.g.* the RCT ADRISK (ClinicalTrials.gov NCT03480672 (10); or NadiHN (EudraCT No. 2016-004787-20). Several phase I and phase II RCTs have been conducted on neoadjuvant therapies with ICI in patients with HNSCC and all achieved promising results with response in up to 52% of cases (11–16). Induction with ICI is likely to be a more effective method of tumor control with fewer side effects compared to adjuvant immunotherapy, as more tumor antigens are present when the tumor is still *in situ* with its higher mass (4, 17, 18). It is expected that the immune system could be better protect against tumor recurrence in the future, whenever immunologic memory develops most early (19, 20). Indeed, immune evasion by the tumor is enhanced by overexpression of the immune checkpoint molecule programmed-death-ligand-1 (PD-L1) on tumor cells and/or tumor-infiltrating immune cells, which is found in around 55% of HNSCC patients and especially after prolonged presence of the tumor. Hence, a combination of immunotherapy with chemotherapy and/or radiotherapy is considered particularly promising in earlier (upfront or neoadjuvant) settings because immunogenic antigens are released during chemotherapy and radiotherapy, which putatively may enhance the effect of ICI (21), and the negative effect exerted by through chemo-induced PD-L1 expression on tumor cells can be abrogated by ICI (22–24). Binding of PD-L1 to its receptor, programmed-death-1 (PD-1) on T, B and NK cells, results in inhibition of proliferation and effector function of these cells (25–27). Thus, cancer may be able to escape immune-mediated destruction (28–30). Although, high PD-L1 expression on tumor and/or immune cells correlates with improved response to anti-PD-1 blockade (28, 31, 32), there is still an immense need for research to improve OS and QoL of patients. Even though therapies performed with an anti-PD-1-ICI in patients with advanced HNSCC have resulted in prolonged survival in the palliative setting compared to standard therapy

(33), not all patients respond equally, and predicting response to PD-1 inhibitor therapy remains challenging (9, 34–38). PD-L1 is currently the only clinically available and routinely used biomarker for optimizing patient selection for anti-PD-1-ICI in non-small cell lung cancer (NSCLC) (39), gastric cancer and HNSCC (9, 34, 35, 38, 40, 41). As use of PD-L1 expression as biomarker is only able to enrich responders among treated patients, clinical characteristics such as T and N category still play the most important role in treatment decision for curative HNSCC (42–47), as (compared to other solid tumors) reliable biomarkers like micro-satellite instability (*e.g.* MSI) for treatment stratification are very infrequent or even missing; *ex-vivo* testing and monitoring of *in vivo* responses via liquid biopsies, however, may overcome the dilemma of missing biomarkers.

Indeed, diverse *ex-vivo* and *in-vitro* testing methods have already been used in the development of pharmaceuticals and have the potential to facilitate or even allow for better stratification of tumor therapies for particular HNSCC subgroups, especially for the use of immunomodulators such as ICI. Reliable prognostication prior to initiation of therapy in patients with cytostatics and targeted therapeutics is useful because HNSCC have a very heterogeneous biology and often low response rates to a given pharmaceutical. However, to date, *ex-vivo* assays have mainly not allowed reliable prediction of treatment success in a clinical context due to so far not available validation studies. Improved methods, however, are leading to a re-evaluation of the *ex-vivo* approach with expanded analysis of the antitumor immune response (48).

The randomized phase II LOP RCT DELOS-II investigated the effect of adding cetuximab to already well-performing therapy with TPF or TP and radiotherapy, also with the hope of LOP in locoregionally advanced LHSCC (2–6, 10, 10). *Ex-vivo* investigations of biopsy samples showed high positive predictive value of reduced colony formation for successful curative treatment and LOP in DeLOS-II (49). Both RCTs, KEYNOTE-048 and DELOS II, form the basis of the randomized controlled phase II LOP trial ELOS in advanced stage III, IVA/B LHNSCC resectable only by total laryngectomy having PD-L1 expression with CPS ≥ 1. ELOS investigates the effect of up to 17 cycles pembrolizumab added to TP treatment. However, as biomarkers allowing to identify responders or nonresponders are missing, we are searching for blood-derived biomarkers as well as *ex-vivo* chemoresponse testing to predict or at least monitor the response to ICI.

Cytokines may have a role as potential biomarkers (50–55) as they are overproduced by many solid tumors including HNSCC (56). Cytokine expression is associated with inflammation and angiogenesis involved in progression of cancer and along growth and progression of the cancer can increase from physiologic pg/ml levels to more than 1000-fold concentrations (57, 58). Our previous research on cytokine expression patterns *in vivo* and *ex vivo* already showed that response to PD-1 blockade is accompanied by shifts in cytokine concentrations closely linked to patient outcome, OS in particular (59). Röhl et al. demonstrated differences between non-responders and responders to PD-1 ICB in terms of levels of various pro-inflammatory and pro-angiogenic cytokines and growth factors before and during/after starting therapy, including MCP-1 (CCL-2) and VEGF-A, but also IFN-γ and chemokines such as IL-8 (CXCL-8) and IP-10 (CXCL-10). Such cytokine expression patterns allow to identify responders with improved survival compared to non-responders. Indeed, there was improved outcome in patients with a low IFN-γ concentration before and after ICB, and especially long-term OS after ICB, whenever serum or plasma concentrations of VEGF, IL-6 and IL-8 were rather low. We recently demonstrated that whenever PD-1-ICB failed to suppress MCP-1 levels, the outcome of HNSCC patients was impaired. Likewise, an increase in IL-6, IL-8 and VEGF was linked to impaired OS (63). In light of our previous research on PD-1 blockade on HNSCC *ex vivo* that revealed subgroups of patients with different response patterns in terms of cytokine release and colony formation *ex vivo* we speculated that response patterns observed in short-time *ex-vivo* tests could be prognostic for outcome independent of treatment.

The question of whether these groups can be identified after treatment *ex vivo* of their tumors remains open for particular treatments. Despite insignificant differences between patients treated with or without chemotherapy (59), a benefit of the combination of pembrolizumab and TP, as will be used in ELOS, remains to be demonstrated. In preparation of the ELOS trial and to check the feasibility of a reliable testing of response to per protocol treatment, we analyzed response of unselected HNSCC biopsies to pembrolizumab, TP and pembrolizumab plus TP to find out if an improved response to the combined treatment can be detected *ex vivo*.

Materials and methods

Study population and patient samples

The study was approved by the ethics committee of the University of Leipzig (vote NICEI-CIH 341-15-ff) and conducted according to the guidelines of the Declaration of Helsinki. Included in the study were samples from histopathological confirmed HNSCC treated in curative or palliative setting at Leipzig University Hospital. From January 2019 to September 2020, patients were informed and gave their written consent for the collection and examination of a tumor sample. Samples of 54 patients, among them 47 HNSCC patients were obtained from tissue biopsies token during panendoscopy or definitive surgery at the Otolaryngology or oral and maxillofacial surgery clinic of the University Hospital Leipzig. The patients were treated according to the decision in the multidisciplinary tumor board (MDTB); the MTDB was blinded regarding the outcome of *ex-vivo* tests (see below). The tumor database of the Department of Otolaryngology served as the source of all clinical data, including staging according to Union for International Cancer Control (UICC) criteria, TNM categories, and clinical follow-up data. The enrolled patients' data were extracted from the tumor database and curated by JW & GW with contributions of LR and TW the patients' characteristics at the time of registration for the study (at which also the biopsy was taken) is shown in Table 1.

TABLE 1 Distribution according to numbers (*n*) and percentage (%) as well as odds ratio (OR) and 95% confidence intervals (95% CI) and 2-sided *p*-value derived from chi-squared tests for categorical measures of various clinical and epidemiologic characteristics and outcome of head and neck squamous cell carcinoma patients providing biopsies for short-time *ex-vivo* chemoresponse testing according the FLAVINO protocol.

Covariate	Characteristic	Total *n* (%)	LHSCC *n* (%)	Other HNSCC *n* (%)	OR (95% CI)	*p* value
Sex						0.391
	Male	40 (85.1)	12 (92.3)	28 (82.4)	1 (95% CI 0.384 - 2.602)	
	Female	7 (14.9)	1 (7.7)	6 (17.6)	2.571 (95% CI 0.279 - 23.73)	
Age						0.484
	< 50	4 (8.5)	0 (–)	4 (11.8)	1 (95% CI 0.016 - 62.30)#	
	51 < 60	22 (46.8)	6 (46.2)	16 (47.1)	0.296 (95% CI 0.014 - 6.375)	
	61 < 70	16 (34)	6 (46.2)	10 (29.4)	0.185 (95% CI 0.008 - 4.079)	
	≥ 70	5 (10.6)	1 (7.7)	4 (11.8)	0.444 (95% CI 0.012 - 17.13)	
Smoking						0.811
	No	12 (25.5)	3 (23.1)	9 (26.5)	1 (95% CI 0.158 - 6.347)	
	Yes	35 (74.5)	10 (76.9)	25 (73.5)	0.833 (95% CI 0.186 - 3.729)	
Smoking						0.070
	Never	12 (25.5)	3 (23.1)	9 (26.5)	1 (95% CI 0.158 - 6.347)	
	Former	6 (12.8)	4 (30.8)	2 (5.9)	0.167 (95% CI 0.02 - 1.42)	
	Current	29 (61.7)	6 (46.2)	23 (67.6)	1.278 (95% CI 0.262 - 6.239)	
Pack years smoking history						0.813
	> 30 PY	23 (48.9)	6 (46.2)	17 (50)	1 (95% CI 0.268 - 3.729)	
	< 30 PY	24 (51.1)	7 (53.8)	17 (50)	0.857 (95% CI 0.238 - 3.086)	
Alcohol						0.931
	Never	14 (29.8)	4 (30.8)	10 (29.4)	1 (95% CI 0.194 - 5.154)	
	Former	6 (12.8)	2 (15.4)	4 (11.8)	0.8 (95% CI 0.102 - 6.25)	
	Current	27 (57.4)	7 (53.8)	20 (58.8)	1.143 (95% CI 0.27 - 4.843)	
Alcohol (g/day)						0.265
	Never	14 (29.8)	4 (30.8)	10 (29.4)	1 (95% CI 0.194 - 5.154)	
	1 - 30	11 (23.4)	2 (15.4)	9 (26.5)	1.8 (95% CI 0.263 - 12.29)	
	31 - 60	5 (10.6)	0 (–)	5 (14.7)	4.714 (95% CI 0.213 - 104.5)#	
	> 60	17 (36.2)	7 (53.8)	10 (29.4)	0.571 (95% CI 0.126 - 2.584)	
Smoking & alcohol consumption						0.824
	Neither risk factor	10 (21.3)	3 (23.1)	7 (20.6)	1 (95% CI 0.148 - 6.772)	
	One risk factor	25 (53.2)	6 (46.2)	19 (55.9)	1.357 (95% CI 0.265 - 6.958)	
	> 30 PY, > 60 g/day	12 (25.5)	4 (30.8)	8 (23.5)	0.857 (95% CI 0.141 - 5.229)	
T category (8^{th} ed.)						0.306
	T1	4 (8.5)	2 (15.4)	2 (5.9)	1 (95% CI 0.063 - 15.98)	
	T2	14 (29.8)	4 (30.8)	10 (29.4)	2.5 (95% CI 0.256 - 24.37)	
	T3	12 (25.5)	1 (7.7)	11 (32.4)	11 (95% CI 0.646 - 187.1)	

(Continued)

10.3389/fimmu.2024.1473897

TABLE 1 Continued

Covariate	Characteristic	Total *n* (%)	LHSCC *n* (%)	Other HNSCC *n* (%)	OR (95% CI)	*p* value
T category (8th ed.)						0.306
	T4	7 (14.9)	2 (15.4)	5 (14.7)	2.5 (95% CI 0.194 - 32.19)	
	T4a	8 (17)	4 (30.8)	4 (11.8)	1 (95% CI 0.091 - 11.02)	
	T4b	2 (4.3)	0 (–)	2 (5.9)	5 (95% CI 0.15 - 166.5)#	
T1 - T3 vs. T4						0.378
	T1 - T3	30 (63.8)	7 (53.8)	23 (67.6)	1.792 (95% CI 0.486 - 6.615)	
	T4	17 (36.2)	6 (46.2)	11 (32.4)	1 (95% CI 0.245 - 4.083)	
N category (8th ed.)						0.477
	N0	16 (34)	6 (46.2)	10 (29.4)	1 (95% CI 0.239 - 4.184)	
	N1	14 (29.8)	4 (30.8)	10 (29.4)	1.5 (95% CI 0.322 - 6.991)	
	N2	1 (2.1)	0,5 (0)	1,5 (2.9)	1.857 (95% CI 0.065 - 52.76)	
	N2b	1 (2.1)	1,5 (7.7)	0 (–)	0.206 (95% CI 0.007 - 5.86)#	
	N2c	5 (10.6)	1 (7.7)	4 (11.8)	2.4 (95% CI 0.215 - 26.82)	
	N3a	1 (2.1)	0 (–)	1 (2.9)	1.857 (95% CI 0.065 - 52.76)#	
	N3b	9 (900)	1 (7.7)	8 (23.5)	4.8 (95% CI 0.475 - 48.46)	
N3						0.159
	other	37 (78.7)	12 (92.3)	25 (73.5)	0.231 (95% CI 0.026 - 2.043)	
	N3	10 (21.3)	1 (7.7)	9 (26.5)	1 (95% CI 0.054 - 18.57)	
M						0.820
	M0	44 (93.6)	12 (92.3)	32 (94.1)	1.333 (95% CI 0.11 - 16.09)	
	M1	3 (6.4)	1 (7.7)	2 (5.9)	1 (95% CI 0.034 - 29.80)	
UICC stage 8th ed.						0.726
	UICC I	7 (14.9)	2 (15.4)	5 (14.7)	1 (95% CI 0.098 - 10.16)	
	UICC II	4 (8.5)	1 (7.7)	3 (8.8)	1.2 (95% CI 0.073 - 19.63)	
	UICC III	16 (34.0)	6 (46.2)	10 (29.4)	0.667 (95% CI 0.097 - 4.58)	
	UICC IVA	6 (12.8)	2 (15.4)	4 (11.8)	0.8 (95% CI 0.076 - 8.474)	
	UICC IVB	11 (23.4)	1 (7.7)	10 (29.4)	4 (95% CI 0.288 - 55.47)	
	UICC IVC	3 (6.4)	1 (7.7)	2 (5.9)	0.8 (95% CI 0.044 - 14.64)	
IVB						0.182
	other	33 (70.2)	11 (84.6)	22 (64.7)	0.333 (95% CI 0.063 - 1.758)	
	IVB or IVC	14 (29.8)	2 (15.4)	12 (35.3)	1 (95% CI 0.12 - 8.307)	
Grading						0.579
	G1	2 (4.3)	1 (7.7)	1 (2.9)	1 (95% CI 0.02 - 50.4)	
	G2	23 (48.9)	5 (38.5)	18 (52.9)	3.6 (95% CI 0.19 - 68.34)	
	G3	22 (46.8)	7 (53.8)	15 (44.1)	2.143 (95% CI 0.116 - 39.47)	
Lymphatic infiltration						0.534
	L1	33 (70.2)	10 (76.9)	23 (67.6)	1 (95% CI 0.35 - 2.857)	
	L0	14 (29.8)	3 (23.1)	11 (32.4)	1.594 (95% CI 0.364 - 6.981)	

(Continued)

TABLE 1 Continued

Covariate	Characteristic	Total *n* (%)	LHSCC *n* (%)	Other HNSCC *n* (%)	OR (95% CI)	*p* value
p16 IHC						0.324
	p16+	12 (25.5)	2 (15.4)	10 (29.4)	1 (95% CI 0.117 - 8.56)	
	p16 neg (or unknown)	35 (74.5)	11 (84.6)	24 (70.6)	0.436 (95% CI 0.082 - 2.336)	
PD-L1 IHC						0.493
	CPS ≥ 1	18 (38.3)	6 (46.2)	12 (35.3)	1 (95% CI 0.25 - 3.999)	
	CPS < 1	29 (61.7)	7 (53.8)	22 (64.7)	1.571 (95% CI 0.429 - 5.752)	
Extranodal extension (ENE)						0.179
	No ENE	20 (42.6)	6 (46.2)	14 (41.2)	1 (95% CI 0.259 - 3.867)	
	ENE+	12 (25.5)	1 (7.7)	11 (32.4)	4.714 (95% CI 0.492 - 45.15)	
	N0 (no ENE)	15 (31.9)	6 (46.2)	9 (26.5)	0.643 (95% CI 0.157 - 2.627)	
Resection margins						0.207
	R0	37 (78.7)	12 (92.3)	25 (73.5)	1 (95% CI 0.378 - 2.647)	
	R1	3 (6.4)	1 (7.7)	2 (5.9)	0.96 (95% CI 0.079 - 11.66)	
	No surgery	7 (14.9)	0 (–)	7 (20.6)	7.353 (95% CI 0.388 - 139.3)#	
Op						0.217
	Yes	38 (80.9)	12 (92.3)	26 (76.5)	1 (95% CI 0.38 - 2.631)	
	No	9 (19.1)	1 (7.7)	8 (23.5)	3.692 (95% CI 0.414 - 32.94)	
Anti-PD-1						0.514
	Yes	5 (10.6)	2 (15.4)	3 (8.8)	1 (95% CI 0.08 - 12.55)	
	No	42 (89.4)	11 (84.6)	31 (91.2)	1.879 (95% CI 0.276 - 12.77)	
Cisplatin						0.596
	Yes	21 (44.7)	5 (38.5)	16 (47.1)	1 (95% CI 0.242 - 4.138)	
	No	26 (55.3)	8 (61.5)	18 (52.9)	0.703 (95% CI 0.191 - 2.592)	
RT						0.917
	Yes	32 (68.1)	9 (69.2)	23 (67.6)	1 (95% CI 0.336 - 2.974)	
	No	15 (31.9)	4 (30.8)	11 (32.4)	1.076 (95% CI 0.271 - 4.276)	
Overall survival (OS)						0.628
	Alive	23 (48.9)	5 (38.5)	18 (52.9)	1 (95% CI 0.246 - 4.06)	
	NCRD	5 (10.6)	2 (15.4)	3 (8.8)	0.417 (95% CI 0.054 - 3.221)	
	CRD	19 (40.4)	6 (46.2)	13 (38.2)	0.602 (95% CI 0.151 - 2.404)	
PFS						0.677
	PFS event	23 (48.9)	7 (53.8)	16 (47.1)	1 (95% CI 0.285 - 3.512)	
	No event	24 (51.1)	6 (46.2)	18 (52.9)	1.313 (95% CI 0.364 - 4.728)	
LRFS (LC)						0.900
	PFS event	21 (44.7)	6 (46.2)	15 (44.1)	1 (95% CI 0.262 - 3.815)	
	No event	26 (55.3)	7 (53.8)	19 (55.9)	1.086 (95% CI 0.301 - 3.919)	
LRRFS (LRC)						0.900
	PFS event	21 (44.7)	6 (46.2)	15 (44.1)	1 (95% CI 0.262 - 3.815)	
	No event	26 (55.3)	7 (53.8)	19 (55.9)	1.086 (95% CI 0.301 - 3.919)	

(Continued)

TABLE 1 Continued

Covariate	Characteristic	Total *n* (%)	LHSCC *n* (%)	Other HNSCC *n* (%)	OR (95% CI)	*p* value
NRFS (NC)						0.421
	PFS event	14 (29.8)	5 (38.5)	9 (26.5)	1 (95% CI 0.213 - 4.693)	
	No event	33 (70.2)	8 (61.5)	25 (73.5)	1.736 (95% CI 0.449 - 6.713)	
DMFS						0.075
	PFS event	10 (21.3)	5 (38.5)	5 (14.7)	1 (95% CI 0.173 - 5.772)	
	No event	37 (78.7)	8 (61.5)	29 (85.3)	3.625 (95% CI 0.837 - 15.70)	

Materials

FLAVINO assay

The FLAVINO assay is a short-time *ex-vivo* assay to test HNSCC regarding response to various treatments. To this end, colony formation and cytokine release of tumor cells exposed to various therapeutic agents are compared with their controls. This allows also the estimation of combinatory effects. Immediately after excision of the biopsy during panendoscopy or tumor surgery, the viable samples were put into cell culture medium and transferred at room temperature into the lab. The cell culture medium was a custom-made phenol- and riboflavin-free RPMI1640 (Bio & Sell GmbH, Feucht, Germany) containing 10% fetal calf serum (FCS; Anprotec, Bruckberg, Germany) with streptomycin, penicillin, amikacin, and nystatin C (all Sigma-Aldrich Chemie GmbH, Deisenhofen, Germany). All steps in handling the biopsy and the cells obtained from the tumor sample were executed under flavin-protective conditions (illumination only by sodium discharge lamps emitting monochromatic light at a wavelength of λ = 589 nm; Philips Medical Systems DMC GmbH, Hamburg, Germany). Mechanically disintegrated tumor tissue was digested via overnight incubation with 230 mIU/ml collagenase IV (Sigma-Aldrich Chemie GmbH, Deisenhofen, Germany) before cell counting utilizing 1:10 diluted Guava® ViaCount™ reagent (Luminex Corp., Austin, TX) for counting of viable cells in the Guava easyCyte 5HT flow-cytometer (Luminex). Flat-bottom cell culture-plates (TPP, Trasadingen, Switzerland) were pre-coated with laminin, collagen I and fibronectin (all from Roche, Mannheim, Germany). Pre-diluted pharmaceuticals were pipetted into six cavities each before seeding of $3x10^4$ viable cells per well to adjust to final concentrations of either 50 µg/ml pembrolizumab (Pemb), the (binary) TP combination of docetaxel (275 nM) and cisplatin (3333 nM) or the ternary combination of 50 mg/ml pembrolizumab plus TP at the same concentrations or medium only (control for reference) each in six replicates. After a further three days of incubation under standard conditions (36.5°C, humidified atmosphere, 3.5% CO_2), 200 µl of culture supernatants were collected and transferred to 384-well plates and stored frozen at -80°C for subsequent cytokine measurement by indirect sandwich enzyme-linked immunosorbent assay (ELISA, see below). Furthermore, cells were step-wise fixed with ethanol (40%, 70%, and 96% ethanol), and air-dried. Before subsequent colony counting, wells were blocked with an assay buffer containing 1% FCS (v/v) to prevent unspecific binding of anti-cytokeratin (Santa-Cruz Biotechnology, Inc., Santa-Cruz, USA) and FITC-labeled secondary antibody (Thermo Fisher Scientific GmbH, Dreieich, Germany). The antibodies were each diluted 1:800 in phosphate-buffered saline (PBS) containing 0.5% FCS and 0.05% Tween-20™. Stained epithelial cells were counted using a fluorescence microscope (Axiovert, Carl Zeiss Microscopy Deutschland GmbH, Oberkochen, Germany).

ELISA

Indirect sandwich ELISAs were performed to measure cytokine concentrations in cell-free supernatants of cell cultures harvested 72 h after exposure to drugs and drug combinations. Using OptEIA™ kits (BD GmbH, Heidelberg, Germany) IL-6, IL-8, IFN-γ, IP-10, MCP-1, and TNF-α, and VEGF-EDK kits for $VEGF_{165}$ (#900-K10, PeproTech GmbH, Hamburg, Germany), cytokine concentrations were measured according to the manufacturer's instructions but using tetramethyl benzidine (TMB 1-Step™ Ultra, Thermo Fisher Scientific) as substrate. Furthermore, measurements were performed at optical densities of λ_1 = 450 nm and λ_2 = 620 nm using the Synergy2™ multimode microplate reader (BioTek Instruments, Inc., Winooski, VT, USA). We used 4-parameter calibration curves to calculate pg/ml concentrations using Gen5™ software (BioTek Instruments, Inc., Winooski, VT, USA). The lower limit of detection (LLD) and the lower limit of quantification (LLQ) for cytokine detection was always < 4 pg/ml.

Evaluation of drug combinations and statistical analysis

For the objective assessment of the interactions between the drugs used, the changes from baseline (untreated control) were used to obtain delta values, which were used to calculate the interaction measure *q* (60–67) using the following formula:

$$q = P(A+B)/((P(A) + P(B) - P(A) \times P(B)) \quad (1)$$

wherein P(A) represents the effect of compound A (for instance, pembrolizumab), P(B) the effect of compound B (here: TP), and P (A+B) the effect of A and B in mixture with the same concentrations (pembrolizumab + TP). The evaluation of the respective mode of action considers the uncertainty of the measurements with regard to the interpretation of the value for q: a result of the equation of $q <$ 0.85 results in antagonism of the effect ratios, while $q = 0.85$ to 1.15 reflects additivity, and $q > 1.15$ indicates synergism. Cut-off analyses were performed for all experiments of sufficient colony formation (CFec ≥ 4). A summary of results for the individual cytokines is shown in graphs depicting the calculation of mean, standard deviation and confidence interval but also median and interquartile range (IQR). Colony formation values were analyzed with a two-tailed *t*-test for paired samples (SPSS Statistics 29.0 for Windows, SPSS Inc., Chicago, IL, USA). When p was < 0.05, the results were considered significant. Patient characteristics and follow-up data were analyzed in relation to the results from ELISA measurements and categorization according to receiver-operating characteristic (ROC) curves as described above. We also analyzed clinical characteristics of patients, and lifestyle-associated risk factors (daily alcohol consumption categorized in 0, 1-30 g, 31-60 g, > 60 g) and status (never, former, current), tobacco smoking (total number of pack years smoked during lifetime), smoking status (never, former, current smoker). Clinical characteristics of patients included age; sex; T, N and M categories; HPV status (according to p16 immune histochemistry), and treatment modalities (curative vs. palliative setting). Associations between categorical variables were examined by *Pearson's Chi-square* test. We calculated OS as time from date of biopsy to date of death (event), or end of follow-up (censored); DSS as time from date of biopsy to date of cancer-related death (event) censoring other causes of death or end of follow-up; PFS from date of biopsy to date of relapse or progressing disease or death from any cause (event), or end of follow-up (censored). Local relapse-free survival (LRFS) was calculated from date of biopsy to date of local relapse (within 2 cm resection margins) or progressing disease or death from any cause (event), or end of follow-up (censored). Nodal relapse-free survival (NRFS) was calculated from date of biopsy to date of diagnosis of locoregional relapse (local metastasis in locoregionary lymph nodes, independent of ipsilateral or contralateral) or progressing disease or death from any cause (event), or end of follow-up (censored). Loco-regional relapse-free survival (LRRFS) was calculated from date of biopsy to date of LRFS or NRFS, whatever came first, or progressing disease or death from any cause (event), or end of follow-up (censored). Distant metastasis-free survival (DMFS) was calculated from date of biopsy to date of diagnosis of distant metastasis (M1, event) or death from any cause (event), or end of follow-up (censored).

We analyzed survival using Kaplan-Meier cumulative survival plots applying log-rank tests and hazard ratios (HR) using multivariate Cox proportional hazard regression models (76) utilizing the conditional logistic regression step-wise forward method, and bootstrapping for internal validation (SPSS version 29, IBM Corporation, Armonk, New York). We considered $p < 0.05$ from 2-sided tests as significant.

Results

A total of $n = 47$ HNSCC patients (40 males, 7 females) out of $N =$ 54 samples (87.0%) obtained allowed for cytokine measurements, whereas only 12 (22.2%) were also reliably analyzable regarding colony formation of adherent epithelial cells (CFec) with mean CFec ≥ 4/well in the 6 replicate wells of sham-treated controls (Supplementary Figure S1). As the small number of 12 HNSCC samples did not allow for suitable subgroup analyses, we focused on treatment effects on cytokine production and compared 13 LHSCC and 34 HNSCC emerging from other sites. The clinical and epidemiological characteristics including distribution of lifestyle-related risk factors, TNM categories and stage as well as treatment of both groups were comparable with unadjusted $p \geq 0.159$ (Table 1). The outcome was also comparable with DMFS being the only measure showing a trend to impaired outcome in LHSCC ($p = 0.075$).

Figure 1 summarizes the treatment-related differences in cytokine production of the 47 samples based on mean and 95% confidence intervals (95%-CI) but also median and interquartile range (IQR) for the seven cytokines measured.

Treatment with pembrolizumab alone had no generalizable effect on production of IL-6, IL-8, MCP-1, TNF-α and VEGF, while IFN-γ was strongly induced. Due to unexpectedly high concentrations of IP-10 produced by sham-treated (medium only) controls, only few samples demonstrated increased IP-10 production without substantial impact toward a generally enhanced IP-10 production according to higher 95%-CI or IQR. The binary combination of docetaxel and cisplatin (TP) demonstrated strong heterogeneity of samples with respect to production of IL-6, as some samples responded with strong induction of IL-6 leading to nearly unchanged mean (1.669 vs. 1.649 ng/ml) but widened 95%-CI (0.832-2.505 vs. 1.114-2.184 ng/ml in controls). The median of 0.622 vs. 1.262 ng/ml was halved (Figure 1H). With IFN-γ again representing the only exception, the production of the other cytokines was found to be suppressed. However, comparing mean and median revealed heterogeneity also in this regard. The stimulating effect of TP on IFN-γ production was below that observed in pembrolizumab-treated samples. However, the combination of TP and pembrolizumab resulted in even stronger deviating amounts of IFN-γ production measured after 72 hours. Whereas production of IL-8, TNF-α and VEGF demonstrated antagonism, as the strong suppression through TP was mostly reduced by simultaneously present pembrolizumab (Figures 1 B, D, F–H), IP-10 release was only slightly modified (often within the range of measurement uncertainty). The production of MCP-1 and IL-6, however, demonstrated also deviating interaction of TP and pembrolizumab when comparing individual samples (compare Supplementary Table S1, available online). Therefore, we systematically investigated differences in outcome of patients related to *ex-vivo* response-patterns of their tumors. To this end,

we used receiver-operating-characteristic (ROC) curves for a binary split of samples according to optimum cut-offs. This, however, failed to demonstrate significant outcome differences (with all $p \geq 0.2$).

In sharp contrast, the response to TP plus pembrolizumab vs. TP and pembrolizumab alone as reflected by changes in production of MCP-1, IFN-γ and IL-6 was related to deviating outcome with significant differences in OS, DSS and PFS (Figure 2). Figure 3

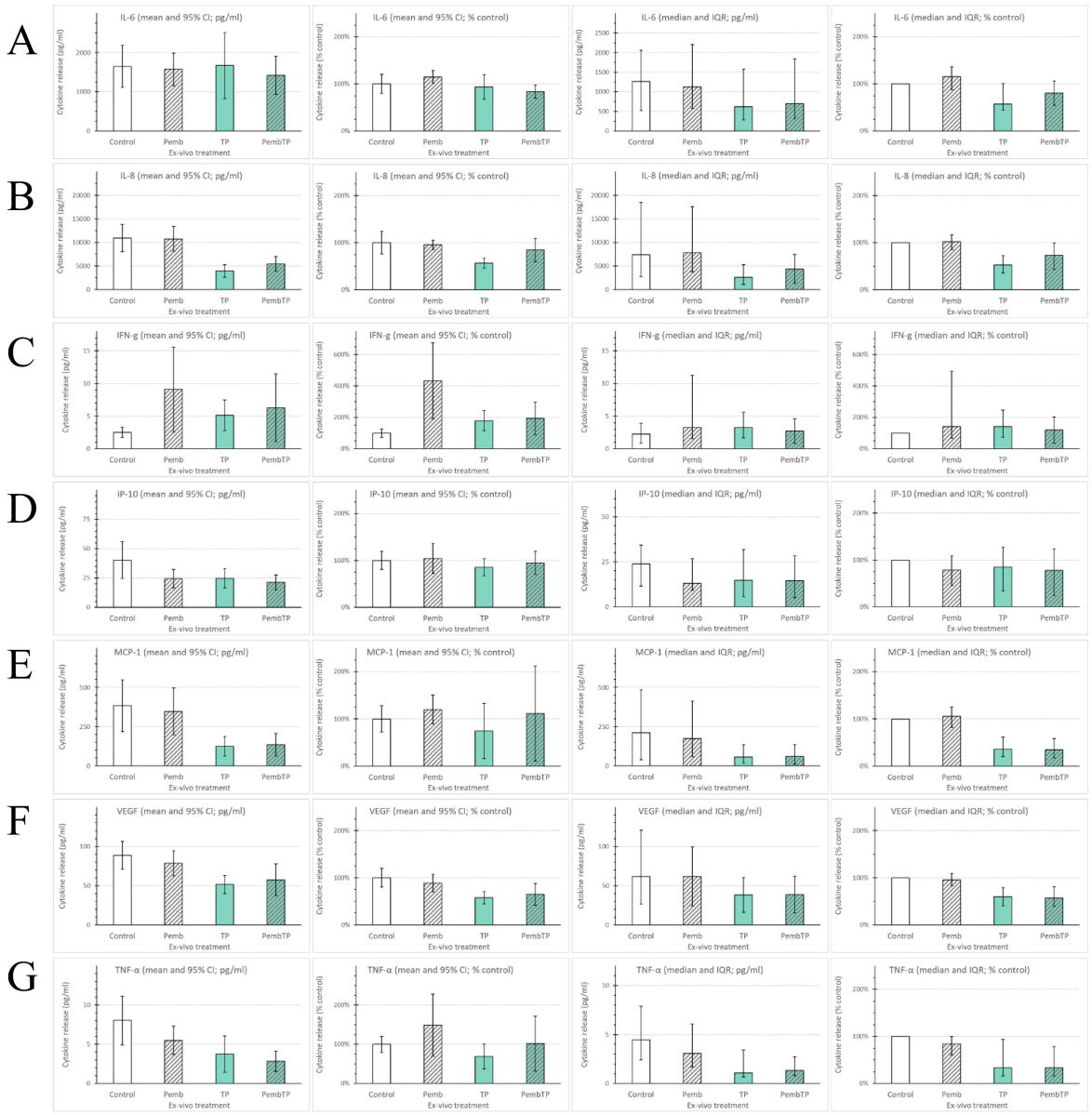

H

	Mean and 95% confidence intervals				Median and interquartile range			
	Control	Pembrolizumab	TP	PembTP	Control	Pembrolizumab	TP	PembTP
IL-6 (ng/ml)	1.649 (1.114 - 2.184)	1.575 (1.159 - 1.990)	1.669 (0.832 - 2.505)	1.419 (0.930 - 1.909)	1.262 (0.525 - 2.057)	1.124 (0.581 - 2.200)	0.622 (0.277 - 1.576)	0.702 (0.315 - 1.834)
IL-8 (ng/ml)	10.91 (8.029 - 13.78)	10.74 (8.120 - 13.36)	3.938 (2.618 - 5.258)	5.432 (3.874 - 6.990)	7.348 (2.735 - 18.44)	7.814 (3.751 - 17.61)	2.620 (1.067 - 5.247)	4.319 (1.355 - 7.478)
IFN-γ (pg/ml)	2.501 (1.716 - 3.285)	9.080 (2.578 - 15.58)	5.152 (2.806 - 7.497)	6.296 (1.112 - 11.48)	2.273 (0.858 - 3.920)	3.238 (1.566 - 11.26)	3.238 (1.696 - 5.623)	2.735 (0.858 - 4.625)
IP-10 (pg/ml)	40.32 (24.67 - 55.97)	24.43 (16.66 - 32.19)	24.69 (16.59 - 32.79)	21.31 (14.94 - 27.68)	23.90 (11.47 - 34.33)	13.03 (9.198 - 26.72)	14.78 (5.652 - 31.78)	14.57 (5.123 - 28.39)
MCP-1 (pg/ml)	383.6 (219.2 - 548.0)	347.0 (198.0 - 496.0)	125.7 (64.51 - 186.9)	135.6 (63.18 - 208.0)	211.5 (39.32 - 482.6)	175.6 (60.37 - 413.1)	57.70 (19.44 - 135.9)	62.85 (12.59 - 136.1)
VEGF-A (pg/ml)	88.43 (70.72 - 106.1)	78.47 (62.29 - 94.64)	51.42 (39.96 - 62.89)	57.40 (37.33 - 77.48)	62.05 (28.04 - 122.1)	62.33 (25.76 - 99.30)	39.28 (21.38 - 60.22)	39.72 (15.77 - 63.50)
TNF-α (pg/ml)	8.049 (4.940 - 11.16)	5.502 (3.698 - 7.306)	3.765 (1.466 - 6.063)	2.853 (1.553 - 4.152)	4.466 (2.423 - 7.876)	3.072 (1.672 - 6.054)	1.106 (0.674 - 3.437)	1.327 (0.808 - 2.720)

FIGURE 1
Cytokine production of head and neck squamous cell carcinoma of 47 patients treated *ex vivo* according the FLAVINO protocol with immune-checkpoint blockade (ICB) utilizing the anti-PD-1 antibody pembrolizumab either alone (Pemb; 50 ng/ml pembrolizumab mono), TP or PembTP, Pemb combined with half maximum tolerable plasma concentrations of docetaxel (T; 275 nM) and cisplatin (P; 3.33 μM). Mean concentrations (pg/ml) and normalized mean (% of untreated control) as well as median concentrations (pg/ml) and normalized mean (% of untreated control) inclusive 95% CI and interquartile range (IQR) measured in 72-hours supernatants are shown for **(A)** interleukin 6 (IL-6); **(B)** IL-8; **(C)** interferon gamma (IFN-γ); **(D)** interferon-induced protein 10 (IP-10; CXCL10); **(E)** monocyte chemo-attractant protein 1(MCP-1; CCL2); **(F)** vascular endothelial growth factor A (VEGF); **(G)** tumor-necrosis-factor alpha (TNF-α); **(H)** mean and 95% CI (left) and median and IQR (right).

shows boxplots for MCP-1, IFN-γ and IL-6 in response groups with deviating outcome. Obviously, patients with superior outcome (depicted blue) had rather high production of MCP-1 that was not substantially elevated by pembrolizumab but suppressed in response to TP, rather lower IL-6 and/or IFN-γ production that was suppressed by TP and/or pembrolizumab plus TP. Contrarily, patients with low MCP-1 production but elevated IL-6 and/or IFN-γ production (depicted red) were at risk for impaired outcome.

As, however, the response to TP plus pembrolizumab regarding MCP-1, IFN-γ and IL-6 production was not strongly correlated on the patient-individual level, we used Cox proportional hazard regression modeling to find out if response patterns emerging after combined treatment are independent predictors of outcome. By including all known clinical prognostic factors for OS of HNSCC patients, we found age at diagnosis, smoking history (according to number of pack-years tobacco smoking), daily alcohol consumption, T and N categories and p16-positivity but not localization in larynx/hypopharynx *vs.* other sites as well as the treatment setting (curative vs. palliative intend) were of prognostic relevance and represented independent predictors (*Pi*) for particular outcome measures, OS, DSS or PFS. The response-

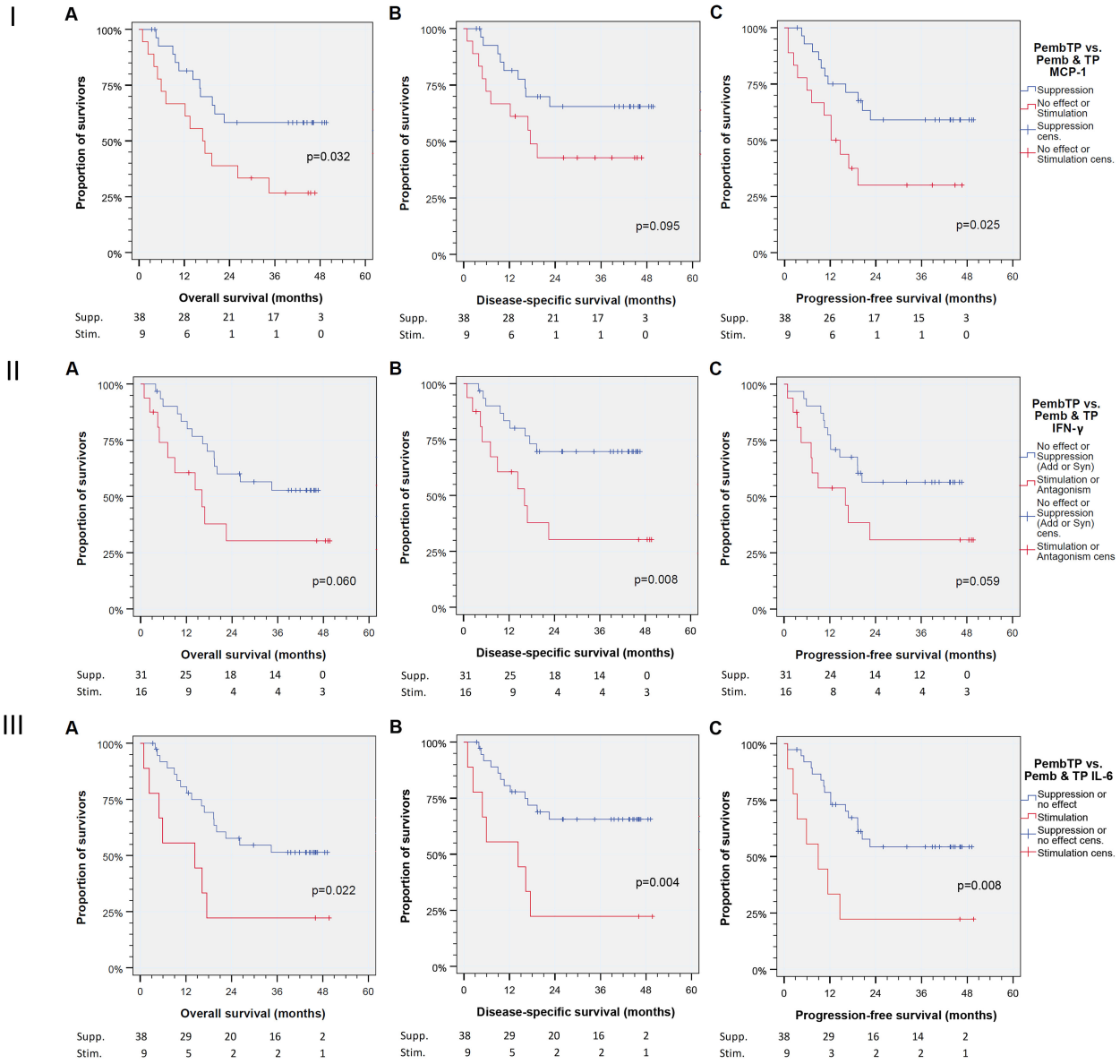

FIGURE 2
Kaplan-Meier cumulative survival plots for (from left to right) overall, disease-specific, and progression-free survival of 47 patients treated *ex vivo* with immune-checkpoint inhibitor (ICI) utilizing the anti-PD-1 antibody pembrolizumab either alone (pembrolizumab mono) vs. TP or pembrolizumab combined with docetaxel (T) and cisplatin (P) according to half maximum tolerable plasma concentration (275 nM and 3.33 µM, respectively) were compared. Binary split of the cohort was according to the mode of action, suppression (Supp.) of MCP-1 or no effect or suppression of IFN-γ or IL-6 production by pembrolizumab + TP vs. those with stimulation (Stim.). Numbers for patients at risk are provided for **(I)** monocyte chemoattractant protein 1 (MCP-1; CCL2); **(II)** interferon gamma (IFN-γ); **(III)** interleukin 6 (IL-6). *P* values shown are from log rank tests (2-sided).

characteristics to TP plus pembrolizumab was introduced into modeling as binary categorized covariates (Table 2).

While some of the clinical *Pi* lost significance and were not included in the step-wise forward build Cox model, MCP-1 emerged as the only *Pi* of PFS (HR 4.698, 95%-CI 1.702-12.97; $p = 0.0028$), it was also *Pi* for DSS (HR 6.392, 95%-CI 2.144-19.06; $p = 0.0009$) and OS (HR 2.732, 95%-CI 1.031-7.240; $p = 0.0433$). Whereas IL-6 was *Pi* only for OS (HR 6.0077, 95%-CI 2.024-17.83; $p = 0.0012$), IFN-γ was *Pi* of DSS (HR 2.592, 95%-CI 1.019-6.591; $p = 0.0455$) and OS (HR 2.391, 95%-CI 1.005-5.689; $p = 0.0488$). Internal validation of the multivariate Cox proportional hazard regression models through bootstrapping applying 1,000 iterations revealed stability of the models and MCP-1 and IL-6 as *Pi* (all $p \leq 0.0310$), while IFN-γ slightly missed this criterion with $p = 0.0589$ for DSS, and $p = 0.0849$ for OS (Table 2).

Discussion

Ex-vivo response-evaluation of HNSCC utilizing ELISA for cytokine measurements allowed for analyzing deviating response to treatment with pembrolizumab, TP and pembrolizumab + TP. Suppression of MCP-1, IL-6 and IFN-γ production by pembrolizumab + TP exceeding the effect of TP or pembrolizumab were found to be independent predictors of outcome according to OS, DSS, and PFS since biopsy. The FLAVINO assay identified a fraction of HNSCC patients among those analyzed with impaired outcome independent from other clinical characteristics and treatment applied. This minor group of patients responded not the same way as the majority of HNSCC samples analyzed as they did not show suppression of MCP-1, IFN-γ, and IL-6 production by pembrolizumab + TP. We interpret this

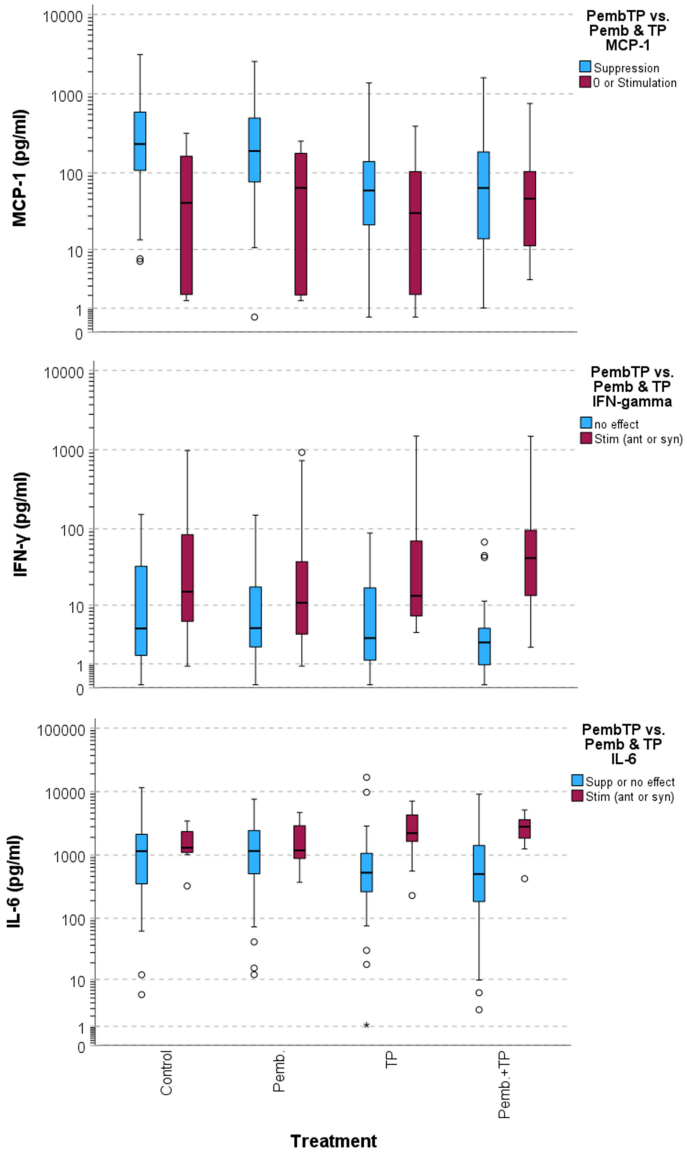

FIGURE 3
Boxplots demonstrating deviating cytokine production of head and neck squamous cell carcinoma in treatment response groups according to binary classification in Figure 2.

TABLE 2 Independent predictors (Pi) of overall survival (OS), disease-specific survival (DSS), and progression-free survival (PFS) of head and neck squamous cell carcinoma patients identified using multivariate Cox proportional hazard regression models build using the step-wise forward likelihood ratio method in SPSS v.29.

	Covariate	Ref.	Characteristic	*n*	Events *n* (%)	*P* value[#]	Cox univariate HR (95% CI)	*P* value[†]	Cox multivariate HR (95% CI)	*P* value[††]	Loss[‡] in χ^2	*P* value[‡]	*P* value[‡‡]
OS	Age at diagnosis	Per year				–	1.009 (0.965 – 1.055)	0.6923	1.075 (1.018 - 1.135)	**0.0097**	6.751	**0.0090**	**0.0110**
	Pack years	Per year				–	1.024 (1.009 - 1.040)	**0.00142**	1.028 (1.010 - 1.046)	**0.0019**	10.469	**0.0010**	**0.0020**
	Treatment setting	curative	palliative	11	9 (81.8%)	**0.0203**	2.601 (1.126 - 6.007)	**0.02524**	3.444 (1.285 - 9.230)	**0.0139**	5.729	**0.0170**	**0.0250**
	p16 IHC	p16 negative or unknown	p16 positive	12	4 (33.3%)	0.2428	0.533 (0.182 - 1.56)	0.2505	0.223 (0.056 - 0.889)	**0.0335**	5.885	**0.0150**	0.0659
	MCP-1 PembTP vs. Pemb & TP	suppression	no effect or stimulation	9	8 (88.9%)	**0.0324**	3.337 (1.392 - 8.000)	**0.00691**	2.732 (1.031 - 7.240)	**0.0433**	3.673	0.0550	**0.0310**
	IFN-γ PembTP vs. Pemb & TP	no effect or suppression (add or syn)	stimulation or antagonism	16	10 (62.5%)	0.0596	2.153 (0.951 - 4.874)	0.06575	2.391 (1.005 - 5.689)	**0.0488**	3.709	0.0540	0.0849
	PembTP vs. Pemb & TP IL-6	no effect or suppression	stimulation (ant or syn)	9	7 (77.8%)	**0.0217**	2.714 (1.117 - 6.594)	**0.02746**	6.007 (2.024 - 17.83)	**0.0012**	9.327	**0.0020**	**0.0020**
DSS	Alcohol (g/day)	<30	≥30	22	13 (59.1%)	**0.0199**	2.989 (1.135 - 7.871)	**0.02668**	5.325 (1.753 - 16.18)	**0.0032**	10.038	**0.0020**	**0.0020**
	N category	N0	N+	31	16 (51.6%)	**0.0157**	4.091 (1.187 - 14.10)	**0.02565**	0.363 (0.184 - 0.717)	**0.0035**	11.771	**0.0010**	**0.0070**
	MCP-1 PembTP vs. Pemb & TP	suppression	no effect or stimulation	9	7 (77.8%)	**0.0095**	3.283 (1.276 - 8.448)	**0.0137**	6.392 (2.144 - 19.06)	**0.0009**	10.086	**0.0010**	**0.0010**
	IFN-γ PembTP vs. Pemb & TP	no effect or suppression (add or syn)	stimulation or antagonism	16	10 (62.5%)	**0.0082**	3.188 (1.288 - 7.890)	**0.01218**	2.592 (1.019 - 6.591)	**0.0455**	3.899	**0.0480**	0.0589
PFS	Alcohol (g/day)	< 30	≥ 30	22	14 (63.6%)	**0.0312**	2.447 (1.056 - 5.671)	**0.03696**	4.273 (1.675 - 10.90)	**0.0024**	9.868	**0.0020**	**0.0040**
	N category	N0	N+	31	19 (61.3%)	**0.0086**	3.872 (1.309 - 11.46)	**0.01445**	7.947 (2.319 - 27.24)	**0.0010**	14.748	**< 0.0001**	**0.0030**
	MCP-1 PembTP	suppression	no effect or stimulation	9	7 (77.8%)	**0.0253**	2.558 (1.036 - 6.319)	**0.04175**	4.698 (1.702 - 12.97)	**0.0028**	7.852	**0.0050**	**0.0010**

P values shown highlighted bold are significant with $p < 0.05$ in 2-sided statistics.

10.3389/fimmu.2024.1473897

finding as patient-individual characteristic regarding deviating immune regulation. Reasons behind this finding could be manifold. It is well investigated that, after prolonged exposure, immune cells, CD4+ T-helper cells (Th) and cytotoxic T cells (Tc) become exhausted or may acquire resistance due to sustained signaling via their interferon receptors, IFNAR and IFNGR (68). We recently published findings about the prognostic value of IFN-γ measured before and during ongoing treatment with antibodies to PD-1, pembrolizumab or nivolumab, and impaired survival of patients with increased IFN-γ concentrations measured in EDTA-anticoagulated plasma (59). Within the same *in-vivo* study, suppression of MCP-1 concentrations ≥ 15% from baseline level was linked to improved survival. Within this *ex-vivo* study, we confirm that compared to pembrolizumab and TP reduced MCP-1 concentrations through combined pembrolizumab + TP is an indicator for HNSCC patients with rather good outcome according to OS, DSS, and PFS. IL-6 is a senescence marker also involved in inflammation and increases IFNGR signaling via facilitation of signal transducer and activator of transcription (STAT 1) phosphorylation (69). Hence, responding to pembrolizumab + TP with reduced production of MCP-1, IFN-γ, and IL-6 might reflect the presence of a well-functioning intratumoral immune infiltrate able to attack the cancerous epithelial cells in HNSCC. An important marker addressed in this study is the pro-inflammatory cytokine MCP-1, which is produced at the site of inflammation. MCP-1 binds to CCR2 and is involved in chemotactic recruitment of monocytes, macrophages and natural killer cells (70). In higher concentrations, this CC chemokine has an effect on the tumor environment and has demonstrated a correlation with tumor invasiveness, tumor angiogenesis and progression of the disease, and spread of metastases (71, 72). Interestingly, both tumor-supporting and tumor-inhibiting effects can be seen through the effects on different cell types and depending on the concentration. Significantly lower OS and DSS were observed in various studies when MCP-1 levels were elevated, suggesting that MCP-1 may be a good prognostic marker for HNSCC (73–75). Results have shown that chemokines produced by tumor cells promote the infiltration of immune cells into the tumor microenvironment (TME), and that MCP-1 (CCL2) plays a decisive role in this context (76). CCL-2 receptor (CCR2) expressing monocytes are recruited along a CCL2 gradient to the tumor periphery (77, 78) where they mature further in the TME and develop pro-tumoral functions (79, 80). This occurs through maturation into tumor-associated macrophages (TAMs), which further fosters tumor growth (79, 81, 82). Based on preclinical models, this growth could be impaired by blocking CCR2/CCL2 binding (83). A correlation between the concentration of CCL2, monocytes in the TME, and the suppression of the T-cell response can be observed in various cancer models (84–87). The resulting immunosuppressive mechanisms cause tumor progression. The CCR2-positive monocytes are thus an antagonist of the antigen-specific T cells.

IFN-γ is a key regulator centrally involved in the initiation of an antitumoral immune response but it can also exert pro-tumoral functions (88). It was shown that exposure to elevated IFN-γ levels and especially a prolonged exposure exerts selective immune pressure on the tumor cell leading to reduced expression of genes involved in antigen presentation, such as MHC class I (89). Persistent IFN-γ signaling also allows the tumor to acquire signal transducer and activator of transcription 1 (STAT1)-related epigenomic changes and augments expression of interferon-stimulated genes and ligands for multiple T-cell inhibitory receptors, which can be seen as a mechanism of adaptive resistance to checkpoint inhibitor therapy. Biomarkers for interferon-driven resistance are reported as being associated with clinical progression after anti-PD-1 therapy (68). Under the combination therapy of pembrolizumab with TP, only a suppression of the MCP-1 concentration occurred in the LHSCC patients. Thus, pembrolizumab can inhibit MCP-1 release in addition to the administration of TP alone. Suppression of MCP-1 showed overall positive results in terms of progression-free survival (PFS) and stimulation proved to be negative for patient survival. An increase in MCP-1 concentration during TP treatment may lead to tumor progression. These results are consistent with a more extensive study in mice with an intravenous CCR2-depleting antibody injection, which showed that depletion of CCR2+ monocytes in a therapeutic tumor setting leads to reduced tumor growth, demonstrating their immunosuppressive capacity. These results indicate that CCR2+ monocytes have a tumor-promoting effect, are counter-regulators of immunological tumor control and contribute to tumor evasion (90). The response to pembrolizumab vs. TP vs. pembrolizumab + TP suggests patient-specific effects of treatment on cytokine production *ex vivo*. The cytokines showing correlation with overall survival or even predicting patient outcome are the same as those found in previous studies *ex vivo* (55) and *in vivo* (59), but require validation in a cohort of patients treated with TP or pembrolizumab + TP, preferably in a randomized clinical trial, while simultaneously tested in FLAVINO using pembrolizumab, TP, and pembrolizumab + TP *ex vivo*. The checkpoint inhibitor used in this assay is pembrolizumab (Keytruda®, MK-3475, MSD Sharp & Dohme Corp, Whitehouse Station, USA), a humanized monoclonal antibody that targets and blocks the protein PD-1 (91). Pembrolizumab was already approved as monotherapy for the treatment of R/M HNSCC with prior platinum-containing chemotherapy. The approval is based in part on results from the KEYNOTE-012, KEYNOTE 040 trials (34, 36). Furthermore, binary and tertiary combinations with docetaxel (Taxotere®, Sanofi-Aventis) and cisplatin were tested. These two therapeutics already showed to dose-dependently reduce the viability and colony formation of HNSCC under laboratory conditions (64). Although efficacy of monoclonal antibodies in relapsed HNSCC has been noted in responders to therapy with consequent prolonged overall survival (OS), the therapy does not lead to the desired response in every patient, resulting in about one third of non-responders with minor (insufficient low) shrinkage of the tumor or disease progression (92). As non-responsiveness or even hyper-progression after pembrolizumab treatment are reported, we have to expect responders and non-responders to the therapy of pembrolizumab in combination with docetaxel and cisplatin as well. Subgroups of HNSCC that respond or do not respond to treatment need to be identified, as pembrolizumab is costly and non-responders who receive ineffective treatment have

an increased risk of early recurrence, reduced quality of life and premature death. Patients who benefit from pembrolizumab despite PD-1 negativity also show need for investigation (38). As we were able to identify a subgroup of patients with adverse stimulation of MCP-1, IFN-γ and IL-6, and the increased levels of the three cytokines emerged as biomarkers for rather poor outcome, we reached the aim of this study by determining deviating effects of pembrolizumab, docetaxel and cisplatin on HNSCC and their cytokine release *ex vivo*. Monitoring these *ex-vivo* effects in parallel to cytokine measurements in blood samples during treatment and clinical follow-up in the ELOS trial will allow for assessing their value as biomarkers for successful pembrolizumab therapy. ELOS is a randomized, two-arm phase II study on organ preservation of the larynx in advanced laryngeal or hypopharyngeal squamous cell carcinoma (LHNSCC) in stage III, IVA/B, which are only resectable by total laryngectomy and have PD-L1 expression with CPS ≥ 1. This study is based on the two studies KEYNOTE-048 and DELOS-II (German Laryngeal Organ Preservation Study II). Positive results were seen in the KEYNOTE-048 trial as a first-line therapy for recurrent and metastatic HNSCC, as well as in the curative setting ADRISK (ClinicalTrials.gov NCT03480672) and NadiHN (EudraCT No. 2016-004787-20). The endpoints of the KEYNOTE-048 study were overall survival and progression-free survival in the intent-to-treat population. The results were positive in terms of efficacy and safety. Therefore, it can be concluded that pembrolizumab plus platinum and 5-fluorouracil is an appropriate first-line therapy for recurrent or metastatic HNSCC, and that pembrolizumab monotherapy is an appropriate first-line therapy for PD-L1-positive recurrent or metastatic HNSCC (9, 93). The randomized phase II DELOS-II trial investigated the effect of adding cetuximab to an already well-functioning therapy with TPF or TP and radiotherapy, also with the hope of laryngeal preservation in LHSCC (NCT00508664 (2–6)). Although cetuximab did not lead to any significant difference in the test group, it was positively noted that the standard group showed an unexpectedly positive development (93). Hence, TP is used for reference (control arm) also in the ongoing ELOS RCT (7, 8). Combination therapy of pembrolizumab in addition to docetaxel with cisplatin in patients with LHSCC identifies *ex vivo* those patients with prolonged PFS irrespective their treatment. Thus, we interpret this finding as an expression of a proper working immune system with potential to eradicate the tumor, provided the tolerance-inducing PD-1:PD-L1 immune-checkpoint can be blocked, for instance using pembrolizumab. This means that addition of pembrolizumab has a potential in these patients to overcome the immunosuppressive cancer microenvironment and may increase the frequency of responders (overall response rate), best response rate, OS, DSS, PFS, EFS and LFS. Further studies are needed to confirm the results and to identify the underlying mechanisms to realize the full potential of specific cancer immunotherapies. In addition to enhancing tumor-specific cytotoxic T cell responses, future immunotherapeutic approaches may need to focus on the immunosuppressive TME, including the role of CCR2+ monocytes, and the interplay with IFN-γ and IL-6 in HNSCC and the patients' blood.

Conclusions

Response evaluation of HNSCC treated *ex vivo* might allow for identification of responsiveness of an individual patient's tumor to combination treatment with pembrolizumab + TP before starting induction chemotherapy. Measuring at least three cytokines, MCP-1, IFN-γ and IL-6 may be able to get very desirable information about principal responsiveness of the tumor to this treatment and, provided suppressed production of these cytokines, predict superior outcome.

Data availability statement

The raw data supporting the conclusions of this article will be made available by the authors, without undue reservation.

Ethics statement

The studies involving humans were approved by the Institutional Human Ethics Committee of the University Leipzig (vote NICEI-CIH 341-15-ff). The studies were conducted in accordance with the local legislation and institutional requirements. The participants provided their written informed consent to participate in this study.

Author contributions

JW: Conceptualization, Data curation, Formal Analysis, Investigation, Methodology, Validation, Visualization, Writing – original draft, Writing – review & editing. LR: Conceptualization, Data curation, Formal Analysis, Investigation, Methodology, Validation, Writing – review & editing. MB: Conceptualization, Investigation, Methodology, Writing – review & editing. IK: Formal Analysis, Investigation, Methodology, Writing – review & editing. VZ: Writing – review & editing. MP: Methodology, Project administration, Resources, Supervision, Writing – review & editing. MS: Investigation, Resources, Writing – review & editing. SW: Conceptualization, Investigation, Project administration, Resources, Supervision, Writing – review & editing. AD: Conceptualization, Funding acquisition, Investigation, Project administration, Resources, Supervision, Writing – review & editing. TW: Conceptualization, Data curation, Formal Analysis, Investigation, Validation, Writing – original draft, Writing – review & editing. GW: Conceptualization, Data curation, Formal Analysis, Funding acquisition, Investigation, Methodology, Project administration, Resources, Software, Supervision, Validation, Visualization, Writing – original draft, Writing – review & editing.

Funding

The author(s) declare that financial support was received for the research, authorship, and/or publication of this article. We

acknowledge support from Leipzig University for Open Access Publishing.

Acknowledgments

We thank all patients and their families who participated in the investigation. We especially thank all contributing physicians for providing clinical data and the entire technical staff, all nurses, and physicians in the involved departments.

Conflict of interest

AD received funding for research the ELOS randomized controlled larynx-organ preservation trial.

The remaining authors declare that the research was conducted in the absence of any commercial or financial relationships that could be construed as a potential conflict of interest.

The author(s) declared that they were an editorial board member of Frontiers, at the time of submission. This had no impact on the peer review process and the final decision.

Publisher's note

Supplementary material

The Supplementary Material for this article can be found online at: https://www.frontiersin.org/articles/10.3389/fimmu.2024.1473897/full#supplementary-material

References

1. Bootz F. S3-Leitlinie Diagnostik, Therapie und Nachsorge des Larynxkarzinoms. *Radiologe*. (2020) 60:1052–7. doi: 10.1007/s00117-020-00760-9

2. Dietz A, Wichmann G, Kuhnt T, Pfreundner L, Hagen R, Scheich M, et al. Induction chemotherapy (IC) followed by radiotherapy (RT) versus cetuximab plus IC and RT in advanced laryngeal/hypopharyngeal cancer resectable only by total laryngectomy-final results of the larynx organ preservation trial DeLOS-II. *Ann Oncol*. (2018) 29:2105–14. doi: 10.1093/annonc/mdy332

3. Wichmann G, Krüger A, Boehm A, Kolb M, Hofer M, Fischer M, et al. Induction chemotherapy followed by radiotherapy for larynx preservation in advanced laryngeal and hypopharyngeal cancer: Outcome prediction after one cycle induction chemotherapy by a score based on clinical evaluation, computed tomography-based volumetry and 18F-FDG-PET/CT. *Eur J Cancer*. (2017) 72:144–55. doi: 10.1016/j.ejca.2016.11.013

4. Wiegand S, Wichmann G, Dietz A. Perspectives of Induction With Chemo and/or Immune Check Point Inhibition in Head and Neck Organ Preservation Treatment. *Front Oncol*. (2019) 9:191. doi: 10.3389/fonc.2019.00191

5. Dietz A, Wiegand S, Kuhnt T, Wichmann G. Laryngeal preservation approaches: considerations for new selection criteria based on the deLOS-II trial. *Front Oncol*. (2019) 9:625. doi: 10.3389/fonc.2019.00625

6. Wichmann G, Wald T, Pirlich M, Stoehr M, Zebralla V, Kuhnt T, et al. Improved survival of locoregional-advanced larynx and hypopharynx cancer patients treated according to the DeLOS-II protocol. *Front Oncol*. (2024) 14:1394691. doi: 10.3389/fonc.2024.1394691

7. Wichmann G, Dietz A, Wald T, Pirlich M, Wiegand S, Napp J, et al. The European Larynx Organ Preservation Study (ELOS) [MK-3475-C44]: STUDY PROTOCOL article Front. *Oncol Sec. Head Neck Cancer*. (2024) 14:1433238. doi: 10.3389/fonc.2024.1433238

8. Dietz A. *ELOS - Induction Chemotherapy With Docetaxel and Cisplatin Followed by Radiation Compared to Additional PD-1 Inhibition in CPS ≥1 Advanced Laryngeal/Hypopharyngeal Cancer Suitable for Laryngectomy Selected After Early Response Evaluation (European Larynx Organ Preservation Study (ELOS)*. European Medicines Agency (CTIS.

9. Burtness B, Harrington KJ, Greil R, Soulières D, Tahara M, Castro G, et al. Pembrolizumab alone or with chemotherapy versus cetuximab with chemotherapy for recurrent or metastatic squamous cell carcinoma of the head and neck (KEYNOTE-048): a randomised, open-label, phase 3 study. *Lancet*. (2019) 394:1915–28. doi: 10.1016/S0140-6736(19)32591-7

10. Wiegand S, Wichmann G, Vogt J, Vogel K, Franke A, Kuhnt T, et al. Postoperative adjuvant radiochemotherapy with cisplatin versus adjuvant radiochemotherapy with cisplatin and pembrolizumab in locally advanced head and neck squamous cell carcinoma- the study protocol of the Adrisk trial. *Front Oncol*. (2023) 13:1128176. doi: 10.3389/fonc.2023.1128176

11. Wu S-G, Wang R-J, Zhou Y, Luo X-Y. Neoadjuvant therapy with chemotherapy and immune checkpoint inhibitor for laryngeal function preservation in locally advanced hypopharyngeal cancer. *Front Immunol*. (2024) 15:1364799. doi: 10.3389/fimmu.2024.1364799

12. Wise-Draper TM, Gulati S, Palackdharry S, Hinrichs BH, Worden FP, Old MO, et al. Phase II clinical trial of neoadjuvant and adjuvant pembrolizumab in resectable local-regionally advanced head and neck squamous cell carcinoma. *Clin Cancer Res*. (2022) 28:1345–52. doi: 10.1158/1078-0432.CCR-21-3351

13. Zhang Z, Wu B, Peng G, Xiao G, Huang J, Ding Q, et al. Neoadjuvant chemoimmunotherapy for the treatment of locally advanced head and neck squamous cell carcinoma: A single-arm phase 2 clinical trial. *Clin Cancer Res*. (2022) 28:3268–76. doi: 10.1158/1078-0432

14. Vos JL, Elbers JBW, Krijgsman O, Traets JJH, Qiao X, van der Leun AM, et al. Neoadjuvant immunotherapy with nivolumab and ipilimumab induces major pathological responses in patients with head and neck squamous cell carcinoma. *Nat Commun*. (2021) 12:7348. doi: 10.1038/s41467-021-26472-9

15. Wang K, Gui L, Lu H, He X, Li D, Liu C, et al. Efficacy and safety of pembrolizumab with preoperative neoadjuvant chemotherapy in patients with resectable locally advanced head and neck squamous cell carcinomas. *Front Immunol*. (2023) 14:1189752. doi: 10.3389/fimmu.2023.1189752

16. Fang Q, Xu P, Cao F, Wu D, Liu X. PD-1 Inhibitors combined with paclitaxel (Albumin-bound) and cisplatin for larynx preservation in locally advanced laryngeal and hypopharyngeal squamous cell carcinoma: a retrospective study. *Cancer Immunol Immunother*. (2023) 72:4161–8. doi: 10.1007/s00262-023-03550-z

17. Heemskerk B, Kvistborg P, Schumacher TNM. The cancer antigenome. *EMBO J*. (2013) 32:194–203. doi: 10.1038/emboj.2012.333

18. Liu J, Blake SJ, Yong MCR, Harjunpää H, Ngiow SF, Takeda K, et al. Improved efficacy of neoadjuvant compared to adjuvant immunotherapy to eradicate metastatic disease. *Cancer Discovery*. (2016) 6:1382–99. doi: 10.1158/2159-8290.CD-16-0577

19. Gajewski TF. Fast forward - neoadjuvant cancer immunotherapy. *N Engl J Med*. (2018) 378:2034–5. doi: 10.1056/NEJMe1803923

20. Forde PM, Chaft JE, Smith KN, Anagnostou V, Cottrell TR, Hellmann MD, et al. Neoadjuvant PD-1 blockade in resectable lung cancer. *N Engl J Med*. (2018) 378:1976–86. doi: 10.1056/NEJMoa1716078

21. Liu WM, Fowler DW, Smith P, Dalgleish AG. Pre-treatment with chemotherapy can enhance the antigenicity and immunogenicity of tumours by promoting adaptive immune responses. *Br J Cancer*. (2010) 102:115–23. doi: 10.1038/sj.bjc.6605465

22. Chen J, Jiang CC, Jin L, Zhang XD. Regulation of PD-L1: a novel role of pro-survival signalling in cancer. *Ann Oncol*. (2016) 27:409–16. doi: 10.1093/annonc/mdv615

23. Peng J, Hamanishi J, Matsumura N, Abiko K, Murat K, Baba T, et al. Chemotherapy Induces Programmed Cell Death-Ligand 1 Overexpression via the Nuclear Factor-κB to Foster an Immunosuppressive Tumor Microenvironment in Ovarian Cancer. *Cancer Res*. (2015) 75:5034–45. doi: 10.1158/0008-5472.CAN-14-3098

24. Zhang P, Ma Y, Lv C, Huang M, Li M, Dong B, et al. Upregulation of programmed cell death ligand 1 promotes resistance response in non-small-cell lung cancer patients treated with neo-adjuvant chemotherapy. *Cancer Sci*. (2016) 107:1563–71. doi: 10.1111/cas.13072

25. Keir ME, Butte MJ, Freeman GJ, Sharpe AH. PD-1 and its ligands in tolerance and immunity. *Annu Rev Immunol*. (2008) 26:677–704. doi: 10.1146/annurev.immunol.26.021607.090331

26. Latchman YE, Liang SC, Wu Y, Chernova T, Sobel RA, Klemm M, et al. PD-L1-deficient mice show that PD-L1 on T cells, antigen-presenting cells, and host tissues negatively regulates T cells. *Proc Natl Acad Sci U. S. A*. (2004) 101:10691–6. doi: 10.1073/pnas.0307252101

27. Yang J, Riella LV, Chock S, Liu T, Zhao X, Yuan X, et al. The novel costimulatory programmed death ligand 1/B7.1 pathway is functional in inhibiting alloimmune responses. *vivo. J Immunol*. (2011) 187:1113–9. doi: 10.4049/jimmunol.1100056

28. Chen S-W, Li S-H, Shi D-B, Jiang W-M, Song M, Yang A-K, et al. Expression of PD-1/PD-L1 in head and neck squamous cell carcinoma and its clinical significance. *Int J Biol Markers*. (2019) 34:398–405. doi: 10.1177/1724600819884722

29. Emancipator K, Huang L, Aurora-Garg D, Bal T, Cohen EEW, Harrington K, et al. Comparing programmed death ligand 1 scores for predicting pembrolizumab efficacy in head and neck cancer. *Mod Pathol*. (2021) 34:532–41. doi: 10.1038/s41379-020-00710-9

30. Chen DS, Irving BA, Hodi FS. Molecular pathways: next-generation immunotherapy–inhibiting programmed death-ligand 1 and programmed death-1. *Clin Cancer Res*. (2012) 18:6580–7. doi: 10.1158/1078-0432.CCR-12-1362

31. Topalian SL, Hodi FS, Brahmer JR, Gettinger SN, Smith DC, McDermott DF, et al. Safety, activity, and immune correlates of anti-PD-1 antibody in cancer. *N Engl J Med*. (2012) 366:2443–54. doi: 10.1056/NEJMoa1200690

32. Caldwell C, Johnson CE, Balaji VN, Balaji GA, Hammer RD, Kannan R. Identification and validation of a PD-L1 binding peptide for determination of PDL1 expression in tumors. *Sci Rep*. (2017) 7:13682. doi: 10.1038/s41598-017-10946-2

33. Stöhr M, Wiegand S, Wichmann G, Dietz A. Aktuelle Therapiekonzepte bei Malignen Kopf-Hals-Tumoren. *TumorDiagn u Ther*. (2017) 38:293–6. doi: 10.1055/s-0043-104004

34. Seiwert TY, Burtness B, Mehra R, Weiss J, Berger R, Eder JP, et al. Safety and clinical activity of pembrolizumab for treatment of recurrent or metastatic squamous cell carcinoma of the head and neck (KEYNOTE-012): an open-label, multicentre, phase 1b trial. *Lancet Oncol*. (2016) 17:956–65. doi: 10.1016/S1470-2045(16)30066-3

35. Chow LQM, Haddad R, Gupta S, Mahipal A, Mehra R, Tahara M, et al. Antitumor Activity of Pembrolizumab in Biomarker-Unselected Patients With Recurrent and/or Metastatic Head and Neck Squamous Cell Carcinoma: Results From the Phase Ib KEYNOTE-012 Expansion Cohort. *J Clin Oncol*. (2016) 34:3838–45. doi: 10.1200/JCO.2016.68.1478

36. Cohen EEW, Soulières D, Le Tourneau C, Dinis J, Licitra L, Ahn M-J, et al. Pembrolizumab versus methotrexate, docetaxel, or cetuximab for recurrent or metastatic head-and-neck squamous cell carcinoma (KEYNOTE-040): a randomised, open-label, phase 3 study. *Lancet*. (2019) 393:156–67. doi: 10.1016/S0140-6736(18)31999-8

37. Bauml J, Seiwert TY, Pfister DG, Worden F, Liu SV, Gilbert J, et al. Pembrolizumab for platinum- and cetuximab-refractory head and neck cancer: results from a single-arm, phase II study. *J Clin Oncol*. (2017) 35:1542–9. doi: 10.1200/JCO.2016.70.1524

38. Mehra R, Seiwert TY, Gupta S, Weiss J, Gluck I, Eder JP, et al. Efficacy and safety of pembrolizumab in recurrent/metastatic head and neck squamous cell carcinoma: pooled analyses after long-term follow-up in KEYNOTE-012. *Br J Cancer*. (2018) 119:153–9. doi: 10.1038/s41416-018-0131-9

39. Ilie M, Hofman V, Dietel M, Soria J-C, Hofman P. Assessment of the PD-L1 status by immunohistochemistry: challenges and perspectives for therapeutic strategies in lung cancer patients. *Virchows Arch*. (2016) 468:511–25. doi: 10.1007/s00428-016-1910-4

40. Kulangara K, Zhang N, Corigliano E, Guerrero L, Waldroup S, Jaiswal D, et al. Clinical utility of the combined positive score for programmed death ligand-1 expression and the approval of pembrolizumab for treatment of gastric cancer. *Arch Pathol Lab Med*. (2019) 143:330–7. doi: 10.5858/arpa.2018-0043-OA

41. Kim HR, Ha S-J, Hong MH, Heo SJ, Koh YW, Choi EC, et al. PD-L1 expression on immune cells, but not on tumor cells, is a favorable prognostic factor for head and neck cancer patients. *Sci Rep*. (2016) 6:36956. doi: 10.1038/srep36956

42. Forastiere AA, Goepfert H, Maor M, Pajak TF, Weber R, Morrison W, et al. Concurrent chemotherapy and radiotherapy for organ preservation in advanced laryngeal cancer. *N Engl J Med*. (2003) 349:2091–8. doi: 10.1056/NEJMoa031317

43. Rutkowski T, Wygoda A, Składowski K, Hejduk B, Rutkowski R, Kołosza Z, et al. Prognostic role of tumor volume for radiotherapy outcome in patient with T2 laryngeal cancer. *Strahlenther. Onkol*. (2013) 189:861–6. doi: 10.1007/s00066-013-0411-5

44. Wichmann G, Rosolowski M, Krohn K, Kreuz M, Boehm A, Reiche A, et al. The role of HPV RNA transcription, immune response-related gene expression and disruptive TP53 mutations in diagnostic and prognostic profiling of head and neck cancer. *Int J Cancer*. (2015) 137:2846–57. doi: 10.1002/ijc.29649

45. Kostareli E, Hielscher T, Zucknick M, Baboci L, Wichmann G, Holzinger D, et al. Gene promoter methylation signature predicts survival of head and neck squamous cell carcinoma patients. *Epigenetics*. (2016) 11:61–73. doi: 10.1080/15592294.2015.1137414

46. Kostareli E, Holzinger D, Bogatyrova O, Hielscher T, Wichmann G, Keck M, et al. HPV-related methylation signature predicts survival in oropharyngeal squamous cell carcinomas. *J Clin Invest*. (2013) 123:2488–501. doi: 10.1172/JCI67010

47. Semrau S, Haderlein M, Schmidt D, Lell M, Wolf W, Waldfahrer F, et al. Single-cycle induction chemotherapy followed by chemoradiotherapy or surgery in patients with head and neck cancer: what are the best predictors of remission and prognosis? *Cancer*. (2015) 121:1214–22. doi: 10.1002/cncr.29188

48. Wichmann G, Dietz A. Präklinische Modelle zur Etablierung innovativer Therapiestrategien: Ex–vivo–Testung der Chemo– und Immunre sponse von Kopf –Hals–Tumoren. *HNO*. (2016) 64:460–9. doi: 10.1007/s00106-016-0160-8

49. Dietz A, Boehm A, Wichmann G, Niederwieser D, Dietzsch S, Fuchs M. Multimodaler Larynxerhalt: Wege zur besseren Patientenselektion. *HNO*. (2012) 60:19–31. doi: 10.1007/s00106-011-2416-7

50. Raufman J-P. Long. The diagnostic and prognostic role of cytokines in colon cancer. *GICTT*. (2011) 1-27-39. doi: 10.2147/GICTT.S18423

51. Chikkaveeraiah BV, Bhirde AA, Morgan NY, Eden HS, Chen X. Electrochemical immunosensors for detection of cancer protein biomarkers. *ACS Nano*. (2012) 6:6546–61. doi: 10.1021/nn3023969

52. Rusling JF, Kumar CV, Gutkind JS, Patel V. Measurement of biomarker proteins for point-of-care early detection and monitoring of cancer. *Analyst*. (2010) 135:2496–511. doi: 10.1039/C0AN00204F

53. Argiris A, Lee SC, Feinstein T, Thomas S, Branstetter BF, Seethala R, et al. Serum biomarkers as potential predictors of antitumor activity of cetuximab-containing therapy for locally advanced head and neck cancer. *Oral Oncol*. (2011) 47:961–6. doi: 10.1016/j.oraloncology.2011.07.034

54. Siemert J, Wald T, Kolb M, Pettinella I, Böhm U, Pirlich M, et al. Pre-therapeutic VEGF level in plasma is a prognostic bio-marker in head and neck squamous cell carcinoma (HNSCC). *Cancers (Basel)*. (2021) 13(15):3781. doi: 10.3390/cancers13153781

55. Berszin M, Michaelides I, Siemert J, Röhl L, Wellhausen J, Wald T, et al. Cytokine profiles of head and neck squamous cell carcinoma undergoing dual immunotherapy with cetuximab and pembrolizumab identify interferon gamma-induced protein 10 as novel biomarker. *Front Oncol*. (2022) 12:795277. doi: 10.3389/fonc.2022.795277

56. Riedel F, Zaiss I, Herzog D, Götte K, Naim R, Hörmann K. Serum levels of interleukin-6 in patients with primary head and neck squamous cell carcinoma. *Anticancer Res*. (2005) 25:2761–5.

57. Schenk T, Irth H, Marko-Varga G, Edholm LE, Tjaden UR, van der Greef J. Potential of on-line micro-LC immunochemical detection in the bioanalysis of cytokines. *J Pharm Biomed Anal*. (2001) 26:975–85. doi: 10.1016/s0731-7085(01)00464-2

58. Stenken JA, Poschenrieder AJ. Bioanalytical chemistry of cytokines–a review. *Anal Chim Acta*. (2015) 853:95–115. doi: 10.1016/j.aca.2014.10.009

59. Röhl L, Wellhausen J, Berszin M, Krücken I, Zebralla V, Pirlich M, et al. Immune checkpoint blockade induced shifts in cytokine expression patterns in peripheral blood of head and neck cancer patients are linked to outcome. *Front Immunol*. (2023) 14:1237623. doi: 10.3389/fimmu.2023.1237623

60. Dietz A, Boehm A, Horn I-S, Kruber P, Bechmann I, Golusinski W, et al. Assay-based response evaluation in head and neck oncology: requirements for better decision making. *Eur Arch Otorhinolaryngol*. (2010) 267:483–94. doi: 10.1007/s00405-009-1191-5

61. Granzow C, Kopun M, Kröber T. Riboflavin-mediated photosensitization of Vinca alkaloids distorts drug sensitivity assays. *Cancer Res*. (1995) 55:4837–43.

62. Mozet C, Stoehr M, Dimitrova K, Dietz A, Wichmann G. Hedgehog targeting by cyclopamine suppresses head and neck squamous cell carcinoma and enhances chemotherapeutic effects. *Anticancer Res*. (2013) 33:2415–24.

63. Schrader C, Boehm A, Reiche A, Dietz A, Mozet C, Wichmann G. Combined effects of lapatinib and cisplatin on colony formation of head and neck squamous cell carcinoma. *Anticancer Res*. (2012) 32:3191–9.

64. Stoehr M, Mozet C, Boehm A, Aigner A, Dietz A, Wichmann G. Simvastatin suppresses head and neck squamous cell carcinoma ex vivo and enhances the cytostatic effects of chemotherapeutics. *Cancer Chemother Pharmacol*. (2014) 73:827–37. doi: 10.1007/s00280-014-2412-1

65. Gessner K, Wichmann G, Boehm A, Reiche A, Bertolini J, Brus J, et al. Therapeutic options for treatment of Merkel cell carcinoma. *Eur Arch Otorhinolaryngol*. (2011) 268:443–8. doi: 10.1007/s00405-010-1354-4

66. Wichmann G, Dietz A. Pharmakologische Charakterisierung von Kopf-Hals-Tumoren in Ex-vivo-Tests. *HNO*. (2011) 59:866–73. doi: 10.1007/s00106-011-2362-4

67. Liebig H, Günther G, Kolb M, Mozet C, Boehm A, Dietz A, et al. Reduced proliferation and colony formation of head and neck squamous cell carcinoma (HNSCC) after dual targeting of EGFR and hedgehog pathways. *Cancer Chemother Pharmacol*. (2017) 79:411–20. doi: 10.1007/s00280-017-3239-3

68. Benci JL, Xu B, Qiu Y, Wu TJ, Dada H, Twyman-Saint Victor C, et al. Tumor interferon signaling regulates a multigenic resistance program to immune checkpoint blockade. *Cell*. (2016) 167:1540–1554.e12. doi: 10.1016/j.cell.2016.11.022

69. Ogata A, Chauhan D, Teoh G, Treon SP, Urashima M, Schlossman RL, et al. IL-6 triggers cell growth via the Ras-dependent mitogen-activated protein kinase cascade. *J Immunol*. (1997) 159:2212–21. doi: 10.4049/jimmunol.159.5.2212

70. Deshmane SL, Kremlev S, Amini S, Sawaya BE. Monocyte chemoattractant protein-1 (MCP-1): an overview. *J Interferon Cytokine Res*. (2009) 29:313–26. doi: 10.1089/jir.2008.0027

71. Ji W-T, Chen H-R, Lin C-H, Lee J-W, Lee C-C. Monocyte chemotactic protein 1 (MCP-1) modulates pro-survival signaling to promote progression of head and neck squamous cell carcinoma. *PloS One*. (2014) 9(2):e88952. doi: 10.1371/journal.pone.0088952

72. Salcedo R, Ponce ML, Young HA, Wasserman K, Ward JM, Kleinman HK, et al. Human endothelial cells express CCR2 and respond to MCP-1: direct role of MCP-1 in angiogenesis and tumor progression. *Blood*. (2000) 96:34–40. doi: 10.1182/blood.V96.1.34

73. Wichmann G, Körner C, Boehm A, Mozet C, Dietz A. Stimulation by monocyte chemoattractant protein-1 modulates the ex-vivo colony formation by head and neck squamous cell carcinoma cells. *Anticancer Res*. (2015) 35:3917–24.

74. Wang H, Zhang Q, Kong H, Zeng Y, Hao M, Yu T, et al. Monocyte chemotactic protein-1 expression as a prognosic biomarker in patients with solid tumor: a meta analysis. *Int J Clin Exp Pathol*. (2014) 7:3876–86.

75. Cedra S, Wiegand S, Kolb M, Dietz A, Wichmann G. Reduced cytokine release in ex vivo response to cilengitide and cetuximab is a marker for improved survival of head and neck cancer patients. *Cancers (Basel)*. (2017) 9:117. doi: 10.3390/cancers9090117

76. Kubli SP, Berger T, Araujo DV, Siu LL, Mak TW. Beyond immune checkpoint blockade: emerging immunological strategies. *Nat Rev Drug Discovery*. (2021) 20:899–919. doi: 10.1038/s41573-021-00155-y

77. Hao Q, Vadgama JV, Wang P. CCL2/CCR2 signaling in cancer pathogenesis. *Cell Commun Signal*. (2020) 18:82. doi: 10.1186/s12964-020-00589-8

78. Hardy LA, Booth TA, Lau EK, Handel TM, Ali S, Kirby JA. Examination of MCP-1 (CCL2) partitioning and presentation during transendothelial leukocyte migration. *Lab Invest*. (2004) 84:81–90. doi: 10.1038/labinvest.3700007

79. Franklin RA, Liao W, Sarkar A, Kim MV, Bivona MR, Liu K, et al. The cellular and molecular origin of tumor-associated macrophages. *Science*. (2014) 344:921–5. doi: 10.1126/science.1252510

80. Liu Y, Cao X. The origin and function of tumor-associated macrophages. *Cell Mol Immunol*. (2015) 12:1–4. doi: 10.1038/cmi.2014.83

81. Noy R, Pollard JW. Tumor-associated macrophages: from mechanisms to therapy. *Immunity*. (2014) 41:49–61. doi: 10.1016/j.immuni.2014.06.010

82. Qian B-Z, Li J, Zhang H, Kitamura T, Zhang J, Campion LR, et al. CCL2 recruits inflammatory monocytes to facilitate breast-tumour metastasis. *Nature*. (2011) 475:222–5. doi: 10.1038/nature10138

83. Mantovani A, Marchesi F, Malesci A, Laghi L, Allavena P. Tumour-associated macrophages as treatment targets in oncology. *Nat Rev Clin Oncol*. (2017) 14:399–416. doi: 10.1038/nrclinonc.2016.217

84. Lesokhin AM, Hohl TM, Kitano S, Cortez C, Hirschhorn-Cymerman D, Avogadri F, et al. Monocytic CCR2(+) myeloid-derived suppressor cells promote immune escape by limiting activated CD8 T-cell infiltration into the tumor microenvironment. *Cancer Res*. (2012) 72:876–86. doi: 10.1158/0008-5472.CAN-11-1792

85. Li X, Yao W, Yuan Y, Chen P, Li B, Li J, et al. Targeting of tumour-infiltrating macrophages via CCL2/CCR2 signalling as a therapeutic strategy against hepatocellular carcinoma. *Gut*. (2017) 66:157–67. doi: 10.1136/gutjnl-2015-310514

86. Movahedi K, Laoui D, Gysemans C, Baeten M, Stangé G, van den Bossche J, et al. Different tumor microenvironments contain functionally distinct subsets of macrophages derived from Ly6C(high) monocytes. *Cancer Res*. (2010) 70:5728–39. doi: 10.1158/0008-5472.CAN-09-4672

87. Sanford DE, Belt BA, Panni RZ, Mayer A, Deshpande AD, Carpenter D, et al. Inflammatory monocyte mobilization decreases patient survival in pancreatic cancer: a role for targeting the CCL2/CCR2 axis. *Clin Cancer Res*. (2013) 19:3404–15. doi: 10.1158/1078-0432.CCR-13-0525

88. Zaidi MR. The interferon-gamma paradox in cancer. *J Interferon Cytokine Res*. (2019) 39:30–8. doi: 10.1089/jir.2018.0087

89. Algarra I, García-Lora A, Cabrera T, Ruiz-Cabello F, Garrido F. The selection of tumor variants with altered expression of classical and nonclassical MHC class I molecules: implications for tumor immune escape. *Cancer Immunol Immunother*. (2004) 53:904–10. doi: 10.1007/s00262-004-0517-9

90. Bartneck J, Hartmann A-K, Stein L, Arnold-Schild D, Klein M, Stassen M, et al. Tumor-infiltrating CCR2+ inflammatory monocytes counteract specific immunotherapy. *Front Immunol*. (2023) 14:1267866. doi: 10.3389/fimmu.2023.1267866

91. Vaddepally RK, Kharel P, Pandey R, Garje R, Chandra AB. Review of Indications of FDA-Approved Immune Checkpoint Inhibitors per NCCN Guidelines with the Level of Evidence. *Cancers (Basel)*. (2020) 12(3):738. doi: 10.3390/cancers12030738

92. Topalian SL, Taube JM, Anders RA, Pardoll DM. Mechanism-driven biomarkers to guide immune checkpoint blockade in cancer therapy. *Nat Rev Cancer*. (2016) 16:275–87. doi: 10.1038/nrc.2016.36

93. Dietz A, Wichmann G, Kuhnt T, Wiegand S. Organerhalt beim fortgeschrittenen Larynx–/Hypopharynxkarzinom: Erfahrungen aus der DELOS-II-Studie. *HNO*. (2020) 68:648–56. doi: 10.1007/s00106-020-00890-5

Frontiers in Immunology

Explores novel approaches and diagnoses to treat immune disorders.

The official journal of the International Union of Immunological Societies (IUIS) and the most cited in its field, leading the way for research across basic, translational and clinical immunology.

Discover the latest Research Topics

See more →

Frontiers

Avenue du Tribunal-Fédéral 34
1005 Lausanne, Switzerland
frontiersin.org

Contact us

+41 (0)21 510 17 00
frontiersin.org/about/contact